

DOCTORAL THESIS

UNIVERSITÀ DEGLI STUDI DI NAPOLI FEDERICO II

PH.D. COURSE IN INFORMATION TECHNOLOGY  
AND ELECTRICAL ENGINEERING

---

MODELLING AND CONTROL  
TECHNIQUES FOR MULTIPHASE  
ELECTRIC DRIVES:  
A PHASE VARIABLE APPROACH

---

ANDREA CERVONE

PH.D. SCHOOL COORDINATOR  
PROF. DANIELE RICCIO

SUPERVISOR  
PROF. GIANLUCA BRANDO

CO-SUPERVISOR  
DR. OBRAD DORDEVIC

XXXIII PH.D. CYCLE – 2020/2021



# Abstract

Multiphase electric drives are today one of the most relevant research topics for the electrical engineering scientific community, thanks to the many advantages they offer over standard three-phase solutions. The employment of a multiphase machine allows to split the input power over multiple phases, thus reducing the voltage and/or current capabilities of the supplying converter, keeps the capability to generate a rotating magnetic field at the air gap even after fault events, and offers a higher number of degrees of freedom which can be conveniently exploited to optimize some desired system performances. For these reasons, multiphase configurations are considered promising solutions in many areas, ranging from industrial to traction applications, and especially in presence of high power or high-reliability requirements.

However, contrarily to the three-phase counterparts, multiphase drives can assume a wider variety of different configurations, concerning both the electrical machine (e.g., symmetrical/asymmetrical windings disposition, concentrated/distributed windings, etc...) and the overall drive topology (e.g., single-star configuration, multiple-star configuration, open-end windings, etc...). This aspect, together with the higher number of variables of the system, can make their analysis and control more challenging.

This Ph.D. thesis is focused on the mathematical modelling and on the control of multiphase electric drives. The aim of this research is to develop a generalized model-based approach that can be used in multiple configurations and scenarios, requiring minimal reconfigurations to deal with different machine designs and/or different converter topologies, and suitable both in healthy and in faulty operating conditions.

Standard field-oriented approaches for the analysis and control of multiphase drives, directly derived as extensions of the three-phase equivalents, despite being relatively easy and convenient solutions to deal with symmetrical machines, may suffer some hurdles when applied to some asymmetrical configurations, including post-fault layouts. Indeed, in these cases, the definition of a proper vector space decomposition may not be a trivial process, and the resulting model may show additional coupling effects, which need to be properly compensated in the machine control.

To address these issues, a different approach, completely derived in the phase variable domain, is here developed. The method does not require any vector space decomposition or rotational transformation but instead explicitly considers the mathematical properties of the multiphase machine and the effects of the drive topology, which typically introduces some constraints on the system variables. The phase variable domain is a natural reference frame for the analysis of the machine and of the drive, because each variable is directly associated with a physical quantity. In this framework, the machine modelling is derived through the standard tools of electromechanical conversion theory, while the drive topology is modelled through a multiport network analysis. The drive control algorithm is also developed in the phase variable domain. It is based on a torque control strategy, aimed at optimally developing the desired electromagnetic torque considering the available degrees of freedom, on a decoupling algorithm, aimed at neutralizing the mutual interaction effects between the machine

variables, and on a feedback current controller, aimed at tracking the required references.

In this thesis work, the proposed approach is particularized for multiphase permanent magnet synchronous machines and for multiphase synchronous reluctance machines. All the results are obtained through rigorous mathematical derivations, and are supported and validated by both numerical analysis and experimental tests. As proven considering many different configurations and scenarios, the main benefits of the proposed methodology are its generality and flexibility, which make it a viable alternative to standard modelling and control algorithms.

Future studies will develop further analysis and extension to other machine types.

# Contents

ABSTRACT .....	I
CONTENTS .....	III
<b>1 INTRODUCTION .....</b>	<b>1</b>
1.1 Literature review .....	2
1.1.1 Applications.....	2
1.1.2 Machine design .....	3
1.1.3 Converter architectures and drive topologies.....	4
1.1.4 Machine modelling and control .....	5
1.1.5 Converter modulation .....	6
1.1.6 Post-fault operations.....	7
1.2 Research objectives.....	8
1.3 Thesis organization.....	9
1.4 List of publications .....	10
<b>2 ELECTRICAL MACHINE MODEL.....</b>	<b>13</b>
2.1 Electrical and mechanical equations.....	13
2.1.1 Electrical equations.....	13
2.1.2 Mechanical equations .....	14
2.2 Magnetic model .....	15
2.2.1 Electromagnetic energy conservation principle .....	15
2.2.2 Energy density, coenergy density and materials .....	17
2.2.3 Energy and coenergy expressions.....	19
2.2.4 Induced flux linkages expression.....	20
2.2.5 Electromagnetic torque expression .....	21
2.2.6 Induced back-EMFs expression .....	23
2.3 Complete machine model.....	24
2.3.1 Phase variable domain .....	24
2.3.2 Fixed reference frame transformations.....	24
2.3.3 Moving reference frame transformations.....	25
2.4 Summary and remarks.....	26
<b>3 CONVERTER ARCHITECTURES AND MODULATION TECHNIQUES .....</b>	<b>29</b>
3.1 VSI architectures .....	29
3.1.1 Leg architectures.....	30
3.1.2 Multiphase architectures .....	32
3.2 Modulation .....	35
3.2.1 Pulse width modulation principles.....	36
3.2.2 Multiphase modulation techniques .....	38
3.2.3 Multilevel modulation techniques .....	42

---

3.3	Multilevel modulation examples .....	44
3.3.1	Hybrid NPC modulation with voltage balancing .....	44
3.3.2	Multistep MPC modulation with voltage balancing.....	52
3.4	Summary and remarks.....	59
<b>4</b>	<b>ELECTRICAL NETWORK MODEL .....</b>	<b>61</b>
4.1	Equivalent sources representation .....	61
4.2	Unconstrained network model .....	62
4.2.1	Electrical equations.....	64
4.2.2	Examples .....	64
4.3	Constrained network model.....	69
4.3.1	Current constraints formalization.....	70
4.3.2	Augmented network model.....	70
4.3.3	Network internal feedback action.....	72
4.3.4	Full order electrical drive model.....	74
4.3.5	Examples .....	75
4.4	Configuration space modelling.....	85
4.4.1	Configuration space.....	85
4.4.2	Configuration space representation.....	85
4.4.3	Machine equations in the configuration space.....	87
4.4.4	Reduced order electrical drive model.....	88
4.4.5	Examples .....	89
4.4.6	Electromagnetic torque expression in the configuration space.....	93
4.5	Summary and remarks.....	93
<b>5</b>	<b>FIELD ORIENTED CONTROL OF ASYMMETRICAL PMSMs.....</b>	<b>95</b>
5.1	Mathematical model .....	96
5.1.1	Phase variable domain .....	97
5.1.2	Space vector formalism .....	98
5.1.3	Vector space decomposition .....	100
5.1.4	Rotational transformation.....	103
5.1.5	Torque expression in the synchronous domain.....	105
5.1.6	Power losses expression.....	106
5.1.7	Mechanical model.....	107
5.2	Torque control strategy .....	108
5.2.1	Fundamental currents control strategy.....	109
5.2.2	Third harmonic injection strategy .....	110
5.2.3	Multi-harmonic injection strategy .....	112
5.2.4	Maximum torque per ampere strategy.....	114
5.3	Current control.....	116
5.3.1	Current controller for symmetrical configurations .....	116
5.3.2	Current controller for asymmetrical configurations.....	118
5.4	Complete drive control algorithm.....	120
5.5	Application example.....	121
5.5.1	Machine under analysis.....	121
5.5.2	Machine model in the synchronous domain .....	124

---

5.5.3	Power losses weighting matrices.....	127
5.6	Numerical and experimental results.....	128
5.6.1	Fundamental currents control strategy.....	128
5.6.2	Third harmonic injection strategy.....	129
5.6.3	Multi-harmonic injection strategy.....	131
5.6.4	Maximum torque per ampere strategy.....	132
5.6.5	Torque control strategies comparison.....	134
5.6.6	Simulation results.....	136
5.6.7	Experimental results.....	138
5.7	Summary and remarks.....	142
<b>6</b>	<b>DECOUPLED PHASE VARIABLE CONTROL OF PMSMs.....</b>	<b>145</b>
6.1	Mathematical model.....	146
6.1.1	Machine model.....	146
6.1.2	Drive electrical model.....	148
6.1.3	Mechanical model.....	149
6.2	Torque control strategy.....	149
6.2.1	Maximum torque per ampere algorithm.....	149
6.2.2	MTPA solution properties.....	152
6.2.3	Torque sharing strategy.....	153
6.3	Decoupling current control algorithm.....	154
6.3.1	Decoupling algorithm principle.....	155
6.3.2	Decoupling algorithm requirements.....	156
6.3.3	Pseudo-inverse based decoupling algorithm.....	157
6.3.4	Decoupling algorithm in the phase variable domain.....	158
6.4	Decoupled current control algorithm.....	161
6.4.1	Decoupled system transfer function.....	161
6.4.2	Decoupled controller.....	162
6.5	Complete drive control algorithm.....	165
6.6	Experimental setup.....	166
6.6.1	Electrical machine.....	166
6.6.2	Power electronics converter.....	169
6.6.3	Interconnection network.....	170
6.6.4	Controller board and algorithm implementation.....	170
6.6.5	Mechanical load.....	171
6.7	Experimental results.....	172
6.7.1	Single neutral point healthy configuration.....	172
6.7.2	Two neutral points healthy configuration.....	175
6.7.3	Two neutral points with one faulty phase.....	177
6.7.4	Two neutral points with two faulty phases.....	182
6.7.5	Three neutral points with one faulty phase.....	185
6.7.6	Highly asymmetrical configuration.....	188
6.7.7	Real-time post-fault reconfiguration.....	190
6.7.8	Torque sharing scenarios.....	194
6.8	Summary and remarks.....	199

---

<b>7</b>	<b>DECOUPLED PHASE VARIABLE CONTROL OF SYNRRMs</b> .....	<b>201</b>
7.1	Mathematical model.....	201
7.1.1	Machine model.....	201
7.1.2	Drive electrical model.....	203
7.1.3	Mechanical model.....	204
7.2	Torque control Strategy.....	204
7.2.1	MTPA problem formulation.....	204
7.2.2	MTPA problem resolution.....	205
7.2.3	MTPA solution properties.....	207
7.3	Current controller.....	208
7.3.1	Decoupling current control algorithm.....	208
7.3.2	Decoupled current control algorithm.....	209
7.4	Overall drive control algorithm.....	210
7.5	Experimental setup.....	211
7.5.1	Electrical machine.....	211
7.5.2	Power electronics converter.....	215
7.5.3	Interconnection network.....	215
7.5.4	Controller board and algorithm implementation.....	215
7.5.5	Mechanical load.....	216
7.6	Experimental results.....	216
7.6.1	MTPA algorithm validation.....	216
7.6.2	Healthy configuration.....	224
7.6.3	Post-fault configuration with one faulty phase.....	229
7.6.4	Post-fault configuration with two faulty phases.....	233
7.7	Summary and remarks.....	237
<b>8</b>	<b>CONCLUSIONS</b> .....	<b>239</b>
8.1	Summary of the thesis contents.....	239
8.2	Original research contributions.....	242
8.3	Future developments.....	243
<b>9</b>	<b>APPENDIX</b> .....	<b>245</b>
9.1	Additional considerations.....	245
9.1.1	Resonant controllers implementation.....	245
9.1.2	Torquemeter measurement.....	247
9.2	Chapter 2 Proofs.....	250
9.2.1	Power balance equation for an electrical machine.....	250
9.2.2	Orthogonality of conservative and solenoidal fields.....	251
9.2.3	Uniqueness of the MQS solution.....	251
9.2.4	Electromagnetic energy and coenergy properties.....	252
9.2.5	Inductances matrix properties.....	254
9.2.6	Torque expression from the electromagnetic energy.....	254
9.2.7	Fixed reference frame transformation parameters.....	255
9.2.8	Moving reference frame transformation parameters.....	256
9.3	Chapter 3 Proofs.....	258

---

9.3.1	PWM for a two-level VSI leg .....	258
9.3.2	Common-mode voltage limits .....	261
9.4	Chapter 4 Proofs .....	263
9.4.1	Tellegen's theorem (virtual powers conservation) .....	263
9.4.2	Reciprocity properties for two-port networks .....	264
9.4.3	Reciprocity properties for multiport networks .....	266
9.4.4	Auxiliary network voltages expression .....	267
9.4.5	Full order electrical drive model parameters .....	268
9.4.6	Range and null-space relationships .....	269
9.4.7	Left singular vectors properties .....	269
9.4.8	Configuration spaces basis .....	270
9.4.9	Reduced order electrical drive model parameters .....	271
9.5	Chapter 5 Proofs .....	273
9.5.1	Torque expression in the space vector formalism .....	273
9.5.2	Clarke matrices orthogonality for symmetrical machines .....	273
9.5.3	Inductances matrix diagonalization for symmetrical machines .....	276
9.5.4	PM-induced back-EMFs for symmetrical machines .....	278
9.5.5	Power losses weighting matrix properties .....	280
9.5.6	Power losses expression for symmetrical machines .....	281
9.5.7	Optimal third harmonic injection strategy solution .....	282
9.5.8	Optimal multi-harmonic injection strategy solution .....	283
9.5.9	Maximum torque per ampere strategy solution .....	284
9.5.10	Neutral point voltage compensation .....	285
9.6	Chapter 6 Proofs .....	287
9.6.1	MTPA problem resolution .....	287
9.6.2	MTPA weighting matrix and configuration space .....	288
9.6.3	MTPA strategy in the configuration space .....	289
9.6.4	A sufficient condition for the decoupling algorithm application .....	289
9.6.5	Injection voltage general formulation .....	290
9.6.6	Voltage injection properties .....	290
9.6.7	Full order decoupling algorithm formulation .....	291
9.6.8	Decoupled system transfer function .....	291
9.7	Chapter 7 Proofs .....	293
9.7.1	Required RMS current for the torque development .....	293
9.7.2	Optimal MTPA current unit vectors .....	293
9.7.3	RMS current with the optimal MTPA solution .....	294
<b>REFERENCES</b> .....		<b>295</b>
<b>ACKNOWLEDGMENTS</b> .....		<b>309</b>



# 1 Introduction

Human progress has always been strictly related to the availability of machines capable of producing power in an effective and controllable way. Today, the electromechanical conversion plays a key role in many aspects of everyday life, and electric drives are of fundamental relevance for both industrial and traction applications.

Up to the late 1980s, DC electric machines were primarily used for variable-speed drives, especially thanks to the simplicity of their control, while AC machines, despite having many advantages in terms of construction and maintenance, were instead primarily used for fixed-speed operations, because of the intrinsic limitations coming from the power grid supply. However, in the last decades, the huge improvements in the power electronics technology have allowed the production of semiconductor devices with increased efficiency and reduced cost. This aspect, together with the development and diffusion of digital control platforms, has made it possible to feed AC machines with controllable power converters and has led to the genesis of variable-frequency AC drives, which have progressively replaced the traditional DC electric drives in almost all power applications.

The power converter acts as a decoupling interface between the electrical machine and the supplying energy source, which can either be in AC (e.g., the main three-phase grid for industry applications) or in DC (e.g., battery packs for automotive and traction applications). This offers several advantages not only for the variable speed control, but also for the electric drive design. For example, the machines do not necessarily need to be designed for 50 Hz or 60 Hz operations, the winding can be configured to operate with non-sinusoidal voltages and currents, and the number of phases is not limited to three. Under this framework, electric drives employing AC machines with more than three phases are named *multiphase electric drives* (Fig. 1.1).

While the first examples and applications of multiphase drives can be traced back to the 1960s, this technology has witnessed the main progress and developments during the 1990s, especially as a solution for high-power applications. Indeed, one of the main benefits of these configurations is the possibility to *split the machine power into multiple phases*, thus allowing the use of semiconductor devices with limited voltage and/or current ratings. This aspect has made their development of great interests in some specific applications (e.g., ship propulsion, wind turbine generation systems, liquified natural gas production plants, etc...).

However, multiphase configurations also have many other benefits which can be considered of practical interests in many applications. One of these is related to the intrinsic *fault-tolerance* capability. Indeed, given the redundancy coming from both the power electronics converter and the electrical machine, the same drive can operate (although with reduced capabilities) even after the fault of one or more phases, as long as the healthy phases can generate a rotating magnetic flux density field at air gap. For this reason, the employment of multiphase machines is of particular interest in some safety-critical applications, like in the aerospace and aircraft industry, where they are

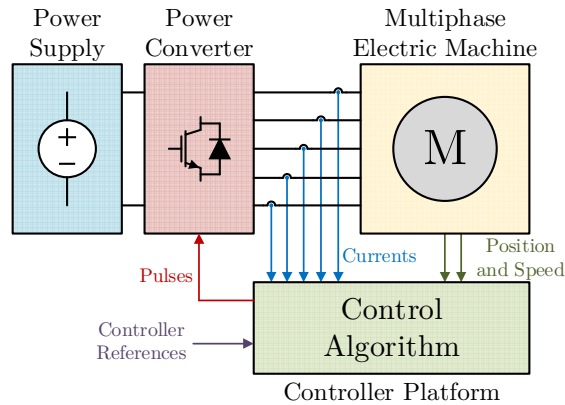


Fig. 1.1 – Schematic representation of a multiphase electric drive.

gaining more and more attention thanks to the concept of a More Electric Aircraft.

Finally, another aspect that is attracting the interests of the scientific community is that the higher number of machine phases offers a higher number of degrees of freedom, which can be exploited for *additional control purposes*. Some examples are the *torque enhancement* through the utilization of multiple spatial harmonics of the air-gap flux-density field, the *independent torque, power or flux control* between multiple machine subsets, and the realization of *multi-motor drives*.

This preliminary chapter, by describing the main research topics and results presented in the technical literature, is aimed at giving some general background regarding the fundamental concepts of multiphase electric drives. It then introduces the main research objectives and provides the structural organization of this Ph.D. thesis.

## 1.1 Literature review

The scientific literature offers many surveys and review papers, which can provide a rich and detailed state of the art on multiphase electrical drives [1]–[8]. This section gives a general overview of the main results regarding different aspects of technical interest.

### 1.1.1 Applications

Multiphase drives are a convenient solution for both high-power and high-reliability systems. Many application areas can benefit from their advantages, including both traction and industry applications.

The *marine applications* are today the most relevant field where multiphase drives are employed, for both the ship propulsion [9]–[17] and for the energy generation onboard [18], [19]. This is especially due to the high installed power that, as previously mentioned, can be more conveniently split among multiple phases.

For the same reason, multiphase drives are successfully being employed also in stationary high-power application areas, like in *wind power generation systems* [20]–[22] or *high power pumps or compressors* [23]–[28], where the installed power ranges from several hundreds of kW to some MW. Another notable application example is for *high-*

*speed elevator systems* [29].

The *aerospace industry* also offers some notable examples of multiphase solutions [30], [31]. The interest is here primarily focused on the fault-tolerant capabilities of these architectures, which have been applied for high-reliability actuators [32]–[38] and for the onboard electrical generation [39], [40]. However, some recent studies have also started investigating these solutions for hybrid aircraft propulsion systems, with the aim to reduce the emissions related to fuel consumptions [31].

Finally, the scientific community is also exploring some possible uses of multiphase drives for *automotive applications* [30]. Some examples regard auxiliary services, like starter/alternators or low-voltage generators [41]–[43]. However, thanks to the increasing interests in Hybrid Electric Vehicles (HEVs), Battery Electric Vehicles (BEVs) and Fuel-Cells (FC) traction systems, in future times multiphase configurations may also represent viable solutions for vehicle traction [44]–[49].

### 1.1.2 Machine design

The different types of designs can be classified in the same categories as for standard three-phase configurations [1]. In other words, a multiphase machine can be designed to be an *induction machine* (IM), an *excited synchronous machine* (ESM) a *permanent magnet synchronous machine* (PMSM, with either *surface-mounted* or *interior-mounted* permanent magnets), a *brushless DC machine* (BLDC), a *synchronous reluctance machine* (SynRM), and so on.

Similarly, each stator phase winding can be realized either with a *distributed* layout or with a *concentrated* layout [1], [3]. The first choice is aimed at producing a sinusoidal magneto-motive force distribution at the air gap, while the second layout allows the generation of non-sinusoidal magnetomotive force distributions with a specific harmonic content. This aspect may be of interest for multiphase configurations because, as also previously mentioned, the higher number of degrees of freedom offered for the machine control can be exploited for torque enhancement purposes by separately controlling multiple spatial harmonic contributions. A special case of concentrated windings design is the *modular* layout, finalized at the minimization of the magnetic, mechanical and thermal influence among different phases, especially for high-reliability applications. A graphical example is depicted in Fig. 1.2.

Contrarily to standard three-phase machines, multiphase configurations may show different winding dispositions along the stator periphery. If the stator windings are uniformly spaced along the stator periphery, the machine has a *symmetrical configuration*, otherwise it has an *asymmetrical configuration*. For a symmetrical  $n$ -phase machine the electrical angle between two consecutive magnetic axes is  $2\pi/n$ . An asymmetrical configuration could, in theory, have an arbitrary angular shift between the magnetic axes. However, most of the asymmetrical configurations examined in the technical literature refer to the case where the  $n$  machine phases can be grouped into  $b$  symmetrical subsets of  $a$  phases each (i.e.,  $n = a \cdot b$ ), and the first phases of two consecutive subsets are shifted by  $\pi/n$ . In this context, machines for which the number of phases  $n$  is a prime number are typically designed with a symmetrical configuration. Conversely, machines for which  $n$  is not a prime number can be designed by either a symmetrical or an asymmetrical winding disposition [1] (as exemplified in Fig. 1.3 for a

nine-phase configuration). A frequently adopted solution is represented by machines designed with multiple symmetrical three-phase subsets, which are also named *multi-three-phase machines* (e.g., dual-three-phase machines).

### 1.1.3 Converter architectures and drive topologies

The supply of a multiphase machine for variable speed operations is normally achieved through a Voltage Source Inverter (VSI). Most of the currently adopted solutions consist of two-level converters. However, the supply of multiphase machines from multilevel converters is currently under development [15], [50]–[53] and has already found some practical uses in high-power applications [15], [25].

Many *drive topologies* can be conceived regarding the electrical connection between the machine and the converter and among the phase windings of the machine itself [7]. A few examples are here provided:

- all the phases can be connected in a star configuration with a single neutral point and supplied by a single inverter unit (single-star configuration),
- the machine phases can be split into different star-connected subsets with multiple isolated neutral points and be supplied either with a common or with multiple independent converter units (multiple-star configuration),
- the phases can be accessed and supplied at both terminals by two independent

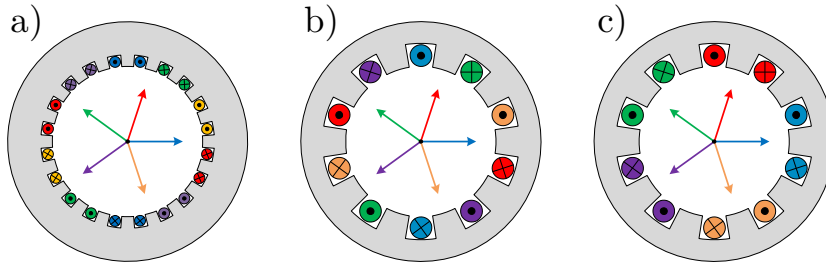


Fig. 1.2 – Different winding designs for a five-phase machine: a) Distributed layout; b) Concentrated layout; c) Modular layout.

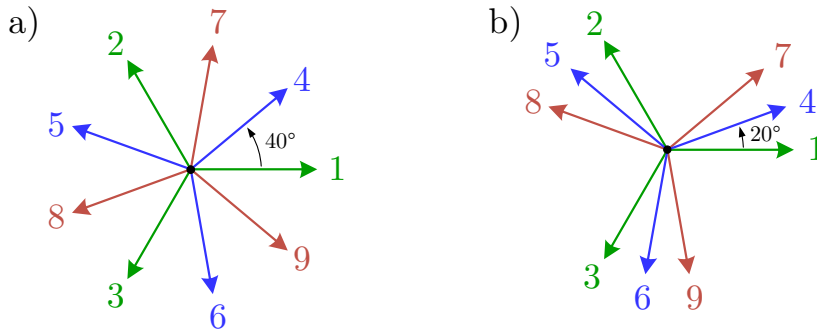


Fig. 1.3 – Different dispositions of the magnetic axes for a nine-phase machine. a) Symmetrical layout; b) Asymmetrical layout.

converters (open-end configuration),

- each phase can be separately supplied by an independent full-bridge converter.

Different topologies can have a different impact on the overall drive control, by introducing some constraints on the machine phase currents and leading to different common-mode voltage injection strategies for the inverter modulation. These aspects will be covered in more detail in Chapter 3 and Chapter 4.

### 1.1.4 Machine modelling and control

The mathematical model of a multiphase machine can be found with the classical tools of electromechanical conversion theory. This approach, which will be analysed and revisited in Chapter 2, results in a set of differential and algebraic equations in the phase variable domain. The mathematical model of the machine is then typically reformulated with some transformations of the phase variables.

Many modelling approaches are based on the *vector space decomposition* (VSD) [1]. The machine variables are combined into a set of space-vector components through the proper definition of a *generalized Clarke's transformation matrix*, which is typically built basing on the magnetic axes disposition of the machine phase windings. For symmetrical configurations, the definition of the transformation matrix is the generalization of the theory of symmetrical components [54] and it leads to the decoupling of the dynamics of all the space vector components of the machine [55]. The definition of a proper transformation matrix for asymmetrical configurations is instead not a trivial process. Many different solutions have been proposed in the technical literature with the aim to give a general solution to this problem but, in general, the dynamic decoupling is not always guaranteed [55]–[58].

For VSD-based modelling approaches, the developed control algorithms are direct extensions of the same approaches adopted for three-phase machines [1], [7].

*Field-oriented control* (FOC) algorithms are today the most commonly adopted approaches for multiphase variable-speed drives. They are based on an additional *rotational transformation* applied to the mathematical model obtained by the VSD. The combined effect of the VSD and rotational transformation is represented by a *generalized Park's transformation matrix*, which projects each space vector in a moving reference frame synchronous with the spatial harmonic components of the magnetic flux density field at the air gap. A set of reference currents is computed from a torque/flux control strategy, and is then controlled either in the stationary or in the synchronous reference frame. In most cases, the reference currents in the synchronous reference frame are constant, and they can be therefore regulated with standard Proportional-Integral (PI) controllers, similarly to the three-phase case. When the reference currents are not constant (e.g., in case the current control is performed in the stationary reference frame, in some asymmetrical configurations, in case of harmonic injections for torque improvements, etc...) the controller is properly modified with additional feedback actions capable of tracking periodic references (e.g., Resonant controllers, multiple Rotating-Integral controllers, Vector Proportional-Integral controllers, etc...) [59]–[63]. Moreover, some other alternative current controllers have also been proposed in the technical literature, like the Model-Predictive Controller (MPC) [64]–[66]. An application of FOC algorithms to asymmetrical PMSMs will be analysed in Chapter 5.

An alternative approach to FOC is represented by the *direct torque control* (DTC) algorithm. It is based on the direct regulation of the electromagnetic torque and of the fundamental component of the stator flux, without relying on inner current control loops [1]–[3], [7]. Its implementation can either rely on optimal switching tables and hysteresis controllers [67]–[71], or on the computation of a set of reference voltages which are then applied through a pulse-width-modulation algorithm [72]. However, the proper definition of optimal switching tables becomes exponentially harder for an increasingly higher number of phases. Additionally, in multiphase configurations, there are generally multiple non-torque and non-flux producing current components, which are not directly limited by standard DTC schemes. Since these current components may assume excessive values and decrease the energetic efficiency of the drive [3], they need to be reduced, for example by properly modifying the definition of the switching tables [70], [73]–[76]. These aspects have strongly limited the spread and extensions of DTC controllers for machines with a high number of phases.

A different modelling method adopted in multiphase configurations is the *multi-stator* approach (MS) [29], [39], [54], [77], [78]. This method is convenient when the machine phases can be grouped in multiple symmetric subsets (e.g., in multi-three-phase configurations), which are analysed and controlled independently from one another. To be more specific, each subset is separately analysed by applying a VSD-based transformation (developed for a reduced number of phases), and is typically controlled in the fundamental synchronous reference frame as in a standard three-phase FOC algorithm. The main benefit of this approach is its intrinsic modularity [54]. Moreover, by independently controlling each subset, it is relatively easy to implement power, torque or flux sharing strategies [79], [80]. However, as a drawback, the resulting model is typically characterized by strong coupling effects between the different subsets [28], [54], [58]. This can severely affect the machine control and may even cause instability [81]. To overcome this issue, some additional decoupling transformations have been proposed in the technical literature [29], [82]–[84].

### 1.1.5 Converter modulation

When the first multiphase drives have been employed, the semiconductor devices technology was still immature, and the voltage source inverters were primarily driven in 180° conduction mode (i.e., six-step mode for three-phase configurations). In that context, multiphase configurations were not only exploited due to their benefits in terms of power segmentation and fault-tolerance, but also to decrease the torque ripple generated by the additional harmonics in the machine supply [1].

Nowadays, given the huge progress in power electronics, the voltage source converters are controlled by means of *pulse width modulation* (PWM) techniques. For two-level architectures, they have been developed with the same approaches as for three-phase converters, and most of them can be classified as *carrier-based* (CBPWM) and the *space-vector* (SVPWM) techniques.

Carrier-based approaches are a direct extension of the analogous techniques developed for single-phase and three-phase systems. They are based on the direct comparison between modulating signals proportional to the voltage references with a common carrier signal. As known, these approaches can use a proper injection of a

common-mode voltage component to extend the linear modulation region of the VSI [50], [85].

Space-vector approaches are instead related to the variable transformations used for the machine modelling (e.g., to the chosen VSD transformation), and are based on the choice of a proper switching pattern between different VSI voltage vectors. However, for multiphase configurations, the selection of a proper set of voltage vectors and of their switching pattern is much more challenging than in three-phase configurations. This is both due to the exponential increase of the overall number of voltage vectors (which, for a two-levels  $n$ -phase converter, are  $2^n$ ) and due to the presence of multiple planes in the transformed coordinates. The technical literature presents many possible approaches to deal with these aspects [86]–[92]. However, it has been proven that most space-vector techniques are completely equivalent to carrier-based algorithms with a proper common-mode voltage injection [50], [88], [93].

Similar considerations can also be applied for multilevel architectures. Again, carrier-based approaches are the easiest and most straightforward implementation [52], [94], while space-vector approaches are strongly affected by the increase of the possible switching states [95], [15], [96], [92], [97], [98]. Again, an equivalence between many space-vector and carrier-based approaches has been proved in the scientific literature [50], [99]–[102]. The redundancy of states in multilevel converters can also be exploited for additional control purposes (e.g., equalization of the DC-bus capacitors voltages, harmonic content optimization, switching losses minimization, etc...) [50], [103]–[105].

These topics will be also discussed in more detail in Chapter 3.

### 1.1.6 Post-fault operations

As previously mentioned, a multiphase machine can operate even after one or more faults, as long as the healthy phases can generate a rotating magnetic field at the air gap. Among the different kinds of faults which can occur in an electric drive, the open-phase fault events are the most analysed in the technical literature [4].

The post-fault operation requires a preliminary diagnosis through a proper detection method [106]–[110] and a subsequent control reconfiguration, which is always accompanied by some performance deratings. Several possible approaches can be implemented according to the specific application.

A possible strategy is to preserve the same electromagnetic torque as in the healthy configuration. This choice can lead to the same mechanical behaviour of the overall drive, but at the expenses of higher currents in the remaining phases [4]. Therefore, assuming the VSI current ratings are not violated, it is a viable option only for short periods because, if prolonged in time, it may increase the thermal stress and reduce the life-span expectations of the drive.

Other more conservative approaches can mitigate this drawback by including some limitations on the phase currents. These limits can be imposed on the maximum current peaks or can be formalized by referring to the stator losses, which are related to the Root Mean Square (RMS) currents [111]–[114]. However, in this case, the electromagnetic torque which can be produced by the machine is reduced with respect to the healthy configuration and, consequently, the mechanical performances of the drive are derated.

The overall impact of a fault on the drive operation and on its performances derating

depends both on the drive topology and on the adopted reconfiguration strategy. For machines designed with multiple independent subsets (e.g., multi-three-phase machines), the easiest fault-tolerant implementation can be achieved by disconnecting the whole subset where the fault has taken place [2], [54], [115]. This approach leads to an easy control reconfiguration and makes the post-fault currents to be equally distributed between the remaining sets, but usually limits the post-fault capabilities more than necessary, since also some healthy phases are penalized by the entire unit disconnection.

Under this perspective, it has been shown that, in most cases, the machine configuration with a single neutral point can achieve better performances [1], [2], [111]. Similar benefits can also be achieved through different kinds of topologies like, for example, the individual supply of each phase winding through a separate full-bridge converter [36], [116], [117].

However, in this case, the post-fault reference currents may show an asymmetrical distribution or additional harmonic components. Therefore, the current controller may also need modifications with respect to the original healthy configuration [4].

## 1.2 Research objectives

This thesis is focused on the modelling and control of multiphase electric drives. In particular, the aim of this research is to develop a generalized model-based approach that can be used in multiple configurations and scenarios. The same approach should apply with minimal reconfigurations to different machine designs (e.g., distributed/concentrated windings layouts, symmetrical/asymmetrical disposition of the phase windings, sinusoidal/non-sinusoidal flux-density field at the air-gap, etc...), to different converter architectures (e.g., single-star, multiple-star with single/multiple DC sources, individual supply of each phase, open-end winding configurations, etc...) and in both healthy and faulty conditions.

The analysis is carried out by first modelling the electric machine and the power converter independently from one another, and then by mathematically formalizing their mutual interaction considering the drive topology. It is shown how different architectures can have a different impact on the electric drive behaviour, by acting as internal feedback actions for its dynamics.

The development of a control algorithm is first examined with a field-oriented approach applied to multiphase PMSMs. Some torque improvement strategies, based on the use of non-sinusoidal currents, are formalized for a generic disposition of the phase windings, and a strong emphasis is given to the main differences between symmetrical and asymmetrical configurations, regarding both the torque and the currents control.

An alternative control strategy is then proposed, and it is first developed for multiphase PMSMs and then extended for multiphase SynRMs. Contrarily to standard approaches, this algorithm is entirely formalized in the phase variable domain, and it explicitly considers the drive architecture. The proposed approach can generalize more easily to different machine configurations and drive topologies, including post-fault operations, and is therefore a viable alternative to standard control algorithms.

The results of this dissertation, obtained through rigorous mathematical derivations, are supported and validated by both numerical analysis and experimental tests.

---

## 1.3 Thesis organization

The thesis is composed of 8 chapters, which can be grouped into two main parts: the first part, which includes Chapter 2, Chapter 3 and Chapter 4, addresses the mathematical modelling of multiphase electric drives, while the second part, which includes Chapter 5, Chapter 6 and Chapter 7, is instead focused on the drive control. A brief overview of the main topics of each chapter is presented as follows.

- Chapter 2 is focused on the *modelling of the electric machine*. The adopted analytical approach is based on the standard theory of electromechanical conversion and, starting from a given set of simplifying assumptions, it derives a generalized mathematical model in the phase variable domain. The main properties of the resulting system are derived and discussed.
- Chapter 3 discusses the main *architectures and modulation strategies for the power electronics converter*. The chapter deals both with two-level and multilevel topologies, and presents some of the different multiphase architectures proposed in the technical literature. A mention and some examples are also provided regarding some pulse-width-modulation strategies.
- Chapter 4 presents a novel modelling approach, based on a *multiport network analysis*, aimed at describing the mutual interactions between the converter and the machine according to the physical configuration of the system. This formalism considerably simplifies the analysis of the same machine under various drive topologies, coming either from different architecture designs or from post-fault reconfigurations. Some of its results are the core of the control algorithm developed in Chapter 6 and Chapter 7.
- Chapter 5 develops a *field-oriented-control* algorithm for *asymmetrical multiphase PMSMs*. This control strategy, which is commonly adopted for symmetrical machines, is particularized for a generic asymmetrical winding configuration, with an arbitrary magnetic axes disposition. The main differences and properties are analysed and discussed. The chapter also presents and compares some *torque enhancement strategies* based on the exploitation of non-sinusoidal currents.
- Chapter 6 presents and discusses a *novel control strategy for multiphase permanent magnet synchronous machines*. The approach is completely derived in the phase variable domain and takes advantage of the results of the modelling approach developed in Chapter 4. It is based on a maximum-torque-per-ampere strategy and on a decoupled current control algorithm, which are both completely general with respect to the machine parameters and winding configuration, and which are also intrinsically suited both in healthy and in faulty operations.
- Chapter 7 shows the *extension of the control strategy* presented in Chapter 6 *to multiphase drives employing synchronous reluctance machines*. It rederives the maximum-torque-per-ampere algorithm basing on the different torque

development mechanism, and discusses the required adaptations for the decoupled current controller.

- Finally, Chapter 8 summarizes the work described in this Ph.D. thesis, and derives the main *conclusions*, emphasising the novel results and contributions, and introducing the main ideas for *future developments*.

All the analysis and results of this dissertation have been addressed and treated with mathematical rigour. However, in order not to overcomplicate the reading, most of the mathematical proofs and derivations, which typically require many analytical computations, have been grouped together and collected in the *Appendix* of Chapter 9. In this way, the reader can proceed more easily with the main thesis chapters, while the mathematical derivations can be explored in a separate reading. The same chapter also includes some other auxiliary technical considerations.

Additionally, a side activity that has been carried out during the Ph.D. is the development of advanced pulse-width-modulation techniques for multilevel converters, aimed at directly addressing the voltage equalization of the DC-bus capacitors. As known, multiphase drives and multilevel converter can benefit from each other, especially in applications that both require high voltage and high reliability (e.g., wind turbine systems, marine transportation, etc...). However, from the mathematical point of view, their control can be analysed separately. For this reason, since a detailed and general analysis of multilevel converters would require much more details, some of the main results related to the developed multilevel converter modulations are briefly presented in Chapter 3.

## 1.4 List of publications

This thesis contains material from the scientific publications listed in the following. Other future technical works, based on still unpublished results shown in this dissertation, are also planned.

### Journal Papers

(Ref. [118]) A. Cervone, O. Dordevic and G. Brando, "General Approach for Modeling and Control of Multiphase PMSM Drives," in *IEEE Transactions on Power Electronics*, vol. 36, no. 9, pp. 10490-10503, Sept. 2021, doi: 10.1109/TPEL.2021.3063791.

(Ref. [119]) A. Cervone, M. Slunjski, E. Levi and G. Brando, "Optimal Third-Harmonic Current Injection for Asymmetrical Multiphase Permanent Magnet Synchronous Machines," in *IEEE Transactions on Industrial Electronics*, vol. 68, no. 4, pp. 2772-2783, April 2021, doi: 10.1109/TIE.2020.2982099.

(Ref. [120]) A. Cervone, G. Brando and O. Dordevic, "Hybrid Modulation Technique With DC-Bus Voltage Control for Multiphase NPC Converters," in *IEEE Transactions on Power Electronics*, vol. 35, no. 12, pp. 13528-13539, Dec. 2020, doi: 10.1109/TPEL.2020.2992226.

---

(Ref. [121]) A. Cervone, G. Brando, O. Dordevic, A. D. Pizzo and S. Meo, "An Adaptive Multistep Balancing Modulation Technique for Multipoint-Clamped Converters," in *IEEE Transactions on Industry Applications*, vol. 56, no. 1, pp. 465-476, Jan.-Feb. 2020, doi: 10.1109/TIA.2019.2949980.

## Conference Papers

(Ref. [122]) A. Cervone, M. Slunjski, E. Levi and G. Brando, "Optimal Multi-Harmonic Current Injection Strategy for an Asymmetrical Nine-Phase PMSM," *2020 International Symposium on Power Electronics, Electrical Drives, Automation and Motion (SPEEDAM)*, Sorrento, Italy, 2020, pp. 787-792, doi: 10.1109/SPEEDAM48782.2020.9161890.

(Ref. [123]) A. Cervone, M. Slunjski, E. Levi and G. Brando, "Optimal Third-Harmonic Current Injection for an Asymmetrical Nine-phase PMSM with Non-Sinusoidal back-EMF," *IECON 2019 - 45th Annual Conference of the IEEE Industrial Electronics Society*, Lisbon, Portugal, 2019, pp. 6223-6228, doi: 10.1109/IECON.2019.8927562.

(Ref. [124]) A. Cervone, G. Brando and O. Dordevic, "A Hybrid Modulation Technique for the DC-Bus Voltage Balancing in a Three-Phase NPC Converter," *IECON 2019 - 45th Annual Conference of the IEEE Industrial Electronics Society*, Lisbon, Portugal, 2019, pp. 3312-3318, doi: 10.1109/IECON.2019.8927047.

(Ref. [125]) G. Brando and A. Cervone, "Novel Balancing Approach for Multilevel Diode Clamped Converters in Medium Voltage Hybrid STATCOM Application," *IECON 2018 - 44th Annual Conference of the IEEE Industrial Electronics Society*, Washington, DC, USA, 2018, pp. 4473-4479, doi: 10.1109/IECON.2018.8592794.

(Ref. [126]) G. Brando, A. Cervone, A. Del Pizzo and S. Meo, "An Adaptive Balancing Modulation for Multilevel Diode Clamped Converters without Common Mode Voltage Injection," *2018 International Symposium on Power Electronics, Electrical Drives, Automation and Motion (SPEEDAM)*, Amalfi, Italy, 2018, pp. 678-684, doi: 10.1109/SPEEDAM.2018.8445262.



# 2 Electrical Machine Model

This chapter is focused on developing a generalized approach for the mathematical modelling of a multiphase electrical machine. As for any physics problem, a good mathematical representation strictly depends on the application where this model is used and, therefore, it is the result of a trade-off between two opposing requirements. The model should be detailed enough to accurately describe the key functional aspects of the system but, at the same time, it should be simple enough to be effectively and adequately used in the application of interests. In other words, different models of the same physical system may be better suited for the design, for the control, for the diagnosis and/or for other purposes.

In what follows, the electrical machine modelling approach, which is based on several simplifying hypothesis and approximations, is derived considering the machine control as the main purpose.

The analysis is conducted as follows. First, Section 2.1 introduces the electrical and mechanical equations of the machine. Section 2.2 describes the machine magnetic behaviour, analysing the properties of the magnetic field inside the machine. The torque and fluxes expressions are then explicitly computed by using the electromagnetic energy conservation principle. Then, Section 2.3 outlines the overall machine model in the phase variable domain, which will be particularized in the next chapters for each specific case study. A brief mention is also given to some reference frame transformations which are typically adopted for the analysis and control of multiphase machines. Finally, Section 2.4 summarizes the main results.

## 2.1 Electrical and mechanical equations

The electrical machine can be considered as an electromechanical energy conversion interface between an electrical network and a mechanical system. Generally, the machine presents  $n$  different current-carrying *phase windings*, connected to the supplying electrical network, and two independent mechanical rigid bodies, named *stator* and *rotor*, in relative motion with one another, and firmly connected to other objects. The schematic model of the machine is depicted in Fig. 2.1.

### 2.1.1 Electrical equations

By using a passive sign convention, for each  $k$ -th machine phase winding (with  $k = 1, \dots, n$ ) it is possible to write the electrical equation:

$$v_k = R_k \cdot i_k + \frac{d\phi_k}{dt} \quad (2.1)$$

which is directly derived from Faraday's law<sup>1</sup>, where:

- $v_k$  denotes the *voltage* between the two terminals of the winding,

---

<sup>1</sup> The plus sign in (2.1) is related to the passive sign convention.

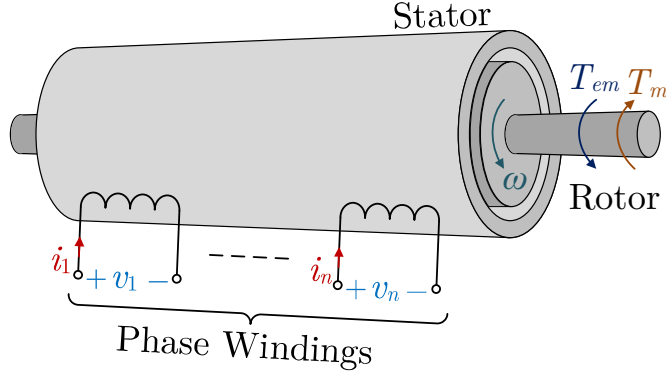


Fig. 2.1 – Schematic model of a rotating electrical machine.

- $i_k$  denotes the *current* flowing into the winding,
- $\phi_k$  denotes the *induced magnetic flux linkage*, and
- $R_k$  denotes the winding *resistance*.

By using a matrix notation, the expression (2.1) can be written as:

$$\mathbf{v} = \mathbf{R} \cdot \mathbf{i} + \frac{d\phi}{dt} \quad (2.2)$$

where:

- $\mathbf{v} = [v_1, \dots, v_n]^T$  is the  $n \times 1$  vector of *windings voltages*,
- $\mathbf{i} = [i_1, \dots, i_n]^T$  is the  $n \times 1$  vector of *windings currents*,
- $\phi = [\phi_1, \dots, \phi_n]^T$  is the  $n \times 1$  vector of *induced flux linkages*, and
- $\mathbf{R}$  is the  $n \times n$  machine *resistances matrix* (which is diagonal and positive definite).

### 2.1.2 Mechanical equations

For a rotating electrical machine, the stator is considered as rigidly connected to a spatial reference frame, while the rotor is in relative motion to it. By using a motoring sign convention, the rotor dynamics is represented by the mechanical equations:

$$\frac{d\theta}{dt} = \omega \quad (2.3)$$

$$J \cdot \frac{d\omega}{dt} + F(\omega) \cdot \omega = T_{em} - T_m \quad (2.4)$$

where:

- $\theta$  is the *rotor position* with respect to a chosen reference (which can vary in the interval  $[0, 2\pi]$ ),
- $\omega$  is the *rotor angular speed*,
- $J$  is the *rotor moment of inertia*,
- $F$  is a mechanical *friction coefficient* (which, generally, can depend on the rotor speed  $\omega$ ),
- $T_{em}$  is the *electromagnetic torque*, generated by the electrical machine by

electromechanical conversion, and

- $T_m$  is the *mechanical braking torque* at the rotor shaft.

## 2.2 Magnetic model

The equations (2.1)-(2.4) are completely general but, by themselves, are unable to describe the electrical machine behaviour, since neither the windings induced flux linkages  $\phi_k$  (with  $k = 1, \dots, n$ ) nor the developed electromagnetic torque  $T_{em}$  have been explicitly linked to the machine internal behaviour. This section derives their expressions in a generalized way by exploiting the energy conservation principle.

### 2.2.1 Electromagnetic energy conservation principle

From the electrical and mechanical equations (2.1)-(2.4), it can be proven that the *electromagnetic energy*  $W_{em}$  of the machine is dynamically governed by the equation<sup>2</sup>:

$$\frac{dW_{em}}{dt} = \mathbf{i}^T \cdot \frac{d\phi}{dt} - T_{em} \cdot \omega = \sum_{k=1}^n i_k \cdot \frac{d\phi_k}{dt} - T_{em} \cdot \frac{d\theta}{dt} \quad (2.5)$$

A first simplifying hypothesis in the machine modelling, which usually is implicitly done, is to consider the electromagnetic energy  $W_{em}$  to be a state function of the system, which only depends on the instantaneous value assumed by the electrical quantities  $i_k$  or  $\phi_k$  and on the instantaneous rotor position  $\theta$ , but which does not depend on their derivatives or their past behaviour [127], [128]. This hypothesis leads to a conservative magnetic model, which neglects the magnetic losses (e.g., the iron losses due to hysteresis and eddy currents)<sup>3</sup>.

Then, assuming the electromagnetic energy  $W_{em}$  to be a function of the induced fluxes  $\phi_k$  (with  $k = 1, \dots, n$ ) and of rotor position  $\theta$ , its time derivative is:

$$\begin{aligned} \frac{dW_{em}}{dt} &= \frac{d}{dt} [W_{em}(\phi_1, \dots, \phi_n, \theta)] = \\ &= \frac{\partial W_{em}}{\partial \phi_1} \cdot \frac{d\phi_1}{dt} + \dots + \frac{\partial W_{em}}{\partial \phi_n} \cdot \frac{d\phi_n}{dt} + \frac{\partial W_{em}}{\partial \theta} \cdot \frac{d\theta}{dt} \end{aligned} \quad (2.6)$$

By comparing (2.5) and (2.6) (which hold for any change of the fluxes and/or the rotor position), it can be concluded that:

$$i_k = \frac{\partial W_{em}}{\partial \phi_k} \quad (\text{with } k = 1, \dots, n) \quad (2.7)$$

<sup>2</sup> Proven in Appendix 9.2.1.

<sup>3</sup> The hysteresis and eddy current losses depend on hysteretic and on dynamical constitution laws for ferromagnetic materials. They could be explicitly introduced in the system model by considering the electromagnetic energy  $W_{em}$  to also have a hysteretic or dynamical functional relationship with respect to the system variables (i.e., currents, fluxes and position). However, this approach usually makes the model much more complex than needed. For this reason, in many cases these effects are either neglected or semi-empirically approximated through additional lumped parameters in the electrical or in the mechanical subsystem model (e.g., with a set of additional resistors).

$$T_{em} = -\frac{\partial W_{em}}{\partial \theta} \quad (2.8)$$

While (2.7) does not give much insight into the machine behaviour (since the aim is to compute the machine flux linkages  $\phi_k$ ), the expression (2.8) allows getting an explicit formulation of the electromagnetic torque  $T_{em}$ , which can be found from the  $\theta$ -derivative of the energy  $W_{em}$ , computed at constant fluxes. Nevertheless,  $W_{em}$  is not generally formalized with respect to the machine fluxes, but it is instead computed in terms of the machine currents, which can be accessed and measured at the phase winding terminals.

A deeper characterization of the machine behaviour can be obtained by introducing the *electromagnetic coenergy*  $W'_{em}$  as<sup>4</sup>:

$$W'_{em} = \mathbf{i}^T \cdot \boldsymbol{\phi} - W_{em} = \sum_{k=1}^n i_k \cdot \phi_k - W_{em} \quad (2.9)$$

Considering (2.5), the time derivative of the coenergy is:

$$\begin{aligned} \frac{dW'_{em}}{dt} &= \frac{d\mathbf{i}^T}{dt} \cdot \boldsymbol{\phi} + \mathbf{i}^T \cdot \frac{d\boldsymbol{\phi}}{dt} - \frac{dW_{em}}{dt} = \\ &= \frac{d\mathbf{i}^T}{dt} \cdot \boldsymbol{\phi} + T_{em} \cdot \frac{d\theta}{dt} = \\ &= \sum_{k=1}^n \phi_k \cdot \frac{di_k}{dt} + T_{em} \cdot \frac{d\theta}{dt} \end{aligned} \quad (2.10)$$

Similarly to the previous case, assuming the electromagnetic coenergy  $W'_{em}$  to be a function of the windings currents  $i_k$  and of rotor position  $\theta$ , its time derivative is also expressed as:

$$\begin{aligned} \frac{dW'_{em}}{dt} &= \frac{d}{dt} [W'_{em}(i_1, \dots, i_n, \theta)] = \\ &= \frac{\partial W'_{em}}{\partial i_1} \cdot \frac{di_1}{dt} + \dots + \frac{\partial W'_{em}}{\partial i_n} \cdot \frac{di_n}{dt} + \frac{\partial W'_{em}}{\partial \theta} \cdot \frac{d\theta}{dt} \end{aligned} \quad (2.11)$$

and by comparing (2.10) and (2.11) (which hold for any change of the currents and/or the rotor position), it can be concluded that:

$$\phi_k = \frac{\partial W'_{em}}{\partial i_k} \quad (\text{with } k = 1, \dots, n) \quad (2.12)$$

$$T_{em} = \frac{\partial W'_{em}}{\partial \theta} \quad (2.13)$$

The expression (2.12) is significantly useful to find an explicit formulation of the flux linkages  $\phi_k$ , each of which is the partial derivative of the coenergy with respect to the corresponding current  $i_k$ . Similarly, (2.13) can be used to find an explicit formulation of the electromagnetic torque  $T_{em}$ , which is the  $\theta$ -derivative of the coenergy  $W'_{em}$ , computed at constant currents.

---

<sup>4</sup> This change of the differential variables in a state function is a *Legendre transformation*, like the analogous transformations adopted in analytical mechanics and in thermodynamics.

### 2.2.2 Energy density, coenergy density and materials

Given the relationships (2.7)-(2.8) and (2.12)-(2.13), the complete characterization of the machine variables can be obtained once the analytic expressions of the electromagnetic energy  $W_{em}$  and of the electromagnetic coenergy  $W'_{em}$  are given.

As known from the theory of electromagnetic fields<sup>5</sup>, the spatial density of the electromagnetic energy in each point of space is:

$$w_{em} = \int \vec{H}(\vec{B}) \cdot d\vec{B} \quad (2.14)$$

where  $\vec{H}$  is the *magnetic field* and  $\vec{B}$  is the *magnetic flux density field*. Similarly, the spatial density of the electromagnetic coenergy is:

$$w'_{em} = \int \vec{B}(\vec{H}) \cdot d\vec{H} \quad (2.15)$$

The two expressions (2.14) and (2.15) depend both on the value of the fields and the constitutive relation of the material at each point of space<sup>6</sup>.

The materials used in an electric machine can be classified as:

- *Dielectric materials*, like the air and the insulating materials: they are mostly a-magnetic and show a proportional relationship between  $\vec{H}$  and  $\vec{B}$  with a relative permeability close to 1,
- *Conductor materials*, like the copper or the aluminium used for the machine windings: they are also almost a-magnetic and show a proportional relationship between  $\vec{H}$  and  $\vec{B}$  with a relative permeability close to 1,
- *Soft ferromagnetic materials*, like the iron used for the stator and rotor cores: they show a hysteretic behaviour between  $\vec{H}$  and  $\vec{B}$ , the coercive magnetic field has reasonably low values (typically  $H_c < 100$  A/m) and the relative permeability around the origin is relatively high (typically  $\mu_{Fe,rel} > 800$ ), and
- *Hard ferromagnetic materials*, like the rare-earth metal alloys (e.g., NdFeB or SmCo) or the hard iron alloys (e.g., AlNiCo) used for permanent magnets: they show a hysteretic behaviour between  $\vec{H}$  and  $\vec{B}$ , the coercive magnetic field is typically high (typically  $H_c > 100$  kA/m) and the local  $(\vec{B}, \vec{H})$  relationship<sup>7</sup> is affine with a relative differential permeability close to 1.

A usual approximation, which is frequently done in electrical machine modelling approaches oriented to control purposes, is to linearize the materials constitutive relations around a rated working point. Then, a constitutive law that can be applied to all the materials is the affine relation:

$$\vec{B} = \mu \vec{H} + \vec{B}_{PM} \quad (2.16)$$

where  $\mu$  identifies the *magnetic permeability* of the material and  $\vec{B}_{PM}$  is a constant

<sup>5</sup> This is a consequence of *Poynting's Theorem* [129].

<sup>6</sup> The expressions (2.14) and (2.15) are given as indefinite integrals because the physical system is only influenced by the change of the energy and coenergy. In other words, any constant offset added to their evaluation would not affect the overall system behaviour.

<sup>7</sup> Far from the bending knees of the hysteresis loop.

permanent magnetization field contribution.

Fig. 2.2 shows a qualitative behaviour of the constitutive relations of the materials and their linearized approximation:

- for dielectric and conductor materials  $\mu \cong \mu_0$  and  $\vec{B}_{PM} = 0$ ,
- for soft ferromagnetic materials  $\mu \cong \mu_{Fe,rel} \cdot \mu_0$  and  $\vec{B}_{PM} = 0$  (i.e., the saturation effects are disregarded), and
- for hard ferromagnetic materials  $\mu \cong \mu_0$  and  $\vec{B}_{PM}$  has the same direction of the permanent magnetization with a non-zero magnitude<sup>8</sup> (i.e., the demagnetization effects are disregarded).

From the constitutive relation (2.16) the integrals (2.14) and (2.15) can be explicitly computed, resulting in:

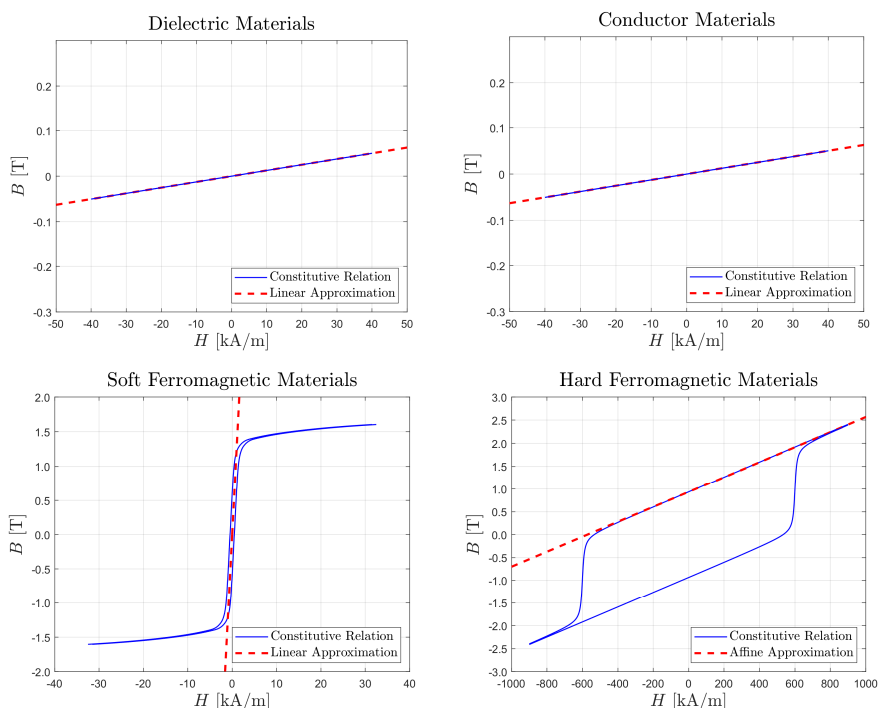


Fig. 2.2 – Qualitative  $(B, H)$  constitutive relations of materials and linearization around a rated working point.

<sup>8</sup> For rare-earth materials (e.g., NdFeB and SmCo), the bending knee of the main hysteresis loop is in the third quadrant of the  $(B, H)$  plane, and the magnitude of  $\vec{B}_{PM}$  is equal to the remanence flux density field of the same characteristic. For ferromagnetic iron alloys (e.g., AlNiCo), the bending knee of the main hysteresis loop is in the second quadrant of the  $(B, H)$  plane, and the linear approximation is to be computed with respect to a *minor hysteresis loop* located inside the main loop. The corresponding magnetic permeability is called *recoil permeability*  $\mu_R$  and the magnitude of  $\vec{B}_{PM}$  is lower than the remanence flux density field. Its value can be computed as  $B_{PM} = \mu_R \cdot H'_c$ , where  $H'_c$  is called *apparent coercivity*, which is typically higher than the real coercive magnetic field of the material [127].

$$w_{em} = \int \vec{H} \cdot d\vec{B} = \int \vec{H} \cdot d(\mu\vec{H} + \vec{B}_{PM}) = \int \mu\vec{H} \cdot d\vec{H} = \frac{1}{2}\mu H^2 \quad (2.17)$$

$$w'_{em} = \int \vec{B} \cdot d\vec{H} = \int \vec{B} \cdot d\left(\frac{\vec{B}}{\mu} - \frac{\vec{B}_{PM}}{\mu}\right) = \int \frac{\vec{B}}{\mu} \cdot d\vec{B} = \frac{1}{2} \frac{B^2}{\mu} \quad (2.18)$$

It is worth emphasizing that, in presence of permanent magnets, the expressions (2.17) and (2.18) for  $w_{em}$  and  $w'_{em}$  are not equivalent, meaning that the electromagnetic energy and coenergy are not equal.

### 2.2.3 Energy and coenergy expressions

The overall electromagnetic energy  $W_{em}$  and coenergy  $W'_{em}$  are found by integrating their density  $w_{em}$  and  $w'_{em}$ , expressed by (2.17) and (2.18) over the whole volume  $\mathfrak{D}$  of the electrical machine:

$$W_{em} = \iiint_{\mathfrak{D}} w_{em} \, dV = \iiint_{\mathfrak{D}} \frac{1}{2} \mu H^2 \, dV \quad (2.19)$$

$$W'_{em} = \iiint_{\mathfrak{D}} w'_{em} \, dV = \iiint_{\mathfrak{D}} \frac{1}{2} \frac{B^2}{\mu} \, dV \quad (2.20)$$

The last step to find a general expression for the electromagnetic energy and coenergy is to compute the magnetic field  $\vec{H}$  and the magnetic flux density field  $\vec{B}$  as a function of the rotor position  $\theta$  and the phase currents  $i_k$  (with  $k = 1, \dots, n$ ). For each rotor position  $\theta$ , the magnetic behaviour of the machine is governed by the *magnetoquasistatic* (MQS) model<sup>9</sup>, which is based on the *Gauss's* and *Ampère's equations*:

$$\begin{cases} \oint_{S_\tau} \vec{B} \cdot \hat{n} \, dS = 0 \\ \oint_{\gamma} \vec{H} \cdot \hat{t} \, dl = \iint_{S_\gamma} \vec{J}_f \cdot \hat{n} \, dS \end{cases} \quad (2.21)$$

where  $\vec{J}_f$  is the *current density field*. In a machine with  $n$  windings,  $\vec{J}_f$  is a linear combination of the phase currents  $i_k$  (with  $k = 1, \dots, n$ ):

$$\vec{J}_f = \sum_{k=1}^n i_k \cdot \vec{J}_{f,k} \quad (2.22)$$

where each  $\vec{J}_{f,k}$  (with  $k = 1, \dots, n$ ) is a known solenoidal vector field being non-zero only in the physical region occupied by the  $k$ -th winding<sup>10</sup>.

A convenient choice for the boundary conditions in the MQS problem for an electrical machine is to consider:

<sup>9</sup> In the MQS model the magnetic fields  $\vec{H}$  and  $\vec{B}$  are computed by solving a magnetostatic problem (as if the system were “frozen” in time), but are then updated dynamically to find the induced back-EMFs through Faraday's law [129].

<sup>10</sup> The MQS model does not consider charge accumulations phenomena inside the machine, meaning that the current density field  $\vec{J}$  (and all the normalized contributions  $\vec{J}_{f,k}$ ) must be solenoidal to respect the electric charge conservation principle [129].

$$\vec{B} \cdot \hat{n} = 0 \quad \text{on } \partial\mathfrak{D} \quad (2.23)$$

where  $\mathfrak{D}$  is the domain occupied by the machine and  $\partial\mathfrak{D}$  its boundary<sup>11</sup>.

The system of equations (2.21), (2.22) and (2.23), together with the constitutive relation (2.16), is linear and has a unique solution<sup>12</sup> which can be expressed as the linear combination:

$$\vec{H} = \vec{H}^{(0)} + \sum_{k=1}^n \vec{h}^{(k)} \cdot i_k \quad \text{and} \quad \vec{B} = \vec{B}^{(0)} + \sum_{k=1}^n \vec{b}^{(k)} \cdot i_k \quad (2.24)$$

where  $(\vec{H}^{(0)}, \vec{B}^{(0)})$  are the fields due to the sole permanent magnets contribution (i.e., when all the currents are zero), while  $(\vec{h}^{(k)}, \vec{b}^{(k)})$  are the fields driven by the sole  $k$ -th phase current contribution (i.e., when  $i_k = 1$  A and  $i_h = 0$  for  $h \neq k$ ) with the permanent magnets fully demagnetized (i.e.,  $\vec{B}_{PM} = 0$  in (2.16)).

Since the fields  $\vec{H}$  and  $\vec{B}$  in (2.24) are linearly dependent on the machine currents, the overall machine energy  $W_{em}$  and coenergy  $W'_{em}$ , which depend on the square magnitude of the fields, are quadratic functions of the machine currents. They can be therefore expressed as:

$$W_{em} = W_{em}^{(0)} + \sum_{k=1}^n W_{em,k}^{(1)} \cdot i_k + \sum_{k_1=1}^n \sum_{k_2=1}^n W_{em,k_1,k_2}^{(2)} \cdot i_{k_1} \cdot i_{k_2} \quad (2.25)$$

$$W'_{em} = W'_{em}{}^{(0)} + \sum_{k=1}^n W'_{em,k}{}^{(1)} \cdot i_k + \sum_{k_1=1}^n \sum_{k_2=1}^n W'_{em,k_1,k_2}{}^{(2)} \cdot i_{k_1} \cdot i_{k_2} \quad (2.26)$$

where the superscript <sup>(0)</sup> has been used to denote the terms independent from the currents, the superscript <sup>(1)</sup> has been used to denote the terms varying linearly with the currents, and the superscript <sup>(2)</sup> has been used to denote the terms varying quadratically with the currents. The coefficients defined in (2.25) and (2.26) are reported in equation (9.8) of Appendix 9.2.4. They are all periodic functions of the rotor position  $\theta$  and satisfy the following properties<sup>13</sup>:

$$\begin{aligned} W_{em}^{(0)} + W'_{em}{}^{(0)} &= \iiint_{\mathfrak{D}} \frac{1}{2} \frac{B_{PM}^2}{\mu} \, dV, & W'_{em,k}{}^{(1)} &= 0, \\ W_{em,k_1,k_2}^{(2)} &= W_{em,k_2,k_1}^{(2)} = W'_{em,k_1,k_2}{}^{(2)} = W'_{em,k_2,k_1}{}^{(2)} \end{aligned} \quad (2.27)$$

## 2.2.4 Induced flux linkages expression

From the coenergy expression (2.26) it is possible to compute the fluxes induced in the machine windings by applying (2.12). By recalling that the coenergy coefficients are periodic functions of the rotor position  $\theta$ , each induced flux linkage can be expressed as:

<sup>11</sup> This boundary condition corresponds to neglecting all the magnetic fields outside the external surface of the machine, and to considering all the magnetic phenomena to only happening inside it. Other boundary conditions can be also considered, leading to similar results.

<sup>12</sup> Proven in Appendix 9.2.3 basing on the results of Appendix 9.2.2.

<sup>13</sup> Proven in Appendix 9.2.4.

$$\begin{aligned}
\phi_{k_1} &= \frac{\partial W'_{em}}{\partial i_{k_1}} = W'_{em,k_1} + \sum_{k_2=1}^n 2 W'_{em,k_1,k_2} \cdot i_{k_2} = \\
&= \psi_{PM,k_1}(\theta) + \sum_{k_2=1}^n L_{k_1,k_2}(\theta) \cdot i_{k_2}
\end{aligned} \tag{2.28}$$

with  $\psi_{PM,k} = W'_{em,k}$  and  $L_{k_1,k_2} = 2 W'_{em,k_1,k_2}$ .

By grouping all the  $n$  machine phases and using a matrix notation, the induced flux linkages can be expressed as:

$$\boldsymbol{\phi} = \boldsymbol{\psi}_{PM}(\theta) + \mathbf{L}(\theta) \cdot \mathbf{i} \tag{2.29}$$

where  $\boldsymbol{\psi}_{PM}(\theta)$  is the  $n \times 1$  vector of *flux linkages induced by the permanent magnets* and  $\mathbf{L}(\theta)$  is the  $n \times n$  *inductances matrix* of the machine. Both  $\boldsymbol{\psi}_{PM}$  and  $\mathbf{L}$  are periodic in  $\theta$ . Their fundamental period defines the *pole pairs periodicity* of the machine and depends on its internal design.

It can be proven that the inductances matrix  $\mathbf{L}(\theta)$  is symmetric and positive definite<sup>14</sup>. Then, it is invertible and its inverse  $\boldsymbol{\Gamma}(\theta) = \mathbf{L}^{-1}(\theta)$ , named *reluctances matrix*, is also a  $n \times n$  symmetric and positive definite matrix periodically varying with the rotor position  $\theta$ . The machine currents can be therefore univocally identified by the machine flux linkages as:

$$\mathbf{i} = \boldsymbol{\Gamma}(\theta) \cdot [\boldsymbol{\phi} - \boldsymbol{\psi}_{PM}(\theta)] \tag{2.30}$$

Given these positions, the energy and coenergy expressions (2.25) and (2.26) can be rewritten in a matrix notation as:

$$W_{em} = W_{em}^{(0)}(\theta) + \frac{1}{2} \mathbf{i}^T \cdot \mathbf{L}(\theta) \cdot \mathbf{i} \tag{2.31}$$

$$W'_{em} = W'_{em}{}^{(0)}(\theta) + \boldsymbol{\psi}_{PM}^T(\theta) \cdot \mathbf{i} + \frac{1}{2} \mathbf{i}^T \cdot \mathbf{L}(\theta) \cdot \mathbf{i} \tag{2.32}$$

### 2.2.5 Electromagnetic torque expression

From the coenergy expression (2.26), which has been rewritten as (2.32), the electromagnetic torque developed by the machine can be computed by applying (2.13):

$$\begin{aligned}
T_{em} &= \frac{\partial W'_{em}}{\partial \theta} = \frac{\partial W'_{em}{}^{(0)}}{\partial \theta} + \left( \frac{\partial \boldsymbol{\psi}_{PM}}{\partial \theta} \right)^T \cdot \mathbf{i} + \frac{1}{2} \mathbf{i}^T \cdot \frac{\partial \mathbf{L}}{\partial \theta} \cdot \mathbf{i} = \\
&= T_0(\theta) + \mathbf{f}_{PM}^T(\theta) \cdot \mathbf{i} + \frac{1}{2} \mathbf{i}^T \cdot \mathbf{L}'(\theta) \cdot \mathbf{i}
\end{aligned} \tag{2.33}$$

with  $T_0(\theta) = \partial W'_{em}{}^{(0)} / \partial \theta$ ,  $\mathbf{f}_{PM}(\theta) = \partial \boldsymbol{\psi}_{PM} / \partial \theta$  and  $\mathbf{L}'(\theta) = \partial \mathbf{L} / \partial \theta$ . It can be proven that the same expression (2.33) can be also obtained by applying (2.8) to the electromagnetic energy expression (2.31)<sup>15</sup>.

<sup>14</sup> Proven in Appendix 9.2.5.

<sup>15</sup> Proven in Appendix 9.2.6.

The electromagnetic torque computed as per (2.33) is given by the superposition of three contributions:

- the term  $T_0(\theta)$ , which is unaffected by the currents and only depends on the field generated by the permanent magnets,
- the term  $\mathbf{f}_{PM}^T(\theta) \cdot \mathbf{i}$ , which is linearly varying with the currents and depends on their interaction with the permanent magnets,
- the term  $(\mathbf{i}^T \cdot \mathbf{L}'(\theta) \cdot \mathbf{i})/2$ , which is quadratically varying with the currents and is independent of the permanent magnets.

The torque contributions can be also classified according to the different stator/rotor interactions. Indeed, the magnetic fields in the machine can be generated or modified from current sources, reluctance variations or permanent magnets. Then, as schematically exemplified in Fig. 2.3, different electromagnetic torque producing mechanisms can be identified:

- *Currents/Currents interaction* (Fig. 2.3.a): it is related to the quadratic term  $(\mathbf{i}^T \cdot \mathbf{L}'(\theta) \cdot \mathbf{i})/2$ . It manifests, for example, in induction machines from the interaction between the currents in the stator windings and the currents in the rotor windings (in case of a wound rotor) or bars (in case of a squirrel cage rotor). It also manifests in excited synchronous machines from the interaction between the currents in the stator windings and the excitation current in the field winding on the rotor.
- *Currents/Reluctance interaction* (Fig. 2.3.b and Fig. 2.3.d): it is related to the quadratic term  $(\mathbf{i}^T \cdot \mathbf{L}'(\theta) \cdot \mathbf{i})/2$ . It manifests, for example, in synchronous reluctance machines because of the flux barriers on the rotor or in excited synchronous machines in case of a rotor with salient poles.
- *Currents/Magnets interaction* (Fig. 2.3.c and Fig. 2.3.g): it is related to the linear term  $\mathbf{f}_{PM}^T(\theta) \cdot \mathbf{i}$ . It manifests, for example, in permanent magnets synchronous machines or brushless DC machines from the interaction of the stator currents and the rotor magnets.
- *Magnets/Reluctance interaction* (Fig. 2.3.f and Fig. 2.3.h): it is related to the uncontrollable term  $T_0(\theta)$ . Usually this is not a desired effect for the machine design. It is the origin of the cogging torque existing in machines with permanent magnets on the rotor due to the interaction with the stator cages.
- *Magnets/Magnets interaction* (Fig. 2.3.i): it is related to the currents independent term  $T_0(\theta)$ . Since it is uncommon for electrical machines to have permanent magnets both on the stator and on the rotor, this term is seldom observed.
- *Reluctance/Reluctance interaction* (Fig. 2.3.e): theoretically, this interaction does not produce any torque, because there would not be magnetic field sources inside the machine. However, due to the remanence field which also exists in soft ferromagnetic materials (and which in the linearized model is neglected), this interaction can be sensed as coming from the interaction between the stator and rotor cages. It behaves similarly to a magnets/reluctance or a magnets/magnets interaction, thus producing a current independent torque contribution like  $T_0(\theta)$ .

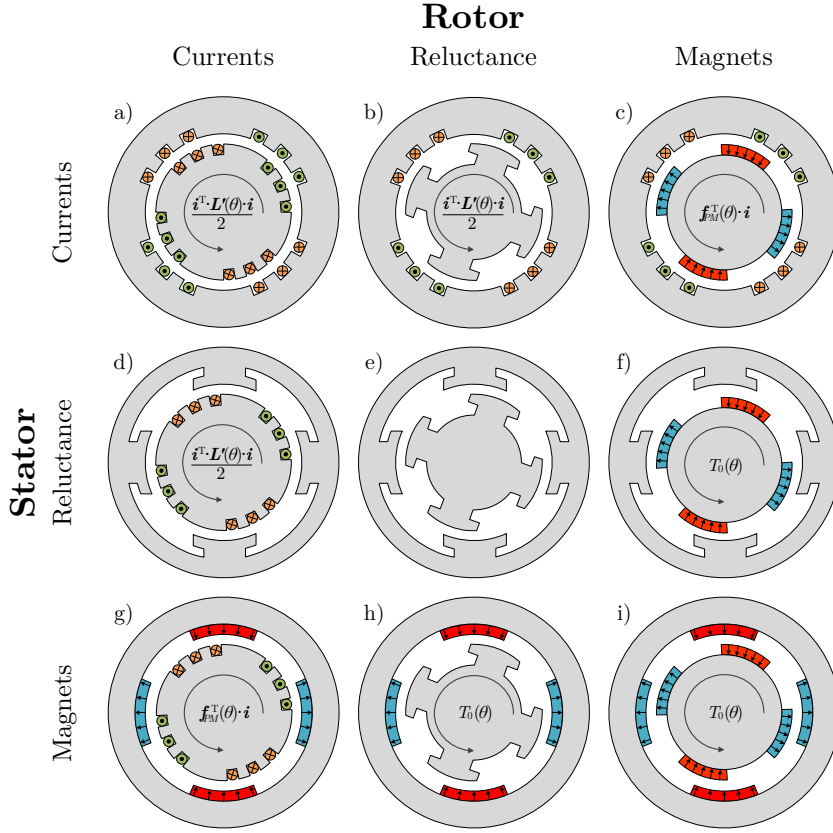


Fig. 2.3 – Electromagnetic torque development mechanisms.

### 2.2.6 Induced back-EMFs expression

For each  $k$ -th machine winding (with  $k = 1, \dots, n$ ), the induced *electromotive force* (EMF) is defined as  $e_{EMF} = -d\phi_k/dt$ . The opposite voltage  $e_{CEMF} = +d\phi_k/dt$  is named *counter-electromotive force* (cEMF) or, more frequently, *back-EMF*.

The explicit expression of the induced back-EMFs in the machine windings can be found by computing the time derivative of the fluxes (2.29), resulting in:

$$\begin{aligned}
 e_{CEMF} &= \frac{d\phi}{dt} = \frac{d\psi_{PM}}{dt} + \frac{d\mathbf{L}}{dt} \cdot \mathbf{i} + \mathbf{L}(\theta) \cdot \frac{d\mathbf{i}}{dt} = \\
 &= \frac{\partial\psi_{PM}}{\partial\theta} \cdot \frac{d\theta}{dt} + \frac{\partial\mathbf{L}}{\partial\theta} \cdot \frac{d\theta}{dt} \cdot \mathbf{i} + \mathbf{L}(\theta) \cdot \frac{d\mathbf{i}}{dt} = \\
 &= \omega \mathbf{f}_{PM}(\theta) + \omega \mathbf{L}'(\theta) \cdot \mathbf{i} + \mathbf{L}(\theta) \cdot \frac{d\mathbf{i}}{dt}
 \end{aligned} \tag{2.34}$$

where, again,  $\mathbf{f}_{PM}(\theta) = \partial\psi_{PM}/\partial\theta$  and  $\mathbf{L}'(\theta) = \partial\mathbf{L}/\partial\theta$ .

It can be seen that the induced back-EMFs are given by three terms:

- the *permanent magnets motional-induced back-EMFs* contribution  $\omega \mathbf{f}_{PM}(\theta)$ , which is proportional to the rotor speed  $\omega$  and is independent of the machine currents  $\mathbf{i}$ ,
- the *phase currents motional-induced back-EMFs* contribution  $\omega \mathbf{L}'(\theta) \cdot \mathbf{i}$ , which is proportional to both the rotor speed  $\omega$  and the machine currents  $\mathbf{i}$ ,
- the *phase currents transformer-induced back-EMFs* contribution  $\mathbf{L}(\theta) \cdot (d\mathbf{i}/dt)$ , which is unaffected by the machine speed  $\omega$  and is proportional to the time derivative of the machine currents  $d\mathbf{i}/dt$ .

## 2.3 Complete machine model

This section formalizes the overall machine model in the phase variable domain and gives a quick overview of some of the variable transformations normally used in standard analysis and control algorithms. Some examples of these reference frame transformations will be provided and analysed in more detail in Chapter 5.

### 2.3.1 Phase variable domain

By focusing on the electrical equations (2.2), with the induced back-EMFs expressed as per (2.34), and on the electromagnetic torque expression (2.33), the overall machine model is given by:

$$\begin{aligned} \mathbf{L}(\theta) \cdot \frac{d\mathbf{i}}{dt} + \mathbf{R} \cdot \mathbf{i} + \mathbf{e} &= \mathbf{v} \\ T_{em} &= T_0(\theta) + \mathbf{f}_{PM}^T(\theta) \cdot \mathbf{i} + \frac{1}{2} \mathbf{i}^T \cdot \mathbf{L}'(\theta) \cdot \mathbf{i} \end{aligned} \quad (2.35)$$

with  $\mathbf{e} = \omega \mathbf{f}_{PM}(\theta) + \omega \mathbf{L}'(\theta) \cdot \mathbf{i}$  representing the overall *motional-induced back-EMFs*.

The set of equations (2.35) represents a dynamic model of order  $n$ , in which the state variables are the machine phase currents  $\mathbf{i}$ , the input variables are the machine voltages  $\mathbf{v}$  and the output variable of interests is the electromagnetic torque  $T_{em}$ . Under the simplifying assumptions made in Section 2.2, this model can be applied to any kind of machine, being it with symmetrical or asymmetrical magnetic axes disposition, concentrated or distributed windings, equal or different number of turns, sinusoidal or non-sinusoidal magnetic field at the air-gap, and so on.

### 2.3.2 Fixed reference frame transformations

Considering any  $n \times n$  invertible transformation matrix  $\mathbf{T}$ , here supposed to be time-invariant, the phase variable model (2.35) can be formulated in a different reference frame by imposing the relationships:

$$\tilde{\mathbf{x}} = \mathbf{T} \cdot \mathbf{x} \quad \Leftrightarrow \quad \mathbf{x} = \mathbf{T}^{-1} \cdot \tilde{\mathbf{x}} \quad (2.36)$$

for any  $n \times 1$  vector  $\mathbf{x}$  of (2.35)<sup>16</sup>. The general expression of the transformed model is:

<sup>16</sup> In general, it is also possible to use different transformation matrices for the different sets of variables (e.g., a transformation matrix  $\mathbf{T}_i$  for the currents and a different transformation matrix  $\mathbf{T}_v$  for the voltages). Similar results and conclusions would apply.

$$\begin{aligned}
\tilde{\mathbf{L}}(\theta) \cdot \frac{d\tilde{\mathbf{i}}}{dt} + \tilde{\mathbf{R}} \cdot \tilde{\mathbf{i}} + \tilde{\mathbf{e}} &= \tilde{\mathbf{v}} \\
\tilde{\mathbf{e}} &= \omega \tilde{\mathbf{f}}_{PM}(\theta) + \omega \tilde{\mathbf{L}}'_E(\theta) \cdot \tilde{\mathbf{i}} \\
T_{em} &= T_0(\theta) + \tilde{\mathbf{f}}_{PM}^T(\theta) \cdot \tilde{\mathbf{Y}} \cdot \tilde{\mathbf{i}} + \frac{1}{2} \tilde{\mathbf{i}}^T \cdot \tilde{\mathbf{L}}'_T(\theta) \cdot \tilde{\mathbf{i}}
\end{aligned} \tag{2.37}$$

whose parameters are reported in equation (9.10) of Appendix 9.2.7.

The transformed model (2.37) is significantly simplified if the transformation matrix  $\mathbf{T}$  is unitary. Indeed, in such a case,  $\mathbf{T}^{-1} = \mathbf{T}^T$  and, from (9.10) it can be verified that:

- $\tilde{\mathbf{Y}} = \mathbf{I}$ ,
- $\tilde{\mathbf{L}}(\theta)$  is symmetric and positive definite,
- $\tilde{\mathbf{L}}'_E(\theta) = \tilde{\mathbf{L}}'_T(\theta) = \partial\tilde{\mathbf{L}}/\partial\theta$  is symmetric,
- $\tilde{\mathbf{R}}$  is symmetric and positive definite.

In these conditions, the transformed model (2.37) has the same form as the model in the phase variable domain (2.35) and can be interpreted as being related to an equivalent machine with different parameters.

This kind of transformation is typically done in the standard multiphase machines analysis with the *vector space decomposition* (VSD) [1], [2], [55]. In this case, the adopted transformation is typically denoted as:

$$\mathbf{x}_{\text{VSD}} = \mathbf{C} \cdot \mathbf{x} \iff \mathbf{x} = \mathbf{C}^{-1} \cdot \mathbf{x}_{\text{VSD}} \tag{2.38}$$

The matrix  $\mathbf{C}$  is named *generalized Clarke's transformation matrix*, and depends on the magnetic axes disposition of the machine phase windings. For machines with both stator and rotor windings (e.g., induction machines), the transformation (2.38) is separately applied to the  $n_s$  stator and to the  $n_r$  rotor phases. Similarly, in *multi-stator* approaches (MS), the reference frame transformation (2.38) is also separately applied to each symmetrical subset of the machine phase windings [29], [39], [54], [77], [78].

### 2.3.3 Moving reference frame transformations

In many cases, the adopted transformation matrix is not constant, but it is time-varying. Usually, the time dependence is defined through a *rotational angle*  $\vartheta$ . The transformation is therefore referred to a moving reference frame and the positions (2.36) are rewritten as:

$$\tilde{\mathbf{x}} = \mathbf{T}(\vartheta) \cdot \mathbf{x} \iff \mathbf{x} = \mathbf{T}^{-1}(\vartheta) \cdot \tilde{\mathbf{x}} \tag{2.39}$$

In this case, the general formulation of the transformed model (2.37) is modified to:

$$\begin{aligned}
\tilde{\mathbf{L}}(\theta, \vartheta) \cdot \frac{d\tilde{\mathbf{i}}}{dt} + \tilde{\mathbf{R}}(\vartheta) \cdot \tilde{\mathbf{i}} + \tilde{\mathbf{e}} &= \tilde{\mathbf{v}} \\
\tilde{\mathbf{e}} &= \omega \tilde{\mathbf{f}}_{PM}(\theta, \vartheta) + \omega \tilde{\mathbf{L}}'_{E1}(\theta, \vartheta) \cdot \tilde{\mathbf{i}} + \Omega \tilde{\mathbf{L}}'_{E2}(\theta, \vartheta) \cdot \tilde{\mathbf{i}} \\
T_{em} &= T_0(\theta) + \tilde{\mathbf{f}}_{PM}^T(\theta, \vartheta) \cdot \tilde{\mathbf{Y}}(\vartheta) \cdot \tilde{\mathbf{i}} + \frac{1}{2} \tilde{\mathbf{i}}^T \cdot \tilde{\mathbf{L}}'_T(\theta, \vartheta) \cdot \tilde{\mathbf{i}}
\end{aligned} \tag{2.40}$$

with  $\Omega = d\vartheta/dt$  denoting the angular speed of the moving reference frame. The transformed parameters, many of which depend both on the rotor angle  $\theta$  and on the moving reference frame angle  $\vartheta$  (which, in general, can be different from each other), are

reported in equation (9.11) of Appendix 9.2.8.

Again, the model is simplified when the transformation matrix  $\mathbf{T}(\vartheta)$  is unitary, because  $\mathbf{T}^{-1}(\vartheta) = \mathbf{T}^T(\vartheta)$ . Then, by considering the parameters defined in (9.11) it can be verified that:

- $\tilde{\mathbf{Y}}(\vartheta) = \mathbf{I}$ ,
- $\tilde{\mathbf{L}}(\theta, \vartheta)$  is symmetric and positive definite,
- $\tilde{\mathbf{L}}'_{E1}(\theta, \vartheta) = \tilde{\mathbf{L}}'_T(\theta, \vartheta)$  is symmetric,
- $\tilde{\mathbf{R}}(\vartheta)$  is symmetric and positive definite.

However, contrarily to the case discussed in Section 2.3.2, now the system (2.40) would still be different from the phase variable model (2.35) because of the additional term  $\Omega \tilde{\mathbf{L}}'_{E2}(\theta, \vartheta) \cdot \tilde{\mathbf{z}}$  in the expression of  $\tilde{\mathbf{e}}$ , which acts as an additional motional induced term related to the moving reference frame time variation.

This kind of transformation is typically used in *field-oriented control* (FOC) algorithms. The adopted transformation is defined as:

$$\mathbf{x}_{dq} = \mathbf{P}(\vartheta) \cdot \mathbf{x} \iff \mathbf{x} = \mathbf{P}^{-1}(\vartheta) \cdot \mathbf{x}_{dq} \quad (2.41)$$

where the transformation matrix  $\mathbf{P}(\vartheta)$ , named *generalized Park's transformation matrix*, is defined as the matrix product:

$$\mathbf{P}(\vartheta) = \mathbf{D}(\vartheta) \cdot \mathbf{C} \quad (2.42)$$

In the expression (2.42),  $\mathbf{C}$  is the generalized Clarke's transformation matrix of the vector space decomposition (2.38) and  $\mathbf{D}(\vartheta)$  is a *rotational transformation matrix* [1], [2]. In multi-stator approaches, the transformation (2.41) is separately applied to each symmetrical phases subset. For permanent magnets machines, the rotational angle  $\vartheta$  is typically chosen to be equal to the rotor electrical angle (i.e.,  $\vartheta = \theta_{el} = P_p \theta$ , where  $P_p$  is the pole pairs number). For induction machines, the transformation (2.41) is instead separately applied to the stator and rotor phases, and the corresponding rotational angles  $\vartheta_s$  and  $\vartheta_r$  are usually chosen to make the moving reference frame to be aligned to the rotor induced field.

## 2.4 Summary and remarks

This chapter has been focused on the formulation of a generalized mathematical model of a multiphase electrical machine.

First, the electrical and mechanical equations have been introduced. They depend on the explicit formulation of the induced fluxes  $\phi_k$  and of the electromagnetic torque  $T_{em}$ , which have been computed in a general way by exploiting the energy conservation principle. By introducing the *electromagnetic coenergy*  $W'_{em}$ , the induced flux  $\phi_k$  in each  $k$ -th winding is the partial derivative of  $W'_{em}$  with respect to the current  $i_k$  flowing in the same winding, while the electromagnetic torque  $T_{em}$  is the partial derivative of  $W'_{em}$  with respect to the rotor position  $\theta$ .

The analytical expression of  $W'_{em}$  has been found by modelling all the machine materials through an *affine  $\vec{B}, \vec{H}$  constitutive relation*, with a proportional term related to the material permeability and with an offset term related to the permanent magnetization. The resulting coenergy expression  $W'_{em}$  is the superposition of three

terms: a term independent from the currents, a term linearly varying with the currents and a term quadratically varying with the currents.

From the knowledge of  $W'_{em}$ , the *induced flux linkages* set  $\phi$  and the developed *electromagnetic torque*  $T_{em}$  have been computed. The fluxes set is the superposition of two terms: a magnets-induced term  $\psi_{PM}(\theta)$  and a currents-induced term  $\mathbf{L}(\theta) \cdot \mathbf{i}$ , which depends on the *inductances matrix*  $\mathbf{L}(\theta)$ . The torque is given by the superposition of three contributions: a term  $T_0(\theta)$  only related to the permanent magnets generated fields, a term  $\mathbf{f}_{PM}^T(\theta) \cdot \mathbf{i}$  proportional to the currents and related to their interaction with the permanent magnets, and a term  $(\mathbf{i}^T \cdot \mathbf{L}'(\theta) \cdot \mathbf{i})/2$  quadratically varying with the currents and related both to the mutual interactions between different windings (e.g., stator and rotor windings) and to variable reluctance effects.

Then, the machine *back-EMFs*, which are the time derivative of the fluxes, have been computed. They are the superposition of three terms: a transformer induced term  $\mathbf{L}(\theta) \cdot (d\mathbf{i}/dt)$  related to the derivatives of the phase currents, a motional induced term  $(d\mathbf{L}/dt) \cdot \mathbf{i}$  related to the variation of the inductances matrix, and a motional induced term  $d\psi_{PM}/dt$  related to the variation of the flux linkages induced by the permanent magnets. The motional terms are proportional to the rotor angular speed  $\omega = d\theta/dt$ .

Finally, the *overall electrical machine model* in the *phase variable domain* has been formalized, resulting in a set of differential and algebraic equations. A brief mention has also been given to some *state transformations* which are typically used in classical multiphase machine analysis approaches and control algorithms.

The results of this chapter represent the starting point for the overall electrical drive analysis and the development of the proposed control algorithms, which are presented in the following chapters.



# 3 Converter Architectures and Modulation Techniques

This chapter presents the most common architectures and modulation techniques for power electronics converters employed in multiphase electrical drives. Again, the analysis is targeted for control purposes, meaning that the physical nature of the semiconductor devices is not relevant for the electrical drive mathematical modelling.

The converter architecture under analysis is a *voltage source inverter* (VSI). It is a circuitual structure realized with controllable power electronics devices which, supplied by a single or multiple voltage sources, is aimed at providing a desired set of voltages to the multiphase electrical machine. Any VSI leg architecture can generate at its output terminals only a discrete set of voltages. Therefore, a *modulation algorithm* is needed to control the converter and make the overall drive evolve, on average, as if it is supplied by the desired set of reference voltages computed by the drive control algorithm.

The chapter is structured as follows. First, Section 3.1 introduces the main VSI architectures adopted in multiphase electrical drives, by first addressing a single VSI leg (in both the two-level and multilevel configurations), and then by focusing on how multiple legs can be organized in different multiphase architectures. Secondly, Section 3.2 recalls the working principle of *pulse width modulation* (PWM) techniques used to supply the converter, and briefly mentions how these techniques are adapted for multiphase and multilevel topologies. Then, Section 3.3 provides some examples of modified modulation techniques specifically addressed to guarantee the DC-bus voltage balancing in a multilevel configuration<sup>1</sup>. Finally, the main contents of this chapter are summarized in Section 3.4.

## 3.1 VSI architectures

This section briefly presents the most common VSI architectures, by first addressing the structure of a single VSI leg and then by showing some of the topologies typically adopted for multiphase drives.

All the VSI architectures are realized through the proper connection of several electronics components. Depending on the operating conditions of the specific application (e.g., rated voltage, current, switching frequency, etc...) different kind of semiconductor devices can be implemented (e.g., MOSFET, IGBT, BJT, GTO, etc...). In the following, the semiconductor devices will be modelled as ideal controllable switches, characterized by a negligible voltage drop in the ON state, a negligible leakage current in the OFF state, and instantaneous switching transitions.

---

<sup>1</sup> As also mentioned in Chapter 1, this topic has been a side research activity carried out during the Ph.D. course. Since these modulation techniques can be analysed separately from the machine control algorithm, some of the main results are here briefly presented.

### 3.1.1 Leg architectures

As previously mentioned, a VSI leg is a power electronics structure that is supplied at the input terminals by a single or multiple voltage sources and which can be actively controlled in a way to generate a desired voltage at its output terminals. If the output voltage can only be controlled to assume two distinct values, the structure is a *two-level converter leg*. If the leg output voltage can assume more than two different values, it represents a *multilevel converter leg*.

The typical two-levels VSI leg architecture is represented in Fig. 3.1. It has two controllable semiconductor devices which are piloted in a complementary way (i.e., when the top device is ON, the bottom device is OFF, and vice-versa)<sup>2</sup>. By taking as reference the negative DC-bus node and by neglecting the semiconductor voltage drops, the leg output voltage  $u_k$  can only assume two possible values, being 0 and the total DC-bus voltage  $V_{DC}$ . The presence of the freewheeling diodes connected in anti-parallel with the controllable switches ensures that the output voltage  $u_k$  is independent of the sign of the output current  $i_k$ .

Several different architectures have been proposed for multilevel voltage source converters, each of which has some benefits and drawbacks. The most common architectures for a multilevel VSI leg can be grouped in [130], [131]<sup>3</sup>:

- *Multi-point clamped* (MPC) converters<sup>4</sup>, where the overall DC-bus is realized through the series connection of multiple DC sources, whose connection point can be linked to the leg output terminal through a proper switching signals configuration (as in Fig. 3.2a),
- *Flying capacitors* (FC) converters, which has a set of isolated capacitive sources, whose connections can be changed by a proper switching signal configuration to generate multiple output voltages (as in Fig. 3.2b), and
- *Modular multi-cell* (MMC) converters, which is built upon the cascaded

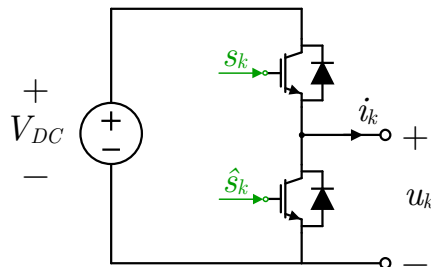


Fig. 3.1 – Schematic representation of a two-level VSI leg.

<sup>2</sup> The subscript  $k$  denotes the generic  $k$ -th phase leg of the converter. The switching signals have been represented as  $s_k \in \{0,1\}$  and  $\hat{s}_k = 1 - s_k$ .

<sup>3</sup> These architectures represent special cases of a generalized multilevel topology [132].

<sup>4</sup> The most common architecture is the three-level one, named *neutral point clamped* (NPC) [133]. Different hardware topologies can be addressed as MPCs (e.g., diode clamped, T-type, etc...); they differ in some design aspects (e.g., number of semiconductor devices, voltage/current ratings, etc...) but behave equivalently from the functional point of view.

connection of multiple conversion modules with a basic VSI architecture<sup>5</sup> (as in Fig. 3.2c).

Similarly to the two-level VSI leg, in multilevel architectures for each controllable semiconductor device it is possible to identify a corresponding device which is piloted in a complementary way (i.e., when the considered device is ON, the complementary one is OFF, and vice-versa). As a result, for a multilevel converter leg with  $N$  couples of complementary devices, there are  $2^N$  possible switching combinations among which to choose. However, some architectures also show additional constraints on the switching signals<sup>6</sup>, while other architectures, instead, may show redundant combinations of the switching signals to supply the same output voltage. These peculiarities influence the modulation strategy used to control the multilevel leg.

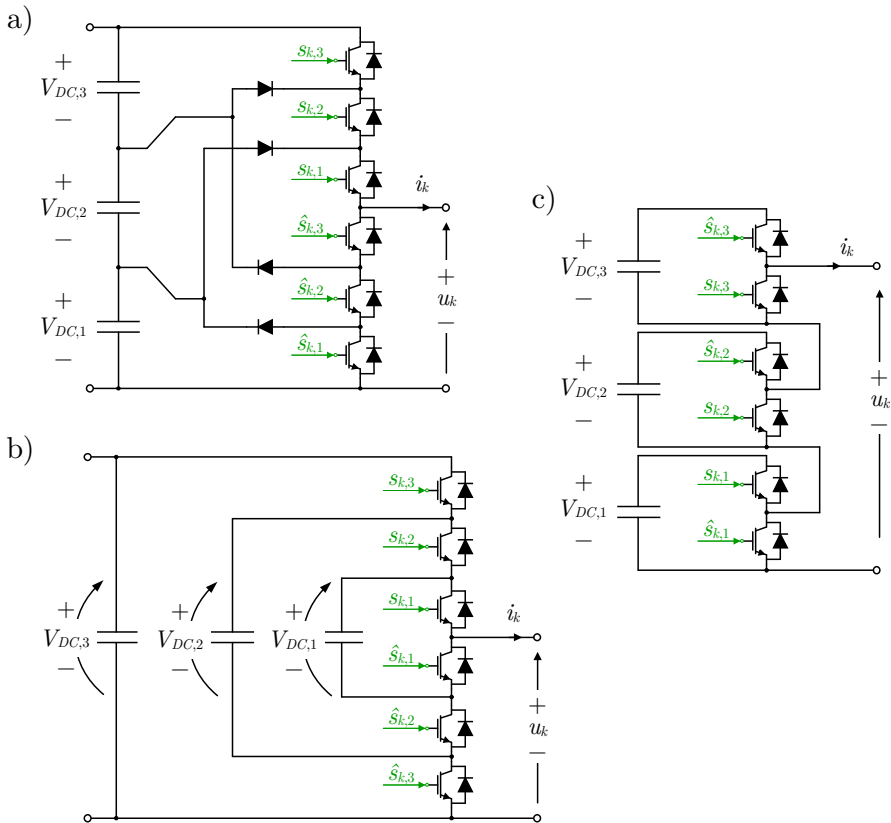


Fig. 3.2 – Schematic representation of different multilevel VSI leg architectures: a) Multi-point clamped (MPC); b) Flying capacitors (FC); c) Modular multi-cell (MMC).

<sup>5</sup> This topology is also called *cascaded multicell inverter* [131]. According to the nature of the basic cell, some special cases are named differently (e.g., cascaded half-bridge, cascaded full-bridge, etc...).

<sup>6</sup> An example is the MPC converter leg where, to guarantee that the leg output voltage is independent of the output current sign, only some switching combinations are allowed. A more detailed explanation is given in the examples of Section 3.3.

### 3.1.2 Multiphase architectures

The control of a multiphase machine requires the use of a multiphase converter, which is built upon multiple legs. In this context, several different multiphase topologies can be realized. They can be either with a single DC voltage source or with multiple independent DC voltage sources [7]; moreover, the corresponding number of legs (further on denoted as  $m$ ) can even be different from the number of phases of the electrical machine (further on denoted as  $n$ ). The following examples illustrate these differences<sup>7</sup>. The mathematical analysis of these configurations will be studied in more detail in Chapter 4 by using a multiport network approach.

In typical configurations with a single DC source, the number of converter legs is equal to the number of machine phases (i.e.,  $m = n$ ). The positive terminal of each  $k$ -th machine phase is connected to the output of the corresponding  $k$ -th converter leg, while the negative terminals are usually connected in a star or multiple-star configurations (see Fig. 3.3a and Fig. 3.3b).

As will be discussed in more detail later on, a star connection with an isolated neutral point introduces a constraint on the machine phase currents, whose sum is forced to be zero. In some cases, to allow the free recirculation of this current, the neutral point is

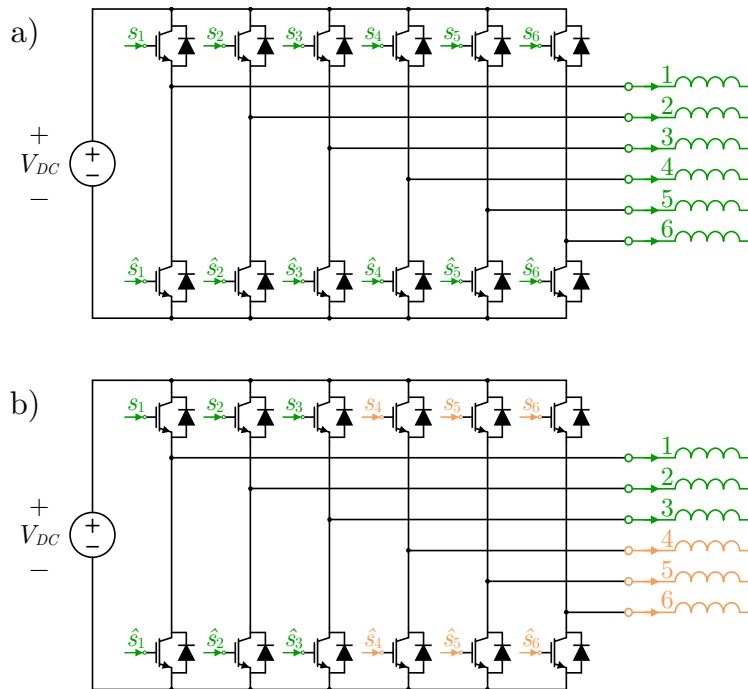


Fig. 3.3 – Star configurations of a six-phase machine with isolated neutrals: a) Single-star; b) Double-star.

<sup>7</sup> All the examples are given for two-level converter architectures, but are also valid for multilevel configurations.

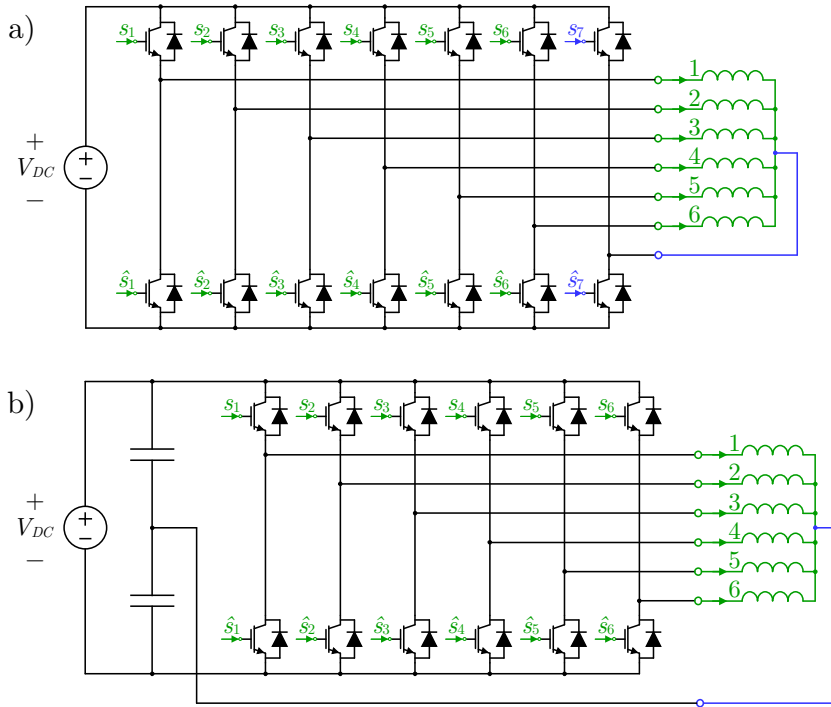


Fig. 3.4 – Star configurations of a six-phase machine with neutral connection: a) Additional VSI leg; b) DC-bus midpoint connection.

either connected to an additional converter leg (as in Fig. 3.4a) or to the DC-bus midpoint (as in Fig. 3.4b). In the first case, it results that  $m > n$ , while in the second case it still results  $m = n$ , but the neutral current may introduce a disbalance among the converter DC-bus capacitors voltages.

Extensions of delta connections are also possible for multiphase drives. A simple example is a pentagon or a pentacle connection for a five-phase machine, as in Fig. 3.5a and Fig. 3.5b, respectively. In this case  $m = n$ , but the cyclic connection of the machine windings leads to a circuit loop whose current (which behaves as a “recirculating current” inside the machine) cannot be directly controlled by the converter voltages.

In presence of multiple isolated DC sources, the previous configurations can also be used for specific subsets of machine windings, as exemplified in Fig. 3.6 for multiple star-connected subsets<sup>8</sup>.

Fig. 3.7 shows another architecture with multiple DC sources, where each machine winding is separately supplied with a dedicated full-bridge converter. This topology, which is of special interests in fault-tolerant applications, leads to  $m = 2n$  and can be considered as a special case of the previous example.

<sup>8</sup> This is a common approach in case the machine is realized with multiple three-phase subsets, each of which is supplied through an isolated three-phase VSI. These multiphase architectures are also known in the technical literature as *Multi-Three-Phase* configurations.

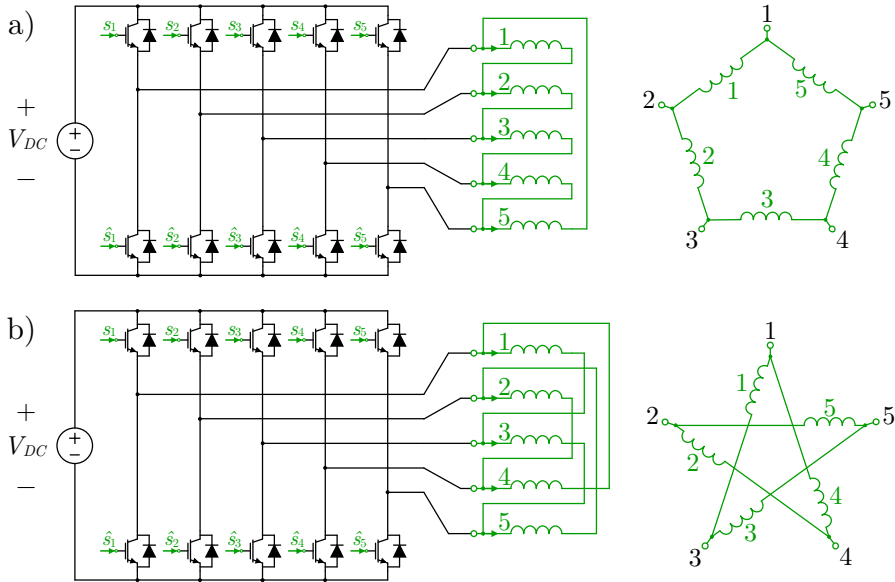


Fig. 3.5 – Cyclical configurations of a five-phase machine: a) Pentagon configuration; b) Pentacle configuration. An alternative representation of the connections has been added to facilitate the circuit understanding.

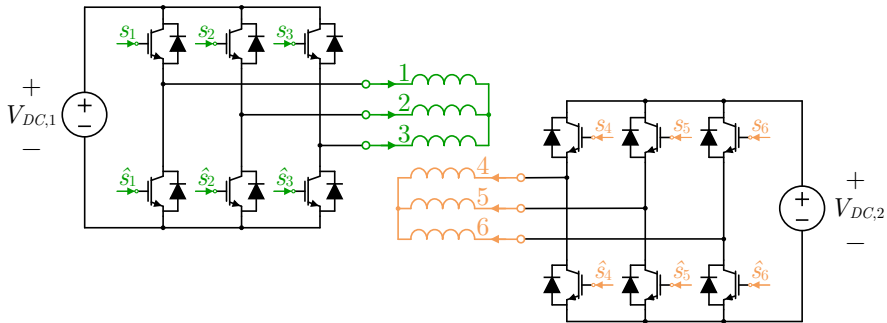


Fig. 3.6 – Six-phase machine in a double-star configuration with two star-connected subsets supplied by isolated DC voltage sources.

Additionally, other configurations are also possible. An example is the double-sided supply configuration of Fig. 3.8, also known as open-end configuration, where the machine phases are separately supplied at both terminals by two isolated  $n$ -phase converters (resulting in  $m = 2n$ ).

All the discussed architectures have a different influence on the mathematical model of the drive. Indeed, both the dependence of the machine voltages from the converter voltages and the constraints on the machine currents are influenced by the chosen configuration. The impact of these architectures on the overall electrical drive mathematical model will be discussed in Chapter 4 by studying the electrical connection between the converter and the machine through a multiport network analysis approach.

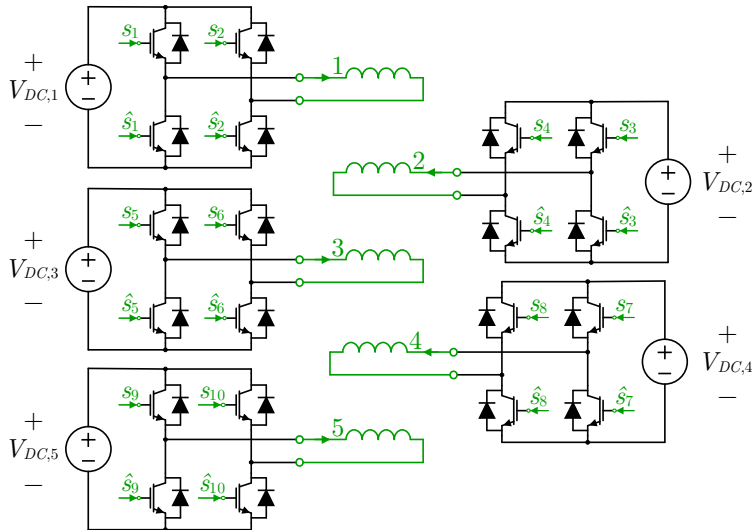


Fig. 3.7 – Five-phase machine with independent supply of each phase winding with an independent full-bridge converter.

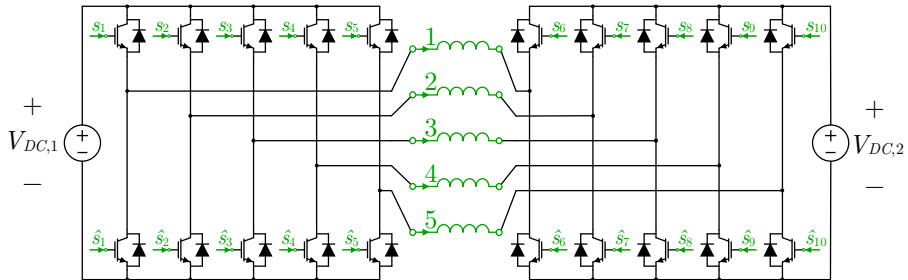


Fig. 3.8 – Five-phase machine in open-end configuration, supplied at both sides by two isolated five-phase converters.

## 3.2 Modulation

As discussed in the previous section, any VSI leg architecture can produce at its output terminal only a finite set of voltages, which are related both to the voltage of the DC sources and to the driving signals applied to the switching devices. Generally, the leg voltage reference computed by the drive control algorithm does not match any of these values. Then, to make the machine variables evolve as closely as possible to the ideal desired behaviour, a modulation technique is required.

The most common modulation approach used in electrical drives is the *pulse width modulation* (PWM) technique. This section briefly recaps its working principle, starting from the analysis for a single two-level VSI leg and then discussing its extension to multiphase and multilevel configurations.

### 3.2.1 Pulse width modulation principles

As discussed in Section 3.1.1, by neglecting the semiconductor voltage drops, the output voltage of a two-level VSI leg can only assume two possible values, being 0 and the total DC-bus voltage  $V_{DC}$ . Then, the inverter output voltage can be realized through a PWM technique, which consists of the application of a sequence of rectangular pulses with a fixed height (equal to  $V_{DC}$ ) and variable temporal width. By properly varying the width of these pulses, the converter voltages can force the electrical machine to follow, on average, the same evolution it would have with the original reference voltages.

For a given *modulation period*  $T_{PWM}$ , the pulse width in each modulation interval is chosen in a way that the average value of the leg voltage matches the average value of the corresponding desired reference. The switching instants of the leg voltage are typically obtained by comparing a *modulating signal*<sup>9</sup> obtained from the reference leg voltage with a *carrier signal*<sup>10</sup> with the period  $T_{PWM}$ .

Consider a generic  $k$ -th converter leg (with  $k = 1, \dots, m$ ) piloted with a PWM technique. By denoting as  $t_h$  the initial instant of the  $h$ -th modulation period, the average voltage  $\langle u_k \rangle[h]$  supplied by the leg in the same period is:

$$\langle u_k \rangle[h] = \frac{1}{T_{PWM}} \cdot \int_{t_h}^{t_h+T_{PWM}} u_k(t) dt = V_{DC} \cdot \frac{T_{k,ON}[h]}{T_{PWM}} = V_{DC} \cdot d_k[h] \quad (3.1)$$

where  $T_{k,ON}$  is the leg output voltage *pulse width* and  $d_k = T_{k,ON}/T_{PWM}$  is the *duty cycle* of the converter leg.

To obtain the same average behaviour, in each modulation period the duty cycle is computed to make the average leg voltage equal to the average reference voltage (i.e.,  $\langle u_k \rangle[h] = \langle u_k^* \rangle[h]$ ). Assuming  $u^*(t)$  does not show a significant variation within the modulation period<sup>11</sup>, it results:

$$\langle u_k^* \rangle[h] = \frac{1}{T_{PWM}} \cdot \int_{t_h}^{t_h+T_{PWM}} u_k^*(t) dt \cong u_k^*(t_h) \quad (3.2)$$

By comparing (3.1) and (3.2), the duty-cycle can be computed to be:

---

<sup>9</sup> If the modulating signal is analogic, the modulation is said to work in *natural sampling* mode. If the modulating signal is digital the modulation is said to work in *regular sampling* mode. In this latter case (which, thanks to the diffusion of digital controllers, is nowadays the most common scenario) the *sampling period*  $T_s$  of the modulating signal is generally synchronized with the carrier period  $T_{PWM}$ .

<sup>10</sup> Typically, the carrier signal is either a *sawtooth* signal or a *triangle wave* signal, in a way that it is piecewise linear in each modulation period. In a digital PWM implementation, for a sawtooth carrier, the modulating signal is updated with the same period of the carrier, meaning that  $T_{PWM} = T_s$ . For a triangular carrier, if the modulating signal is updated with the same period of the triangular wave (i.e.,  $T_{PWM} = T_s$ ), the modulation is called *symmetrical* or *single edge*; if the modulating signal is updated twice for each carrier period, (i.e.,  $T_{PWM} = 2T_s$ ) the modulation is called *asymmetrical* or *double edge*.

<sup>11</sup> Which is an exact (i.e., not approximate) condition in case of a regular sampling mode, since  $u_k^*$  is digitally implemented and is kept constant for each modulation interval.

$$d_k[h] = \frac{u_k^*(t_h)}{V_{DC}} \quad (3.3)$$

To guarantee a feasible behaviour for the converter leg, the reference leg voltage must be in the range  $0 \leq u_k^* \leq V_{DC}$ , meaning that  $0 \leq d_k \leq 1$ . The duty-cycle computed as per (3.3) is used as the modulating signal for the PWM and compared to the chosen carrier signal varying from 0 to 1 to compute the switching instants for the converter leg. The schematic representation of this carrier-based PWM technique is schematically shown in Fig. 3.9.

It can be proven<sup>12</sup> that, if the bandwidth of the reference voltage  $u_k^*$  is low enough if compared to the modulation frequency  $f_{PWM}$ , then the leg output voltage  $u_k(t)$  (which is a pulses sequence) has the same low-frequency harmonic content of  $u_k^*(t)$ , but it is applied with a time delay of  $T_{PWM}/2$ . In other words, the leg output voltage can be written as:

$$u_k(t) = u_k^* \left( t - \frac{T_{PWM}}{2} \right) + \Delta u_k(t) \cong u_k^* \left( t - \frac{T_{PWM}}{2} \right) \quad (3.4)$$

where  $\Delta u_k(t)$  is a residual voltage, whose low-frequency harmonic content is negligible with respect to the reference  $u_k^*(t)$ .

This is exemplified in the diagram of Fig. 3.10, which shows the time and frequency behaviour of a reference analog signal  $u_k^*$  and of the corresponding pulse-width-modulated signal  $u_k$ , both normalized by  $V_{DC}$ . The analog signal has a fundamental frequency of 50 Hz, while the carrier signal (red triangle-wave of Fig. 3.10) has a frequency of 1 kHz. As can be seen, while the analog signal  $u_k^*$  has a smooth behaviour, the PWM signal  $u_k$  is a sequence of rectangular pulses of fixed height and variable width. However, the low-frequency harmonic content of both signals (for  $f < 500$  Hz) is almost identical. The high frequency harmonics of the PWM signal  $u_k$  are centered around the multiple integers of the carrier frequency.

Therefore, by applying the pulse width modulated voltage  $u_k(t)$  to a dynamical system with a low-pass filter behaviour, the voltage  $\Delta u_k(t)$  is neutralized and its effect can be neglected. This is what usually happens in an electrical drive, where the ohmic-

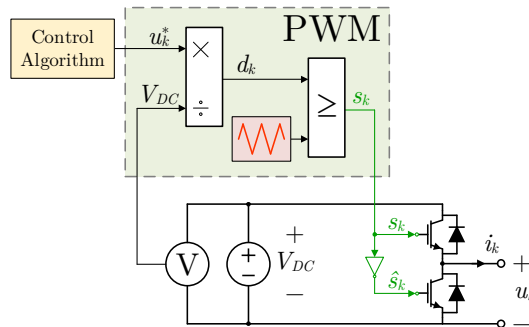


Fig. 3.9 – Carrier-based PWM technique for a two-level VSI leg.

<sup>12</sup> Proven in Appendix 9.3.1.

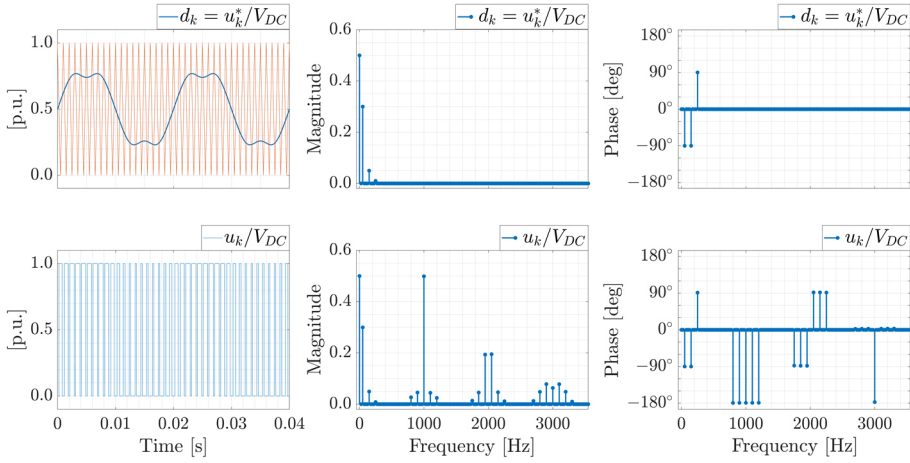


Fig. 3.10 – Example of a two-level PWM technique.

inductive nature of the electrical machine can filter out the effect of the high-frequency harmonic content of the voltages on the machine currents. Then,  $\Delta u(t)$  only produces a current ripple which, for the drive control purposes, can be disregarded.

For a digital controller working with a sampling period of  $T_s$ , the duty-cycles computed as per (3.3) during a generic  $h$ -th sampling interval are usually applied at the beginning of the  $(h + 1)$ -th sampling interval<sup>13</sup>. This introduces an additional time delay to the modulation. Therefore, for control purposes, by neglecting the effect of  $\Delta u_k(t)$ , the combined action of the discrete-time behaviour and the pulse width modulation technique can be modelled through the relation:

$$u_k(t) \cong u_k^* \left( t - T_s - \frac{T_{PWM}}{2} \right) = u_k^*(t - \tau_{del}) \quad (3.5)$$

where  $\tau_{del} = T_s + T_{PWM}/2$  is the *overall time delay* introduced by both the digital control and by the modulation technique.

### 3.2.2 Multiphase modulation techniques

Several different approaches have been proposed for the modulation of multiphase converters [50], [93], [134]–[136]. They are typically referred to  $m$ -phase star connected systems with a single isolated neutral point but, with relatively few changes, they can be also easily extended to other configurations (for example, in case of a multiple star-connected configuration, the same modulation approach can be separately applied to each star-connected subsystem).

The most simple and straightforward approach is to use a carrier-based PWM method to separately control each converter leg independently from the others. In other words, the switching signals for the semiconductor devices are obtained by comparing  $m$  modulation signals with a common carrier signal with the period  $T_{PWM}$ .

<sup>13</sup> This is typically called *shadow mode*.

Similarly to the approach used in most of the standard three-phase drives, a common-mode voltage injection can be superimposed to the leg voltage references. Indeed, for a  $m$ -phase/ $m$ -wires architecture, the common-mode voltage does not affect the supplied system, because the converter imposes the phase-to-phase voltages, which are unaffected by the common-mode component. To be more specific, given a  $m \times 1$  set of reference voltages  $\tilde{\mathbf{u}}^* = [\tilde{u}_1^*, \tilde{u}_2^*, \dots, \tilde{u}_m^*]^T$ , the reference leg voltages for the carrier-based modulation can be obtained as:

$$\mathbf{u}^* = \tilde{\mathbf{u}}^* + u_{CM}^* \cdot \mathbf{1}_m \quad \Rightarrow \quad u_k^* = \tilde{u}_k^* + u_{CM}^* \quad (3.6)$$

where  $\mathbf{1}_m = [1, 1, \dots, 1]^T$ , while  $u_{CM}^*$  is the aforementioned *common-mode voltage* component.

Since the basic two-level VSI leg architecture is not capable of generating negative output voltages, the common-mode component must be chosen in a way that  $0 \leq u_k^* \leq V_{DC}$  for all  $k = 1, \dots, m$ , where  $V_{DC}$  is the DC-bus voltage. As a result, the common-mode voltage must be in the range<sup>14</sup>:

$$-\min\{\tilde{\mathbf{u}}^*\} \leq u_{CM}^* \leq V_{DC} - \max\{\tilde{\mathbf{u}}^*\} \quad (3.7)$$

The condition (3.7) simply requires that the maximum phase-to-phase voltage (i.e.,  $\max\{\tilde{\mathbf{u}}^*\} - \min\{\tilde{\mathbf{u}}^*\}$ ) is lower than the overall DC-bus voltage  $V_{DC}$ .

The simplest common-mode voltage injection is:

$$u_{CM}^* = \frac{V_{DC}}{2} \quad (3.8)$$

which is just a shift of the reference voltages towards the DC-bus midrange. Again, similarly to the techniques employed for three-phase systems, different injections can be used to improve some converter performances. Among the different approaches which have been presented in the technical literature, it is worth mentioning the so-called *min-max injection* [50], [85], which computes the common-mode component  $u_{CM}^*$  at the midrange of its feasibility range, as:

$$u_{CM}^* = \frac{(V_{DC} - \max\{\tilde{\mathbf{u}}^*\}) + (-\min\{\tilde{\mathbf{u}}^*\})}{2} = \frac{V_{DC}}{2} - \frac{\max\{\tilde{\mathbf{u}}^*\} + \min\{\tilde{\mathbf{u}}^*\}}{2} \quad (3.9)$$

in a way that the reference voltages  $u_k^* = \tilde{u}_k^* + u_{CM}^*$  are centred around  $V_{DC}/2$ . In this way, similarly to three-phase drives, the DC-bus utilization in the linear modulation region is maximized. However, as proven in [85], for symmetrical and sinusoidal drives, the benefit of the min-max injection technique (3.9) over the basic DC injection (3.8) is lower and lower for an increasing number of phases.

An example of a common-mode voltage injection is given in Fig. 3.11 for a five-phase symmetrical set of purely sinusoidal voltage references. As expected, the injection (3.8) (top subplot of Fig. 3.11) keeps all the voltage waveforms sinusoidal and only shifts them by  $V_{DC}/2$ . On the contrary, the min-max injection (3.9) (bottom subplot of Fig. 3.11) modifies the waveform of the leg voltage references, which are not sinusoidal anymore. The injected common-mode voltage reference (black dashed trace) has a pseudo-

<sup>14</sup> Proven in Appendix 9.3.2.

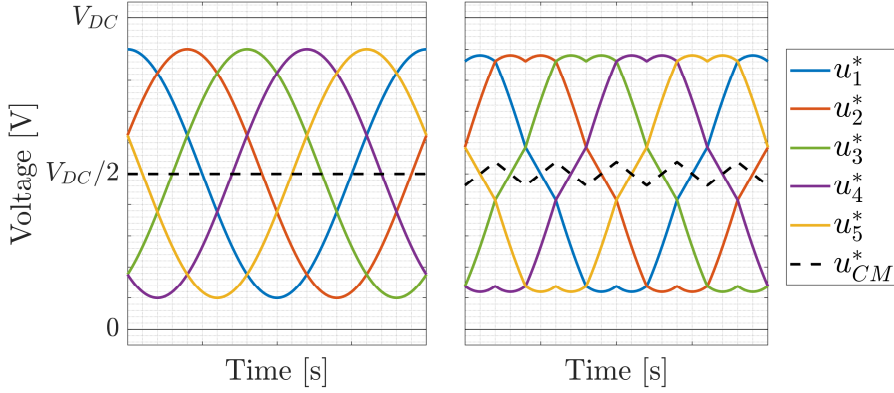


Fig. 3.11 – Example of a common-mode voltage injection to a five-phase symmetrical set of sinusoidal voltage references. Left: DC-bus midrange voltage injection; Right: min-max injection.

triangular waveform and, as previously explained, can reduce the peak values of the leg voltage references without altering the supplied phase-to-phase voltages.

A different approach for the generation of the switching signals is the *space vector modulation*, which is based on the computation of voltage vectors (which are defined with the variable transformations introduced in Section 2.3) and on the generation of proper switching patterns among the vector combinations which can be supplied through the converter legs [88]. This approach, which is commonly adopted for standard three-phase drives, is not of straightforward application in multiphase configurations, both because of the rapid increase in the number of possible output voltage vectors (which grows up exponentially as  $2^m$ ) and the presence of multiple planes which must be controlled simultaneously [50].

As an example, by considering a five-phase converter ( $m = 5$ ) and by referring to the transformation:

$$\begin{bmatrix} u_{x1} \\ u_{y1} \\ u_{x3} \\ u_{y3} \\ u_0 \end{bmatrix} = \sqrt{\frac{2}{5}} \cdot \begin{bmatrix} \cos(0\alpha) & \cos(1\alpha) & \cos(2\alpha) & \cos(3\alpha) & \cos(4\alpha) \\ \sin(0\alpha) & \sin(1\alpha) & \sin(2\alpha) & \sin(3\alpha) & \sin(4\alpha) \\ \cos(0\alpha) & \cos(3\alpha) & \cos(6\alpha) & \cos(9\alpha) & \cos(12\alpha) \\ \sin(0\alpha) & \sin(3\alpha) & \sin(6\alpha) & \sin(9\alpha) & \sin(12\alpha) \\ 1/\sqrt{2} & 1/\sqrt{2} & 1/\sqrt{2} & 1/\sqrt{2} & 1/\sqrt{2} \end{bmatrix} \cdot \begin{bmatrix} u_1 \\ u_2 \\ u_3 \\ u_4 \\ u_5 \end{bmatrix}$$

with  $\alpha = 2\pi/5$ , Fig. 3.12 shows the mapping of all the  $2^5 = 32$  voltage vectors which can be generated, both in the  $\{u_{x1}, u_{y1}\}$  and in the  $\{u_{x3}, u_{y3}\}$  planes.

Given a reference voltage vector, the space vector algorithm applies it on average in a modulation period by using some of the nearest applicable vectors. However, the choice of the voltage vectors to be applied and of their application pattern is not straightforward. Moreover, it has been shown that most of the available space vectors techniques are completely equivalent to carrier-based methods, once a proper selection

of the common-mode voltage injection is given<sup>15</sup> [50], [93], [99], [137].

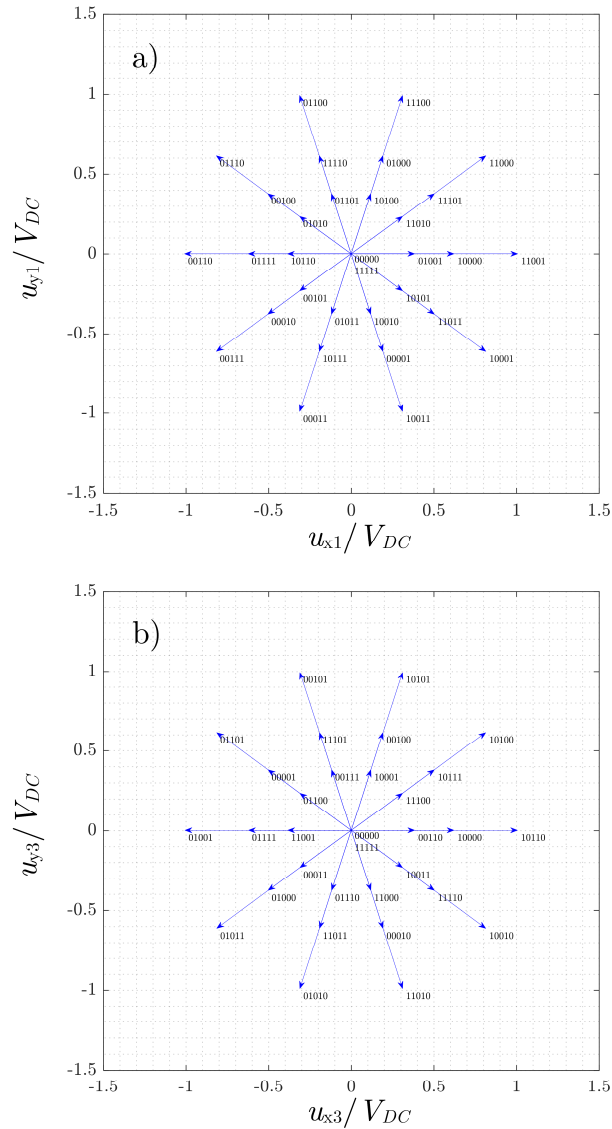


Fig. 3.12 – Representation of the voltage vectors of a two-level five-phase VSI in the  $\{u_{x1}, u_{y1}\}$  and in the  $\{u_{x3}, u_{y3}\}$  planes.

<sup>15</sup> This is not surprising, since the space vector approach can be interpreted as applying a carrier-based technique in a different reference frame. Under this point of view, the common-mode voltage injection is implicitly done with the space vector approaches, while it is explicitly imposed in carrier-based ones.

### 3.2.3 Multilevel modulation techniques

For multilevel VSI architectures, the presence of multiple devices for each leg results in a higher number of degrees of freedom for the converter control, which can be exploited to optimize some desired performances. Some of the improvements which are usually demanded to the converter modulation include, for example, the optimization of the switching harmonic content, the losses minimization or the voltage balancing among multiple DC sources. When the voltage sources are implemented by capacitors, a voltage equalization technique is required to guarantee the correct behaviour of the converter [131], [138], [139].

When the number of levels is sufficiently high, the switching signals are typically chosen in a way to approximate the reference leg voltage  $u_k^*$  with the closest feasible level. This approach is called *nearest level modulation* and is mainly characterized by a reduced switching transitions rate [138] (see Fig. 3.13a).

In case the number of levels is not sufficiently high to neglect the approximation error introduced by the nearest level modulation, it is possible to use extensions of PWM techniques. Contrarily to a two-level leg, for a multilevel leg the same average output voltage  $\langle u_k^* \rangle$  can be generated in multiple different ways. Different PWM techniques can be classified according to the waveform of the leg output voltage  $u_k$  corresponding to the reference  $u_k^*$ . A possible classification is:

- *single-step* mode (SS), if in each modulation period the voltage  $u_k$  only switches among the two feasible levels closest to  $u_k^*$  (see Fig. 3.13b),
- *multi-step* mode (MS), if in each modulation period the voltage  $u_k$  switches among multiple feasible levels (see Fig. 3.13c), and
- *two-level* mode (TL, which is the extreme case of an MS mode), if the multilevel leg behaves similarly to a two-level VSI leg by only switching among the extreme feasible output voltage levels (see Fig. 3.13d).

Generally speaking, the generation of the switching signals to supply the semiconductor devices can still be obtained through a carrier comparison approach, similarly to the two-level case. However, given the higher number of devices, the comparison approaches can be performed in different ways and can be classified as:

- *single reference/multiple carriers* approaches (as in Fig. 3.14a), where a single reference (i.e., modulating) signal is compared with multiple carrier signals<sup>16</sup> (each of which refers to a couple of complementary devices),
- *multiple references/single carrier* approaches (as in Fig. 3.14b), where a single carrier signal is compared with multiple references (each of which refers to a couple of complementary devices), and
- *multiple references/multiple carriers* approaches (as in Fig. 3.14c), where each couple of complementary devices is separately controlled by comparing a reference and a carrier signal.

---

<sup>16</sup> These are the most commonly used techniques and, according to the nature of the different carrier signals, they are further classified in different subcategories, like *Phase Shifted* (PS), *In-Phase Disposition Level Shifted* (PD-LS), *Phase Opposition Disposition Level Shifted* (POD-LS), *Alternate Phase Opposition Disposition Level Shifted* (APOD-LS), etc... [140], [141].

For what concerns multilevel multiphase architectures, the independent control of each leg is nowadays the most common approach. Indeed, the application of space vector modulation approaches to multilevel architectures drastically increases the algorithm complexity and is not suited for multiphase scenarios. Some space vector approaches have been proposed in the technical literature but, again, most of them are completely equivalent to an independent control of each converter leg with a superposition of a properly chosen common-mode voltage component [50], [99]–[102].

The proper choice of the modulation technique to be used is strictly related to the converter architecture (which, as previously mentioned, may have its specific constraints or redundancies) and to the desired performances to be met. Section 3.3 presents some examples of PWM techniques aimed at the voltage balancing in multilevel converters.

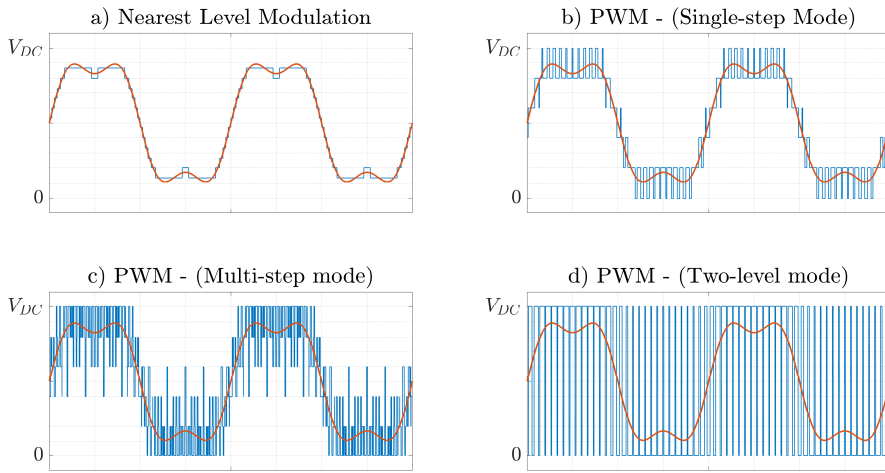


Fig. 3.13 – Example of output voltage waveforms with different modulation techniques for a multilevel converter leg.

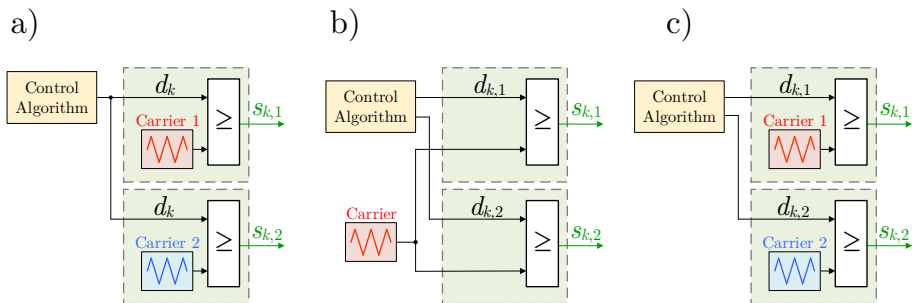


Fig. 3.14 – Some possible carrier comparison techniques for multilevel converters.

- a) Single reference/multiple carriers;
- b) Multiple references/single carrier;
- c) Multiple references/multiple carriers.

### 3.3 Multilevel modulation examples

The present section gives some examples concerning the application of multilevel pulse width modulation techniques with voltage balancing capabilities. The analysis is focused on *neutral point clamped* (NPC) and *multi-point clamped* (MPC) architectures, and briefly addresses the main results proposed in [120], [121], [124]–[126].

#### 3.3.1 Hybrid NPC modulation with voltage balancing

Considering some of the basic three-level neutral point clamped converter leg architectures represented in Fig. 3.15a and Fig. 3.15b, it can be noted that the output node can be connected to any of the three DC-bus nodes through proper control of the semiconductor devices. This connection not only determines the output voltage  $u_k$  of the converter leg, but also the current  $i_{NP,k}$  absorbed from the neutral point. Consequently, from the functional point of view, the converter behaves as the ideal switching circuit of Fig. 3.15c. Generally speaking, the overall DC-bus voltage  $V_{DC} = V_{DC,T} + V_{DC,B}$  is imposed externally and can be approximately considered to be constant, while the voltages of the top and bottom DC-bus capacitors  $V_{DC,T}$  and  $V_{DC,B}$  dynamically depend on the converter operating condition. In other words, they can vary in time and can be different from one another. Since the converter operation can lead to high steady-state voltage fluctuations and, in some cases, even to instability [142]–[145], a voltage balancing technique is required to equalize  $V_{DC,T}$  and  $V_{DC,B}$ .

As previously mentioned, the four active semiconductor devices of each leg are grouped in two couples which are controlled in a complementary way. The  $2^2 = 4$  possible switching states, together with the corresponding values of the leg output voltage  $u_k$  and of the neutral point current  $i_{NP,k}$ , are summarized in Table 3.I. The correct operation of the converter requires the state  $\{1,0\}$  to be avoided: indeed, for the diode clamped architecture of Fig. 3.15a, it would make the output leg voltage to be dependent on the sign of the output current (i.e., it would result  $u_k = V_{DC} \cdot (1 - \text{sign}(i_k))/2$ ), which is not desirable, whereas for the T-type architecture it would short-circuit the whole DC-bus, thus compromising the converter safety. A simple way to avoid the exploitation of the state  $\{1,0\}$  is to guarantee that  $0 \leq s_{T,k} \leq s_{B,k} \leq 1$ , which can be interpreted as a functional constraint imposed to the switching signals.

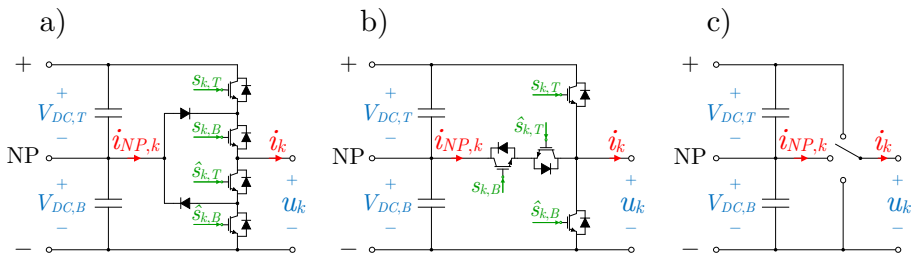


Fig. 3.15 – Neutral Point Clamped converter leg architectures: a) Diode clamped; b) T-type; c) Ideal topology.

Table 3.I – SWITCHING STATES FOR AN NPC LEG.

State	$s_{T,k}$	$s_{B,k}$	$u_k$	$i_{NP,k}$
{0,0}	0	0	0	0
{0,1}	0	1	$V_{DC,B}$	$i_k$
{1,0}	1	0	(undetermined)	0
{1,1}	1	1	$V_{DC}$	0

To consider all the possible operating mode of the pulse width modulation technique (being the SS, MS and TL modes), the switching signals are considered as obtained through a multiple references/single carrier comparison<sup>17</sup>. This means that each signal  $s_{(T/B),k}$  is obtained by comparing a duty-cycle  $d_{(T/B),k}$  with a common triangular carrier signal, with period  $T_{PWM}$ . The different switching modes are represented in Fig. 3.16 for a general case in which the top and bottom DC-bus capacitors have different voltage levels (i.e.,  $V_{DC,T} \neq V_{DC,B} \neq V_{DC}/2$ ).

As can be deduced from the graphical interpretation, the aforementioned constraints  $0 \leq s_{T,k} \leq s_{B,k} \leq 1$  are automatically satisfied once the same relationship holds for the duty cycles (i.e., once  $0 \leq d_{T,k} \leq d_{B,k} \leq 1$ ). It can also be noticed how for SS and TL mode the duty cycles are univocally determined for a given reference voltage  $u_k^*$ , while this is not the case for the MS mode, which allows to freely choose  $d_{T,k}$  and  $d_{B,k}$  in multiple ways, while still developing the desired average output voltage.

By applying a standard averaging procedure over a  $T_{PWM}$  time interval, the average  $k$ -th converter leg voltage and NP current are<sup>18</sup>:

$$\begin{aligned} u_k &= d_{B,k} \cdot V_{DC,B} + d_{T,k} \cdot V_{DC,T} \\ i_{NP,k} &= (d_{B,k} - d_{T,k}) \cdot i_k = d_{NP,k} \cdot i_k \end{aligned} \quad (3.10)$$

The difference  $d_{NP,k} = d_{B,k} - d_{T,k}$  in (3.10) is an important parameter, which represents the fraction of the modulation period for which the output node is connected to the neutral point. A graphical interpretation of  $d_{NP,k}$  is shown in Fig. 3.16. Its minimum value is 0 and is obtained in TL mode (i.e., the output node of the leg is never connected to the NP). Its maximum value is obtained in SS mode and depends on the output voltage reference  $u_k^*$  according to the rule:

$$d_{NP,\max}(u_k^*) = \min \left\{ \frac{u_k^*}{V_{DC,B}}, \frac{V_{DC} - u_k^*}{V_{DC,T}} \right\} \quad (3.11)$$

which is a piece-wise linear function of  $u_k^*$ . All the intermediate values of  $d_{NP,k}$  represent a possible MS mode and can be identified through the normalized parameter:

$$\alpha_k = d_{NP,k} / d_{NP,\max}(u_k^*) \quad (3.12)$$

<sup>17</sup> Many single references/multiple carrier approaches (like, for example, the level shifted PWM) can be also realized with a multiple references/single carrier approach with a proper choice of the modulation signals.

<sup>18</sup> For notation ease, all the variables (unless otherwise specified) implicitly refer to the corresponding average value in a single modulation period.

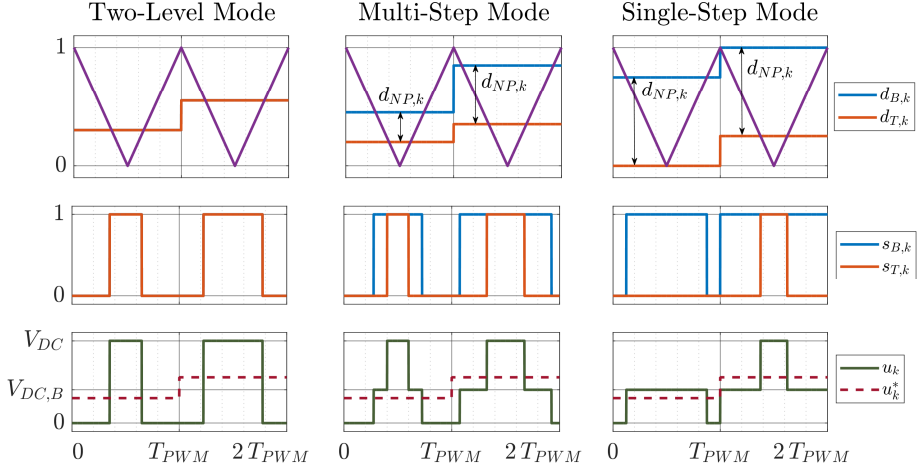


Fig. 3.16 – Qualitative behaviour of the different switching modes of an NPC leg for the same output voltage reference: Top) Duty-cycles; Middle) Switching signals; Bottom) NPC leg output voltage.

named *MS gain factor*. When  $\alpha_k = 0\%$  the  $k$ -th NPC leg works in TL mode, when  $\alpha_k = 100\%$  the NPC leg works in SS mode, and in all the other cases it works in MS mode.

The previous reasoning can be applied to all the converter phases, which share the same DC-bus capacitors.

As also mentioned in Section 3.2.2, in absence of a neutral wire connection, a common-mode voltage  $u_{CM}^*$  can be injected in the reference leg voltages without affecting the overall behaviour of the supplied load (which, in this case, is the electrical machine). As a result, each  $k$ -th leg voltage references can be written as  $u_k^* = \tilde{u}_k^* + u_{CM}^*$ , coherently with (3.6). The common-mode voltage  $u_{CM}^*$  is a degree of freedom for the modulation.

Therefore, by considering the superimposed contribution of all the  $m$  converter legs, the dynamics of the voltage disbalance between the two DC-bus capacitors is given by:

$$\begin{aligned}
 C \cdot \frac{d}{dt} (V_{DC,T} - V_{DC,B}) &= i_{NP} = \\
 &= \sum_{k=1}^m i_{NP,k} = \sum_{k=1}^m i_k \cdot \alpha_k \cdot d_{NP,\max} (\tilde{u}_k^* + u_{CM}^*)
 \end{aligned} \tag{3.13}$$

In (3.13), all the reference voltages  $\tilde{u}_k^*$  are known (e.g., they are imposed by the machine control algorithm), while all the phase currents  $i_k$  behave as uncontrollable inputs for the DC-bus capacitors voltage disbalance dynamics.

Standard modulation techniques, like the single reference/multiple carriers ones, by default, only work in SS mode by taking all the gain factors  $\alpha_k$  to 100%. The common-mode voltage  $u_{CM}^*$  is chosen with a standard min-max injection strategy and, consequently, there is not any active control of the NP current  $i_{NP}$ . As previously stated, in some operating conditions the effect of the load might lead to high DC-bus voltage fluctuations and even instability. To counteract these drawbacks, some techniques have

been proposed to achieve control of the NP current by modifying the modulation technique, without any need for external balancing circuits.

The voltage balancing can be obtained by controlling in feedback the voltage difference ( $V_{DC,T} - V_{DC,B}$ ) and, according to the model equation (3.13), by computing a reference neutral point current  $i_{NP}^*$  to be injected into the DC-bus midpoint. Since the voltages  $\tilde{u}_k^*$  and the currents  $i_k$  (which are related to the drive control algorithm) should not be altered by the balancing technique, the available degrees of freedom to control  $i_{NP}$  are the common-mode voltage  $u_{CM}^*$  and the gain factors  $\alpha_1, \dots, \alpha_m$ .

Some of the proposed strategies only work in SS mode (i.e., all  $\alpha_k$  at 100%) and use a proper common-mode voltage injection to minimize (or, if possible, to nullify), the error between the NP current  $i_{NP}$  and the reference NP current  $i_{NP}^*$  [104], [146], [147]. The expression (3.13) (for any given choice of the gain factors  $\alpha_k$ ) is a piecewise linear function of the common-mode voltage  $u_{CM}^*$ , whose breaking points<sup>19</sup> are obtained when one phase is such that  $d_{NP,max}(\tilde{u}_k^* + u_{CM}^*)$  is either 0 or 1. Then, the choice of the optimal common-mode voltage reference can be graphically interpreted through a diagram like the one depicted in Fig. 3.17. To be more specific, in the function  $i_{NP}(u_{CM}^*)$  it is always possible to identify a breaking point which minimizes the distance from  $i_{NP}^*$  (e.g., the voltage  $u_{CM,opt,me}^*$  in Fig. 3.17) and, in some cases, it is also possible to identify a common-mode voltage for which  $i_{NP}^* = i_{NP}$  (e.g., the voltage  $u_{CM,opt,ec}^*$  in Fig. 3.17). Then, the optimal common-mode voltage to guarantee the DC-bus voltage balancing is chosen to minimize (and, if possible, to nullify) the error  $|i_{NP}^* - i_{NP}|$ . This approach leads to a reduced number of switching transitions, but it becomes unreliable for operating conditions with high modulation index values, since the feasible interval for the common-mode voltage injection may be too narrow to control  $i_{NP}$ .

Other proposed algorithms, instead, only uses the MS mode operation by properly

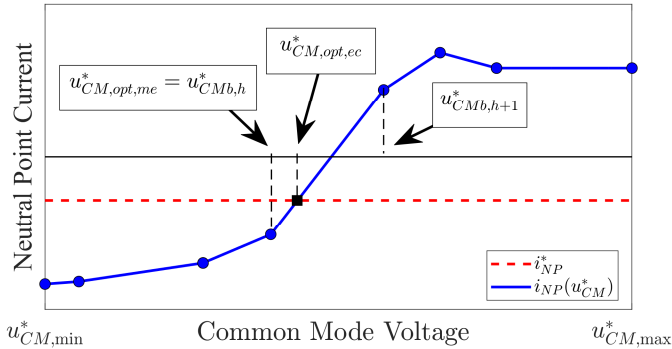


Fig. 3.17 – Neutral point current function with the common-mode voltage injection-based balancing algorithm.

<sup>19</sup> The breaking points (i.e., the points where the slope of the function  $i_{NP}(u_{CM}^*)$  changes) are obtained when the output terminal of one of the converter legs is clamped to one of the DC-bus nodes. Therefore, for a  $m$ -phase NPC there are, at most,  $m + 2$  breaking points.

reducing the gain factors  $\alpha_k$  in a way to condition the function (3.13) and again, if possible, to nullify the error  $|i_{NP}^* - i_{NP}|$  [103], [148]–[150]. The common-mode voltage  $u_{CM}^*$  is instead chosen according to a standard approach, like the min-max injection strategy (3.9) [103]. A graphical interpretation of these kind of approaches is given in Fig. 3.18, where it can be seen that the decrease of one gain factor  $\alpha_k$  from 100% (i.e., SS mode) to a lower value (i.e., MS mode) can change the shape of the overall function  $i_{NP}(u_{CM}^*)$ . For a given (i.e., fixed) common-mode voltage injection, changing one or more  $\alpha_k$  can allow to find an intersection with the reference current  $i_{NP}^*$ . However, despite always being able to guarantee the equalization (even in operations with high modulation index values), the MS mode introduces additional switching transitions to the system, and therefore reduces the converter energetic efficiency.

A proper combination of a simultaneous common-mode voltage injection and MS operation allows the modulation to take advantage of the main benefits of the proposed approaches, while at the same time neutralizing their respective drawbacks. This has led to the development of the hybrid technique proposed in [120], [124], whose graphical interpretation is given in Fig. 3.19. In this case, the reduction of one gain factor  $\alpha_k$  is

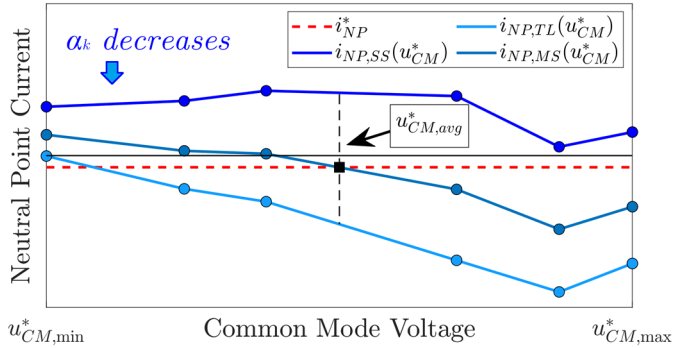


Fig. 3.18 – Neutral point current functions with the MS-based balancing algorithm.

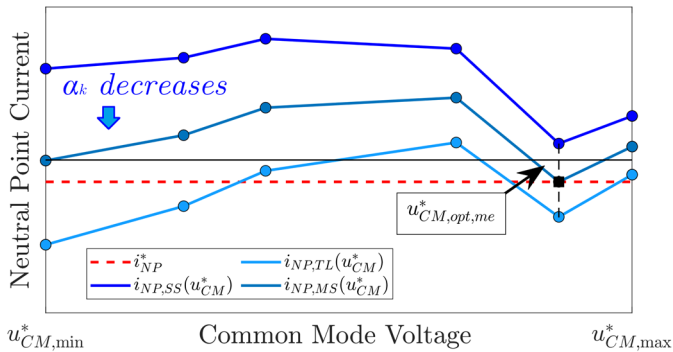


Fig. 3.19 – Neutral point current functions with the proposed hybrid balancing algorithm.

supported by the choice of a common-mode voltage at the breaking point of one phase (e.g., the voltage  $u_{CM,opt,me}^*$  in Fig. 3.19). In this way one converter leg is clamped to one of the DC-bus nodes, and partially neutralizes the increase of the switching transitions rate. In other words, if one NPC leg is required to work in MS mode (with more switching transitions), another leg is clamped to one of the DC-bus nodes (and does not have any switching transition in the same modulation interval).

The logical flow-chart of this hybrid technique is depicted in Fig. 3.20. The algorithm starts with all the NPC leg in SS mode (i.e., all the gain factors  $\alpha_k = 100\%$ ) and finds all the available breaking points of  $i_{NP}(u_{CM}^*)$ . Then, it first looks for possible intersections between  $i_{NP}(u_{CM}^*)$  and  $i_{NP}^*$  and, if present, it uses the same approach as in Fig. 3.17 to compute the reference common-mode voltage injection. In case there is no intersection, the algorithm chooses the breaking point which minimizes the distance from  $i_{NP}^*$  (i.e., the voltage  $u_{CM,opt,me}^*$  of the previous examples) and evaluates the corresponding evolution of  $(V_{DC,T} - V_{DC,B})$  via (3.13). In case the disbalance decreases

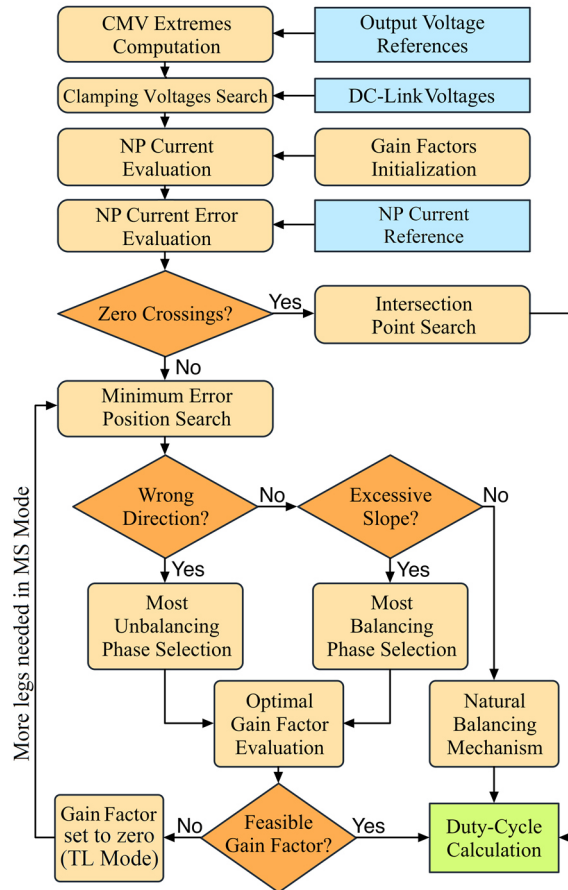


Fig. 3.20 – Flow-chart of the proposed hybrid NPC modulation technique.

with an acceptable slope, a “*Natural balancing*” mechanism is recognized, and the algorithm stops. Otherwise, one NPC leg is selected to work in MS mode and the shape of the function  $i_{NP}(u_{CM}^*)$  is changed as in Fig. 3.19 until an intersection with the reference neutral point current  $i_{NP}^*$  is found. For three-phase converters, it is always guaranteed that at most only one phase is needed to work in MS mode [124]. However, for multiphase converters this may not be the case, and the same approach is iteratively repeated until the balancing conditions are met [120].

The proposed technique has been experimentally validated with a multiphase NPC converter based on Semikron SKM50GB12T4 modules. The results are depicted from Fig. 3.21 to Fig. 3.25. In all operating conditions, the total DC-bus voltage is stabilized at 300 V (through a Sorensen SGI 600/25 voltage supply), while the converter switching frequency has been set to 2 kHz. The proposed hybrid approach (column *a* of all the figures) has been compared to the purely Common-Mode-Injection based technique of [146] (CMI method – column *b* of all the figures), and to the purely Multi-Step based technique of [103] (MS method – column *c* of all the figures). Additionally, a standard NPC modulation technique (i.e., not addressing the balancing requirement) has been added as a reference for comparisons (CBPWM method – column *d* of all the figures). All the modulation techniques have been implemented on a dSpace ds1006 platform with a 2 kHz sampling rate, while the measurements have been recorded through a Tektronix DPO/MSO 2014 oscilloscope and LEM transducers. The figures show the voltages  $V_{DC,T}$

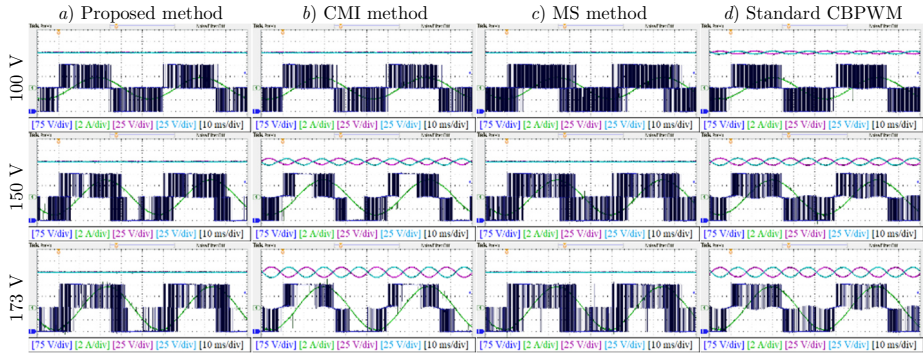


Fig. 3.21 – Comparisons between different NPC modulation algorithms (Symmetrical three-phase RL load, steady-state conditions).

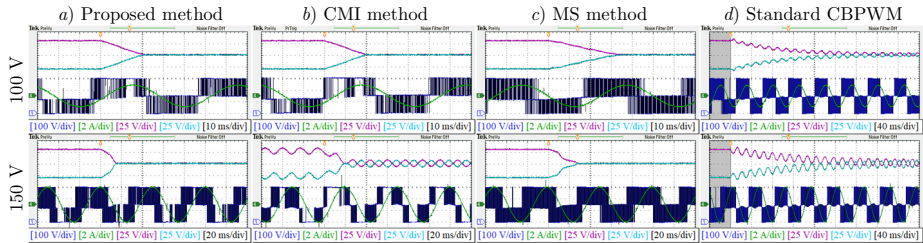


Fig. 3.22 – Comparisons between different NPC modulation algorithms (Symmetrical three-phase RL load, transient results).

and  $V_{DC,B}$  of the DC-bus capacitors (light blue and magenta traces), one leg voltage  $u_k$  (dark blue trace) and the corresponding leg phase current  $i_k$  (green trace).

Different operating conditions have been analysed. Fig. 3.21 and Fig. 3.22 depict the steady-state and transient results for a three-phase symmetrical ohmic-inductive load (with  $R \cong 20 \Omega$  and  $L \cong 360$  mH). Fig. 3.23 and Fig. 3.24 show the steady-state and transient result for a five-phase symmetrical induction machine (with  $R_s \cong R'_r \cong 0.75 \Omega$ ,  $L_{ls} \cong 11.25$  mH,  $L'_{lr} \cong 3.75$  mH and  $L_m \cong 128.75$  mH). Finally, Fig. 3.25 shows the steady-state result for an unbalanced five-phase induction machine (with an external  $5 \Omega$  resistor connected in series to phase 5).

From the results, it can be seen that the pure CMI based approach works effectively for low modulation index values (i.e., with output voltages with a peak value of 100 V), but, instead, it performs poorly for higher modulation index values. On the contrary, the pure MS-based method is always capable of guaranteeing the DC-bus voltages equalization, but at the price of a higher number of switching transitions (as can be noted from the leg output voltage waveforms, which also switch between all the three

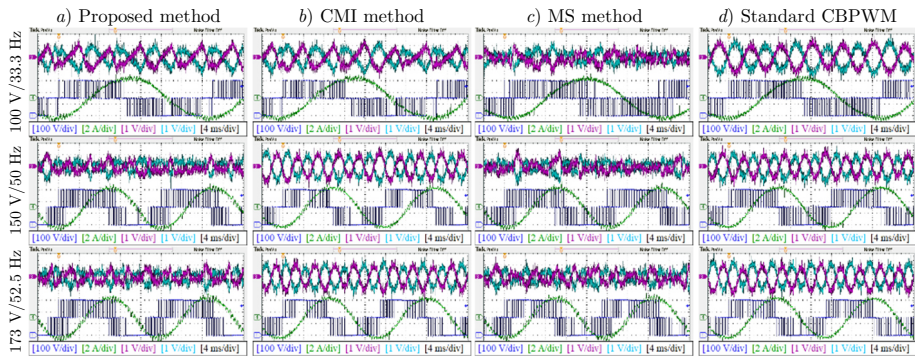


Fig. 3.23 – Comparisons between different NPC modulation algorithms (Symmetrical five-phase induction machine, steady-state conditions).

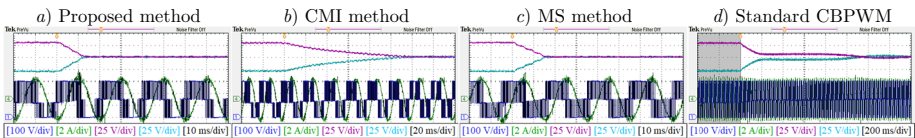


Fig. 3.24 – Comparisons between different NPC modulation algorithms (Symmetrical five-phase induction machine, transient results, 150 V/50 Hz).

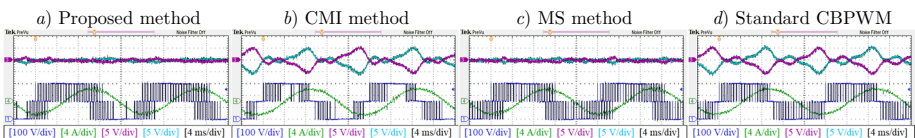


Fig. 3.25 – Comparisons between different NPC modulation algorithms (Unbalanced five-phase induction machine, steady-state conditions, 150 V/50 Hz).

NPC voltage levels). The proposed hybrid technique can also always guarantee the desired voltage balancing but, thanks to the voltage clamping due to the simultaneous common-mode voltage injection, it has fewer transitions than the MS-based approach.

A quantitative comparison of the average switching transitions per leg in a single modulation period is reported in Table 3.II. The results reveal that, in the examined conditions, the total number of switching transitions obtained with the proposed approach are around 22% – 25% less than with the baseline MS approach (which is the only other balancing method that always guarantees the active control of the DC-bus voltages). Moreover, the proposed approach also results in faster transient dynamic performances (as can be noted from the results obtained during the equalization tests).

To sum up, it can be concluded that, thanks to the combination of the MS working mode with a proper CMI, it is possible to achieve both better transient responses and less switching transitions, leading to a better energetic efficiency. For more details, including additional quantitative comparisons of switching transition rates, losses, and equalization effectiveness, the reader can refer to [120].

### 3.3.2 Multistep MPC modulation with voltage balancing

The generalization of the balancing modulation algorithm for multi-point clamped converters is not straightforward.

Again, different topologies can be addressed as MPC (e.g., Diode Clamped, T-Type, etc..., see Fig. 3.26). They differ in some design aspects (e.g., number, voltage and/or current ratings of semiconductor devices) but behave equivalently from the functional point of view. Generally speaking, a  $N$ -level MPC is built upon the series connection of  $(N - 1)$  DC-bus capacitors, and the output terminal of each leg can be connected to one of their terminals through a proper switching signals control. This means that all the MPC architectures can be referred to the ideal topology of Fig. 3.26d. Therefore, the DC-bus has 2 extreme terminals, and  $(N - 2)$  accessible internal points.

As a direct extension of the NPC architecture, a  $N$ -level MPC leg is realized through  $(N - 1)$  couples of controllable semiconductor devices, which are switched in a complementary way (as exemplified in Fig. 3.26). However, the correct operation of the system also imposes the switching signals to respect the additional condition:

Table 3.II – AVERAGE SWITCHING TRANSITIONS RATE COMPARISON.

Operating Conditions	Proposed method	CMI method	MS method	Standard CBPWM
Three-phase RL load				
100 V/20 Hz	199	201	267	198
150 V/20 Hz	207	140	266	198
173 V/20 Hz	211	135	272	198
Five-phase Induction Machine				
100 V/33.3 Hz	110	112	138	120
150 V/50 Hz	81	64	98	83
158 V/52.5 Hz	77	63	84	76
Unbalanced Five-phase Induction Machine				
150 V/50 Hz	91	53	102	80

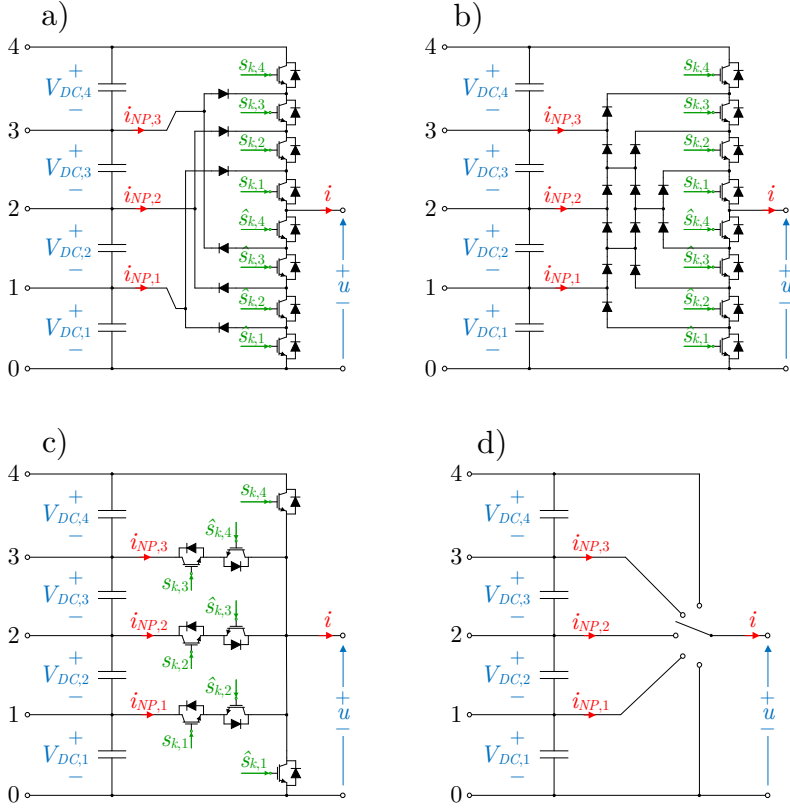


Fig. 3.26 – Multi-point clamped converter architectures (5 level example): a) Standard Diode Clamped; b) Pyramidal Diode Clamped; c) T-Type; d) Ideal topology.

$$0 \leq s_{N-1} \leq \dots \leq s_{h+1} \leq s_h \leq \dots \leq s_1 \leq 1 \quad (3.14)$$

This means that the number of feasible combinations for the switching signals is reduced from  $2^N$  to just  $N$ .

Again, by using the same reasoning of Section 3.3.1, the condition (3.14) can be automatically verified by using a multiple references/single carrier comparison once the duty-cycles of the semiconductor devices satisfy the same conditions:

$$0 \leq d_{N-1} \leq \dots \leq d_{h+1} \leq d_h \leq \dots \leq d_1 \leq 1 \quad (3.15)$$

(for a graphical interpretation it is possible to refer to Fig. 3.16).

Under these conditions, and by using an averaging procedure<sup>20</sup> over a time period of  $T_{PWM}$ , the output leg voltage  $u$  can be expressed as a linear combination of the DC-bus voltages  $\{V_{DC,1}, \dots, V_{DC,N-1}\}$  as:

<sup>20</sup> For notation ease, all the variables (unless otherwise specified) implicitly refer to the corresponding average value in a single modulation period. Additionally, the subscript  $k$  denoting the converter phase will be omitted in this section to simplify the notation.

$$u = \sum_{h=1}^{N-1} d_h \cdot V_{DC,h} \quad (3.16)$$

while the current driven from the  $h$ -th DC-bus node is:

$$i_{DC,h} = (d_h - d_{h+1}) \cdot i = d_{NP,h} \cdot i \quad (3.17)$$

The current  $i_{DC,h}$  actively influences the dynamics of the DC-bus capacitors. In other words, a positive  $i_{DC,h}$  has a charging effect on all the capacitors located above the  $h$ -th DC-bus node, and a discharging effect on all the capacitors located below the  $h$ -th DC-bus node. Since it always results  $d_h - d_{h+1} \geq 0$ , the sign of  $i_{DC,h}$  in (3.17) cannot be controlled, and these currents typically have an unbalancing effect on the whole converter.

Many standard modulation techniques do not address this problem, which often leads to an unstable behaviour. In these cases, the voltage balancing is typically done with external equalization circuits, resulting in a more complex converter architecture. However, by properly acting on the converter modulation, it is possible to reverse this phenomenon and exploit the output leg currents to equalize the DC-bus capacitors.

A possible MS technique, developed in [121], [126], derives as an extension of the NPC modulation presented in Section 3.3.1, and is again based on the reformulation of the  $h$ -th node duty cycle as:

$$d_{NP,h} = d_h - d_{h+1} = \alpha_h \cdot \sigma \quad (3.18)$$

where  $\alpha_h$  is a normalization *gain factor*, which varies from node to node in a way that  $\sum_{h=1}^{N-2} \alpha_h = 1$ , while  $\sigma$  is named *balancing strength factor* and is equal for all the nodes of a single MPC leg. To give a physical interpretation,  $\sigma$  represents the time for which the output leg node is connected to the MPC DC-bus internal points, while  $\alpha_h$  is the percentage of this time referred to the  $h$ -th node. For example,  $\sigma = 0.8$  means that the MPC leg output node is connected to the DC-bus internal nodes for 80% of the modulation period. Then, if  $\alpha_h = 0.3$ , the  $h$ -th node duty-cycle is  $d_{NP,h} = 0.3 \cdot 0.8 = 0.24$ , meaning that the MPC leg output node is connected to the  $h$ -th DC-bus node for 24% of the entire modulation period.

To guarantee the equalization with the considered converter leg, it is possible to set the gain factors as:

$$\alpha_h = \begin{cases} 0 & \text{if } \Delta V_{DC,h} \cdot i < 0 \\ \frac{\Delta V_{DC,h}}{\sum_k |\Delta V_{DC,k}|} & \text{if } \Delta V_{DC,h} \cdot i \geq 0 \end{cases} \quad (3.19)$$

with  $\Delta V_{DC,h} = V_{DC,h} - V_{DC,h+1}$  denoting the voltage disbalance between the  $h$ -th and the  $(h+1)$ -th DC-bus capacitor.

In this way, if the current  $i$  has an unbalancing effect on the voltage disbalance  $\Delta V_{DC,h}$ , the choice  $\alpha_h = 0$  bypasses the  $h$ -th DC-bus node leading to  $i_{NP,h} = 0$ . On the contrary, if the current  $i$  has a balancing effect on  $\Delta V_{DC,h}$ , the  $h$ -th gain factor  $\alpha_h$  and, consequently, the  $h$ -th NP current  $i_{NP,h}$  are set to be proportional to the measured voltage disbalance (i.e., the couple of capacitors with higher disbalance are given a higher

priority on the equalization algorithm). Naturally, the relationship between  $\alpha_h$  and  $\Delta V_{DC,h}$  given in (3.19) can also be replaced by a different strategy (e.g., by using a quadratic proportionality relation).

The choice (3.19) guarantees that, in every operating condition, the modulation of the chosen MPC leg has a balancing effect on the DC-bus capacitors. Then, to maximize the equalization effectiveness, the control strategy requires to choose the strength factor  $\sigma$  (defined in (3.18)) to be the maximum feasible value compatible with the supply of the average reference output voltage  $u^*$ .

With some algebraic manipulations it can be proven that this approach can be studied as the balancing modulation of an equivalent three-level NPC converter with the equivalent top and bottom voltages:

$$V_{\Sigma T} = \sum_{h=1}^{N-2} \left( \alpha_h \cdot \sum_{k=h+1}^{N-1} V_{DC,k} \right) \quad \text{and} \quad V_{\Sigma B} = \sum_{h=1}^{N-2} \left( \alpha_h \cdot \sum_{k=1}^h V_{DC,k} \right) \quad (3.20)$$

In particular, with these positions, the balancing strength factor  $\sigma$  corresponds to the equivalent NP duty cycle  $d_{NP}$  of this equivalent NPC converter leg, whose maximum value is given by the same expression (3.11) which is:

$$\sigma_{\max}(u_k^*) = \min \left\{ \frac{u^*}{V_{\Sigma B}}, \frac{V_{DC} - u^*}{V_{\Sigma T}} \right\} \quad (3.21)$$

Then, the same approach developed in Section 3.3.1 can be followed, and once  $\sigma$  has been chosen, the duty-cycles of all the MPC leg devices can be computed as:

$$\begin{aligned} d_1 = 1, \quad d_2 = d_1 - \sigma \cdot \alpha_1, \dots & \quad \text{if } \frac{u^*}{V_{\Sigma B}} \geq \frac{V_{DC} - u^*}{V_{\Sigma T}} \\ \dots \quad d_{N-1} = d_{N-2} - \sigma \cdot \alpha_{N-2} & \\ \\ d_{N-1} = 0, \quad d_{N-2} = d_{N-1} + \sigma \cdot \alpha_{N-2}, \dots & \quad \text{if } \frac{u^*}{V_{\Sigma B}} < \frac{V_{DC} - u^*}{V_{\Sigma T}} \\ \dots \quad d_1 = d_2 + \sigma \cdot \alpha_1 & \end{aligned} \quad (3.22)$$

This modulation technique is always guaranteed to achieve the voltage equalization of all the DC-bus capacitors. The drawback of this procedure is that, being based on an intrinsic MS approach, it may result in a higher switching transition rate, which can reduce the overall efficiency and worsen the output voltage harmonic content.

To neutralize this effect, it is possible to apply it only to a subset  $M \in \{2, \dots, N\}$  of the converter levels, which is properly selected to reduce the switching transitions rate. In this context, since the output voltage can only switch among the levels between  $N_{Bot}$  and  $N_{Top}$ , the converter behaves like an equivalent  $M$ -level MPC connected to the overall DC-bus through additional capacitors. A graphical interpretation of this concept is given in Fig. 3.27.

To adapt the previous strategy to this configuration, it is only necessary to apply the following substitutions:

$$N \rightarrow M, \quad h \rightarrow h + N_{Bot}, \quad u^* \rightarrow u^* - V_{DC,Bot} \quad (3.23)$$

where  $V_{DC,Bot}$  is the DC-bus voltage of the bottom  $N_{Bot}$  capacitors.

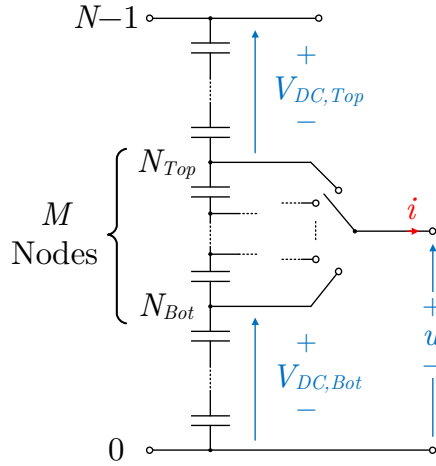


Fig. 3.27 – Equivalent circuit for a  $N$ -level MPC in  $M$ -level operating mode.

The number of levels  $M$  can be chosen with an iterative procedure aimed at guaranteeing a stable behaviour of each converter leg. This has been done by initializing  $M = 2$  (i.e., SS mode) and by changing the minimum and maximum levels  $N_{Bot}$  and  $N_{Top}$  until either an extreme level is reached or it results:

$$\begin{cases} \Delta V_{DC,Bot} \cdot i = (V_{DC,N_{Bot}} - V_{DC,N_{Bot}+1}) \cdot i \geq 0 \\ \Delta V_{DC,Top} \cdot i = (V_{DC,N_{Top}} - V_{DC,N_{Top}+1}) \cdot i \geq 0 \end{cases} \quad (3.24)$$

In this way, it is guaranteed that the NP current absorbed from both the extreme levels  $N_{Bot}$  and  $N_{Top}$  has an overall balancing effect on the structure.

The flowchart of the described algorithm, which is separately applied to each MPC leg, is schematically depicted in Fig. 3.28.

This approach has been validated through hardware-in-the-loop (HIL) tests and compared to other MS-based modulation techniques for MPC converters. The tests have been carried out with respect to a three-phase nine-level grid-connected MPC. Since the proposed algorithm is separately applied to each single MPC leg, analogous results could be obtained by considering a multiphase architecture. The comparisons have been carried out concerning the multi-step technique previously developed in [126] and the multi-step technique of [151], which has been considered as a baseline approach for the voltage balancing of an MPC converter using a modified PWM technique. The proposed technique has been implemented by considering a hysteresis threshold of 1.5% – 5% of the rated DC-bus voltage to activate the adaptation rule (3.23).

Fig. 3.29 shows the results for different power absorption values (i.e., at no-load, at half of the rated load and at the full rated load). The acquisitions show two of the MPC output currents (yellow and green traces), one phase-to-phase output voltage (blue traces) and one output leg voltage (red traces). The corresponding quantitative results are summarized in Table 3.III.

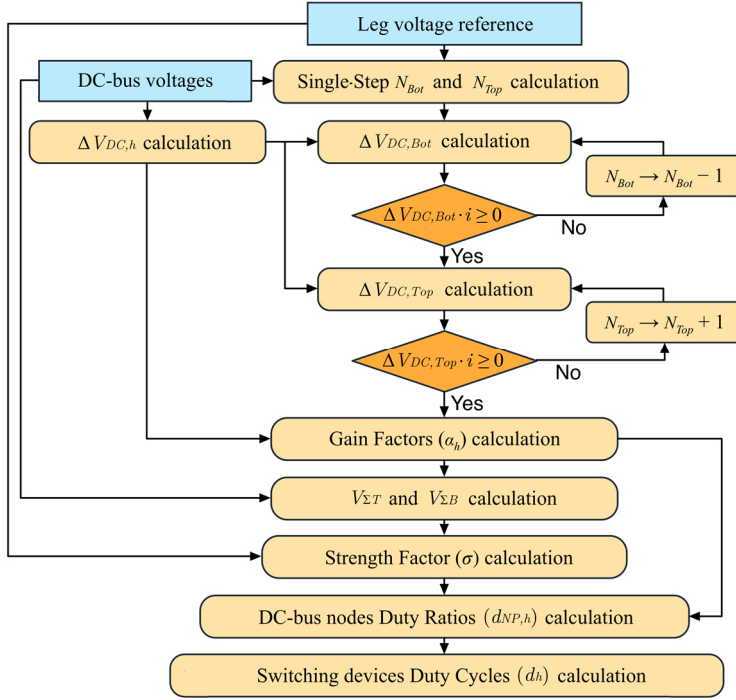


Fig. 3.28 – Flow-chart of the proposed adaptive multistep modulation technique.

From the leg voltage waveforms and from the transitions count, it can be noted that, if compared with the other approaches, the proposed solution can effectively reduce the overall number of switching transitions needed to guarantee the correct MPC functioning. This result is achieved thanks to the adaptive choice of the switching levels.

All the methods can keep all the DC-bus voltages within a desired threshold, and they also lead to similar total harmonic distortion (THD) values for the line-to-line voltages and for the line currents. However, with the proposed adaptive approach, the average number of switching transitions can be reduced by around 30% – 45% with respect to the adaptive MS technique presented in [126] and by around 49% – 80% with respect to the MS technique of [151]. Generally speaking, the best improvements are obtained for reduced loads, since the disbalance effect on the internal DC-bus capacitors is less intense and can be neutralized more easily.

Fig. 3.30 shows the results of the proposed approach for different values of the modulation index, defined as  $m_{ind} = \tilde{u}_{peak}^*/(V_{DC}/2)$ . These results have been obtained by changing the overall DC-bus voltage while keeping the output reference voltages and the corresponding currents unaltered (at the full rated load of the converter). The corresponding quantitative results are summarized in Table 3.IV.

As can be noted, despite a small increase in the maximum DC-bus capacitors voltage disbalances, the highest modulation index values are characterized by the lowest switching transitions rate. This effect can be explained by considering that the common mode voltage injection needed when  $m_{ind} > 1$  (which allows to extend the linear

modulation region) produces in some intervals a clamping of the leg output voltage either to 0 or to  $V_{DC}$ , and forces the corresponding devices not to switch for several modulation periods. This behavior has also a positive influence on the THD of the line-to-line voltages and of the output currents.

Table 3.III – COMPARISONS OF MULTISTEP MPC MODULATION TECHNIQUES.

		a) Proposed Adaptive Technique	b) Original Adaptive Technique	c) Baseline Multistep Technique
0% Load	Number of Switching Transitions	1150	2350	7372
	Maximum DC Voltage Deviation	1.92%	1.07%	1.03%
	Leg Voltages THD	0.216	0.607	1.028
	Line-to-Line Voltages THD	0.093	0.348	0.607
50% Load	Number of Switching Transitions	3671	5145	7372
	Maximum DC Voltage Deviation	3.26%	2.34%	0.38%
	Leg Voltages THD	0.681	0.824	1.010
	Line-to-Line Voltages THD	0.421	0.502	0.593
	AC Grid Currents THD	0.070	0.085	0.103
100% Load	Number of Switching Transitions	3820	6950	7372
	Maximum DC Voltage Deviation	5.01%	5.00%	0.35%
	Leg Voltages THD	0.728	0.923	1.003
	Line-to-Line Voltages THD	0.452	0.564	0.591
	AC Grid Currents THD	0.038	0.047	0.049

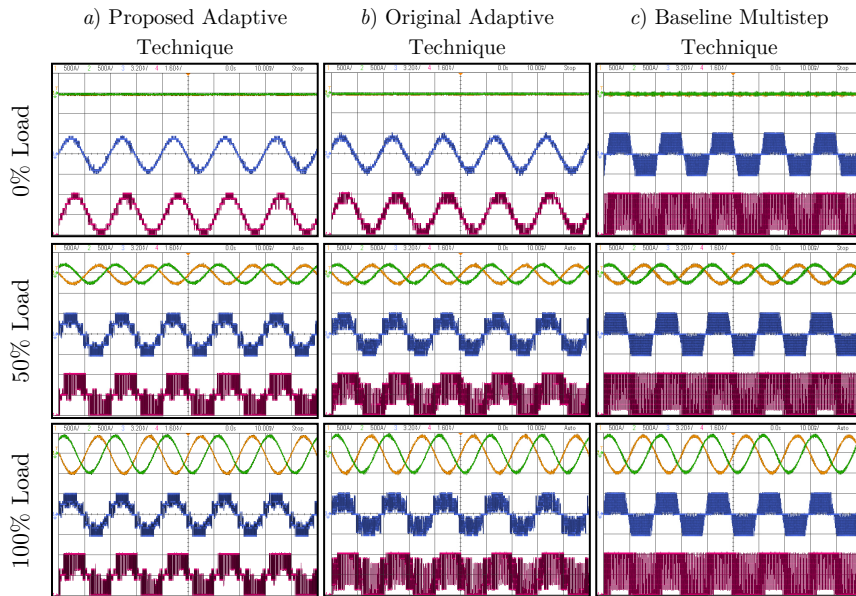
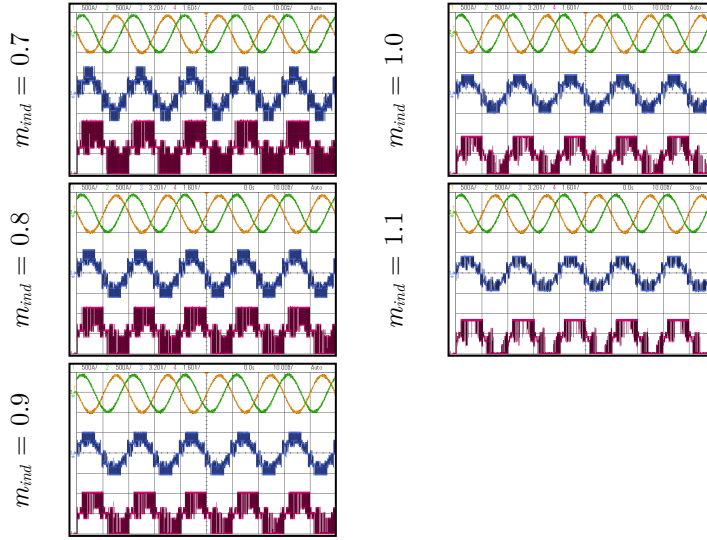


Fig. 3.29 – Comparison between different MPC modulation algorithms.

Table 3.IV – RESULTS FOR DIFFERENT MODULATION INDEX VALUES.

	$m_{ind} = 0.7$	$m_{ind} = 0.8$	$m_{ind} = 0.9$	$m_{ind} = 1.0$	$m_{ind} = 1.1$
Total DC Voltage	4230 V	3700 V	3300 V	2965 V	2700 V
Number of Switching Transitions	3860	3870	3820	3690	3140
Maximum DC Voltage Deviation	4.07%	4.65%	5.01%	5.06%	5.07%
Leg Voltages THD	0.974	0.849	0.728	0.635	0.519
Line-to-Line Voltages THD	0.480	0.468	0.452	0.409	0.341
AC Grid Currents THD	0.043	0.040	0.038	0.038	0.034

Fig. 3.30 – Effectiveness of the proposed algorithm for different modulation index values ( $m_{ind} = \tilde{u}_{peak}^*/(V_{DC}/2)$ ).

For more details, including both the DC-bus capacitors voltages waveforms and quantitative comparisons of switching transition rates, losses and harmonic content the reader can refer to [121].

### 3.4 Summary and remarks

This chapter has focused on the analysis of voltage source inverter (VSI) architectures used in multiphase electrical drives and of their modulation strategies.

The circuitual architectures have been first shown concerning a single *VSI leg*, both in the classic *two-level* configuration and in some common *multilevel* configurations. Since the nature of the semiconductor devices is not relevant for control purposes, the power electronics components have been treated as ideal controllable switches.

Then, several *multiphase topologies*, commonly adopted in electrical drives, have been presented. Different circuitual architectures can be used, with either a single or multiple independent DC sources. The same machine can be supplied in many different

configurations and, in general, the number of converter legs can also differ from the number of machine phases. As will be discussed in detail in Chapter 4, some circuit configurations introduce some constraints on the machine currents, which should be properly considered in the drive modelling.

The output voltage generated by any VSI leg architecture can only assume a discrete number of different values. Then, to make the supplied electrical drive follow a desired behaviour, a modulation technique is required.

The most common modulation technique for a two-level VSI is the *pulse width modulation* (PWM) technique, whose working principle has been briefly recalled. The switching signals to control the semiconductor devices are typically found with a reference/carrier comparison, and the leg output voltage is a sequence of rectangular pulses with fixed height and variable width. The low-frequency harmonic content of the leg voltage is the same as the desired reference voltage, while its high-frequency content is filtered out by the ohmic-inductive nature of the electrical machine and can be neglected for control purposes.

The modulation of a two-level multiphase converter can be implemented by separately controlling each VSI leg. In absence of a neutral wiring connection, a common-mode voltage can be superimposed to the leg reference voltages without altering the overall converter behaviour. Similarly to some of the approaches used in three-phase drives, this *common-mode voltage injection* can be exploited to maximize the DC-bus utilization. *Space vector modulation* approaches have also been proposed in the technical literature, but their implementation for multiphase converters is much more challenging than in three-phase systems because of the higher number of available vectors, modulation planes and switching sequences to combine.

For a multilevel VSI leg with many levels, the output voltage can be approximated as the closest feasible level to the desired reference voltage. This approach, called *nearest level modulation*, is however not suited in case the voltage modulation error is not negligible. In such cases, it is possible to use *multilevel PWM approaches*. Given the high number of levels, the extension of a PWM technique can be implemented in many different ways. This redundancy allows more degrees of freedom which can be used to improve the converter performances.

In case the multilevel converter has multiple capacitive sources, a *voltage balancing* among different capacitors is required to guarantee its correct behaviour. Some proposed algorithms able to guarantee the voltage balancing through the modulation technique are finally shown regarding *neutral point clamped* (NPC) and *multi-point clamped* (MPC) converters.

# 4 Electrical Network Model

The electrical machine model found in Chapter 2 depends on the set of voltages applied to each phase winding. For the drive analysis and control, it is necessary to know how the machine windings voltages are linked to the converter leg voltages. This relationship does not only depend on the connection between the converter and machine terminals, but is also strictly related to how the machine windings are connected to one another. Indeed, many typical electrical drive configurations (both in healthy and in faulty cases) introduce some algebraic constraints on the machine currents, which strongly influence the overall drive dynamical behaviour and, therefore, should be explicitly considered in the overall electrical drive mathematical model.

This chapter is then focused on formalizing in a general fashion the electrical interconnection network linking the electrical machine to the power electronics converter. This approach, seldom applied in standard multiphase drives analysis, can be adequately exploited to study the same machine under different configurations, which can result either from architecture designs or from post-fault reconfigurations. For this reason, the main properties and results of this analysis will be the core of the control algorithms developed in Chapter 6 and Chapter 7.

The chapter is structured as follows. First, Section 4.1 briefly introduces the equivalent representations of both the machine phase windings and the converter legs for the considered network analysis. Secondly, Section 4.2 discusses the proposed multiport analysis in case the machine currents are not subject to any algebraic constraint coming from the hardware configuration. The presence of these hardware-related constraints is explicitly addressed in Section 4.3, which extends the previous results to a more general configuration. Then, a different formulation of the constrained drive model is presented in Section 4.4 by introducing the concept of the configuration space of the system, which allows obtaining an equivalent reduced-order model of a multiphase electrical drive subject to current constraints. Finally, Section 4.5 summarizes the main results of this chapter.

To facilitate the reading, in the following analysis the electrical machine variables will be denoted with the subscript “*EM*” and the power electronics converter variables will be denoted with the subscript “*VSI*”. All the voltages and currents will be denoted as  $v$  and  $i$ , respectively. Additionally, the explicit dependence of the machine parameters on the position  $\theta$  will be omitted for notation simplicity.

## 4.1 Equivalent sources representation

The machine electrical behaviour is governed by the electrical equations (2.1), which have been expressed in a matrix notation in (2.2). This set of equations describes a dynamical system in which the fluxes  $\phi_{EM} = [\phi_{EM,1}, \dots, \phi_{EM,n}]^T$  are the state variables. By considering the electromagnetic energy of the machine as a state function of the system, the machine currents  $i_{EM} = [i_{EM,1}, \dots, i_{EM,n}]^T$  are univocally identified by the instantaneous value of the fluxes  $\phi_{EM}$  and of the rotor position  $\theta_{EM}$ . Indeed, they can

always be found from the expression (2.7) and, by considering the simplifying hypothesis adopted in Chapter 2, they can be explicitly computed from the expression (2.30). As a result, the currents can also be considered as state variables for the machine and, from the circuital point of view, each  $k$ -th winding (with  $k = 1, \dots, n$ ) can be modelled as an ideal current source<sup>1</sup> forcing the corresponding machine current  $i_{EM,k}$ .

The converter electrical behaviour depends on the switching signals used to control the semiconductor devices. For a voltage source converter, all the feasible states univocally identify the output voltage of all the legs. As a result, from the circuital point of view, each  $k$ -th converter leg (with  $k = 1, \dots, m$ ) can be modelled as an ideal voltage source forcing the corresponding leg voltage  $v_{EM,k}$ .

A schematic depiction of these equivalent source modelling is depicted in Fig. 4.1. It is worth emphasizing again that, for a generic drive configuration, it may be  $m \neq n$ .

## 4.2 Unconstrained network model

Consider a drive configuration in which all the currents are free to flow independently from one another. The connection between the power electronics converter and the electrical machine can be modelled through a linear a-dynamical multi-port network, whose forcing inputs are the  $m$  converter voltages  $\mathbf{v}_{VSI} = [v_{VSI,1}, \dots, v_{VSI,m}]^T$  and the  $n$  machine currents  $\mathbf{i}_{EM} = [i_{EM,1}, \dots, i_{EM,n}]^T$ .

The *complementary variables* are the converter currents  $\mathbf{i}_{VSI} = [i_{VSI,1}, \dots, i_{VSI,m}]^T$  and the electrical machine windings voltages  $\mathbf{v}_{EM} = [v_{EM,1}, \dots, v_{EM,n}]^T$ . They can be expressed as linear combinations of the forcing inputs. By using an active sign convention for the  $m$  converter ports and a passive sign convention for the  $n$  machine ports, the linear relationship can be synthetically represented by the *hybrid matrix* of the network<sup>2</sup>:

$$\begin{bmatrix} \mathbf{i}_{VSI} \\ -\mathbf{v}_{EM} \end{bmatrix} = \begin{bmatrix} \mathbf{H}_{VSI,VSI} & \mathbf{H}_{VSI,EM} \\ \mathbf{H}_{EM,VSI} & \mathbf{H}_{EM,EM} \end{bmatrix} \cdot \begin{bmatrix} \mathbf{v}_{VSI} \\ \mathbf{i}_{EM} \end{bmatrix} \quad (4.1)$$

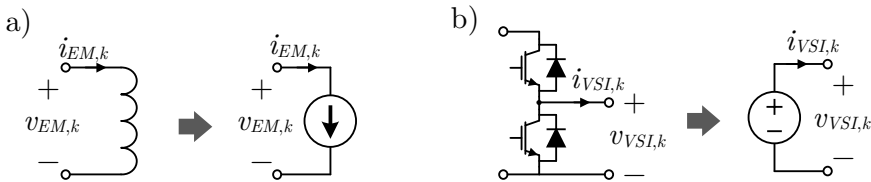


Fig. 4.1 – Equivalent sources representation for the network analysis: a) Electrical machine phase winding; b) Voltage source inverter leg.

<sup>1</sup> This can be also interpreted in terms of the *associated resistive circuit* of a dynamical electrical network, where all the inductive elements are replaced by current sources forcing their instantaneous current (which is the corresponding state variable), called *substitution sources*.

<sup>2</sup> The negative sign appearing at the first term for  $\mathbf{v}_{EM}$  is because the characterization of multiport systems through a hybrid matrix is typically done by using the active sign notation for all the forcing inputs.

From the *reciprocity properties* of linear multiport networks, it can be proven<sup>3</sup> that:

$$\begin{aligned} \mathbf{H}_{VSI,VSI} &= \mathbf{H}_{VSI,VSI}^T = \mathbf{G}_{NET} \\ \mathbf{H}_{EM,EM} &= \mathbf{H}_{EM,EM}^T = \mathbf{R}_{NET} \\ \mathbf{H}_{VSI,EM} &= -\mathbf{H}_{EM,VSI}^T = \mathbf{N} \end{aligned} \quad (4.2)$$

where:

- $\mathbf{G}_{NET}$  is a  $m \times m$  *network conductances matrix* related to the converter variables, and is responsible for the leakage currents. Indeed, its parameters represent the currents that would be absorbed from the converter if the machine windings are open (i.e.,  $\mathbf{i}_{EM} = \mathbf{0}$ ). Usually, they are only related to shunt parasitic effects, which can be disregarded leading to  $\mathbf{G}_{NET} \cong \mathbf{0}$ .
- $\mathbf{R}_{NET}$  is a  $n \times n$  *network resistances matrix* related to the electrical machine variables, and is responsible for the voltage drops across the network. Indeed, its parameters represent the voltages that would be measured on the machine windings if all the converter legs are short-circuited (i.e.,  $\mathbf{v}_{VSI} = \mathbf{0}$ ). Usually, they are only related to the wiring resistances, which also can be disregarded leading to  $\mathbf{R}_{NET} \cong \mathbf{0}$ .
- $\mathbf{N}$  is a  $n \times m$  matrix here named *network interconnection matrix*. Its parameters define both the effect of the converter voltages on the machine voltages and the effect of the machine currents on the converter currents.

Then, the expression (4.1) can be rewritten as:

$$\begin{bmatrix} \mathbf{i}_{VSI} \\ \mathbf{v}_{EM} \end{bmatrix} = \begin{bmatrix} \mathbf{G}_{NET} & \mathbf{N}^T \\ \mathbf{N} & -\mathbf{R}_{NET} \end{bmatrix} \cdot \begin{bmatrix} \mathbf{v}_{VSI} \\ \mathbf{i}_{EM} \end{bmatrix} \cong \begin{bmatrix} \mathbf{0} & \mathbf{N}^T \\ \mathbf{N} & \mathbf{0} \end{bmatrix} \cdot \begin{bmatrix} \mathbf{v}_{VSI} \\ \mathbf{i}_{EM} \end{bmatrix} \quad (4.3)$$

A schematic depiction of the analysed network representation is depicted in Fig. 4.2.

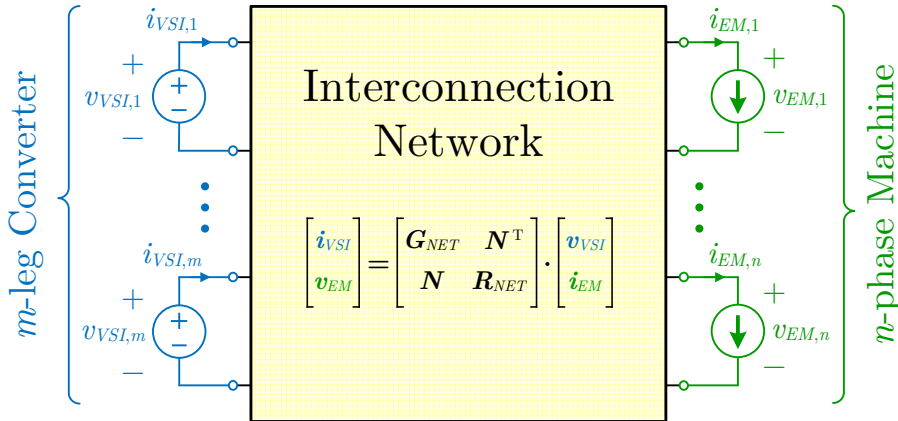


Fig. 4.2 – Multiport representation of an unconstrained electrical network.

<sup>3</sup> Proven in Appendix 9.4.3 basing on the results of Appendix 9.4.2 and Appendix 9.4.1.

### 4.2.1 Electrical equations

By isolating the voltages of the machine phase windings in (4.3), it results that:

$$\mathbf{v}_{EM} = \mathbf{N} \cdot \mathbf{v}_{VSI} - \mathbf{R}_{NET} \cdot \mathbf{i}_{EM} \cong \mathbf{N} \cdot \mathbf{v}_{VSI} \quad (4.4)$$

The expression (4.4) shows that, once the converter leg voltages set  $\mathbf{v}_{VSI}$  (and, eventually, the machine currents  $\mathbf{i}_{EM}$ ) are known, the machine phase voltages  $\mathbf{v}_{EM}$  are univocally identified. By combining the voltages expressed by (4.4) with the electrical machine dynamic model (2.35), the overall drive satisfies the equation:

$$\mathbf{L}_{EM} \cdot \frac{d\mathbf{i}_{EM}}{dt} + (\mathbf{R}_{EM} + \mathbf{R}_{NET}) \cdot \mathbf{i}_{EM} + \mathbf{e}_{EM} = \mathbf{N} \cdot \mathbf{v}_{VSI} \quad (4.5)$$

The equation (4.5) describes a dynamical system of order  $n$ , whose functional block diagram is schematically represented in Fig. 4.3. The input of this system is represented by the  $m \times 1$  set of converter voltages  $\mathbf{v}_{VSI}$ , and acts through the input matrix  $\mathbf{N}$ , which is only related to the network configuration.

The dynamical model (4.5) is represented in the *descriptor form*. The *canonical state-space representation* of the system is obtained by multiplying both sides of (4.5) by the matrix  $\mathbf{\Gamma}_{EM} = \mathbf{L}_{EM}^{-1}$  and by isolating the current derivatives, resulting in:

$$\begin{aligned} \frac{d\mathbf{i}_{EM}}{dt} &= [-\mathbf{\Gamma}_{EM} \cdot (\mathbf{R}_{EM} + \mathbf{R}_{NET})] \cdot \mathbf{i}_{EM} + \dots \\ &\dots + [\mathbf{\Gamma}_{EM} \cdot \mathbf{N}] \cdot \mathbf{v}_{VSI} + [-\mathbf{\Gamma}_{EM} \cdot \mathbf{e}_{EM}] = \\ &= \mathbf{A}_{EM} \cdot \mathbf{i}_{EM} + \mathbf{B}_{EM} \cdot \mathbf{v}_{VSI} + \mathbf{d}_{EM} \end{aligned} \quad (4.6)$$

where  $\mathbf{A}_{EM}$  is the *state matrix* of the system,  $\mathbf{B}_{EM}$  is the *state space input matrix* of the system and  $\mathbf{d}_{EM}$  is an equivalent *disturbance input* for the system. Note that, in the canonical form (4.6), all these terms depend on the machine parameters, including the rotor position  $\theta$ , meaning that they are time-variant. Moreover, in presence of variable reluctance effects, the term  $\mathbf{d}_{EM}$  may also depend on the machine currents through the effect of the motional induced back-EMFs  $\omega \mathbf{L}'_{EM}(\theta) \cdot \mathbf{i}_{EM}$ .

### 4.2.2 Examples

To better explain the proposed modelling approach of the electrical network in case the phase currents are not subject to any constraint, some examples are here provided to show how the matrices in (4.3) can be computed. The examples refer to some of the

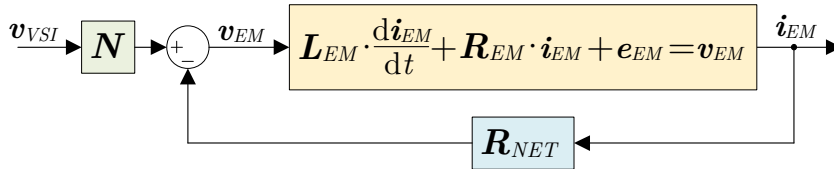


Fig. 4.3 – Functional block diagram of the electrical equations in case of an unconstrained interconnection network.

configurations introduced in Section 0. All the examples will assume the effects of wiring resistances and parasitic conductances to be negligible, leading to  $\mathbf{R}_{NET} = \mathbf{0}$  and  $\mathbf{G}_{NET} = \mathbf{0}$  as in the simplified results of (4.3).

Note that all the following examples, by focusing on the electrical interconnection network, are valid regardless of the kind of machine which is supplied (e.g., PMSM, IM, SynRM, etc...).

### Separately excited windings

Consider a five-phase machine ( $n = 5$ ) whose windings are all supplied by isolated full-bridge converters ( $m = 10$ ), as schematically represented in Fig. 4.4. By neglecting the wiring resistances and leakage conductances of the semiconductor devices, the relationship between the machine and converter variables can be immediately derived as the system of equations:

$$\begin{aligned} i_{VSI,1} &= i_{EM,1}, & i_{VSI,2} &= -i_{EM,1}, & v_{EM,1} &= v_{VSI,1} - v_{VSI,2}, \\ i_{VSI,3} &= i_{EM,2}, & i_{VSI,4} &= -i_{EM,2}, & v_{EM,2} &= v_{VSI,3} - v_{VSI,4}, \\ i_{VSI,5} &= i_{EM,3}, & i_{VSI,6} &= -i_{EM,3}, & v_{EM,3} &= v_{VSI,5} - v_{VSI,6}, \\ i_{VSI,7} &= i_{EM,4}, & i_{VSI,8} &= -i_{EM,4}, & v_{EM,4} &= v_{VSI,7} - v_{VSI,8}, \\ i_{VSI,9} &= i_{EM,5}, & i_{VSI,10} &= -i_{EM,5}, & v_{EM,5} &= v_{VSI,9} - v_{VSI,10} \end{aligned}$$

By using a matrix notation, the converter voltages and currents can be grouped in the  $10 \times 1$  sets  $\mathbf{v}_{VSI} = [v_{VSI,1}, \dots, v_{VSI,10}]^T$  and  $\mathbf{i}_{VSI} = [i_{VSI,1}, \dots, i_{VSI,10}]^T$ , respectively. Similarly, the electrical machine voltages and currents can be grouped in the  $5 \times 1$  sets  $\mathbf{v}_{EM} = [v_{EM,1}, \dots, v_{EM,5}]^T$  and  $\mathbf{i}_{EM} = [i_{EM,1}, \dots, i_{EM,5}]^T$ , respectively.

From the previous equations, it results that:

- the VSI current set  $\mathbf{i}_{VSI}$  is independent of the VSI voltages set  $\mathbf{v}_{VSI}$ , meaning that  $\mathbf{G}_{NET} = \mathbf{0}$ ,

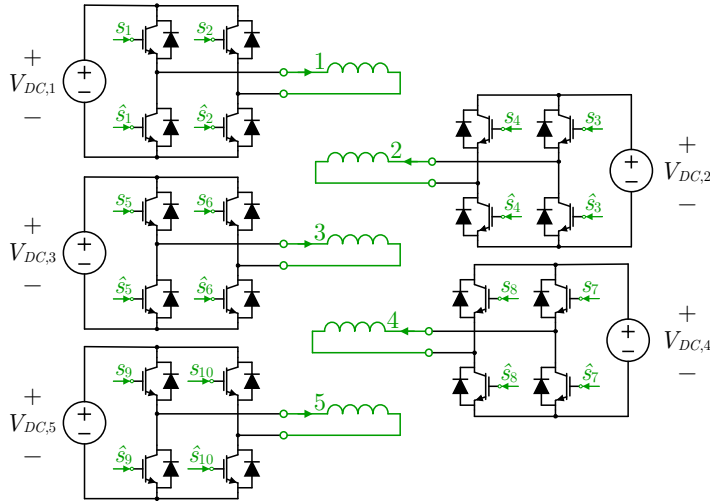


Fig. 4.4 – Five-phase machine with independent supply of each phase winding with an independent full-bridge converter.

- the EM voltages set  $\mathbf{v}_{EM}$  are unaffected by the EM currents set  $\mathbf{i}_{EM}$ , meaning that  $\mathbf{R}_{NET} = \mathbf{0}$ , and
- the mutual relationship between  $\mathbf{v}_{EM}$  and  $\mathbf{v}_{VSI}$  and between  $\mathbf{i}_{EM}$  and  $\mathbf{i}_{VSI}$  are identified by the  $5 \times 10$  network interconnection matrix

$$\mathbf{N} = \begin{bmatrix} 1 & -1 & 0 & 0 & 0 & 0 & 0 & 0 & 0 & 0 \\ 0 & 0 & 1 & -1 & 0 & 0 & 0 & 0 & 0 & 0 \\ 0 & 0 & 0 & 0 & 1 & -1 & 0 & 0 & 0 & 0 \\ 0 & 0 & 0 & 0 & 0 & 0 & 1 & -1 & 0 & 0 \\ 0 & 0 & 0 & 0 & 0 & 0 & 0 & 0 & 1 & -1 \end{bmatrix}$$

Note that the same model would have been also valid in case all the full-bridges were with a common DC-bus (and not isolated with each other). In this case, the configuration could also be interpreted as a five-phase machine supplied by a ten-leg converter.

### Single-star configuration with additional VSI leg

Consider a six-phase machine ( $n = 6$ ), with the windings which are star-connected with an accessible neutral point, which is itself connected to an independent VSI leg as in Fig. 4.5. In this case,  $m = 7$  and, by using the same assumptions of the previous example, the following equations can be written:

$$\begin{aligned} i_{VSI,1} &= i_{EM,1}, & v_{EM,1} &= v_{VSI,1} - v_{VSI,7}, \\ i_{VSI,2} &= i_{EM,2}, & v_{EM,2} &= v_{VSI,2} - v_{VSI,7}, \\ i_{VSI,3} &= i_{EM,3}, & v_{EM,3} &= v_{VSI,3} - v_{VSI,7}, \\ i_{VSI,4} &= i_{EM,4}, & v_{EM,4} &= v_{VSI,4} - v_{VSI,7}, \\ i_{VSI,5} &= i_{EM,5}, & v_{EM,5} &= v_{VSI,5} - v_{VSI,7}, \\ i_{VSI,6} &= i_{EM,6}, & v_{EM,6} &= v_{VSI,6} - v_{VSI,7}, \\ i_{VSI,7} &= -i_{EM,1} - i_{EM,2} - i_{EM,3} - i_{EM,4} - i_{EM,5} - i_{EM,6} \end{aligned}$$

With the same approach of the previous example, the converter voltages and currents can be grouped in the  $7 \times 1$  sets  $\mathbf{v}_{VSI} = [v_{VSI,1}, \dots, v_{VSI,7}]^T$  and  $\mathbf{i}_{VSI} = [i_{VSI,1}, \dots, i_{VSI,7}]^T$ , respectively, while the electrical machine voltages and currents can be grouped in the  $6 \times 1$  sets  $\mathbf{v}_{EM} = [v_{EM,1}, \dots, v_{EM,6}]^T$  and  $\mathbf{i}_{EM} = [i_{EM,1}, \dots, i_{EM,6}]^T$ , respectively.

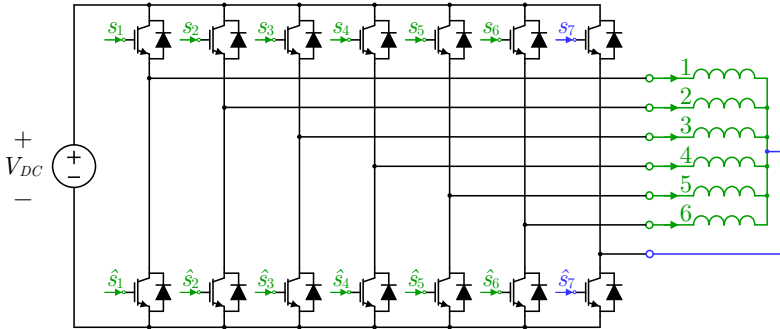


Fig. 4.5 – Six-phase machine in a single-star configuration with neutral point connected to an additional VSI leg.

From the previous equations it results that:

- the VSI current set  $\mathbf{i}_{VSI}$  is independent of the VSI voltages set  $\mathbf{v}_{VSI}$ , meaning that  $\mathbf{G}_{NET} = \mathbf{0}$ ,
- the EM voltages set  $\mathbf{v}_{EM}$  are unaffected by the EM currents set  $\mathbf{i}_{EM}$ , meaning that  $\mathbf{R}_{NET} = \mathbf{0}$ , and
- the mutual relationship between  $\mathbf{v}_{EM}$  and  $\mathbf{v}_{VSI}$  and between  $\mathbf{i}_{EM}$  and  $\mathbf{i}_{VSI}$  are identified by the  $6 \times 7$  network interconnection matrix

$$\mathbf{N} = \begin{bmatrix} 1 & 0 & 0 & 0 & 0 & 0 & -1 \\ 0 & 1 & 0 & 0 & 0 & 0 & -1 \\ 0 & 0 & 1 & 0 & 0 & 0 & -1 \\ 0 & 0 & 0 & 1 & 0 & 0 & -1 \\ 0 & 0 & 0 & 0 & 1 & 0 & -1 \\ 0 & 0 & 0 & 0 & 0 & 1 & -1 \end{bmatrix}$$

### Single-star configuration with DC-bus midpoint connection

Consider again a star-connected six-phase machine ( $n = 6$ ), but in this case with the neutral point connected at the DC-bus midpoint of the supplying converter, as in Fig. 4.6. In this case,  $m = 6$  and the equations describing the system are:

$$\begin{aligned} i_{VSI,1} &= i_{EM,1}, & v_{EM,1} &= v_{VSI,1} - V_{DC}/2, \\ i_{VSI,2} &= i_{EM,2}, & v_{EM,2} &= v_{VSI,2} - V_{DC}/2, \\ i_{VSI,3} &= i_{EM,3}, & v_{EM,3} &= v_{VSI,3} - V_{DC}/2, \\ i_{VSI,4} &= i_{EM,4}, & v_{EM,4} &= v_{VSI,4} - V_{DC}/2, \\ i_{VSI,5} &= i_{EM,5}, & v_{EM,5} &= v_{VSI,5} - V_{DC}/2, \\ i_{VSI,6} &= i_{EM,6}, & v_{EM,6} &= v_{VSI,6} - V_{DC}/2 \end{aligned}$$

The presence of  $V_{DC}/2$  can be easily dropped out by referring the VSI voltages to the DC-bus midpoint instead of referring them to the DC-bus negative node. In this case, the same expressions become:

$$\begin{aligned} i_{VSI,1} &= i_{EM,1}, & v_{EM,1} &= v_{VSI,1}, \\ i_{VSI,2} &= i_{EM,2}, & v_{EM,2} &= v_{VSI,2}, \\ i_{VSI,3} &= i_{EM,3}, & v_{EM,3} &= v_{VSI,3}, \\ i_{VSI,4} &= i_{EM,4}, & v_{EM,4} &= v_{VSI,4}, \\ i_{VSI,5} &= i_{EM,5}, & v_{EM,5} &= v_{VSI,5}, \\ i_{VSI,6} &= i_{EM,6}, & v_{EM,6} &= v_{VSI,6} \end{aligned}$$

Then, the converter voltages and currents can be grouped in the  $6 \times 1$  sets  $\mathbf{v}_{VSI} = [v_{VSI,1}, \dots, v_{VSI,6}]^T$  and  $\mathbf{i}_{VSI} = [i_{VSI,1}, \dots, i_{VSI,6}]^T$ , while the electrical machine voltages and currents can be grouped in the  $6 \times 1$  sets  $\mathbf{v}_{EM} = [v_{EM,1}, \dots, v_{EM,6}]^T$  and  $\mathbf{i}_{EM} = [i_{EM,1}, \dots, i_{EM,6}]^T$ , respectively.

From the previous equations, it results that:

- the VSI current set  $\mathbf{i}_{VSI}$  is independent of the VSI voltages set  $\mathbf{v}_{VSI}$ , meaning that  $\mathbf{G}_{NET} = \mathbf{0}$ ,
- the EM voltages set  $\mathbf{v}_{EM}$  are unaffected by the EM currents set  $\mathbf{i}_{EM}$ , meaning that  $\mathbf{R}_{NET} = \mathbf{0}$ , and
- the mutual relationship between  $\mathbf{v}_{EM}$  and  $\mathbf{v}_{VSI}$  and between  $\mathbf{i}_{EM}$  and  $\mathbf{i}_{VSI}$  are

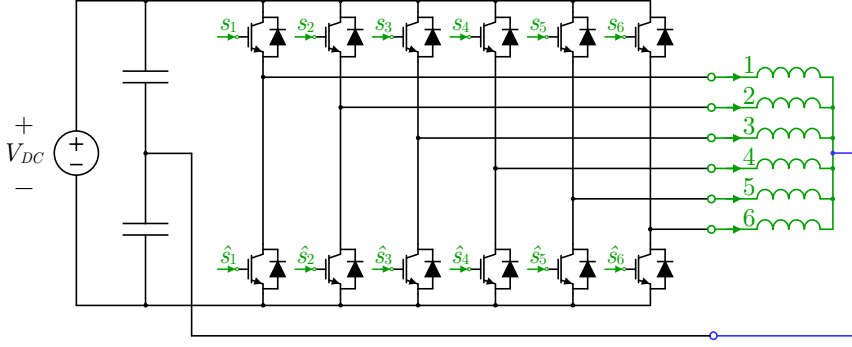


Fig. 4.6 – Six-phase machine in a single-star configuration with neutral point connected the DC-bus midpoint.

identified by the  $6 \times 6$  network interconnection matrix

$$\mathbf{N} = \begin{bmatrix} 1 & 0 & 0 & 0 & 0 & 0 \\ 0 & 1 & 0 & 0 & 0 & 0 \\ 0 & 0 & 1 & 0 & 0 & 0 \\ 0 & 0 & 0 & 1 & 0 & 0 \\ 0 & 0 & 0 & 0 & 1 & 0 \\ 0 & 0 & 0 & 0 & 0 & 1 \end{bmatrix} = \mathbf{I}$$

If compared to the previous example, this configuration does not require an additional converter leg. However, in case the DC-bus is realized with capacitors, the presence of a DC component or of low-frequency AC components in the neutral point current could lead to a significant disbalance or to heavy fluctuations between the voltages of the DC-bus capacitors, which may negatively affect the converter behaviour.

## Pentagon configuration

Consider a five-phase machine ( $n = 5$ ), where this time the windings are cyclically connected in a pentagon configuration as in Fig. 4.7. The equations of the system are:

$$\begin{aligned} i_{VSI,1} &= i_{EM,1} - i_{EM,5}, & v_{EM,1} &= v_{VSI,1} - v_{VSI,2} \\ i_{VSI,2} &= i_{EM,2} - i_{EM,1}, & v_{EM,2} &= v_{VSI,2} - v_{VSI,3} \\ i_{VSI,3} &= i_{EM,3} - i_{EM,2}, & v_{EM,3} &= v_{VSI,3} - v_{VSI,4} \\ i_{VSI,4} &= i_{EM,4} - i_{EM,3}, & v_{EM,4} &= v_{VSI,4} - v_{VSI,5} \\ i_{VSI,5} &= i_{EM,5} - i_{EM,4}, & v_{EM,5} &= v_{VSI,5} - v_{VSI,1} \end{aligned}$$

The converter voltages and currents can be grouped in the  $5 \times 1$  sets  $\mathbf{v}_{VSI} = [v_{VSI,1}, \dots, v_{VSI,5}]^T$  and  $\mathbf{i}_{VSI} = [i_{VSI,1}, \dots, i_{VSI,5}]^T$ , respectively, while the electrical machine voltages and currents can be grouped in the  $5 \times 1$  sets  $\mathbf{v}_{EM} = [v_{EM,1}, \dots, v_{EM,5}]^T$  and  $\mathbf{i}_{EM} = [i_{EM,1}, \dots, i_{EM,5}]^T$ , respectively.

From the previous equations, it results that:

- the VSI current set  $\mathbf{i}_{VSI}$  is independent of the VSI voltages set  $\mathbf{v}_{VSI}$ , meaning that  $\mathbf{G}_{NET} = \mathbf{0}$ ,

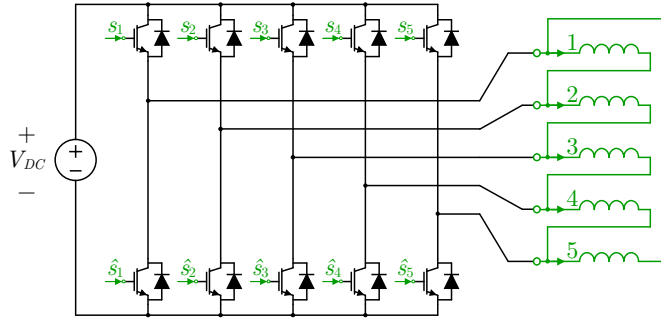


Fig. 4.7 – Five-phase machine in pentagon configuration.

- the EM voltages set  $\mathbf{v}_{EM}$  are unaffected by the EM currents set  $\mathbf{i}_{EM}$ , meaning that  $\mathbf{R}_{NET} = \mathbf{0}$ , and
- the mutual relationship between  $\mathbf{v}_{EM}$  and  $\mathbf{v}_{VSI}$  and between  $\mathbf{i}_{EM}$  and  $\mathbf{i}_{VSI}$  are identified by the  $5 \times 5$  network interconnection matrix

$$\mathbf{N} = \begin{bmatrix} 1 & -1 & 0 & 0 & 0 \\ 0 & 1 & -1 & 0 & 0 \\ 0 & 0 & 1 & -1 & 0 \\ 0 & 0 & 0 & 1 & -1 \\ -1 & 0 & 0 & 0 & 1 \end{bmatrix}$$

In this case, contrarily to the previous examples,  $\mathbf{N}$  is not a full-ranked matrix. This is the direct consequence of the cyclical connection and means that the 5 electrical machine voltages cannot be controlled independently from one another. Indeed, they are always subject to:

$$v_{EM,1} + v_{EM,2} + v_{EM,3} + v_{EM,4} + v_{EM,5} = 0$$

A similar model can be also applied to other cyclical configurations (e.g., to the pentacle configuration of the examples in Section 3.1.2).

## 4.3 Constrained network model

Most typical electrical drive configurations include some physical constraints on the machine currents. The most common example is a star connection of a group of windings with an isolated neutral point, in which the sum of the corresponding currents is forced to be zero, but another example of practical interests is the case of an open-circuit fault on one phase, which forces the current of the same winding to zero.

This section mathematically formalizes these constraints in a way to model them with the same multi-port formalism adopted in the previous case. It is also shown how the presence of algebraic constraints for the phase currents can alter the machine behaviour by introducing some internal feedback actions on its dynamical model<sup>4</sup>.

<sup>4</sup> It is worth emphasizing that this modified modelling approach is required because the

### 4.3.1 Current constraints formalization

Each  $h$ -th physical constraint (with  $h = 1, \dots, n_c$ ) can be found by applying *Kirchhoff's current law* (KCL) to the node (or, more generally, to the cutset) involving the constrained machine phases, and is represented by an algebraic equation in the form:

$$\sum_{k=1}^n M_{hk} \cdot i_k = 0 \quad (4.7)$$

where  $M_{hk} \neq 0$  only if the  $h$ -th constraint involves the  $k$ -th machine winding. The set of all the  $n_c$  algebraic constraints can be written in matrix form as:

$$\mathbf{M}^T \cdot \mathbf{i}_{EM} = \mathbf{0} \quad (4.8)$$

and  $\mathbf{M}$  is a  $n \times n_c$  matrix, here named *constraints matrix*. Each column of  $\mathbf{M}$  represents a single specific algebraic constraint introduced by the physical connection of the machine windings.

By neglecting the linearly dependent columns of  $\mathbf{M}$  (which identify the same algebraic constraints and, therefore, are redundant), the rank of  $\mathbf{M}$  is  $n_c$ . The maximum number of constraints is limited by the number of windings itself (because there cannot be more constraints than the number of currents). This means that  $n_c \leq n$ .

Note that the same set of algebraic constraints can be modelled in different ways. This means that the same electrical configuration can be associated with different constraints matrix  $\mathbf{M}$ . As explained and exemplified in the following, this does not affect the validity of the resulting mathematical model.

### 4.3.2 Augmented network model

The presence of algebraic constraints on the machine currents makes the interconnection network harder to model as a multiport system, because it forces the machine currents (which are input variables for the system) to be dependent on one another. Therefore, it is convenient to modify the interconnection network topology to obtain an equivalent unconstrained system with the same behaviour as the original (i.e., physical) one. This can be done by adding, for each  $h$ -th node or cutset identifying a current constraint (with  $h = 1, \dots, n_c$ ) an *auxiliary voltage source*  $v_{NET,h}$  connected to the rest of the physical system. In this modified circuit topology, the current  $i_{NET,h}$  flowing in the  $h$ -th auxiliary voltage source with a passive sign convention is:

$$i_{NET,h} = \sum_{k=1}^n M_{hk} \cdot i_k \quad (4.9)$$

which, in the original system, was constrained to zero. Fig. 4.8 exemplifies how an algebraic constraint on the machine phase currents can be modelled with a modified system with an auxiliary voltage source.

---

constraints are applied to the machine currents, which are state variables for the system. In other words, since the state variables of the dynamical system cannot evolve freely, the whole drive exhibits a different behaviour. On the contrary, other constraints related to the electrical configuration (like, for example, constraints on the converter currents), would not require any modification in the mathematical model as long as they do not involve any state variable.

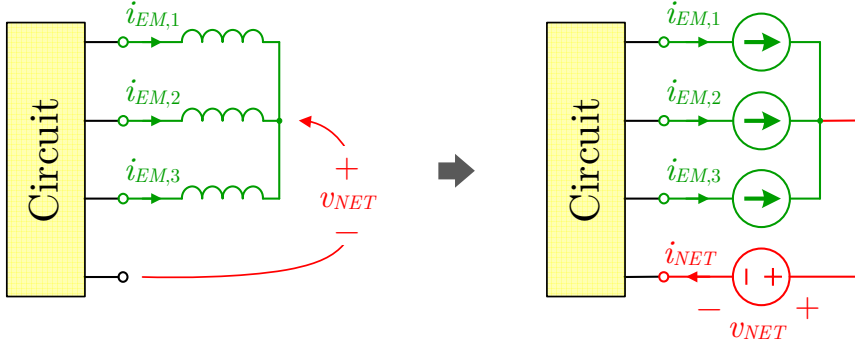


Fig. 4.8 – Network representation of a constraint through the introduction of an auxiliary voltage source.

In this unconstrained augmented system, the relationship between the independent sources and the complementary variables is similar to the expression (4.1) and can be formalized through a hybrid matrix as:

$$\begin{bmatrix} \mathbf{i}_{VSI} \\ -\mathbf{v}_{EM} \\ -\mathbf{i}_{NET} \end{bmatrix} = \begin{bmatrix} \mathbf{H}_{VSI,VSI} & \mathbf{H}_{VSI,EM} & \mathbf{H}_{VSI,NET} \\ \mathbf{H}_{EM,VSI} & \mathbf{H}_{EM,EM} & \mathbf{H}_{EM,NET} \\ \mathbf{H}_{NET,VSI} & \mathbf{H}_{NET,EM} & \mathbf{H}_{NET,NET} \end{bmatrix} \cdot \begin{bmatrix} \mathbf{v}_{VSI} \\ \mathbf{i}_{EM} \\ \mathbf{v}_{NET} \end{bmatrix} \quad (4.10)$$

where  $\mathbf{v}_{NET} = [v_{NET,1}, \dots, v_{NET,n_c}]^T$  is the set of auxiliary net voltages, which act as independent sources, and  $\mathbf{i}_{NET} = [i_{NET,1}, \dots, i_{NET,n_c}]^T$  is the set of auxiliary net current, which act as complementary variables.

Similarly to (4.2), from the reciprocity properties of linear multiport networks and from (4.9), it can be proven that:

$$\begin{aligned} \mathbf{H}_{VSI,VSI} &= \mathbf{H}_{VSI,VSI}^T = \mathbf{G}_{NET} \cong \mathbf{0}, & \mathbf{H}_{VSI,NET} &= -\mathbf{H}_{NET,VSI}^T = \mathbf{0} \\ \mathbf{H}_{EM,EM} &= \mathbf{H}_{EM,EM}^T = \mathbf{R}_{NET} \cong \mathbf{0}, & \mathbf{H}_{NET,NET} &= \mathbf{H}_{NET,NET}^T = \mathbf{0} \\ \mathbf{H}_{VSI,EM} &= -\mathbf{H}_{EM,VSI}^T = \mathbf{N}, & \mathbf{H}_{EM,NET} &= -\mathbf{H}_{NET,EM}^T = \mathbf{M} \end{aligned} \quad (4.11)$$

where the matrices  $\mathbf{G}_{NET}$ ,  $\mathbf{R}_{NET}$  and  $\mathbf{N}$  have the same meaning of (4.2), while  $\mathbf{M}$  is the constraint matrix defined in (4.8).

The expression (4.10) can be therefore rewritten as:

$$\begin{aligned} \begin{bmatrix} \mathbf{i}_{VSI} \\ \mathbf{v}_{EM} \\ \mathbf{i}_{NET} \end{bmatrix} &= \begin{bmatrix} \mathbf{G}_{NET} & \mathbf{N}^T & \mathbf{0} \\ \mathbf{N} & \mathbf{R}_{NET} & -\mathbf{M} \\ \mathbf{0} & \mathbf{M}^T & \mathbf{0} \end{bmatrix} \cdot \begin{bmatrix} \mathbf{v}_{VSI} \\ \mathbf{i}_{EM} \\ \mathbf{v}_{NET} \end{bmatrix} \cong \\ &\cong \begin{bmatrix} \mathbf{0} & \mathbf{N}^T & \mathbf{0} \\ \mathbf{N} & \mathbf{0} & -\mathbf{M} \\ \mathbf{0} & \mathbf{M}^T & \mathbf{0} \end{bmatrix} \cdot \begin{bmatrix} \mathbf{v}_{VSI} \\ \mathbf{i}_{EM} \\ \mathbf{v}_{NET} \end{bmatrix} \end{aligned} \quad (4.12)$$

A schematic illustration of the analysed network representation is depicted in Fig. 4.9.

Note that the auxiliary voltages set  $\mathbf{v}_{EM}$  is strictly related to the choice of the constraints matrix  $\mathbf{M}$ . As previously stated, the same electrical configuration can be

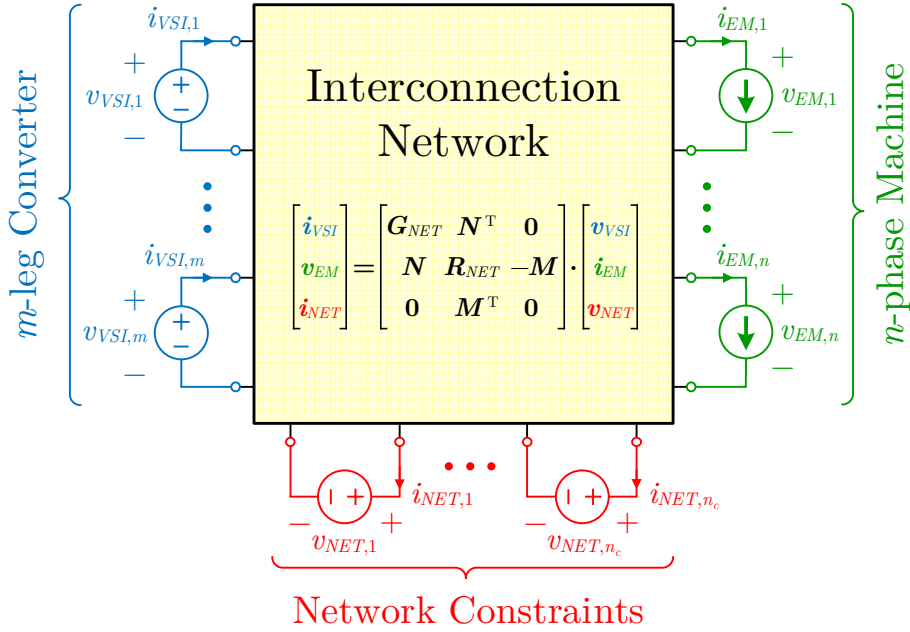


Fig. 4.9 – Multiport representation of a constrained electrical network with the introduction of the auxiliary network voltages.

associated with different algebraic equations and, therefore, to different constraints matrices  $\mathbf{M}$ . This means that the auxiliary voltages set  $\mathbf{v}_{EM}$  must be chosen depending on  $\mathbf{M}$ , in a way to meet (4.9). However, as also explained and exemplified in the following, this does not affect the overall model validity and only changes the physical interpretation given to the elements of  $\mathbf{v}_{EM}$ .

### 4.3.3 Network internal feedback action

The introduction of the auxiliary set of voltages  $\mathbf{v}_{NET}$  has made it possible to replace the constrained physical network with an unconstrained augmented network, which can be modelled through (4.12) as a linear a-dynamical multiport system.

From (4.12) the machine voltages set can be written as:

$$\mathbf{v}_{EM} = \mathbf{N} \cdot \mathbf{v}_{VSI} - \mathbf{R}_{NET} \cdot \mathbf{i}_{EM} - \mathbf{M} \cdot \mathbf{v}_{NET} \cong \mathbf{N} \cdot \mathbf{v}_{VSI} - \mathbf{M} \cdot \mathbf{v}_{NET} \quad (4.13)$$

By comparing (4.13) with (4.4) it can be seen that the set  $\mathbf{v}_{NET}$  of additional auxiliary voltage sources actively affects the phase windings voltages set  $\mathbf{v}_{EM}$  of the electrical machine, according to the same matrix  $\mathbf{M}$  which defines the currents constraints. In this case, the sole knowledge of the converter leg voltages set  $\mathbf{v}_{VSI}$  and of the machine currents  $\mathbf{i}_{EM}$  is not enough to completely analyse the system, and the block diagram of Fig. 4.3 is modified to the diagram of Fig. 4.10.

To make this augmented system behave exactly like the physical one (i.e., like the original constrained system), the set  $\mathbf{v}_{NET}$  cannot assume any arbitrary value, but it must adapt itself in a way that it always results  $\mathbf{i}_{NET} = \mathbf{M}^T \cdot \mathbf{i}_{EM} = \mathbf{0}$ . This happens when  $\mathbf{v}_{NET}$  is exactly equal to the open-circuit voltage measured in the physical system.

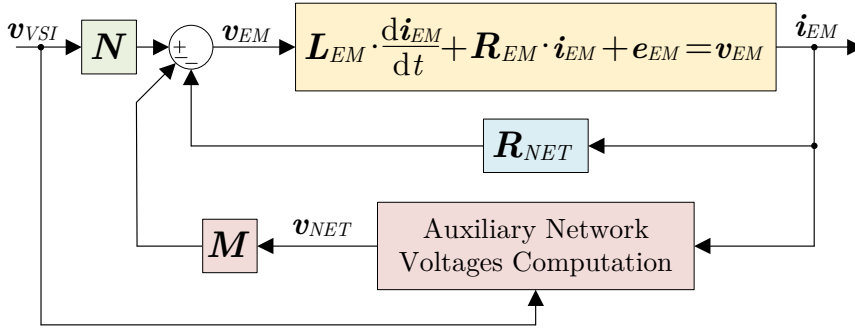


Fig. 4.10 – Functional block diagram of the electrical equations in case of a constrained interconnection network.

Then, from a different perspective, each auxiliary voltage  $v_{NET,h}$  (with  $h = 1, \dots, n_c$ ) can be interpreted as the electrical potential shift between two different nodes of the real physical system. In this context, the possibility to model the same physical system with multiple formulations (depending on the choice of  $\mathbf{M}$ ) can be interpreted as modelling the same network with respect to the open-circuit voltage between different nodes.

However, the auxiliary voltage set  $v_{NET}$  does not only depend on the converter voltages  $v_{VSI}$ , but it is also influenced by the internal behaviour of the electrical machine, as schematically represented by the “*Auxiliary Network Voltages Computation*” block of Fig. 4.10. Consequently, the voltages  $v_{EM}$  at the machine windings are also linked to the machine parameters.

As an example, it can be proven that, for the machine model provided in (2.35), the general expression of the auxiliary voltages set is<sup>5</sup>:

$$\mathbf{v}_{NET} = (\mathbf{M}^T \cdot \boldsymbol{\Gamma}_{EM} \cdot \mathbf{M})^{-1} \cdot \mathbf{M}^T \cdot \boldsymbol{\Gamma}_{EM} \cdot [\mathbf{N} \cdot \mathbf{v}_{VSI} + \dots - (\mathbf{R}_{EM} + \mathbf{R}_{NET}) \cdot \mathbf{i}_{EM} - \mathbf{e}_{EM}] \quad (4.14)$$

This expression is influenced by all the electrical machine parameters. By substituting it in (4.13) and by defining the matrix:

$$\mathbf{F} = \mathbf{M} \cdot (\mathbf{M}^T \cdot \boldsymbol{\Gamma}_{EM} \cdot \mathbf{M})^{-1} \cdot \boldsymbol{\Gamma}_{EM} \quad (4.15)$$

the machine voltages could be rewritten as:

$$\mathbf{v}_{EM} = \mathbf{N}_{ext} \cdot \mathbf{v}_{VSI} - \mathbf{R}_{NET,ext} \cdot \mathbf{i}_{EM} + \mathbf{e}_{EM,ext} \quad (4.16)$$

where the expression of these equivalent parameters is:

$$\begin{aligned} \mathbf{N}_{ext} &= (\mathbf{I} - \mathbf{F}) \cdot \mathbf{N} \\ \mathbf{R}_{ext} &= (\mathbf{I} - \mathbf{F}) \cdot \mathbf{R}_{NET} - \mathbf{F} \cdot \mathbf{R}_{EM} \\ \mathbf{e}_{EM,ext} &= -\mathbf{F} \cdot \mathbf{e}_{EM} \end{aligned} \quad (4.17)$$

Physically, the expressions (4.14) and (4.16) can be interpreted as a result of a

<sup>5</sup> Proven in Appendix 9.4.4.

feedback action acting inside the constrained electrical network, which automatically links the voltages set  $\mathbf{v}_{NET}$  to the internal machine dynamical behaviour. This feedback action is weighted by the matrix  $\mathbf{F}$  defined in (4.15) which, for this reason, is here named *network internal feedback matrix*. This matrix is non-dimensional and depends both on the network configuration (via the constraint matrix  $\mathbf{M}$ ) and on the machine parameters (via the reluctances matrix  $\mathbf{\Gamma}_{EM}$ , which is worth recalling that, in general, is a function of the rotor position  $\theta$ ). For an unconstrained network, the expression (4.16) is reduced to the expression (4.4) by simply putting  $\mathbf{F} = \mathbf{0}$ , which can be interpreted as the absence of any internal feedback action.

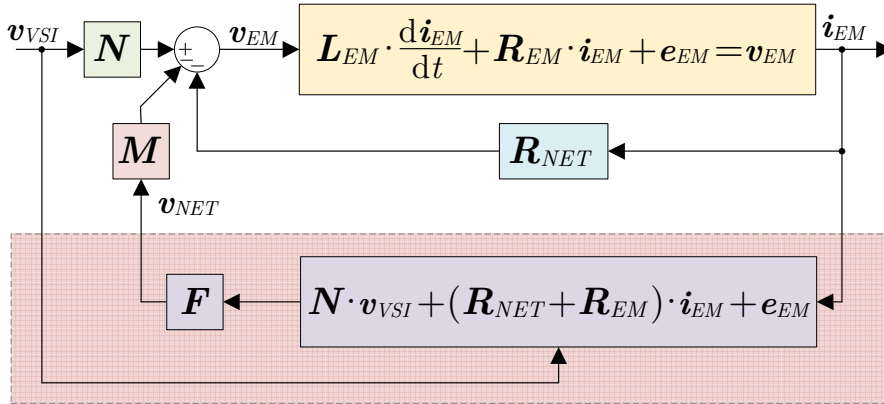
Considering (4.14), a more detailed representation of the schematic block diagram of Fig. 4.10 is reported in Fig. 4.11, where the functional dependence of  $\mathbf{v}_{NET}$  on  $\mathbf{v}_{VSI}$  and  $\mathbf{i}_{EM}$  is given explicitly.

#### 4.3.4 Full order electrical drive model

By combining the machine model (2.35) with the network equation (4.13), it is possible to describe the electrical machine equations as:

$$\begin{aligned} \mathbf{L}_{EM} \cdot \frac{d\mathbf{i}_{EM}}{dt} + \mathbf{R}_{EM} \cdot \mathbf{i}_{EM} + \mathbf{e}_{EM} &= \mathbf{v}_{EM} = \\ &= \mathbf{N} \cdot \mathbf{v}_{VSI} - \mathbf{R}_{NET} \cdot \mathbf{i}_{EM} - \mathbf{M} \cdot \mathbf{v}_{NET} = \\ &= \mathbf{N}_{ext} \cdot \mathbf{v}_{VSI} - \mathbf{R}_{NET,ext} \cdot \mathbf{i}_{EM} + \mathbf{e}_{EM,ext} \end{aligned} \quad (4.18)$$

By substituting the parameters expression (4.17) and by properly grouping the various terms, the overall drive electrical equations are<sup>6</sup>:



#### Auxiliary Network Voltages Computation

Fig. 4.11 – Explicit representation of the functional block diagram of the electrical equations for the machine model developed in Chapter 2.

<sup>6</sup> Proven in Appendix 9.4.5.

$$\begin{aligned} \mathbf{L}_{EM} \cdot \frac{d\mathbf{i}_{EM}}{dt} + (\mathbf{I} - \mathbf{F}) \cdot [(\mathbf{R}_{EM} + \mathbf{R}_{NET}) \cdot \mathbf{i}_{EM} + \mathbf{e}_{EM}] = \\ = (\mathbf{I} - \mathbf{F}) \cdot \mathbf{N} \cdot \mathbf{v}_{VSI} \end{aligned} \quad (4.19)$$

The equation (4.19) represents a dynamical system of order  $n$ , which again refers to the schematic block diagram given in Fig. 4.11. Similarly to (4.5), the input of this system is represented by the  $m \times 1$  set of converter voltages  $\mathbf{v}_{VSI}$ , but in this case the input matrix  $(\mathbf{I} - \mathbf{F}) \cdot \mathbf{N}$  depends both on the network configuration and on the system parameters (in general, including also the rotor position  $\theta$ ).

Together with the electromagnetic torque equation (2.33) and to the mechanical equations (2.3)-(2.4), the equation (4.19) completely describes the electrical behaviour of the considered drive and, through the matrix  $\mathbf{F}$ , this model automatically includes the effects of the current constraints on the machine behaviour. Again, for an unconstrained network, the expression (4.19) can be reduced to the expression (4.5) by simply putting  $\mathbf{F} = \mathbf{0}$ .

Similarly to (4.6), the *canonical state-space representation* corresponding to (4.19) can be found by multiplying both terms by  $\mathbf{\Gamma}_{EM}$  and by isolating the current derivatives, resulting in:

$$\begin{aligned} \frac{d\mathbf{i}_{EM}}{dt} = [-\mathbf{\Gamma}_{EM} \cdot (\mathbf{I} - \mathbf{F}) \cdot (\mathbf{R}_{EM} + \mathbf{R}_{NET})] \cdot \mathbf{i}_{EM} + \dots \\ \dots + [\mathbf{\Gamma}_{EM} \cdot (\mathbf{I} - \mathbf{F}) \cdot \mathbf{N}] \cdot \mathbf{v}_{VSI} + [-\mathbf{\Gamma}_{EM} \cdot (\mathbf{I} - \mathbf{F}) \cdot \mathbf{e}_{EM}] = \\ = \mathbf{A}_{EM} \cdot \mathbf{i}_{EM} + \mathbf{B}_{EM} \cdot \mathbf{v}_{VSI} + \mathbf{d}_{EM} \end{aligned} \quad (4.20)$$

where  $\mathbf{A}_{EM}$  is the state matrix of the system,  $\mathbf{B}_{EM}$  is the state space input matrix of the system and  $\mathbf{d}_{EM}$  is an equivalent disturbance input.

### 4.3.5 Examples

To better explain the proposed modelling approach of the electrical network in presence of constraints on the phase currents, some examples are here provided to show how the matrices in (4.12) can be computed. Again, most of the examples refer to the architectures introduced in Section 3.1.2. In the following, the wiring resistances and parasitic conductances will always be neglected, meaning that it will always result  $\mathbf{R}_{NET} = \mathbf{0}$  and  $\mathbf{G}_{NET} = \mathbf{0}$ . Then, the examples will focus on the computation of  $\mathbf{N}$  and  $\mathbf{M}$ . Again, all the following examples, by focusing only on the network model, are valid regardless of the nature of the supplied machine (e.g., PMSM, IM, SynRM, etc...). The effect of the machine internal behaviour (which, as previously explained, act as an internal feedback in the overall model through (4.14)), depends on the specific machine parameters and is not here explicitly addressed.

#### Single-star configuration

Consider a six-phase machine ( $n = 6$ ) supplied by a six-leg converter ( $m = 6$ ) and connected in a single-star configuration with a single isolated neutral point, as depicted in Fig. 4.12.

The single isolated neutral point forces the sum of all the phase currents to be zero, meaning that there is a single current constraint ( $n_c = 1$ ) which can be expressed as:

$$i_{EM,1} + i_{EM,2} + i_{EM,3} + i_{EM,4} + i_{EM,5} + i_{EM,6} = 0$$

By considering the auxiliary network voltage  $v_{NET}$  to be the voltage between the machine neutral point and the converter reference node, by applying Kirchhoff's laws it results that:

$$\begin{aligned} i_{VSI,1} &= i_{EM,1}, & v_{EM,1} &= v_{VSI,1} - v_{NET}, \\ i_{VSI,2} &= i_{EM,2}, & v_{EM,2} &= v_{VSI,2} - v_{NET}, \\ i_{VSI,3} &= i_{EM,3}, & v_{EM,3} &= v_{VSI,3} - v_{NET}, \\ i_{VSI,4} &= i_{EM,4}, & v_{EM,4} &= v_{VSI,4} - v_{NET}, \\ i_{VSI,5} &= i_{EM,5}, & v_{EM,5} &= v_{VSI,5} - v_{NET}, \\ i_{VSI,6} &= i_{EM,6}, & v_{EM,6} &= v_{VSI,6} - v_{NET} \end{aligned}$$

The converter voltages and currents can be grouped in the  $6 \times 1$  sets  $\mathbf{v}_{VSI} = [v_{VSI,1}, \dots, v_{VSI,6}]^T$  and  $\mathbf{i}_{VSI} = [i_{VSI,1}, \dots, i_{VSI,6}]^T$ , respectively, while the electrical machine voltages and currents can be grouped in the  $6 \times 1$  sets  $\mathbf{v}_{EM} = [v_{EM,1}, \dots, v_{EM,6}]^T$  and  $\mathbf{i}_{EM} = [i_{EM,1}, \dots, i_{EM,6}]^T$ , respectively.

From the previous equations, it results that:

- the constraint on the phase currents set  $\mathbf{i}_{EM}$  and the effect of the auxiliary network voltage  $v_{NET}$  to the machine voltages set  $\mathbf{v}_{EM}$  can be modelled by the  $6 \times 1$  constraint matrix:

$$M = \begin{bmatrix} 1 \\ 1 \\ 1 \\ 1 \\ 1 \\ 1 \end{bmatrix}$$

- the VSI current set  $\mathbf{i}_{VSI}$  is independent of the VSI voltages set  $\mathbf{v}_{VSI}$ , meaning that  $\mathbf{G}_{NET} = \mathbf{0}$ ,
- the EM voltages set  $\mathbf{v}_{EM}$  are unaffected by the EM currents set  $\mathbf{i}_{EM}$ , meaning

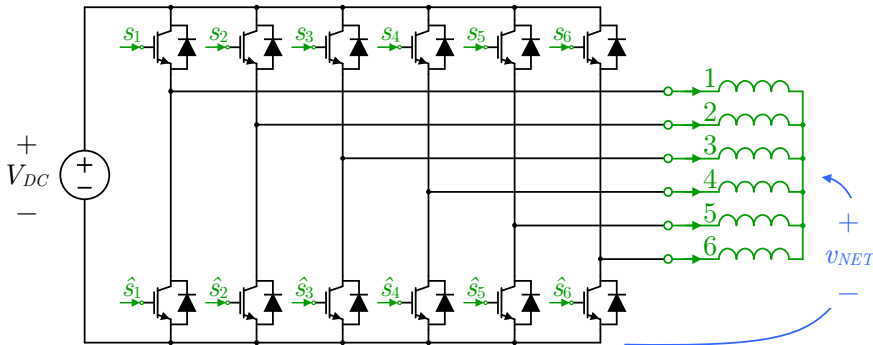


Fig. 4.12 – Six-phase machine in a single-star configuration.

that  $\mathbf{R}_{NET} = \mathbf{0}$ , and

- the mutual relationship between  $\mathbf{v}_{EM}$  and  $\mathbf{v}_{VSI}$  and between  $\mathbf{i}_{EM}$  and  $\mathbf{i}_{VSI}$  are identified by the  $6 \times 6$  network interconnection matrix

$$\mathbf{N} = \mathbf{I} = \begin{bmatrix} 1 & 0 & 0 & 0 & 0 & 0 \\ 0 & 1 & 0 & 0 & 0 & 0 \\ 0 & 0 & 1 & 0 & 0 & 0 \\ 0 & 0 & 0 & 1 & 0 & 0 \\ 0 & 0 & 0 & 0 & 1 & 0 \\ 0 & 0 & 0 & 0 & 0 & 1 \end{bmatrix}$$

### Multiple-star configuration

Consider again a six-phase machine ( $n = 6$ ) supplied by a six-leg converter ( $m = 6$ ), but connected in a double-star configuration with two isolated neutral points, as shown in Fig. 4.13

The two isolated neutral points force the sum of the corresponding phase currents to be zero, meaning that there are two current constraints ( $n_c = 2$ ) which can be expressed as the equations:

$$\begin{aligned} i_{EM,1} + i_{EM,2} + i_{EM,3} &= 0, \\ i_{EM,4} + i_{EM,5} + i_{EM,6} &= 0 \end{aligned}$$

By considering the auxiliary network voltages  $v_{NET,1}$  and  $v_{NET,2}$  to be the voltages between the machine neutral points and the converter reference node, by applying Kirchhoff's laws it results that:

$$\begin{aligned} i_{VSI,1} &= i_{EM,1}, & v_{EM,1} &= v_{VSI,1} - v_{NET,1}, \\ i_{VSI,2} &= i_{EM,2}, & v_{EM,2} &= v_{VSI,2} - v_{NET,1}, \\ i_{VSI,3} &= i_{EM,3}, & v_{EM,3} &= v_{VSI,3} - v_{NET,1}, \\ i_{VSI,4} &= i_{EM,4}, & v_{EM,4} &= v_{VSI,4} - v_{NET,2}, \\ i_{VSI,5} &= i_{EM,5}, & v_{EM,5} &= v_{VSI,5} - v_{NET,2}, \\ i_{VSI,6} &= i_{EM,6}, & v_{EM,6} &= v_{VSI,6} - v_{NET,2} \end{aligned}$$

The converter variables can be grouped in the  $6 \times 1$  sets  $\mathbf{v}_{VSI} = [v_{VSI,1}, \dots, v_{VSI,6}]^T$

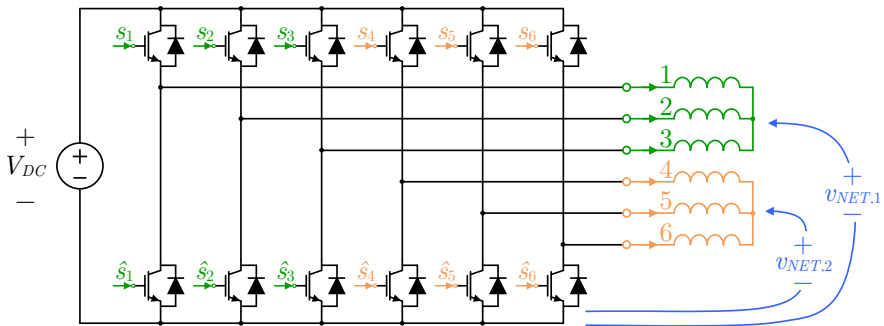


Fig. 4.13 – Six-phase machine in a double-star configuration.

and  $\mathbf{i}_{VSI} = [i_{VSI,1}, \dots, i_{VSI,6}]^T$ , respectively, while the electrical machine variables can be grouped in the  $6 \times 1$  sets  $\mathbf{v}_{EM} = [v_{EM,1}, \dots, v_{EM,6}]^T$  and  $\mathbf{i}_{EM} = [i_{EM,1}, \dots, i_{EM,6}]^T$ , respectively. The auxiliary voltages can be grouped in the  $2 \times 1$  set  $\mathbf{v}_{NET} = [v_{NET,1}, v_{NET,2}]^T$ .

From the previous equations, it results that:

- the constraints on the phase currents set  $\mathbf{i}_{EM}$  and the effect of the auxiliary network voltages set  $\mathbf{v}_{NET}$  on the machine voltages set  $\mathbf{v}_{EM}$  can be modelled by the  $6 \times 2$  constraint matrix:

$$\mathbf{M} = \begin{bmatrix} 1 & 0 \\ 1 & 0 \\ 1 & 0 \\ 0 & 1 \\ 0 & 1 \\ 0 & 1 \end{bmatrix}$$

- the VSI current set  $\mathbf{i}_{VSI}$  is independent of the VSI voltages set  $\mathbf{v}_{VSI}$ , meaning that  $\mathbf{G}_{NET} = \mathbf{0}$ ,
- the EM voltages set  $\mathbf{v}_{EM}$  are unaffected by the EM currents set  $\mathbf{i}_{EM}$ , meaning that  $\mathbf{R}_{NET} = \mathbf{0}$ , and
- the mutual relationship between  $\mathbf{v}_{EM}$  and  $\mathbf{v}_{VSI}$  and between  $\mathbf{i}_{EM}$  and  $\mathbf{i}_{VSI}$  are identified by the  $6 \times 6$  network interconnection matrix

$$\mathbf{N} = \mathbf{I} = \begin{bmatrix} 1 & 0 & 0 & 0 & 0 & 0 \\ 0 & 1 & 0 & 0 & 0 & 0 \\ 0 & 0 & 1 & 0 & 0 & 0 \\ 0 & 0 & 0 & 1 & 0 & 0 \\ 0 & 0 & 0 & 0 & 1 & 0 \\ 0 & 0 & 0 & 0 & 0 & 1 \end{bmatrix}$$

Generally speaking, when the number of machine phases is equal to the number of converter legs and each machine phase is directly connected to the positive terminal of the corresponding converter leg, all the single and multiple-star configurations are such that  $\mathbf{N} = \mathbf{I}$ . As will be shown in Chapter 6, this can drastically simplify the machine control.

The same configuration could also have been studied by modelling the constraints differently. Indeed, the same algebraic constraints could have also been modelled as:

$$\begin{aligned} i_{EM,1} + i_{EM,2} + i_{EM,3} + i_{EM,4} + i_{EM,5} + i_{EM,6} &= 0, \\ i_{EM,1} + i_{EM,2} + i_{EM,3} &= 0 \end{aligned}$$

which is a different set of equations describing the same constraints (they are linear combinations of the previously computed constraints equations). In this case, the corresponding constraints matrix would be:

$$\mathbf{M} = \begin{bmatrix} 1 & 1 \\ 1 & 1 \\ 1 & 1 \\ 1 & 0 \\ 1 & 0 \\ 1 & 0 \end{bmatrix}$$

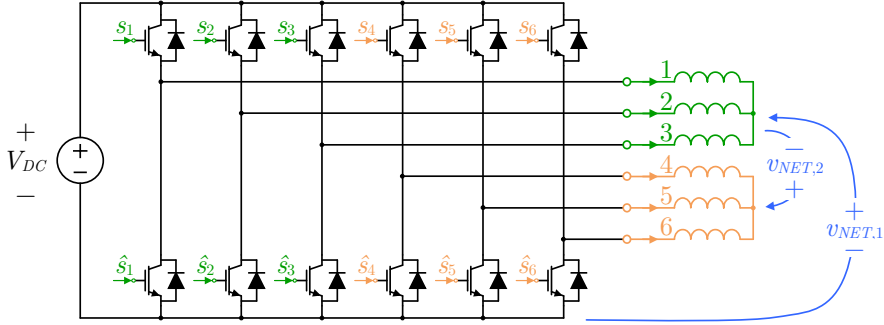


Fig. 4.14 – Six-phase machine in a double-star configuration; alternative formalization of the auxiliary network voltages.

and it can be directly found by the previous equations since  $\mathbf{M}^T \cdot \mathbf{i} = \mathbf{0}$ .

In this case, the auxiliary network voltages  $v_{NET,1}$  and  $v_{NET,2}$  related to  $\mathbf{M}$  must be chosen with a different physical interpretation. Indeed, to meet the conditions (4.9), the voltage sources of  $v_{NET,1}$  and  $v_{NET,2}$  must be chosen to identify the voltages between the neutral point  $N_1$  and the converter node  $O$  and the voltage between the neutral point  $N_2$  and the neutral point  $N_1$ , respectively. A physical interpretation can be deduced by Fig. 4.14. By applying Kirchhoff's laws it is possible to write:

$$\begin{aligned}
 i_{VSI,1} &= i_{EM,1}, & v_{EM,1} &= v_{VSI,1} - v_{NET,1}, \\
 i_{VSI,2} &= i_{EM,2}, & v_{EM,2} &= v_{VSI,2} - v_{NET,1}, \\
 i_{VSI,3} &= i_{EM,3}, & v_{EM,3} &= v_{VSI,3} - v_{NET,1}, \\
 i_{VSI,4} &= i_{EM,4}, & v_{EM,4} &= v_{VSI,4} - v_{NET,1} - v_{NET,2}, \\
 i_{VSI,5} &= i_{EM,5}, & v_{EM,5} &= v_{VSI,5} - v_{NET,1} - v_{NET,2}, \\
 i_{VSI,6} &= i_{EM,6}, & v_{EM,6} &= v_{VSI,6} - v_{NET,1} - v_{NET,2}
 \end{aligned}$$

By using a matrix notation, it can be verified that  $\mathbf{N}$  is still the  $6 \times 6$  identity matrix, while the effect of the new set of auxiliary voltages  $\mathbf{v}_{NET} = [v_{NET,1}, v_{NET,2}]^T$  on the machine voltages set  $\mathbf{v}_{EM}$  refers to the new constraint matrix  $\mathbf{M}$ .

The two models are completely equivalent and only differ in the physical interpretation given to  $\mathbf{v}_{NET}$ . Generally speaking, since there can be multiple approaches to model the same drive, it is convenient to first compute  $\mathbf{M}$  from the equations of the constraints applied to the machine currents (which can be written in an arbitrary way) and then deduce the physical meaning of  $\mathbf{v}_{NET}$  from the matrix  $\mathbf{M}$  via (4.9). However, as shown later on, a physical interpretation of  $\mathbf{v}_{NET}$ , although useful to better understand the drive behaviour, is not required for control purposes, for which the simple computation of  $\mathbf{M}$  from the constraints equations is typically enough.

## Open-circuit faults

Consider the same six-phase machine example of the previous case and suppose there is a fault on phase 1, as in Fig. 4.15.

Again, the two isolated neutral points force the sum of the corresponding phase currents to be zero, but in this case an additional constraint is introduced by the open-circuit fault. Then,  $n_c = 3$  and the expressions of these constraints can be written as:

$$\begin{aligned} i_{EM,1} + i_{EM,2} + i_{EM,3} &= 0, \\ i_{EM,4} + i_{EM,5} + i_{EM,6} &= 0, \\ i_{EM,1} &= 0, \end{aligned}$$

By considering the auxiliary network voltages  $v_{NET,1}$  and  $v_{NET,2}$  to be the voltages between the machine neutral points and the converter reference node, and the network voltage  $v_{NET,3}$  to be the voltage at the open-circuit fault, by applying Kirchoff's laws it results that:

$$\begin{aligned} i_{VSI,1} &= i_{EM,1}, & v_{EM,1} &= v_{VSI,1} - v_{NET,1} - v_{NET,3}, \\ i_{VSI,2} &= i_{EM,2}, & v_{EM,2} &= v_{VSI,2} - v_{NET,1}, \\ i_{VSI,3} &= i_{EM,3}, & v_{EM,3} &= v_{VSI,3} - v_{NET,1}, \\ i_{VSI,4} &= i_{EM,4}, & v_{EM,4} &= v_{VSI,4} - v_{NET,2}, \\ i_{VSI,5} &= i_{EM,5}, & v_{EM,5} &= v_{VSI,5} - v_{NET,2}, \\ i_{VSI,6} &= i_{EM,6}, & v_{EM,6} &= v_{VSI,6} - v_{NET,2} \end{aligned}$$

The converter voltages and currents can be grouped in the  $6 \times 1$  sets  $\mathbf{v}_{VSI} = [v_{VSI,1}, \dots, v_{VSI,6}]^T$  and  $\mathbf{i}_{VSI} = [i_{VSI,1}, \dots, i_{VSI,6}]^T$ , respectively, while the electrical machine voltages and currents can be grouped in the  $6 \times 1$  sets  $\mathbf{v}_{EM} = [v_{EM,1}, \dots, v_{EM,6}]^T$  and  $\mathbf{i}_{EM} = [i_{EM,1}, \dots, i_{EM,6}]^T$ , respectively. The three auxiliary voltages can be grouped in the  $3 \times 1$  set  $\mathbf{v}_{NET} = [v_{NET,1}, v_{NET,2}, v_{NET,3}]^T$ .

From the previous equations, it results that:

- the constraints on the phase currents set  $\mathbf{i}_{EM}$  and the effect of the auxiliary network voltages set  $\mathbf{v}_{NET}$  on the machine voltages set  $\mathbf{v}_{EM}$  can be modelled by the  $6 \times 2$  constraint matrix:

$$M = \begin{bmatrix} 1 & 0 & 1 \\ 1 & 0 & 0 \\ 1 & 0 & 0 \\ 0 & 1 & 0 \\ 0 & 1 & 0 \\ 0 & 1 & 0 \end{bmatrix}$$

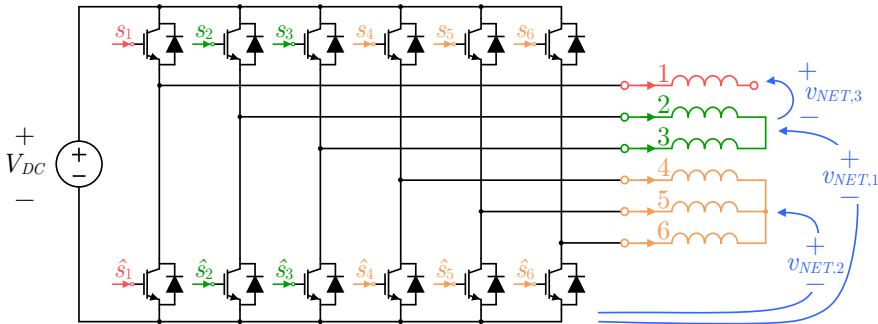


Fig. 4.15 – Six-phase machine in a double-star configuration with an open-circuit fault on phase 1.

- the VSI current set  $\mathbf{i}_{VSI}$  is independent of the VSI voltages set  $\mathbf{v}_{VSI}$ , meaning that  $\mathbf{G}_{NET} = \mathbf{0}$ ,
- the EM voltages set  $\mathbf{v}_{EM}$  are unaffected by the EM currents set  $\mathbf{i}_{EM}$ , meaning that  $\mathbf{R}_{NET} = \mathbf{0}$ , and
- the mutual relationship between  $\mathbf{v}_{EM}$  and  $\mathbf{v}_{VSI}$  and between  $\mathbf{i}_{EM}$  and  $\mathbf{i}_{VSI}$  are identified by the  $6 \times 6$  network interconnection matrix

$$\mathbf{N} = \mathbf{I} = \begin{bmatrix} 1 & 0 & 0 & 0 & 0 & 0 \\ 0 & 1 & 0 & 0 & 0 & 0 \\ 0 & 0 & 1 & 0 & 0 & 0 \\ 0 & 0 & 0 & 1 & 0 & 0 \\ 0 & 0 & 0 & 0 & 1 & 0 \\ 0 & 0 & 0 & 0 & 0 & 1 \end{bmatrix}$$

As can be seen, the fault did not change  $\mathbf{N}$ , which is still equal to the identity matrix. For machine modelling and control purposes, this is very convenient, since the adaptation of the drive model to the faulty configuration only requires changing the constraints matrix  $\mathbf{M}$ . Additional faults can also be analysed in the same way.

Again, it is worth recalling that the fault could have also been modelled with a different set of constraints equations. The resulting matrix  $\mathbf{M}$  would have been different, but the system behaviour would have been the same (it would have only changed the physical interpretation of  $\mathbf{v}_{NET}$ ).

### Open-end winding configuration

Consider a five-phase machine ( $n = 5$ ) whose windings are supplied at the two terminals by two independent five-leg converters ( $m = 10$ ) as in Fig. 4.16.

Since, for the considered configuration, the two converters are isolated from one another, the sum of all the phase currents is zero. Then, there is a single constraint ( $n_c = 1$ ) which is:

$$i_{EM,1} + i_{EM,2} + i_{EM,3} + i_{EM,4} + i_{EM,5} = 0$$

By considering the auxiliary network voltage  $v_{NET}$  to be the voltage between the reference nodes of the two converters, by applying Kirchhoff's laws it results that:

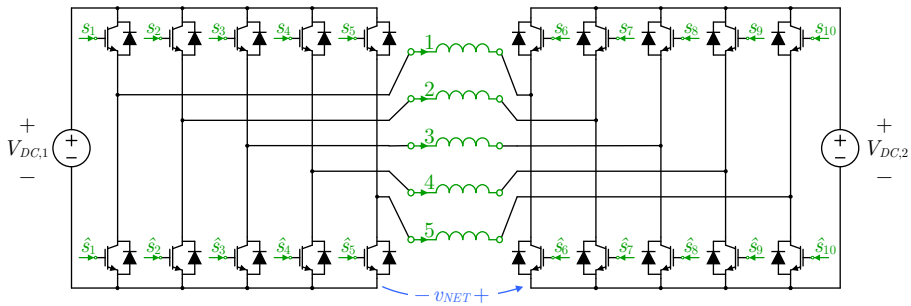


Fig. 4.16 – Five-phase machine with open-end winding supplied at both sides by two isolated five-phase converters.

$$\begin{aligned}
i_{VSI,1} &= i_{EM,1}, & i_{VSI,6} &= -i_{EM,1}, & v_{EM,1} &= v_{VSI,1} - v_{VSI,6} - v_{NET}, \\
i_{VSI,2} &= i_{EM,2}, & i_{VSI,7} &= -i_{EM,1}, & v_{EM,2} &= v_{VSI,2} - v_{VSI,7} - v_{NET}, \\
i_{VSI,3} &= i_{EM,3}, & i_{VSI,8} &= -i_{EM,1}, & v_{EM,3} &= v_{VSI,3} - v_{VSI,8} - v_{NET}, \\
i_{VSI,4} &= i_{EM,4}, & i_{VSI,9} &= -i_{EM,1}, & v_{EM,4} &= v_{VSI,4} - v_{VSI,9} - v_{NET}, \\
i_{VSI,5} &= i_{EM,5}, & i_{VSI,10} &= -i_{EM,1}, & v_{EM,5} &= v_{VSI,5} - v_{VSI,10} - v_{NET}
\end{aligned}$$

The converter voltages and currents can be grouped in the  $10 \times 1$  sets  $\mathbf{v}_{VSI} = [v_{VSI,1}, \dots, v_{VSI,10}]^T$  and  $\mathbf{i}_{VSI} = [i_{VSI,1}, \dots, i_{VSI,10}]^T$ , respectively, while the electrical machine voltages and currents can be grouped in the  $5 \times 1$  sets  $\mathbf{v}_{EM} = [v_{EM,1}, \dots, v_{EM,5}]^T$  and  $\mathbf{i}_{EM} = [i_{EM,1}, \dots, i_{EM,5}]^T$ , respectively.

From the previous equations, it results that:

- the constraint on the phase currents set  $\mathbf{i}_{EM}$  and the effect of the auxiliary network voltage  $v_{NET}$  to the machine voltages set  $\mathbf{v}_{EM}$  can be modelled by the  $5 \times 1$  constraint matrix:

$$\mathbf{M} = \begin{bmatrix} 1 \\ 1 \\ 1 \\ 1 \\ 1 \end{bmatrix}$$

- the VSI current set  $\mathbf{i}_{VSI}$  is independent of the VSI voltages set  $\mathbf{v}_{VSI}$ , meaning that  $\mathbf{G}_{NET} = \mathbf{0}$ ,
- the EM voltages set  $\mathbf{v}_{EM}$  are unaffected by the EM currents set  $\mathbf{i}_{EM}$ , meaning that  $\mathbf{R}_{NET} = \mathbf{0}$ , and
- the mutual relationship between  $\mathbf{v}_{EM}$  and  $\mathbf{v}_{VSI}$  and between  $\mathbf{i}_{EM}$  and  $\mathbf{i}_{VSI}$  are identified by the  $5 \times 10$  network interconnection matrix

$$\mathbf{N} = \begin{bmatrix} 1 & 0 & 0 & 0 & 0 & -1 & 0 & 0 & 0 & 0 \\ 0 & 1 & 0 & 0 & 0 & 0 & -1 & 0 & 0 & 0 \\ 0 & 0 & 1 & 0 & 0 & 0 & 0 & -1 & 0 & 0 \\ 0 & 0 & 0 & 1 & 0 & 0 & 0 & 0 & -1 & 0 \\ 0 & 0 & 0 & 0 & 1 & 0 & 0 & 0 & 0 & -1 \end{bmatrix}$$

Note that the constraint on the phase currents would not have been present in case a common-mode current had a possible flowing path. This would have been the case, for example, of converters with the same DC-bus or simply with the same common ground.

## Symmetrical/Asymmetrical reconfiguration

Consider a nine-phase machine ( $n = 9$ ) supplied by a nine-leg converter ( $m = 9$ ) in a single-star configuration ( $n_c = 1$ ).

As explained in [152], a nine-phase machine can be rearranged in a symmetrical configuration or in an asymmetrical configuration by just changing the order of the phase windings. In the first case, the machine windings can be grouped in three symmetrical three-phase sets mutually shifted by  $40^\circ$  with each other. In the second case, the machine windings can be grouped in three symmetrical three-phase sets mutually shifted by  $20^\circ$  with each other.

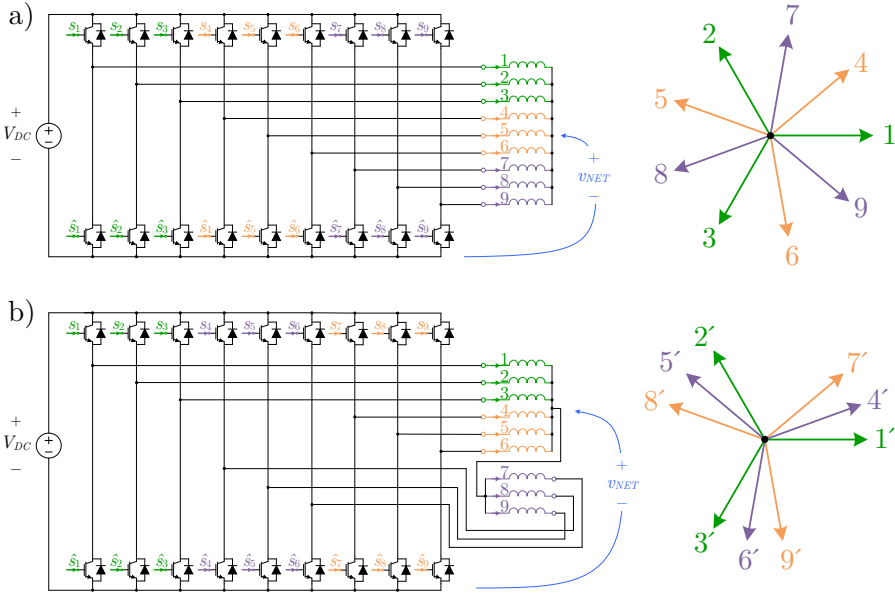


Fig. 4.17 – Two possible reconfigurations of a nine-phase machine: a) Symmetrical; b) Asymmetrical. The magnetic axes disposition has been added to facilitate the physical interpretation.

When the machine is in a symmetrical configuration, by using the same approach as in the previous examples, it can be easily verified that the drive model results in  $\mathbf{N} = \mathbf{I}$  and in  $\mathbf{M} = [1, 1, 1, 1, 1, 1, 1, 1, 1]^T$ .

With reference to Fig. 4.17, in the asymmetrical configuration it is sufficient to do the following rearrangements:

- the set  $\{1, 2, 3\}$  of the symmetrical configuration is equal to the set  $\{1', 2', 3'\}$  of the asymmetrical configuration,
- the set  $\{4, 5, 6\}$  of the symmetrical configuration becomes the set  $\{7', 8', 9'\}$  of the asymmetrical configuration, and
- the set  $\{7, 8, 9\}$  of the symmetrical configuration is connected with opposite polarity and becomes the set  $\{6', 4', 5'\}$  of the asymmetrical configuration.

By taking as reference the symmetrical configuration, the electrical connection in the asymmetrical scenario can be done as in Fig. 4.17b.

In this case, the single isolated neutral point constraint is:

$$\begin{aligned} i_{EM,1'} + i_{EM,2'} + i_{EM,3'} + i_{EM,4'} + i_{EM,5'} + i_{EM,6'} + i_{EM,7'} + i_{EM,8'} + i_{EM,9'} &= \\ &= i_{EM,1} + i_{EM,2} + i_{EM,3} - i_{EM,7} - i_{EM,8} - i_{EM,9} + i_{EM,4} + i_{EM,5} + i_{EM,6} = 0 \end{aligned}$$

The auxiliary network voltage can be again considered as the voltage between the single isolated neutral point and the converter reference node. By applying Kirchhoff's laws it results that:

$$\begin{array}{ll}
i_{VSI,1} = i_{EM,1'} = i_{EM,1}, & v_{EM,1'} = v_{EM,1} = v_{VSI,1} - v_{NET} \\
i_{VSI,2} = i_{EM,2'} = i_{EM,2}, & v_{EM,2'} = v_{EM,2} = v_{VSI,2} - v_{NET} \\
i_{VSI,3} = i_{EM,3'} = i_{EM,3}, & v_{EM,3'} = v_{EM,3} = v_{VSI,3} - v_{NET} \\
i_{VSI,4} = i_{EM,4'} = -i_{EM,8}, & v_{EM,4'} = -v_{EM,8} = v_{VSI,4} - v_{NET} \\
i_{VSI,5} = i_{EM,5'} = -i_{EM,9}, & v_{EM,5'} = -v_{EM,9} = v_{VSI,5} - v_{NET} \\
i_{VSI,6} = i_{EM,6'} = -i_{EM,7}, & v_{EM,6'} = -v_{EM,7} = v_{VSI,6} - v_{NET} \\
i_{VSI,7} = i_{EM,7'} = i_{EM,4}, & v_{EM,7'} = v_{EM,4} = v_{VSI,7} - v_{NET} \\
i_{VSI,8} = i_{EM,8'} = i_{EM,5}, & v_{EM,8'} = v_{EM,5} = v_{VSI,8} - v_{NET} \\
i_{VSI,9} = i_{EM,9'} = i_{EM,6}, & v_{EM,9'} = v_{EM,6} = v_{VSI,9} - v_{NET}
\end{array}$$

The converter voltages and currents can be grouped in the  $9 \times 1$  sets  $\mathbf{v}_{VSI} = [v_{VSI,1}, \dots, v_{VSI,9}]^T$  and  $\mathbf{i}_{VSI} = [i_{VSI,1}, \dots, i_{VSI,9}]^T$ , respectively. The electrical machine voltages and currents can be grouped in the  $9 \times 1$  sets  $\mathbf{v}_{EM} = [v_{EM,1}, \dots, v_{EM,9}]^T$  and  $\mathbf{i}_{EM} = [i_{EM,1}, \dots, i_{EM,9}]^T$ , respectively, in a way to identify the same variables of the symmetrical configuration (and using the same machine model to analyse the system).

From the previous equations it results that:

- the constraint on the phase currents set  $\mathbf{i}_{EM}$  and the effect of the auxiliary network voltage  $v_{NET}$  to the machine voltages set  $\mathbf{v}_{EM}$  can be modelled by the  $9 \times 1$  constraint matrix:

$$\mathbf{M} = \begin{bmatrix} 1 \\ 1 \\ 1 \\ 1 \\ 1 \\ 1 \\ 1 \\ -1 \\ -1 \\ -1 \end{bmatrix}$$

- the VSI current set  $\mathbf{i}_{VSI}$  is independent of the VSI voltages set  $\mathbf{v}_{VSI}$ , meaning that  $\mathbf{G}_{NET} = \mathbf{0}$ ,
- the EM voltages set  $\mathbf{v}_{EM}$  are unaffected by the EM currents set  $\mathbf{i}_{EM}$ , meaning that  $\mathbf{R}_{NET} = \mathbf{0}$ , and
- the mutual relationship between  $\mathbf{v}_{EM}$  and  $\mathbf{v}_{VSI}$  and between  $\mathbf{i}_{EM}$  and  $\mathbf{i}_{VSI}$  are identified by the  $9 \times 9$  network interconnection matrix

$$\mathbf{N} = \begin{bmatrix} 1 & 0 & 0 & 0 & 0 & 0 & 0 & 0 & 0 \\ 0 & 1 & 0 & 0 & 0 & 0 & 0 & 0 & 0 \\ 0 & 0 & 1 & 0 & 0 & 0 & 0 & 0 & 0 \\ 0 & 0 & 0 & 0 & 0 & 0 & 1 & 0 & 0 \\ 0 & 0 & 0 & 0 & 0 & 0 & 0 & 1 & 0 \\ 0 & 0 & 0 & 0 & 0 & 0 & 0 & 0 & 1 \\ 0 & 0 & 0 & 0 & 0 & -1 & 0 & 0 & 0 \\ 0 & 0 & 0 & -1 & 0 & 0 & 0 & 0 & 0 \\ 0 & 0 & 0 & 0 & -1 & 0 & 0 & 0 & 0 \end{bmatrix}$$

Once again, the set of equations describing the system can be represented synthetically with the matrix formalism as (4.12)-(4.13). Thanks to this approach, the change of the machine configuration can be studied with the same mathematical model of the original machine formulation, with the only difference being in  $\mathbf{M}$  and  $\mathbf{N}$ . In other words, once the machine parameters have been identified in the symmetrical configuration, the asymmetrical machine (which is simply obtained by rearranging the windings connection) does not need a new parameters identification.

## 4.4 Configuration space modelling

The electrical equation (4.19) completely describes the electrical drive behaviour in presence of currents constraints through the introduction of the network internal feedback matrix  $\mathbf{F}$ . However, the resulting model, despite correctly describing the machine dynamics, is not convenient for control purposes, since the matrix  $\mathbf{F}$ , which depends on the machine parameters, also multiplies the converter voltages set  $\mathbf{v}_{VSI}$ .

A different formulation, which is more convenient for control purposes, is here derived basing on the algebraic properties of the constrained system. This formalism will be useful for the decoupled control of the machine phase currents developed in Chapter 6.

### 4.4.1 Configuration space

Mathematically speaking, the machine currents set  $\mathbf{i}_{EM}$  is a vector of the  $n$ -dimensional space  $\mathbb{R}^n$ . All the feasible currents, which satisfy the constraints (4.8), belong to the null-space<sup>7</sup>  $\mathcal{N}(\mathbf{M}^T)$  of the constraints matrix  $\mathbf{M}^T$ , which is identified from the equation  $\mathbf{M}^T \cdot \mathbf{x} = \mathbf{0}$ . This null-space  $\mathcal{N}(\mathbf{M}^T)$  is a vector subspace of  $\mathbb{R}^n$  and can be mathematically interpreted as a hyperplane. It is here named *configuration space* of the system<sup>8</sup>. The orthogonal complement<sup>9</sup> of the configuration space  $\mathcal{N}^\perp(\mathbf{M}^T)$  is here named *complementary configuration space* of the system. For a known linear algebra property<sup>10</sup>, this space is equal to the range<sup>11</sup>  $\mathcal{R}(\mathbf{M})$  of the constraint matrix  $\mathbf{M}$ .

### 4.4.2 Configuration space representation

As previously stated, the configuration space  $\mathcal{N}(\mathbf{M}^T)$  is a subspace of  $\mathbb{R}^n$ . Since it is defined by  $n_c$  constraints, the dimension of  $\mathcal{N}(\mathbf{M}^T)$  is  $n_f = n - n_c$  and represents the number of degrees of freedom for the machine currents. Similarly, the complementary configuration space  $\mathcal{R}(\mathbf{M}) = \mathcal{N}^\perp(\mathbf{M}^T)$  is a subspace of  $\mathbb{R}^n$  with dimension  $n_c$ . To better identify the properties of the system, it is convenient to explore the properties of these vector spaces.

<sup>7</sup> The *null-space*, or *kernel*, of a  $r \times c$  matrix  $\mathbf{A}$ , is the set of all vectors  $\mathbf{x} \in \mathbb{R}^c$  such that  $\mathbf{A} \cdot \mathbf{x} = \mathbf{0}$ .

<sup>8</sup> This name has been chosen due to the similarity to the configuration space introduced in analytical mechanics to study the motion of rigid bodies in presence of mechanical constraints.

<sup>9</sup> Given a subspace  $\mathcal{S} \subseteq \mathbb{R}^n$ , its *orthogonal complement*  $\mathcal{S}^\perp$  is the set of vectors  $\mathbf{x} \in \mathbb{R}^n$  such that, for any  $\mathbf{y} \in \mathcal{S}$ , it results that  $\mathbf{x}^T \cdot \mathbf{y} = 0$ .

<sup>10</sup> Recalled and proven in Appendix 9.4.6.

<sup>11</sup> The *range*, or *column space*, of a  $r \times c$  matrix  $\mathbf{A}$ , is the set of all the vectors  $\mathbf{y} \in \mathbb{R}^r$  which can be expressed as  $\mathbf{y} = \mathbf{A} \cdot \mathbf{x}$ .

This operation can be done through the *singular value decomposition* (SVD) of the constraints matrix  $\mathbf{M}$ . The  $n \times n_c$  constraints matrix  $\mathbf{M}$  can be expressed as [118]:

$$\mathbf{M} = \mathbf{U} \cdot \boldsymbol{\Sigma} \cdot \mathbf{V}^T = [\mathbf{U}_c \quad \mathbf{U}_f] \cdot \begin{bmatrix} \tilde{\boldsymbol{\Sigma}} \\ \mathbf{0} \end{bmatrix} \cdot \mathbf{V}^T = \mathbf{U}_c \cdot \tilde{\boldsymbol{\Sigma}} \cdot \mathbf{V}^T \quad (4.21)$$

where:

- $\mathbf{U}$  is a  $n \times n$  unitary matrix (i.e.,  $\mathbf{U} \cdot \mathbf{U}^T = \mathbf{U}^T \cdot \mathbf{U} = \mathbf{I}$ ) whose columns are called *left singular vectors* of  $\mathbf{M}$ , which has been split into two rectangular submatrices:
  - $\mathbf{U}_c$ , which is the set of the first  $n_c$  left singular vectors,
  - $\mathbf{U}_f$ , which is the set of the last  $n_f$  left singular vectors,
- $\mathbf{V}$  is a  $n_c \times n_c$  unitary matrix (i.e.,  $\mathbf{V} \cdot \mathbf{V}^T = \mathbf{V}^T \cdot \mathbf{V} = \mathbf{I}$ ) whose columns are called *right singular vectors* of  $\mathbf{M}$ , and
- $\boldsymbol{\Sigma}$  is a  $n \times n_c$  rectangular matrix, whose non-diagonal elements are all zero (i.e.,  $\Sigma_{k,h} = 0$  with  $k \neq h$ ) and whose diagonal elements, called *singular values* of  $\mathbf{M}$ , are all positive (i.e.,  $\Sigma_{k,k} = \sigma_k > 0$ , with  $k = 1, \dots, n_c$ ). The singular values have been grouped in the  $n_c \times n_c$  diagonal matrix  $\tilde{\boldsymbol{\Sigma}}$ , which is therefore symmetric (i.e.,  $\tilde{\boldsymbol{\Sigma}} = \tilde{\boldsymbol{\Sigma}}^T$ ) and positive definite (i.e.,  $\mathbf{y}^T \cdot \tilde{\boldsymbol{\Sigma}} \cdot \mathbf{y} > 0, \forall \mathbf{y} \neq \mathbf{0}$ ) and, as a consequence, it is invertible.

A graphical representation of the decomposition (4.21) is depicted in Fig. 4.18.

The left singular vectors satisfy the following properties<sup>12</sup>:

$$\begin{aligned} \mathbf{U}_c^T \cdot \mathbf{U}_c &= \mathbf{I}, & \mathbf{U}_f^T \cdot \mathbf{U}_f &= \mathbf{I}, \\ \mathbf{U}_f^T \cdot \mathbf{U}_c &= \mathbf{0}, & \mathbf{U}_c^T \cdot \mathbf{U}_f &= \mathbf{0}, \end{aligned} \quad (4.22)$$

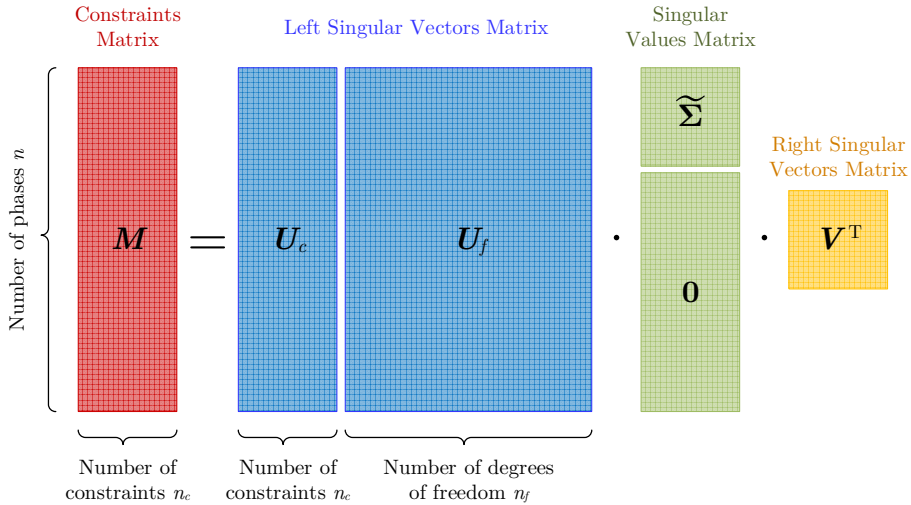


Fig. 4.18 – Singular Value Decomposition of the constraints matrix  $\mathbf{M}$ .

<sup>12</sup> Proven in Appendix 9.4.7.

$$\mathbf{U}_c \cdot \mathbf{U}_c^T + \mathbf{U}_f \cdot \mathbf{U}_f^T = \mathbf{I} \quad (4.23)$$

$$\mathbf{M}^T \cdot \mathbf{U}_c = \mathbf{V} \cdot \tilde{\Sigma}, \quad \mathbf{M}^T \cdot \mathbf{U}_f = \mathbf{0} \quad (4.24)$$

From these properties it is possible to derive the following important conclusions<sup>13</sup>:

- the matrix  $\mathbf{U}_f$  is a basis of the configuration space  $\mathcal{N}(\mathbf{M}^T)$  and, for this reason, is here named *configuration matrix*, and
- the matrix  $\mathbf{U}_c$  is a basis of the complementary configuration space  $\mathcal{N}^\perp(\mathbf{M}^T) = \mathcal{R}(\mathbf{M})$  and, for this reason, is here named *complementary configuration matrix*.

Since  $\mathbf{U}$  is a  $n \times n$  unitary matrix, it can be used as a different basis for the whole space  $\mathbb{R}^n$ . Therefore, any vector  $\mathbf{x} \in \mathbb{R}^n$  can be written as:

$$\mathbf{x} = \mathbf{U} \cdot \mathbf{y} = [\mathbf{U}_c \quad \mathbf{U}_f] \cdot \begin{bmatrix} \mathbf{y}_c \\ \mathbf{y}_f \end{bmatrix} = \mathbf{U}_c \cdot \mathbf{y}_c + \mathbf{U}_f \cdot \mathbf{y}_f \quad (4.25)$$

where, from the properties (4.22), it can be verified that:

$$\mathbf{y} = \mathbf{U}^T \cdot \mathbf{x}, \quad \mathbf{y}_c = \mathbf{U}_c^T \cdot \mathbf{x}, \quad \mathbf{y}_f = \mathbf{U}_f^T \cdot \mathbf{x} \quad (4.26)$$

The  $n \times 1$  vector  $\mathbf{y}$  represents the coordinates of  $\mathbf{x}$  expressed in the new reference frame defined by  $\mathbf{U}$ . The  $n_f \times 1$  vector  $\mathbf{y}_f$  and the  $n_c \times 1$  vector  $\mathbf{y}_c$  represent the components of the vector  $\mathbf{y}$  in the directions defined from the configuration matrix  $\mathbf{U}_f$  and from the complementary configuration matrix  $\mathbf{U}_c$ , respectively.

By combining (4.25) and (4.26), any vector  $\mathbf{x} \in \mathbb{R}^n$  can be written as:

$$\mathbf{x} = (\mathbf{U}_f \cdot \mathbf{U}_f^T) \cdot \mathbf{x} + (\mathbf{U}_c \cdot \mathbf{U}_c^T) \cdot \mathbf{x} \quad (4.27)$$

The  $n \times 1$  vector  $(\mathbf{U}_f \cdot \mathbf{U}_f^T) \cdot \mathbf{x}$  represents the projection of  $\mathbf{x}$  in  $\mathcal{N}(\mathbf{M}^T)$ , and the matrix  $(\mathbf{U}_f \cdot \mathbf{U}_f^T)$  is the projection operator in the configuration space. Similarly, the  $n \times 1$  vector  $(\mathbf{U}_c \cdot \mathbf{U}_c^T) \cdot \mathbf{x}$  represents the projection of  $\mathbf{x}$  in  $\mathcal{R}(\mathbf{M}) = \mathcal{N}^\perp(\mathbf{M}^T)$  and the matrix  $(\mathbf{U}_c \cdot \mathbf{U}_c^T)$  is the projection operator in the complementary configuration space.

### 4.4.3 Machine equations in the configuration space

As discussed in Section 4.3, the constrained network model makes the electrical machine satisfy the vector equations:

$$\begin{aligned} \mathbf{M}^T \cdot \mathbf{i}_{EM} &= \mathbf{i}_{NET} = \mathbf{0} \\ \mathbf{v}_{EM} &= \mathbf{N} \cdot \mathbf{v}_{VSI} - \mathbf{R}_{NET} \cdot \mathbf{i}_{EM} - \mathbf{M} \cdot \mathbf{v}_{NET} \end{aligned} \quad (4.28)$$

Having introduced the configuration space, these equations can be reinterpreted in a different way.

The first equation of (4.28) means that the feasible machine currents set  $\mathbf{i}_{EM}$  must belong to the configuration space  $\mathcal{N}(\mathbf{M}^T)$ . From the results obtained in Section 4.4.2, this means that  $\mathbf{i}_{EM,c} = \mathbf{U}_c^T \cdot \mathbf{i}_{EM} = \mathbf{0}$  and that the vector  $\mathbf{i}_{EM}$  can be expressed as:

$$\mathbf{i}_{EM} = \mathbf{U}_f \cdot \mathbf{i}_{EM,f}, \quad \text{with} \quad \mathbf{i}_{EM,f} = \mathbf{U}_f^T \cdot \mathbf{i}_{EM} \quad (4.29)$$

<sup>13</sup> Proven in Appendix 9.4.8.

The  $n_f \times 1$  vector  $\dot{\mathbf{i}}_{EM,f}$  represents the unconstrained current components of the system, which are the available degrees of freedom in the constrained system.

The second equation of (4.28) highlights that the electrical machine voltages depend on the auxiliary network voltages set  $\mathbf{v}_{NET}$  through the constraints matrix  $\mathbf{M}$ . By projecting both sides of the equation in the configuration space  $\mathcal{N}(\mathbf{M}^T)$  through the projection operator  $(\mathbf{U}_f \cdot \mathbf{U}_f^T)$  it results that:

$$\begin{aligned} (\mathbf{U}_f \cdot \mathbf{U}_f^T) \cdot \mathbf{v}_{EM} &= (\mathbf{U}_f \cdot \mathbf{U}_f^T) \cdot (\mathbf{N} \cdot \mathbf{v}_{VSI} - \mathbf{R}_{NET} \cdot \dot{\mathbf{i}}_{EM} - \mathbf{M} \cdot \mathbf{v}_{NET}) = \\ &= (\mathbf{U}_f \cdot \mathbf{U}_f^T) \cdot (\mathbf{N} \cdot \mathbf{v}_{VSI} - \mathbf{R}_{NET} \cdot \dot{\mathbf{i}}_{EM}) \end{aligned} \quad (4.30)$$

The equation (4.30) shows that the electrical machine voltages set  $\mathbf{v}_{EM}$  in the configuration space is only related to the converter voltages set  $\mathbf{v}_{VSI}$  and to the electrical machine currents  $\dot{\mathbf{i}}_{EM}$ , and is therefore independent of the auxiliary network voltages set  $\mathbf{v}_{NET}$ , contrarily to the full-order model (4.13).

#### 4.4.4 Reduced order electrical drive model

The electrical drive mathematical model (4.19) can be simplified by considering the configuration space concept. By pre-multiplying both sides of (4.18) for  $\mathbf{U}_f^T$  and by considering (4.29), it can be proven<sup>14</sup> that the machine behaviour in the configuration space satisfies the equation:

$$\mathbf{L}_{EM,f} \cdot \frac{d\dot{\mathbf{i}}_{EM,f}}{dt} + (\mathbf{R}_{EM,f} + \mathbf{R}_{NET,f}) \cdot \dot{\mathbf{i}}_{EM,f} + \mathbf{e}_{EM,f} = \mathbf{N}_f \cdot \mathbf{v}_{VSI} \quad (4.31)$$

where the equivalent parameters are:

$$\begin{aligned} \mathbf{L}_{EM,f} &= \mathbf{U}_f^T \cdot \mathbf{L}_{EM} \cdot \mathbf{U}_f, & \dot{\mathbf{i}}_{EM,f} &= \mathbf{U}_f^T \cdot \dot{\mathbf{i}}_{EM} \\ \mathbf{R}_{EM,f} &= \mathbf{U}_f^T \cdot \mathbf{R}_{EM} \cdot \mathbf{U}_f, & \mathbf{e}_{EM,f} &= \mathbf{U}_f^T \cdot \mathbf{e}_{EM} \\ \mathbf{R}_{NET,f} &= \mathbf{U}_f^T \cdot \mathbf{R}_{NET} \cdot \mathbf{U}_f, & \mathbf{N}_f &= \mathbf{U}_f^T \cdot \mathbf{N} \end{aligned} \quad (4.32)$$

The equation (4.31) is a dynamical system of order  $n_f \leq n$ . Similarly to the model (4.19), this equation automatically includes the machine current constraints. However, contrarily to (4.19), in this case the  $m \times 1$  input vector of the converter voltages  $\mathbf{v}_{VSI}$  is weighted by the input matrix  $\mathbf{N}_f = \mathbf{U}_f^T \cdot \mathbf{N}$ , which only depends on the network configuration (i.e., it is independent of the machine parameters). The block diagram of this system is schematically represented in Fig. 4.19. This model will be used to develop the control algorithm proposed in Chapter 6 and Chapter 7.

The equation (4.31) describes the evolution of the machine currents within the

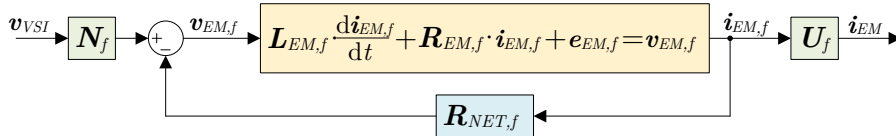


Fig. 4.19 – Functional block diagram of the reduced order system.

<sup>14</sup> Proven in Appendix 9.4.9.

configuration space, which has fewer degrees of freedom than the number of phases of the electrical machine. For this reason, it represents a *reduced order drive model*. It has the same form of the equation (4.5) for the unconstrained system and, in case the network is not subject to any constraint, it can be reconducted to the model (4.5) (schematically depicted in Fig. 4.3) by simply putting  $\mathbf{U}_f = \mathbf{I}$ .

Since the matrix  $\mathbf{L}_{EM,f}$  defined in (4.32) is symmetric and positive definite, there exists its inverse  $\mathbf{\Gamma}_{EM,f} = \mathbf{L}_{EM,f}^{-1}$ . Then, the canonical state-space representation of the reduced-order system (4.31) can be found by pre-multiplying both sides for  $\mathbf{\Gamma}_{EM,f}$  and by isolating the current derivatives, resulting in:

$$\begin{aligned} \frac{d\mathbf{i}_{EM,f}}{dt} &= [-\mathbf{\Gamma}_{EM,f} \cdot (\mathbf{R}_{EM,f} + \mathbf{R}_{NET,f})] \cdot \mathbf{i}_{EM,f} + \dots \\ &\dots + [\mathbf{\Gamma}_{EM,f} \cdot \mathbf{N}_f] \cdot \mathbf{v}_{VSI} + [-\mathbf{\Gamma}_{EM,f} \cdot \mathbf{e}_{EM,f}] = \\ &= \mathbf{A}_{EM,f} \cdot \mathbf{i}_{EM,f} + \mathbf{B}_{EM,f} \cdot \mathbf{v}_{VSI} + \mathbf{d}_{EM,f} \end{aligned} \quad (4.33)$$

where  $\mathbf{A}_{EM,f}$ ,  $\mathbf{B}_{EM,f}$  and  $\mathbf{d}_{EM,f}$  are the state matrix, the state space input matrix and the equivalent disturbance input of the reduced-order system, respectively. Similarly to the unconstrained system (4.6), also for the canonical representation (4.33) these terms also depend on the machine parameters, including the rotor position  $\theta$ , thus making the canonical representation (4.33) a time-variant system.

It is worth emphasizing that the variable transformation introduced through this configuration space approach is conceptually different from a Vector Space Decomposition (VSD). Indeed, the VSD is a variable transformation intrinsically linked to the machine design and parameters (e.g., to the disposition of the magnetic axes of the phase windings), while the proposed configuration space approach only depends on the electrical connection of the windings and to the corresponding constraints introduced to the machine phase currents (which are unrelated to the machine design and parameters). However, in some specific cases (e.g., symmetrical machines in a star configuration with a single isolated neutral point), the two approaches might lead to similar results, and the VSD transformation may also separate the configuration space variables from the complementary configuration space variables.

### 4.4.5 Examples

Two examples are here given about the computation of the configuration matrix  $\mathbf{U}_f$  and of the complementary configuration matrix  $\mathbf{U}_c$  starting from the knowledge of the constraints matrix  $\mathbf{M}$ . They are referred to the first two configurations exemplified in Section 4.3.5. The extension to all the other examples are straightforward and only requires numerical computations from the knowledge of  $\mathbf{M}$ . Other examples will also be given in Chapter 6 and in Chapter 7.

#### Single-star configuration

Consider again the six-phase configuration of Fig. 4.12, previously exemplified in Section 4.3.5. In this case  $n = 6$  and  $n_c = 1$ ; the constraint matrix has been found to be:

$$\mathbf{M} = \begin{bmatrix} 1 \\ 1 \\ 1 \\ 1 \\ 1 \\ 1 \end{bmatrix}$$

Its singular value decomposition has been computed numerically<sup>15</sup> and the corresponding matrices are:

$$\mathbf{U} = \begin{bmatrix} 0.41 & -0.41 & -0.41 & -0.41 & -0.41 & -0.41 \\ 0.41 & 0.88 & -0.12 & -0.12 & -0.12 & -0.12 \\ 0.41 & -0.12 & 0.88 & -0.12 & -0.12 & -0.12 \\ 0.41 & -0.12 & -0.12 & 0.88 & -0.12 & -0.12 \\ 0.41 & -0.12 & -0.12 & -0.12 & 0.86 & -0.12 \\ 0.41 & -0.12 & -0.12 & -0.12 & -0.12 & -0.12 \end{bmatrix}, \quad \mathbf{\Sigma} = \begin{bmatrix} 2.45 \\ 0 \\ 0 \\ 0 \\ 0 \\ 0 \end{bmatrix}, \quad \mathbf{V} = [1]$$

It can be verified that  $\mathbf{U}^T \cdot \mathbf{U} = \mathbf{U} \cdot \mathbf{U}^T = \mathbf{I}$  (i.e., it is the  $6 \times 6$  identity matrix) and that  $\mathbf{V}^T \cdot \mathbf{V} = \mathbf{V} \cdot \mathbf{V}^T = 1$  (i.e., it is the  $1 \times 1$  identity matrix).

The configuration matrix  $\mathbf{U}_f$  is given by the last  $n - n_c = 4 - 1 = 5$  columns of  $\mathbf{U}$ , while the complementary configuration matrix  $\mathbf{U}_c$  is instead only the first column of  $\mathbf{U}$ :

$$\mathbf{U}_c = \begin{bmatrix} 0.41 \\ 0.41 \\ 0.41 \\ 0.41 \\ 0.41 \\ 0.41 \end{bmatrix}, \quad \mathbf{U}_f = \begin{bmatrix} -0.41 & -0.41 & -0.41 & -0.41 & -0.41 \\ 0.88 & -0.12 & -0.12 & -0.12 & -0.12 \\ -0.12 & 0.88 & -0.12 & -0.12 & -0.12 \\ -0.12 & -0.12 & 0.88 & -0.12 & -0.12 \\ -0.12 & -0.12 & -0.12 & 0.86 & -0.12 \\ -0.12 & -0.12 & -0.12 & -0.12 & -0.12 \end{bmatrix}$$

It can be verified that the properties (4.22)-(4.24) are satisfied, and that  $\mathbf{U}_c^T \cdot \mathbf{U}_c = 1$  (i.e., it is the  $1 \times 1$  identity matrix),  $\mathbf{U}_f^T \cdot \mathbf{U}_f = \mathbf{I}$  (i.e., it is the  $5 \times 5$  identity matrix), and  $\mathbf{U}_f^T \cdot \mathbf{U}_c = \mathbf{0}$  (i.e., it is a  $5 \times 1$  vector with all the elements equal to zero).

Finally, the projection matrices in the configuration space and in the complementary configuration space are:

$$\mathbf{U}_f \cdot \mathbf{U}_f^T = \begin{bmatrix} 0.83 & -0.17 & -0.17 & -0.17 & -0.17 & -0.17 \\ -0.17 & 0.83 & -0.17 & -0.17 & -0.17 & -0.17 \\ -0.17 & -0.17 & 0.83 & -0.17 & -0.17 & -0.17 \\ -0.17 & -0.17 & -0.17 & 0.83 & -0.17 & -0.17 \\ -0.17 & -0.17 & -0.17 & -0.17 & 0.83 & -0.17 \\ -0.17 & -0.17 & -0.17 & -0.17 & -0.17 & 0.83 \end{bmatrix},$$

<sup>15</sup> The singular value decompositions in the proposed examples have been computed in MATLAB through the “svd” command. The results here reported have been rounded to the second decimal unit.

$$\mathbf{U}_c \cdot \mathbf{U}_c^T = \begin{bmatrix} 0.17 & 0.17 & 0.17 & 0.17 & 0.17 & 0.17 \\ 0.17 & 0.17 & 0.17 & 0.17 & 0.17 & 0.17 \\ 0.17 & 0.17 & 0.17 & 0.17 & 0.17 & 0.17 \\ 0.17 & 0.17 & 0.17 & 0.17 & 0.17 & 0.17 \\ 0.17 & 0.17 & 0.17 & 0.17 & 0.17 & 0.17 \\ 0.17 & 0.17 & 0.17 & 0.17 & 0.17 & 0.17 \end{bmatrix}$$

Note that, while  $\mathbf{U}_f^T \cdot \mathbf{U}_f = \mathbf{I}$  and  $\mathbf{U}_c^T \cdot \mathbf{U}_c = \mathbf{I}$  (i.e., the columns of  $\mathbf{U}_f$  and  $\mathbf{U}_c$  are orthogonal),  $\mathbf{U}_f \cdot \mathbf{U}_f^T \neq \mathbf{I}$  and  $\mathbf{U}_c \cdot \mathbf{U}_c^T \neq \mathbf{I}$  (i.e., the rows of  $\mathbf{U}_f$  and  $\mathbf{U}_c$  are not orthogonal). Again, it can be verified that the property (4.23) is satisfied.

From the numerical evaluation of the projection matrices, it can be noted that the matrix  $\mathbf{U}_f \cdot \mathbf{U}_f^T$ , once applied to any  $6 \times 1$  vector  $\mathbf{x} = [x_1, \dots, x_6]^T$ , results in subtracting the average value  $\frac{1}{6} \sum_{k=1}^6 x_k$  from all the terms of  $\mathbf{x}$ . The projection matrix  $\mathbf{U}_c \cdot \mathbf{U}_c^T$ , instead, results in a  $6 \times 1$  vector whose elements are all equal to  $\frac{1}{6} \sum_{k=1}^6 x_k$ . These considerations may help to better understand the physical meaning of the configuration space and of the complementary configuration space.

### Multiple-star configuration

Consider again the six-phase configuration of Fig. 4.13, previously exemplified in Section 4.3.5. In this case  $n = 6$  and  $n_c = 2$ ; the constraint matrix has been found to be:

$$\mathbf{M} = \begin{bmatrix} 1 & 0 \\ 1 & 0 \\ 1 & 0 \\ 0 & 1 \\ 0 & 1 \\ 0 & 1 \end{bmatrix}$$

Its singular value decomposition has been computed numerically, resulting in:

$$\mathbf{U} = \begin{bmatrix} -0.58 & 0 & -0.58 & 0.33 & 0.33 & 0.33 \\ -0.58 & 0 & -0.21 & -0.46 & -0.46 & -0.46 \\ -0.58 & 0 & 0.79 & 0.12 & 0.12 & 0.12 \\ 0 & -0.58 & 0 & 0.67 & -0.33 & -0.33 \\ 0 & -0.58 & 0 & -0.33 & 0.67 & -0.33 \\ 0 & -0.58 & 0 & -0.33 & -0.33 & 0.67 \end{bmatrix}, \mathbf{\Sigma} = \begin{bmatrix} 1.73 & 0 \\ 0 & 1.73 \\ 0 & 0 \\ 0 & 0 \\ 0 & 0 \\ 0 & 0 \end{bmatrix},$$

$$\mathbf{V} = \begin{bmatrix} -1 & 0 \\ 0 & -1 \end{bmatrix}$$

and, again,  $\mathbf{U}^T \cdot \mathbf{U} = \mathbf{U} \cdot \mathbf{U}^T = \mathbf{I}$  (with dimension  $6 \times 6$ ) and  $\mathbf{V}^T \cdot \mathbf{V} = \mathbf{V} \cdot \mathbf{V}^T = \mathbf{I}$  (with dimension  $2 \times 2$ ).

The configuration matrix  $\mathbf{U}_f$  is given by the last  $n - n_c = 6 - 2 = 4$  columns of  $\mathbf{U}$ . The complementary configuration matrix  $\mathbf{U}_c$  is given by the first  $n_c = 2$  columns of  $\mathbf{U}$ . Again, it can be verified that the properties (4.22)-(4.24) are satisfied.

The projection matrices in the configuration space and in the complementary configuration space are:

$$\mathbf{U}_f \cdot \mathbf{U}_f^T = \begin{bmatrix} 0.67 & -0.33 & -0.33 & 0 & 0 & 0 \\ -0.20 & 0.67 & -0.33 & 0 & 0 & 0 \\ -0.33 & -0.33 & 0.67 & 0 & 0 & 0 \\ 0 & 0 & 0 & 0.67 & -0.33 & -0.33 \\ 0 & 0 & 0 & -0.20 & 0.67 & -0.33 \\ 0 & 0 & 0 & -0.33 & -0.33 & 0.67 \end{bmatrix},$$

$$\mathbf{U}_c \cdot \mathbf{U}_c^T = \begin{bmatrix} 0.33 & 0.33 & 0.33 & 0 & 0 & 0 \\ 0.33 & 0.33 & 0.33 & 0 & 0 & 0 \\ 0.33 & 0.33 & 0.33 & 0 & 0 & 0 \\ 0 & 0 & 0 & 0.33 & 0.33 & 0.33 \\ 0 & 0 & 0 & 0.33 & 0.33 & 0.33 \\ 0 & 0 & 0 & 0.33 & 0.33 & 0.33 \end{bmatrix}$$

and again it can be easily verified that  $\mathbf{U}_f \cdot \mathbf{U}_f^T + \mathbf{U}_c \cdot \mathbf{U}_c^T = \mathbf{I}$ .

From the numerical matrices, it can be observed that the projection matrix  $\mathbf{U}_f \cdot \mathbf{U}_f^T$ , once applied to any  $6 \times 1$  vector  $\mathbf{x} = [x_1, \dots, x_6]^T$ , results in subtracting the average value  $\frac{1}{3} \sum_{k=1}^3 x_k$  from the three-phase set  $\{x_1, x_2, x_3\}$  and the average value  $\frac{1}{3} \sum_{k=4}^6 x_k$  from the set  $\{x_4, x_5, x_6\}$ , which are the two star-connected subsets of the considered configuration. The projection matrix  $\mathbf{U}_c \cdot \mathbf{U}_c^T$ , instead, results in a  $6 \times 1$  vector whose first three elements are all equal to  $\frac{1}{3} \sum_{k=1}^3 x_k$  and the last three elements are all equal to  $\frac{1}{3} \sum_{k=4}^6 x_k$ . Again, this helps to get a better physical insight into the meaning of the configuration space and of the complementary configuration space.

If, alternatively, the system had been represented with the matrix:

$$\mathbf{M} = \begin{bmatrix} 1 & 1 \\ 1 & 1 \\ 1 & 1 \\ 1 & 0 \\ 1 & 0 \\ 1 & 0 \end{bmatrix}$$

obtained from the same electrical configuration, the singular value decomposition would have been:

$$\mathbf{U} = \begin{bmatrix} -0.49 & -0.30 & -0.41 & -0.41 & 0.41 & 0.41 \\ -0.49 & -0.30 & -0.41 & 0.41 & 0.41 & 0.41 \\ -0.49 & -0.30 & 0.82 & 0 & 0 & 0 \\ -0.30 & 0.49 & 0 & 0.67 & -0.33 & -0.33 \\ -0.30 & 0.49 & 0 & -0.33 & 0.67 & -0.33 \\ -0.30 & 0.49 & 0 & -0.33 & -0.33 & 0.67 \end{bmatrix}, \quad \mathbf{\Sigma} = \begin{bmatrix} 2.80 & 0 \\ 0 & 1.07 \\ 0 & 0 \\ 0 & 0 \\ 0 & 0 \\ 0 & 0 \end{bmatrix},$$

$$\mathbf{V} = \begin{bmatrix} -0.85 & 0.53 \\ -0.53 & -0.85 \end{bmatrix}$$

This means that, by choosing a different  $\mathbf{M}$  to analyze the same electrical network, the matrices  $\mathbf{U}_f$  and  $\mathbf{U}_c$  are also different. However, it can be verified that the new matrices still satisfy all the conditions (4.22)-(4.24) and that the projection matrices  $\mathbf{U}_f \cdot \mathbf{U}_f^T$  and  $\mathbf{U}_c \cdot \mathbf{U}_c^T$  are equal to the previously computed ones.

### 4.4.6 Electromagnetic torque expression in the configuration space

The electromagnetic torque  $T_{em}$  developed by the electrical machine has been formalized through the equation (2.33). It is worth recalling that it is composed of the superposition of three terms:

- a term  $T_0(\theta)$  which is independent of the machine currents and which mainly identifies the cogging torque phenomena,
- a term  $\mathbf{f}_{PM}^T(\theta) \cdot \mathbf{i}_{EM}$  which is linearly depending on the machine currents and which identifies their interaction with the permanent magnets,
- a term  $(\mathbf{i}_{EM}^T \cdot \mathbf{L}'_{EM}(\theta) \cdot \mathbf{i}_{EM})/2$  which is quadratically depending on the machine currents and which identifies both the variable reluctance phenomena and the mutual interaction between the stator and the rotor currents.

When the machine currents  $\mathbf{i}_{EM}$  are subject to the algebraic constraints (4.8), since the relationship (4.29) holds, the torque expression can be formalized with respect to the  $n_f \times 1$  set of unconstrained current components  $\mathbf{i}_{EM,f} = \mathbf{U}_f^T \cdot \mathbf{i}_{EM}$ , resulting in:

$$\begin{aligned} T_{em} &= T_0(\theta) + \mathbf{f}_{PM}^T(\theta) \cdot \mathbf{i}_{EM} + \frac{1}{2} \cdot \mathbf{i}_{EM}^T \cdot \mathbf{L}'_{EM}(\theta) \cdot \mathbf{i}_{EM} = \\ &= T_0(\theta) + \mathbf{f}_{PM,f}^T(\theta) \cdot \mathbf{i}_{EM,f} + \frac{1}{2} \cdot \mathbf{i}_{EM,f}^T \cdot \mathbf{L}'_{EM,f}(\theta) \cdot \mathbf{i}_{EM,f} \end{aligned} \quad (4.34)$$

where the equivalent parameters are:

$$\mathbf{L}'_{EM,f}(\theta) = \mathbf{U}_f^T \cdot \mathbf{L}'_{EM}(\theta) \cdot \mathbf{U}_f, \quad \mathbf{f}_{PM,f}(\theta) = \mathbf{U}_f^T \cdot \mathbf{f}_{PM}(\theta) \quad (4.35)$$

Since the configuration matrix  $\mathbf{U}_f$  is only linked to the machine current constraints, which are constant in time, it can be easily proven that the parameters in (4.32) and the parameters in (4.35) satisfy the relationships:

$$\begin{aligned} \mathbf{L}'_{EM,f}(\theta) &= \frac{\partial \mathbf{L}_{EM,f}}{\partial \theta}, \\ \mathbf{e}_{EM,f} &= \omega \mathbf{f}_{PM,f}(\theta) + \omega \mathbf{L}'_{EM,f}(\theta) \cdot \mathbf{i}_{EM,f} \end{aligned} \quad (4.36)$$

As a result, by considering both the equations (4.31) and (4.34) it can be concluded that an electrical machine with  $n$  windings, supplied through a constrained network with  $n_c$  current constraints, behaves, both electrically and mechanically, exactly as an equivalent machine with only  $n_f = n - n_c$  windings.

## 4.5 Summary and remarks

This section has developed the mathematical modelling of the electrical drive basing on the *interconnection network* between the electrical machine and the power electronics converter. The interconnection network, which has been formalized as a linear time-invariant multiport system, is responsible for both the link between the machine windings and the converter leg voltages and for the presence of algebraic constraints on the machine currents.

The direct relationship between the converter voltages and the machine voltages has

been represented through a *network interconnection matrix*  $\mathbf{N}$ . The effects of resistive and conductive elements in the network (if present) can also be included through a *network resistances matrix*  $\mathbf{R}_{NET}$  and a *network conductances matrix*  $\mathbf{G}_{NET}$ , respectively. Their contributions can almost always be neglected for electrical drive modelling targeted at control purposes.

The presence of *current constraints* is particularly relevant for the whole drive functioning, because it has the same effect of an internal feedback action which alters the machine voltages according to the system overall functioning. It has been modelled by introducing a *constraint matrix*  $\mathbf{M}$  and a set of *auxiliary network voltages*  $\mathbf{v}_{NET}$ , which can physically be interpreted as the voltages existing between some nodes of the physical system.

By explicitly considering the effect of the auxiliary voltages set  $\mathbf{v}_{NET}$  it has been possible to develop the complete model of the electrical drive in presence of currents constraints. This model depends on a *network internal feedback matrix*  $\mathbf{F}$ , which is related both to the constraints and to the machine parameters.

A different formulation of the constrained drive model has been then obtained by introducing the concept of the *configuration space* of the system. The constrained drive equations, projected in the configuration space, result in a *reduced order model*, which can describe the dynamic evolution of the electrical drive while at the same time intrinsically taking into account the constraints on the machine currents. This set of equations depends on a *configuration matrix*  $\mathbf{U}_f$ , which is only related to the current constraints and does not depend on the machine parameters.

The modelling approach adopted in this chapter is heavily based on linear algebra properties. A rich set of examples has been provided for each case, in a way to make the results and the applications more intuitive. The results and properties of this analysis are the core basis of the control algorithms developed in Chapter 6 and in Chapter 7.

# 5 Field Oriented Control of Asymmetrical PMSMs

The Field Oriented Control (FOC) is currently the most common approach for the control of multiphase machines. It is directly derived from three-phase machines and is based on a proper reference transformation of the machine phase variables. The chosen reference frame is directly related to the spatial displacement of the magnetic flux density field in the air-gap<sup>1</sup> of the machine, and is based on the proper definition of space vectors related to the electrical variables of the machine.

Symmetrical machines have, by design, many special properties which make their modelling to be particularly convenient in this moving reference frame, and FOC algorithms for this kind of machines have been deeply analysed in the technical literature. On the contrary, asymmetrical machines do not meet many of those features and, by using the same field-oriented approach, their analysis and control become more challenging.

The present chapter derives and analyses the field-oriented control approach for a generic  $n$ -phase surface-mounted *permanent magnet synchronous machine* (PMSM)<sup>2</sup>. The analysis is presented for a generic winding disposition (i.e., asymmetrical, with an arbitrary angular shift) and with a single isolated neutral point configuration. The presence of multiple spatial harmonics of the magnetic field at the air gap is explicitly addressed to identify the field-oriented reference frames and to introduce some torque enhancement control strategies based on the injection of harmonic currents.

For the present analysis, the asymmetry is either resulting from the machine design (i.e., intrinsically asymmetrical configurations) or coming from a post-fault configuration of an originally symmetrical machine<sup>3</sup>. One of the aims of this analysis is to emphasize the main differences between symmetrical and asymmetrical machines, in a way to point out which properties are kept, and which properties are lost.

The chapter is structured as follows. Section 5.1 focuses on the machine mathematical model. First, the phase variable model (whose generalized formulation has been given in Chapter 2), is particularized to the specific case study. Then, coherently with the field-oriented approach, the model is reformulated in a reference frame whose components are synchronous with a set of spatial harmonics of the magnetic field at the air gap, which allows to emphasize the currents/fluxes interactions for the electromagnetic torque generation. Section 5.2 is then focused on the torque control strategy, which is finalized at computing a set of reference currents to develop a desired electromagnetic torque. As known, for a multiphase machine it is possible to exploit

---

<sup>1</sup> Hence the name “Field Oriented”.

<sup>2</sup> The same approach can also be used for a Brushless DC (BLDC) machine.

<sup>3</sup> As an example, a  $n_1$ -phase machine subject to  $n_2$  open-circuit faults is here analysed as an asymmetrical machine with  $n = n_1 - n_2$  phases.

higher-order spatial harmonics for the torque development through a proper injection of harmonic currents. Some different strategies are presented to generalize this torque enhancement to asymmetrical machines while, at the same time, optimizing the drive energetic performances. Section 5.3 addresses the current control strategy, by first presenting the standard control strategy applied in symmetrical machines, and then by showing how it can be adapted to deal with asymmetrical configurations. The overall control scheme is summarized in Section 5.4, and is then particularized to a specific nine-phase case study in Section 5.5 and Section 5.6. Finally, Section 5.7 sums up the conclusions of this chapter.

For notation simplicity, the subscripts “EM” and “VSI” adopted in Chapter 4 will not be used anymore. The output voltages of the converter legs will be further on denoted as  $u$ , while the voltages at the machine winding terminals will be denoted as  $v$ . Moreover, the network wiring resistances will be neglected.

## 5.1 Mathematical model

The PMSM under analysis is assumed to have  $n$  identical stator windings arranged in  $P_p$  pole pairs and distributed along the stator periphery of the machine so that their magnetic axes have an electrical phase displacement of  $\alpha_k$  (with  $k = 1, \dots, n$  being the phase index) measured from an arbitrary reference position. All the windings are star-connected with a single isolated neutral point. This architecture is schematically represented in Fig. 5.1.

For a symmetrical machine design, all the windings are evenly placed along the stator periphery, with a reciprocal displacement of  $(2\pi/n)$ . This leads to magnetic axis displacement of the  $k$ -th phase which can be simply expressed as  $\alpha_k = (2\pi/n) \cdot (k - 1)$ . On the contrary, for an asymmetrical configuration, the magnetic axes angles  $\alpha_k$  can assume any arbitrary value.

This section particularizes the generalized machine model presented in Chapter 2 to the examined configuration.

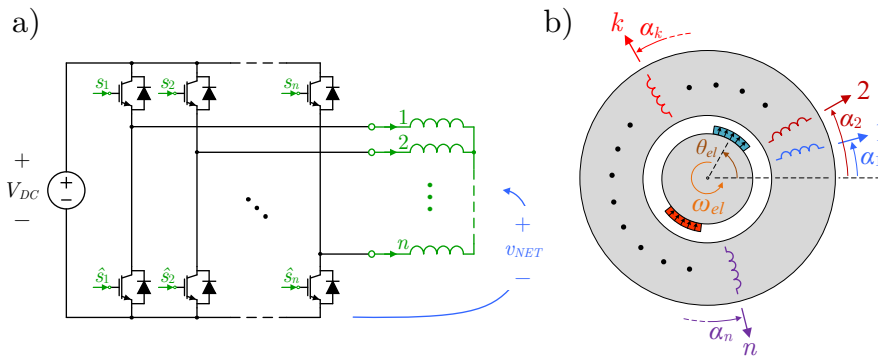


Fig. 5.1 – Schematic representation of the multiphase drive under analysis: a) Circuitual architecture; b) Phase windings magnetic axes disposition.

### 5.1.1 Phase variable domain

Under the linearity hypothesis, the fluxes induced in the  $n$  stator windings are given by the superimposed contribution of the magnetic field generated by all the phase currents and by the permanent magnets on the rotor. The generalized model (2.29) is particularized into:

$$\phi = \mathbf{L} \cdot \mathbf{i} + \psi_{PM}(\theta) \quad (5.1)$$

The magnetic flux density field generated at the air gap by the permanent magnets, once decomposed in a Fourier series with respect to the stator angle, is given by the superposition of an infinite number of spatial harmonics. These harmonics produce in each  $k$ -th machine winding an induced flux linkage  $\psi_{PM,k}$ , which is a periodic function of the rotor electrical position  $\theta_{el} = P_p \cdot \theta$ .

Then, the flux linkage induced in the  $k$ -th machine phase (with  $k = 1, \dots, n$ ) can be expressed as the Fourier series:

$$\psi_{PM,k}(\theta_{el}) = \sum_{h=1}^{+\infty} \Psi_{Mh} \cdot \cos(h \cdot (\theta_{el} - \alpha_k) + \varphi_h) \quad (5.2)$$

with  $\Psi_{Mh}$  and  $\varphi_h$  denoting the magnitude and the phase displacement of the  $h$ -th spatial harmonic contribution<sup>4</sup>. The magnitudes  $\Psi_{Mh}$  depend both on the rotor magnets and on the stator windings design. For a purely sinusoidal machine, only the fundamental harmonic (with index  $h = 1$ ) is present, whereas, for a non-sinusoidal machine, multiple harmonics are present.

For a surface-mounted PMSM, once the variable reluctance effects linked to the stator slots are disregarded, the  $n \times n$  inductances matrix  $\mathbf{L}$  in (5.1) can be assumed to be invariant with respect to the rotor position. Moreover, as proven in Chapter 2,  $\mathbf{L}$  is always symmetric and positive definite. Finally, in the particular case of symmetrical windings designs,  $\mathbf{L}$  is a *circulant matrix*, meaning that  $L_{k,h} = L_{k+1,h+1}$  for all the couples  $k, h = 1, \dots, n$  [55], [153]<sup>5</sup>.

From the fluxes expression (5.1), the induced back-EMFs can be split in the transformer induced contribution and in the motional-induced contribution as:

$$\frac{d\phi}{dt} = \mathbf{L} \cdot \frac{d\mathbf{i}}{dt} + \frac{d\psi_{PM}}{dt} = \mathbf{L} \cdot \frac{d\mathbf{i}}{dt} + e \quad (5.3)$$

From the expression (5.2), the PM-induced back-EMF in the  $k$ -th phase is equal to:

$$\begin{aligned} e_k = e_{PM,k} &= \frac{d\psi_{PM,k}}{dt} = \frac{\partial \theta_{el}}{\partial t} \cdot \frac{\partial \psi_{PM,k}}{\partial \theta_{el}} = \\ &= -\omega_{el} \cdot \sum_{h=1}^{+\infty} h \cdot \Psi_{Mh} \cdot \sin(h \cdot (\theta_{el} - \alpha_k) + \varphi_h) \end{aligned} \quad (5.4)$$

where  $\omega_{el} = P_p \cdot \omega$  is the rotor electrical speed.

<sup>4</sup> The harmonic index  $h$  is a strictly positive integer, ranging from 1 to  $+\infty$ . The spatial harmonic of order 0 is absent because the magnetic flux density  $\vec{B}$  is a solenoidal field.

<sup>5</sup> This is because any permutation of the phase indexes leaves the overall structure unaffected. This property is not guaranteed for an asymmetrical windings design.

Given the single isolated neutral point machine configuration, the sum of all the phase currents is forced to be zero. The network model developed in Chapter 4 is therefore simply represented by imposing  $\mathbf{N} = \mathbf{I}$  and  $\mathbf{M} = \mathbf{1}_n = [1 \ 1 \ \dots \ 1]^T$ . The constraint equation is then represented as:

$$\mathbf{1}_n^T \cdot \mathbf{i} = \sum_{k=1}^n i_k = 0 \quad (5.5)$$

while the machine phase voltages set is:

$$\mathbf{v} = \mathbf{u} - \mathbf{1}_n \cdot v_{NET} \quad (5.6)$$

where  $v_{NET}$  represents the voltage between the inverter reference node  $O$  and the neutral point  $N$  of the machine phase windings (as represented in Fig. 5.1).

Since the windings have been supposed to be equal, the resistances matrix is simply  $\mathbf{R} = R \cdot \mathbf{I}$ .

To sum up, the electrical equations of the considered PMSM multiphase drive can be written in the phase variable domain as:

$$\mathbf{L} \cdot \frac{d\mathbf{i}}{dt} + R \cdot \mathbf{i} + \mathbf{e} = \mathbf{v} = \mathbf{u} - \mathbf{1}_n \cdot v_{NET} \quad (5.7)$$

The electromagnetic torque developed by the machine, expressed in terms of phase variables, is instead expressed as:

$$T_{em} = \mathbf{f}_{PM}^T(\theta) \cdot \mathbf{i} = \sum_{k=1}^n \frac{\partial \psi_{PM,k}}{\partial \theta} \cdot i_k = P_p \cdot \sum_{k=1}^n \frac{\partial \psi_{PM,k}}{\partial \theta_{el}} \cdot i_k \quad (5.8)$$

### 5.1.2 Space vector formalism

The stator currents flowing in the machine windings modify the overall flux density field at the air gap by generating a field distribution which, similarly to the one generated by the PMs, can also be decomposed in the superposition of an infinite number of spatial harmonics. Each  $h$ -th spatial harmonic of this magnetic flux density field at the air-gap can be synthetically identified through a single complex variable, which is proportional to the  $h$ -th order *space vector* of the machine currents, defined as<sup>6</sup>:

$$\underline{i}_h = i_{xh} + j \cdot i_{yh} = \sqrt{\frac{2}{n}} \cdot \sum_{k=1}^n i_k \cdot e^{jh\alpha_k} \quad (5.9)$$

In other words,  $\underline{i}_h$  identifies, through its magnitude and phase, the intensity and local displacement of a spatial harmonic of the magnetic flux density field generated at the air gap by the stator currents<sup>7</sup>.

<sup>6</sup> The definition (5.9) is typically named *power invariant*. Other space vectors definitions (e.g. amplitude invariant) have also been introduced in the technical literature. They would lead to similar analysis and results.

<sup>7</sup> To be more specific, the radial component of the magnetic flux density at the air-gap can be expressed as  $B(\gamma) = \sum_{h=1}^{+\infty} \text{Re}\{b_h \cdot \underline{i}_h \cdot e^{-jhP_p\gamma}\} = \sum_{h=1}^{+\infty} b_h \cdot |\underline{i}_h| \cdot \cos(hP_p\gamma - \angle \underline{i}_h)$ , where  $b_h$  is a weighting factor depending on the machine design (e.g., number of turns, winding factor,

Coherently with the *field-oriented approach*, and extending what is typically done for three-phase machines, each current space vector can be expressed in a reference frame synchronous to the corresponding harmonic of the PM induced fluxes (and, consequently, synchronous to the corresponding spatial harmonic of the magnetic field at the air-gap). In this context, the space vector  $\underline{i}_h$  can be redefined by applying a complex rotation as:

$$\underline{i}_h^{(dq)} = i_{dh} + j \cdot i_{qh} = \underline{i}_h \cdot e^{-j(h\theta_{el} + \varphi_h)} \quad (5.10)$$

The complex variable  $\underline{i}_h^{(dq)}$  defined as per (5.10) represents the same space vector  $\underline{i}_h$  in a synchronous “field-oriented” reference frame, which rotates at the speed  $h \cdot \omega_{el}$ . The real part  $i_{dh} = \text{Re}\{\underline{i}_h^{(dq)}\}$  and the imaginary part  $i_{qh} = \text{Im}\{\underline{i}_h^{(dq)}\}$  represent the *direct axis component* and the *quadrature axis component* of  $\underline{i}_h^{(dq)}$ , respectively.

Given the positions (5.9) and (5.10), with simple algebraic manipulations the electromagnetic torque  $T_{em}$  developed by the machine and expressed via (5.8) can be rewritten through the space vector formalism as<sup>8</sup>:

$$T_{em} = \sum_{h=1}^{+\infty} \left( \sqrt{\frac{n}{2}} \cdot h \cdot P_p \cdot \Psi_{Mh} \right) \cdot i_{qh} = \sum_{h=1}^{+\infty} \kappa_h \cdot i_{qh} \quad (5.11)$$

with  $\kappa_h = \sqrt{n/2} \cdot P_p \cdot h \cdot \Psi_{Mh}$  being a *torque gain* coefficient related to the  $h$ -th spatial harmonic. It is also worth noticing that each gain  $\kappa_h$  (which, dimensionally, is equivalent to a flux) is proportional to the magnitude of the  $h$ -th harmonic in the motional induced back-EMFs (5.4).

By using this field-oriented approach, from (5.11) it can be deduced that only the quadrature axis components of the space vectors of the machine currents, by interacting with the corresponding harmonics of the fluxes induced by the PMs, are contributing to the electromagnetic torque production. From (5.11), each  $h$ -th spatial harmonic contributes to the torque  $T_{em}$  as if it were produced by an equivalent machine with  $h \cdot P_p$  pole pairs and with an induced flux magnitude equal to  $\Psi_{Mh}$ . Usually, the lowest odd-order harmonics have the highest gains  $\kappa_h$  and, therefore, they are preferable for torque control.

Together with the space vectors defined in (5.9), it is also convenient to introduce the *zero-sequence component* of the machine phase currents as the scalar variable:

$$i_0 = \frac{1}{\sqrt{n}} \cdot \sum_{k=1}^n i_k \quad (5.12)$$

With the position (5.12), the phase currents constraint (5.5) due to the isolated neutral point configuration is simply expressed as:

$$i_0 = 0 \quad (5.13)$$

---

mechanical dimensions, etc...) and  $\gamma$  is the angle with respect to the magnetic axis of the first machine phase. This expression, which is a Fourier series in the spatial angle  $P_p \cdot \gamma$ , highlights how the magnitude and phase of the space vector  $\underline{i}_h$  influence the  $h$ -th spatial harmonic of the flux-density field generated by the machine stator currents.

<sup>8</sup> Proven in Appendix 9.5.1.

### 5.1.3 Vector space decomposition

As typically done, the mathematical model of the multiphase machine can be reformulated through a variable transformation known as *vector space decomposition* (VSD) [1].

As mentioned in Section 2.3.2, this change of variables is identified by the linear transformation (2.38), which is here repeated:

$$\mathbf{x}_{\text{VSD}} = \mathbf{C} \cdot \mathbf{x} \iff \mathbf{x} = \mathbf{C}^{-1} \cdot \mathbf{x}_{\text{VSD}} \quad (5.14)$$

where  $\mathbf{C}$  is the *generalized Clarke's transformation matrix* and  $\mathbf{x}$  is a generic  $n \times 1$  phase variable vector.

The field-oriented approach consists in choosing the transformation matrix  $\mathbf{C}$  in a way that the transformed currents vector  $\mathbf{i}_{\text{VSD}} = \mathbf{C} \cdot \mathbf{i}$  includes a set of space vector components  $\{i_{xh}, i_{yh}\}$  to be controlled. Given (5.9), the components of the  $h$ -th space vector  $\dot{i}_h = i_{xh} + j \cdot i_{yh}$  can be included in the transformed set  $\mathbf{i}_{\text{VSD}}$  through the rows:

$$\mathbf{C}_h = \sqrt{\frac{2}{n}} \cdot \begin{bmatrix} \cos(h\alpha_1) & \cos(h\alpha_2) & \cdots & \cos(h\alpha_n) \\ \sin(h\alpha_1) & \sin(h\alpha_2) & \cdots & \sin(h\alpha_n) \end{bmatrix} \quad (5.15)$$

Similarly, given (5.12), the zero-sequence component  $i_0$  can be included in the transformed set  $\mathbf{i}_{\text{VSD}}$  through the row:

$$\mathbf{C}_0 = \frac{1}{\sqrt{n}} \cdot [1 \quad 1 \quad 1 \quad \cdots \quad 1] \quad (5.16)$$

Indeed, with the positions (5.15)-(5.16), it can be verified that:  $[i_{xh} \ i_{yh}]^T = \mathbf{C}_h \cdot \mathbf{i}$  and  $i_0 = \mathbf{C}_0 \cdot \mathbf{i}$ .

The proper choice of the transformation matrix  $\mathbf{C}$ , which can be built as the concatenation of the  $1 \times n$  row vector  $\mathbf{C}_0$  defined as per (5.16) and of several  $2 \times n$  submatrices  $\mathbf{C}_h$  defined as per (5.15), is crucial for proper machine control.

From (5.11), to achieve a complete control of all the (infinite) spatial harmonics interactions, it would be desirable to control all the (infinite) space vectors of the machine currents. However, since the set of machine phase currents constitutes a system of  $n$  variables, the number of degrees of freedom is limited, and only up to  $n$  scalar components can be set arbitrarily. Moreover, the winding configuration further reduces the number of controllable components by forcing to 0 the zero-sequence component  $i_0$ , which should be therefore included in the set  $\mathbf{i}_{\text{VSD}}$ .

Then, for a machine with an odd number of phases, it is possible to freely control at most  $(n-1)/2$  space vectors at the same time whereas, for a machine with an even number of phases, the number of independently controllable space vectors is  $(n-2)/2$ . In this latter case, the transformed set  $\mathbf{i}_{\text{VSD}}$  can be completed by introducing a *second zero-sequence component*  $i_0^-$  through an additional row  $\mathbf{C}_0^-$ , typically built as [2], [154]:

$$\mathbf{C}_0^- = \frac{1}{\sqrt{n}} \cdot [1 \quad -1 \quad 1 \quad \cdots \quad -1] \quad (5.17)$$

Moreover, the generalized Clarke transformation matrix  $\mathbf{C}$  must be a full rank matrix to guarantee the existence of its inverse  $\mathbf{C}^{-1}$  and, therefore, to preserve the overall

number of state variables (i.e., to allow for the inverse transformation  $\mathbf{i} = \mathbf{C}^{-1} \cdot \mathbf{i}_{\text{VSD}}$ ). This means that a chosen set of space vectors can be controlled only if the corresponding rows  $\mathbf{C}_h$  in the transformation matrix are linearly independent.

As a result, a practical way to establish whether a set of space vectors can be freely controlled is to compute the rank of the matrix  $\mathbf{C}$  built upon the submatrices  $\mathbf{C}_h$  and the zero-sequence row  $\mathbf{C}_0$  (and, eventually, of the second zero-sequence row  $\mathbf{C}_0^-$ ), which only depend on the magnetic axes disposition of the machine windings. If some rows are linearly dependent on some others, there are certain algebraic constraints between the corresponding space vector components, which therefore cannot be imposed arbitrarily<sup>9</sup>.

In many applications the Clarke transformation matrix is built by considering the lowest order space vectors [57], resulting in<sup>10</sup>:

$$\mathbf{C} = \begin{bmatrix} \mathbf{C}_1 \\ \mathbf{C}_2 \\ \mathbf{C}_3 \\ \vdots \\ (\mathbf{C}_0^-) \\ \mathbf{C}_0 \end{bmatrix} = \sqrt{\frac{2}{n}} \cdot \begin{bmatrix} \cos(\alpha_1) & \cos(\alpha_2) & \cdots & \cos(\alpha_n) \\ \sin(\alpha_1) & \sin(\alpha_2) & \cdots & \sin(\alpha_n) \\ \cos(2\alpha_1) & \cos(2\alpha_2) & \cdots & \cos(2\alpha_n) \\ \sin(2\alpha_1) & \sin(2\alpha_2) & \cdots & \sin(2\alpha_n) \\ \cos(3\alpha_1) & \cos(3\alpha_2) & \cdots & \cos(3\alpha_n) \\ \sin(3\alpha_1) & \sin(3\alpha_2) & \cdots & \sin(3\alpha_n) \\ \vdots & \vdots & \ddots & \vdots \\ (1/\sqrt{2}) & (-1/\sqrt{2}) & \cdots & (-1/\sqrt{2}) \\ 1/\sqrt{2} & 1/\sqrt{2} & \cdots & 1/\sqrt{2} \end{bmatrix} \quad (5.18)$$

with  $\mathbf{i}_{\text{VSD}} = [i_{x1}, i_{y1}, i_{x2}, i_{y2}, i_{x3}, i_{y3}, \dots, (i_0^-), i_0]^T$ .

Another common choice is to select only the lowest odd-order space vectors [57] as:

$$\mathbf{C} = \begin{bmatrix} \mathbf{C}_1 \\ \mathbf{C}_3 \\ \mathbf{C}_5 \\ \vdots \\ (\mathbf{C}_0^-) \\ \mathbf{C}_0 \end{bmatrix} = \sqrt{\frac{2}{n}} \cdot \begin{bmatrix} \cos(\alpha_1) & \cos(\alpha_2) & \cdots & \cos(\alpha_n) \\ \sin(\alpha_1) & \sin(\alpha_2) & \cdots & \sin(\alpha_n) \\ \cos(3\alpha_1) & \cos(3\alpha_2) & \cdots & \cos(3\alpha_n) \\ \sin(3\alpha_1) & \sin(3\alpha_2) & \cdots & \sin(3\alpha_n) \\ \cos(5\alpha_1) & \cos(5\alpha_2) & \cdots & \cos(5\alpha_n) \\ \sin(5\alpha_1) & \sin(5\alpha_2) & \cdots & \sin(5\alpha_n) \\ \vdots & \vdots & \ddots & \vdots \\ (1/\sqrt{2}) & (-1/\sqrt{2}) & \cdots & (-1/\sqrt{2}) \\ 1/\sqrt{2} & 1/\sqrt{2} & \cdots & 1/\sqrt{2} \end{bmatrix} \quad (5.19)$$

<sup>9</sup> A simple example of this incompatible control is related to the mapping of different space vectors to the same transformed components. For instance, considering a symmetric five-phase machine, since  $\alpha_k = (k-1) \cdot (2\pi/5)$ , it can be immediately verified by application of (5.9) that  $\underline{i}_9$  is the complex conjugate of  $\underline{i}_1$ . This means that the ninth spatial harmonic torque contribution cannot be controlled independently from the fundamental component contribution. Similar relationship can also be found for different space vectors and for different number of phases. For a generic (i.e., asymmetrical) winding configuration the relationship between different space vectors components might be harder to directly investigate through (5.9), but it can easily be addressed by evaluating the rank of  $\mathbf{C}$ . Some examples can be found in [119].

<sup>10</sup> For symmetrical machines the definition (5.18) represents a special case of a Discrete Fourier Transformation (DFT) applied to a set of  $n$  equally spaced samples [154].

with  $\mathbf{i}_{\text{VSD}} = [i_{x1}, i_{y1}, i_{x3}, i_{y3}, i_{x5}, i_{y5}, \dots, (i_0^-), i_0]^T$ . In this way, it is possible to take advantage of the lowest odd-order spatial harmonics of the machine, which are usually related to the highest torque gains  $\kappa_h$ .

Other approaches are also possible. Generally, the most convenient choice depends on the machine design through the effect of both the torque gains  $\kappa_h$  and of the magnetic axes disposition.

It is worth noticing that, in case the required number of rows of  $\mathbf{C}$  exceeds the number of spatial harmonics to be controlled (like in case of sinusoidal machines, where only  $\Psi_{M1} \neq 0$ ), the other rows of  $\mathbf{C}$  can be arbitrarily chosen.

By using the VSD transformation (5.14), the model (5.7) is modified into:

$$\mathbf{L}_{\text{VSD}} \cdot \frac{d\mathbf{i}_{\text{VSD}}}{dt} + \mathbf{R} \cdot \mathbf{i}_{\text{VSD}} + \mathbf{e}_{\text{VSD}} = \mathbf{v}_{\text{VSD}} = \mathbf{u}_{\text{VSD}} - \mathbf{c} \cdot v_{\text{NET}} \quad (5.20)$$

with:

- $\mathbf{L}_{\text{VSD}} = \mathbf{C} \cdot \mathbf{L} \cdot \mathbf{C}^{-1}$  being the inductances matrix in the chosen VSD reference frame, and
- $\mathbf{c} = \mathbf{C} \cdot \mathbf{1}_n$  being responsible for the mutual interaction among the VSD components related to the isolated neutral point configuration.

The constraint (5.5) is instead simply modified to:

$$i_0 = [0 \ 0 \ 0 \ \dots \ (0) \ 1] \cdot \mathbf{i}_{\text{VSD}} = 0 \quad (5.21)$$

The model (5.20) represents the particularization of (2.37) to this specific case study.

Several simplifications apply for symmetrical machines, which are instead generally not true for asymmetrical configurations.

First, for a symmetrical machine with an odd number of phases, it can be proven<sup>11</sup> that the generalized Clarke transformation matrix  $\mathbf{C}$  chosen either as (5.18) or as (5.19) not only is invertible, but it is also unitary (i.e.,  $\mathbf{C}^{-1} = \mathbf{C}^T$ ).

Moreover, since the inductances matrix  $\mathbf{L}$  in the phase variable domain is a circulant matrix, (i.e.,  $L_{j,k} = L_{j+1,k+1}$ ), it can be proven<sup>12</sup> that the columns of the generalized Clarke transformation matrix  $\mathbf{C}$  chosen either as (5.18) or as (5.19) are the eigenvectors of  $\mathbf{L}$ . Consequently, the computation of the transformed matrix  $\mathbf{L}_{\text{VSD}} = \mathbf{C} \cdot \mathbf{L} \cdot \mathbf{C}^{-1} = \mathbf{C} \cdot \mathbf{L} \cdot \mathbf{C}^T$  performs the diagonalization of  $\mathbf{L}$ .

Additionally, the transformed self-inductance parameters related to the same space vector components are equal (i.e.,  $L_{xh} = L_{yh} = L_h$ ).

Finally, since the magnetic axes are equally shifted from one another, it also results  $\mathbf{c} = \mathbf{C} \cdot \mathbf{1}_n = [0 \ 0 \ 0 \ \dots \ (0) \ \sqrt{n}]^T$ .

Given these properties, all the components of (5.20) are decoupled from one another and can be written element by element. The  $h$ -th space vector components satisfy the set of first-order differential equations:

<sup>11</sup> Proven in Appendix 9.5.2.

<sup>12</sup> Proven in Appendix 9.5.3. A similar proof can also be found in [55] basing on the properties of the complex Fortescue transformation.

$$\begin{cases} L_h \cdot \frac{di_{xh}}{dt} + R \cdot i_{xh} + e_{xh} = v_{xh} = u_{xh} \\ L_h \cdot \frac{di_{yh}}{dt} + R \cdot i_{yh} + e_{yh} = v_{yh} = u_{yh} \end{cases} \quad (5.22)$$

The second zero-sequence component (if present) satisfies the differential equation:

$$L_0^- \cdot \frac{di_0^-}{dt} + R \cdot i_0^- + e_0^- = v_0^- = u_0^- \quad (5.23)$$

The zero-sequence component equation in (5.20), since  $i_0 = 0$ , is the algebraic equation:

$$e_0 = v_0 = u_0 - \sqrt{n} \cdot v_{NET} \quad (5.24)$$

and it only defines the neutral point potential shift<sup>13</sup>  $v_{NET} = (u_0 - e_0)/\sqrt{n}$ .

These properties drastically simplify the modelling and control of symmetrical machines, which can be analysed with the same well-known techniques of three-phase machines. However, they are instead not guaranteed for a generic (i.e., asymmetrical) winding configuration. In such cases, there might be coupling effects among different transformed variables, due both to the magnetic effects (through  $\mathbf{L}_{VSD}$ ) and to the electrical winding configuration (through  $\mathbf{c}$ ).

#### 5.1.4 Rotational transformation

Once the generalized Clarke transformation matrix  $\mathbf{C}$  has been built, the VSD current set  $\mathbf{i}_{VSD}$  can be further modified by transforming each couple  $\{i_{xh}, i_{yh}\}$  related to the  $h$ -th space vector  $\mathbf{i}_h$  into the corresponding couple  $\{i_{dh}, i_{qh}\}$  of the synchronous space vector  $\mathbf{i}_h^{(dq)}$ .

Given (5.10), this operation can be done with the matrix formalism by defining, for each  $h$ -th space vector, a rotational submatrix built as:

$$\mathbf{D}_h(\theta_{el}) = \begin{bmatrix} \cos(h\theta_{el} + \varphi_h) & \sin(h\theta_{el} + \varphi_h) \\ -\sin(h\theta_{el} + \varphi_h) & \cos(h\theta_{el} + \varphi_h) \end{bmatrix} \quad (5.25)$$

in a way that:

$$\begin{bmatrix} i_{dh} \\ i_{qh} \end{bmatrix} = \mathbf{D}_h(\theta_{el}) \cdot \begin{bmatrix} i_{xh} \\ i_{yh} \end{bmatrix}, \quad \text{and} \quad \begin{bmatrix} \dot{i}_{xh} \\ \dot{i}_{yh} \end{bmatrix} = \mathbf{D}_h^T(\theta_{el}) \cdot \begin{bmatrix} \dot{i}_{dh} \\ \dot{i}_{qh} \end{bmatrix} \quad (5.26)$$

This operation, applied to all the chosen components, defines a further variable transformation as:

$$\mathbf{x}_{dq} = \mathbf{D}(\theta_{el}) \cdot \mathbf{x}_{VSD} \quad \Leftrightarrow \quad \mathbf{x}_{VSD} = \mathbf{D}^{-1}(\theta_{el}) \cdot \mathbf{x}_{dq} \quad (5.27)$$

where  $\mathbf{D}(\theta_{el})$  is a *rotational transformation matrix*, which is built as a block-diagonal matrix by combining the rotational submatrices  $\mathbf{D}_h(\theta_{el})$  defined as per (5.25). No rotation is instead applied to the zero-sequence component  $i_0$  and to the second zero-sequence component  $i_0^-$  (if present).

<sup>13</sup> It can be interpreted as the particularization of (4.14).

Given the property (5.26), the rotational matrix  $\mathbf{D}(\theta_{el})$  is always unitary, meaning that  $\mathbf{D}^{-1}(\theta_{el}) = \mathbf{D}^T(\theta_{el})$ .

The cascaded application of the Clarke's transformation matrix  $\mathbf{C}$  and of the rotational transformation matrix  $\mathbf{D}(\theta_{el})$  represents a *generalized Park's transformation* from the phase variable domain into the multiple synchronous variable domain.

Different choices of the Clarke transformation matrix  $\mathbf{C}$  also lead to different rotational matrices  $\mathbf{D}(\theta_{el})$ . For instance, the rotational matrix associated with the matrix  $\mathbf{C}$  defined via (5.18) is:

$$\mathbf{D}(\theta_{el}) = \begin{bmatrix} \mathbf{D}_1(\theta_{el}) & \mathbf{0} & \mathbf{0} & \cdots & (\mathbf{0}) & \mathbf{0} \\ \mathbf{0} & \mathbf{D}_2(\theta_{el}) & \mathbf{0} & \cdots & (\mathbf{0}) & \mathbf{0} \\ \mathbf{0} & \mathbf{0} & \mathbf{D}_3(\theta_{el}) & \cdots & (\mathbf{0}) & \mathbf{0} \\ \vdots & \vdots & \vdots & \ddots & \vdots & \vdots \\ (\mathbf{0}) & (\mathbf{0}) & (\mathbf{0}) & \cdots & (1) & (0) \\ \mathbf{0} & \mathbf{0} & \mathbf{0} & \cdots & (0) & 1 \end{bmatrix} \quad (5.28)$$

with  $\mathbf{i}_{dq} = [i_{d1}, i_{q1}, i_{d2}, i_{q2}, i_{d3}, i_{q3}, \dots, (i_0^-), i_0]^T$ , while the rotational matrix associated with the definition (5.19) is:

$$\mathbf{D}(\theta_{el}) = \begin{bmatrix} \mathbf{D}_1(\theta_{el}) & \mathbf{0} & \mathbf{0} & \cdots & (\mathbf{0}) & \mathbf{0} \\ \mathbf{0} & \mathbf{D}_3(\theta_{el}) & \mathbf{0} & \cdots & (\mathbf{0}) & \mathbf{0} \\ \mathbf{0} & \mathbf{0} & \mathbf{D}_5(\theta_{el}) & \cdots & (\mathbf{0}) & \mathbf{0} \\ \vdots & \vdots & \vdots & \ddots & \vdots & \vdots \\ (\mathbf{0}) & (\mathbf{0}) & (\mathbf{0}) & \cdots & (1) & (0) \\ \mathbf{0} & \mathbf{0} & \mathbf{0} & \cdots & (0) & 1 \end{bmatrix} \quad (5.29)$$

with  $\mathbf{i}_{dq} = [i_{d1}, i_{q1}, i_{d3}, i_{q3}, i_{d5}, i_{q5}, \dots, (i_0^-), i_0]^T$ .

By applying the rotational transformation (5.27) to the system (5.20), the electrical equation of the machine, expressed with the matrix formalism, becomes:

$$\begin{aligned} \mathbf{L}_{dq1}(\theta_{el}) \cdot \frac{d\mathbf{i}_{dq}}{dt} + \omega_{el} \cdot \mathbf{L}_{dq2}(\theta_{el}) \cdot \mathbf{i}_{dq} + R \cdot \mathbf{i}_{dq} + \mathbf{e}_{dq}(\theta_{el}) &= \\ &= \mathbf{v}_{dq} = \mathbf{u}_{dq} - \mathbf{g}(\theta_{el}) \cdot v_{NET} \end{aligned} \quad (5.30)$$

with:

- $\mathbf{L}_{dq1}(\theta_{el}) = \mathbf{D}(\theta_{el}) \cdot \mathbf{L}_{VSD} \cdot \mathbf{D}^T(\theta_{el})$  being responsible for the transformer induced back-EMFs in the synchronous domain,
- $\mathbf{L}_{dq2}(\theta_{el}) = \mathbf{D}(\theta_{el}) \cdot \mathbf{L}_{VSD} \cdot (\partial \mathbf{D} / \partial \theta_{el})^T$  being responsible for the motional induced back-EMFs due to the moving reference frame transformation, and
- $\mathbf{g}(\theta_{el}) = \mathbf{D}(\theta_{el}) \cdot \mathbf{c}$  being responsible for the mutual interaction among different synchronous components related to the isolated neutral point configuration.

The model (5.30) represents the particularization of (2.40) to the specific case study. If the chosen set of space vectors completely describes all the spatial harmonics of interests, the rotational submatrices (5.25) constraint to zero the direct axis components of the motional induced back-EMFs set  $e_{dq}$ .

Again, in case of a symmetrical machine, several simplifications can apply. Indeed, in such a case, the application of the rotational transformation can be applied to each space vector related couple (5.22), resulting in the familiar synchronous equations:

$$\begin{cases} L_h \cdot \frac{di_{dh}}{dt} - h \omega_{el} L_h i_{qh} + R \cdot i_{dh} + e_{dh} = v_{dh} = u_{dh} \\ L_h \cdot \frac{di_{qh}}{dt} + h \omega_{el} L_h i_{dh} + R \cdot i_{qh} + e_{qh} = v_{qh} = u_{qh} \end{cases} \quad (5.31)$$

while the equations for the zero-sequence component and the second zero-sequence component (if present) are the same as in (5.23)-(5.24). If the chosen space vectors completely identify all the spatial harmonics of the machine, it can be proven that<sup>14</sup> the transformed PM-induced back-EMFs are simply  $e_{dh} = 0$  and  $e_{qh} = \sqrt{n/2} \cdot h \omega_{el} \cdot \Psi_{Mh}$ .

However, similarly to the VSD model (5.20), this decoupling is not guaranteed in case of an asymmetrical winding disposition, and the differential equations governing the machine behaviour show additional interactions among different subsets. As exemplified further on in a specific case study, this can have an important impact on the multiphase machine control.

### 5.1.5 Torque expression in the synchronous domain

In case the chosen set of space vectors can completely describe all the spatial harmonics of interests, the expression (5.11) is simplified and can be reformulated in the matrix formalism as:

$$T_{em} = \boldsymbol{\kappa}^T \cdot \boldsymbol{i}_{dq} \quad (5.32)$$

where  $\boldsymbol{\kappa}$  is a  $n \times 1$  vector grouping the gain factors of the considered spatial harmonics.

As an example, under the reasonable assumption that all the even-order spatial harmonics of the magnetic flux density field at the air-gap are absent, and that the odd-order harmonics with index  $h \geq n$  are negligible, by using the VSD transformation (5.19) the vector  $\boldsymbol{\kappa}$  would be expressed as:

$$\begin{aligned} \boldsymbol{\kappa} &= [0 \quad \kappa_1 \quad 0 \quad \kappa_3 \quad 0 \quad \kappa_5 \quad \cdots \quad (0) \quad 0]^T = \\ &= P_p \cdot \sqrt{\frac{n}{2}} \cdot [0 \quad \Psi_{M1} \quad 0 \quad 3 \Psi_{M3} \quad 0 \quad 5 \Psi_{M5} \quad \cdots \quad (0) \quad 0]^T \end{aligned} \quad (5.33)$$

where the terms related to the direct axes components  $i_{dh}$  and to the zero-sequence component  $i_0$  (and, eventually, to the second zero-sequence component  $i_0^-$ ) are zero.

The corresponding electromagnetic torque would be:

$$T_{em} = P_p \cdot \sqrt{\frac{n}{2}} \cdot (\Psi_{M1} \cdot i_{q1} + 3 \Psi_{M3} \cdot i_{q3} + 5 \Psi_{M5} \cdot i_{q5} + \cdots) \quad (5.34)$$

---

<sup>14</sup> Proven in Appendix 9.5.4.

### 5.1.6 Power losses expression

By only considering the Joule losses in the stator windings<sup>15</sup>, the instantaneous power dissipated by the machine can be expressed as:

$$p_R = \sum_{k=1}^n R \cdot i_k^2 = R \cdot (\mathbf{i}^T \cdot \mathbf{i}) = R \cdot I_{RMS}^2 \quad (5.35)$$

where the term

$$I_{RMS} = \|\mathbf{i}\| = \sqrt{\mathbf{i}^T \cdot \mathbf{i}} = \sqrt{\sum_{k=1}^n i_k^2} \quad (5.36)$$

is an *equivalent root mean square* (RMS) current for the whole machine.

Considering the variable transformations (5.14) and (5.27), the instantaneous power losses can be written in terms of the synchronous current set  $\mathbf{i}_{dq}$  as:

$$\begin{aligned} p_R &= R \cdot I_{RMS}^2 = R \cdot \mathbf{i}^T \cdot \mathbf{i} = \\ &= R \cdot (\mathbf{C}^{-1} \cdot \mathbf{D}^T(\theta_{el}) \cdot \mathbf{i}_{dq})^T \cdot (\mathbf{C}^{-1} \cdot \mathbf{D}^T(\theta_{el}) \cdot \mathbf{i}_{dq}) = \\ &= R \cdot \mathbf{i}_{dq}^T \cdot (\mathbf{D}(\theta_{el}) \cdot \mathbf{C}^{-T} \cdot \mathbf{C}^{-1} \cdot \mathbf{D}^T(\theta_{el})) \cdot \mathbf{i}_{dq} = \\ &= R \cdot \mathbf{i}_{dq}^T \cdot \mathbf{G}(\theta) \cdot \mathbf{i}_{dq} \end{aligned} \quad (5.37)$$

where  $\mathbf{G}(\theta) = \mathbf{D}(\theta_{el}) \cdot \mathbf{C}^{-T} \cdot \mathbf{C}^{-1} \cdot \mathbf{D}^T(\theta_{el})$  is a *weighting matrix* for the instantaneous power losses computation<sup>16</sup>. The matrix  $\mathbf{G}(\theta)$  only depends on the chosen VSD and rotational transformations and, therefore, it can be computed analytically.

The steady-state average power losses  $P_R$  of the machine can be simply found by averaging  $p_R$  over a full  $2\pi$  electrical rotor cycle. If the synchronous current set  $\mathbf{i}_{dq}$  is constant, this results in:

$$\begin{aligned} P_R &= \frac{1}{2\pi} \int_0^{2\pi} p_R(\theta_{el}) d\theta_{el} = \frac{1}{2\pi} \int_0^{2\pi} R \cdot \mathbf{i}_{dq}^T \cdot \mathbf{G}(\theta) \cdot \mathbf{i}_{dq} d\theta_{el} = \\ &= R \cdot \mathbf{i}_{dq}^T \cdot \left( \frac{1}{2\pi} \int_0^{2\pi} \mathbf{G}(\theta) d\theta_{el} \right) \cdot \mathbf{i}_{dq} = R \cdot \mathbf{i}_{dq}^T \cdot \mathbf{H} \cdot \mathbf{i}_{dq} \end{aligned} \quad (5.38)$$

where  $\mathbf{H} = (1/2\pi) \int_0^{2\pi} \mathbf{G}(\theta_{el}) d\theta_{el}$  is a weighting matrix for the average power losses computation. The matrix  $\mathbf{H}$  is simply given by the element-by-element average of  $\mathbf{G}(\theta_{el})$  and can also be computed analytically.

It can be proven that all the non-diagonal terms of  $\mathbf{G}(\theta_{el})$  are trigonometric functions with a zero average value over a full cycle of  $\theta_{el}$ , and that the diagonal terms related to the same  $h$ -th space vector components have an equal average value  $H_h > 0$  over a full electrical rotor cycle<sup>17</sup>. Therefore,  $\mathbf{H}$  is a positive definite diagonal matrix.

<sup>15</sup> This is coherent with the approximations introduced in the generalized mathematical model developed in Chapter 2.

<sup>16</sup> It is worth recalling that the notation  $\mathbf{C}^{-T}$  stands for  $\mathbf{C}^{-T} = (\mathbf{C}^{-1})^T = (\mathbf{C}^T)^{-1}$ .

<sup>17</sup> Proven in Appendix 9.5.5.

Considering, as an example, the VSD and rotational transformations (5.19) and (5.29), the corresponding matrix  $\mathbf{H}$  is:

$$\mathbf{H} = \begin{bmatrix} H_1 & 0 & 0 & 0 & 0 & 0 & \dots & (0) & 0 \\ 0 & H_1 & 0 & 0 & 0 & 0 & \dots & (0) & 0 \\ 0 & 0 & H_3 & 0 & 0 & 0 & \dots & (0) & 0 \\ 0 & 0 & 0 & H_3 & 0 & 0 & \dots & (0) & 0 \\ 0 & 0 & 0 & 0 & H_5 & 0 & \dots & (0) & 0 \\ 0 & 0 & 0 & 0 & 0 & H_5 & \dots & (0) & 0 \\ \vdots & \vdots & \vdots & \vdots & \vdots & \vdots & \ddots & \vdots & \vdots \\ (0) & (0) & (0) & (0) & (0) & (0) & \dots & (H_0^-) & (0) \\ 0 & 0 & 0 & 0 & 0 & 0 & \dots & (0) & H_0 \end{bmatrix} \quad (5.39)$$

meaning that the corresponding expression (5.38) for the average power losses is:

$$P_R = R \cdot \left( H_1 \cdot i_{d1}^2 + H_1 \cdot i_{q1}^2 + H_3 \cdot i_{d3}^2 + H_3 \cdot i_{q3}^2 + \dots \right. \\ \left. \dots + H_5 \cdot i_{d5}^2 + H_5 \cdot i_{q5}^2 + \dots + (H_0^- \cdot i_0^{-2}) + H_0 \cdot i_0^2 \right) \quad (5.40)$$

Again, a drastic simplification is obtained for symmetrical machines. Indeed, as previously stated, for a symmetrical machine the Clarke transformation matrix  $\mathbf{C}$  is unitary, meaning that  $\mathbf{C}^{-1} = \mathbf{C}^T$ . Therefore, the power losses weighing matrix are simplified to<sup>18</sup>  $\mathbf{H} = \mathbf{G}(\theta_{el}) = \mathbf{I}$ . Therefore, the power losses expression simply becomes:

$$P_R = p_R = R \cdot (\mathbf{i}_{dq}^T \cdot \mathbf{i}_{dq}) = R \cdot \|\mathbf{i}_{dq}\|^2 = \\ = R \cdot \left( i_{d1}^2 + i_{q1}^2 + i_{d3}^2 + i_{q3}^2 + i_{d5}^2 + i_{q5}^2 + \dots + (i_0^{-2}) + i_0^2 \right) \quad (5.41)$$

meaning that it simply results  $I_{RMS} = \|\mathbf{i}\| = \|\mathbf{i}_{dq}\|$ . In this case, the average power losses are equal to the instantaneous power losses, and all the components of the synchronous current set  $\mathbf{i}_{dq}$  are equally weighted in their computation<sup>19</sup>. On the contrary, for an asymmetrical machine configuration, this property is not generally true, meaning that different components of  $\mathbf{i}_{dq}$  may have a different impact on the overall power losses.

### 5.1.7 Mechanical model

The electrical machine mechanical model is governed by the dynamical equations (2.3)-(2.4), which are here reported:

$$J \cdot \frac{d\omega}{dt} + F(\omega) \cdot \omega = T_{em} - T_m \quad (5.42)$$

$$\frac{d\theta}{dt} = \omega \quad (5.43)$$

<sup>18</sup> Proven in Appendix 9.5.6.

<sup>19</sup> This explains why the definition (5.9) is also known as *power invariant*.

where it is worth recalling that  $J$  represents the rotor inertia of the electrical machine,  $F(\omega)$  represents a mechanical friction coefficient and  $T_m$  is the mechanical braking torque applied to the rotor shaft.

The electrical machine rotor shaft is typically connected to other rigid bodies through a mechanical transmission system. Both the rigid bodies and the transmission system can actively influence the mechanical behaviour of the electrical machine. This effect depends on the mechanical braking torque  $T_m$  which, in many common applications, can be modelled through the simple equation:

$$T_m = J_m \cdot \frac{d\omega}{dt} + F_m(\omega) \cdot \omega + T_{load} \quad (5.44)$$

This simplified model considers three contributions:

- the term  $J_m \cdot d\omega/dt$  represents an *inertial torque* contribution, which is related to the *moment of inertia* of the rotating mechanical bodies  $J_m$ ,
- the term  $F_m(\omega) \cdot \omega$  represents a *friction torque* contribution, and
- the term  $T_{load}$  represents a *loading mechanical torque*, related to the mechanical power absorbed by the connected system.

By properly combining (5.44) with (5.42), the dynamics of the rotor speed is:

$$J_{eq} \cdot \frac{d\omega}{dt} + F_{eq}(\omega) \cdot \omega = (J + J_m) \cdot \frac{d\omega}{dt} + [F(\omega) + F_m(\omega)] \cdot \omega = T_{em} - T_{load} \quad (5.45)$$

which has the same form as the expression (5.42), but with different values for the parameters. Therefore, the speed control can just refer to the overall mechanical group inertia  $J_{eq} = (J + J_m)$  and friction coefficient  $F_{eq}(\omega) = [F(\omega) + F_m(\omega)]$  of (5.45).

The difference between (5.42) and (5.45) can be relevant in case of torque measurements done at the joint between the electrical machine and the mechanical load, which would provide the value of  $T_m$ . However,  $T_m$  is generally not equal to the actual torque  $T_{em}$  developed by the electrical machine or to the torque  $T_{load}$  required by the mechanical load, because it does not consider the machine inertia and friction contributions. Further details are given in Appendix 9.1.2.

## 5.2 Torque control strategy

The machine control strategy is aimed at developing a desired electromagnetic torque  $T_{em}^*$  coming, for example, from a speed feedback controller. Since the electromagnetic torque is produced by the mutual interaction between fluxes and currents, this requirement can be obtained by formulating a proper strategy to compute the reference currents for the machine.

In field-oriented control algorithms, the problem is formalized in the multiple synchronous domain by considering the torque expression (5.32), which is used to compute a reference current set  $i_{dq}^*$  to be tracked. Once the synchronous reference current set  $i_{dq}^*$  has been computed, the corresponding set of phase reference currents can be simply found through an inverse Park transformation, as:

$$\mathbf{i}^* = \mathbf{C}^{-1} \cdot \mathbf{D}^T(\theta_{el}) \cdot \mathbf{i}_{dq}^* \quad (5.46)$$

Considering the general case in which multiple spatial harmonics are present in the

magnetic field at the air gap, different strategies can be formulated to compute  $\hat{\mathbf{i}}_{dq}^*$  for a given reference torque  $T_{em}^*$ . This section presents some of these torque control strategies, specifically addressed to asymmetrical machine configurations.

### 5.2.1 Fundamental currents control strategy

This torque development strategy is directly derived from standard FOC algorithms developed for three-phase PMSMs. It consists of controlling only the component  $i_{q1}^*$  of the synchronous current set  $\hat{\mathbf{i}}_{dq}$ , while keeping all the other terms to zero.

With this choice, the torque expression (5.34) simply becomes:

$$T_{em} = \kappa_1 \cdot i_{q1} = P_p \cdot \sqrt{\frac{n}{2}} \cdot \Psi_{M1} \cdot i_{q1} \quad (5.47)$$

and the reference current to develop a desired electromagnetic torque  $T_{em}^*$  is simply found by inverting (5.47), resulting in:

$$i_{q1}^* = \frac{T_{em}^*}{\kappa_1} = \frac{T_{em}^*}{\sqrt{n/2} \cdot P_p \cdot \Psi_{M1}} \quad (5.48)$$

The functional block diagram of this torque control strategy is schematically represented in Fig. 5.2.

The synchronous current set  $\hat{\mathbf{i}}_{dq}^* = [0 \quad i_{q1}^* \quad 0 \quad 0 \quad \dots \quad (0) \quad 0]^T$  can be transformed into the phase variable domain by applying (5.46). The only rotational submatrix to multiply non-zero terms is  $\mathbf{D}_1(\theta_{el})$ . Consequently, the optimal phase currents are sinusoidal functions of the rotor electrical position  $\theta_{el}$  and, in steady-state conditions with a constant angular speed and a constant reference torque, they are also sinusoidal in time.

The average losses obtained when only the fundamental current component is used can be found via (5.40) to be:

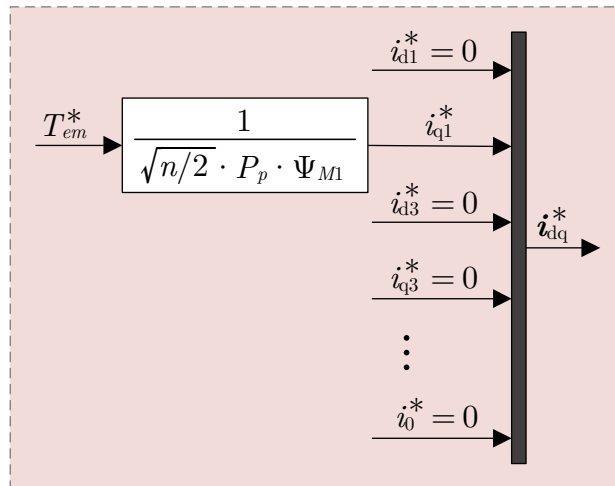


Fig. 5.2 – Functional block scheme of the fundamental current control algorithm.

$$P_R^{(\text{FUND})} = R \cdot H_1 \cdot i_{q1}^{*2} = R \cdot T_{em}^* \cdot \frac{H_1}{\kappa_1} \quad (5.49)$$

and are quadratically increasing with the reference torque  $T_{em}^*$ .

An example of this strategy will be given in Section 5.6.1.

### 5.2.2 Third harmonic injection strategy

For machines with significant higher-order spatial harmonics in the PM-induced flux linkages, it is possible to exploit the quadrature components of some higher-order space vector components to contribute to the electromagnetic torque development. This results in a higher number of degrees of freedom, which can be used to optimize some performances of the drive.

The simplest enhancement can be obtained by also controlling the  $i_{q3}$  current component. In steady-state conditions at a constant speed and constant torque, due to the  $3\theta_{el}$  rotation in the  $\mathbf{D}(\theta_{el})$  matrix, the application of a constant  $i_{q3}$  corresponds to a *third harmonic injection* (THI) into the machine phase currents [119], [123].

In this case, the torque expression (5.34) becomes:

$$T_{em} = \kappa_1 \cdot i_{q1} + \kappa_3 \cdot i_{q3} = P_p \cdot \sqrt{\frac{n}{2}} \cdot \left( \Psi_{M1} \cdot i_{q1} + 3 \Psi_{M3} \cdot i_{q3} \right) \quad (5.50)$$

Contrarily to the previous case, there are now two available degrees of freedom for the torque control (being  $i_{q1}$  and  $i_{q3}$ ). Therefore, their reference value can be chosen to optimize some system performances while, at the same time, developing the desired reference torque  $T_{em}^*$ .

The choice of the proposed optimization is to minimize the average power losses  $P_R$ . Considering (5.40), their expression is:

$$P_R = R \cdot I_{RMS}^2 = R \cdot (H_1 \cdot i_{q1}^2 + H_3 \cdot i_{q3}^2) \quad (5.51)$$

As a result, the proposed strategy can be formalized as the constrained minimization problem:

$$\min_{\{i_{q1}, i_{q3}\}} \{H_1 \cdot i_{q1}^2 + H_3 \cdot i_{q3}^2\} \quad \text{subject to} \quad \kappa_1 \cdot i_{q1} + \kappa_3 \cdot i_{q3} = T_{em}^* \quad (5.52)$$

This problem can be easily reformulated in terms of a *third-harmonic injection ratio*, defined as [119], [123]:

$$k = i_{q3}/i_{q1} \quad (5.53)$$

With the position (5.53), the torque development requirement becomes:

$$T_{em}^* = \kappa_1 \cdot i_{q1}^* + \kappa_3 \cdot k \cdot i_{q1}^* = (\kappa_1 + k \cdot \kappa_3) \cdot i_{q1}^* \quad (5.54)$$

and the currents  $i_{q1}$  and  $i_{q3}$  can be expressed as:

$$i_{q1} = \frac{T_{em}^*}{\kappa_1 + k \cdot \kappa_3} \quad \text{and} \quad i_{q3} = \frac{k \cdot T_{em}^*}{\kappa_1 + k \cdot \kappa_3} \quad (5.55)$$

The minimising function is therefore reformulated as a function of  $k$ :

$$P_R(k) = R \cdot I_{RMS}^2(k) = R \cdot T_{em}^*{}^2 \cdot \frac{H_1 + H_3 \cdot k^2}{(\kappa_1 + k \cdot \kappa_3)^2} \quad (5.56)$$

The function (5.56) is convex with respect to the injection ratio  $k$  and its minimum can be found by nullifying its derivative  $\partial P_R / \partial k$ . Then, the optimal injection ratio is<sup>20</sup>:

$$k^* = \frac{\kappa_3 / \kappa_1}{H_3 / H_1} \quad (5.57)$$

and the corresponding optimal currents are:

$$i_{q1}^* = \frac{H_3 \cdot \kappa_1}{H_1 \cdot \kappa_3^2 + H_3 \cdot \kappa_1^2} \cdot T_{em}^* \quad \text{and} \quad i_{q3}^* = \frac{H_1 \cdot \kappa_3}{H_1 \cdot \kappa_3^2 + H_3 \cdot \kappa_1^2} \cdot T_{em}^* \quad (5.58)$$

A schematic block diagram of this strategy is represented in Fig. 5.3.

From (5.57) and (5.58) it can be concluded that currents are proportional to the reference electromagnetic torque  $T_{em}^*$  and their ratio depends both on the induced fluxes magnitudes (via  $\kappa_1$  and  $\kappa_3$ ) and on the magnetic axes disposition (via  $H_1$  and  $H_3$ ).

The average losses with the optimal injection ratio are:

$$P_R^{(THI)} = P_R(k^*) = R \cdot T_{em}^*{}^2 \cdot \frac{H_1 \cdot H_3}{H_1 \cdot \kappa_3^2 + H_3 \cdot \kappa_1^2} \quad (5.59)$$

They can be compared with the losses  $P_R^{(FUND)}$  obtained when only the current  $i_{q1}$  is exploited. Their ratio is:

$$\frac{P_R^{(THI)}}{P_R^{(FUND)}} = \frac{H_3 \cdot \kappa_1^2}{H_1 \cdot \kappa_3^2 + H_3 \cdot \kappa_1^2} \quad (5.60)$$

which can be easily verified to always be less than 1, meaning that  $P_R^{(THI)} \leq P_R^{(FUND)}$ . In other words, from the energetic point of view, it is always convenient to exploit (whenever possible), this third harmonic injection strategy.

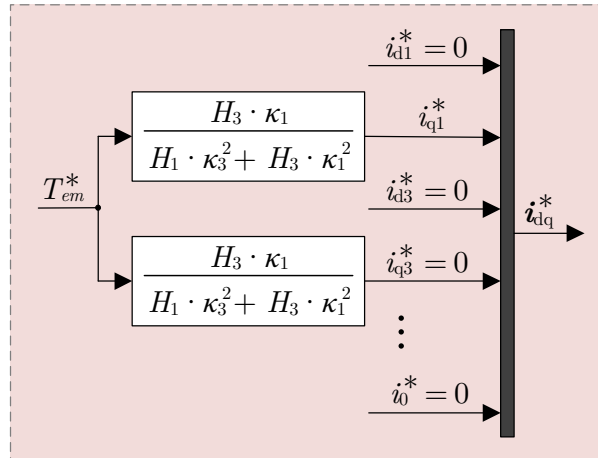


Fig. 5.3 – Functional block scheme of the third harmonic injection strategy.

<sup>20</sup> Proven in Appendix 9.5.7.

In case  $\Psi_{M3} = 0$  (like in machines with a sinusoidal magnetic field at the air-gap), since it results  $\kappa_3 = 0$ , the expression (5.57) simply becomes  $k^* = 0$ , meaning that  $i_{q3}^* = 0$  and that the third harmonic injection cannot be exploited for torque enhancement.

It is worth emphasizing that the proposed harmonic injection strategy does not lead to torque ripple, since it is formalized basing on the instantaneous torque expression, which is forced to be constant. It is also worth noticing that the same strategy can also be applied for different harmonic injection (e.g., fifth-harmonic injection).

An example of this strategy will be given in Section 5.6.2.

### 5.2.3 Multi-harmonic injection strategy

The previous strategy can be extended to allow for the simultaneous exploitation of multiple harmonics at the same time. Indeed, considering (5.40), all the quadrature components  $i_{qh}$  of the transformed set  $i_{dq}$  can contribute to the torque development.

By choosing a constant  $i_{dq}$  set each subset  $\{i_{dh}, i_{qh}\}$  is subject to a rotation of  $h\theta_{el}$  in the inverse transformation (5.46). Then, in steady-state conditions at a constant speed and constant torque, this corresponds to a *multi-harmonic injection* (MHI) into the machine phase currents [122].

Again, the higher number of degrees of freedom can be used to minimize the average stator power losses in the machine. Considering the general expressions (5.32) and (5.38), this strategy can be mathematically formalized as the constrained optimization problem:

$$\min_{i_{dq}} \{ i_{dq}^T \cdot \mathbf{H} \cdot i_{dq} \} \quad \text{subject to} \quad \boldsymbol{\kappa}^T \cdot i_{dq} = T_{em}^* \quad (5.61)$$

which is the generalization of the problem (5.52).

The problem (5.61) can be solved analytically by using the Lagrange multiplier method. A Lagrangian function for (5.61) can be chosen as:

$$\mathcal{L}(i_{dq}, \mu) = \frac{1}{2} i_{dq}^T \cdot \mathbf{H} \cdot i_{dq} - \mu \cdot (\boldsymbol{\kappa}^T \cdot i_{dq} - T_{em}^*) \quad (5.62)$$

where  $\mu$  is the Lagrange multiplier associated with the torque development requirement. The solution to the constrained optimization problem is found by nullifying the gradient of  $\mathcal{L}(i_{dq}, \mu)$ , which results in the linear algebraic system:

$$\begin{aligned} \frac{\partial \mathcal{L}}{\partial i_{dq}} &= \mathbf{H} \cdot i_{dq} - \mu \cdot \boldsymbol{\kappa} = \mathbf{0} \\ \frac{\partial \mathcal{L}}{\partial \mu} &= \boldsymbol{\kappa}^T \cdot i_{dq} - T_{em}^* = 0 \end{aligned} \quad (5.63)$$

which leads to the optimal synchronous current set<sup>21</sup>:

$$i_{dq}^* = \frac{\mathbf{H}^{-1} \cdot \boldsymbol{\kappa}}{\boldsymbol{\kappa}^T \cdot \mathbf{H}^{-1} \cdot \boldsymbol{\kappa}} \cdot T_{em}^* \quad (5.64)$$

and to the simple functional block diagram of Fig. 5.4.

<sup>21</sup> Proven in Appendix 9.5.8.

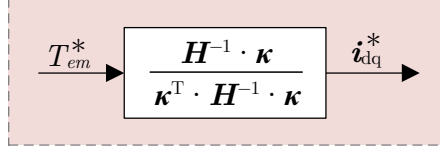


Fig. 5.4 – Functional block scheme of the multiple harmonic injection strategy.

Generally speaking, by using (5.64), the zero-sequence component  $i_0^*$ , the second zero-sequence component  $i_0^{-*}$  (if present) and all the direct axes components  $i_{dh}^*$  are zero, because they dissipate power without actively contributing to the torque development. The quadrature axis components  $i_{qh}^*$  are instead non-zero and each one of them is proportional to the reference electromagnetic torque  $T_{em}^*$  and to the ratio  $(\kappa_h/H_h)$  of the corresponding harmonic. This result is also expected because it favours the spatial harmonic components with the highest induced fluxes  $\Psi_{Mh}$  (and, hence, the highest values of  $\kappa_h$ , which does not depend on the magnetic axes disposition) and the lowest contribution to the average power losses (and, hence, the lowest values of  $H_h$ , which are instead related to the magnetic axes disposition).

To give an example, given the VSD and rotational transformations (5.19) and (5.29), the expression (5.64) is particularized in:

$$\mathbf{i}_{dq}^* = \frac{[0 \quad \kappa_1/H_1 \quad 0 \quad \kappa_3/H_3 \quad 0 \quad \kappa_5/H_5 \quad \cdots \quad (0) \quad 0]^T}{\kappa_1^2/H_1 + \kappa_3^2/H_3 + \kappa_5^2/H_5 + \cdots} \cdot T_{em}^* \quad (5.65)$$

The average machine losses with the optimal currents set (5.64) are:

$$P_R^{(\text{MHI})} = P_R(i_{dq}^*) = R \cdot T_{em}^{*2} \cdot \frac{1}{\kappa^T \cdot \mathbf{H}^{-1} \cdot \kappa} \quad (5.66)$$

They can be compared with the losses  $P_R^{(\text{FUND})}$  obtained when only the current  $i_{q1}$  is exploited. Their ratio is:

$$\frac{P_R^{(\text{MHI})}}{P_R^{(\text{FUND})}} = \frac{H_1/\kappa_1}{\kappa^T \cdot \mathbf{H}^{-1} \cdot \kappa} = \frac{H_1/\kappa_1}{\sum_h (H_h/\kappa_h)} \quad (5.67)$$

which can be easily verified to always be less than 1, meaning that  $P_R^{(\text{MHI})} \leq P_R^{(\text{FUND})}$ . Similarly, by comparing (5.66) with the losses expression (5.59) obtained with the optimal third harmonic injection strategy of Section 0, it can be verified that it also results  $P_R^{(\text{MHI})} \leq P_R^{(\text{THI})}$ . This means that, from the energetic point of view, it is always convenient to exploit this multi-harmonic harmonic injection strategy.

In case of a symmetrical machine, since  $\mathbf{H} = \mathbf{I}$ , the expression (5.65) is simplified to:

$$\begin{aligned} \mathbf{i}_{dq}^* &= \frac{[0 \quad \kappa_1 \quad 0 \quad \kappa_3 \quad 0 \quad \kappa_5 \quad \cdots \quad (0) \quad 0]^T}{\kappa_1^2 + \kappa_3^2 + \kappa_5^2 + \cdots} \cdot T_{em}^* = \\ &= \sqrt{\frac{2}{n}} \cdot \frac{[0 \quad \Psi_{M1} \quad 0 \quad 3\Psi_{M3} \quad 0 \quad 5\Psi_{M5} \quad \cdots \quad (0) \quad 0]^T}{\Psi_{M1}^2 + 9\Psi_{M3}^2 + 25\Psi_{M5}^2 + \cdots} \cdot \frac{T_{em}^*}{P_p} \end{aligned} \quad (5.68)$$

Given the common denominator, each  $h$ -th quadrature current component is proportional to  $h \Psi_{Mh}$ , which is the same proportionality ratio of the induced back-

EMFs. This means that, for a symmetrical  $n$ -phase machine with only the odd-order harmonics with index  $h \leq n$ , the optimal phase currents have the same waveform of the induced back-EMFs.

An example of this strategy will be given in Section 5.6.3.

### 5.2.4 Maximum torque per ampere strategy

The injection strategies proposed in the previous sections made use of a constant reference current set  $\mathbf{i}_{dq}^*$  and exploited the higher number of degrees of freedom to minimize the average stator losses  $P_R$  expressed by (5.38). The choice of a constant  $\mathbf{i}_{dq}^*$  allow for an easier implementation of the control strategy in a real-time application, since the optimization can be conveniently computed offline. Moreover, as discussed later on, by computing a constant synchronous set  $\mathbf{i}_{dq}^*$ , the current control can be performed with standard regulators (e.g., PI controllers).

However, the drive energetic performances can be further improved by allowing the reference current set  $\mathbf{i}_{dq}^*$  to be variable with the electrical rotor position  $\theta_{el}$  and by aiming at the minimization of the instantaneous power losses  $p_R$ .

Since  $p_R = R \cdot I_{RMS}^2$ , the minimization of  $p_R$  for a given reference torque  $T_{em}^*$  can be also interpreted as the maximization of the developed torque  $T_{em}$  for a given overall RMS current  $I_{RMS}$ . As a result, this approach represents a *maximum torque per ampere* (MTPA) strategy.

Considering the generalized formulation of the torque (5.32) and the instantaneous power losses (5.37), the problem can be formalized as:

$$\min_{\mathbf{i}_{dq}} \{ \mathbf{i}_{dq}^T \cdot \mathbf{G}(\theta_{el}) \cdot \mathbf{i}_{dq} \} \quad \text{subject to} \quad \begin{cases} \boldsymbol{\kappa}^T \cdot \mathbf{i}_{dq} = T_{em}^* \\ i_0 = 0 \end{cases} \quad (5.69)$$

where the additional constraint  $i_0 = 0$  (required by the isolated neutral point configuration) must now be directly enforced in the optimization procedure because  $\mathbf{G}(\theta_{el})$  is, in general, not diagonal<sup>22</sup>.

The problem can be reformulated similarly to (5.61) and solved analytically through the Lagrange multipliers method. The optimal current set is<sup>23</sup>:

$$\mathbf{i}_{dq}^*(\theta_{el}) = \frac{\mathbf{G}'_{eq}(\theta_{el}) \cdot \boldsymbol{\kappa}}{\boldsymbol{\kappa}^T \cdot \mathbf{G}'_{eq}(\theta_{el}) \cdot \boldsymbol{\kappa}} \cdot T_{em}^* \quad (5.70)$$

where the weighting matrix  $\mathbf{G}'_{eq}(\theta_{el})$  is defined as<sup>24</sup>:

$$\mathbf{G}'_{eq}(\theta_{el}) = \begin{bmatrix} \hat{\mathbf{G}}^{-1}(\theta_{el}) & \mathbf{0} \\ \mathbf{0} & 0 \end{bmatrix} \quad (5.71)$$

and  $\hat{\mathbf{G}}(\theta_{el})$  is a  $(n-1) \times (n-1)$  matrix obtained by removing the last row and the last

<sup>22</sup> The additional constraint  $i_0 = 0$  was not needed in the problem formulation (5.61) because it was always inferred by the optimal solution (5.64). This is because  $\mathbf{H}$  is diagonal and does not lead to coupling effects among different components of  $i_{dq}$  in the evaluation of  $P_R$ .

<sup>23</sup> Proven in Appendix 9.5.9.

<sup>24</sup> This operation is needed to enforce  $i_0^* = 0$ , which is required by the hardware configuration.

column from of  $\mathbf{G}(\theta_{el})$  (i.e., the row and the column related to the zero-sequence component  $i_0$ ). The functional block diagram of this control strategy is represented in Fig. 5.5.

Again, the optimal currents in (5.70) are proportional to the reference torque  $T_{em}^*$ . However, contrarily to the reference currents set (5.64) the solution (5.70) now depends on the instantaneous electrical rotor position  $\theta_{el}$ .

Since  $\mathbf{G}'_{eq}(\theta_{el})$  is, in general, not diagonal, the set  $\mathbf{i}_{dq}^*(\theta_{el})$  can also present non-zero direct axis components  $i_{dh}^*$ . These components, despite not developing any torque, can reduce the overall machine losses by interacting with the other components of  $\mathbf{i}_{dq}^*$ .

Since  $\mathbf{i}_{dq}^*$  periodically depends on  $\theta_{el}$ , when applying the inverse transformation (5.46), the resulting optimal phase currents set may also show additional harmonics which are absent in the fluxes and induced back-EMFs spectra (even in case of sinusoidal machines). These additional harmonics do not develop any average electromagnetic torque (because they do not interact with any corresponding term in the induced fluxes), but they can neutralize the torque ripple introduced by the interaction of the other harmonics.

The expression of the instantaneous power losses obtained with this current references computation strategy is:

$$p_R^{(\text{MTPA})}(\theta_{el}) = R \cdot T_{em}^{*2} \cdot \frac{1}{\boldsymbol{\kappa}^T \cdot \mathbf{G}'_{eq}(\theta_{el}) \cdot \boldsymbol{\kappa}} \quad (5.72)$$

The corresponding average losses  $P_R$  can be found by averaging the expression (5.72) over a full  $2\pi$  electrical rotor cycle:

$$P_R^{(\text{MTPA})} = R \cdot T_{em}^{*2} \cdot \frac{1}{2\pi} \int_0^{2\pi} \frac{1}{\boldsymbol{\kappa}^T \cdot \mathbf{G}'_{eq}(\theta_{el}) \cdot \boldsymbol{\kappa}} d\theta_{el} \quad (5.73)$$

About  $P_R^{(\text{MTPA})}$ , for which an analytical expression is not given (since the resolution of (5.73) is, in general, not easily computed) it can still be said that, since the expression  $\mathbf{i}_{dq}^*(\theta_{el})$  given by (5.70) results in the minimization of  $p_R$  for any value of  $\theta_{el}$ , by averaging, it results  $P_R^{(\text{MTPA})} \leq P_R^{(\text{MHI})} \leq P_R^{(\text{THI})} \leq P_R^{(\text{FUND})}$ . This means that, from the energetic point of view, the proposed MTPA strategy is always more convenient than the other injection strategies developed in the previous subsections. A comparison example is provided in Section 5.6.5.

However, for real time applications, the computation of (5.70) should be based on the value of the electrical rotor position  $\theta_{el}$ , which might not be easily addressed given

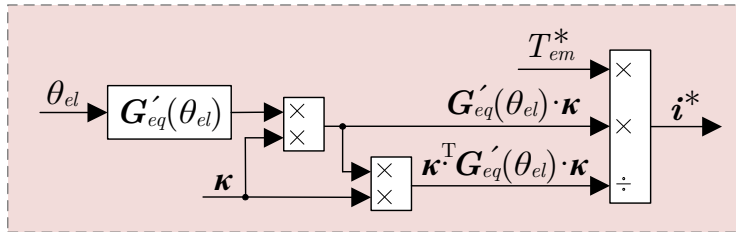


Fig. 5.5 – Functional block scheme of the MTPA strategy.

the matrix inversion in (5.71). Moreover, as will be discussed further on, the presence of a non-constant reference  $\mathbf{i}_{dq}^*$  may require a more complex current controller to effectively track the higher-order current harmonics.

As previously stated, for symmetrical machines it results  $p_R = P_R = R \cdot \mathbf{i}_{dq}^T \cdot \mathbf{i}_{dq}$ . In this case, the proposed MTPA strategy is equal to the multi-harmonic injection strategy developed in Section 5.2.3, and the optimal current set  $\mathbf{i}_{dq}^*$  computed via (5.70) is equal to the set provided in (5.64) (which it is worth recalling to be independent of  $\theta_{el}$ ).

An example of this strategy will be given in Section 5.6.4. A generalization of this MTPA approach, directly derived in the phase variable domain and computationally more convenient for real-time applications, will be derived in Chapter 6.

## 5.3 Current control

Once the chosen torque development strategy is executed, the controller must compute a set of converter voltages in a way to drive the synchronous current set  $\mathbf{i}_{dq}$  towards the desired references set  $\mathbf{i}_{dq}^*$ . In field-oriented controllers this is typically done in the multiple synchronous domain by referring to the mathematical model (5.30).

In other words, the current controller, by properly processing the error  $(\mathbf{i}_{dq}^* - \mathbf{i}_{dq})$ , computes a set  $\mathbf{u}_{dq}^*$  of reference voltages for the converter, which are then transformed back into the phase variable domain through the inverse Park transformation:

$$\mathbf{u}^* = \mathbf{C}^{-1} \cdot \mathbf{D}^T(\theta_{el}) \cdot \mathbf{u}_{dq}^* \quad (5.74)$$

The set  $\mathbf{u}^*$  is then used as the input of a pulse-width modulation technique, which computes the switching signals for the converter devices.

This section describes how the computation of  $\mathbf{u}_{dq}^*$  is typically accomplished by standard techniques developed for symmetrical machines, and what are instead the differences in case of asymmetrical configurations.

### 5.3.1 Current controller for symmetrical configurations

For symmetrical machines, the electrical equations in the synchronous reference frame are given by (5.31). As previously discussed, each space vector couple  $\{i_{dh}, i_{qh}\}$  is decoupled from the others, while the mutual coupling between  $i_{dh}$  and  $i_{qh}$  is only due to the rotational transformation (5.27). Moreover, in symmetrical machines, all the torque control strategies presented in Section 5.2 result in a constant reference synchronous current set.

As a result, in this case, similarly to how it is done for three-phase machines, the control can be easily achieved with proportional-integral (PI) controllers and simple compensation actions. The reference converter voltages in the synchronous domain are computed as:

$$\begin{cases} u_{dh}^* = w_{dh}^* - h\omega_{el} L_h i_{qh} + e_{dh} \\ u_{qh}^* = w_{qh}^* + h\omega_{el} L_h i_{dh} + e_{qh} \end{cases} \quad (5.75)$$

and correspond to the functional block diagram of Fig. 5.6, where:

- the terms  $w_{dh}^*$  and  $w_{qh}^*$  are the output of PI controllers respectively acting on

- the errors  $(i_{dh}^* - i_{dh})$  and  $(i_{qh}^* - i_{qh})$ ,
- the terms  $(-h\omega_{el} L_h i_{qh})$  and  $(+h\omega_{el} L_h i_{dh})$  are the compensation terms for the motional-induced back-EMFs due to the rotational transformation (5.27), and
- the terms  $e_{dh}$  and  $e_{qh}$  are the compensation terms for the motional-induced back-EMFs due to the permanent magnets on the rotor (and it is worth recalling that, typically,  $e_{dh} = 0$  and  $e_{qh} = \sqrt{n/2} \cdot h\omega_{el} \cdot \Psi_{Mh}$ ).

The second zero-sequence current component (if present), whose dynamical behaviour is governed by the differential equation (5.23), can be controlled by computing the second zero-sequence voltage as:

$$u_0^{-*} = w_0^{-*} + e_0^{-*} \tag{5.76}$$

and corresponds to the functional block diagram of Fig. 5.7, where:

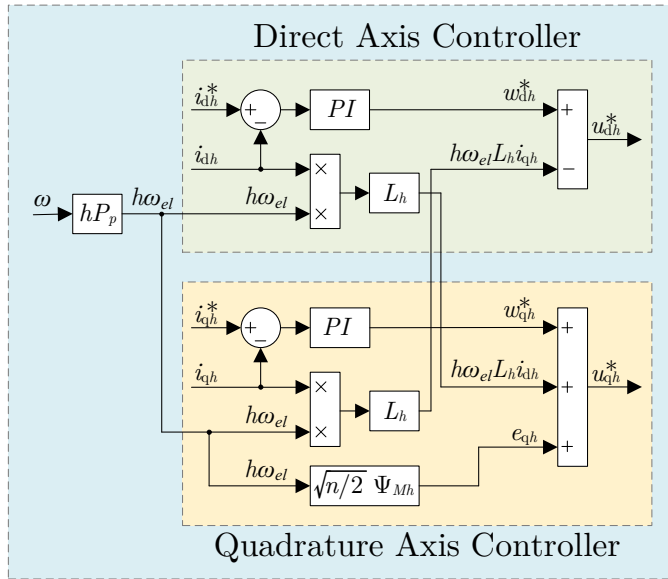


Fig. 5.6 – Functional block diagram of the decoupled current controller in the  $h$ -th synchronous reference frame for a symmetrical machine.

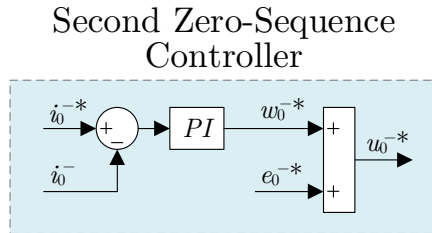


Fig. 5.7 – Functional block diagram of the second zero-sequence current controller for a symmetrical machine.

- the term  $w_0^-$  is the output of a PI controller acting on  $(i_0^- - i_0^-)$ , and
- the term  $e_0^-$  compensate (if present) the second zero-sequence component of the motional induced back-EMF related to the permanent magnets.

Naturally, since  $i_0 = 0$  because of the isolated neutral point configuration, no control action is needed for the zero-sequence current component. Consequently, the zero-sequence voltage  $u_0^*$  can be arbitrarily chosen with any typical common-mode injection strategy proposed for star-connected systems (e.g., min-max injection, higher-order harmonic injection, etc..., as mentioned in Section 3.2.2).

The equations (5.75)-(5.76) can be grouped and rewritten with a matrix notation as:

$$\mathbf{u}_{dq}^* = \mathbf{w}_{dq}^* + \omega_{el} \cdot \mathbf{L}_{dq2} \cdot \mathbf{i}_{dq} + \mathbf{e}_{dq} \quad (5.77)$$

which corresponds to the schematic block diagram of Fig. 5.8, where

- the set  $\mathbf{w}_{dq}^*$  is composed of the output voltage references computed by all the feedback PI controllers,
- the term  $\omega_{el} \cdot \mathbf{L}_{dq2} \cdot \mathbf{i}_{dq}$  is the compensation of all the motional induced back-EMFs generated by the machine model transformation into a moving reference frame, and
- the term  $\mathbf{e}_{dq}$  is the compensation of the motional induced back-EMFs due to the permanent magnets on the rotor (which, for a symmetrical machine, can be computed as  $\mathbf{e}_{dq} = \omega \cdot \boldsymbol{\kappa}$ ).

### 5.3.2 Current controller for asymmetrical configurations

As previously discussed, for asymmetrical configurations the dynamical model (5.30) presents additional mutual interactions between the state variables, which not only depend on the magnetic behaviour of the machine (through the effect of the inductances matrices  $\mathbf{L}_{dq1}$  and  $\mathbf{L}_{dq2}$ ), but also on the electrical connections of the phase windings, which are represented by the term  $\mathbf{g}(\theta_{el}) \cdot v_{NET}$  in (5.30). In this case, the current control may be more challenging.

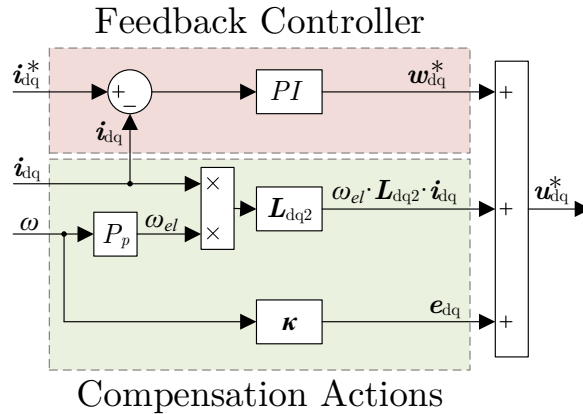


Fig. 5.8 – Functional block diagram of the field-oriented current controller for a symmetrical machine.

A possible way to adapt the current controller to this new configuration without significantly altering the basic control scheme<sup>25</sup> (5.77) is to compute the references voltage set as:

$$\mathbf{u}_{dq}^* = \mathbf{w}_{dq}^* + \omega_{el} \cdot \mathbf{L}_{dq2}(\theta_{el}) \cdot \mathbf{i}_{dq} + \mathbf{e}_{dq}(\theta_{el}) + \mathbf{g}(\theta_{el}) \cdot v_{NET}^* \quad (5.78)$$

The block scheme of this controller structure is represented in Fig. 5.9. Its structure is similar to the one of Fig. 5.8, but with the additional term  $\mathbf{g}(\theta_{el}) \cdot v_{NET}^*$ , aimed at compensating the mutual interactions due to the electrical configuration.

The term  $v_{NET}^*$  can be computed from the zero-sequence equation in (5.30) to compensate for the steady-state effects of the electrical network. A general formulation in case of a constant synchronous current set  $\mathbf{i}_{dq}^*$  is provided in (9.21) of Appendix 9.5.10, while a simple application example in which this additional compensation is computed analytically will be given in Section 5.5 and Section 5.6. Since the strategy (5.78), by keeping the same structure of (5.77), compensates only the motional-induced coupling

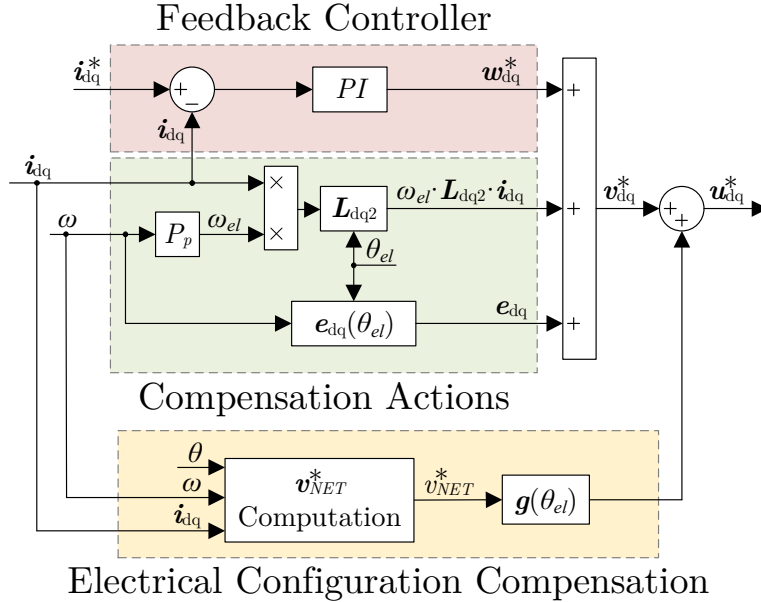


Fig. 5.9 – Functional block diagram of the field-oriented current controller for an asymmetrical machine.

<sup>25</sup> Other approaches can also be applied for the current control. For example, in case the asymmetry is coming from the post-fault reconfiguration of an originally symmetrical machine, another convenient option is to use the same VSD transformation and compensation terms of the healthy machine. In this case, however, the current references computed by any of the strategy presented in Section 5.2 are always non-sinusoidal and, contrarily to the healthy configuration, the current controller would also require additional control terms to follow the higher order harmonics (e.g., negative sequence synchronous PI controllers, resonant controllers, VPI controllers, etc...).

terms of  $v_{NET}$ , and neglects the transformer-induced terms (i.e., the terms related to  $di_{dh}/dt$  and  $di_{qh}/dt$ ), the stability robustness of the controller may be negatively affected, thus requiring a more conservative tuning of the controller parameters.

Moreover, for a generic winding configuration, the expressions of the PM-induced back-EMFs  $e_{dh} = 0$  and  $e_{qh} = \sqrt{n/2} \cdot h \omega_{el} \cdot \Psi_{Mh}$  (which have been adopted in the schemes of Fig. 5.6 and Fig. 5.8) are not generally guaranteed, meaning that  $e_{dq}$  may also depend on  $\theta_{el}$ . In this case  $e_{dq}$ , if not properly compensated, behaves as a periodic disturbance input for the current control.

In case of a constant reference current set  $\mathbf{i}_{dq}^*$  the same PI-based structure of symmetrical configurations can still be applied for the computation of  $\mathbf{w}_{dq}^*$ . On the contrary, the feedback controller structure might also need additional changes in case the reference current set  $\mathbf{i}_{dq}^*$  is not constant (e.g., for the MTPA strategy developed in Section 5.2.4). Indeed, for a non-constant synchronous current set, the feedback control may require additional control terms to follow the higher harmonics of  $\mathbf{i}_{dq}^*(\theta_{el})$  (e.g., negative sequence synchronous PI controllers, resonant controllers, etc...) [62], [63].

## 5.4 Complete drive control algorithm

The functional block scheme of the overall field-oriented controller is represented in Fig. 5.10.

First, the “*Speed Controller*” compares the reference speed  $\omega^*$  with the machine speed  $\omega$  and computes the reference electromagnetic torque  $T_{em}^*$  to be applied. The machine speed dynamics is described by the model (5.48), which is unrelated to the electrical machine parameters and configuration. As a result, any standard speed controller structure, like a PI regulator, can be used (as represented in Fig. 5.10).

The “*Torque Control Strategy*” block is then executed, by using one of the strategies presented in Section 5.2 to compute the reference currents set  $\mathbf{i}_{dq}^*$  to be tracked. In case the MTPA algorithm is chosen, this block also needs to know the instantaneous rotor electrical position  $\theta_{el}$ .

The generalized *Park transformation*, obtained by the cascaded application of the Clarke transformation matrix  $\mathbf{C}$  and of the rotational transformation matrix  $\mathbf{D}(\theta_{el})$ , is

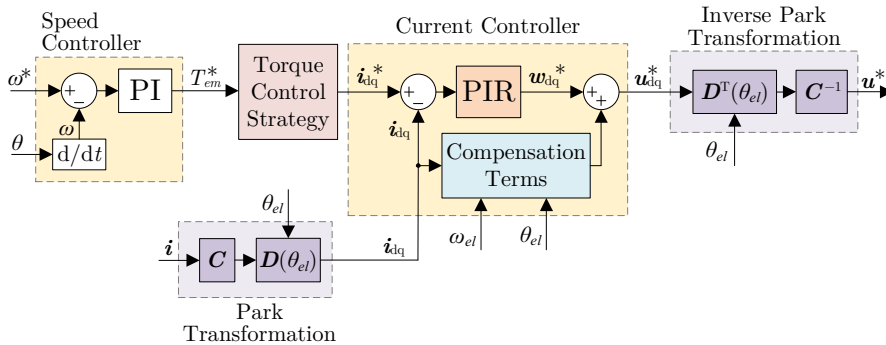


Fig. 5.10 – Functional block diagram of the field-oriented controller.

applied to compute the transformed currents set  $\hat{\mathbf{i}}_{dq}$  from the knowledge of the phase currents set  $\mathbf{i}$ .

The “*Current Controller*” block can then be executed. Following the discussion of Section 5.3, this block compares the reference currents set  $\hat{\mathbf{i}}_{dq}^*$  with the measured currents set  $\hat{\mathbf{i}}_{dq}$ , and processes this error with a feedback controller to compute the reference voltage  $\mathbf{w}_{dq}^*$ . As previously mentioned, for a generic machine configuration a simple PI controller may not be suited to properly track the reference current  $\hat{\mathbf{i}}_{dq}^*$ . Therefore, the scheme of Fig. 5.10 has been explicitly represented considering a Proportional-Integral-Resonant (PIR) controller architecture. As discussed in Section 5.3, the reference voltages set  $\mathbf{u}_{dq}^*$  is found by adding the proper compensation actions to the set  $\mathbf{w}_{dq}^*$ .

The transformed voltages set  $\mathbf{u}_{dq}^*$  is finally transformed back into the phase variable domain by applying an *inverse Park transformation* (5.74). The resulting set  $\mathbf{u}^*$  is processed by a pulse width modulator to compute the switching signals for the semiconductor devices.

The generalized Clarke transformation matrix  $\mathbf{C}$  and its inverse  $\mathbf{C}^{-1}$  (which it is worth recalling that, for asymmetrical machine configurations, may be different from  $\mathbf{C}^T$ ) can be computed offline or during the algorithm initialization to reduce the overall computational burden of the algorithm for a real-time application. The rotational transformation matrix must be instead computed in real time for each measured value of the rotor electrical position  $\theta_{el}$ .

## 5.5 Application example

The general analysis of the previous sections has been particularized to a specific application, which has been selected as an asymmetrical nine-phase PMSM. This section describes the mathematical modelling of the machine, by mainly focusing on the variable transformations adopted for the selected configuration. The numerical and experimental results regarding the same machine are then discussed in Section 5.6.

### 5.5.1 Machine under analysis

The electrical machine under analysis is based on the prototype represented in Fig. 5.11. It is a nine-phase surface mounted PMSM with 1 pole pair, obtained by rewinding an originally three-phase machine.

All the 18 machine windings are available externally and, according to their connection, the machine configuration can be either symmetrical or asymmetrical<sup>26</sup>. For the present analysis, the machine has been arranged in an asymmetrical configuration. The 9 machine phases are star connected with a single isolated neutral point.

The stator windings (geometrically identical) can be grouped into three symmetrical

---

<sup>26</sup> Further information about multiphase machine design compatible with both symmetrical and asymmetrical configurations can be found in [152]. The analysis of this same machine in the symmetrical configuration can be found in [155]–[157]. An example of the asymmetrical reconfiguration of a symmetrical nine-phase machine has been previously given in Section 4.3.5.

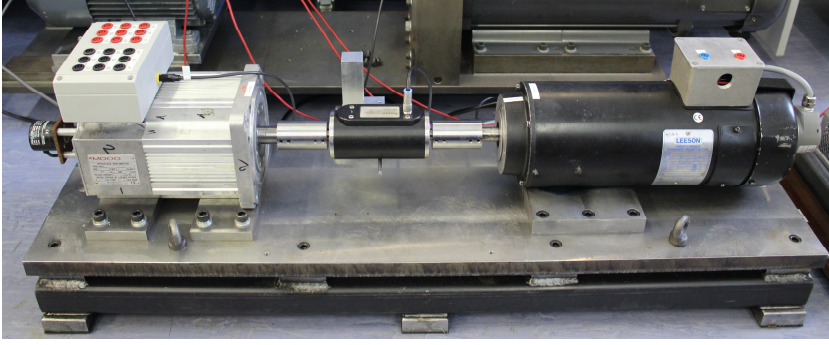


Fig. 5.11 – Nine-phase PMSM under analysis (left) coupled to a DC machine used for loading (right).

three-phase sets whose magnetic axes are mutually shifted by  $20^\circ$  from each other. It is, therefore, possible to define the angles set:

$$\alpha = [0^\circ \quad 120^\circ \quad 240^\circ \quad 20^\circ \quad 140^\circ \quad 260^\circ \quad 40^\circ \quad 160^\circ \quad 280^\circ]$$

which identifies the magnetic axes angles of all the machine phase windings.

The PM-induced back-EMFs have been found by measuring the terminal voltages while the machine was spinning at a constant speed and all the phases were disconnected. The back-EMFs have the same waveforms for all the 9 phases and are not sinusoidal. The back-EMF induced by the permanent magnets in phase 1, found by spinning the machine at around 1500 rpm, is depicted in Fig. 5.12.

For the present analysis, all the even-order harmonics and the odd-order harmonics with index  $h \geq 9$  are neglected.

As a result, the  $k$ -th PM-induced flux linkage (with  $k = 1, \dots, 9$ ) can be modelled as:

$$\begin{aligned} \psi_{PM,k}(\theta) &= \sum_{h=1,3,5,7} \Psi_{Mh} \cdot \cos(h \cdot (\theta - \alpha_k) + \varphi_h) = \\ &= \Psi_{M1} \cdot \cos(\theta - \alpha_k) + \Psi_{M3} \cdot \cos(3(\theta - \alpha_k) + \varphi_3) + \dots \\ &\dots + \Psi_{M5} \cdot \cos(5(\theta - \alpha_k) + \varphi_5) + \Psi_{M7} \cdot \cos(7(\theta - \alpha_k) + \varphi_7) \end{aligned}$$

The corresponding induced back-EMFs is then modelled as:

$$\begin{aligned} f_{PM,k}(\theta) &= \frac{\partial \psi_{PM,k}}{\partial \theta} = - \sum_{h=1,3,5,7} h \cdot \Psi_{Mh} \cdot \sin(h \cdot (\theta - \alpha_k) + \varphi_h) = \\ &= -\Psi_{M1} \cdot \sin(\theta - \alpha_k) - 3 \Psi_{M3} \cdot \sin(3(\theta - \alpha_k) + \varphi_3) + \dots \\ &\dots - 5 \Psi_{M5} \cdot \sin(5(\theta - \alpha_k) + \varphi_5) - 7 \Psi_{M7} \cdot \sin(7(\theta - \alpha_k) + \varphi_7) \end{aligned}$$

The fluxes magnitudes and phases are reported in Table 5.I.

The inductances parameters have been computed with the machine in the symmetrical configuration by individually exciting a single space vector at a time. The

inductances matrix, reported in Table 5.II, has been found by computing the inverse VSD transformation from the parameters found in the symmetrical configuration. It can

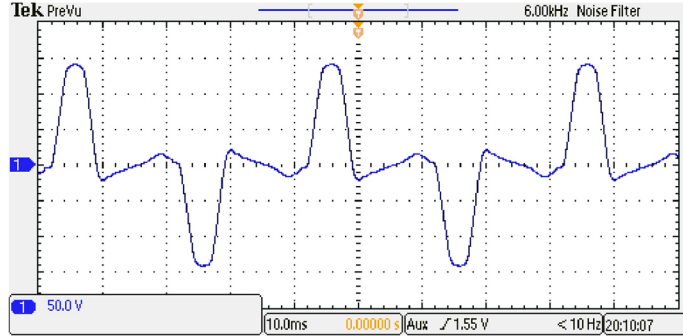


Fig. 5.12 – Waveforms of the PM-induced back-EMF in phase 1 (acquired at no load at 1500 rpm).

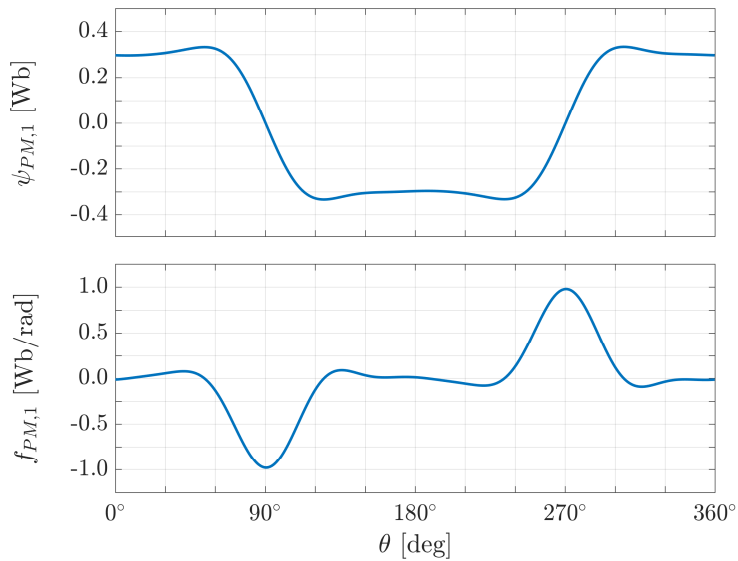


Fig. 5.13 – Waveforms of the PM induced flux and normalized back-EMF in phase 1 as a function of the rotor position (modelled only considering the 1<sup>st</sup>, 3<sup>rd</sup>, 5<sup>th</sup> and 7<sup>th</sup> harmonics).

Table 5.I – PMSM INDUCED FLUXES HARMONICS

$h$	1	3	5	7
$\Psi_{Mh}$ [mWb]	385	119	38	7
$\varphi_h$ [deg]	0°	180°	0°	165°

Table 5.II – PMSM INDUCTANCES MATRIX PARAMETERS

$L_{k_1 k_2}$ [mH]	$k_2$									
	1	2	3	4	5	6	7	8	9	
$k_1$	1	263	-35	-35	81	-58	-12	58	-81	12
	2	-35	263	-35	-12	81	-58	12	58	-81
	3	-35	-35	263	-58	-12	81	-81	12	58
	4	81	-12	-58	263	-35	-35	81	-58	-12
	5	-58	81	-12	-35	263	-35	-12	81	-58
	6	-12	-58	81	-35	-35	263	-58	-12	81
	7	58	12	-81	81	-12	-58	263	-35	-35
	8	-81	58	12	-58	81	-12	-35	263	-35
	9	12	-81	58	-12	-58	81	-35	-35	263

be verified that, coherently with the mathematical model presented in Chapter 2,  $\mathbf{L}$  is symmetric and positive definite<sup>27</sup>.

All the windings have approximately the same resistance  $R \cong 31.3 \Omega$  (which has been measured in DC).

### 5.5.2 Machine model in the synchronous domain

For the control of the analysed machine, the generalized Clarke transformation matrix  $\mathbf{C}$  has been built according to (5.19), in a way to control the space vectors  $\dot{i}_1$ ,  $\dot{i}_3$ ,  $\dot{i}_5$  and  $\dot{i}_7$  and, therefore, take advantage of the fundamental, the third, the fifth and the seventh spatial harmonics in the machine. Its explicit formulation is<sup>28</sup>:

$$\mathbf{C} = \begin{bmatrix} \mathbf{C}_1 \\ \mathbf{C}_3 \\ \mathbf{C}_5 \\ \mathbf{C}_7 \\ \mathbf{C}_0 \end{bmatrix} = \sqrt{\frac{2}{9}} \cdot \begin{bmatrix} \cos(\alpha_1) & \cos(\alpha_2) & \cos(\alpha_3) & \cos(\alpha_4) \\ \sin(\alpha_1) & \sin(\alpha_2) & \sin(\alpha_3) & \sin(\alpha_4) \\ \cos(3\alpha_1) & \cos(3\alpha_2) & \cos(3\alpha_3) & \cos(3\alpha_4) \\ \sin(3\alpha_1) & \sin(3\alpha_2) & \sin(3\alpha_3) & \sin(3\alpha_4) \\ \cos(5\alpha_1) & \cos(5\alpha_2) & \cos(5\alpha_3) & \cos(5\alpha_4) & \dots \\ \sin(5\alpha_1) & \sin(5\alpha_2) & \sin(5\alpha_3) & \sin(5\alpha_4) \\ \cos(7\alpha_1) & \cos(7\alpha_2) & \cos(7\alpha_3) & \cos(7\alpha_4) \\ \sin(7\alpha_1) & \sin(7\alpha_2) & \sin(7\alpha_3) & \sin(7\alpha_4) \\ 1/\sqrt{2} & 1/\sqrt{2} & 1/\sqrt{2} & 1/\sqrt{2} \end{bmatrix}$$

<sup>27</sup> The inductances matrix could have also been found directly in the phase variable domain, by separately supplying each phase at a time and measuring the induced voltage in the other windings. This method has been used to characterize the machine analysed in Chapter 6. It has a more general applicability, but typically requires more measurements to be done.

<sup>28</sup> The numerical values have been rounded to the second decimal unit.

$$\begin{array}{ccccc}
\cos(\alpha_5) & \cos(\alpha_6) & \cos(\alpha_7) & \cos(\alpha_8) & \cos(\alpha_9) \\
\sin(\alpha_5) & \sin(\alpha_6) & \sin(\alpha_7) & \sin(\alpha_8) & \sin(\alpha_9) \\
\cos(3\alpha_5) & \cos(3\alpha_6) & \cos(3\alpha_7) & \cos(3\alpha_8) & \cos(3\alpha_9) \\
\sin(3\alpha_5) & \sin(3\alpha_6) & \sin(3\alpha_7) & \sin(3\alpha_8) & \sin(3\alpha_9) \\
\cdots & \cos(5\alpha_5) & \cos(5\alpha_6) & \cos(5\alpha_7) & \cos(5\alpha_8) & \cos(5\alpha_9) \\
\sin(5\alpha_5) & \sin(5\alpha_6) & \sin(5\alpha_7) & \sin(5\alpha_8) & \sin(5\alpha_9) \\
\cos(7\alpha_5) & \cos(7\alpha_6) & \cos(7\alpha_7) & \cos(7\alpha_8) & \cos(7\alpha_9) \\
\sin(7\alpha_5) & \sin(7\alpha_6) & \sin(7\alpha_7) & \sin(7\alpha_8) & \sin(7\alpha_9) \\
1/\sqrt{2} & 1/\sqrt{2} & 1/\sqrt{2} & 1/\sqrt{2} & 1/\sqrt{2}
\end{array} \Bigg] =$$

$$= \begin{bmatrix}
0.47 & -0.24 & -0.24 & 0.44 & -0.36 & -0.08 & 0.36 & -0.44 & 0.08 \\
0 & 0.41 & -0.41 & 0.16 & 0.30 & -0.46 & 0.30 & 0.16 & -0.46 \\
0.47 & 0.47 & 0.47 & 0.24 & 0.24 & 0.24 & -0.24 & -0.24 & -0.24 \\
0 & 0 & 0 & 0.41 & 0.41 & 0.41 & 0.41 & 0.41 & 0.41 \\
0.47 & -0.24 & -0.24 & -0.08 & 0.44 & -0.36 & -0.44 & 0.08 & 0.36 \\
0 & -0.41 & 0.41 & 0.46 & -0.16 & -0.30 & -0.16 & 0.46 & -0.30 \\
0.47 & -0.24 & -0.24 & -0.36 & -0.08 & 0.44 & 0.08 & 0.36 & -0.44 \\
0 & 0.41 & -0.41 & 0.30 & -0.46 & 0.16 & -0.46 & 0.30 & 0.16 \\
0.33 & 0.33 & 0.33 & 0.33 & 0.33 & 0.33 & 0.33 & 0.33 & 0.33
\end{bmatrix}$$

It can be verified that the rank of  $\mathbf{C}$  is equal to 9, meaning that all the chosen space vector components can be controlled simultaneously.

The inverse matrix  $\mathbf{C}^{-1}$ , computed analytically<sup>29</sup>, is:

$$\mathbf{C}^{-1} = \sqrt{\frac{2}{9}} \cdot \begin{bmatrix}
\cos(\alpha_1) & \sin(\alpha_1) & \cos(3\alpha_1) - 1 & \sin(3\alpha_1) - \sqrt{3} \\
\cos(\alpha_2) & \sin(\alpha_2) & \cos(3\alpha_2) - 1 & \sin(3\alpha_2) - \sqrt{3} \\
\cos(\alpha_3) & \sin(\alpha_3) & \cos(3\alpha_3) - 1 & \sin(3\alpha_3) - \sqrt{3} \\
\cos(\alpha_4) & \sin(\alpha_4) & \cos(3\alpha_4) + 1 & \sin(3\alpha_4) + \sqrt{3} \\
\cos(\alpha_5) & \sin(\alpha_5) & \cos(3\alpha_5) + 1 & \sin(3\alpha_5) + \sqrt{3} \cdots \\
\cos(\alpha_6) & \sin(\alpha_6) & \cos(3\alpha_6) + 1 & \sin(3\alpha_6) + \sqrt{3} \\
\cos(\alpha_7) & \sin(\alpha_7) & \cos(3\alpha_7) - 1 & \sin(3\alpha_7) - \sqrt{3} \\
\cos(\alpha_8) & \sin(\alpha_8) & \cos(3\alpha_8) - 1 & \sin(3\alpha_8) - \sqrt{3} \\
\cos(\alpha_9) & \sin(\alpha_9) & \cos(3\alpha_9) - 1 & \sin(3\alpha_9) - \sqrt{3}
\end{bmatrix}$$

$$\begin{array}{ccccc}
\cos(5\alpha_1) & \sin(5\alpha_1) & \cos(7\alpha_1) & \sin(7\alpha_1) & 1/\sqrt{2} + \sqrt{2} \\
\cos(5\alpha_2) & \sin(5\alpha_2) & \cos(7\alpha_2) & \sin(7\alpha_2) & 1/\sqrt{2} + \sqrt{2} \\
\cos(5\alpha_3) & \sin(5\alpha_3) & \cos(7\alpha_3) & \sin(7\alpha_3) & 1/\sqrt{2} + \sqrt{2} \\
\cos(5\alpha_4) & \sin(5\alpha_4) & \cos(7\alpha_4) & \sin(7\alpha_4) & 1/\sqrt{2} - 2\sqrt{2} \\
\cdots & \cos(5\alpha_5) & \sin(5\alpha_5) & \cos(7\alpha_5) & \sin(7\alpha_5) & 1/\sqrt{2} - 2\sqrt{2} \\
\cos(5\alpha_6) & \sin(5\alpha_6) & \cos(7\alpha_6) & \sin(7\alpha_6) & 1/\sqrt{2} - 2\sqrt{2} \\
\cos(5\alpha_7) & \sin(5\alpha_7) & \cos(7\alpha_7) & \sin(7\alpha_7) & 1/\sqrt{2} + \sqrt{2} \\
\cos(5\alpha_8) & \sin(5\alpha_8) & \cos(7\alpha_8) & \sin(7\alpha_8) & 1/\sqrt{2} + \sqrt{2} \\
\cos(5\alpha_9) & \sin(5\alpha_9) & \cos(7\alpha_9) & \sin(7\alpha_9) & 1/\sqrt{2} + \sqrt{2}
\end{array} \Bigg] =$$

<sup>29</sup> With the aid of the Symbolic Math Toolbox of MATLAB. The numerical values are approximated to the second decimal unit.

$$= \begin{bmatrix} 0.47 & 0 & 0 & -0.82 & 0.47 & 0 & 0.47 & 0 & 1 \\ -0.24 & 0.41 & 0 & -0.82 & -0.24 & -0.41 & -0.24 & 0.41 & 1 \\ -0.24 & -0.41 & 0 & -0.82 & -0.24 & 0.41 & -0.24 & -0.41 & 1 \\ 0.44 & 0.16 & 0.71 & 1.22 & -0.08 & 0.46 & -0.36 & 0.30 & -1 \\ -0.36 & 0.30 & 0.71 & 1.22 & 0.44 & -0.16 & -0.08 & -0.46 & -1 \\ -0.08 & -0.46 & 0.71 & 1.22 & -0.36 & -0.30 & 0.44 & 0.16 & -1 \\ 0.36 & 0.30 & -0.71 & -0.41 & -0.44 & -0.16 & 0.08 & -0.46 & 1 \\ -0.44 & 0.16 & -0.71 & -0.41 & 0.08 & 0.46 & 0.36 & 0.30 & 1 \\ 0.08 & -0.46 & -0.71 & -0.41 & 0.36 & -0.30 & -0.44 & 0.16 & 1 \end{bmatrix}$$

The corresponding rotational matrix  $\mathbf{D}(\theta_{el}) = \mathbf{D}(\theta)$  takes the structure of (5.29).

Through the matrices  $\mathbf{C}$  and  $\mathbf{D}(\theta)$  it has been possible to apply the generalized Park transformation to the machine mathematical model.

It can be verified that the equations describing the first, the fifth and the seventh space vector components are decoupled from each other and assume the standard form:

$$\begin{cases} L_h \cdot \frac{di_{dh}}{dt} - h\omega L_h i_{qh} + R \cdot i_{dh} = v_{dh} = u_{dh} \\ L_h \cdot \frac{di_{qh}}{dt} + h\omega L_h i_{dh} + R \cdot i_{qh} + e_{qh} = v_{qh} = u_{qh} \end{cases} \quad (5.79)$$

with  $h = 1, 5, 7$  and  $e_{qh} = \sqrt{9/2} \cdot h\omega \Psi_{Mh}$ .

The third space vector components show, instead, the additional coupling effect of the neutral point potential shift through  $\mathbf{g}(\theta)$ , and are:

$$\begin{cases} L_3 \cdot \frac{di_{d3}}{dt} - 3\omega L_3 i_{q3} + R \cdot i_{d3} = v_{d3} = \\ \quad = u_{d3} - 2\sqrt{2} \cos\left(3\theta + \varphi_3 - \frac{\pi}{3}\right) \cdot v_{NET} \\ L_3 \cdot \frac{di_{q3}}{dt} + 3\omega L_3 i_{d3} + R \cdot i_{q3} + e_{q3} = v_{q3} = \\ \quad = u_{d3} - 2\sqrt{2} \cos\left(3\theta + \varphi_3 + \frac{\pi}{6}\right) \cdot v_{NET} \end{cases} \quad (5.80)$$

with  $e_{q3} = \sqrt{9/2} \cdot 3\omega \Psi_{M3} = 3/\sqrt{2} \cdot \omega \Psi_{M3}$ .

Additionally, given the asymmetrical configuration, the voltage  $v_{NET}$  is itself dependent on  $i_{d3}$  and  $i_{q3}$ . The explicit dependence can be found from the zero-sequence equation of the mathematical model in the synchronous domain and by imposing the constraints  $i_0 = 0$  and  $di_0/dt = 0$  (which are hardware-related). The following functional relationship is obtained:

$$\begin{aligned} v_{NET} = & -\frac{L_{m3}}{9} \cdot \left[ 2\sqrt{2} \sin\left(3\theta + \varphi_3 + \frac{\pi}{6}\right) \cdot \left(\frac{di_{d3}}{dt} - 3\omega i_{q3}\right) + \dots \right. \\ & \left. \dots + 2\sqrt{2} \cos\left(3\theta + \varphi_3 + \frac{\pi}{6}\right) \cdot \left(\frac{di_{q3}}{dt} + 3\omega i_{d3}\right) \right] - \frac{e_0 - u_0}{3} \end{aligned} \quad (5.81)$$

where  $L_{m3} = L_3 - L_0$  is the mutual inductance related to the space vector  $\dot{i}_3$  (i.e., it does not include the leakage effects) and  $e_0 = -6\omega \Psi_{M3} \sin(3\theta + \varphi_3 - \pi/6)$ .

The transformed inductance parameters appearing in the equations (5.79)-(5.81) are reported in Table 5.III.

From the equations (5.80) and (5.81) it might seem that the common-mode inverter voltage, by changing the voltage  $u_0$  and, consequently, the neutral point potential shift  $v_{NET}$  via (5.81), might affect the dynamics of  $i_{d3}$  and  $i_{q3}$  through (5.80). However, this dependence (that would negate the exploitation of a common-mode voltage injection for modulation purposes) is only apparent. Indeed, given the asymmetrical configuration of the machine axes (and, consequently, the asymmetrical nature of the VSD and rotational transformation matrices), any change in the common-mode voltage of the supplying inverter not only affects the zero-sequence component  $u_0$ , but at the same time it also changes the components  $u_{d3}$  and  $u_{q3}$ . Their simultaneous variations perfectly compensate and does not affect the dynamics of  $i_{d3}$  and  $i_{q3}$ . Similarly, it can be verified from inspection of  $\mathbf{C}^{-1}$  that the change of the zero-sequence component  $u_0$  (while keeping the components  $u_{d3}$  and  $u_{q3}$  unchanged) is not equivalent to the change of the VSI common-mode voltage (which, indeed, also requires a coherent change of  $u_{d3}$  and  $u_{q3}$ ). As a result, for control purposes, the compensation of  $e_0$  in (5.81) can also be achieved by changing  $u_0$  (as it will be exemplified in Section 5.6.6). This imbalance effect appearing in asymmetrical machines with a single isolated neutral point configuration has also been verified in [56]–[58].

### 5.5.3 Power losses weighting matrices

From the chosen VSD and rotational transformation matrices, it is possible to compute the instantaneous power losses weighting matrix  $\mathbf{G}(\theta) = \mathbf{D}(\theta) \cdot \mathbf{C}^{-T} \cdot \mathbf{C}^{-1} \cdot \mathbf{D}^T(\theta)$  introduced in Section 5.1.6.

The computation has been performed analytically<sup>30</sup>, and results in:

$$\mathbf{G}(\theta) = \begin{bmatrix} 1 & 0 & 0 & 0 & 0 & 0 & 0 & 0 & 0 \\ 0 & 1 & 0 & 0 & 0 & 0 & 0 & 0 & 0 \\ 0 & 0 & G_{d3,d3}(\theta) & G_{d3,q3}(\theta) & 0 & 0 & 0 & 0 & G_{d3,0}(\theta) \\ 0 & 0 & G_{q3,d3}(\theta) & G_{q3,q3}(\theta) & 0 & 0 & 0 & 0 & G_{q3,0}(\theta) \\ 0 & 0 & 0 & 0 & 1 & 0 & 0 & 0 & 0 \\ 0 & 0 & 0 & 0 & 0 & 1 & 0 & 0 & 0 \\ 0 & 0 & 0 & 0 & 0 & 0 & 1 & 0 & 0 \\ 0 & 0 & 0 & 0 & 0 & 0 & 0 & 1 & 0 \\ 0 & 0 & G_{0,d3}(\theta) & G_{0,q3}(\theta) & 0 & 0 & 0 & 0 & 9 \end{bmatrix} \quad (5.82)$$

where the  $\theta$ -dependent terms have the following expressions:

Table 5.III – INDUCTANCES PARAMETERS IN THE SYNCHRONOUS DOMAIN.

$L_1$ [mH]	$L_3$ [mH]	$L_5$ [mH]	$L_7$ [mH]	$L_0$ [mH]
460	120	96	87	85

<sup>30</sup> With the aid of the Symbolic Math Toolbox of MATLAB.

$$\begin{aligned}
G_{d3,d3}(\theta) &= 5 - 4 \cos(6\theta + 2\varphi_3 + \pi/3) \\
G_{q3,q3}(\theta) &= 5 + 4 \cos(6\theta + 2\varphi_3 + \pi/3) \\
G_{d3,q3}(\theta) &= G_{q3,d3}(\theta) = 4 \sin(6\theta + 2\varphi_3 + \pi/3) \\
G_{d3,0}(\theta) &= G_{0,d3}(\theta) = -3\sqrt{6} \sin(3\theta + \varphi_3) - 3\sqrt{2} \cos(3\theta + \varphi_3) \\
G_{q3,0}(\theta) &= G_{0,q3}(\theta) = 3\sqrt{2} \sin(3\theta + \varphi_3) - 3\sqrt{6} \cos(3\theta + \varphi_3)
\end{aligned} \tag{5.83}$$

Since  $i_0 = 0$ , the instantaneous power losses are expressed by:

$$\begin{aligned}
p_R &= i_{d1}^2 + i_{q1}^2 + 5 i_{d3}^2 + 5 i_{q3}^2 + \dots \\
&\quad \dots + 4 \cos(6\theta + 2\varphi_3 + \pi/3) \cdot (i_{q3}^2 - i_{d3}^2) + \dots \\
&\quad \dots + 8 \sin(6\theta + 2\varphi_3 + \pi/3) \cdot (i_{d3} \cdot i_{q3}) + \dots \\
&\quad \dots + i_{d5}^2 + i_{q5}^2 + i_{d7}^2 + i_{q7}^2
\end{aligned} \tag{5.84}$$

The average power losses weighting matrix  $\mathbf{H}$ , introduced in Section 5.1.6, is obtained by simply averaging  $\mathbf{G}(\theta)$  in a  $2\pi$  period of  $\theta$ . Only the constant terms of (5.82) are preserved, resulting in the simplified expression:

$$\mathbf{H} = \begin{bmatrix} 1 & 0 & 0 & 0 & 0 & 0 & 0 & 0 & 0 \\ 0 & 1 & 0 & 0 & 0 & 0 & 0 & 0 & 0 \\ 0 & 0 & 5 & 0 & 0 & 0 & 0 & 0 & 0 \\ 0 & 0 & 0 & 5 & 0 & 0 & 0 & 0 & 0 \\ 0 & 0 & 0 & 0 & 1 & 0 & 0 & 0 & 0 \\ 0 & 0 & 0 & 0 & 0 & 1 & 0 & 0 & 0 \\ 0 & 0 & 0 & 0 & 0 & 0 & 1 & 0 & 0 \\ 0 & 0 & 0 & 0 & 0 & 0 & 0 & 1 & 0 \\ 0 & 0 & 0 & 0 & 0 & 0 & 0 & 0 & 9 \end{bmatrix} \tag{5.85}$$

This means that, by using a constant set  $\mathbf{i}_{dq}$ , the average machine losses are:

$$P_R = i_{d1}^2 + i_{q1}^2 + 5 i_{d3}^2 + 5 i_{q3}^2 + i_{d5}^2 + i_{q5}^2 + i_{d7}^2 + i_{q7}^2 \tag{5.86}$$

Then, it can be concluded that, contrarily to what would happen for a symmetrical machine, in this asymmetrical configuration the third space vector components  $\{i_{d3}, i_{q3}\}$  are weighted 5 times more than the other components for the power losses computation.

## 5.6 Numerical and experimental results

This section presents the numerical and experimental results obtained for the analysed asymmetrical nine-phase PMSM, with special focus on the different torque development strategies introduced in Section 5.2.

### 5.6.1 Fundamental currents control strategy

The fundamental current control strategy, as explained in Section 5.2.1, only exploits the quadrature current  $i_{q1}$  for the machine torque control. For the present analysis the expression (5.48) is particularized in:

$$i_{q1}^* = \frac{T_{em}^*}{\kappa_1} = \frac{T_{em}^*}{\sqrt{9/2} \cdot \Psi_{M1}}$$

The synchronous current set is  $i_{dq}^* = [0 \ i_{q1}^* \ 0 \ 0 \ 0 \ 0 \ 0 \ 0]^T$  and it can be transformed into the phase variable domain by applying (5.46).

The optimal phase currents waveforms<sup>31</sup> and their harmonic spectra are shown in Fig. 5.14. They are normalized by the peak current  $I_{\text{FUND}} = (2/9) \cdot (T_{em}^*/\Psi_{M1})$ .

It can be noted that all the current waveforms are perfectly sinusoidal in  $\theta$  (i.e., only the 1<sup>st</sup> harmonic is present). Moreover, the currents have the same magnitude for all the phases. This means that the overall stator power losses are equally shared by all the 9 machine windings. The currents in each of the symmetrical three-phase subsets  $\{1,2,3\}$ ,  $\{4,5,6\}$  and  $\{7,8,9\}$  are shifted by  $120^\circ$  from each other, while the different sets are mutually shifted by  $20^\circ$  (i.e., they follow the same phase shift of the magnetic axes angles set  $\alpha$ ).

### 5.6.2 Third harmonic injection strategy

This section particularized the third harmonic injection strategy presented in Section 5.2.2 to the specific case study<sup>32</sup>. This strategy exploits both  $i_{q1}$  and  $i_{q3}$  for the torque development. By particularizing (5.57) to the present case study, the optimal injection ratio is:

$$k^* = \frac{i_{q1}^*}{i_{q3}^*} = \frac{3\Psi_{M3}/\Psi_{M1}}{5/1} \cong 0.19$$

and the corresponding values (5.58) of the optimal quadrature axes currents are:

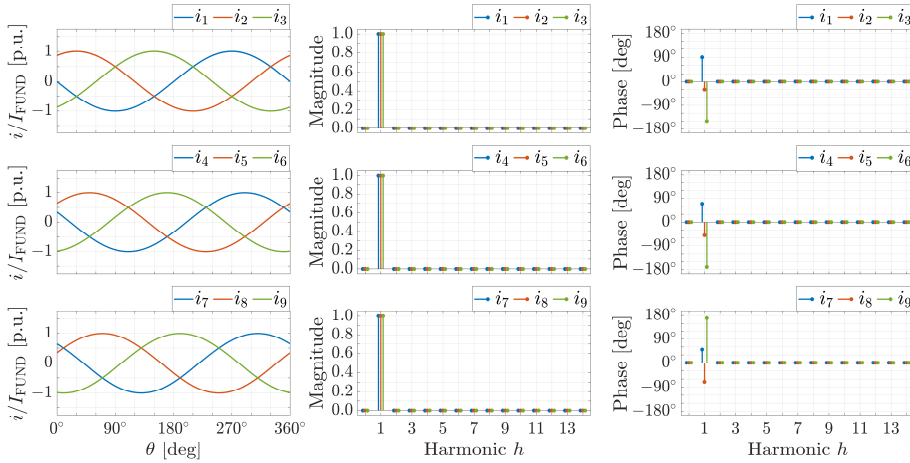


Fig. 5.14 – Waveforms and harmonic spectra of the reference currents obtained with the fundamental current control strategy.

<sup>31</sup> Obtained for varying  $\theta$  and for a constant reference torque  $T_{em}^*$ .

<sup>32</sup> Additional details, and further examples for machines with different number of phases, can be found in [119].

$$i_{q1}^* = \sqrt{\frac{9}{2}} \cdot \frac{5 \Psi_{M1}}{9 \Psi_{M3}^2 + 5 \Psi_{M1}^2} \cdot T_{em}^* \quad \text{and} \quad i_{q3}^* = \sqrt{\frac{9}{2}} \cdot \frac{3 \Psi_{M3}}{9 \Psi_{M3}^2 + 5 \Psi_{M1}^2} \cdot T_{em}^*$$

The power losses reduction can be computed via (5.60) and is:

$$\frac{P_R^{(\text{THI})}}{P_R^{(\text{FUND})}} = \frac{5 \Psi_{M1}^2}{9 \Psi_{M3}^2 + 5 \Psi_{M1}^2} \cong 0.853$$

To highlight that the computed injection ratio does indeed minimize the power losses, Fig. 5.15 shows the normalized<sup>33</sup> ratio  $P_R(k)/P_R^{(\text{FUND})}$  for different values of  $k = i_{q3}/i_{q1}$ . It can be noted that, coherently with the analytical expressions, the minimum ratio of the power losses (denoted by the red point in Fig. 5.15) is around 0.85 and is obtained for an injection ratio of  $k \cong 0.19$ . This means that the proposed optimal third harmonic injection allows reducing the power losses of around 15% if compared to the sole fundamental currents exploitation.

The corresponding optimal phase currents are shown in Fig. 5.16, together with their harmonic spectra. Again, they are normalized by  $I_{\text{FUND}} = (2/9) \cdot (T_{em}^*/\Psi_{M1})$ , which is the peak phase current needed to supply the same electromagnetic torque by only exploiting the fundamental component  $i_{q1}$ .

In agreement with the analytical results, only the first and the third harmonics are present in the Fourier decomposition of the phase currents. The waveforms within each of the symmetrical three-phase subsets  $\{1,2,3\}$ ,  $\{4,5,6\}$  and  $\{7,8,9\}$  are identical and just mutually shifted by  $120^\circ$ . Nevertheless, it can be noted that the three subsets behave differently from one another. This leads to an unequal distribution of the third-harmonic current components among the different phase sets, which is required to satisfy the condition  $i_0 = 0$  imposed by the hardware configuration.

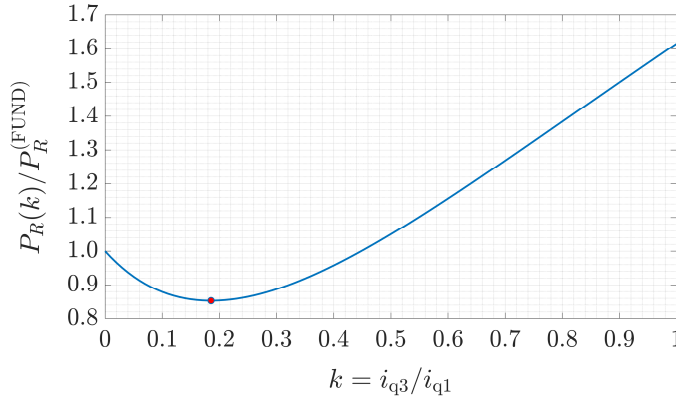


Fig. 5.15 – Normalized power losses obtained with the proposed third harmonic injection strategy, as a function of the third harmonic injection ratio.

<sup>33</sup> It is here recalled that the power  $P_R^{(\text{FUND})}$  represents the overall machine power losses obtained when only the fundamental current components related to  $i_{q1}$  are exploited.

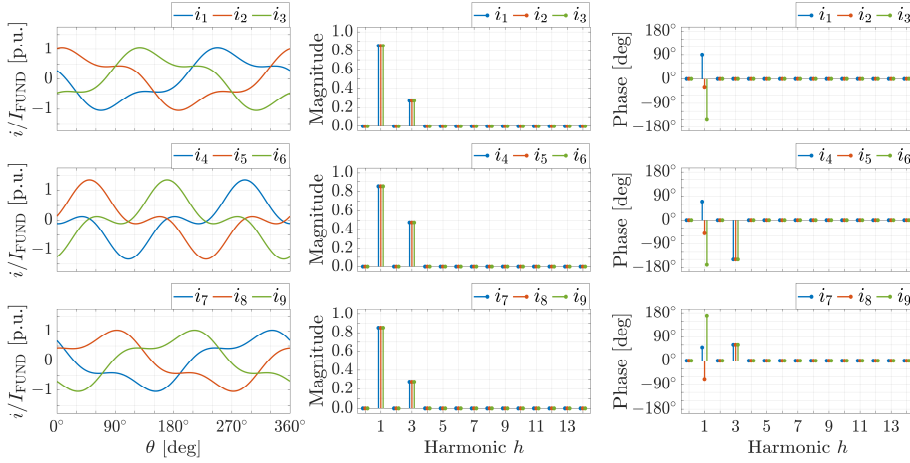


Fig. 5.16 – Waveforms and harmonic spectra of the reference currents obtained with the third harmonic injection strategy.

To be more specific, the magnitude of the third harmonic components are equal in the sets  $\{1,2,3\}$  and  $\{7,8,9\}$ , but are  $\sqrt{3}$  times higher in the set  $\{4,5,6\}$ . This unequal distribution of the currents also leads to an unequal distribution of the overall stator power losses: they can be computed to be 31.3% for the subsets  $\{1,2,3\}$  and  $\{7,8,9\}$ , and 37.4% for the subset  $\{4,5,6\}$ .

Finally, despite the reduction of the RMS current with respect to the sole exploitation of  $i_{q1}$ , it can be noted that the normalized peak currents are higher than 1, with the most affected set being  $\{4,5,6\}$ .

### 5.6.3 Multi-harmonic injection strategy

The multi-harmonic injection strategy developed in Section 5.2.3 is here particularized for the analysed asymmetrical nine-phase machine<sup>34</sup>. The optimal synchronous current set is now computed as:

$$\mathbf{i}_{dq}^* = \sqrt{\frac{2}{9}} \cdot \frac{[0 \quad 5 \Psi_{M1} \quad 0 \quad 3 \Psi_{M3} \quad 0 \quad 25 \Psi_{M5} \quad 0 \quad 35 \Psi_{M7} \quad 0]^T}{5 \Psi_{M1}^2 + 9 \Psi_{M3}^2 + 125 \Psi_{M5}^2 + 245 \Psi_{M7}^2} \cdot T_{em}^*$$

which is the particularization of (5.64) and (5.65).

The power losses reduction can be computed via (5.67) and is:

$$\frac{P_R^{(MHI)}}{P_R^{(FUND)}} = \frac{5 \Psi_{M1}^2}{5 \Psi_{M1}^2 + 9 \Psi_{M3}^2 + 125 \Psi_{M5}^2 + 245 \Psi_{M7}^2} \cong 0.698$$

which represents a reduction of the losses of around 30% with respect to the sole fundamental harmonic exploitation.

Fig. 5.17 shows the corresponding optimal phase currents (normalized by  $I_{FUND}$ ),

<sup>34</sup> Additional details can be found in [122].

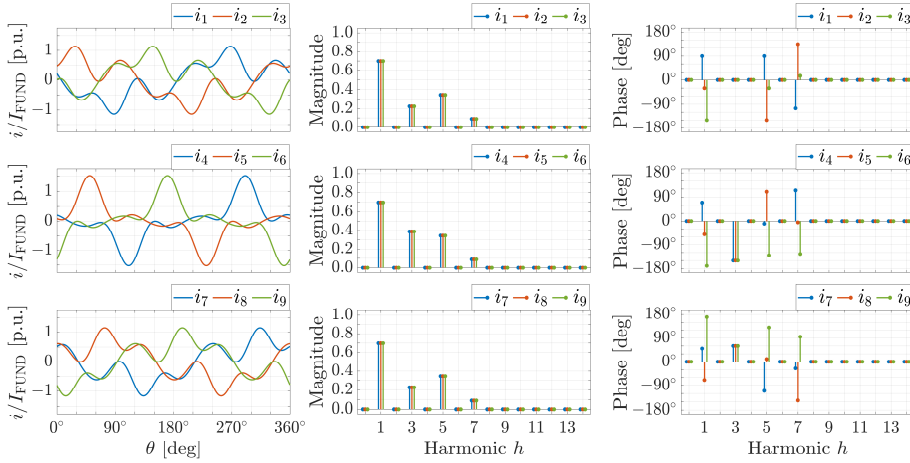


Fig. 5.17 – Waveforms and harmonic spectra of the reference currents obtained with the multi-harmonic injection strategy.

together with their harmonic spectra. Coherently with the theoretical analysis, the Fourier decomposition shows the presence of the 1<sup>st</sup>, the 3<sup>rd</sup>, the 5<sup>th</sup> and the 7<sup>th</sup> harmonics.

Similarly to the previous case, the currents of a single three-phase subset (i.e., the subset  $\{1,2,3\}$ ,  $\{4,5,6\}$  or  $\{7,8,9\}$ ) are equal and just mutually shifted by 120°. On the contrary, the three subsets behave differently from one another. Again, this is due to the 3<sup>rd</sup> harmonic contributions which, to satisfy the single isolated neutral point constraint, are again unequally distributed among the sets, and are  $\sqrt{3}$  times higher in the set  $\{4,5,6\}$ . All the other harmonics (i.e., the 1<sup>st</sup>, the 5<sup>th</sup> and the 7<sup>th</sup>) are instead equally shared by all phases.

Once again, the unequal distribution of the currents also leads to an unequal distribution of the power losses. In this case the losses in the subsets  $\{1,2,3\}$  and  $\{7,8,9\}$  are around 31.7% of the overall losses, while the subset  $\{4,5,6\}$  is responsible for the remaining 36.6%.

Finally, despite the RMS current reduction, the normalized peak currents are again higher than 1, and the most affected subset is  $\{4,5,6\}$  where the peak current is around 50% higher than in case of the sole fundamental harmonic exploitation.

#### 5.6.4 Maximum torque per ampere strategy

The MTPA strategy developed in Section 5.2.4 is here applied to the analysed machine. The optimal synchronous currents are now computed by processing (5.70) for each value of the rotor position  $\theta$ .

The results of the optimization procedure (5.69) are depicted in Fig. 5.18, which shows the synchronous current components and their harmonic spectra<sup>35</sup> in the whole range  $[0^\circ; 360^\circ]$  of  $\theta$ . They have been normalized by  $I_{q1} = \sqrt{2/9} \cdot T_{em}^* / \Psi_{M1}$ , which is the

<sup>35</sup> The currents in the synchronous domain have not been shown for the other strategies because they all lead to constant references.

value of the quadrature current  $i_{q1}$  when the fundamental current control strategy is implemented. The zero-sequence current  $i_0$  is always null (to meet the isolated neutral point constraint) and, therefore, is not shown.

As can be noted, now the synchronous current components are not constant but, instead, they are varying with the rotor position with a  $6\theta$  periodicity. While  $i_{d1}$ ,  $i_{d5}$  and  $i_{d7}$  are zero, the direct axis component  $i_{d3}$  is actively controlled during the machine functioning and is also an alternating function of  $6\theta$ , but with a zero average value.

It has been numerically computed that the normalized average power losses with this strategy are:

$$\frac{P_R^{(MTPA)}}{P_R^{(FUND)}} = \sqrt{\frac{2}{9}} \cdot \frac{1}{\Psi_{M1}} \cdot \frac{1}{2\pi} \int_0^{2\pi} \frac{1}{\boldsymbol{\kappa}^T \cdot \mathbf{G}'_{eq}(\theta) \cdot \boldsymbol{\kappa}} d\theta \cong 0.590$$

which represents a reduction of the losses of around 41% with respect to the sole fundamental harmonic exploitation.

The corresponding optimal phase currents, obtained through the inverse transformation (5.46), are depicted in Fig. 5.19, together with their harmonic spectra. Similarly to the previous cases, they are normalized by  $I_{FUND} = \sqrt{2/9} \cdot I_{q1} = (2/9) \cdot (T_{em}^*/\Psi_{M1})$ , which is the peak current obtained with the fundamental current control strategy presented in Section 5.6.1.

Contrarily to the previous case, now also higher-order harmonics (i.e., 9<sup>th</sup>, 11<sup>th</sup>, 13<sup>th</sup>, etc...) are present in the Fourier decomposition of the optimal currents. This is expected, because of the interaction between the rotational transformation  $\mathbf{D}(\theta)$  and the  $\theta$ -varying set  $\mathbf{i}_{dq}^*(\theta)$ .

Once again, the currents of the same three-phase subset (i.e., {1,2,3}, {4,5,6} or

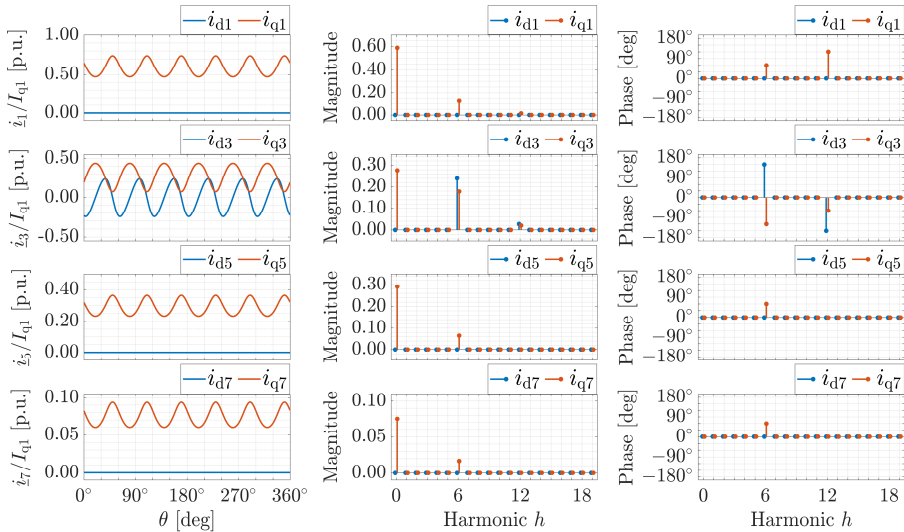


Fig. 5.18 – Waveforms and harmonic spectra of the reference currents obtained in the synchronous domain with the MTPA strategy.

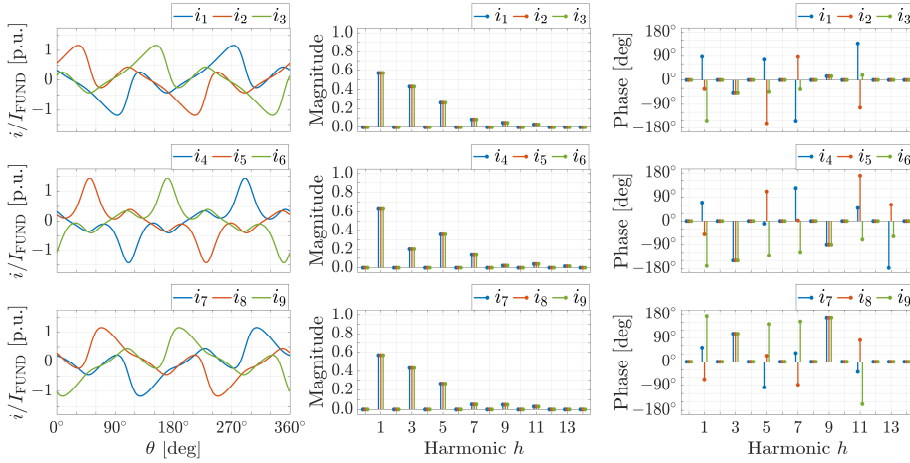


Fig. 5.19 – Waveforms and harmonic spectra of the reference currents obtained with the MTPA strategy.

{7,8,9}) are equal and only shifted by  $120^\circ$  from each other, while the currents in the three sets are different. The magnitude differences are now not only limited to the 3<sup>rd</sup> harmonic components but are also present in the other orders.

Similarly to the previous cases, this asymmetry leads to an unequal distribution of the power losses. In this case the losses in the subset {1,2,3} are around 33.5%, the losses in the subset {4,5,6} are around 33.3% and the losses in the subset {7,8,9} are around 33.2% of the overall dissipation. If compared with the other harmonic injection strategies, it can be noted that the proposed MTPA algorithm also leads to a more uniform redistribution of the power losses among the machine phases.

Again, despite the RMS current reduction following the power losses minimization, the peak currents are higher than in case of the sole fundamental current exploitation.

As explained in Section 5.2.4, the additional harmonics introduced by the MTPA strategy do not develop any average electromagnetic torque, but are needed to cancel out the ripple introduced by the interaction of the other harmonic components. In other words, if these higher-order current harmonics are not fully controlled in a real-time application, the electromagnetic torque developed by the machine would show a periodic ripple, but its average value would be unaffected.

### 5.6.5 Torque control strategies comparison

The analysed torque control strategies working principles and main properties can be summarized as follows:

- the fundamental current control strategy only exploits  $i_{q1}^*$  for the torque development and results in all the phase currents to be sinusoidal with the same magnitude;
- the THI strategy exploits a constant  $i_{q1}^*$  and a constant  $i_{q3}^*$  to develop the electromagnetic torque, the phase currents show both a fundamental and a

third harmonic component, and their waveforms are not equal for all the windings;

- the MHI strategy exploits a constant synchronous current set  $i_{dq}^*$  for the torque development, the phase currents are not sinusoidal but also include a 3<sup>rd</sup>, a 5<sup>th</sup> and a 7<sup>th</sup> harmonic, and the 3<sup>rd</sup> harmonic is unequally shared by different phase windings; and
- the MTPA strategy exploits a  $\theta$ -varying synchronous current set  $i_{dq}^*(\theta)$  for the torque development, the phase currents show multiple harmonics (even with an order higher than 7), which are all unequally shared by the different phase windings.

Table 5.IV summarizes some of the overall features obtained from the previous numerical analysis, while Fig. 5.20 shows the comparison of the overall machine stator losses obtained with the analysed strategies in the whole range  $[0; 360^\circ]$  of the rotor position  $\theta$  (considering a constant reference torque  $T_{em}^*$ ). The solid traces represent the instantaneous power losses  $p_R = R \cdot \sum_{k=1}^9 i_k^2$ , while the dashed traces represent the average losses  $P_R = (1/2\pi) \cdot \int_0^{2\pi} p_R(\theta) d\theta$  of the machine in a full rotor cycle. All the traces of Fig. 5.20 have been normalized by the power  $P_R^{(FUND)} = R \cdot (2/9) \cdot (T_{em}^*/\Psi_{M1})^2$ , which is the average dissipation in case of the sole fundamental harmonic exploitation.

From the results of Fig. 5.20 it can be noted that the instantaneous power losses are constant when only the fundamental current components are exploited whereas, for all the other strategies, they depend on the rotor position with a  $6\theta$  periodicity. As expected, and as confirmed both by Table 5.IV and by Fig. 5.20, it can be concluded that  $P_R^{(FUND)} \geq P_R^{(THI)} \geq P_R^{(MHI)} \geq P_R^{(MTPA)}$ , meaning that a progressive reduction of the power losses can be fulfilled by implementing more advanced control strategies.

Given the machine asymmetrical configuration, the higher-order harmonics are not

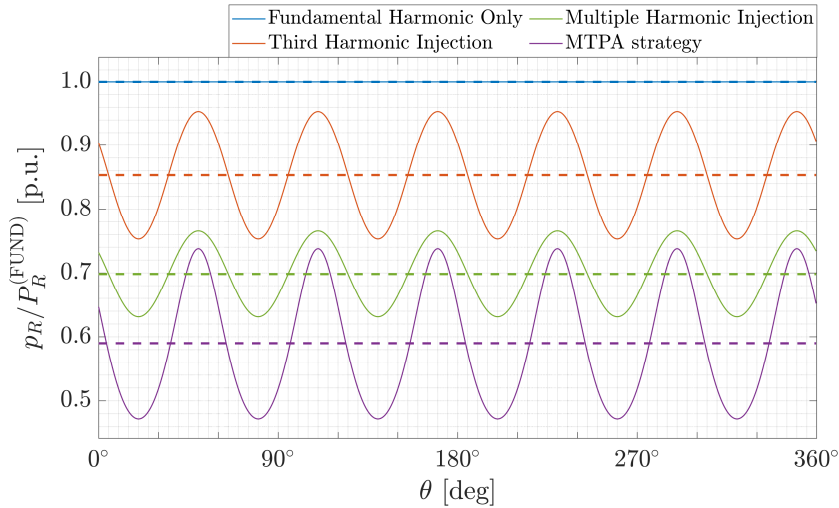


Fig. 5.20 – Comparison of the overall power losses obtained with the different torque development strategies.

Table 5.IV – TORQUE CONTROL STRATEGIES COMPARISON.

	Fundamental Only	THI strategy	MHI strategy	MTPA strategy
Synchronous current components	$i_{q1}$ (constant)	$i_{q1}$ and $i_{q3}$ (constant)	$i_{q1}, i_{q3}, i_{q5}, i_{q7}$ (constant)	$i_{q1}, i_{d3}, i_{q3}, i_{q5}, i_{q7}$ ( $\theta$ -varying)
Phase currents harmonics	1 <sup>st</sup>	1 <sup>st</sup> and 3 <sup>rd</sup>	1 <sup>st</sup> , 3 <sup>rd</sup> , 5 <sup>th</sup> and 7 <sup>th</sup>	1 <sup>st</sup> , 3 <sup>rd</sup> , 5 <sup>th</sup> , 7 <sup>th</sup> , 9 <sup>th</sup> , 11 <sup>th</sup> , 13 <sup>th</sup> , ...
Average stator losses reduction	0%	15%	30%	41%
Losses in the subset {1,2,3}	33.3%	31.3%	31.7%	33.5%
Losses in the subset {4,5,6}	33.3%	37.4%	36.6%	33.3%
Losses in the subset {7,8,9}	33.3%	31.3%	31.7%	33.2%

equally distributed in all the phases, leading also to an unequal distribution of the power losses, which however becomes progressively less relevant as the number of exploited harmonics increases.

### 5.6.6 Simulation results

The proposed control strategies have been tested numerically in the MATLAB/Simulink environment.

The machine model has been realized in the phase variable domain using the parameters described in Section 5.5.

The supplying inverter has been simulated with an average model in a way to filter out the effects of the harmonics introduced by the PWM technique. Its overall DC-bus voltage has been set to 450 V.

A digital implementation of the controller described in Section 5.4 has been applied and executed with a 10 kHz sampling frequency.

The feedback controller has been implemented in the multiple synchronous domain and it has been realized with a proportional action, an integral action and a single resonant action synchronized with  $6\omega$ .

Given the model equations (5.79), the controller for the fundamental, the fifth and the seventh space vectors components of the currents have been set similarly to a traditional FOC algorithm as:

$$\begin{cases} u_{dh}^* = w_{dh}^* - h\omega_{el} L_h i_{qh} + e_{dh} \\ u_{qh}^* = w_{qh}^* + h\omega_{el} L_h i_{dh} + e_{qh} \end{cases} \quad (5.87)$$

with  $h = 1, 5, 7$  and  $e_{qh} = \sqrt{9/2} \cdot h\omega \Psi_{Mh}$  (where  $w_{dh}^*$  and  $w_{qh}^*$  are the output of the feedback PIR controllers).

On the contrary, the compensation terms of the third space vector components have been set differently to neutralize the effect of  $v_{NET}$ . Basing on the equations (5.80), they have been set as:

$$\begin{cases} u_{d3}^* = w_{d3}^* - 3\omega L_3 i_{q3} - 2\sqrt{2} \cos\left(3\theta + \varphi_3 - \frac{\pi}{3}\right) \cdot \tilde{v}_{NET}^* \\ u_{q3}^* = w_{q3}^* + 3\omega L_3 i_{d3} - 2\sqrt{2} \cos\left(3\theta + \varphi_3 - \frac{\pi}{3}\right) \cdot \tilde{v}_{NET}^* + e_{q3} \end{cases} \quad (5.88)$$

where  $w_{d3}^*$  and  $w_{q3}^*$  are the output of the feedback PIR controllers, while  $\tilde{v}_{NET}^*$  has been chosen as:

$$\tilde{v}_{NET}^* = \frac{2\sqrt{2}\omega L_{m3}}{3} \cdot \left[ i_{d3} \cdot \cos\left(3\theta + \varphi_3 + \frac{\pi}{6}\right) - i_{q3} \cdot \sin\left(3\theta + \varphi_3 + \frac{\pi}{6}\right) \right] \quad (5.89)$$

The term  $\tilde{v}_{NET}^*$  expressed in (5.89) has been computed from (5.81) by neglecting the transformer induced back-EMFs and by compensating the effect of  $e_0$  with the injection:

$$u_0^* = e_0 = -6\omega \Psi_{M3} \sin\left(3\theta + \varphi_3 - \frac{\pi}{3}\right) \quad (5.90)$$

The computed reference set  $\mathbf{u}_{dq}^*$  has been transformed back into the phase variable domain by using the inverse Park transformation (5.46). A constant common-mode voltage injection of 225 V (i.e., half of the total DC-bus voltage) has been added after the inverse Park transformation to obtain positive reference voltages for the computation of the duty-cycles for the semiconductor devices.

The testing scenario is described as follows. During the whole simulation, the machine is controlled to be at a constant speed of 600 rpm and is subject to an external mechanical loading torque of 2 Nm. The test involves 4 different time intervals of 200 ms each (i.e., 2 fundamental periods). Initially, in the interval  $[t_0, t_1]$ , the machine is controlled by only using the fundamental current harmonic components by following the torque control strategy presented in Section 5.2.1 and particularized in Section 5.6.1. Then, in the  $[t_1, t_2]$  time interval, the current references are changed and are computed by using the third harmonic injection strategy described in Section 0 and particularized in Section 5.6.2. In the third time interval  $[t_2, t_3]$  the strategy is modified into the multiple harmonic injection approach described in Section 5.2.3 and particularized in Section 5.6.3. Finally, in the interval  $[t_3, t_4]$ , the MTPA algorithm of Section 5.2.4 and Section 5.6.4 is executed. Since the machine is always kept at the same speed and subject to the same loading torque, the analysis of the proposed torque control strategies can be done through the machine currents and power losses.

The results are depicted in Fig. 5.21. All the currents are shown both in the multiple synchronous domain and in the phase variable domain. The numerical results also include the developed electromagnetic torque  $T_{em}$  and the average machine power losses  $P_R$ , which have been computed from the instantaneous losses through a moving average algorithm as:

$$P_R(t) = \frac{1}{T_0} \cdot \int_{t-T_0}^t p_R(\tau) d\tau = \frac{1}{T_0} \cdot \int_{t-T_0}^t \sum_{k=1}^9 R \cdot i_k^2(\tau) d\tau \quad (5.91)$$

where  $T_0 = 100$  ms is one fundamental period.

As can be seen, for the first 200 ms only the current component  $i_{q1}$  is controlled to a constant non-zero value, and the resulting phase currents are perfectly sinusoidal in time, as in Fig. 5.14. The average power losses are around 188 W.

When the third harmonic injection is executed, a constant  $i_{d3}$  is applied and the current  $i_{q1}$  is reduced accordingly (because the machine is asked to develop the same electromagnetic torque). The average power losses, after a 100 ms transient due to the moving average procedure (5.91), stabilize around 160 W. The waveforms of the currents follow the ideal references of Fig. 5.16.

Then, the multiple harmonic injection of Section 5.6.3 is performed, and all the quadrature current components (i.e.,  $i_{q1}$ ,  $i_{q3}$ ,  $i_{q5}$  and  $i_{q7}$ ) are exploited for the torque development. The phase currents become highly non-sinusoidal, coherently with the waveforms of Fig. 5.17, and the average losses further decrease to around 131 W.

Finally, the MTPA algorithm is implemented. Coherently with the results of Section 5.6.4, the synchronous currents are no longer constant but, instead, show a periodic variation with a  $6\omega$  angular frequency (with the same waveform of Fig. 5.18). While the direct axis components  $i_{d1}$ ,  $i_{d5}$  and  $i_{d7}$  are still kept to zero, the component  $i_{d3}$  is now actively controlled to track a non-zero reference. The corresponding phase currents follow the waveforms depicted in Fig. 5.19 and the average power losses decrease down to the final value of around 111 W.

For each of the torque control algorithm, the numerical results are coherent with the theoretical results discussed in Section 5.6.5. The electromagnetic torque, apart from small transient deviations during the control strategy transitions, is always kept to 2 Nm.

### 5.6.7 Experimental results

Some of the theoretical analysis of this chapter have been also validated experimentally.

In this case, the machine prototype (represented in Fig. 5.11) has been supplied by two custom-made two-level multiphase voltage source inverters, based on Infineon FS50R12KE3 IGBT modules. All the 9 inverter legs have a common DC-bus, whose voltage is supplied by a Sorensen SGI600/25 single quadrant DC-voltage source and has been set to  $V_{DC} = 450$  V. A standard triangular carrier-based PWM algorithm, working with a modulation frequency of 5 kHz, has been implemented to operate the converter. The dead-time is implemented via hardware and is approximately equal to 5  $\mu$ s.

The control algorithm has been implemented with a dSPACE DS1006 platform. It is executed with a 10 kHz sampling rate and it is synchronized with the converter PWM period. All the 9 machine currents have been measured through external LEM transducers, which are connected to a DS2004 ADC board. The machine speed and position have been provided through an incremental encoder and acquired through a DS3002 encoder board. Additional measurements have been recorded using a Tektronix DPO/MSO 2014 oscilloscope, equipped with TCP0030A current probes.

The testing scenario has been developed to validate the third harmonic injection strategy developed in Section 5.6.2 and it has been conducted as follows. The machine is feedback-controlled to keep a constant angular speed of 500 rpm. It has been mechanically coupled to a DC machine, whose armature terminals are connected to an external resistor in a way that the PMSM subject to a mechanical loading torque of around 2 Nm.

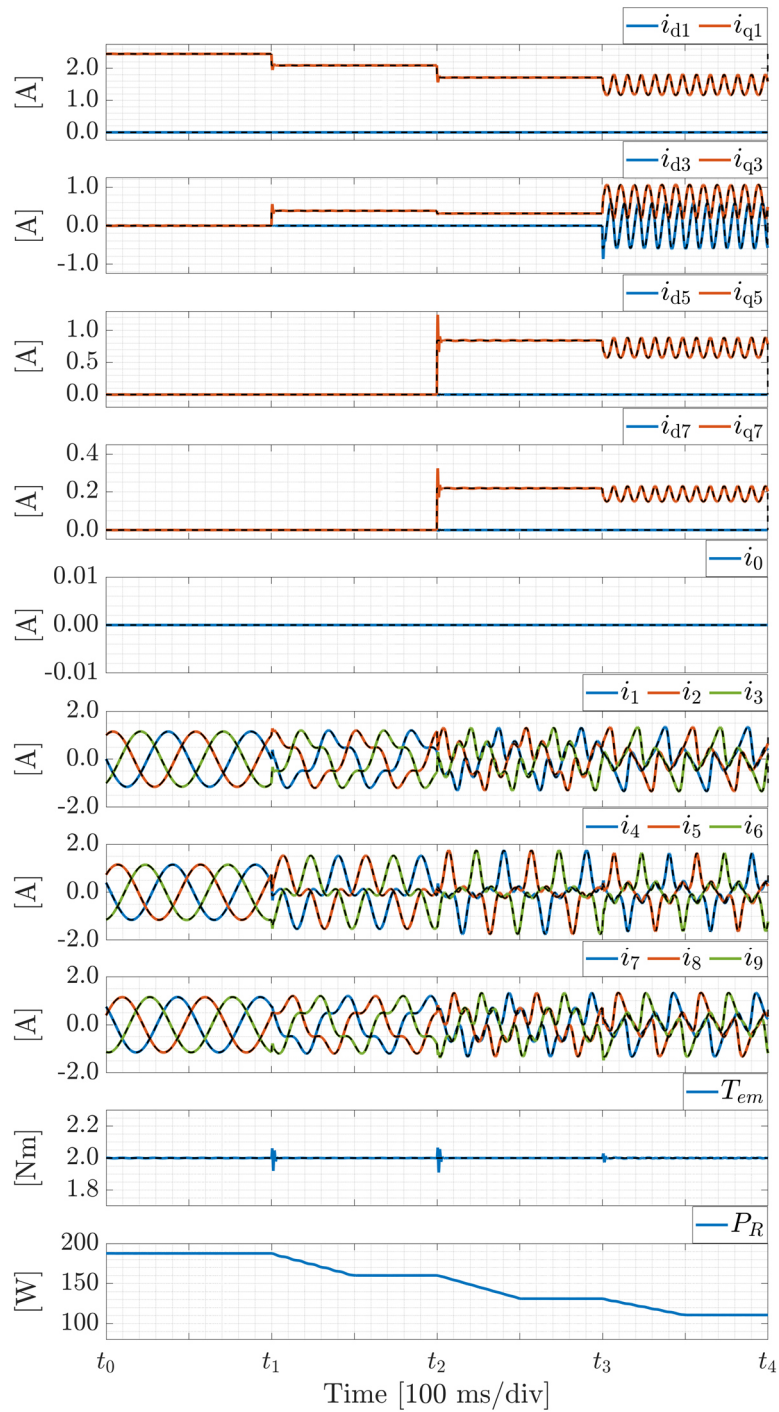


Fig. 5.21 – Simulation results.

The torque control strategy has been performed by linearly varying the third harmonic injection ratio  $k = i_{q3}/i_{q1}$  in a 20 s time window. All the other component of the reference synchronous set  $i_{dq}^*$  have been kept to zero. Since the reference current set  $i_{dq}^*$  is constant, a simple PI controller has been used to drive all the components of the synchronous current set  $i_{dq}$ . The compensation terms in the current controller have been set as in (5.87)-(5.89).

Fig. 5.22 shows the average power losses  $P_R$  and the quadrature currents  $i_{q1}$  and  $i_{q3}$  during the testing interval. The obtained waveform is similar to the theoretical results depicted in Fig. 5.15. The minimum dissipation is obtained for  $k \cong 0.22$  which is reasonably close to the theoretical optimal ratio  $k^* \cong 0.19$  obtained from (5.57).

An oscilloscope capture of the results is also shown in Fig. 5.23. It shows the measured currents  $i_1$ ,  $i_4$  and  $i_7$  (measured with current probes with 4 turns) without and with the optimal third harmonic injection. They have been obtained by step-changing the injection ratio  $k$  from zero to the theoretical optimal value  $k^* \cong 0.19$ . As it is evident, after an initial transient, the current controller can track the desired references and there is good agreement with the corresponding theoretical current waveforms of Fig. 5.14 and Fig. 5.16.

For comparison, Fig. 5.24 shows the same currents when the neutral point potential shift  $v_{NET}$  is not properly compensated in the current control algorithm. In this case, it can be noted that the current waveforms are distorted, especially in the first 500 ms.

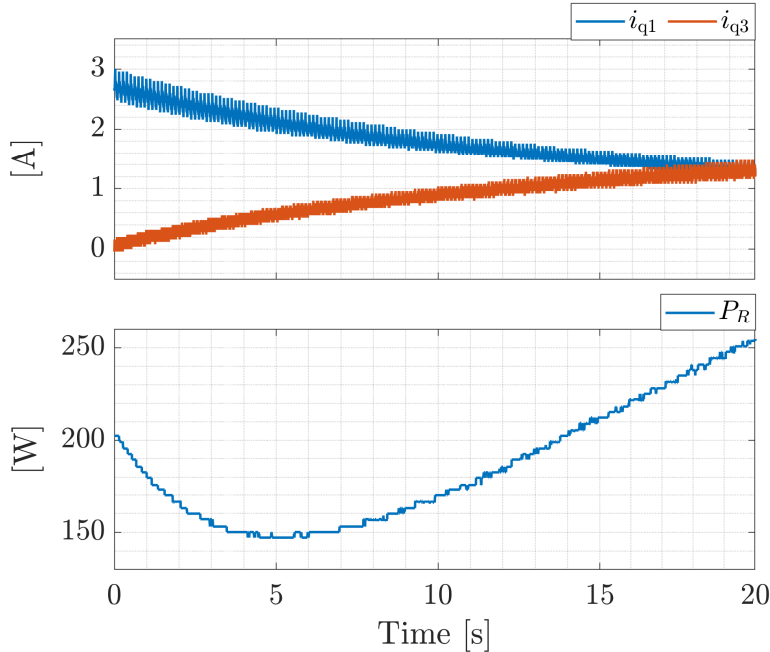


Fig. 5.22 – Quadrature current components and average power losses for a linearly varying third harmonic injection ratio in a 20 s time window.

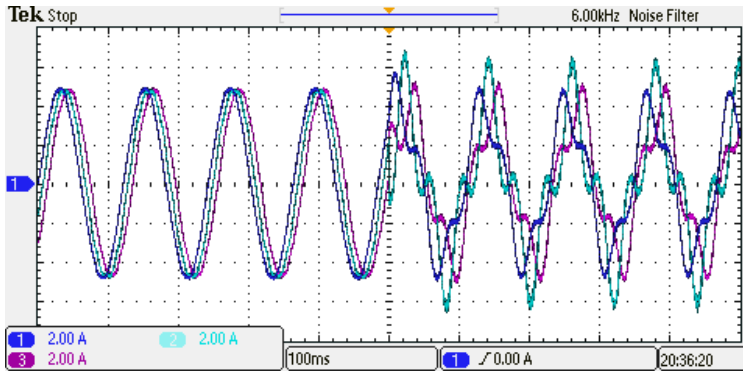


Fig. 5.23 – Phase currents  $i_1$ ,  $i_4$  and  $i_7$  without and with the optimal third harmonic injection (with the correct compensation of  $v_{NET}$ ).

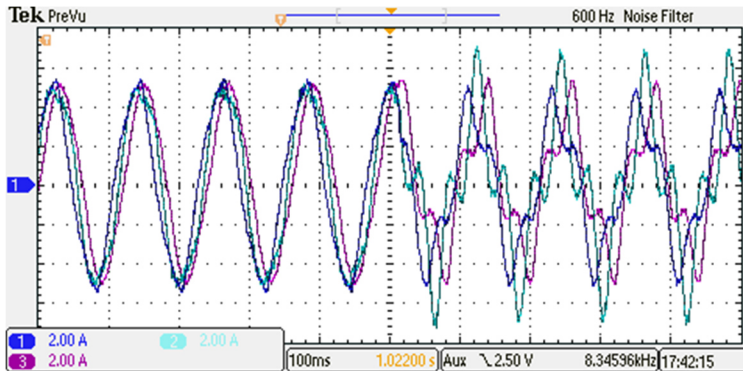


Fig. 5.24 – Phase currents  $i_1$ ,  $i_4$  and  $i_7$  without and with the optimal third harmonic injection (with an incomplete compensation of  $v_{NET}$ ).

This highlights that the proper compensation of  $v_{NET}$  is crucial to ensure the current controller effectiveness.

Finally, Fig. 5.25 shows the measured rotor speed  $\omega$  (reported with a scale of 40 mA/(rad/s)) and the torque  $T_m$  developed at the rotor shaft (reported with a scale of 1 A/Nm) in the same operating conditions of Fig. 5.23. They have been measured by a Datum Electronics M425 torque meter positioned at the joint between the PMSM and the DC machine. As can be noted, the adopted third harmonic injection does not alter the depicted waveforms, which are practically the same both before and after the change of the torque development strategy. This is a further confirmation that it is possible to alter the waveforms of the machine phase currents in a way to take advantage of the available degrees of freedom without affecting the overall torque developed by the machine<sup>36</sup>.

<sup>36</sup> For the analysed setup, the oscillations of  $T_m$  are mainly due to unmodelled or neglected phenomena (e.g., cogging torque, imperfect mechanical coupling, etc...).

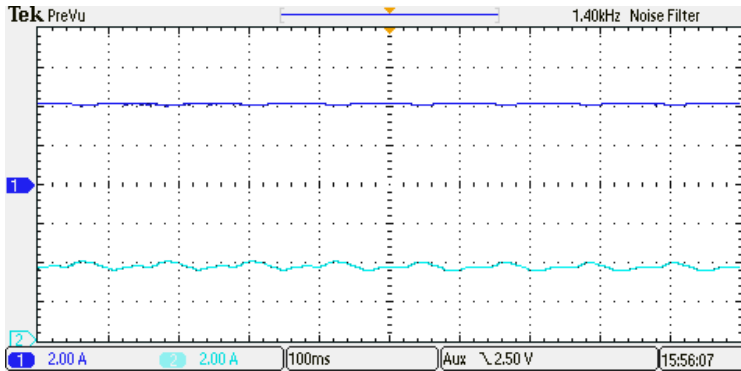


Fig. 5.25 – Speed and torque acquisitions without and with the optimal third harmonic injection.

## 5.7 Summary and remarks

The present chapter has focused on the *control of permanent magnet synchronous machine using a field-oriented approach*. The analysis has been carried out considering a generic winding configuration (i.e., asymmetrical, with an arbitrary angular shift), in a way to explicitly emphasize the main difference with respect to standard symmetrical configurations.

First, Section 5.1 has focused on the modelling of the machine. A *space vector formalism* has been introduced to link the spatial harmonics of the magnetic field at the air gap to the machine currents. It has been shown that the electromagnetic torque can be expressed as a linear combination of the quadrature components of the currents space vectors, each of which is related to a specific spatial harmonic.

However, for control purposes, only a limited set of space vector components can be controlled at the same time. The choice of these components is done by a *vector space decomposition* (VSD), by properly selecting a full-ranked Clarke transformation matrix. In asymmetrical configurations, many transformation matrices chosen with a field-oriented approach are usually not unitary. This affects the power losses expression (which can weight differently each current harmonic component) and the transformed mathematical model (which may show additional coupling effects among different space vector components).

After the model analysis, some torque control strategies have been developed in Section 5.2. It has been shown that also for asymmetrical machine configurations it is possible to exploit higher-order spatial harmonic contributions for torque development. Considering the fundamental current control as a baseline technique, a *third harmonic injection*, a *multi-harmonic injection* and a *maximum torque per ampere* strategies have been formulated, emphasizing their benefits and, once again, what are the differences between symmetrical and asymmetrical machine configurations.

Then, Section 5.3 has focused on the current control strategy, by first introducing the standard field-oriented control approach used in symmetrical configurations, and then by indicating some changes (like additional compensation terms) to adapt it to asymmetrical cases.

The theoretical analysis, which has been done for a generic machine, has then been particularized for a specific asymmetrical nine-phase PMSM, whose details have been given in Section 5.5. Finally, Section 5.6 has shown the numerical analysis of the proposed torque control approaches, the simulation results in a closed-loop control and the experimental results with a real machine prototype.



# 6 Decoupled Phase Variable Control of PMSMs

In Chapter 5 it has been shown that field-oriented controllers, despite being viable and convenient solutions for symmetrical machines, suffer significant hurdles when applied for asymmetrical configurations, including post-fault layouts. Indeed, in such cases, the implementation of a proper VSD and rotational transformation may be more complex, while the coupling effects between different current components can make the current control more challenging. The aim of the present chapter is to propose an alternative control algorithm that can automatically overcome the aforementioned drawbacks and limitations, therefore being suitable for any machine design and configuration [118].

The basic idea of the proposed approach is to re-derive the control algorithm without using any VSD or rotational transformation, but instead by addressing it directly in the phase variable domain. This is done while explicitly taking into account the electrical topology of the drive, by exploiting the properties and results of the network modelling approach developed in Chapter 4.

The concept of developing a machine control directly in the phase variable domain is not new, but its application has never spread out if compared to FOC algorithms, since the majority of electrical drives (both in industrial and in traction applications) are three-phase and are intrinsically symmetrical. On the contrary, as it has been previously discussed, multiphase drives can be realized in several different configurations, regarding both the machine design and the electrical topology. Moreover, even symmetrical multiphase machines may expose an asymmetrical behaviour when subject to faults.

The main benefit of the proposed approach is its generality. Indeed, the same controller structure can be applied for any machine design (e.g., different magnetic axes disposition, back-EMFs waveforms, etc...) and for any electrical configuration (e.g., single or multiple neutral points, open-end windings, etc...). This also makes it possible to use the same controller in case of post-fault reconfigurations of the same machine, which is an undoubted benefit for fault-tolerant multiphase drives. Based on these properties, the proposed approach can be considered a viable alternative to standard multiphase drives control algorithms.

The chapter is structured as follows. Section 6.1 summarizes the mathematical model of the analysed PMSM drive, which strongly relies on the network model properties derived in Chapter 4 and represents the analytical core for the control derivation. Section 6.2 describes a current references computation strategy based on a maximum torque per ampere (MTPA) approach, analyses its properties and explains how it can also be implemented for independent torque control strategies. Then, the current control is examined. The proposed current controller consists of two components, which are described in detail in Section 6.3 and in Section 6.4, respectively. The first component is

a decoupling algorithm, aimed at neutralizing the mutual interactions among the different machine phases, which come both from the magnetic phenomena inside the machine and from the electrical connection among the phase windings. The second component is a decoupled controller, which individually drives each phase current to seek the corresponding reference computed by the MTPA algorithm. The overall control algorithm is summarized in Section 6.5. Its experimental validation is described in Section 6.6 (which describes the adopted nine-phase PMSM setup) and in Section 6.7 (which discusses different testing scenarios). Finally, Section 6.8 sums up the conclusion of the work.

Again, as done in Chapter 5, the subscripts “*EM*” and “*VSI*” adopted in Chapter 4 will not be used anymore. The converter leg voltages set will be denoted as  $\mathbf{u}$  and the electrical machine phase voltages set will be denoted as  $\mathbf{v}$ . Additionally, the network resistance matrix  $\mathbf{R}_{NET}$  is supposed to be negligible.

## 6.1 Mathematical model

The drive under analysis consists of a  $n$ -phase PM machine supplied by a  $m$ -leg converter. All the  $n$  machine windings are located on the stator and the permanent magnets are placed on the rotor surface. The analysis is done considering magnetically isotropic machines, for which the rotor does not present any variable reluctance effect. Additionally, the effects of the stator slots are also disregarded.

Contrarily to the analysis of Chapter 5, no other assumptions are made regarding the machine phase windings design and the converter architecture.

This section particularizes the generalized machine model presented in Chapter 2 to the examined configuration, explicitly considering the drive architecture model analysed in Chapter 4 through the multiport network approach. Fig. 6.1 shows a schematic representation of a multiphase drive with the explicit identification of the PMSM, of the VSI (average model) and of the interconnection network.

### 6.1.1 Machine model

As also presented in Chapter 2, under the linearity hypothesis, the fluxes induced in each of the  $n$  stator windings is given by the superimposed contribution of the magnetic field generated by all the phase currents and by the permanent magnets on the rotor. The generalized model (2.29) is particularized into:

$$\boldsymbol{\phi} = \mathbf{L} \cdot \mathbf{i} + \boldsymbol{\psi}_{PM}(\theta) \quad (6.1)$$

For magnetically isotropic machines the  $n \times n$  inductances matrix  $\mathbf{L}$  does not depend on the rotor position  $\theta$ . As shown in Chapter 2, for energy-related reasons,  $\mathbf{L}$  is always symmetric and positive definite. As discussed in Chapter 5, in the special case of a symmetrical machine design (i.e., when all the windings are identical and equally shifted along the stator periphery),  $\mathbf{L}$  is also a *circulant matrix*, meaning that it also results  $L_{k,h} = L_{k+1,h+1}$  for all  $k, h = 1, \dots, n$ .

The  $n \times 1$  PM induced fluxes set  $\boldsymbol{\psi}_{PM}$  is a periodic function of the rotor position  $\theta$ . The waveforms of the flux linkages depend both on the magnetic field distribution generated at the air gap by the permanent magnets (e.g., sinusoidal, trapezoidal, etc.)

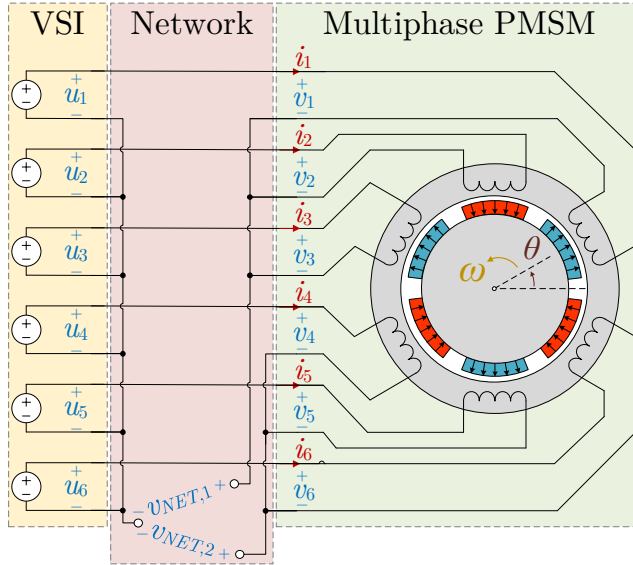


Fig. 6.1 – Schematic representation of a six-phase multiphase PMSM drive architecture, with explicit identification of the VSI (average model) and of the electrical interconnection network (double-star configuration with two isolated neutral points).

and on the spatial distribution of the stator windings (e.g., distributed or concentrated windings). A Fourier decomposition can be applied with respect to the mechanical position  $0 \leq \theta < 2\pi$  to identify the different harmonic contributions, each of which is related to a specific spatial harmonic of the magnetic field at the air gap. The fundamental harmonic of this Fourier decomposition identifies the pole pair periodicity of the machine. In other words, for a machine with  $P_p$  pole pairs, the set  $\psi_{PM}$  varies with the electrical angle  $\theta_{el} = P_p \cdot \theta$ . For purely sinusoidal machine only one fundamental harmonic is present. On the contrary, for a non-sinusoidal machine, multiple harmonics are present. In the special case of a symmetrical machine design, the flux linkages induced by the PMs in two consecutive phases expose identical waveforms, which are shifted from one another by the angle  $\alpha = 2\pi/nP_p$ . This property is not guaranteed for a generic machine configuration, for which the flux linkages induced in different phase windings can also differ from one another.

From the fluxes expression (6.1), the induced back-EMFs can be split in the transformer induced contribution and the motional induced contribution as:

$$\frac{d\phi}{dt} = \mathbf{L} \cdot \frac{d\mathbf{i}}{dt} + \omega \mathbf{f}_{PM}(\theta) \quad (6.2)$$

where it is here recalled that  $\omega = d\theta/dt$  is the rotor mechanical speed, and  $\mathbf{f}_{PM}(\theta) = \partial\psi_{PM}/\partial\theta$  is the  $n \times 1$  set of normalized PM-induced back-EMFs. Similarly to  $\psi_{PM}$ , also  $\mathbf{f}_{PM}$  periodically varies with the rotor position  $\theta$  and can be studied as the superposition of different harmonics of its Fourier spectrum. The same properties regarding the pole pair periodicity and harmonic content are also valid.

By denoting as  $\mathbf{e} = \omega \mathbf{f}_{PM}(\theta)$  the motional-induced back-EMFs, the machine electrical equations can be written in a matrix formalism as:

$$\mathbf{L} \cdot \frac{d\mathbf{i}}{dt} + \mathbf{R} \cdot \mathbf{i} + \mathbf{e} = \mathbf{v} \quad (6.3)$$

Since for magnetically isotropic PM machines the variable reluctance effects are absent, the electromagnetic torque expression (2.33) only depends on the interaction between the stator currents and the rotor magnets, and is therefore simplified to:

$$T_{em} = \mathbf{f}_{PM}^T(\theta) \cdot \mathbf{i} \quad (6.4)$$

### 6.1.2 Drive electrical model

As explained in Chapter 4, the machine phase windings are connected with each other and to the supplying converter through a known interconnection network, which typically introduces some algebraic constraints to the machine currents. The  $n_c \leq n$  constraints be modelled through the vector equation:

$$\mathbf{M}^T \cdot \mathbf{i} = \mathbf{0} \quad (6.5)$$

where  $\mathbf{M}$  is the  $n \times n_c$  constraints matrix. By neglecting the network resistive voltage drops<sup>1</sup>, the machine electrical equation (4.18) is therefore expressed as:

$$\mathbf{L} \cdot \frac{d\mathbf{i}}{dt} + \mathbf{R} \cdot \mathbf{i} + \mathbf{e} = \mathbf{v} = \mathbf{N} \cdot \mathbf{u} - \mathbf{M} \cdot \mathbf{v}_{NET} \quad (6.6)$$

where  $\mathbf{u}$  is the  $m \times 1$  set of converter leg voltages and  $\mathbf{v}_{NET}$  is the  $n_c \times 1$  set of auxiliary network voltages representing the potential shift due to the constraints on the currents.

As explained in Chapter 4, the model dependence on the auxiliary network voltages set  $\mathbf{v}_{NET}$  can be dropped out by projecting the system equation (6.6) in the configuration space, which is identified by the  $n \times n_f$  configuration matrix  $\mathbf{U}_f$  (with  $n_f = n - n_c$ ). As explained in Section 4.4, the matrix  $\mathbf{U}_f$  can be computed from the singular value decomposition of  $\mathbf{M}$  and is such that:

$$\mathbf{i} = \mathbf{U}_f \cdot \mathbf{i}_f, \quad \text{and} \quad \mathbf{U}_f^T \cdot \mathbf{M} = \mathbf{0} \quad (6.7)$$

where  $\mathbf{i}_f$  is a  $n_f \times 1$  set of free current components and can be found from the original set of phase currents as  $\mathbf{i}_f = \mathbf{U}_f^T \cdot \mathbf{i}$ .

The electrical equations (6.6) of the drive model can be therefore transformed in the reduced-order equations:

$$\mathbf{L}_f \cdot \frac{d\mathbf{i}_f}{dt} + \mathbf{R}_f \cdot \mathbf{i}_f + \mathbf{e}_f = \mathbf{v}_f = \mathbf{N}_f \cdot \mathbf{u} \quad (6.8)$$

where, coherently with the definitions of Section 4.4.4, the projections of the variables and the parameters in the configuration space is given by:

<sup>1</sup> The network resistive drops could however also be explicitly considered by merging the network resistances matrix  $\mathbf{R}_{NET}$  to the machine resistances matrix  $\mathbf{R}$ .

$$\begin{aligned}
\mathbf{L}_f &= \mathbf{U}_f^T \cdot \mathbf{L} \cdot \mathbf{U}_f \\
\mathbf{R}_f &= \mathbf{U}_f^T \cdot \mathbf{R} \cdot \mathbf{U}_f \\
\mathbf{N}_f &= \mathbf{U}_f^T \cdot \mathbf{N} \\
\mathbf{v}_f &= \mathbf{U}_f^T \cdot \mathbf{v} \\
\mathbf{e}_f &= \mathbf{U}_f^T \cdot \mathbf{e} = \mathbf{U}_f^T \cdot \omega \mathbf{f}_{PM}(\theta)
\end{aligned} \tag{6.9}$$

### 6.1.3 Mechanical model

Similarly to how it has been discussed in Section 5.1.7, the equivalent mechanical model of the electrical machine and of the connected rigid bodies can be represented through the equations:

$$J_{eq} \cdot \frac{d\omega}{dt} + F_{eq}(\omega) \cdot \omega = T_{em} - T_{load} \tag{6.10}$$

$$\frac{d\theta}{dt} = \omega \tag{6.11}$$

where it is recalled that  $J_{eq} = J + J_m$  and  $F_{eq}(\omega) = [F(\omega) + F_m(\omega)]$  respectively represent the *overall inertia* and the *overall friction coefficient* of the mechanical group (i.e., including both the electrical machine and the mechanical load). In this framework,  $T_{load}$  identifies the *loading torque* applied to the drive (which it is worth recalling to be different from the mechanical torque  $T_m$  applied at the rotor shaft of the electrical machine).

## 6.2 Torque control strategy

The machine control strategy is aimed at developing a desired electromagnetic torque  $T_{em}^*$ , typically coming from a speed controller. Given (6.4), this requirement can be obtained by formulating a proper strategy to compute the reference currents set  $\mathbf{i}^*$ .

Naturally, for the reference currents to be feasible, the  $n \times 1$  set  $\mathbf{i}^*$  must satisfy the algebraic constraints  $\mathbf{M}^T \cdot \mathbf{i}^* = \mathbf{0}$  related to the network configuration. This means that, for a  $n$ -phase machine subject to  $n_c$  algebraic constraints, there are  $n_f = n - n_c$  free current components which can be chosen. Moreover, the torque development requirement can be also formalized as an additional constraint for choosing the current references set. As a result, there are  $n_f - 1$  degrees of freedom to choose the set  $\mathbf{i}^*$  while producing the desired torque  $T_{em}^*$  and respecting the network algebraic constraints at the same time.

These degrees of freedom can be properly exploited to optimize some system performances by choosing a convenient objective function. The present section proposes a *maximum torque per ampere* (MTPA) strategy to compute  $\mathbf{i}^*$ .

### 6.2.1 Maximum torque per ampere algorithm

The MTPA strategy is aimed at developing the maximum possible electromagnetic torque for a given *machine equivalent current*  $I_{eq}$ . This requirement is perfectly equivalent to develop the given reference torque  $T_{em}^*$  while minimizing  $I_{eq}$ .

In the present analysis, the machine equivalent current is chosen to be an overall *root mean square* (RMS) current  $I_{RMS}$  computed as the Euclidean norm of the machine

currents set  $\mathbf{i}$ :

$$I_{RMS} = \|\mathbf{i}\| = \sqrt{\mathbf{i}^T \cdot \mathbf{i}} = \sqrt{\sum_{k=1}^n i_k^2} \quad (6.12)$$

For a machine with equal windings resistances, the current  $I_{RMS}$  is directly related to the machine losses. Indeed, in such a case, the instantaneous Joule losses of the machine would be expressed as:

$$p_R = \sum_{k=1}^n R \cdot i_k^2 = R \cdot I_{RMS}^2 \quad (6.13)$$

Therefore, the minimization of  $I_{RMS}$  would lead to the minimization of the Joule losses in the machine windings. Consequently, the thermal stress on the machine would be reduced and the energetic efficiency of the drive would be optimized<sup>2</sup>.

Since the minimization of  $I_{RMS}$  can be also addressed by minimizing  $I_{RMS}^2$ , the proposed MTPA algorithm is formalized as the constrained optimization problem<sup>3</sup>:

$$\min_{\mathbf{i}} \{\mathbf{i}^T \cdot \mathbf{i}\} \quad \text{subject to} \quad \begin{cases} \mathbf{f}_{PM}^T \cdot \mathbf{i} = T_{em}^* \\ \mathbf{M}^T \cdot \mathbf{i} = \mathbf{0} \end{cases} \quad (6.14)$$

The optimization problem (6.14) is the minimization of a quadratic function of  $n$  variables subject to a set of  $n_c + 1$  linear constraints. As known, it could be solved with a pseudo-inverse algorithm. However, since the set  $\mathbf{f}_{PM}$  of normalized PM-induced back-EMFs varies with the rotor position  $\theta$ , the corresponding pseudo-inverse matrix could not be computed offline. Therefore, this resolution approach is unfeasible for real-time applications using typical digital controllers.

For this reason, an analytical solution for (6.14), suitable for a real-time implementation, is here derived by using the *Lagrange's multiplier method*. By considering both the objective function  $I_{RMS}^2 = \mathbf{i}^T \cdot \mathbf{i}$  and the linear constraints  $\mathbf{f}_{PM}^T \cdot \mathbf{i} = T_{em}^*$  and  $\mathbf{M}^T \cdot \mathbf{i} = \mathbf{0}$ , a possible choice for the *Lagrangian function* is:

$$\mathfrak{L}(\mathbf{i}, \mu, \boldsymbol{\nu}) = \frac{1}{2} \mathbf{i}^T \cdot \mathbf{i} - \mu \cdot (\mathbf{f}_{PM}^T \cdot \mathbf{i} - T_{em}^*) - \boldsymbol{\nu}^T \cdot (\mathbf{M}^T \cdot \mathbf{i}) \quad (6.15)$$

where:

- $\mu$  is the Lagrange multiplier related to the reference torque development requirement, and
- $\boldsymbol{\nu}$  is the  $n_c \times 1$  vector of Lagrange multipliers related to the  $n_c$  algebraic constraints on the machine currents expressed by (6.5).

The optimal solution to the minimization problem (6.14) is found by nullifying the

<sup>2</sup> For a machine with different windings resistances, the windings losses minimization can be achieved by formulating the overall machine RMS current differently. For example, a possible formulation would be  $I_{RMS} = (\sqrt{R_k \cdot i_k^2})/R_0 = (\sqrt{\mathbf{i}^T \cdot \mathbf{R} \cdot \mathbf{i}})/R_0$  for any value of  $R_0$ . The overall machine windings losses would be  $p_R = R_0 \cdot I_{RMS}^2$  and all the proposed arguments of this section would still be valid, with only some slightly different formulations for the final results.

<sup>3</sup> The explicit dependence of  $\mathbf{f}_{PM}$  on the rotor position  $\theta$  has been omitted for notation compactness.

gradient of the Lagrangian  $\mathcal{L}(\mathbf{i}, \mu, \boldsymbol{\nu})$ . This leads to the following linear algebraic system of  $(n + n_c + 1)$  equations in  $(n + n_c + 1)$  variables:

$$\begin{aligned}\frac{\partial \mathcal{L}}{\partial \mathbf{i}} &= \mathbf{i} - \mu \cdot \mathbf{f}_{PM} - \mathbf{M} \cdot \boldsymbol{\nu} = \mathbf{0} \\ \frac{\partial \mathcal{L}}{\partial \mu} &= \mathbf{f}_{PM}^T \cdot \mathbf{i} - T_{em}^* = 0 \\ \frac{\partial \mathcal{L}}{\partial \boldsymbol{\nu}} &= \mathbf{M}^T \cdot \mathbf{i} = \mathbf{0}\end{aligned}\tag{6.16}$$

The linear system (6.16) has a unique solution which, since the objective function (6.12) is convex, is the global minimum of the optimization problem (6.14). Then, the analytical formulation of the optimal current set  $\mathbf{i}^*$  is<sup>4</sup>:

$$\mathbf{i}^* = \frac{\mathbf{W} \cdot \mathbf{f}_{PM}}{\mathbf{f}_{PM}^T \cdot \mathbf{W} \cdot \mathbf{f}_{PM}} \cdot T_{em}^*\tag{6.17}$$

where  $\mathbf{W}$  is a  $n \times n$  *MTPA weighting matrix* defined as:

$$\mathbf{W} = \mathbf{I} - \mathbf{M} \cdot (\mathbf{M}^T \cdot \mathbf{M})^{-1} \cdot \mathbf{M}^T\tag{6.18}$$

The matrix  $\mathbf{W}$  only depends on the algebraic constraints imposed on the machine currents. Therefore, it can be computed offline, and the computation of  $\mathbf{i}^*$  via (6.17) is suitable for real-time applications. The set  $\mathbf{i}^*$  is then the input reference for the current control algorithm.

The functional block scheme of the algorithm (6.17) is schematically represented in Fig. 6.2.

It can be proven<sup>5</sup> that the weighting matrix is equal to the configuration space projection matrix  $\mathbf{W} = \mathbf{U}_f \cdot \mathbf{U}_f^T$ . This property may be convenient for the algorithm numerical implementation, especially in case of  $\mathbf{N} = \mathbf{I}$ , because it provides an alternative way to compute the projection matrix  $\mathbf{U}_f \cdot \mathbf{U}_f^T$  via (6.18), without using the singular value decomposition of  $\mathbf{M}$ . As will be seen in Section 6.3, the matrix  $\mathbf{U}_f \cdot \mathbf{U}_f^T$  has an important role for the decoupled current control.

The same MTPA strategy can also be completely formalized in the configuration space, resulting in the expression (9.23), which gives the same reference currents obtained via (6.17)<sup>6</sup>.

In case of a single isolated neutral point configuration (in which the constraint matrix is simply  $\mathbf{M} = [1, 1, 1, \dots, 1]^T$ ) the solution (6.17) is completely equivalent to the solution (5.70) obtained in the synchronous domain (it is indeed the same optimization problem, which is only formulated with a different variable representation).

<sup>4</sup> Proven in Appendix 9.6.1.

<sup>5</sup> Proven in Appendix 9.6.2.

<sup>6</sup> Proven in Appendix 9.6.3.

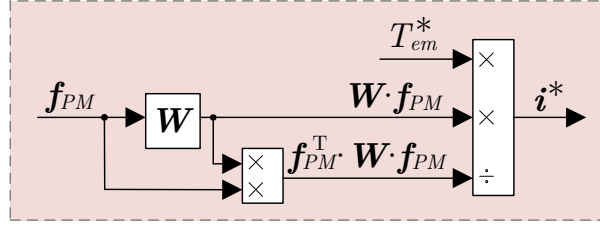


Fig. 6.2 – Functional block scheme of the MTPA algorithm.

### 6.2.2 MTPA solution properties

Several properties can be deduced from the inspection of (6.17).

First, as expected, the optimal phase currents set  $\mathbf{i}^*$  is proportional to the reference torque  $T_{em}^*$  and depends periodically on the rotor position  $\theta$  through the effect of  $\mathbf{f}_{PM}(\theta)$ . As a result, when the machine works in steady-state conditions at a constant speed and with a constant loading torque, the reference currents are periodic in time and their period is proportional to the rotor speed  $\omega$  (to be more specific, their period is linked to the machine electrical speed  $\omega_{el} = P_p \cdot \omega$ ).

In many typical operating conditions, the denominator ( $\mathbf{f}_{PM}^T \cdot \mathbf{W} \cdot \mathbf{f}_{PM}$ ) in the expression (6.17) is constant and the optimal reference current set  $\mathbf{i}^*$  is proportional to the normalized back-EMFs set  $\mathbf{f}_{PM}$ . As a result, in steady state conditions, the currents have the same harmonic content as the PM-induced back-EMFs. All the harmonics contribute to the development of the electromagnetic torque and their mutual interaction does not lead to any torque ripple. This is, for example, what typically happens for sinusoidal machines in healthy configurations, either when the magnetic axes disposition is symmetrical or when the  $n$  windings can be split in multiple symmetric subsets (e.g., multiple three-phase configurations). In other words, for these configurations, the optimal currents are also sinusoidal functions of  $\theta$ .

On the contrary, in all the other cases when ( $\mathbf{f}_{PM}^T \cdot \mathbf{W} \cdot \mathbf{f}_{PM}$ ) is not constant, the optimal currents set  $\mathbf{i}^*$  is not proportional to  $\mathbf{f}_{PM}$  and, in steady-state conditions, it shows also harmonic components which are absent in the PM-induced back-EMFs spectra. These additional harmonics do not develop any average electromagnetic torque, but are only needed to neutralize the torque ripple caused by the mutual interactions of the other harmonics appearing in both  $\mathbf{i}^*$  and  $\mathbf{f}_{PM}$  harmonic spectra at the same time. This behaviour not only exists in machines with highly non-sinusoidal back-EMFs but can also be observed for machines with sinusoidal PM-induced back-EMFs in case of post-fault reconfigurations. In other words, the optimal currents computed via (6.19) in healthy configurations might be sinusoidal, while in case of post-fault conditions (where the only difference is in the weighting matrix  $\mathbf{W}$ ) they might be non-sinusoidal.

Some problems may arise when the denominator ( $\mathbf{f}_{PM}^T \cdot \mathbf{W} \cdot \mathbf{f}_{PM}$ ) of (6.17) is close to zero. Indeed, in this case, the computed reference currents would tend towards infinity and be unfeasible for real applications. When this happens, it means that the machine is not capable of supplying the required electromagnetic torque  $T_{em}^*$  while satisfying the

hardware constraints at the same time<sup>7</sup>. For example, this is what would happen in case the stator currents cannot generate a rotating magnetic field at the air gap (as it happens for a single-phase machine). Anyway, this occurrence seldom occurs to multiphase drives<sup>8</sup> and, therefore, it can be disregarded in this context. A proper saturation of the set  $\mathbf{i}^*$  computed by (6.17) should be nevertheless implemented in order to avoid unreasonable high values of the reference currents, thus preventing overcurrent phenomena.

### 6.2.3 Torque sharing strategy

The proposed MTPA strategy (6.14) can also be applied to some machine windings subsets. This may be useful in case different groups of windings are supplied by independent sources, because it allows the control to transfer power between them, as depicted in Fig. 6.3.

By considering a total number  $n_{SET}$  of isolated windings groups, this capability is met by simply partitioning both the vector  $\mathbf{f}_{PM}$  and the vector  $\mathbf{i}$  into  $n_{SET}$  subsets and applying (6.14) to each one of them. Mathematically speaking, the expressions (6.17) and (6.18) are particularized in:

$$\mathbf{i}_{SET_h}^* = \frac{\mathbf{W}_{SET_h} \cdot \mathbf{f}_{PM,SET_h}}{\mathbf{f}_{PM,SET_h}^T \cdot \mathbf{W}_{SET_h} \cdot \mathbf{f}_{PM,SET_h}} \cdot T_{em,SET_h}^* \quad (6.19)$$

$$\mathbf{W}_{SET_h} = \mathbf{I} - \mathbf{M}_{SET,h} \cdot (\mathbf{M}_{SET_h}^T \cdot \mathbf{M}_{SET_h})^{-1} \cdot \mathbf{M}_{SET_h}^T \quad (6.20)$$

which must be applied to each  $h$ -th subset (with  $h = 1, \dots, n_{SET}$ ), as schematically represented in Fig. 6.4.

The constraint matrix  $\mathbf{M}_{SET_h}$  and, consequently, the weighting matrix  $\mathbf{W}_{SET_h}$  only

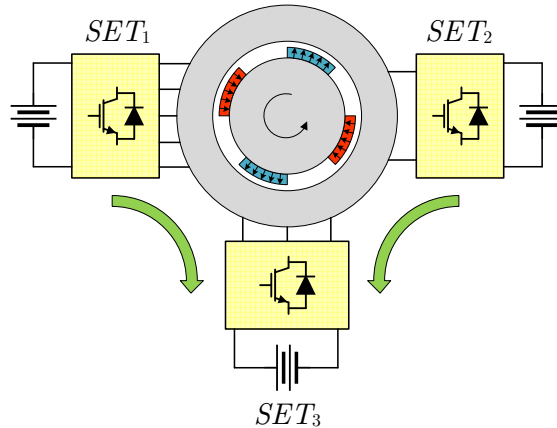


Fig. 6.3 – Power transfer between isolated phase windings subsets.

<sup>7</sup> This limitation is unrelated to the electrical drive control algorithm, and is instead intrinsically related to the drive configuration. When this happens, the torque development strategy cannot be imposed instantaneously as in (6.14) but, for example, only on average in a full rotor cycle (like it is done in single-phase machines).

<sup>8</sup> Given the presence of many phases, being unable to generate a rotating field at the air-gap would require a high number of faults.

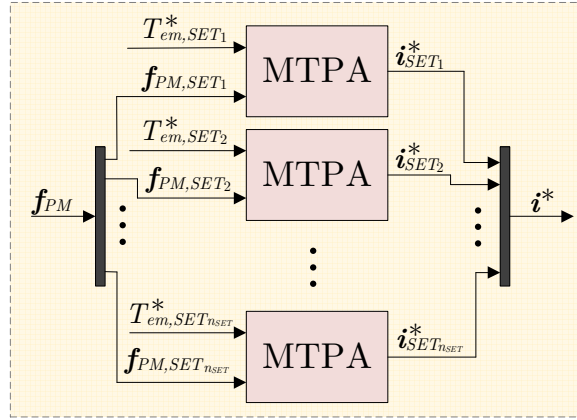


Fig. 6.4 – Application of the MTPA strategy for torque sharing purposes.

refer to the phases of the  $h$ -th windings group, just as if they were referred to a different PMSM with a reduced number of phases. Also, note that the different windings groups can also have a different number of phases (as exemplified in the illustration of Fig. 6.3).

The reference torque  $T_{em,SET_h}^*$  of each  $h$ -th subset can be chosen according to a desired power-sharing requirement. To give a practical example a windings subset with a higher reference torque will provide more power than one with a lower reference torque. Similarly, a subset with a reference torque in opposition to the rotor speed would absorb mechanical power instead of supplying it (i.e., it would behave as a “braking” subset instead of a “motoring” subset). The only condition to meet to keep guaranteeing the overall torque development (which is usually needed for the speed control), is:

$$\sum_{h=1}^{n_{SET}} T_{em,SET_h}^* = T_{em}^* \quad (6.21)$$

From the electromechanical point of view, this approach can be interpreted as applying the MTPA strategy to different PM machines having the same rotor. However, it is worth emphasizing that generally, from the electromagnetic point of view, the different subsets dynamically interact with one another. Consequently, contrarily to the current references computation strategy, the current control (which will be discussed in the following sections) cannot be separately applied to the different subsets.

### 6.3 Decoupling current control algorithm

Once the reference currents set  $\mathbf{i}^*$  has been computed, the control algorithm must find a set of reference converter voltages  $\mathbf{u}^*$  to drive the measured currents set  $\mathbf{i}$  towards  $\mathbf{i}^*$ . However, the dynamical equation (6.6) regulating the machine currents can be interpreted as a multi-input/multi-output control problem and, therefore, the simultaneous control of all the phase currents is not a trivial process.

Indeed, as already discussed, the currents are subject to multiple mutual interactions, which can be caused both by the magnetic phenomena in the machine (through the effect

of the mutually induced back-EMFs) and by the phase windings connection (due to the internal feedback actions caused by the constraints of the current).

This section presents and discusses a decoupling algorithm scheme, aimed at neutralizing the aforementioned mutual interactions. In this way, the machine phase currents can be controlled independently from one another by using a decoupled controller design, which will be analysed in Section 6.4.

### 6.3.1 Decoupling algorithm principle

The basic idea of the proposed solution is simple. It consists of replicating the equation (6.8) describing the drive model (in the configuration space), but by substituting the real current derivatives  $d\mathbf{i}_f/dt$  with a set  $\delta\mathbf{i}_f^*$  of reference current derivatives. This operation results in a desired set of voltages  $\mathbf{v}_f^*$  which is computed as:

$$\mathbf{L}_f \cdot \delta\mathbf{i}_f^* + \mathbf{R}_f \cdot \mathbf{i}_f + \mathbf{e}_f = \mathbf{v}_f^* \quad (6.22)$$

The reference derivative set  $\delta\mathbf{i}_f^*$  is computed basing on  $\mathbf{i}^*$  and  $\mathbf{i}$  through the procedure which will be described in Section 6.4.

Proving that the position (6.22) does achieve the desired currents dynamics decoupling is straightforward. Indeed, if  $\mathbf{v}_f = \mathbf{v}_f^*$  (i.e., if the voltage supply is done properly), (6.22) can be substituted into the reduced-order drive model (6.8) and the following formula is obtained:

$$\mathbf{L}_f \cdot \frac{d\mathbf{i}_f}{dt} + \mathbf{R}_f \cdot \mathbf{i}_f + \mathbf{e}_f = \mathbf{L}_f \cdot \delta\mathbf{i}_f^* + \mathbf{R}_f \cdot \mathbf{i}_f + \mathbf{e}_f \quad (6.23)$$

Then, by cancelling out the resistive term  $\mathbf{R}_f \cdot \mathbf{i}_f$  and the motional induced back-EMFs term  $\mathbf{e}_f$  and by grouping the remaining terms, it results that:

$$\mathbf{L}_f \cdot \left( \frac{d\mathbf{i}_f}{dt} - \delta\mathbf{i}_f^* \right) = \mathbf{0} \quad (6.24)$$

Since  $\mathbf{L}_f$  is a  $n_f \times n_f$  symmetric and positive definite matrix, the only solution to the homogeneous vector equation (6.24) is obtained when the multiplying vector is zero or, in other words, when:

$$\frac{d\mathbf{i}_f}{dt} = \delta\mathbf{i}_f^* \quad (6.25)$$

This equation can be separately applied to each of the  $n_f$  current components, resulting in the system of equations:

$$\frac{di_{f,k}}{dt} = \delta i_{f,k}^* \quad (\text{with } k = 1, \dots, n_f) \quad (6.26)$$

This means that, by only acting on the  $k$ -th reference derivative  $\delta i_{f,k}^*$ , each  $k$ -th current component  $i_{f,k}$  can be controlled independently from all the others. Therefore, thanks to the position (6.22), it has been possible to achieve the dynamic decoupling of the current components in the configuration space. The working principle of this decoupling algorithm is schematically represented in the block diagram of Fig. 6.5.

### 6.3.2 Decoupling algorithm requirements

This paragraph shows what are the mathematical properties that the drive model must satisfy to meet the condition (6.22), which achieves the desired decoupling.

The controller must compute a set of reference converter voltages set  $\mathbf{u}^*$  in a way to supply the desired  $\mathbf{v}_f^*$ . This requirement can be interpreted as the resolution of the linear system:

$$\mathbf{N}_f \cdot \mathbf{u}^* = \mathbf{v}_f^* \quad (6.27)$$

where  $\mathbf{v}_f^*$  is known and has been computed as per (6.22).

Since  $\mathbf{N}_f = \mathbf{U}_f^T \cdot \mathbf{N}$  is a  $n_f \times m$  matrix, the vector equation (6.27) is a system of  $n_f$  equations in  $m$  unknowns. Usually  $m \neq n_f$  and special attention must be given to the resolution of (6.27). Indeed, the existence and uniqueness of the solution may not be satisfied.

To guarantee the existence of the solution for any possible value of the reference vector  $\mathbf{v}_f^*$ , the number of equations  $n_f$  should not be greater than the number of unknowns  $m$ . Therefore, it must result  $m \geq n_f$ , meaning that  $\mathbf{N}_f$  should be either a square matrix or a horizontal rectangular matrix (i.e. the number of converter legs  $m$  should be greater than the number of free current components  $n_f = n - n_c$ ).

As a trivial example, a three-leg converter ( $m = 3$ ) cannot fully control the phase currents of a five-phase machine ( $n = 5$ ) with a single isolated neutral point configuration ( $n_c = 1$ ), because it would result  $n_f = n - n_c = 5 - 1 = 4 > 3 = m$ .

The condition  $m \geq n_f$  is not sufficient, by itself, to always guarantee the solvability of the system (6.27). Indeed, another requirement is that all the  $n_f$  equations of (6.27) must be compatible with each other. This condition is satisfied when all the rows of  $\mathbf{N}_f$  are linearly independent from one another (i.e., when the rank of  $\mathbf{N}_f$  is equal to  $n_f$ ). If this prerequisite is not met, the equation (6.27) may not have a solution because two or more equations conflict with one another. Physically, this condition would mean that some winding voltages (or some combinations of winding voltages) in the electrical machine cannot be directly affected by the VSI leg voltages.

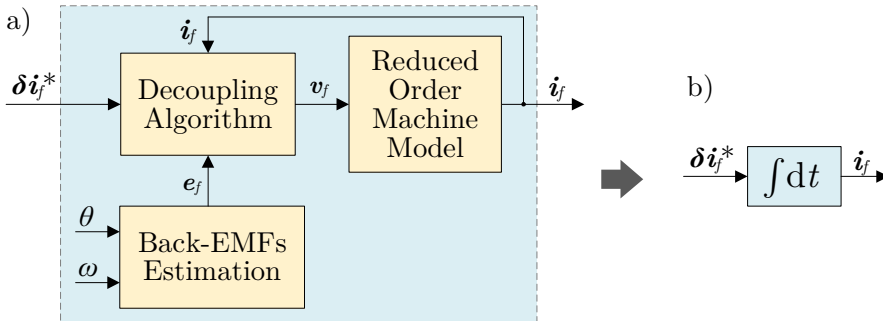


Fig. 6.5 – Working principle of the proposed decoupling algorithm: a) Expanded functional block diagram; b) Equivalent block diagram of the decoupled system (i.e., simple integrator).

As a trivial example, a converter leg that is not connected to any machine terminal cannot influence any machine winding voltage and the matrix  $\mathbf{N}_f$  would have a row with all zeros.

Another trivial example is represented by the parallel connection of two windings: in this case, the corresponding voltages would always be equal, and the converter would not be able to individually influence them. The matrix  $\mathbf{N}_f$  would have two identical (and therefore, linearly dependent) rows, meaning that its rank would be lower than  $n_f$ .

To sum up the results of this section, the decoupling algorithm (6.22) can be applied if that the matrix  $\mathbf{N}_f$  is full-ranked and with  $m \geq n_f$ . This prerequisite is met by most of the typical multiphase drive configurations, and is automatically verified if  $\mathbf{N}$  is a full-ranked  $n \times m$  matrix<sup>9</sup>. For this reason, the solvability of (6.27) will be further on taken for granted.

### 6.3.3 Pseudo-inverse based decoupling algorithm

Provided that (6.27) can be solved and, therefore, that the decoupling algorithm (6.22) can be applied, it is here shown what is the resulting analytical expression of the converter references voltages set  $\mathbf{u}^*$ .

If  $\mathbf{N}_f$  is a square matrix, the system (6.27) only has one solution which can be computed by a simple matrix inversion as:

$$\mathbf{u}^* = \mathbf{N}_f^{-1} \cdot \mathbf{v}_f^* = \mathbf{N}_f^{-1} \cdot (\mathbf{L}_f \cdot \delta \mathbf{i}_f^* + \mathbf{R}_f \cdot \mathbf{i}_f + \mathbf{e}_f) \quad (6.28)$$

If  $\mathbf{N}_f$  is a rectangular matrix, the system (6.27) has infinite solutions. The general formulation of a solution can be decomposed into two parts:

$$\mathbf{u}^* = \mathbf{u}_{opt}^* + \mathbf{u}_0^* \quad (6.29)$$

The voltage set  $\mathbf{u}_{opt}^*$  in (6.29) is the minimum-norm solution<sup>10</sup> of (6.27), and can be computed as:

$$\mathbf{u}_{opt}^* = \mathbf{N}_f^\dagger \cdot \mathbf{v}_f^* = \mathbf{N}_f^\dagger \cdot (\mathbf{L}_f \cdot \delta \mathbf{i}_f^* + \mathbf{R}_f \cdot \mathbf{i}_f + \mathbf{e}_f) \quad (6.30)$$

where  $\mathbf{N}_f^\dagger$  is the *Moore-Penrose pseudo-inverse* of  $\mathbf{N}_f$ , and is such that  $\mathbf{N}_f \cdot \mathbf{N}_f^\dagger = \mathbf{I}$ . It can be noted that the expression (6.30) takes the same form of (6.28) and can be interpreted as being its generalization when  $\mathbf{N}_f$  is not a square matrix.

The voltage set  $\mathbf{u}_0^*$  is any  $m \times 1$  vector belonging to the null-space of  $\mathbf{N}_f$  (i.e., such that  $\mathbf{N}_f \cdot \mathbf{u}_0^* = \mathbf{0}$ ). Since  $\mathbf{N}_f$  has a rank  $n_f \leq m$ , the number of degrees of freedom for choosing  $\mathbf{u}_0^*$  is  $m - n_f = (m - n) + n_c$ . This means that  $\mathbf{u}_0^*$  can be related both to the presence of more converter legs than the number of machine phases (i.e., when  $m > n$ ) and to the presence of algebraic constraints for the machine currents (i.e., when  $n_c > 0$ ).

<sup>9</sup> Proven in Appendix 9.6.4.

<sup>10</sup> This means that the vector  $\mathbf{u}_{opt}^*$  is the solution of (6.27) which minimizes the *Euclidean Norm* of the VSI reference voltages set, which is  $\|\mathbf{u}^*\| = \sqrt{(\mathbf{u}^*)^T \cdot \mathbf{u}^*}$ .

In this latter case,  $\mathbf{u}_0^*$  can be interpreted as the generalized formulation of the common-mode voltage injection which is typically applied in star connected system with isolated neutrals. This means that a lack of degrees of freedom for the machine phase currents leads to the presence of more degrees of freedom for the converter leg voltages.

Since the minimum norm set  $\mathbf{u}_{opt}^*$  computed as per (6.30) usually requires some converter leg voltages to be negative, and given that this requirement cannot be achieved through most of the inverter architectures, the set  $\mathbf{u}_0^*$  can be chosen to properly condition the overall leg voltages set  $\mathbf{u}^*$  to be in a feasible range. Then, a general formulation for this injection set is<sup>11</sup>:

$$\mathbf{u}_0^* = (\mathbf{I} - \mathbf{N}_f^\dagger \cdot \mathbf{N}_f) \cdot \mathbf{u}_{off}^* \quad (6.31)$$

where  $\mathbf{u}_{off}^*$  is a desired offset voltages vector, which can be chosen as the set of midrange voltages values associated with each converter leg (e.g., half of the DC-bus voltage) or through other known common-mode voltage injection algorithms (e.g., min-max injection, higher harmonic injections, etc.). It can be proven<sup>12</sup> that, with the position (6.31), the voltage set  $\mathbf{u}^* = \mathbf{u}_{opt}^* + \mathbf{u}_0^*$  is the solution of (6.27) that minimizes the Euclidean norm  $\|\mathbf{u} - \mathbf{u}_{off}^*\|$ , which represents a distance between the leg voltages set  $\mathbf{u}$  and the desired offset voltage vector  $\mathbf{u}_{off}^*$ .

The proposed decoupling algorithm is general and can be applied to a wide range of different machine and drive configurations, including concentrated or distributed windings design, symmetrical or asymmetrical magnetic axes configuration, sinusoidal or non-sinusoidal induced back-EMFs, single or multiple-star connections, healthy and faulty scenarios, and so on. Its schematic block diagram is represented in Fig. 6.6.

### 6.3.4 Decoupling algorithm in the phase variable domain

The decoupled algorithm presented in the previous sections has been completely formalized within the configuration space of the drive, concerning the reduced-order model (6.8). This approach can be directly reformulated for the whole full-order drive model (6.6) with relatively few changes.

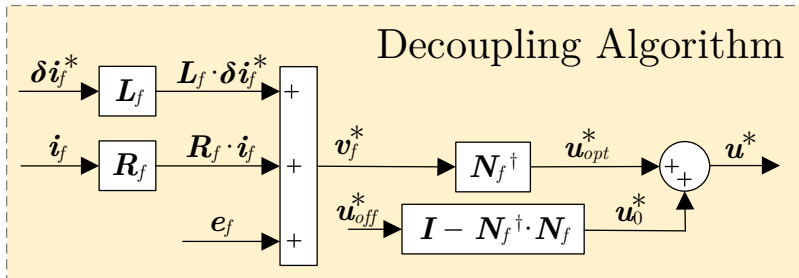


Fig. 6.6 – Functional block scheme of the decoupling algorithm implemented in the configuration space.

<sup>11</sup> Proven in Appendix 9.6.5.

<sup>12</sup> Proven in Appendix 9.6.6.

Consider the reference derivative set for the free current components  $\delta \mathbf{i}_f^*$ . This set is a  $n_f \times 1$  vector of the configuration space. The corresponding reference derivatives set for the real machine currents is a  $n \times 1$  vector  $\delta \mathbf{i}^*$  such that:

$$\mathbf{M}^T \cdot \delta \mathbf{i}^* = \mathbf{0}, \quad \delta \mathbf{i}^* = \mathbf{U}_f \cdot \delta \mathbf{i}_f^*, \quad \text{and} \quad \delta \mathbf{i}_f^* = \mathbf{U}_f^T \cdot \delta \mathbf{i}^* \quad (6.32)$$

By pre-multiplying both sides of (6.25) for  $\mathbf{U}_f$  and by considering (6.32), it results:

$$\frac{d\mathbf{i}}{dt} = \delta \mathbf{i}^* \quad (6.33)$$

which, once expressed in components, is:

$$\frac{di_k}{dt} = \delta i_k^* \quad (\text{with } k = 1, \dots, n) \quad (6.34)$$

This consideration means that, by using a reference set  $\delta \mathbf{i}^*$  compatible the hardware constraints, the proposed decoupling algorithm not only works for the configuration space components  $\mathbf{i}_f$ , but also for the actual (i.e.,  $n$ -dimensional) set of the machine phase currents  $\mathbf{i}$ .

The expressions (6.30) of the minimum-norm voltage reference  $\mathbf{u}^*$  is computed as<sup>13</sup>:

$$\mathbf{u}_{opt}^* = [(\mathbf{U}_f^T \cdot \mathbf{N})^\dagger \cdot \mathbf{U}_f^T] \cdot (\mathbf{L} \cdot \delta \mathbf{i}^* + \mathbf{R} \cdot \mathbf{i} + \mathbf{e}) \quad (6.35)$$

This expression is given by the product of two terms:

- the  $m \times n$  matrix  $[(\mathbf{U}_f^T \cdot \mathbf{N})^\dagger \cdot \mathbf{U}_f^T]$ , which is only related to the interconnection network and does not depend on the machine parameters, and
- the  $n \times 1$  vector  $(\mathbf{L} \cdot \delta \mathbf{i}^* + \mathbf{R} \cdot \mathbf{i} + \mathbf{e})$ , which is only related to the machine parameters and does not depend on the interconnection network.

The expression (6.31) of the injection voltage set  $\mathbf{u}_0^*$  is instead unaltered by referring to the full-order drive model. By recalling that  $\mathbf{N}_f = \mathbf{U}_f^T \cdot \mathbf{N}$ , the same expression is here explicitly rewritten as:

$$\mathbf{u}_0^* = [\mathbf{I} - (\mathbf{U}_f^T \cdot \mathbf{N})^\dagger \cdot (\mathbf{U}_f^T \cdot \mathbf{N})] \cdot \mathbf{u}_{off}^* \quad (6.36)$$

The schematic diagram of the decoupling algorithm implemented directly in the phase variable domain is depicted in Fig. 6.7. As can be seen, the algorithm can be grouped in two separate sections:

- the “*Machine Compensation*” block, that identifies the machine-related terms, which are independent of the electrical topology of the system, and
- the “*Network Compensation*” block, that identifies the network-related terms, which are independent of the machine parameters.

---

<sup>13</sup> Proven in Appendix 9.6.7.

The expressions (6.35)-(6.36) are simplified when  $\mathbf{N} = \mathbf{I}$ , which is the case of most star and multiple-star connected drive configurations (both in healthy and in faulty scenarios). Indeed, in such a case, the expressions simply become:

$$\mathbf{u}_{opt}^* = (\mathbf{U}_f \cdot \mathbf{U}_f^T) \cdot (\mathbf{L} \cdot \delta \mathbf{i}^* + \mathbf{R} \cdot \mathbf{i} + \mathbf{e}) \quad (6.37)$$

$$\mathbf{u}_0^* = (\mathbf{U}_c \cdot \mathbf{U}_c^T) \cdot \mathbf{u}_{off}^* \quad (6.38)$$

Then, in this case, it can be concluded that:

- the minimum-norm voltages set  $\mathbf{u}_{opt}^*$  is the projection of the reference vector  $(\mathbf{L} \cdot \delta \mathbf{i}^* + \mathbf{R} \cdot \mathbf{i} + \mathbf{e})$  in the configuration space,
- the injection vector  $\mathbf{u}_0^*$  can be computed by projecting any offset vector  $\mathbf{u}_{off}^*$  in the complementary configuration space.

The functional block diagram of Fig. 6.7 is modified into the diagram of Fig. 6.8. As can be seen, the machine compensation block is still the same, while the network compensation block is simplified and does not require any Moore-Penrose pseudo-inversion.

All the formerly addressed generality properties of the proposed decoupling algorithm are still valid. Additionally, by directly formulating it in the phase variable domain, it can be concluded that:

- Once the electrical machine parameters are given, the vector  $\mathbf{v}^* = (\mathbf{L} \cdot \delta \mathbf{i}^* + \mathbf{R} \cdot \mathbf{i} + \mathbf{e})$  (i.e., the machine compensation blocks of Fig. 6.7 and Fig. 6.8) is always computed with the same expression, regardless of how the different phases influence each other. Any detectable change in the machine parameters (for example, related to thermal effects) can be directly considered by properly updating the corresponding terms.
- Once the network configuration is given, all the pre-multiplying matrices in (6.35)-(6.36) (i.e., the network compensation blocks of Fig. 6.7 and Fig. 6.8) are univocally identified. For a real-time implementation, they can be computed during the algorithm initialization and can be updated only in case of network reconfigurations (for example, after a fault recognition).

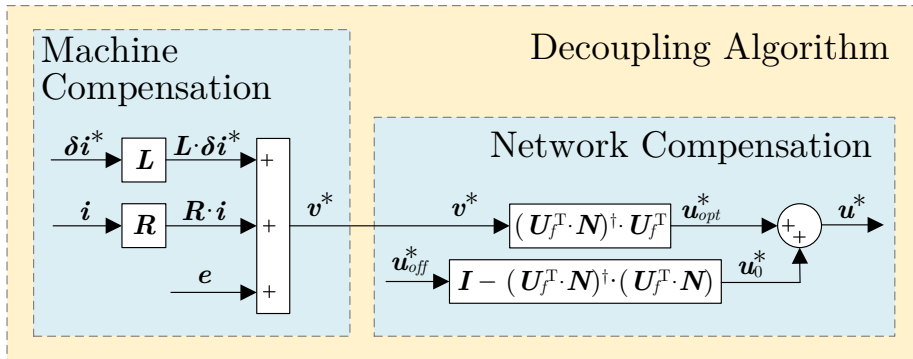


Fig. 6.7 – Functional block scheme of the decoupling algorithm implemented in the phase variable domain.

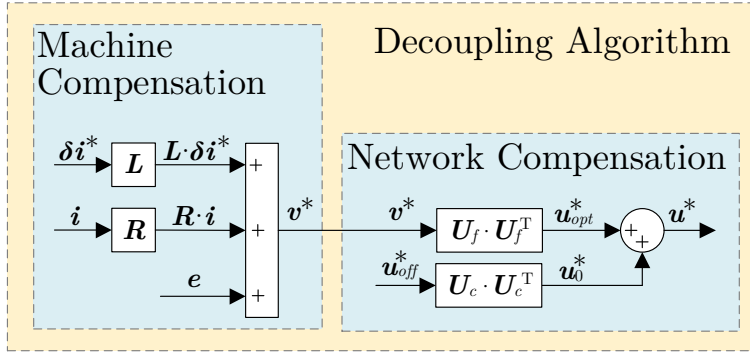


Fig. 6.8 – Functional block scheme of the decoupling algorithm if  $N = I$ .

## 6.4 Decoupled current control algorithm

Once the proposed decoupling algorithm is implemented, the machine currents can be independently controlled from one another. This means that the multi-input/multi-output control problem is conveniently reduced in multiple single-input/single-output control problems, which can be solved through well-known tools of control theory.

The decoupled current control aims to drive the  $n \times 1$  machine currents set  $\mathbf{i}$  towards the desired references current set  $\mathbf{i}^*$ . Naturally, to be feasible, the reference current set  $\mathbf{i}^*$  must satisfy the same hardware constraint  $\mathbf{M}^T \cdot \mathbf{i}^* = \mathbf{0}$  of the actual machine currents, which is automatically guaranteed by the current references computation strategy presented in Section 6.2.

If executed in the configuration space, the decoupled current control algorithm is asked to compute the  $n_f \times 1$  reference derivatives set  $\delta \mathbf{i}_f^*$  to be used in (6.30). If executed in the phase variable domain, the decoupled current control algorithm is instead asked to compute the  $n \times 1$  reference derivatives set  $\delta \mathbf{i}^*$  to be used in (6.35). The two approaches are perfectly equivalent.

Any single-input/single-output feedback controller structure can be used (e.g., linear, hysteresis, dead-beat, sliding mode, model-predictive, etc.). The different current components could also be driven by different controller architectures. Moreover, the feedback controller structure can be also supported by an additional feedforward action.

The present section proposes a simple linear controller architecture which can be used in most of the typical applications. Given the linearity, the proposed controller properties can be conveniently studied both in the Laplace domain and in the frequency domain by using standard dynamical systems analysis tools (e.g., transfer functions, Bode diagrams, etc.).

### 6.4.1 Decoupled system transfer function

When the decoupling algorithm (6.35) is implemented, it has been shown that each  $k$ -th current  $i_k$  (with  $k = 1, \dots, n$ ) is governed by the corresponding reference derivative  $\delta i_k^*$  through the dynamical equation (6.34), which represents a simple integrator. Then, the transfer function of the decoupled system in the Laplace domain would be:

$$\mathcal{G}(s) = \frac{\mathcal{L}[i_k](s)}{\mathcal{L}[\delta i_k^*](s)} = \frac{1}{s} \quad (6.39)$$

Nevertheless, as explained in Chapter 3, the actual leg voltages set  $\mathbf{u}$  does not coincide with the reference voltages set  $\mathbf{u}^*$ . Indeed, it has been shown that for a pulse-width modulated converter driven by a digital controller, by focusing on the low-frequency harmonic content of the output voltages, from (3.5) it results that:

$$u_k(t) \cong u_k^*(t - \tau_{del}) \quad (6.40)$$

where  $\tau_{del} = T_s + T_{PWM}/2$  is the overall time delay introduced by both the discrete-time control and by the modulation technique. This time delay can be represented, in the Laplace domain, by the transfer function:

$$\mathcal{M}(s) = \frac{\mathcal{L}[u_k](s)}{\mathcal{L}[u_k^*](s)} \cong e^{-s \tau_{del}} \quad (6.41)$$

which, in the frequency domain, has unitary magnitude but introduces a phase delay which increases with the frequency.

As a result, by explicitly taking into account this delay effect, the overall decoupled system transfer function (6.39) can be better approximated as<sup>14</sup>:

$$\mathcal{G}(s) = \frac{\mathcal{L}[i_k](s)}{\mathcal{L}[\delta i_k^*](s)} \cong \frac{1}{s} \cdot e^{-s \tau_{del}} \quad (6.42)$$

This additional delay effect is particularly important for the decoupled controller tuning, since it significantly affects the stability margin of the system.

## 6.4.2 Decoupled controller

The proposed feedback controller architecture is equal for all the  $n$  machine phase currents. Each  $k$ -th single-input/single-output linear controller (with  $k = 1, \dots, n$ ) processes the  $k$ -th current tracking error ( $i_k^* - i_k$ ) and computes the reference derivative set  $\delta i_k^*$  which is then used in the decoupling algorithm (6.35).

As shown in Section 6.2, each reference current  $i_k^*$  is a periodic function of the electrical angle  $\theta_{el} = P_p \theta$ . This means that, in steady state conditions at a constant rotor speed, all the reference currents are periodic in time, with the fundamental angular frequency  $\omega_{el} = P_p \omega$ .

Contrarily to standard FOC algorithms, since the proposed controller directly works in the phase variable domain, a simple *proportional-integral* (PI) structure is not effective, since it cannot nullify the tracking error in case of periodic current references. Therefore, to guarantee the steady-state tracking error to be zero, the standard PI structure is enforced by adding multiple *resonant controllers* actions.

Indeed, similarly to how an integral action results into an infinite magnitude gain for constant references (which are at zero frequency) each  $h$ -th resonant action leads to an infinite magnitude gain at its resonance frequency  $\omega_h$ , and is therefore suited to track sinusoidal references [158]–[161]. The total number of resonant actions  $n_{res}$  required to

<sup>14</sup> Proven in Appendix 9.6.8.

track a generic periodic reference is related to the number of harmonics of its Fourier series expression.

The proposed controller transfer function in the Laplace domain is:

$$\mathcal{C}(s) = \frac{\mathcal{L}[\delta i_k^*](s)}{\mathcal{L}[i_k^* - i_k](s)} = K_P + \frac{K_I}{s} + \sum_{h=1}^{n_{res}} K_{R,h} \cdot \frac{s}{s^2 + \omega_h^2} \quad (6.43)$$

where:

- $K_P$  is the *proportional controller constant*,
- $K_I$  is the *integral controller constant*, and
- $K_{R,h}$  is the  *$h$ -th resonant controller constant*.

An additional benefit of this multiple resonant structure is that, similarly to how an integral action can perfectly reject constant disturbances, each  $h$ -th resonant action can perfectly reject sinusoidal disturbances at its resonance frequency  $\omega_h$ . In real applications, these disturbances may come, for example, from an imperfect compensation of the induced back-EMFs vector  $\mathbf{e} = \omega \mathbf{f}_{PM}(\theta)$  or from an imperfect knowledge of the machine parameters in the decoupling algorithm (6.35).

To allow the controller to work with variable speed drives, each  $h$ -th resonance frequency  $\omega_h$  should be synchronized in real-time with the measured machine angular speed  $\omega$ . The implementation algorithm used in this work is described in Appendix 9.1.1 and relies on the synchronization with the rotor position  $\theta$ . Because of sampling effects, for a digital control, the maximum resonance frequency is limited by the Nyquist frequency  $f_s/2$  and, therefore, it should be sufficiently lower than  $\omega_s = 2\pi \cdot f_s/2 = \pi f_s$ . The resonant actions in (6.43) can also be replaced by different controllers with an equivalent behaviour (e.g., multiple rotating integrators, vector proportional-integral controllers, repetitive controllers, etc...).

As known, for feedback-controlled systems many properties can be found from the analysis of the open-loop transfer function:

$$\mathcal{H}(s) = \mathcal{C}(s) \cdot \mathcal{G}(s) \quad (6.44)$$

For the proposed current control algorithm a qualitative open-loop frequency response is graphically represented in the Bode diagram of Fig. 6.9. In this example, the feedback controller transfer function  $\mathcal{C}(s)$  in (6.43) has been realized with three resonant terms synchronized with  $\omega_{el}$ ,  $3\omega_{el}$  and  $5\omega_{el}$ . It can be clearly seen that the magnitude gain for these frequencies is infinite, meaning that the resonant actions can perfectly track the fundamental, the third and the fifth harmonic of the desired current reference. Each resonant term is also responsible for a  $180^\circ$  jump of the phase diagram.

The progressive increase of the phase delay with the frequency is instead due to the time delay effect introduced by the term  $e^{-s\tau_{del}}$  in (6.42), which approximately describes the combined effect of the PWM technique and of the discrete-time control.

As for any linear controller, the 0 dB *crossover frequency*<sup>15</sup>  $\omega_{0dB}$  of the open-loop

<sup>15</sup> For a feedback controlled system with open-loop transfer function  $\mathcal{H}(s)$ , the 0 dB *crossover frequency* is the angular frequency  $\omega_{0dB}$  for which  $|\mathcal{H}(j\omega_{0dB})| = 1$ , [162]. Under the normally adopted assumption that  $|\mathcal{H}(j\omega)| \gg 1$  for  $\omega < \omega_{0dB}$  and  $|\mathcal{H}(j\omega)| \ll 1$  for  $\omega > \omega_{0dB}$ , the 0 dB

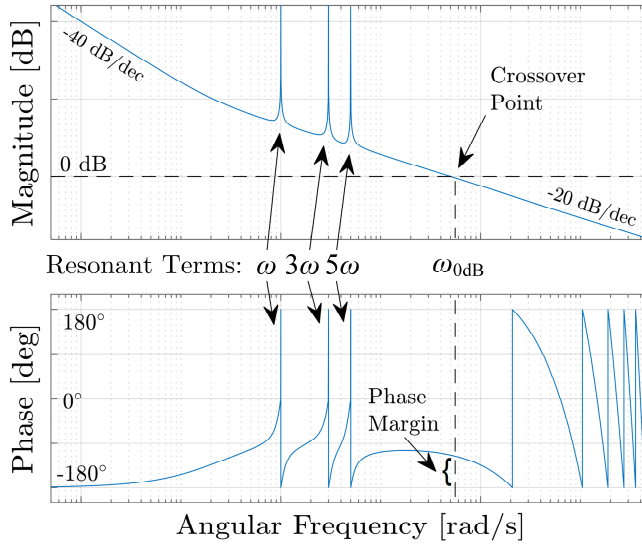


Fig. 6.9 – Qualitative Bode diagram of the open-loop decoupled system.

transfer function frequency response (which mostly depend on  $K_P$ ) should be chosen as a trade-off between the closed-loop controller dynamic requirements and its robustness. Indeed, higher values of  $\omega_{0dB}$  would be preferable to make the closed-loop transient performances to be faster but, given the phase delay in (6.42) caused by the modulation procedure and by the digital controller implementation, high values of  $\omega_{0dB}$  may also lead to low values for the *stability phase margin*<sup>16</sup> of  $\mathcal{H}(s)$ , which might compromise the stability of the closed-loop system.

The choice of the integral and resonant parameters  $K_I$  and  $K_{R,h}$  (with  $h = 1, \dots, n_{res}$ ) also depend on the required dynamic response of the system towards tracking errors. Generally speaking, higher values lead to faster settling transients, but too high values may also lead to overshooting effects. Moreover, as previously stated, an imperfect compensation of the machine parameters in the decoupling algorithm (due, for example, to measurement uncertainties and neglected or unmodelled phenomena) can be neutralized in steady-state thanks to the resonant controllers. However, these effects can also reduce the stability robustness of the closed-loop control. To avoid instability phenomena, it is possible to reduce the 0 dB crossover frequency  $\omega_{0dB}$  with respect to

---

crossover frequency can give an estimation of the dynamic performances of the closed-loop system: the higher is  $\omega_{0dB}$ , the faster is its transient behaviour.

<sup>16</sup> For a feedback controlled system with open-loop transfer function  $\mathcal{H}(s)$ , the *phase margin* is the angle  $\varphi_m = \pi - |\angle \mathcal{H}(j\omega_{0dB})|$ , [162]. Under the normally adopted assumption that  $|\mathcal{H}(j\omega)| \gg 1$  for  $\omega < \omega_{0dB}$  and  $|\mathcal{H}(j\omega)| \ll 1$  for  $\omega > \omega_{0dB}$ , the phase margin can give an estimation of the stability properties of the closed-loop system: the higher is  $\varphi_m$ , the more robust is the system stability with respect to parameter uncertainty and unmodelled dynamics. However, in case of more 0 dB crossover frequencies, the stability properties of the system cannot be directly addressed through  $\varphi_m$  and the use of *Nyquist's theorem* may be required.

the theoretical value<sup>17</sup>. The required reduction should be verified on the specific machine.

Finally, it is worth recalling that the chosen structure of (6.43) is only a possible choice for the current controller, which could have also been realized with different architectures or implementations, naturally resulting in different transient performances and different parameter tuning approaches.

## 6.5 Complete drive control algorithm

The overall structure of the proposed drive control algorithm is schematically represented in Fig. 6.10.

First, the “*Speed Controller*” compares the reference speed  $\omega^*$  with the machine speed  $\omega$  and computes the reference electromagnetic torque  $T_{em}^*$  to be applied. The machine speed dynamics is described by the model (6.10)-(6.11), which is unrelated to the electrical machine parameters and configuration. As a result, any standard speed controller structure, like a PI regulator, can be used (as represented in Fig. 6.10).

Next, the “*Back-EMFs Estimation*” block is executed to compute both the normalized PM-induced back-EMFs vector  $\mathbf{f}_{PM}$  (which is required from the current references computation strategy) and to estimate the motional induced back-EMFs vector  $\mathbf{e} = \omega \cdot \mathbf{f}_{PM}$  (which is instead used in the decoupling algorithm).

The “*MTPA*” block (whose structure has been previously represented in Fig. 6.2) is then executed to find the references currents set  $\mathbf{i}^*$  via equation (6.17). In case of torque sharing strategies, as explained in Section 6.2.3, this block is separately executed for all the chosen subsets of the machine windings (as it will be exemplified in Section 6.7.8).

The “*Current Controller*” block is finally executed. The Proportional-Integral-Resonant (PIR) feedback controller described in Section 6.4 compares the reference currents set  $\mathbf{i}^*$  with the actual currents set  $\mathbf{i}$  and, through this error, it computes the reference derivative currents set  $\delta \mathbf{i}^*$  to be applied<sup>18</sup>. The *decoupling algorithm* (6.35)-

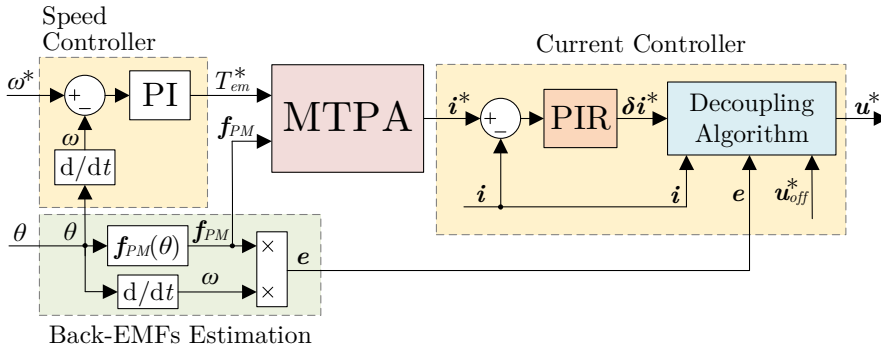


Fig. 6.10 – Functional block diagram of the proposed controller.

<sup>17</sup> The value which would have been chosen in presence of a perfect decoupling algorithm.

<sup>18</sup> To guarantee the feasibility of the current control, it is convenient to pre-multiply both  $\mathbf{i}^*$  and  $\mathbf{i}$  for the projection matrix  $(\mathbf{U}_f^T \cdot \mathbf{U}_f)$  before the execution of the decoupled controller, in a

(6.36) (whose functional block diagram has been previously represented in Fig. 6.7) is then executed to find the reference voltages set  $\mathbf{u}^*$ , which is finally applied through a pulse width modulation algorithm.

All the matrices needed for the execution of the proposed algorithm can be conveniently computed offline or during the algorithm initialization to reduce the computational burden for real-time applications (and, therefore, to make the algorithm execution faster). In case of configuration or parameters changes, these matrices can be updated in real-time without altering the drive control scheme (as it will be exemplified in Section 6.7.7).

## 6.6 Experimental setup

The proposed control algorithm has been experimentally validated with the setup depicted in Fig. 6.11.

### 6.6.1 Electrical machine

The electrical machine under analysis (see Fig. 6.12) is a nine-phase surface-mounted PMSM with 3 pole pairs<sup>19</sup>.

The machine windings have been designed as 3 symmetrical three-phase sets whose magnetic axes are mutually shifted by  $15^\circ$  in the electrical reference frame (i.e.,  $5^\circ$  mechanically). It is, therefore, possible to define the angles set:

$$\boldsymbol{\alpha} = [0^\circ \quad 120^\circ \quad 240^\circ \quad 15^\circ \quad 135^\circ \quad 255^\circ \quad 30^\circ \quad 150^\circ \quad 270^\circ]$$

The set  $\boldsymbol{\alpha}$  identifies the magnetic axes electrical angles. All the 18 windings terminals (the positive/negative couples for all the  $n = 9$  machine phases) are available externally.

The PM-induced back-EMFs have been found by measuring the terminal voltages while the machine was spinning at a constant speed and all the phases were disconnected. All the back-EMFs are sinusoidal functions of the electrical rotor position  $\theta_{el} = 3\theta$  and are mutually shifted with each other according to their magnetic axes angles. As a result, the  $k$ -th PM induced flux linkage and the corresponding normalized back-EMF (with  $k = 1, \dots, 9$ ) can be respectively modelled as:

$$\begin{aligned} \psi_{PM,k}(\theta) &= \Psi_{PM,k} \cdot \cos(3\theta - \alpha_k) \\ f_{PM,k}(\theta) &= \frac{\partial \psi_{PM,k}}{\partial \theta} = -3 \cdot \Psi_{PM,k} \cdot \sin(3\theta - \alpha_k) \end{aligned}$$

---

way to enforce (6.32). In theory, this operation would not be required. However, in real applications, it can neutralize both the effects of computation errors for the reference set  $\mathbf{i}^*$  and of measurement noises in the actual currents set  $\mathbf{i}$ .

<sup>19</sup> The machine has been obtained by re-winding an originally three-phase PMSM. The analysis of this machine with a VSD-based approach can be found in [84].

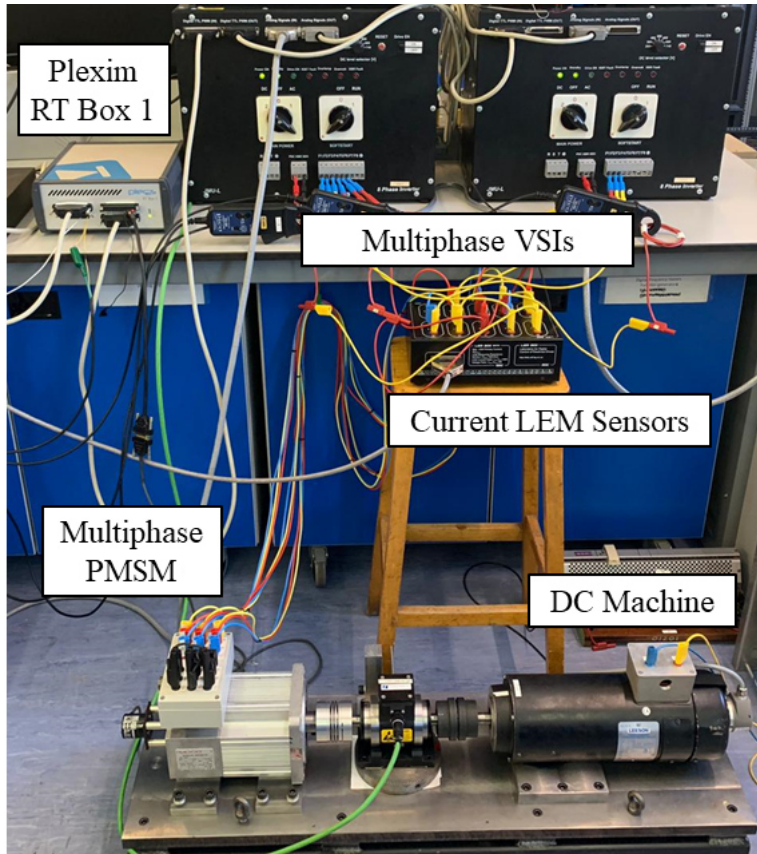


Fig. 6.11 – Experimental setup.

The flux magnitudes  $\Psi_{PM,k}$  are reported in Table 6.I. It can be noted that they are equal for the windings belonging to the same symmetrical three-phase set. They also have the same value for the sets  $\{1,2,3\}$  and  $\{7,8,9\}$ , but are lower for the set  $\{4,5,6\}$ <sup>20</sup>.

Table 6.I – PMSM INDUCED FLUXES MAGNITUDES.

$k$	1	2	3	4	5	6	7	8	9
$\Psi_{PM,k}$ [mWb]	268	268	268	259	259	259	268	268	268

<sup>20</sup> It is worth emphasizing that the machine analysed in this chapter is fundamentally different from the machine analysed in Chapter 5. Indeed, while both are nine-phase PMSMs with an asymmetrical configuration, the machine of Chapter 5 was with a single pole pair and with non-sinusoidal back-EMFs (being equal for all the phases). On the contrary, the machine analysed in this chapter has 3 pole pairs and sinusoidal back-EMFs (but they are not equal for all the phases).

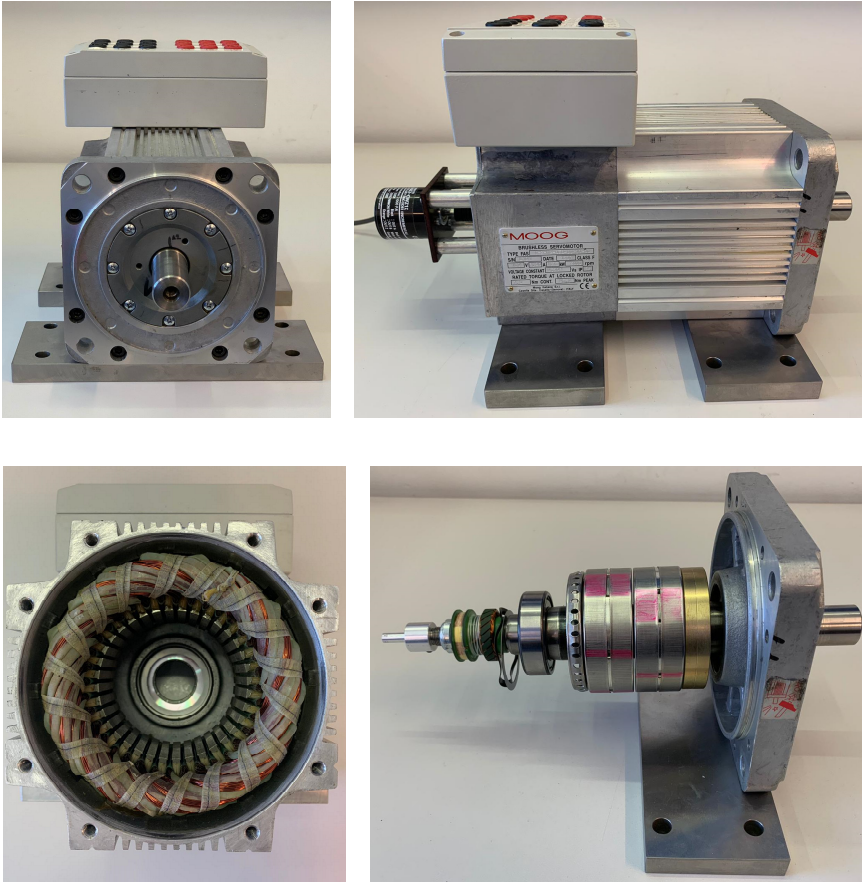


Fig. 6.12 – Nine-phase PMSM under analysis. Top-left: Front view; Top-right: Side view; Bottom-left: Stator; Bottom-right: Rotor.

All the windings have approximately the same resistance  $R \cong 8 \Omega$  (measured in DC). As a result, the resistances matrix is the scalar matrix  $\mathbf{R} = R \cdot \mathbf{I}$ .

The machine inductances matrix parameters  $L_{k_1, k_2}$  have been found at blocked rotor by individually supplying each  $k_1$ -th machine phase with a 50 Hz voltage  $v_{k_1}(t)$  and by measuring the corresponding current  $i_{k_1}(t)$  and the induced voltage  $v_{k_2}$  (with  $k_2 \neq k_1$ ) in all the other phases, which have been left in open circuit. The results have been reported in Table 6.II. It can be verified that, coherently with the mathematical model,  $\mathbf{L}$  is symmetric and positive definite.

The rotor inertia has been estimated to be around  $J \cong 2 \cdot 10^{-3} \text{ kg m}^2$ . The mechanical friction due to the bearings is approximately linear with the rotor speed and it has been estimated to develop a braking torque of about 0.2 N m when the machine speed is 500 rpm, meaning that the friction coefficient is  $F \cong 4 \cdot 10^{-3} \text{ (N m)/(rad/s)}$ .

Table 6.II – PMSM INDUCTANCES MATRIX PARAMETERS.

$L_{k_1 k_2}$ [mH]	$k_2$									
	1	2	3	4	5	6	7	8	9	
$k_1$	1	25.2	-3.3	-3.3	13.9	-6.2	-2.1	8.3	-7.3	0.4
	2	-3.3	25.2	-3.3	-2.1	13.9	-6.2	0.4	8.3	-7.3
	3	-3.3	-3.3	25.2	-6.2	-2.1	13.9	-7.3	0.4	8.3
	4	13.9	-2.1	-6.2	17.2	-3.3	-3.3	13.9	-6.2	-2.1
	5	-6.2	13.9	-2.1	-3.3	17.2	-3.3	-2.1	13.9	-6.2
	6	-2.1	-6.2	13.9	-3.3	-3.3	17.2	-6.2	-2.1	13.9
	7	8.3	0.4	-7.3	13.9	-2.1	-6.2	25.2	-3.3	-3.3
	8	-7.3	8.3	0.4	-6.2	13.9	-2.1	-3.3	25.2	-3.3
	9	0.4	-7.3	8.3	-2.1	-6.2	13.9	-3.3	-3.3	25.2

### 6.6.2 Power electronics converter

The machine has been supplied by two custom-made two-level multiphase voltage source inverters, based on Infineon FS50R12KE3 IGBT modules (see Fig. 6.13). All the  $m = 9$  inverter legs have a common DC-bus, whose voltage is supplied by a Sorensen SGI600/25 single quadrant DC-voltage source and has been set to  $V_{DC} = 200$  V.



Fig. 6.13 – Voltage Source Inverter.

A standard triangular carrier-based PWM algorithm, working with a modulation frequency of 10 kHz, has been implemented to operate the converter. The modulation dead-time is implemented via hardware and is approximately equal to 5  $\mu$ s.

### 6.6.3 Interconnection network

Each converter leg output node is directly connected to one machine phase positive terminal. As a result, the network interconnection matrix  $\mathbf{N}$  is always the  $9 \times 9$  identity matrix. On the contrary, the machine negative terminals have been connected differently for each testing scenario, meaning that the constraints matrix  $\mathbf{M}$  is not always the same.

### 6.6.4 Controller board and algorithm implementation

The proposed control algorithm has been implemented with a Plexim RT Box 1 platform (see Fig. 6.14). The control is executed with a 10 kHz sampling rate and it is synchronized with the converter PWM period.

All the 9 machine currents have been measured through external LEM transducers, which are connected to the platform ADC channels. The machine speed and position have been provided through the incremental encoder Omron E6B2-CWZ1X, with a resolution of 1000 pulses/revolution.

For each testing scenario, the configuration matrix  $\mathbf{U}_f$ , the complementary configuration matrix  $\mathbf{U}_c$  and the MTPA weighting matrix  $\mathbf{W}$  have been computed during the algorithm initialization, basing on the provided constraint matrix  $\mathbf{M}$ .

For all the tests the network interconnection matrix is always equal to  $\mathbf{N} = \mathbf{I}$ . As a result, the decoupling algorithm described in Section 6.3.4 does not require any pseudo-inverse matrix computation and simplifies to the one described in equations (6.37)-(6.38).

The implemented speed controller has a standard PI-based structure. For safety reasons the reference torque  $T_{em}^*$  computed by the speed controller has been limited to a feasible range of  $\pm 5$  N m.

The feedback current controller has been implemented in the phase variable domain



Fig. 6.14 – Plexim RT Box 1 controller board.

with the transfer function (6.43). It has been designed with a proportional action, an integral action and six resonant actions synchronized with the lowest odd-order integer multiples of the machine electrical speed  $\omega_{el} = 3\omega$ . In other words, the chosen resonance frequencies are  $\omega_h = h \cdot 3\omega$ , with  $h = 1, 3, 5, 7, 9, 11$ .

The offset vector  $\mathbf{u}_{off}^*$  for the VSI leg voltage injection (6.38) has been set to half of the DC-bus voltage (i.e., 100 V) for all the 9 converter legs.

### 6.6.5 Mechanical load

The PMSM has been mechanically coupled to a DC machine, used for loading (see Fig. 6.15).

The DC machine inertia is around  $J_m \cong 6 \cdot 10^{-3} \text{ kg m}^2$ , making the overall group inertia to be  $J_{eq} \cong 6 \cdot 10^{-3} \text{ kg m}^2$ , approximately. Similarly to the PMSM, the mechanical friction of the DC machine has also been estimated to be roughly linear with the machine speed and with a similar friction coefficient  $F_m \cong 4 \cdot 10^{-3} \text{ (N m)/(rad/s)}$ .

The armature of the DC machine has been connected to an external resistor through a controllable contactor. When the contactor is open, the only braking torque acting on the system is due to the mechanical friction. When the contactor is closed, the DC machine develops the additional torque  $T_{load}$ , which is proportional to the speed  $\omega$  and is such that  $T_{load} \cong 2 \text{ N m}$  when the machine speed is equal to 500 rpm.

A Magtrol Torquemaster TM 210 has been positioned between the PMSM and the DC machine rotor shafts. This torque meter has been used to measure the torque  $T_m$  developed at the joint between the two machines<sup>21</sup>.

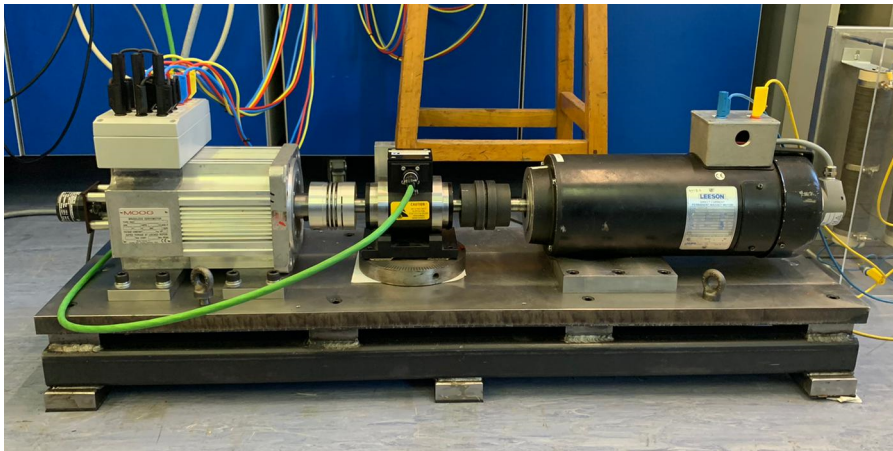


Fig. 6.15 – Mechanical coupling between the nine-phase PMSM under analysis and the DC machine used for loading. The torquemeter has been positioned at the joint between the two machines.

<sup>21</sup> Note that this measurement does not correspond to the overall electromagnetic torque  $T_{em}$  developed by the PMSM, since it neglects the PMSM inertia and friction torque contributions.

## 6.7 Experimental results

To validate the proposed algorithm and to emphasize its generality and flexibility, it has been tested in several different scenarios, discussed and analysed in this section<sup>22</sup>.

For each scenario, the constraint matrix  $\mathbf{M}$ , the configuration matrix  $\mathbf{U}_f$  and the MTPA weighting matrix  $\mathbf{W}$  are explicitly shown<sup>23</sup>. However, note that for a real-time implementation only  $\mathbf{M}$  is required, and that the other matrices can be numerically computed from it (i.e., the user does not need to provide them). The figure representing the layout of each examined configuration also shows the corresponding constraint matrix  $\mathbf{M}$  and the corresponding physical interpretation of the auxiliary voltages set  $\mathbf{v}_{NET}$ . To facilitate the interpretation of the constraints, different colours have been used to denote both the machine phase windings and the columns of  $\mathbf{M}$ . The DC-bus negative node has been considered as the reference node for the VSI leg output voltages.

### 6.7.1 Single neutral point healthy configuration

This testing scenario is aimed at showing the effectiveness of the proposed control algorithm in a healthy machine configuration, both at varying speed and at varying load.

The configuration under analysis is represented in Fig. 6.16. All the machine phases are star-connected to a single isolated neutral point. The sum of all  $n = 9$  phase currents is forced to be zero, meaning that the system is subject to  $n_c = 1$  algebraic constraint. The constraints matrix  $\mathbf{M}$  and the configuration matrix  $\mathbf{U}_f$  are:

$$\mathbf{M} = \begin{bmatrix} 1 \\ 1 \\ 1 \\ 1 \\ 1 \\ 1 \\ 1 \\ 1 \\ 1 \\ 1 \end{bmatrix}, \quad \mathbf{U}_f = \begin{bmatrix} -0.33 & -0.33 & -0.33 & -0.33 & -0.33 & -0.33 & -0.33 & -0.33 \\ 0.92 & -0.08 & -0.08 & -0.08 & -0.08 & -0.08 & -0.08 & -0.08 \\ -0.08 & 0.92 & -0.08 & -0.08 & -0.08 & -0.08 & -0.08 & -0.08 \\ -0.08 & -0.08 & 0.92 & -0.08 & -0.08 & -0.08 & -0.08 & -0.08 \\ -0.08 & -0.08 & -0.08 & 0.92 & -0.08 & -0.08 & -0.08 & -0.08 \\ -0.08 & -0.08 & -0.08 & -0.08 & 0.92 & -0.08 & -0.08 & -0.08 \\ -0.08 & -0.08 & -0.08 & -0.08 & -0.08 & 0.92 & -0.08 & -0.08 \\ -0.08 & -0.08 & -0.08 & -0.08 & -0.08 & -0.08 & 0.92 & -0.08 \\ -0.08 & -0.08 & -0.08 & -0.08 & -0.08 & -0.08 & -0.08 & 0.92 \end{bmatrix}$$

The corresponding MTPA weighting matrix  $\mathbf{W}$  is:

$$\mathbf{W} = \begin{bmatrix} 0.89 & -0.11 & -0.11 & -0.11 & -0.11 & -0.11 & -0.11 & -0.11 & -0.11 \\ -0.11 & 0.89 & -0.11 & -0.11 & -0.11 & -0.11 & -0.11 & -0.11 & -0.11 \\ -0.11 & -0.11 & 0.89 & -0.11 & -0.11 & -0.11 & -0.11 & -0.11 & -0.11 \\ -0.11 & -0.11 & -0.11 & 0.89 & -0.11 & -0.11 & -0.11 & -0.11 & -0.11 \\ -0.11 & -0.11 & -0.11 & -0.11 & 0.89 & -0.11 & -0.11 & -0.11 & -0.11 \\ -0.11 & -0.11 & -0.11 & -0.11 & -0.11 & 0.89 & -0.11 & -0.11 & -0.11 \\ -0.11 & -0.11 & -0.11 & -0.11 & -0.11 & -0.11 & 0.89 & -0.11 & -0.11 \\ -0.11 & -0.11 & -0.11 & -0.11 & -0.11 & -0.11 & -0.11 & 0.89 & -0.11 \\ -0.11 & -0.11 & -0.11 & -0.11 & -0.11 & -0.11 & -0.11 & -0.11 & 0.89 \end{bmatrix}$$

<sup>22</sup> These tests have also been analysed in [118].

<sup>23</sup> The configuration matrix has been found through the “`svd`” command in Matlab. The MTPA weighting matrix has been found by applying equation (6.18). All the parameters reported here are rounded to the second decimal unit.

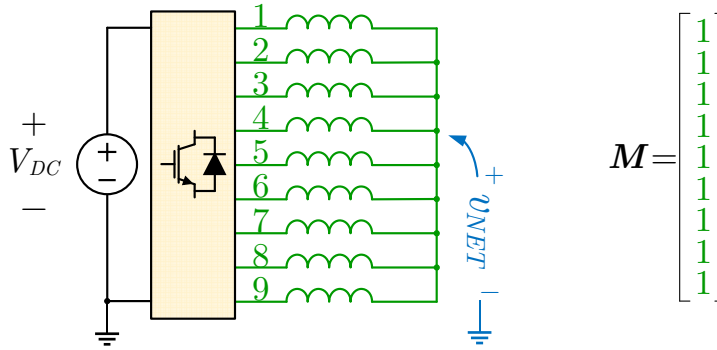


Fig. 6.16 – Schematic diagram and constraint matrix for the single neutral point healthy configuration.

It can be verified that, in this configuration, the denominator  $f_{PM}^T \cdot \mathbf{W} \cdot f_{PM}$  of the MTPA algorithm (6.17) is independent of  $\theta$ , meaning that the steady state reference currents are sinusoidal. This is expected since the machine windings are designed in a multiple three-phase configuration and that the only constraint involves the overall common-mode current. The waveforms and harmonic spectra of the optimal phase currents are depicted in Fig. 6.17 for a whole  $[0^\circ; 360^\circ]$  electrical cycle. Since the optimal current set  $i^*$  computed via (6.17) is proportional to the torque, the results of Fig. 6.17 are normalized by  $T_{em}$ .

Note that the matrix  $\mathbf{W}$ , once applied to any  $9 \times 1$  vector  $\mathbf{x}$ , simply subtracts its average value  $\frac{1}{9} \sum_{k=1}^9 x_k$ . This provides a much easier physical interpretation of the weighting matrix related to the MTPA algorithm. This property comes from the fact that  $\mathbf{W}$  is equal to the configuration space projection matrix  $\mathbf{U}_f \cdot \mathbf{U}_f^T$ .

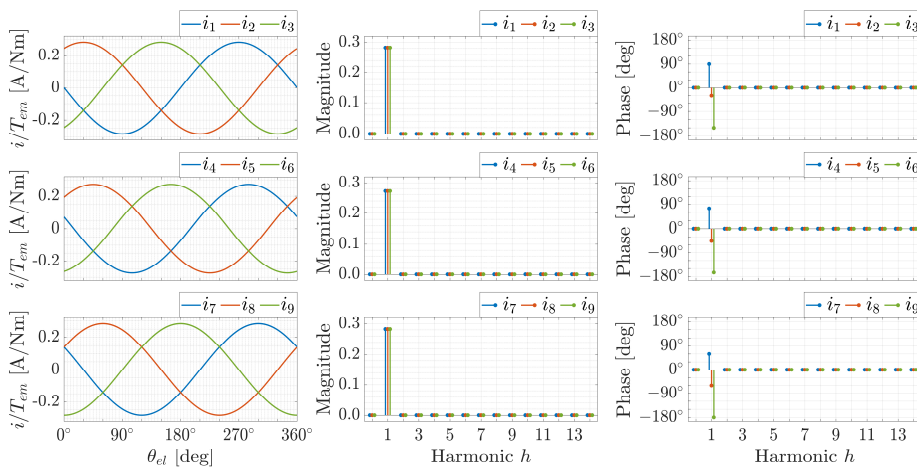


Fig. 6.17 – Waveforms and harmonic spectra of the optimal reference currents in the single neutral point healthy configuration.

The experimental test has been conducted as follows. Initially, the machine works at no load at the speed of  $-500$  rpm, and therefore the electromagnetic torque  $T_{em}$  only needs to balance the mechanical friction. Then, the machine reference speed  $\omega^*$  is changed to  $+500$  rpm. After the speed inversion has been performed and the machine has reached the steady-state conditions, the mechanical load is changed by commanding (via RT Box platform) the closing of the DC machine contactor.

The results are depicted in Fig. 6.18. The first three subplots show the machine phase currents (solid lines) and the corresponding references (black dashed lines). The fourth subplot shows the developed electromagnetic torque  $T_{em}$  (solid line) and the controller reference torque  $T_{em}^*$  (dashed line); the torque has been estimated by computing (6.4) with the measured currents. The last subplot shows the machine speed  $\omega$  (solid line) and the corresponding reference value  $\omega^*$  (dashed line); a zoomed version of the speed dynamics after the load torque step change is shown in a box inside the same subplot<sup>24</sup>.

For the first 100 ms, the machine is in steady-state conditions at  $-500$  rpm. The currents are sinusoidal and develop a torque of around  $-0.5$  Nm to neutralize the overall drive train friction.

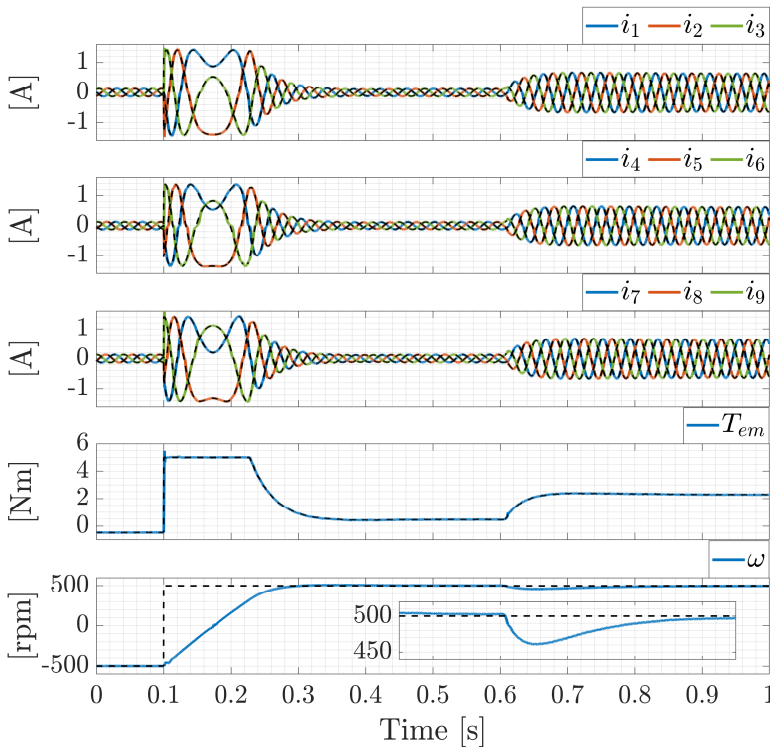


Fig. 6.18 – Experimental results in the single neutral point healthy configuration. Solid lines: measured variables; Dashed lines: reference variables.

<sup>24</sup> Note that the timing instants are shared by all the subplots, including the zoom of the speed.

Immediately after the speed reference change, the torque reference jumps to the maximum value of +5 Nm and the reference currents increase accordingly (coherently with the MTPA strategy). When the machine speed approaches its reference value, the torque decreases down to the final value of around 0.5 Nm (which is again only related to the drive train friction). The speed inversion is completed in around 250 ms and the steady-state currents are again sinusoidal functions of time, but their phase displacement is reversed (e.g., initially  $i_2$  was ahead of  $i_1$ , while now it is the opposite).

At around 600 ms the controlled contactor is closed, and the DC machine terminals are connected to the external resistor. The drive loading torque increases and the speed drops down from the reference value. Then, to counteract this drop, the speed controller increases the reference torque  $T_{em}^*$  and, because of the MTPA strategy, the PMSM current references  $i_k^*$  (with  $k = 1, \dots, 9$ ) increase proportionally to it. The speed reaches the minimum value of around 460 rpm after 50 ms and is regulated back to the reference value of 500 rpm in around 350 ms. At steady-state conditions, the currents are again sinusoidal functions of time and develop an overall torque of around 2.3 Nm.

As can be seen, all the steady-state currents of the experimental results depicted in Fig. 6.18 are consistent with the theoretical currents computed numerically and represented in Fig. 6.17.

An oscilloscope capture of the experimental results is also shown in Fig. 6.19. It includes the measured currents  $i_1$ ,  $i_4$  and  $i_7$  (measured with current probes with 4 turns) and the torque  $T_m$  developed at the rotor shaft (measured by the torque meter at the joint between the PMSM and the DC machine and reported with a scale of 100 mV/Nm).

### 6.7.2 Two neutral points healthy configuration

This testing scenario is very similar to the previous one, with the only difference being represented by a different machine windings connection.

In this case, the machine configuration is schematically represented in Fig. 6.20. The machine windings are divided into two star-connected groups with two isolated neutral

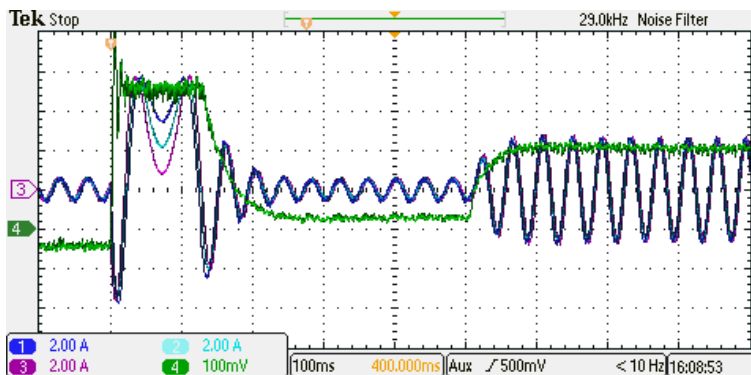


Fig. 6.19 – Oscilloscope capture of the experimental results in the single neutral point healthy configuration.

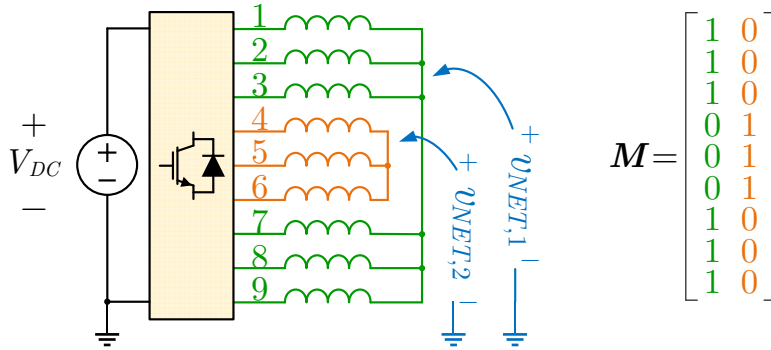


Fig. 6.20 – Schematic diagram and constraint matrix for the two neutral points healthy configuration.

points. The first group includes the windings  $\{1,2,3,7,8,9\}$  and, given the machine design, it behaves like an equivalent six-phase machine (with two symmetrical three-phase windings sets mutually shifted by  $30^\circ$ , electrically). The second winding group includes the remaining windings sets  $\{4,5,6\}$  and is equivalent to a symmetrical three-phase machine. The  $n = 9$  phase currents are now subject to  $n_c = 2$  constraints, identified by the two isolated neutral points.

The constraint matrix  $M$  and the configuration matrix  $U_f$  are:

$$M = \begin{bmatrix} 1 & 0 \\ 1 & 0 \\ 1 & 0 \\ 0 & 1 \\ 0 & 1 \\ 0 & 1 \\ 1 & 0 \\ 1 & 0 \\ 1 & 0 \end{bmatrix}, \quad U_f = \begin{bmatrix} -0.41 & 0.24 & 0.24 & 0.24 & -0.41 & -0.41 & -0.41 \\ -0.12 & -0.51 & -0.51 & -0.51 & -0.12 & -0.12 & -0.12 \\ 0.88 & 0.07 & 0.07 & 0.07 & -0.12 & -0.12 & -0.12 \\ 0 & 0.67 & -0.33 & -0.33 & 0 & 0 & 0 \\ 0 & -0.33 & 0.67 & -0.33 & 0 & 0 & 0 \\ 0 & -0.33 & -0.33 & 0.67 & 0 & 0 & 0 \\ -0.12 & 0.07 & 0.07 & 0.07 & 0.88 & -0.12 & -0.12 \\ -0.12 & 0.07 & 0.07 & 0.07 & -0.12 & 0.88 & -0.12 \\ -0.12 & 0.07 & 0.07 & 0.07 & -0.12 & -0.12 & 0.88 \end{bmatrix}$$

The corresponding MTPA weighting matrix, computed via (6.18), is:

$$W = \begin{bmatrix} 0.83 & -0.17 & -0.17 & 0 & 0 & 0 & -0.17 & -0.17 & -0.17 \\ -0.17 & 0.83 & -0.17 & 0 & 0 & 0 & -0.17 & -0.17 & -0.17 \\ -0.17 & -0.17 & 0.83 & 0 & 0 & 0 & -0.17 & -0.17 & -0.17 \\ 0 & 0 & 0 & 0.67 & -0.33 & -0.33 & 0 & 0 & 0 \\ 0 & 0 & 0 & -0.33 & 0.67 & -0.33 & 0 & 0 & 0 \\ 0 & 0 & 0 & -0.33 & -0.33 & 0.67 & 0 & 0 & 0 \\ -0.17 & -0.17 & -0.17 & 0 & 0 & 0 & 0.83 & -0.17 & -0.17 \\ -0.17 & -0.17 & -0.17 & 0 & 0 & 0 & -0.17 & 0.83 & -0.17 \\ -0.17 & -0.17 & -0.17 & 0 & 0 & 0 & -0.17 & -0.17 & 0.83 \end{bmatrix}$$

Again, it has been verified that, in this configuration, the product  $f_{PM}^T \cdot W \cdot f_{PM}$  appearing as the denominator of the MTPA algorithm (6.17) is independent of  $\theta$ ,

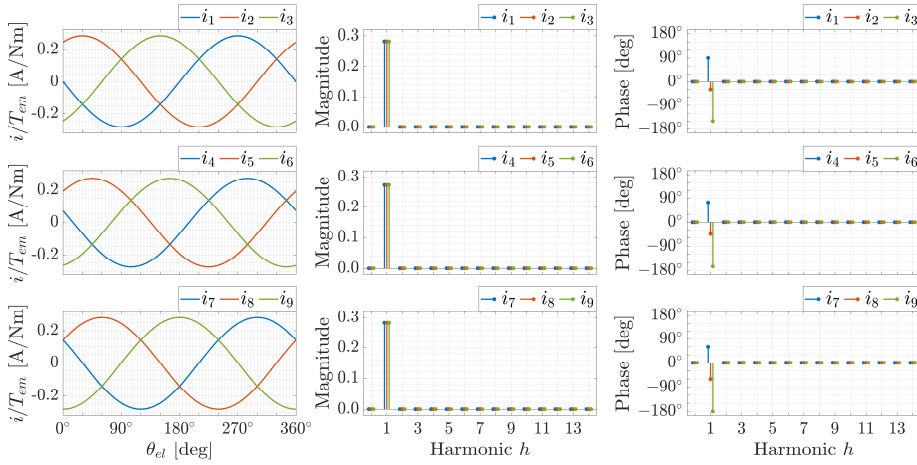


Fig. 6.21 – Waveforms and harmonic spectra of the optimal reference currents in the two neutral points healthy configuration.

meaning that the optimal reference currents are still sinusoidal in steady-state conditions. They have been reported in Fig. 6.21. As could be expected, they are identical to the previous case. This is because, as a result of the multiple three-phase symmetry, the optimal currents obtained in the single neutral configuration were already satisfying  $i_1^* + i_2^* + i_3^* + i_7^* + i_8^* + i_9^* = 0$  and  $i_4^* + i_5^* + i_6^* = 0$ , which are the constraints of this new machine configuration.

Similarly to the previous case, a physical interpretation of the weighting procedure of the proposed MTPA strategy can be obtained by observing that, in this case, the matrix  $\mathbf{W}$ , once applied to any  $9 \times 1$  vector  $\mathbf{x}$ , subtracts the average value  $\frac{1}{6}(\sum_{k=1}^3 x_k + \sum_{k=7}^9 x_k)$  from the set  $\{1,2,3,7,8,9\}$  and the average value  $\frac{1}{3}\sum_{k=4}^6 x_k$  from the set  $\{4,5,6\}$ , which correspond to the isolated windings subsets of the analyzed machine configuration.

The testing scenario is the same as the previous case study. The results, shown in Fig. 6.22, are almost identical to the single neutral point configuration. Again, an oscilloscope capture has been reported in Fig. 6.23 to show the measured currents  $i_1$ ,  $i_4$  and  $i_7$  and the torque developed at the rotor shaft  $T_m$ .

### 6.7.3 Two neutral points with one faulty phase

This test is aimed at showing the performances of the proposed controller in a post-fault machine configuration.

The windings configuration, schematically represented in Fig. 6.24, is modified from the previous case study by physically disconnecting phase 1 of the machine. This introduces an additional algebraic constraint on the phase currents (which is  $i_1 = 0$ ) and the constraints matrix  $\mathbf{M}$  is therefore modified to include an extra column.

The numerical values of the matrices  $\mathbf{M}$  and  $\mathbf{U}_f$  are:

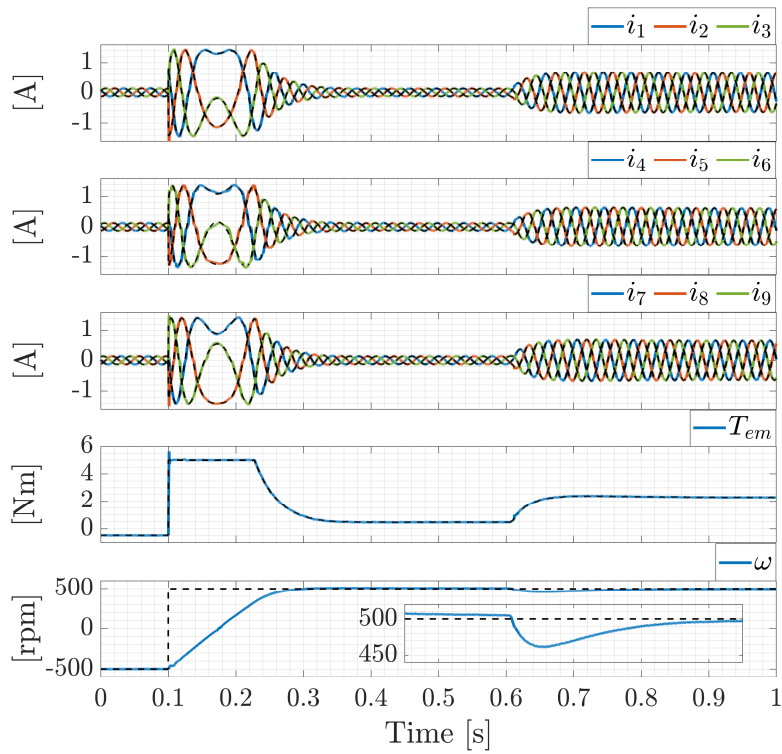


Fig. 6.22 – Experimental results in the two neutral points healthy configuration. Solid lines: measured variables; Dashed lines: reference variables.

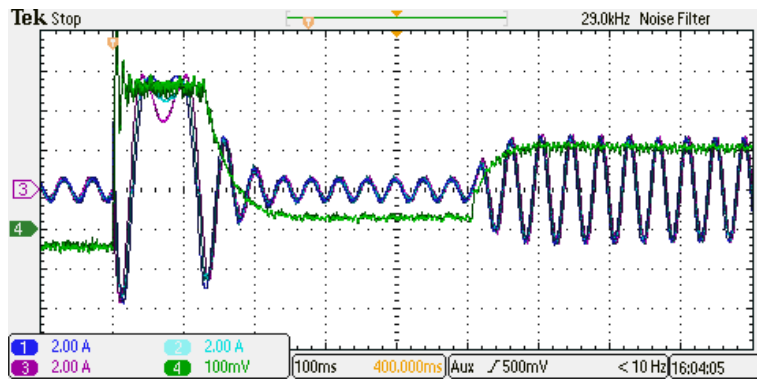


Fig. 6.23 – Oscilloscope capture of the experimental results in the two neutral points healthy configuration.

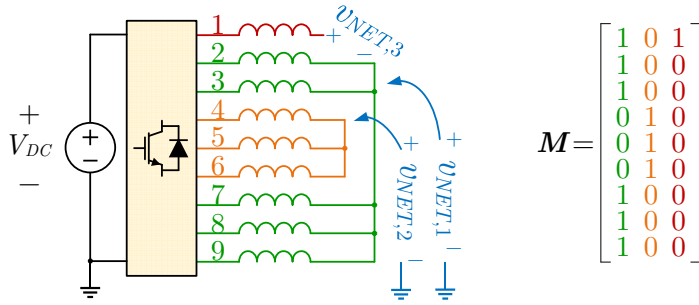


Fig. 6.24 – Schematic diagram and constraint matrix for the two neutral points configuration with one faulty phase.

$$M = \begin{bmatrix} 1 & 0 & 1 \\ 1 & 0 & 0 \\ 1 & 0 & 0 \\ 0 & 1 & 0 \\ 0 & 1 & 0 \\ 0 & 1 & 0 \\ 1 & 0 & 0 \\ 1 & 0 & 0 \\ 1 & 0 & 0 \end{bmatrix}, \quad U_f = \begin{bmatrix} 0 & 0 & 0 & 0 & 0 & 0 \\ -0.50 & -0.50 & -0.50 & -0.14 & -0.14 & -0.14 \\ 0.26 & 0.26 & 0.26 & -0.45 & -0.45 & -0.45 \\ 0.67 & -0.33 & -0.33 & 0 & 0 & 0 \\ -0.33 & 0.67 & -0.33 & 0 & 0 & 0 \\ -0.33 & -0.33 & 0.67 & 0 & 0 & 0 \\ 0.08 & 0.08 & 0.08 & 0.86 & -0.14 & -0.14 \\ 0.08 & 0.08 & 0.08 & -0.14 & 0.86 & -0.14 \\ 0.08 & 0.08 & 0.08 & -0.14 & -0.14 & 0.86 \end{bmatrix}$$

To have an easier physical interpretation, the open phase winding and the corresponding column of  $M$  have been denoted with a different colour in Fig. 6.24. Note that, with the chosen constraint matrix, the auxiliary network voltages  $v_{NET,1}$  and  $v_{NET,2}$  still represent the potential of the two isolated neutral points (as in the previous example), while the new auxiliary voltage  $v_{NET,3}$  is the voltage between the neutral point of the six-phase group and the open terminal of phase 1.

The MTPA weighting matrix is modified to:

$$W = \begin{bmatrix} 0 & 0 & 0 & 0 & 0 & 0 & 0 & 0 & 0 \\ 0 & 0.80 & -0.20 & 0 & 0 & 0 & -0.20 & -0.20 & -0.20 \\ 0 & -0.20 & 0.80 & 0 & 0 & 0 & -0.20 & -0.20 & -0.20 \\ 0 & 0 & 0 & 0.67 & -0.33 & -0.33 & 0 & 0 & 0 \\ 0 & 0 & 0 & -0.33 & 0.67 & -0.33 & 0 & 0 & 0 \\ 0 & 0 & 0 & -0.33 & -0.33 & 0.67 & 0 & 0 & 0 \\ 0 & -0.20 & -0.20 & 0 & 0 & 0 & 0.80 & -0.20 & -0.20 \\ 0 & -0.20 & -0.20 & 0 & 0 & 0 & -0.20 & 0.80 & -0.20 \\ 0 & -0.20 & -0.20 & 0 & 0 & 0 & -0.20 & -0.20 & 0.80 \end{bmatrix}$$

In this case, it can be verified that the denominator  $\mathbf{f}_{PM}^T \cdot \mathbf{W} \cdot \mathbf{f}_{PM}$  of the MTPA algorithm is not anymore constant with the rotor position  $\theta$ . As a result, the optimal currents computed by the MTPA algorithm (6.17) are not anymore sinusoidal functions of the rotor electrical angle  $\theta_{el} = 3\theta$ . This is a direct consequence of the symmetry loss due to the open-circuit fault and means that, in steady-state, the optimal currents are not sinusoidal in time. Their waveforms and harmonic spectra are depicted in Fig. 6.25

for a full  $[0^\circ, 360^\circ]$  electrical rotor cycle. Coherently with the open phase constraint, all the harmonics of  $i_1$  are zero, while the other phases now also show some higher-order harmonics, and especially a third-harmonic contribution. As previously explained, only their fundamental components develop a non-zero average torque (in a full rotor cycle), while all the other higher-order harmonics are only needed to neutralize the torque ripple.

The magnitude of the currents is not equally distributed among all the phases and is higher than in the healthy configuration. From the optimal reference current waveforms of Fig. 6.25, it can be computed that the overall RMS current  $I_{RMS}$  is (on average in a full rotor cycle) around 9% higher than in the healthy configuration. This behaviour is expected because the faulty machine is asked to develop the same electromagnetic torque of the healthy configuration, but at the same time it is subject to an additional constraint (which is  $i_1 = 0$ )<sup>25</sup>.

In this case, the weighting matrix  $\mathbf{W}$ , once applied to any  $9 \times 1$  vector  $\mathbf{x}$ , nullifies the component  $x_1$  and subtracts the average value  $\frac{1}{5}(\sum_{k=2}^3 x_k + \sum_{k=7}^9 x_k)$  from the set  $\{2,3,7,8,9\}$  and the average value  $\frac{1}{3}\sum_{k=4}^6 x_k$  from the set  $\{4,5,6\}$  (which, again, are related to the isolated windings groups in this new machine configuration).

The same testing scenario of the previous cases has been repeated here. The

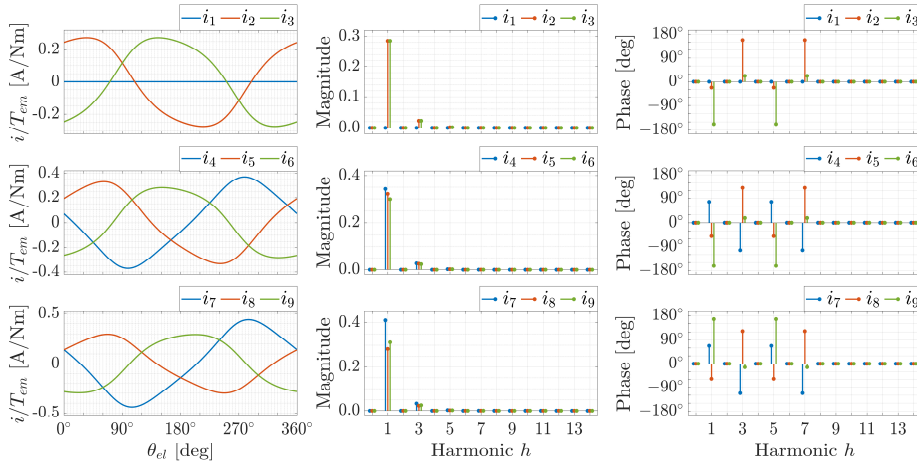


Fig. 6.25 – Waveforms and harmonic spectra of the optimal reference currents in the two neutral points configuration with one faulty phase.

<sup>25</sup> As also previously mentioned in Section 1.1.6, the choice of not limiting the currents in the post-fault configuration (and to develop the same torque) allows to keep the machine mechanical behaviour unchanged but, if prolonged in time, it may increase the thermal stress and reduce the machine life-span expectations with respect to the healthy configuration. Different options can also be chosen to deal with post-fault conditions. For example, a different approach is to fix the maximum allowed RMS current or the maximum allowed peak current. These other options are more conservative and can be tolerated for longer operations, but the maximum electromagnetic torque of the drive would be lower than in the healthy configuration, meaning that the machine mechanical capabilities would be changed.

experimental results are depicted in Fig. 6.26 and the corresponding oscilloscope captures are reported in Fig. 6.27.

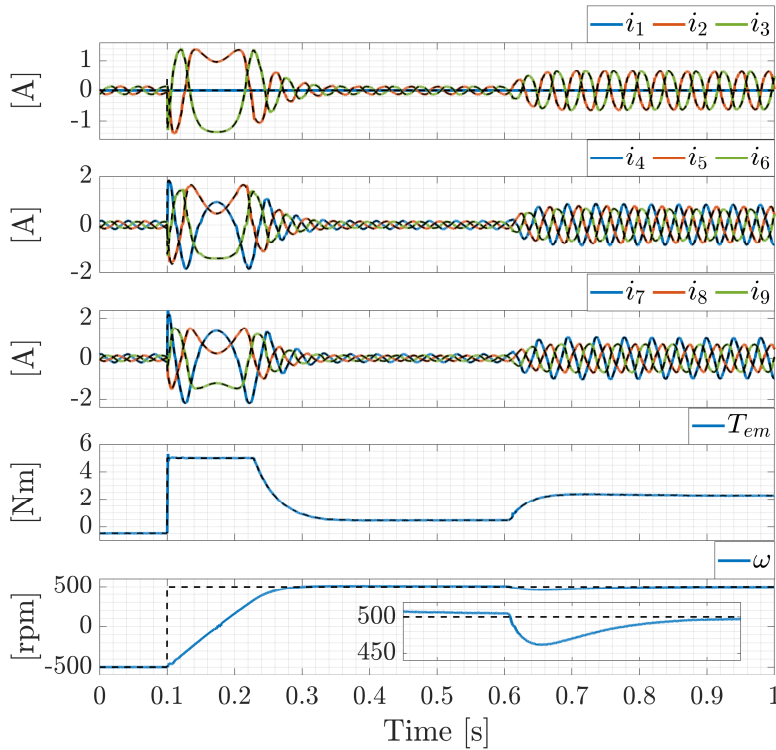


Fig. 6.26 – Experimental results in the two neutral points configuration with one faulty phase. Solid lines: measured variables; Dashed lines: reference variables.

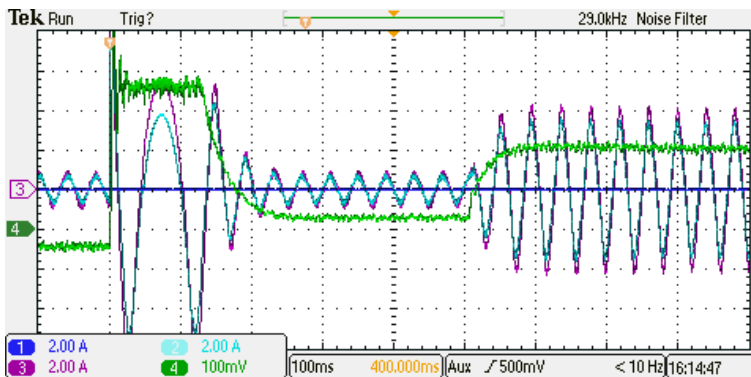


Fig. 6.27 – Oscilloscope capture of the experimental results in the two neutral points configuration with one faulty phase.

If compared with the healthy configuration, both the speed and the torque show the same dynamics (because they refer to the same speed controller). On the contrary, the current waveforms are different and it can be immediately noticed that they are not sinusoidal anymore. These non-sinusoidal references can still be perfectly tracked thanks to the resonant actions included in the feedback current controller. It is worth emphasising that the controller structure and parameters have not been altered at all, and only a different constraint matrix has been provided.

#### 6.7.4 Two neutral points with two faulty phases

The same strategy of the previous tests can be also applied in case of more than one fault is present.

In this test, the winding configuration is represented in Fig. 6.28. If compared to the configuration of the previous case study, an additional fault has been simulated by physically opening phase 6 of the machine. The matrices  $\mathbf{M}$  and  $\mathbf{U}_f$  are now:

$$\mathbf{M} = \begin{bmatrix} 1 & 0 & 1 & 0 \\ 1 & 0 & 0 & 0 \\ 1 & 0 & 0 & 0 \\ 0 & 1 & 0 & 0 \\ 0 & 1 & 0 & 0 \\ 0 & 1 & 0 & 1 \\ 1 & 0 & 0 & 0 \\ 1 & 0 & 0 & 0 \\ 1 & 0 & 0 & 0 \end{bmatrix}, \quad \mathbf{U}_f = \begin{bmatrix} 0 & 0 & 0 & 0 & 0 \\ -0.35 & -0.79 & -0.14 & -0.14 & -0.14 \\ 0.18 & 0.41 & -0.45 & -0.45 & -0.45 \\ -0.64 & 0.29 & 0 & 0 & 0 \\ 0.64 & -0.29 & 0 & 0 & 0 \\ 0 & 0 & 0 & 0 & 0 \\ 0.06 & 0.13 & 0.86 & -0.14 & -0.14 \\ 0.06 & 0.13 & -0.14 & 0.86 & -0.14 \\ 0.06 & 0.13 & -0.14 & -0.14 & 0.86 \end{bmatrix}$$

and the last column of  $\mathbf{M}$  identifies the additional constraint  $i_6 = 0$ . Again, different colors have been used to identify the two open-circuit faults in Fig. 6.28. The physical interpretation of the voltages  $v_{NET,1}$ ,  $v_{NET,2}$  and  $v_{NET,3}$  is the same of the previous case study, while the additional auxiliary voltage  $v_{NET,4}$  is the voltage between the neutral point of the three-phase subset and the open terminal of phase 6.

The MTPA weighting matrix is now:

$$\mathbf{W} = \begin{bmatrix} 0 & 0 & 0 & 0 & 0 & 0 & 0 & 0 & 0 \\ 0 & 0.80 & -0.20 & 0 & 0 & 0 & -0.20 & -0.20 & -0.20 \\ 0 & -0.20 & 0.80 & 0 & 0 & 0 & -0.20 & -0.20 & -0.20 \\ 0 & 0 & 0 & 0.50 & -0.50 & 0 & 0 & 0 & 0 \\ 0 & 0 & 0 & -0.50 & 0.50 & 0 & 0 & 0 & 0 \\ 0 & 0 & 0 & 0 & 0 & 0 & 0 & 0 & 0 \\ 0 & -0.20 & -0.20 & 0 & 0 & 0 & 0.80 & -0.20 & -0.20 \\ 0 & -0.20 & -0.20 & 0 & 0 & 0 & -0.20 & 0.80 & -0.20 \\ 0 & -0.20 & -0.20 & 0 & 0 & 0 & -0.20 & -0.20 & 0.80 \end{bmatrix}$$

and, similarly to the previous post-fault scenario, the denominator of the MTPA algorithm is not constant and, therefore, the optimal currents are not sinusoidal. Their waveforms and harmonic spectra are depicted in Fig. 6.29. It can be seen that, because of the opening of phase 6, the currents in phases 4 and 5 are opposite (in other words, they behave as an equivalent single-phase winding).

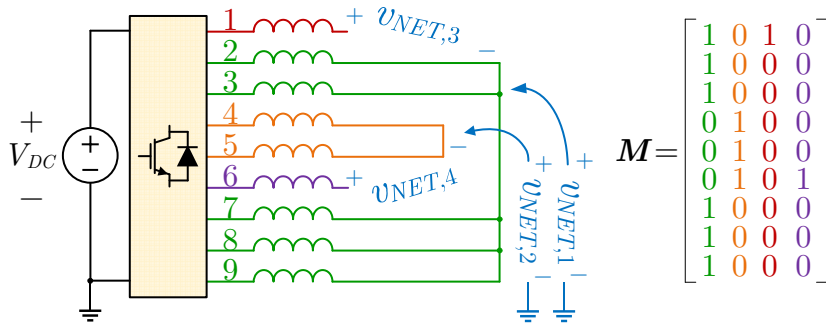


Fig. 6.28 – Schematic diagram and constraint matrix for the two neutral points configuration with two faulty phases.

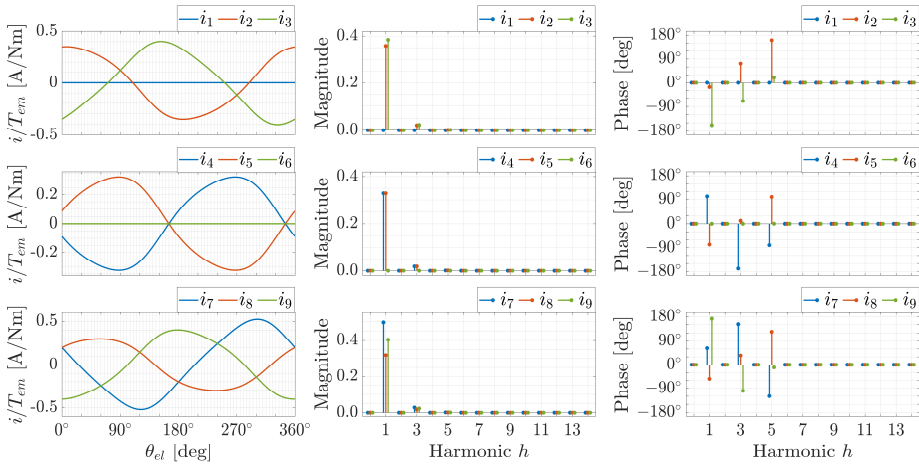


Fig. 6.29 – Waveforms and harmonic spectra of the optimal reference currents in the two neutral points configuration with two faulty phases.

Given the additional constraint, the overall machine RMS current is, on average, around 19% higher than in the healthy configuration and a similar reasoning to the previous example can also be applied to obtain a physical interpretation for the weighting matrix  $\mathbf{W}$ .

The experimental results are reported in Fig. 6.30 and Fig. 6.31. Again, the speed and torque responses are the same, while the currents follow the waveforms of Fig. 6.29.

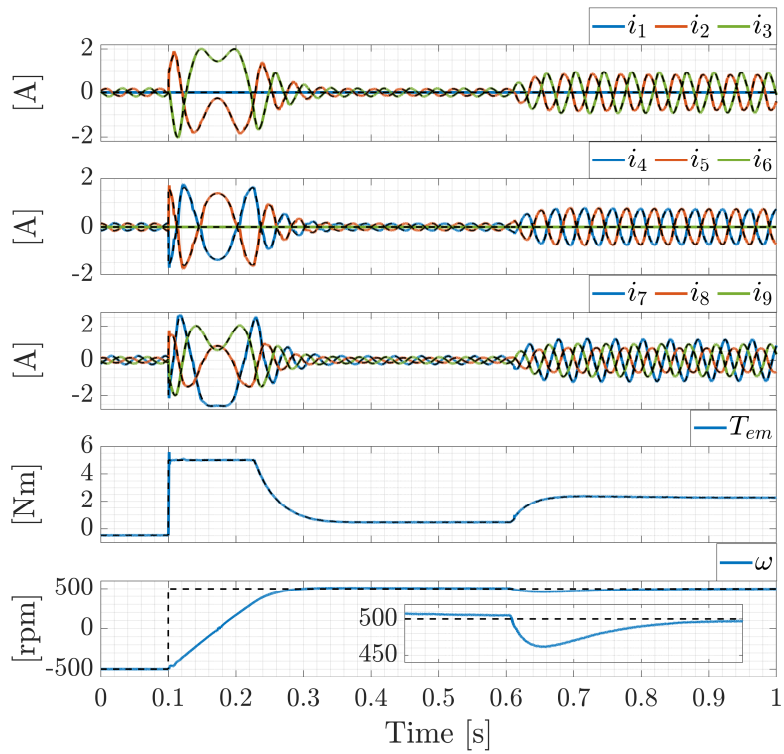


Fig. 6.30 – Experimental results in the two neutral points configuration with two faulty phases. Solid lines: measured variables; Dashed lines: reference variables.

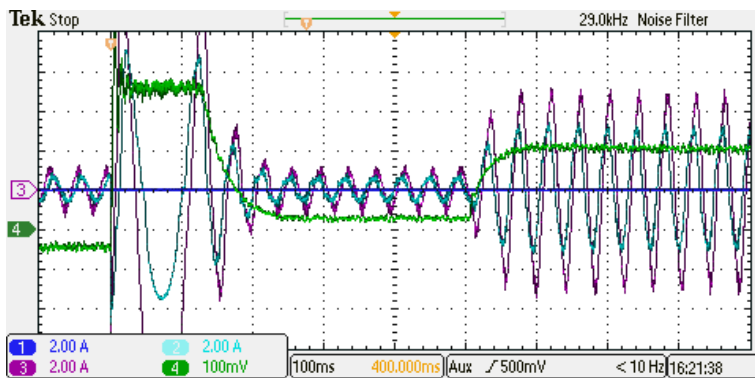


Fig. 6.31 – Oscilloscope capture of the experimental results in the two neutral points configuration with two faulty phases.

### 6.7.5 Three neutral points with one faulty phase

The windings configuration is represented in Fig. 6.32.

The nine machine phases have been grouped into the three symmetrical three-phase groups  $\{1,2,3\}$ ,  $\{4,5,6\}$  and  $\{7,8,9\}$ , each of which is star connected and with an isolated neutral point. Additionally, phase 1 has been physically disconnected. As a result, the system is subject to  $n_c = 4$  algebraic constraints and the constraints and configuration matrices are:

$$M = \begin{bmatrix} 1 & 0 & 0 & 1 \\ 1 & 0 & 0 & 0 \\ 1 & 0 & 0 & 0 \\ 0 & 1 & 0 & 0 \\ 0 & 1 & 0 & 0 \\ 0 & 1 & 0 & 0 \\ 0 & 0 & 1 & 0 \\ 0 & 0 & 1 & 0 \\ 0 & 0 & 1 & 0 \end{bmatrix}, \quad U_f = \begin{bmatrix} 0 & 0 & 0 & 0 & 0 \\ -0.21 & -0.21 & 0.37 & 0.37 & 0.37 \\ 0.21 & 0.21 & -0.37 & -0.37 & -0.37 \\ -0.53 & -0.53 & -0.19 & -0.19 & -0.19 \\ 0.76 & -0.24 & 0.10 & 0.10 & 0.10 \\ -0.24 & 0.76 & 0.10 & 0.10 & 0.10 \\ 0 & 0 & 0.67 & -0.33 & -0.33 \\ 0 & 0 & -0.33 & 0.67 & -0.33 \\ 0 & 0 & -0.33 & -0.33 & 0.67 \end{bmatrix}$$

where the first three columns of  $M$  identify the constraints on the three neutral points, while the last column represents the constraint  $i_1 = 0$ .

The MTPA weighting matrix is:

$$W = \begin{bmatrix} 0 & 0 & 0 & 0 & 0 & 0 & 0 & 0 & 0 \\ 0 & 0.50 & -0.50 & 0 & 0 & 0 & 0 & 0 & 0 \\ 0 & -0.50 & 0.50 & 0 & 0 & 0 & 0 & 0 & 0 \\ 0 & 0 & 0 & 0.67 & -0.33 & -0.33 & 0 & 0 & 0 \\ 0 & 0 & 0 & -0.33 & 0.67 & -0.33 & 0 & 0 & 0 \\ 0 & 0 & 0 & -0.33 & -0.33 & 0.67 & 0 & 0 & 0 \\ 0 & 0 & 0 & 0 & 0 & 0 & 0.67 & -0.33 & -0.33 \\ 0 & 0 & 0 & 0 & 0 & 0 & -0.33 & 0.67 & -0.33 \\ 0 & 0 & 0 & 0 & 0 & 0 & -0.33 & -0.33 & 0.67 \end{bmatrix}$$

and, once again, it leads to non-sinusoidal optimal currents, as shown in Fig. 6.33.

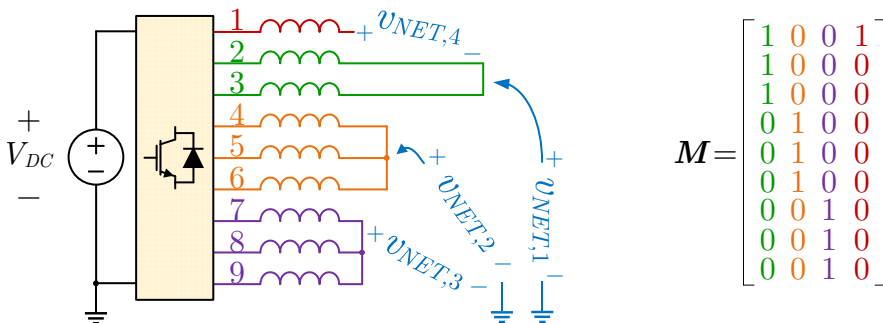


Fig. 6.32 – Schematic diagram and constraint matrix for the three neutral points configuration with one faulty phase.

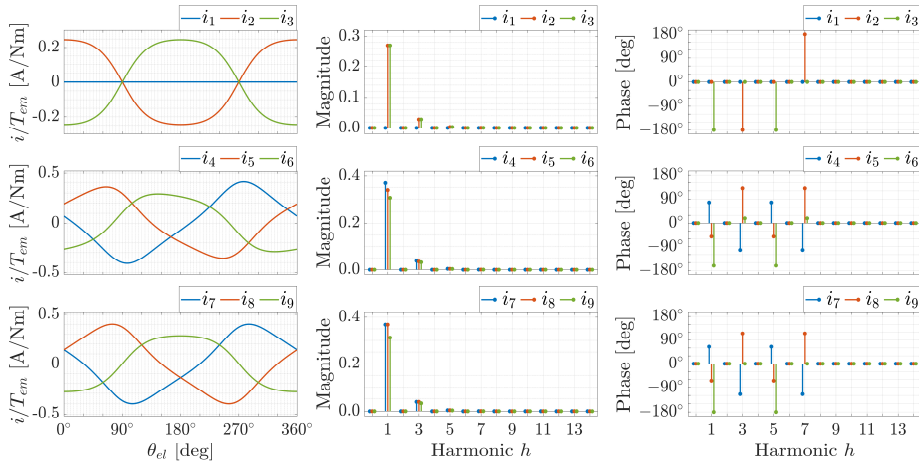


Fig. 6.33 – Waveforms and harmonic spectra of the optimal reference currents in the three neutral points configuration with one faulty phase.

As expected, the optimal currents are different from the ones of Fig. 6.25, which were computed after the fault of phase 1 in case of two isolated neutral points. In particular, it can be observed that the currents in phases 2 and 3 are opposite, meaning that they behave as an equivalent single-phase winding.

Under this perspective, it can be also realized that, in a machine configured with multiple isolated three-phase windings sets (which is a commonly adopted solution in practical multiphase drives applications), the opening of one phase does not require the disconnection of the entire three-phase subset where the fault has occurred. Indeed, the two remaining phases of the subset behave as an equivalent single-phase winding, which can still contribute to the overall electromagnetic torque development.

Moreover, these optimal currents also behave differently on the torque development algorithm. Indeed, it has been verified that the average RMS current in this condition is around 10% higher than in the healthy configuration (against 9% of the case study of Section 6.7.3). This confirms that, as could be expected, different constraints can change the machine behaviour and that the same open-circuit fault is more penalising in case of three isolated neutral points ( $n_c = 3 + 1 = 4$ ) than in case of two isolated neutral points ( $n_c = 2 + 1 = 3$ ).

Finally, if compared to the results of Section 6.7.4 (where it also results  $n_c = 4$ ), it is also confirmed that, as could be expected, different winding configurations, although characterized by the same number of constraints, can have a different impact on the drive performances.

The experimental results obtained under the same dynamical tests of the previous subsections are depicted in Fig. 6.34 and in Fig. 6.35.

Once again, the dynamic behaviour of the system is the same as in the previous examples, and the phase currents can effectively track their non-sinusoidal references thanks to the contribution of the resonant controller actions.

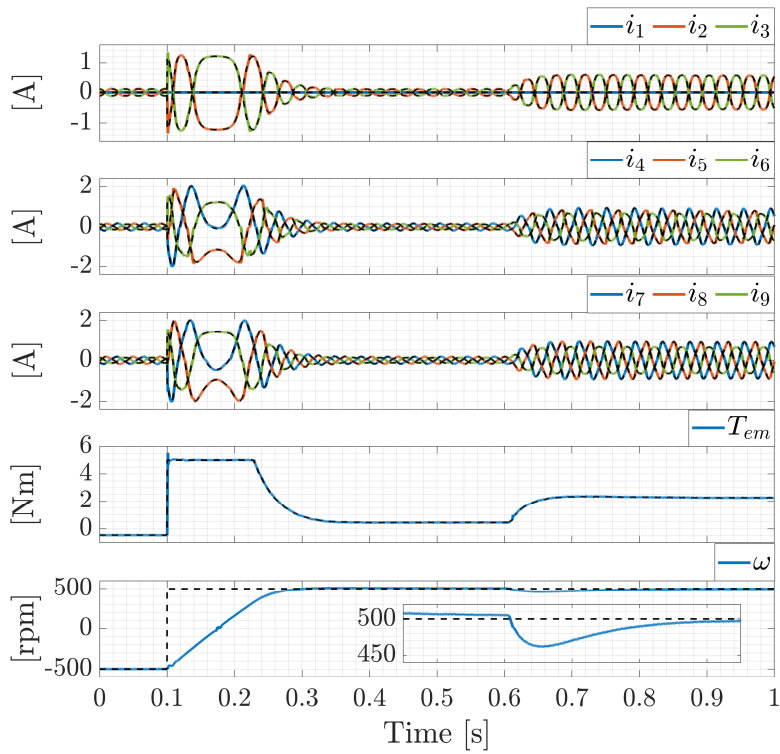


Fig. 6.34 – Experimental results in the three neutral points configuration with one faulty phase. Solid lines: measured variables; Dashed lines: reference variables.

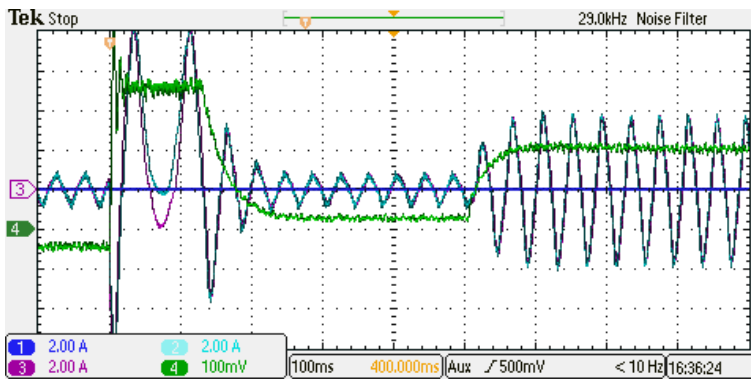


Fig. 6.35 – Oscilloscope capture of the experimental results in the three neutral points configuration with one faulty phase.

### 6.7.6 Highly asymmetrical configuration

This testing scenario considers an unrealistic machine configuration, with the aim to emphasize the generality of the proposed approach.

In this case, the machine windings are divided into two star-connected groups with two isolated neutral points, as schematically depicted in Fig. 6.36. The first group includes the five phases {1,5,6,7,8}, while the second group include the remaining four phases {2,3,4,9}. The corresponding constraints and configuration matrices are:

$$M = \begin{bmatrix} 1 & 0 \\ 0 & 1 \\ 0 & 1 \\ 0 & 1 \\ 1 & 0 \\ 1 & 0 \\ 1 & 0 \\ 1 & 0 \\ 0 & 1 \end{bmatrix}, \quad U_f = \begin{bmatrix} 0 & 0 & -0.45 & -0.45 & -0.45 & -0.45 & 0 \\ -0.50 & -0.50 & 0 & 0 & 0 & 0 & -0.50 \\ 0.83 & -0.17 & 0 & 0 & 0 & 0 & -0.17 \\ -0.17 & 0.83 & 0 & 0 & 0 & 0 & -0.17 \\ 0 & 0 & 0.86 & -0.14 & -0.14 & -0.14 & 0 \\ 0 & 0 & -0.14 & 0.86 & -0.14 & -0.14 & 0 \\ 0 & 0 & -0.14 & -0.14 & 0.86 & -0.14 & 0 \\ 0 & 0 & -0.14 & -0.14 & -0.14 & 0.86 & 0 \\ -0.17 & -0.17 & 0 & 0 & 0 & 0 & 0.83 \end{bmatrix}$$

while the MTPA weighting matrix, computed via (6.18), is:

$$W = \begin{bmatrix} 0.80 & 0 & 0 & 0 & -0.20 & -0.20 & -0.20 & -0.20 & 0 \\ 0 & 0.75 & -0.25 & -0.25 & 0 & 0 & 0 & 0 & -0.25 \\ 0 & -0.25 & 0.75 & -0.25 & 0 & 0 & 0 & 0 & -0.25 \\ 0 & -0.25 & -0.25 & 0.75 & 0 & 0 & 0 & 0 & -0.25 \\ -0.20 & 0 & 0 & 0 & 0.80 & -0.20 & -0.20 & -0.20 & 0 \\ -0.20 & 0 & 0 & 0 & -0.20 & 0.80 & -0.20 & -0.20 & 0 \\ -0.20 & 0 & 0 & 0 & -0.20 & -0.20 & 0.80 & -0.20 & 0 \\ -0.20 & 0 & 0 & 0 & -0.20 & -0.20 & -0.20 & 0.80 & 0 \\ 0 & -0.25 & -0.25 & -0.25 & 0 & 0 & 0 & 0 & 0.75 \end{bmatrix}$$

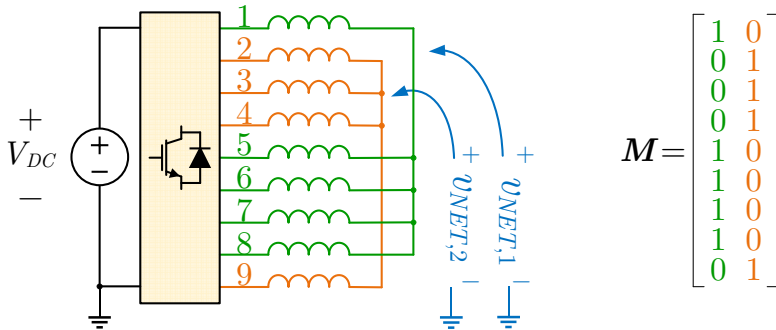


Fig. 6.36 – Schematic diagram and constraint matrix for the highly asymmetrical configuration.

The optimal phase currents computed by the MTPA algorithm (6.17) are depicted<sup>26</sup> in Fig. 6.37. They are almost sinusoidal, and only a small third-harmonic contribution (following the machine asymmetry) is present. Again, the currents harmonics (and the resulting losses) are not evenly distributed between all the machine phases. This may be more or less relevant for thermal analysis depending on the machine internal design.

The experimental results in this testing scenario are shown in Fig. 6.38 and Fig. 6.39.

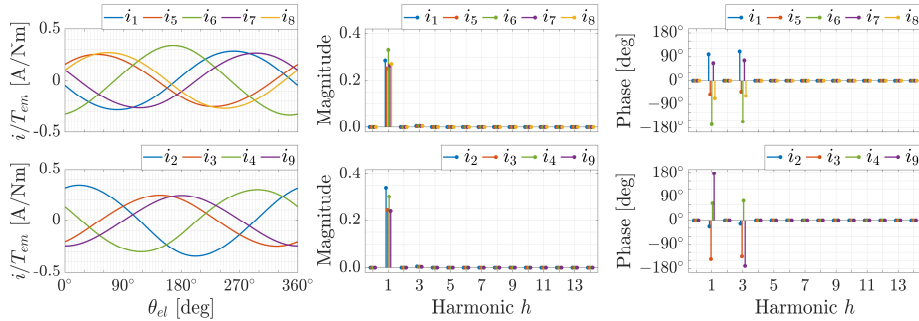


Fig. 6.37 – Waveforms and harmonic spectra of the optimal reference currents in the highly asymmetrical configuration.

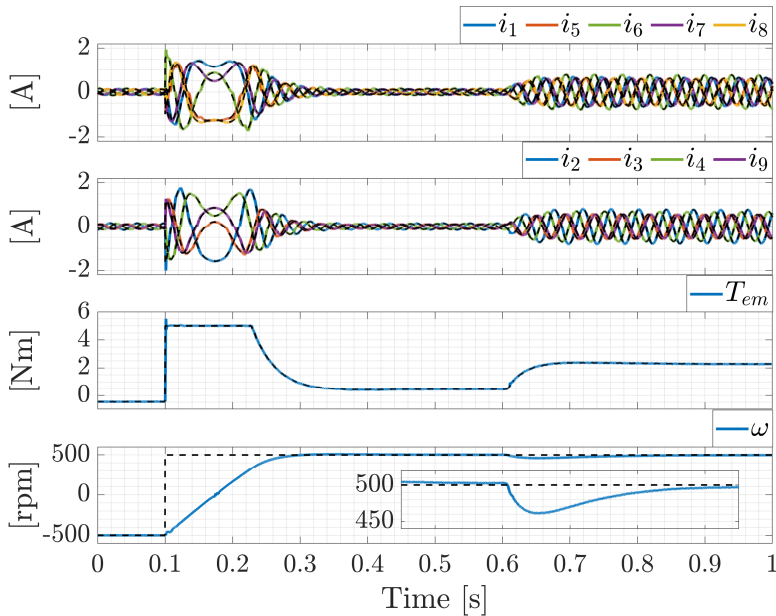


Fig. 6.38 – Experimental results in the highly asymmetrical configuration. Solid lines: measured variables; Dashed lines: reference variables.

<sup>26</sup> The currents depicted in the numerical and experimental results have been grouped differently than in the previous cases.

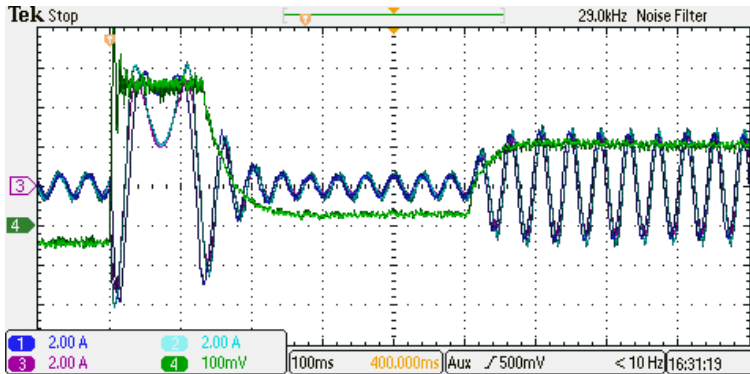


Fig. 6.39 – Oscilloscope capture of the experimental results in the highly asymmetrical configuration.

In this case, the speed and torque still have the same dynamics, while the currents, follow the waveforms of Fig. 6.37. The combined effect of the decoupling algorithm and the resonant actions in the feedback controller make the currents follow their desired references even in such an uncommon winding configuration.

Again, it is worth emphasising that the controller structure and parameters have been kept unaltered from the previous cases, and only a different constraint matrix  $\mathbf{M}$  has been provided to the initialization routine. Similarly to the post-fault scenarios of the previous sections, minimal changes are required to adapt the algorithm to this new configuration. Conversely, the control implementation would have been much more challenging if carried out with a FOC-based approach.

### 6.7.7 Real-time post-fault reconfiguration

This testing scenario is aimed at showing the fundamental role of the configuration matrix  $\mathbf{U}_f$  for the machine current control. This is done by emulating an open-winding fault event and the consequent real-time controller reconfiguration<sup>27</sup>.

The circuit configuration is schematically depicted in Fig. 6.40. At the beginning of this experiment, the contactor in series to phase 1 is closed, and the machine windings are star connected with a single isolated neutral point. This configuration, which represents a healthy machine, is the same as the case study developed in Section 6.7.1 and represented in Fig. 6.16.

After 80 ms from the beginning of the experiment, phase 1 of the machine is physically disconnected by commanding (via the RT Box platform) the opening of the serially connected contactor.

The controller matrices (which depend on the constraint matrix  $\mathbf{M}$ ) are kept unaltered for another 200 ms (i.e., they still refer to the healthy configuration of Fig. 6.16) and are finally updated to the post-fault condition by considering the correct system matrices.

For the whole test, the machine is kept at an angular speed of around 500 rpm and

<sup>27</sup> The fault detection algorithm has not been considered in this study.

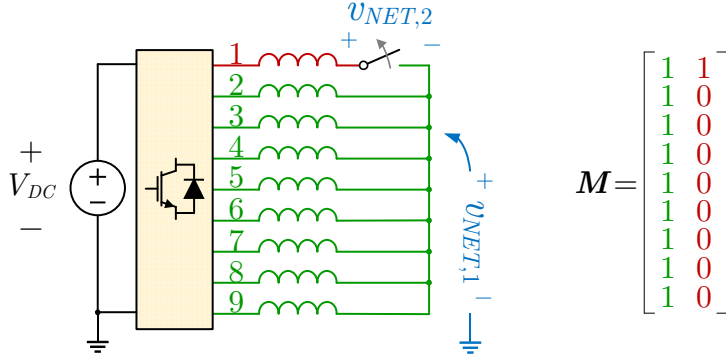


Fig. 6.40 – Schematic diagram for the real-time post-fault reconfiguration scenario, with the constraint matrix after the opening of the contactor.

is subject to a mechanical load of around 2.3 Nm applied at the shaft through the DC machine.

The constraints matrix  $M$ , the configuration matrix  $U_f$  and the MTPA weighting matrix  $W$  of the healthy configuration are the same as the case study of Section 6.7.1. The same matrices in the post-fault configuration are, instead:

$$M = \begin{bmatrix} 1 & 1 \\ 1 & 0 \\ 1 & 0 \\ 1 & 0 \\ 1 & 0 \\ 1 & 0 \\ 1 & 0 \\ 1 & 0 \\ 1 & 0 \end{bmatrix}, \quad U_f = \begin{bmatrix} 0 & 0 & 0 & 0 & 0 & 0 & 0 & 0 \\ -0.35 & -0.35 & -0.35 & -0.35 & -0.35 & -0.35 & -0.35 & -0.35 \\ 0.91 & -0.09 & -0.09 & -0.09 & -0.09 & -0.09 & -0.09 & -0.09 \\ -0.09 & 0.91 & -0.09 & -0.09 & -0.09 & -0.09 & -0.09 & -0.09 \\ -0.09 & -0.09 & 0.91 & -0.09 & -0.09 & -0.09 & -0.09 & -0.09 \\ -0.09 & -0.09 & -0.09 & 0.91 & -0.09 & -0.09 & -0.09 & -0.09 \\ -0.09 & -0.09 & -0.09 & -0.09 & 0.91 & -0.09 & -0.09 & -0.09 \\ -0.09 & -0.09 & -0.09 & -0.09 & -0.09 & 0.91 & -0.09 & -0.09 \\ -0.09 & -0.09 & -0.09 & -0.09 & -0.09 & -0.09 & -0.09 & 0.91 \end{bmatrix}$$

$$W = \begin{bmatrix} 0 & 0 & 0 & 0 & 0 & 0 & 0 & 0 & 0 \\ 0 & 0.88 & -0.12 & -0.12 & -0.12 & -0.12 & -0.12 & -0.12 & -0.12 \\ 0 & -0.12 & 0.88 & -0.12 & -0.12 & -0.12 & -0.12 & -0.12 & -0.12 \\ 0 & -0.12 & -0.12 & 0.88 & -0.12 & -0.12 & -0.12 & -0.12 & -0.12 \\ 0 & -0.12 & -0.12 & -0.12 & 0.88 & -0.12 & -0.12 & -0.12 & -0.12 \\ 0 & -0.12 & -0.12 & -0.12 & -0.12 & 0.88 & -0.12 & -0.12 & -0.12 \\ 0 & -0.12 & -0.12 & -0.12 & -0.12 & -0.12 & 0.88 & -0.12 & -0.12 \\ 0 & -0.12 & -0.12 & -0.12 & -0.12 & -0.12 & -0.12 & 0.88 & -0.12 \\ 0 & -0.12 & -0.12 & -0.12 & -0.12 & -0.12 & -0.12 & -0.12 & 0.88 \end{bmatrix}$$

The optimal currents in the post-fault scenario, together with the corresponding harmonic spectra, are depicted in Fig. 6.41. As in all the other analysed post-fault configurations, they are not sinusoidal and show some higher-order harmonics (especially a third-harmonic contribution). Moreover, the currents harmonics (and the corresponding losses) are not equally shared by all the healthy phases.

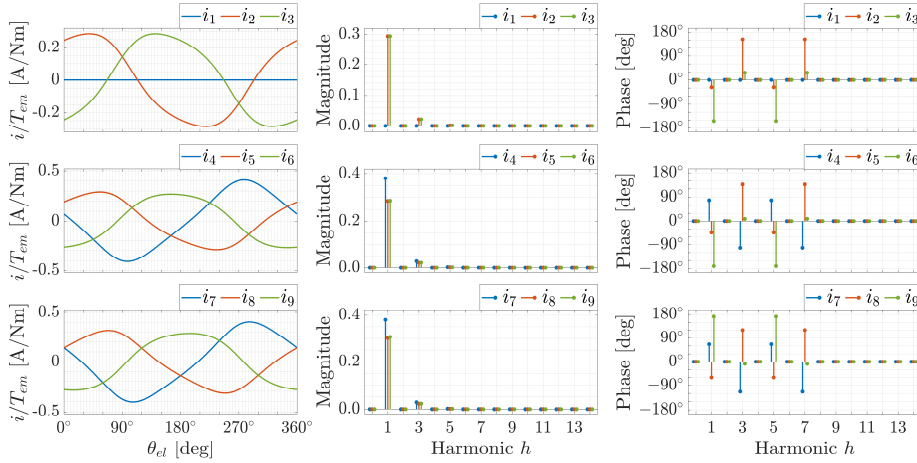


Fig. 6.41 – Waveforms and harmonic spectra of the optimal reference currents in the single neutral post-fault configuration.

The experimental results are depicted in Fig. 6.42, while Fig. 6.43 shows the corresponding oscilloscope acquisitions.

During the first 80 ms, coherently with the results of Section 6.7.1, all the machine currents follow the corresponding references, which are sinusoidal. Then, the current  $i_1$  is forced to zero (via hardware), without altering the controller parameters.

All the current references (dashed traces) are still sinusoidal waveforms, but the measured currents are unable to follow them. This is expected because the references are not compatible with the new system configuration. This effect is particularly evident in the current  $i_4$ , which is severely increased with respect to the others. Since the currents cannot follow their references, also the developed torque  $T_{em}$  cannot follow the desired value  $T_{em}^*$  and periodically oscillates between around 2 Nm and 2.3 Nm. This torque decrease also leads to a slight reduction of the machine angular speed  $\omega$ .

At the time  $t = 280$  ms the controller parameters are finally updated by using the correct constraint matrix  $\mathbf{M}$  (i.e., the one corresponding to the faulty scenario) and by coherently updating  $\mathbf{U}_f$  and  $\mathbf{W}$ . All the other controller parameters (e.g., speed and current feedback controller coefficients, inductances and resistances matrix, estimated back-EMFs, etc.) are kept unchanged. Again, the structure update required no changes to the controller architecture and minimal modifications to the control matrices.

Coherently with the post-fault configuration, the reference current  $i_1^*$  is kept to zero, while all the other current references become non-sinusoidal. Again, this is expected because of the asymmetrical structure of the post-fault machine configuration. The machine currents are quickly and effectively driven towards the corresponding references, the electromagnetic torque can again follow the reference value  $T_{em}^*$  and the machine speed  $\omega$  is slowly kept back to the reference  $\omega^* = 500$  rpm.

The analysed results highlight how the proposed approach can be a viable and interesting solution for fault-tolerant applications.

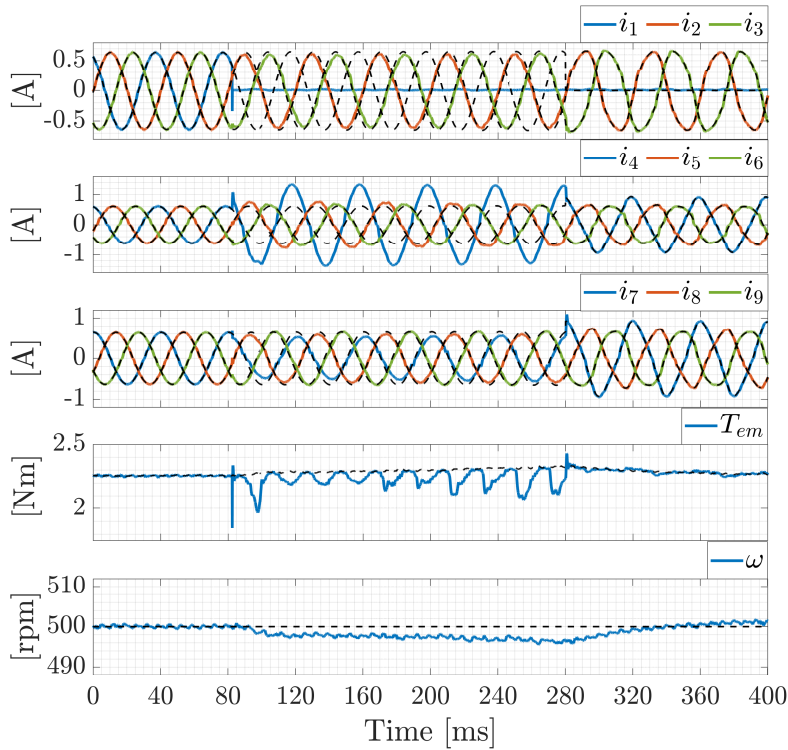


Fig. 6.42 – Experimental results in the real-time post-fault reconfiguration scenario. Solid lines: measured variables; Dashed lines: reference variables.

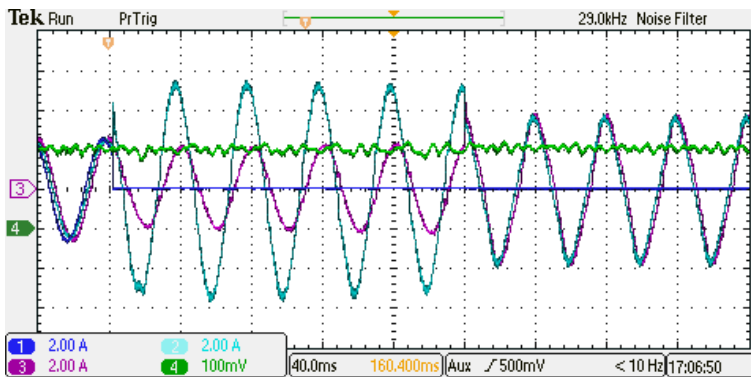


Fig. 6.43 – Oscilloscope capture of the experimental results in the real-time post-fault reconfiguration scenario.

### 6.7.8 Torque sharing scenarios

This testing scenario is aimed at showing the torque sharing capabilities of the proposed current references computation strategy.

In this case, the machine windings are divided into two independent subsets, further on identified as  $SET_1$  and  $SET_2$ , respectively. The first windings subset works in “motoring” mode, with the aim to keep the angular speed of the machine at the reference value of  $\omega^* = 500$  rpm. The second windings subset, instead, works in “braking” mode and is controlled to develop a desired braking torque  $T_{em,br}^*$  in opposition to the mechanical speed. In such a way it is possible to transfer power from the motoring windings set to the braking windings set. For the whole test, the machine is subject to the sole mechanical friction torque, which is around 0.5 Nm.

The experiment is here done with the healthy machine configuration analysed in Section 6.7.2 and schematically represented in Fig. 6.20. The machine windings are divided into two star-connected groups with isolated neutral points. The motoring group includes the windings  $\{1,2,3,7,8,9\}$ , while the breaking group includes the remaining windings  $\{4,5,6\}$ . The decoupling algorithm is executed considering the constraints and configuration matrices  $\mathbf{M}$  and  $\mathbf{U}_f$  given in Section 6.7.2.

The current references are found by separately applying the MTPA strategy presented in Section 6.2.3 to the two windings subsets. Their waveforms and harmonic spectra are shown<sup>28</sup> in Fig. 6.44.

To be more specific, the reference currents  $\mathbf{i}_{SET_1}^* = [i_1^*, i_2^*, i_3^*, i_7^*, i_8^*, i_9^*]^T$  of the six-phase motoring group are found by applying (6.19) with  $\mathbf{f}_{PM,SET_1} = [f_{PM,1}, f_{PM,2}, f_{PM,3}, f_{PM,7}, f_{PM,8}, f_{PM,9}]^T$ . The reference torque for the motoring set is computed as:

$$T_{em,SET_1}^* = T_{em}^* + T_{em,br}^*$$

where  $T_{em}^*$  is the overall electromagnetic torque computed by the speed controller, while  $T_{em,br}^*$  is the compensation of the torque applied by the braking windings group. The MTPA weighting matrix  $\mathbf{W}_{SET_1}$  of the motoring group is:

$$\mathbf{W}_{SET_1} = \begin{bmatrix} 0.83 & -0.17 & -0.17 & -0.17 & -0.17 & -0.17 \\ -0.17 & 0.83 & -0.17 & -0.17 & -0.17 & -0.17 \\ -0.17 & -0.17 & 0.83 & -0.17 & -0.17 & -0.17 \\ -0.17 & -0.17 & -0.17 & 0.83 & -0.17 & -0.17 \\ -0.17 & -0.17 & -0.17 & -0.17 & 0.83 & -0.17 \\ -0.17 & -0.17 & -0.17 & -0.17 & -0.17 & 0.83 \end{bmatrix}$$

and it has been found by computing (6.20) with the matrix

$$\mathbf{M}_{SET_1} = [1 \ 1 \ 1 \ 1 \ 1 \ 1]^T$$

which identifies isolated neutral point constraint of the six-phase group. Given the symmetry of the considered subset, the corresponding currents of Fig. 6.44 are sinusoidal.

<sup>28</sup> Note that, contrarily to the previous cases, now the currents of each of the two subsets are normalized by the corresponding reference torques, which can be different from one another.

Similarly, the references  $\mathbf{i}_{SET_2}^* = [i_4^*, i_5^*, i_6^*]^T$  of the three-phase braking group are found by applying the same equation (6.19), but with the set  $\mathbf{f}_{PM,SET_2} = [f_{PM,4}, f_{PM,5}, f_{PM,6}]^T$ . The reference torque for this group is simply imposed to be the desired braking torque:

$$T_{em,SET_2}^* = -T_{em,br}^*$$

The MTPA weighting matrix  $\mathbf{W}_{SET_2}$  of the braking group is simply:

$$\mathbf{W}_{SET_2} = \begin{bmatrix} 0.67 & -0.33 & -0.33 \\ -0.33 & 0.67 & -0.33 \\ -0.33 & -0.33 & 0.67 \end{bmatrix}$$

and, once again, it has been computed via (6.20) with the matrix:

$$\mathbf{M}_{SET_2} = [1 \quad 1 \quad 1]^T$$

which identifies the three-phase group isolated neutral point constraint. Again, since the three-phase subset is symmetrical, the corresponding currents in Fig. 6.44 are sinusoidal.

Note that, despite the different current references computation strategy, the current control algorithm of this testing scenario is equal to the one described in Section 6.7.2 (i.e., it refers to the same  $\mathbf{M}$  and  $\mathbf{U}_f$  matrices).

Fig. 6.45 and Fig. 6.46 show the experimental results obtained in this testing scenario. Initially,  $T_{em,br}^*$  is set to 0 Nm; then, after 80 ms,  $T_{em,br}^*$  is changed to 2 Nm.

By observing the machine phase currents it can be noted that, since for the first 80 ms the three-phase set is asked not to produce any torque, the corresponding currents are zero. The currents of the six-phase windings group are sinusoidal and with the same

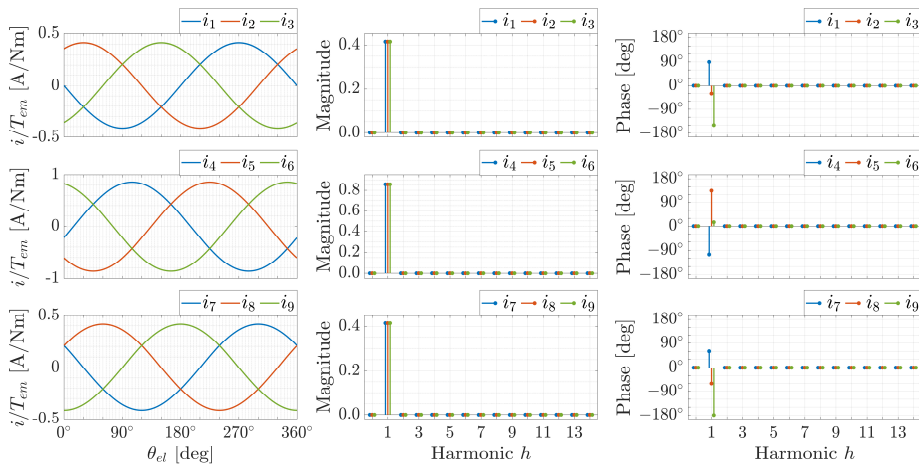


Fig. 6.44 – Waveforms and harmonic spectra of the optimal reference currents for the torque sharing scenario. The currents of the motoring set  $\{1,2,3,7,8,9\}$  are referred to the torque  $T_{em,SET_1}^* = T_{em}^* + T_{em,br}^*$ . The currents of the braking set  $\{4,5,6\}$  are referred to the torque  $T_{em,SET_2}^* = -T_{em,br}^*$ .

magnitude (coherently with Fig. 6.44). They only need to balance the mechanical loading torque due to the friction.

After the reference torque  $T_{em,br}^*$  is changed to 2 Nm, the currents of the braking group increase to follow the corresponding references which, given the symmetrical configuration of the three-phase set, are also sinusoidal waveforms (coherently with Fig. 6.44). To balance the braking torque, the currents of the six-phase motoring set have their magnitude increased of around 5 times. Indeed, to compensate for the effect of  $T_{em,br}^*$ , they now need to develop an overall torque of around 2.5 Nm against the initial value of around 0.5 Nm which was only due to the mechanical load. Following an initial transient, all the currents can perfectly track their references.

The fourth subplot of Fig. 6.45 shows both the overall torque  $T_{em}$  and the torques  $T_{em,SET_1}$  and  $T_{em,SET_2}$  developed by the two windings subsets<sup>29</sup>. As can be noted, after an initial transient,  $T_{em,SET_2}$  reaches the desired value of  $-2$  Nm and  $T_{em,SET_1}$  the corresponding value of 2.5 Nm. The overall torque  $T_{em}$  developed at the rotor shaft, which is given by the combined contribution of the two subsets, is almost unaffected by

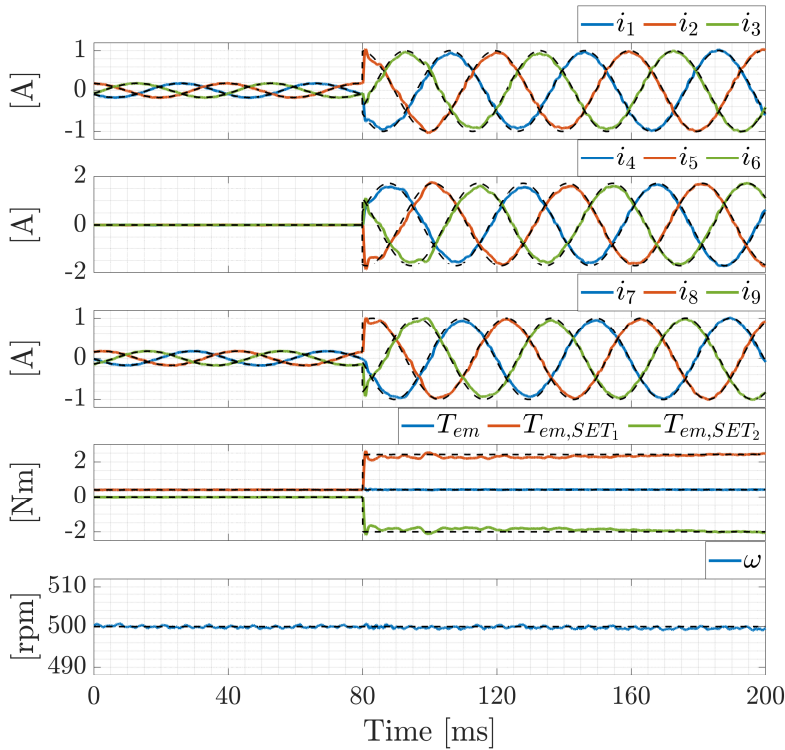


Fig. 6.45 – Experimental results for the torque sharing scenario in healthy conditions. Solid lines: measured variables; Dashed lines: reference variables.

<sup>29</sup> Again, these are torque estimations computed by applying the analytical expression (6.4) and by only selecting the phase indexes related to the two subsets.

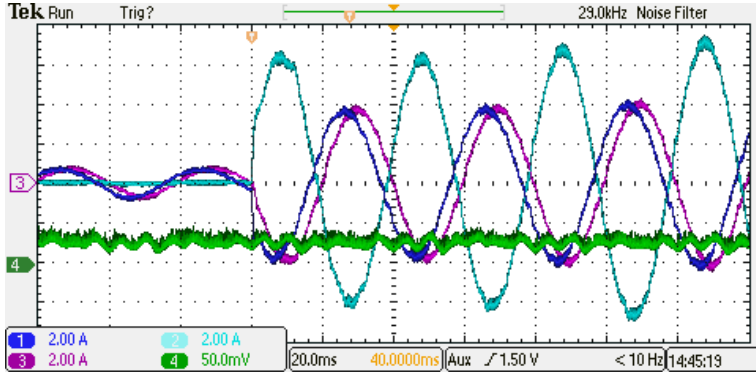


Fig. 6.46 – Oscilloscope capture of the experimental results for the torque sharing scenario in healthy conditions.

the current transient and is kept to the constant value of around 0.5 Nm. This is also confirmed by the measurement of the torque meter (the green trace of Fig. 6.46).

As can be seen from the last subplot of Fig. 6.45, the machine speed  $\omega$  is unaffected by the change of  $T_{em,br}^*$  and stays at the value of 500 rpm.

As also analysed in Section 6.2.3, this torque sharing capability can be conveniently used to transfer power between different sets (e.g., from the motoring subset to the braking subset).

The same torque sharing strategy can be also applied to a faulty machine configuration. This is here exemplified by repeating the same testing scenario for the post-fault configuration analysed in Section 6.7.3 and represented in Fig. 6.24, in which phase 1 of the machine has been physically disconnected.

In this case, the only difference in the current references computation strategy is related to the weighting matrix  $\mathbf{W}_{SET_1}$ , which is now computed with the constraints matrix:

$$\mathbf{M}_{SET_1} = \begin{bmatrix} 1 & 1 & 1 & 1 & 1 & 1 \\ 1 & 0 & 0 & 0 & 0 & 0 \end{bmatrix}^T$$

which includes the additional constraint  $i_1 = 0$ . From (6.20), it results:

$$\mathbf{W}_{SET_1} = \begin{bmatrix} 0 & 0 & 0 & 0 & 0 & 0 \\ 0 & 0.80 & -0.20 & -0.20 & 0.20 & -0.20 \\ 0 & -0.20 & 0.80 & -0.20 & -0.20 & -0.20 \\ 0 & -0.20 & -0.20 & 0.80 & -0.20 & -0.20 \\ 0 & -0.20 & -0.20 & -0.20 & 0.80 & -0.20 \\ 0 & -0.20 & -0.20 & -0.20 & -0.20 & 0.80 \end{bmatrix}$$

The optimal current references in this scenario are depicted in Fig. 6.47, while the experimental results are shown in Fig. 6.48 and Fig. 6.49.

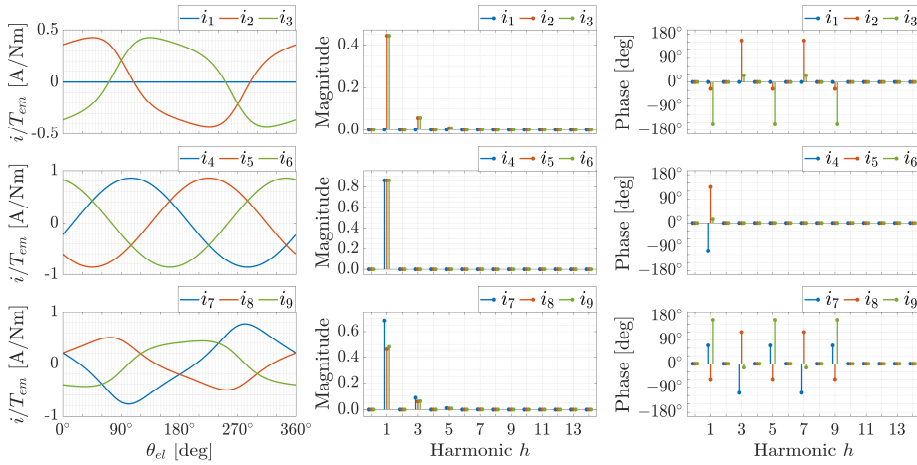


Fig. 6.47 – Waveforms and harmonic spectra of the optimal reference currents for the torque sharing scenario in faulty conditions. The currents of the motoring set  $\{1,2,3,7,8,9\}$  are referred to the torque  $T_{em,SET1}^* = T_{em}^* + T_{em,br}^*$ . The currents of the braking set  $\{4,5,6\}$  are referred to the torque  $T_{em,SET2}^* = -T_{em,br}^*$ .

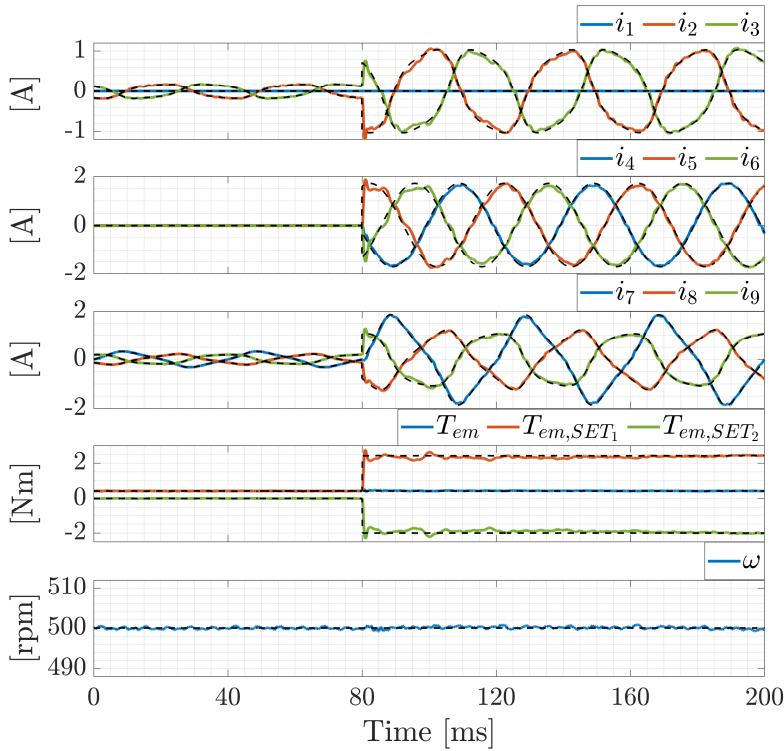


Fig. 6.48 – Experimental results for the torque sharing scenario in faulty conditions. Solid lines: measured variables; Dashed lines: reference variables.

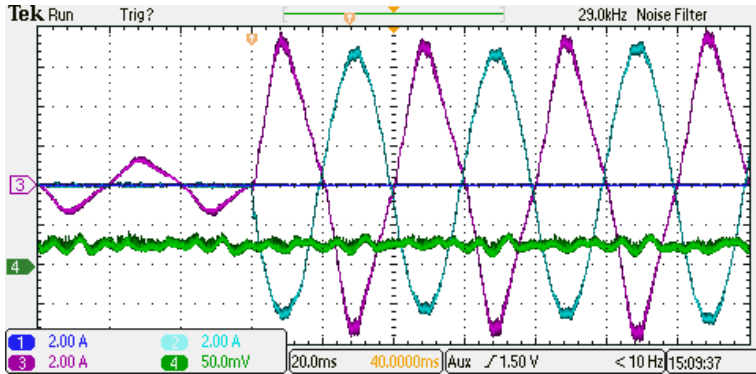


Fig. 6.49 – Oscilloscope capture of the experimental results for the torque sharing scenario in faulty conditions.

Again, the currents of the three-phase braking set are initially zero (because  $T_{em,br}^*$  is 0 Nm) and after the settling transient, they follow the same sinusoidal references of the healthy configuration, coherently with the references currents of Fig. 6.47 (indeed, the three-phase set has not been changed).

On the contrary, the currents of the motoring set are not sinusoidal anymore, because of the asymmetrical structure of the post-fault configuration. In particular, the corresponding waveforms do not change during the entire experiment (i.e., they have the same waveform of Fig. 6.47) and only their magnitude is modified after the braking torque change. Initially, when  $T_{em,br}^* = 0$  Nm, they only need to balance the mechanical torque of around 0.5 Nm due to the drive train friction. When, after 80 ms, the reference braking torque is changed to  $T_{em,br}^* = 2$  Nm, the magnitude of the currents of the motoring group increases by around 5 times to balance the overall braking torque of around 2.5 Nm.

Once again, the overall electromagnetic torque  $T_{em}$  is not affected by the change of the torques of the two subsets and, consequently, the machine speed  $\omega$  is always kept to the reference value of 500 rpm.

## 6.8 Summary and remarks

This chapter has presented a *generalized control algorithm for a multiphase surface-mounted PMSM drive*. Contrarily to standard approaches, the proposed solution is completely derived in the phase variable domain and does not require any VSD or rotational transformation, but instead it explicitly considers the hardware connection among the machine phase windings and with the supplying power converter.

First, the mathematical model of the drive has been derived. The electrical machine model is the particularization of the general model developed in Chapter 2, while the effect of the interconnection network has been done through the *network interconnection matrix*  $\mathbf{N}$  and the *constraints matrix*  $\mathbf{M}$ , coherently with the analysis of Chapter 4.

Then, an *MTPA algorithm* has been presented to compute the machine current references needed to develop a desired electromagnetic torque. The approach has been

formalized as a constrained optimization problem aimed at minimizing the overall machine RMS current while, at the same time, producing the desired reference torque and satisfying the algebraic constraints introduced by the drive hardware configuration. It has been solved analytically and only requires the computation of an *MTPA weighing matrix*  $\mathbf{W}$ , which only depends on the constraints matrix  $\mathbf{M}$ . The same MTPA approach can also be applied to chosen subsets of the machine windings, and is therefore suitable for independent torque control strategies.

The current controller has then been developed.

The core of the proposed solution is a *decoupling algorithm* that, coherently with the system constraints, is aimed at neutralizing all the mutual interactions due both to the magnetic couplings and to the electrical drive topology. The proposed decoupling algorithm is composed of a *machine compensation* term (which replicates the machine model) and of a *network compensation* term (which implements a pseudo-inverse algorithm and depends on the *configuration matrix*  $\mathbf{U}_f$ ).

Thanks to the decoupled algorithm, the machine currents can be independently controlled through any standard single-input/single-output controller structure. The chosen *decoupled current controller* is linear and, since the steady-state currents are periodic, is composed of a proportional action, an integral action, and several resonant actions synchronized with the machine angular speed. The presence of the resonant terms guarantees the steady-state tracking errors to be zero.

The whole control algorithm has been experimentally validated with a nine-phase PMSM drive. Several testing scenarios have been analysed and discussed in detail. All the results are satisfactory and coherent with the theoretical analysis.

The main benefit of the proposed approach is its generality and flexibility. The same controller architecture can be applied to any machine design (e.g., different magnetic axes disposition, back-EMFs waveforms, etc...) and to any electrical configuration (e.g., single or multiple neutral points, healthy or post-fault configurations, etc...). It can also be adapted in real-time to different drive configurations with minimal changes, thus being a viable solution for fault-tolerant applications.

# 7 Decoupled Phase Variable Control of SynRMs

Chapter 6 has proposed an innovative control algorithm for multiphase PMSMs, which is directly derived in the phase variable domain and explicitly considers the drive architecture. Thanks to detailed mathematical analysis and to many experimental tests, the proposed approach has proven its benefits in terms of generality with respect to both machine designs and drive configurations, thus representing a viable alternative to standard multiphase control algorithms.

This chapter is aimed at showing how this approach can be extended to an electric drive employing a multiphase synchronous reluctance machine (SynRM). Here, the main differences are related to the torque development mechanism and, consequently, to the generation of the motional induced back-EMFs, which are not related to the presence of permanent magnets but, instead, depend on variable reluctance effects.

The chapter is structured as follows. Section 7.1.6.1 summarizes the mathematical model of the analysed SynRM drive which, again, combines the machine model developed in Chapter 2 and the network model developed in Chapter 4. Section 7.2 describes a current references computation strategy based on a maximum torque per ampere (MTPA) approach and analyses its properties and implementation. Next, Section 7.3 examines the current control algorithm, which follows the same approach developed in Chapter 6 and is based on a decoupling algorithm and on a decoupled feedback controller. The overall control algorithm is then summarized in Section 7.4. The experimental setup used to validate the proposed approach is described in Section 7.5, while the corresponding results are discussed in Section 7.6. Finally, Section 7.7 summarizes the main conclusions of this study.

## 7.1 Mathematical model

The drive under analysis consists of a  $n$ -phase SynRM supplied by a  $m$ -leg converter. All the  $n$  machine windings are located on the stator, and the variable reluctance is realized through the rotor design.

This section particularizes the generalized machine model presented in Chapter 2 to the examined configuration, explicitly considering the drive architecture model analysed in Chapter 4 through the multiport network approach. Fig. 7.1 shows a schematic representation of the analysed multiphase drive, with the explicit identification of the SynRM, of the VSI (average model) and of the interconnection network.

### 7.1.1 Machine model

As presented in Chapter 2, under the linearity hypothesis, the fluxes induced in each of the  $n$  stator windings is given by the superimposed contribution of the magnetic field generated by all the machine phase currents. The model (2.29) is particularized into:

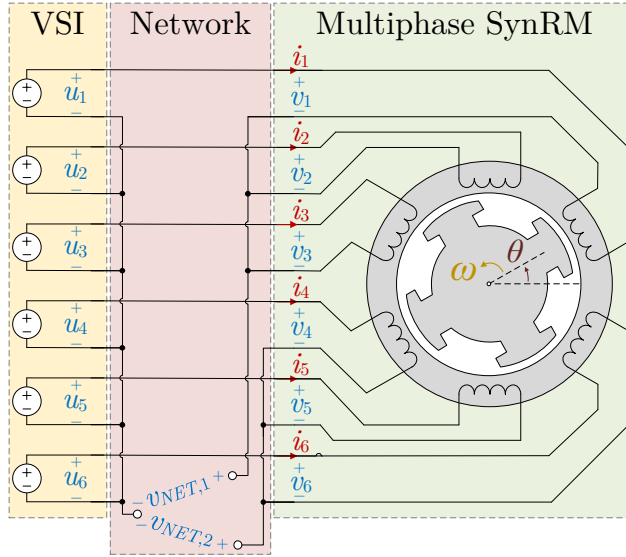


Fig. 7.1 – Schematic representation of a six-phase multiphase SynRM drive architecture, with explicit identification of the VSI (average model) and of the electrical interconnection network (double-star configuration with two isolated neutral points).

$$\phi = \mathbf{L}(\theta) \cdot \mathbf{i} \quad (7.1)$$

Given the variable reluctance effects, the  $n \times n$  inductances matrix  $\mathbf{L}$  periodically depends on the rotor position  $\theta$ . As shown in Chapter 2, for each rotor position,  $\mathbf{L}(\theta)$  is symmetric and positive definite. A Fourier decomposition can be applied with respect to the mechanical position  $0 \leq \theta \leq 2\pi$  to identify the different harmonic contribution of each coefficient of  $\mathbf{L}(\theta)$ . For typical designs, considering a machine with  $P_p$  pole pairs, the inductances matrix is characterized by only even-order harmonics of the electrical rotor position  $\theta_{el} = P_p \cdot \theta$  (i.e., by the harmonics of order  $h = 0, 2, 4, \dots$ <sup>1</sup>).

From (7.1), the induced back-EMFs can be split in the transformer-induced contribution (related to the time variation of the phase currents) and in the motional-induced contribution (related to the time variation of the rotor position) as:

$$\frac{d\phi}{dt} = \mathbf{L}(\theta) \cdot \frac{d\mathbf{i}}{dt} + \omega \cdot \mathbf{L}'(\theta) \cdot \mathbf{i} \quad (7.2)$$

with  $\omega = d\theta/dt$  identifying the mechanical speed of the rotor, and  $\mathbf{L}'(\theta) = \partial\mathbf{L}/\partial\theta$  identifying the  $\theta$ -derivative of the inductances matrix, whose coefficients are related to the variable reluctance effects. The matrix  $\mathbf{L}'(\theta)$  is also a symmetric matrix that periodically depends on  $\theta$  but, generally, it is not positive definite.

By denoting as  $\mathbf{e} = \omega \cdot \mathbf{L}'(\theta) \cdot \mathbf{i}$  the motional-induced back-EMFs, the machine electrical equations can be written in a matrix formalism as:

<sup>1</sup> This is because the rotor is typically designed with an even number of saliencies (or flux barriers) for each pole pair of the machine.

$$\mathbf{L}(\theta) \cdot \frac{d\mathbf{i}}{dt} + \mathbf{R} \cdot \mathbf{i} + \mathbf{e} = \mathbf{v} \quad (7.3)$$

This equation takes the same form of the model (6.3), where the only differences are the dependence of the inductances matrix  $\mathbf{L}$  by the rotor position  $\theta$  and the different definition of the motional-induced back-EMFs vector  $\mathbf{e}$ , which in (6.3) was related to the permanent magnets, while in (7.3) is related to the variable reluctance effects.

Given the absence of PMs, the electromagnetic torque generated by the machine is only due to the mutual interaction between the different phase currents, which depends on the variable reluctance effects, and the general expression (2.33) is simplified to:

$$T_{em} = \frac{1}{2} \cdot \mathbf{i}^T \cdot \mathbf{L}'(\theta) \cdot \mathbf{i} \quad (7.4)$$

### 7.1.2 Drive electrical model

As explained in Chapter 4, and similarly to how it has been discussed in Chapter 6, the machine phase windings are connected with each other and to the supplying converter through a known interconnection network which may introduce  $n_c$  algebraic constraints to the  $n$  machine currents. Again, as previously done in Section 6.1.2, the overall effect of the network can be modelled through the equations:

$$\mathbf{M}^T \cdot \mathbf{i} = \mathbf{0} \quad (7.5)$$

$$\mathbf{L}(\theta) \cdot \frac{d\mathbf{i}}{dt} + \mathbf{R} \cdot \mathbf{i} + \mathbf{e} = \mathbf{v} = \mathbf{N} \cdot \mathbf{u} - \mathbf{M} \cdot \mathbf{v}_{NET} \quad (7.6)$$

where  $\mathbf{M}$  is the  $n \times n_c$  constraints matrix,  $\mathbf{u}$  is the  $m \times 1$  set of converter leg voltages,  $\mathbf{N}$  is the  $n \times m$  network interconnection matrix, and  $\mathbf{v}_{NET}$  is the  $n_c \times 1$  set of auxiliary network voltages related to the constraints on the machine currents.

As explained in Chapter 4, the model (7.5)-(7.6) can be simplified by considering a configuration matrix  $\mathbf{U}_f$  (which can be computed from the singular value decomposition of  $\mathbf{M}$ ), in a way that:

$$\mathbf{i} = \mathbf{U}_f \cdot \mathbf{i}_f, \quad \text{and} \quad \mathbf{U}_f^T \cdot \mathbf{M} = \mathbf{0} \quad (7.7)$$

This allows reducing the  $n$ -dimensional set of equations (7.4) and (7.6) in a set of equations with dimension  $n_f = n - n_c$ , which are:

$$\mathbf{L}_f(\theta) \cdot \frac{d\mathbf{i}_f}{dt} + \mathbf{R}_f \cdot \mathbf{i}_f + \mathbf{e}_f = \mathbf{v}_f = \mathbf{N}_f \cdot \mathbf{u} \quad (7.8)$$

$$T_{em} = \frac{1}{2} \cdot \mathbf{i}_f^T \cdot \mathbf{L}'_f(\theta) \cdot \mathbf{i}_f \quad (7.9)$$

In (7.8) and (7.9), the  $n \times 1$  vectors  $\mathbf{i}$ ,  $\mathbf{e}$  and  $\mathbf{v}$  have been reduced to the  $n_f \times 1$  vectors  $\mathbf{i}_f$ ,  $\mathbf{e}_f$  and  $\mathbf{v}_f$  through the transformations:

$$\mathbf{i}_f = \mathbf{U}_f^T \cdot \mathbf{i}, \quad \mathbf{e}_f = \mathbf{U}_f^T \cdot \mathbf{e}, \quad \mathbf{v}_f = \mathbf{U}_f^T \cdot \mathbf{v} \quad (7.10)$$

while the  $n \times n$  matrices  $\mathbf{L}(\theta)$ ,  $\mathbf{L}'(\theta)$  and  $\mathbf{R}$ , and the  $n \times m$  matrix  $\mathbf{N}$ , have been reduced to the  $n_f \times n_f$  matrices  $\mathbf{L}_f(\theta)$ ,  $\mathbf{L}'_f(\theta)$  and  $\mathbf{R}_f$ , and in the  $n_f \times m$  matrix  $\mathbf{N}_f$  as:

$$\begin{aligned} \mathbf{L}_f(\theta) &= \mathbf{U}_f^T \cdot \mathbf{L}(\theta) \cdot \mathbf{U}_f, & \mathbf{R}_f &= \mathbf{U}_f^T \cdot \mathbf{R} \cdot \mathbf{U}_f \\ \mathbf{L}'_f(\theta) &= \mathbf{U}_f^T \cdot \mathbf{L}'(\theta) \cdot \mathbf{U}_f, & \mathbf{N}_f &= \mathbf{U}_f^T \cdot \mathbf{N} \end{aligned} \quad (7.11)$$

### 7.1.3 Mechanical model

The mechanical model of the system is the same as the previously discussed model presented in Section 5.1.7 and in Section 6.1.3. The corresponding equations of the overall group are here repeated:

$$J_{eq} \cdot \frac{d\omega}{dt} + F_{eq}(\omega) \cdot \omega = T_{em} - T_{load} \quad (7.12)$$

$$\frac{d\theta}{dt} = \omega \quad (7.13)$$

## 7.2 Torque control Strategy

The torque control strategy is aimed at computing a set of reference currents  $\mathbf{i}^*$  to be tracked to develop a desired electromagnetic torque  $T_{em}^*$ . As also explained in Section 6.2, for a  $n$ -phase machine subject to  $n_c$  constraints (7.5), there are  $n_f = n - n_c$  free current components which can be chosen. Then, the torque development requirement can be addressed as an additional constraint on the machine currents, and the remaining  $n_f - 1$  degrees of freedom can be exploited to optimize some system performances. The present section proposes a *maximum torque per ampere* (MTPA) strategy to compute the references currents set  $\mathbf{i}^*$  to be tracked.

### 7.2.1 MTPA problem formulation

Similarly to how it has been done in Section 6.2, the proposed algorithm is aimed at the minimization of an overall instantaneous *root mean square* (RMS) current for the whole machine, which is defined as in (6.12) to be:

$$I_{RMS} = \|\mathbf{i}\| = \sqrt{\mathbf{i}^T \cdot \mathbf{i}} = \sqrt{\sum_{k=1}^n i_k^2} \quad (7.14)$$

Then, considering (7.4) and (7.5), the proposed MTPA strategy can be formalized as the constrained optimization problem<sup>2</sup>:

$$\min_{\mathbf{i}} \{\mathbf{i}^T \cdot \mathbf{i}\} \quad \text{subject to} \quad \begin{cases} \frac{1}{2} \cdot \mathbf{i}^T \cdot \mathbf{L}' \cdot \mathbf{i} = T_{em}^* \\ \mathbf{M}^T \cdot \mathbf{i} = \mathbf{0} \end{cases} \quad (7.15)$$

The resolution of the problem (7.15) could in theory be addressed with the same approach adopted in Section 6.2. However, while the torque development requirement in (6.14) was a linear function of the currents set  $\mathbf{i}$ , the same requirement in (7.15) is a

<sup>2</sup> The explicit dependence of  $\mathbf{L}'$  on the rotor position  $\theta$  has been omitted for notation compactness.

quadratic function of  $\mathbf{i}$ . This means that the problem (7.15) is a minimization of a quadratic function subject, at the same time, to both linear and quadratic constraints. This makes its analytical resolution much more challenging.

As will be shown, a drastic simplification is obtained by reformulating the problem (7.15) in the configuration space. Considering (7.7), and since  $\mathbf{U}_f^T \cdot \mathbf{U}_f = \mathbf{I}$ , the RMS current (7.14) can be rewritten as:

$$I_{RMS} = \|\mathbf{i}\| = \sqrt{\mathbf{i}^T \cdot \mathbf{i}} = \sqrt{\mathbf{i}_f^T \cdot \mathbf{U}_f^T \cdot \mathbf{U}_f \cdot \mathbf{i}_f} = \sqrt{\mathbf{i}_f^T \cdot \mathbf{i}_f} = \|\mathbf{i}_f\| \quad (7.16)$$

Moreover, by referring the problem to the set  $\mathbf{i}_f$ , the torque development requirement is given by the similar expression (7.9), while the constraints equation (7.5) is automatically verified.

As a result, the problem (7.15) can be rewritten as:

$$\min_{\mathbf{i}_f} \{\mathbf{i}_f^T \cdot \mathbf{i}_f\} \quad \text{subject to} \quad \frac{1}{2} \cdot \mathbf{i}_f^T \cdot \mathbf{L}'_f \cdot \mathbf{i}_f = T_{em}^* \quad (7.17)$$

The simplification motivated by the fact that, contrarily to the formulation (7.15), the problem (7.17) is a minimization of a quadratic function subject to a single quadratic constraint. Moreover, it does not depend on the  $n \times 1$  set  $\mathbf{i}$ , but it is formalized with the reduced order set  $\mathbf{i}_f$ , which is a  $n_f \times 1$  vector (with  $n_f \leq n$ ).

### 7.2.2 MTPA problem resolution

This section is aimed at analytically solving the problem (7.17). For this purpose, the current set  $\mathbf{i}_f$  is decomposed as:

$$\mathbf{i}_f = I_{RMS} \cdot \hat{\mathbf{i}}_f \quad (7.18)$$

Considering (7.16), it can be derived that  $\|\hat{\mathbf{i}}_f\| = \hat{\mathbf{i}}_f^T \cdot \hat{\mathbf{i}}_f = 1$ . This means that  $I_{RMS}$  represents the magnitude of the vector  $\mathbf{i}_f$ , while  $\hat{\mathbf{i}}_f$ , which is a unit vector (i.e., a versor), represents its direction in the  $n_f$ -dimensional space  $\mathbb{R}^{n_f}$ .

For a given unit vector  $\hat{\mathbf{i}}_f$ , the corresponding current  $I_{RMS}$  can be immediately found<sup>3</sup> by the torque development requirement in (7.17). Indeed, on the condition that the quadratic form ( $\hat{\mathbf{i}}_f^T \cdot \mathbf{L}'_f \cdot \hat{\mathbf{i}}_f$ ) has the same sign of the reference torque  $T_{em}^*$ , the current RMS magnitude is:

$$I_{RMS} = \sqrt{\frac{2 \cdot T_{em}^*}{\hat{\mathbf{i}}_f^T \cdot \mathbf{L}'_f \cdot \hat{\mathbf{i}}_f}} \quad (7.19)$$

Therefore, considering (7.19) it can be deduced that:

- if  $T_{em}^* > 0$ , the minimization of  $I_{RMS}$  is obtained by maximizing the denominator ( $\hat{\mathbf{i}}_f^T \cdot \mathbf{L}'_f \cdot \hat{\mathbf{i}}_f$ ) (which must be positive), and
- if  $T_{em}^* < 0$ , the minimization of  $I_{RMS}$  is obtained by minimizing the denominator ( $\hat{\mathbf{i}}_f^T \cdot \mathbf{L}'_f \cdot \hat{\mathbf{i}}_f$ ) (which must be negative).

The maximization or minimization of the quadratic form ( $\hat{\mathbf{i}}_f^T \cdot \mathbf{L}'_f \cdot \hat{\mathbf{i}}_f$ ) can be solved by computing the *eigenvalues* and *eigenvectors* of the matrix  $\mathbf{L}'_f$ . To be more specific, it

<sup>3</sup> Proven in Appendix 9.7.1.

can be proven that<sup>4</sup>:

- if  $T_{em}^* > 0$ , the optimal solution is given by the eigenvector  $\hat{\mathbf{i}}_{f,\max}$  corresponding to the *maximum (positive) eigenvalue*  $\nu_{\max} > 0$  of the matrix  $\mathbf{L}'_f$ , and it results that  $(\hat{\mathbf{i}}_{f,\max}^T \cdot \mathbf{L}'_f \cdot \hat{\mathbf{i}}_{f,\max}) = \nu_{\max}$ , while
- if  $T_{em}^* < 0$ , the optimal solution is given by the eigenvector  $\hat{\mathbf{i}}_{f,\min}$  corresponding to the *minimum (negative) eigenvalue*  $\nu_{\min} < 0$  of the matrix  $\mathbf{L}'_f$ , and it results that  $(\hat{\mathbf{i}}_{f,\min}^T \cdot \mathbf{L}'_f \cdot \hat{\mathbf{i}}_{f,\min}) = \nu_{\min}$ .

Naturally, if  $T_{em}^* = 0$ , it is sufficient to set  $I_{RMS} = 0$  for any unit vector  $\hat{\mathbf{i}}_f$ .

To sum up, the solution to the MTPA algorithm (7.17) is obtained by computing the matrix  $\mathbf{L}'_f = \mathbf{U}_f^T \cdot \mathbf{L}' \cdot \mathbf{U}_f$  and by calculating its maximum and minimum eigenvalues  $\nu_{\max} > 0$  and  $\nu_{\min} < 0$ , and the corresponding unitary-norm eigenvectors  $\hat{\mathbf{i}}_{f,\max}$  and  $\hat{\mathbf{i}}_{f,\min}$ . Once the reference current direction set  $\hat{\mathbf{i}}_f^*$  has been chosen either as  $\hat{\mathbf{i}}_{f,\max}$  or as  $\hat{\mathbf{i}}_{f,\min}$  (depending on the sign of the reference torque  $T_{em}^*$ ), the term  $I_{RMS}$  can be computed via (7.19) and the optimal current set  $\mathbf{i}_f^*$  in the configuration space can be reconstructed via (7.18). Finally, the reference currents set in the phase variable domain, which is the solution to the original problem (7.15), can be found via (7.7) as  $\mathbf{i}^* = \mathbf{U}_f \cdot \mathbf{i}_f^*$ .

However, by combining these last considerations, the solution can also be directly formalized in the phase variable domain. Indeed, considering (7.18), it is possible to define a reference current direction versor in the phase variable domain as  $\hat{\mathbf{i}}^* = \mathbf{U}_f \cdot \hat{\mathbf{i}}_f^*$  and, through (7.19), it can be easily verified that:

$$\hat{\mathbf{i}}_f^{*\text{T}} \cdot \mathbf{L}'_f \cdot \hat{\mathbf{i}}_f^* = (\mathbf{U}_f \cdot \hat{\mathbf{i}}_f^*)^T \cdot \mathbf{L}' \cdot (\mathbf{U}_f \cdot \hat{\mathbf{i}}_f^*) = \hat{\mathbf{i}}^{*\text{T}} \cdot \mathbf{L}' \cdot \hat{\mathbf{i}}^* \quad (7.20)$$

Therefore, the optimal solution to the MTPA problem (7.15) is:

$$\mathbf{i}^* = \sqrt{\frac{2 \cdot T_{em}^*}{\hat{\mathbf{i}}^{*\text{T}} \cdot \mathbf{L}' \cdot \hat{\mathbf{i}}^*}} \cdot \hat{\mathbf{i}}^*, \quad \text{with} \quad \hat{\mathbf{i}}^* = \begin{cases} \mathbf{U}_f \cdot \hat{\mathbf{i}}_{f,\max} & \text{if } T_{em}^* \geq 0 \\ \mathbf{U}_f \cdot \hat{\mathbf{i}}_{f,\min} & \text{if } T_{em}^* < 0 \end{cases} \quad (7.21)$$

The schematic block diagram of this algorithm is represented in Fig. 7.2. Note that, since  $\mathbf{L}'$  periodically varies with the rotor position  $\theta$ , also  $\hat{\mathbf{i}}_{f,\max}$  and  $\hat{\mathbf{i}}_{f,\min}$  (and, consequently,  $\hat{\mathbf{i}}^*$ ) should be computed considering the measured value of  $\theta$ .

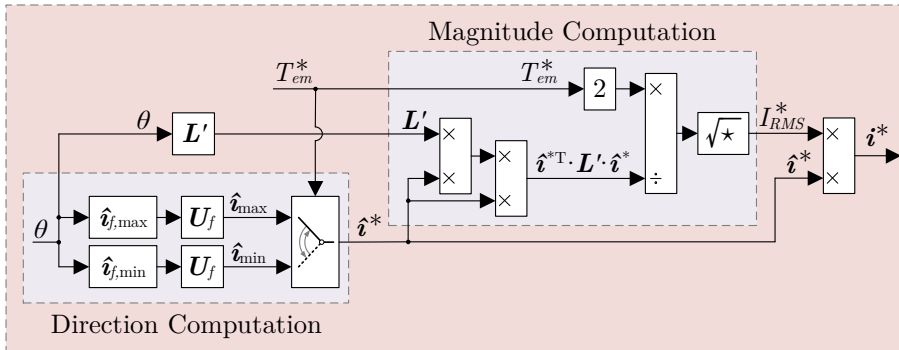


Fig. 7.2 – Functional block scheme of the MTPA algorithm.

<sup>4</sup> Proven in Appendix 9.7.2.

### 7.2.3 MTPA solution properties

Several interesting properties can be observed from inspection of the MTPA problem (7.15) and of the corresponding solution (7.21).

The first property which can be immediately observed from (7.15) is that, since both the objective function and the constraint are quadratic in  $\mathbf{i}$ , the solution to (7.17) is not unique. Indeed, opposite sets of phase currents develop the same torque. This is coherent with (7.21), considering that opposite eigenvectors relate to the same eigenvalue. This aspect, if not properly considered in a real-time implementation, might generate sharp transitions in the reference currents set  $\mathbf{i}^*$  to be tracked. However, this inconvenience is easy to neutralize by conditioning the reference unit vector  $\hat{\mathbf{i}}^*$  to have a smooth evolution in time. The easiest way for this implementation is to evaluate the scalar product  $\hat{\mathbf{i}}^*(t_k)^T \cdot \hat{\mathbf{i}}(t_{k-1})$  between the reference vector  $\hat{\mathbf{i}}^*(t_k)$  computed at a given time instant and the reference vector  $\hat{\mathbf{i}}(t_{k-1})$  computed at a previous time instant. If this scalar product is negative, this indicates that a sharp transition would occur, and it can be prevented by just replacing  $\hat{\mathbf{i}}^*(t_k)$  with  $-\hat{\mathbf{i}}^*(t_k)$ .

Another interesting aspect is that, contrarily to the MTPA for PMSMs derived in Section 6.2, the reference currents given by (7.21) are proportional to the square root of the reference electromagnetic torque  $T_{em}^*$ . As a consequence, the overall machine stator losses (which depend on the term  $I_{RMS}^2$ ) are proportional to the torque  $T_{em}^*$ . This means that, to double the torque developed by the machine, the overall losses also double, but the currents only need to be increased by  $\sqrt{2} \cong 1.41$  times.

However, the RMS current of (7.21) may not be constant with  $\theta$  and may not be the same for positive or negative reference torques. Indeed, it is easy to prove that, with the optimal reference currents, the RMS current is equal to<sup>5</sup>:

$$I_{RMS} = \begin{cases} \sqrt{2 \cdot T_{em}^* / \nu_{\max}} & \text{if } T_{em}^* \geq 0 \\ \sqrt{2 \cdot T_{em}^* / \nu_{\min}} & \text{if } T_{em}^* < 0 \end{cases} \quad (7.22)$$

Since the matrix  $\mathbf{L}'_f = \mathbf{U}_f^T \cdot \mathbf{L}' \cdot \mathbf{U}_f$  varies with the rotor position, also its corresponding eigenvalues  $\nu_{\max}$  and  $\nu_{\min}$  are, in general, periodic functions of  $\theta$ . In case they are not constant, according to (7.22), the overall RMS current needed to develop the same electromagnetic torque  $T_{em}^*$  would also depend on  $\theta$ , meaning that some rotor positions would be favourable for the torque development than other rotor positions. Moreover, in general, it may also happen that  $|\nu_{\max}| \neq |\nu_{\min}|$ . In this case, it would mean that the machine has (at least locally) a preferred spin direction, which would require a smaller overall RMS current to develop the same spinning torque.

The average losses in a full rotor cycle are given by:

$$P_R = \sum_{k=1}^n R \cdot i_k^2 \quad (7.23)$$

Similarly to the corresponding considerations done in Section 6.2, some problems may arise when the denominator ( $\hat{\mathbf{i}}^{*T} \cdot \mathbf{L}' \cdot \hat{\mathbf{i}}^*$ ) in (7.21) gets close to zero (i.e., when  $\nu_{\max}$

<sup>5</sup> Proven in Appendix 9.7.3.

or  $\nu_{\min}$  have a small absolute value). Indeed, in this case, the phase currents required to develop a desired electromagnetic torque may become very high and be unfeasible for real applications. This phenomenon may happen in case of multiple faults on the machine phases but, again, it can be prevented by limiting the phase currents computed via (7.21) within a chosen feasible range, chosen for safety reasons.

Finally, for a real-time implementation of (7.21), the computation of the directions  $\mathbf{U}_f \cdot \hat{\mathbf{i}}_{f,\max}$  and  $\mathbf{U}_f \cdot \hat{\mathbf{i}}_{f,\min}$  can either be entirely executed online through a fast eigenvalue computation algorithm (e.g., with the inverse iteration method, Rayleigh quotient iteration method, etc...) or can be partially executed offline or during an algorithm initialization routine, and then implemented in real-time with an interpolation algorithm (e.g., through a Fourier-based interpolation).

## 7.3 Current controller

Once the reference currents set  $\mathbf{i}^*$  has been computed, the control algorithm must find a set of reference converter voltages  $\mathbf{u}^*$  to drive the measured currents set  $\mathbf{i}$  towards  $\mathbf{i}^*$ . The same strategy previously presented in Chapter 6 is here applied. It is based on a *decoupling algorithm* (derived as in Section 6.3) and on a *decoupled controller* (chosen as in Section 6.4).

### 7.3.1 Decoupling current control algorithm

The basic idea of the proposed decoupling algorithm is the same described in Section 6.3.1. Indeed, by comparing the reduced-order model (7.8) obtained in Section 7.1.2 for a generic multiphase SynRM with the corresponding model (6.8) obtained in Section 6.1.2 for a generic PMSM, it can be observed that they have the same structure, the only difference being the dependence of  $\mathbf{L}_f$  by  $\theta$ .

Then, as done in Section 6.3, the VSI voltages set  $\mathbf{u}^*$  which leads to the decoupling of the phase currents dynamics can be computed as:

$$\mathbf{u}^* = \mathbf{u}_{opt}^* + \mathbf{u}_0^* \quad (7.24)$$

where  $\mathbf{u}_{opt}^*$  and  $\mathbf{u}_0^*$  are respectively given by:

$$\begin{aligned} \mathbf{u}_{opt}^* &= \mathbf{N}_f^\dagger \cdot \mathbf{v}_f^* = \mathbf{N}_f^\dagger \cdot [\mathbf{L}_f(\theta) \cdot \delta \mathbf{i}_f^* + \mathbf{R}_f \cdot \mathbf{i}_f + \mathbf{e}_f] = \\ &= [(\mathbf{U}_f^T \cdot \mathbf{N})^\dagger \cdot \mathbf{U}_f^T] \cdot [\mathbf{L}(\theta) \cdot \delta \mathbf{i}^* + \mathbf{R} \cdot \mathbf{i} + \mathbf{e}] \end{aligned} \quad (7.25)$$

$$\begin{aligned} \mathbf{u}_0^* &= (\mathbf{I} - \mathbf{N}_f^\dagger \cdot \mathbf{N}_f) \cdot \mathbf{u}_{off}^* = \\ &= [\mathbf{I} - (\mathbf{U}_f^T \cdot \mathbf{N})^\dagger \cdot (\mathbf{U}_f^T \cdot \mathbf{N})] \cdot \mathbf{u}_{off}^* \end{aligned} \quad (7.26)$$

with  $\dagger$  denoting the Moore-Penrose pseudo-inverse,  $\delta \mathbf{i}^* = \mathbf{U}_f \cdot \delta \mathbf{i}_f^*$  being a  $n \times 1$  references derivatives currents set, and  $\mathbf{u}_{off}^*$  being a  $m \times 1$  offset vector for the VSI leg voltages (which is the generalization of a standard common-mode voltage injection).

The schematic block diagram of this decoupling algorithm is depicted in Fig. 7.3. It is perfectly identical to the same diagram previously shown in Fig. 6.7, with the only differences being in the  $\theta$ -dependence of  $\mathbf{L}$ . Again, in case  $\mathbf{N} = \mathbf{I}$ , the expression of the

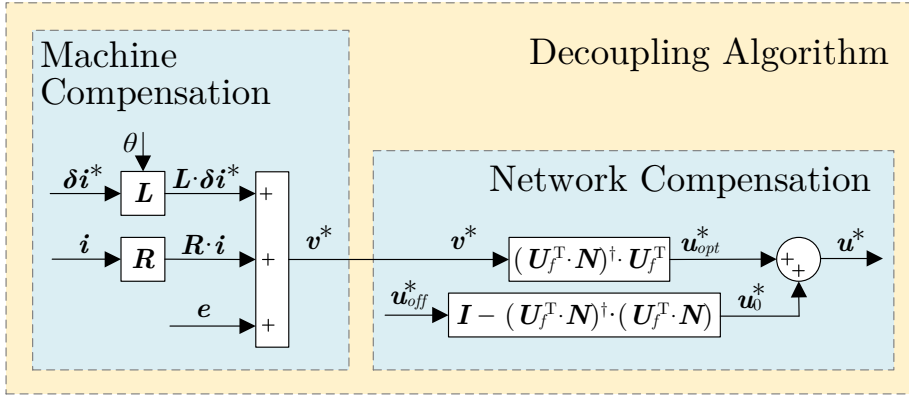


Fig. 7.3 – Functional block scheme of the decoupling algorithm.

optimal solution is simplified by considering that  $[(U_f^T \cdot N)^\dagger \cdot U_f^T] = (U_f \cdot U_f^T)$  in (7.25) and  $[I - (U_f^T \cdot N)^\dagger \cdot (U_f^T \cdot N)] = (U_c \cdot U_c^T)$  in (7.26), and the corresponding block diagram would be the same depicted in Fig. 6.8.

### 7.3.2 Decoupled current control algorithm

Once the decoupling control algorithm is executed, the dynamics of the machine phase currents are independent of one another and are governed by the simple dynamical relation:

$$\frac{di}{dt} = \delta i^* \Leftrightarrow \frac{di_k}{dt} = \delta i_k^* \quad (\text{with } k = 1, \dots, n) \quad (7.27)$$

As done in Section 6.4, each term  $\delta i_k^*$  can be properly computed by a single-input/single-output controller acting on the tracking error  $i_k^* - i_k$ .

To guarantee a perfect steady-state tracking of periodic references synchronized with the machine angular speed, the proposed solution is again a Proportional-Integral-Resonant controller, with multiple resonant actions synchronized with multiple integers of  $\omega$ . Its transfer function in the Laplace domain has been previously given in (6.43) and is here repeated:

$$\mathcal{C}(s) = \frac{\mathcal{L}[\delta i_k^*](s)}{\mathcal{L}[i_k^* - i_k](s)} = K_P + \frac{K_I}{s} + \sum_{h=1}^{n_{res}} K_{R,h} \cdot \frac{s}{s^2 + \omega_h^2} \quad (7.28)$$

where:

- $K_P$  is the *proportional controller constant*,
- $K_I$  is the *integral controller constant*, and
- $K_{R,h}$  is the *h-th resonant controller constant*.

The same considerations done in Section 6.4 are also valid for this case.

Additional details regarding the implementation of the resonant controller actions are reported in Appendix 9.1.1.

## 7.4 Overall drive control algorithm

The overall structure of the proposed drive control algorithm is schematically represented in Fig. 7.4. As can be noted, it takes the same structure of the PMSM controller previously described in Section 6.5 and represented in Fig. 6.10.

First, the “*Speed Controller*”, here implemented as a simple PI regulator, compares the reference speed  $\omega^*$  with the measured machine speed  $\omega$ , and computes the reference electromagnetic torque  $T_{em}^*$  to be applied.

Next, the “*Inductances and Back-EMFs Estimation*” block is executed to compute the matrices  $\mathbf{L}(\theta)$  and  $\mathbf{L}'(\theta) = \partial\mathbf{L}/\partial\theta$  from the measured rotor position  $\theta$ . The same block also computes the motional-induced back-EMFs vector  $\mathbf{e} = \omega \cdot \mathbf{L}'(\theta) \cdot \mathbf{i}$  (which is used in the decoupling algorithm).

The “*MTPA*” block is then executed to find the references currents set  $\mathbf{i}^*$  as described in Section 7.2. The schematic block diagram of the MTPA algorithm has been formerly represented in Fig. 7.2. As also previously mentioned, the eigenvalues and eigenvectors of the matrix  $\mathbf{L}'_f(\theta) = \mathbf{U}_f^T \cdot \mathbf{L}'(\theta) \cdot \mathbf{U}_f$  can either be computed in real-time with a fast eigenvalue research algorithm or can be calculated during an algorithm initialization and then reconstructed from offline computed coefficients (e.g., through the coefficients of their Fourier decomposition).

The “*Current Controller*” block is finally executed. The Proportional-Integral-Resonant (PIR) feedback controller compares the reference currents set  $\mathbf{i}^*$  with the actual currents set  $\mathbf{i}$  and, through this error, it computes the reference derivative currents set  $\delta\mathbf{i}^*$  to be applied. The *decoupling algorithm* of (7.24)-(7.26) (whose functional block diagram has been previously represented in Fig. 7.3) is then executed to find the reference voltages set  $\mathbf{u}^*$ , which is finally applied through a pulse width modulation algorithm.

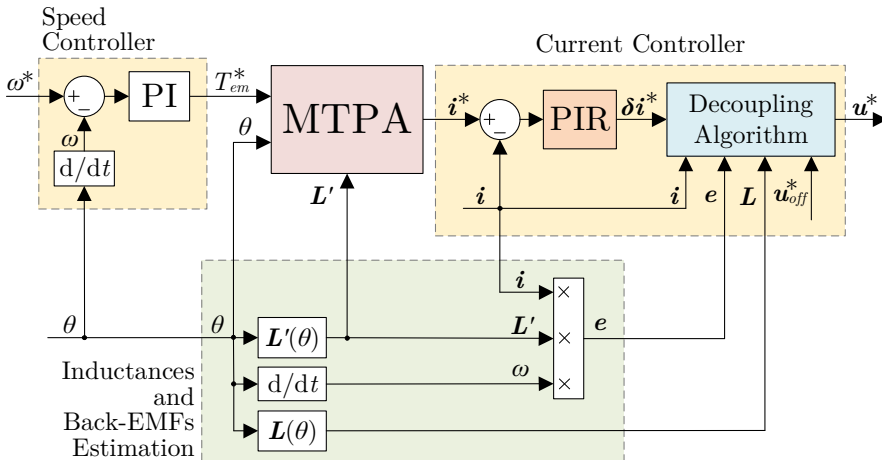


Fig. 7.4 – Functional block diagram of the proposed controller.

## 7.5 Experimental setup

The proposed control algorithm has been experimentally validated with the machine depicted in Fig. 7.5.

### 7.5.1 Electrical machine

The electrical machine under analysis is a five-phase synchronous reluctance machine with two pole pairs<sup>6</sup>.

The machine has been obtained from an originally three-phase induction machine. The stator has 40 slots and the winding have been arranged in a way that the magnetic axes of two consecutive phases are mutually shifted by  $72^\circ$  electrically (i.e.,  $36^\circ$  mechanically). The variable reluctance rotor has been obtained by cutting the original squirrel-cage rotor to realize four salient poles. A geometric representation of the machine is shown in Fig. 7.6. The main geometrical data are reported in Table 7.I. The terminals of all the phase windings are available externally.

The machine winding resistances have been measured in DC. They are identical for all five phases and equal to  $R = 1.8 \Omega$ .

The machine inductances parameters have been found in the phase variable domain with the following procedure. Phase 1 of the machine has been supplied with a sinusoidal

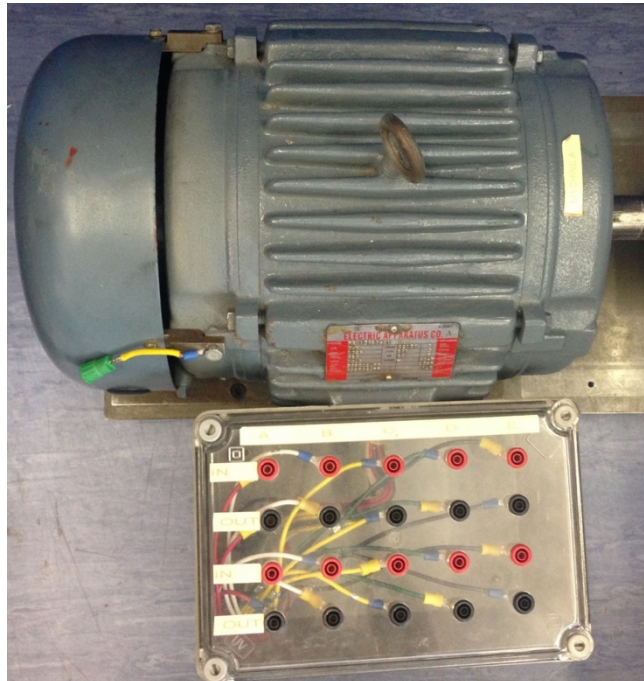


Fig. 7.5 – Five-phase synchronous reluctance machine under analysis.

<sup>6</sup> Additional information regarding the design of this machine can be found in [163], [164].

voltage with a peak value of 20 V and a 50 Hz frequency, while all the other phases have been left in open-circuit. The current in phase 1 and the induced voltages in all the other phases  $\{2,3,4,5\}$  have been measured at blocked rotor for different positions of the electrical angle  $\theta_{el} = 2\theta$  (the position at  $0^\circ$  has been considered to be coincident with the magnetic axis of phase 1). From the voltage and current measurements, it has been possible to estimate the fluxes induced in the machine phases:

$$\begin{cases} \lambda_1(t) = \int (v_1(t) - R \cdot i_1(t)) dt \\ \lambda_k(t) = \int v_k(t) dt, \quad (\text{with } k = 2,3,4,5) \end{cases} \quad (7.29)$$

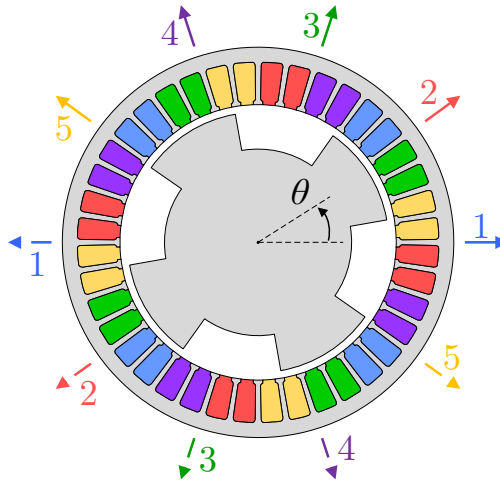


Fig. 7.6 – Geometric representation of the five-phase synchronous reluctance machine under analysis.

Table 7.I – SYNRM GEOMETRICAL DATA.

Pole pairs	2	
Internal stator diameter	127	mm
External stator diameter	180	mm
Stator slots depth	20	mm
Number of wires per slot	54	
Number of turns per phase	216	
Minimum rotor diameter	86	mm
Maximum rotor diameter	126	mm
Salient poles height	20	mm
Minimum air-gap width	0.5	mm
Maximum air-gap width	20.5	mm
Axial length	101.6	mm

All the fluxes have been plotted with respect to the machine current  $i_1(t)$ , in a way to obtain different hysteresis loops for each rotor position under test. The results are depicted in Fig. 7.7.

Then, the parameters  $L_{k,1}(\theta_{el})$  (with  $k = 1, \dots, 5$ ) of the inductances matrix  $\mathbf{L}(\theta_{el})$  have been found with a linear regression procedure as the slope of the linear characteristics  $\lambda/i$  which better approximate the different hysteresis loops. Finally, considering the machine symmetry, the values of the functions  $L_{k,1}(\theta_{el})$  have been extrapolated with an additional regression procedure based on the computation of the lowest even-order harmonics in  $\theta_{el}$ . The results of this parameter identification procedure, considering the harmonics of order 0, 2, 6, 10 and 14, are shown in Fig. 7.8, together with the corresponding values  $L'_{k,1}(\theta_{el})$  of the inductances derivative matrix. The corresponding numerical parameters are summarized in Table 7.II. It is worth recalling that, because of the machine symmetry,  $L_{4,1}(\theta_{el}) = L_{3,1}(-\theta_{el})$  and  $L_{5,1}(\theta_{el}) = L_{2,1}(-\theta_{el})$ .

As can be noted, the self-inductance  $L_{1,1}(\theta_{el})$  is always positive. Its maximum values are obtained for  $\theta_{el} = 0^\circ$  and  $\theta_{el} = 180^\circ$  (which are the positions of minimum reluctance). Its minimum values are instead obtained for  $\theta_{el} = \pm 90^\circ$  (which are the positions of maximum reluctance). The mutual inductances functions  $L_{3,1}(\theta_{el})$  and  $L_{4,1}(\theta_{el})$  have a mirrored symmetry and are always negative (coherently with the negative slopes of the corresponding hysteresis loops in Fig. 7.7).

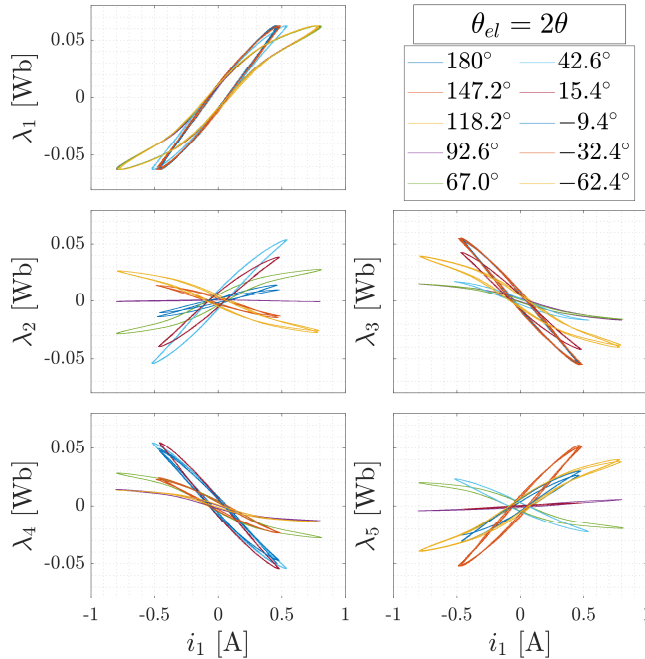


Fig. 7.7 – Hysteresis loops obtained for different rotor positions by supplying the phase 1 with all the other phases left in open circuit.

The functions  $L_{2,1}(\theta_{el})$  and  $L_{5,1}(\theta_{el})$  also have a mirrored symmetry, but show both positive and negative values (coherently with the slope change in the corresponding hysteresis loops of Fig. 7.7). Given the machine symmetry, all the other inductances parameters  $L_{h,k}(\theta_{el})$  (with  $h = 2,3,4,5$ ) are obtained by just shifting the functions  $L_{1,k}(\theta_{el})$  by  $72^\circ$ ,  $144^\circ$ ,  $216^\circ$  and  $288^\circ$ . The same is also true for the matrix  $\mathbf{L}'(\theta_{el})$ .

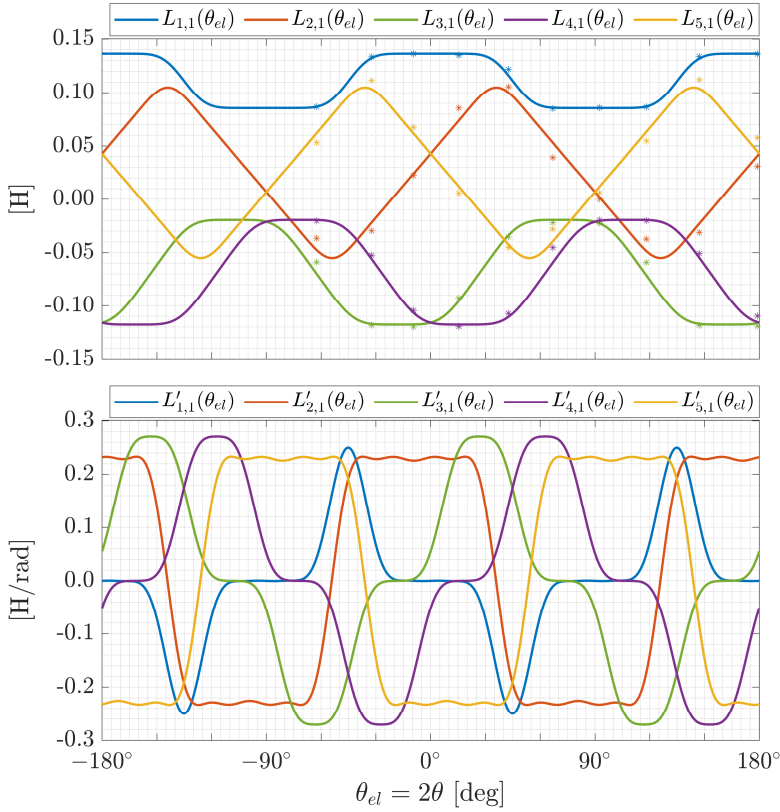


Fig. 7.8 – Parameters of  $\mathbf{L}(\theta_{el})$  and of  $\mathbf{L}'(\theta_{el})$  of the examined SynRM.

Table 7.II – SYNRM EXTRAPOLATED INDUCTANCES HARMONICS.

Inductance Function	Harmonic order (varying with $\theta_{el}$ )				
	0	2	6	10	14
$L_{1,1}(\theta_{el})$	111 mWb -	30.9 mWb $0^\circ$	6.9 mWb $180^\circ$	1.8 mWb $0^\circ$	0.3 mWb $180^\circ$
$L_{2,1}(\theta_{el})$	24.9 mWb -	71.5 mWb $-72^\circ$	6.6 mWb $144^\circ$	1.5 mWb $0^\circ$	0.4 mWb $-144^\circ$
$L_{3,1}(\theta_{el})$	-68.6 mWb -	55.5 mWb $-144^\circ$	6.0 mWb $108^\circ$	0.7 mWb $180^\circ$	0.3 mWb $72^\circ$

## 7.5.2 Power electronics converter

The machine has been supplied by one of the multiphase converters previously described in Section 6.6.2. For this application, the DC-bus voltage has been set to  $V_{DC} = 600$  V. Again, the VSI has been operated with a PWM algorithm working with a modulation frequency of 10 kHz.

## 7.5.3 Interconnection network

Similarly to the experiments of Chapter 6, each converter leg output node is directly connected to one machine phase positive terminal. As a result, the network interconnection matrix  $\mathbf{N}$  is always the  $5 \times 5$  identity matrix. On the contrary, the machine negative terminals have been connected differently according to the analysed scenario, meaning that the constraints matrix  $\mathbf{M}$  is not always the same.

## 7.5.4 Controller board and algorithm implementation

The proposed control algorithm has been implemented with the same Plexim RT Box 1 platform described in Section 6.6.4. The control is executed with a 10 kHz sampling rate and it is synchronized with the converter PWM period. The same LEM transducers have also been used to measure the five machine phase currents. The speed and position have instead been measured through a resolver integrated into the machine, whose signals have been properly adapted to the RT Box platform through a Resolver/Encoder interface.

The implemented speed controller has a standard PI-based structure. For safety reasons, the reference torque  $T_{em}^*$  computed by the speed controller has been limited to a feasible range of  $\pm 15$  Nm.

Again, as for the analogous control algorithm of Chapter 6, the constraint matrix  $\mathbf{M}$  has been provided for each testing scenario, and an offline initialization routine has been configured to compute the corresponding configuration matrices  $\mathbf{U}_f$  and  $\mathbf{U}_c$ .

The same initialization routine has been used to implement the MTPA algorithm (7.21). The matrix  $\mathbf{L}'_f(\theta) = \mathbf{U}_f^T \cdot \mathbf{L}'(\theta) \cdot \mathbf{U}_f$  and the corresponding eigenvectors  $\hat{\mathbf{i}}_{f,\max}$  and  $\hat{\mathbf{i}}_{f,\min}$  have been numerically computed for multiple rotor positions. Then, the corresponding directions  $\hat{\mathbf{i}}_{\max} = \mathbf{U}_f \cdot \hat{\mathbf{i}}_{f,\max}$  and  $\hat{\mathbf{i}}_{\min} = \mathbf{U}_f \cdot \hat{\mathbf{i}}_{f,\min}$  have been calculated, and have been decomposed as Fourier series in  $\theta_{el}$ . The resulting coefficients have been stored in the RT Box platform memory, and have been used to recompute the optimal reference directions of (7.21) in real-time.

For safety reasons, all the phase currents of the reference set  $\mathbf{i}^*$  have been limited to the feasibility range of  $\pm 8.5$  A before the execution of the current controller.

The decoupling algorithm has been executed with the estimated inductances parameters given in Section 7.5.1. The feedback current controller has been implemented in the phase variable domain with the transfer function (6.43). The implemented resonant actions have been chosen for all the odd-order multiple integers of the machine electrical speed  $\omega_{el} = 2\omega$ , up to the 19<sup>th</sup> harmonic. Finally, the offset vector  $\mathbf{u}_{off}^*$  for the common-mode voltage injection of the VSI has been set to half of the DC-bus voltage (i.e., 300 V) for all the five converter legs.

### 7.5.5 Mechanical load

The five-phase SynRM has been mechanically coupled to a DC machine, used for loading. The overall group inertia has been estimated to be  $J_{eq} \cong 50 \cdot 10^{-3} \text{ kg m}^2$ , while the overall friction coefficient has been estimated to be  $F_{eq}(\omega) \cong 6 \cdot 10^{-3} \text{ (Nm)/(rad/s)}$ .

The armature of the DC machine has been connected to an external  $20 \Omega$  resistor, chosen in a way that the machine develops a loading torque  $T_{load}$  proportional to the speed  $\omega$  and is such that  $T_{load} \cong 2 \text{ Nm}$  when the machine speed is equal to 500 rpm.

An additional  $20 \Omega$  resistor has been connected in parallel to the DC machine armature terminals through a controllable contactor. In this way, when the contactor is closed, the equivalent resistance connected at the DC machine terminals is reduced to  $10 \Omega$ , and the applied loading torque is doubled (i.e.,  $T_{load} \cong 4 \text{ Nm}$  when the machine speed is 500 rpm).

A Datum Electronics M425 Torque transducer has been positioned between the SynRM and the DC machine rotor shafts. This torque meter has been used to measure the torque  $T_m$  developed at the joint between the two machines.

## 7.6 Experimental results

To validate the proposed algorithm and to emphasize its generality and flexibility, it has been tested in several different scenarios, which are discussed and analysed in this section.

For each scenario, the constraint matrix  $\mathbf{M}$  and the configuration matrix  $\mathbf{U}_f$  are explicitly shown<sup>7</sup>. However, similarly to the results of Chapter 6, it is worth recalling that for a real-time implementation only  $\mathbf{M}$  is required, and that  $\mathbf{U}_f$  is automatically computed during the algorithm initialization.

### 7.6.1 MTPA algorithm validation

This testing scenario is aimed at giving an implementation example of the MTPA strategy developed in Section 7.2 and compares it with other current references computation algorithms.

The test refers to the single-star configuration depicted in Fig. 7.9. To clarify the working principle of the proposed MTPA algorithm, it is here explained for the considered case study.

The constraints and configuration matrices for the analysed setup are:

$$\mathbf{M} = \begin{bmatrix} 1 \\ 1 \\ 1 \\ 1 \\ 1 \end{bmatrix}, \quad \mathbf{U}_f = \begin{bmatrix} -0.45 & -0.45 & -0.45 & -0.45 \\ 0.86 & -0.14 & -0.14 & -0.14 \\ -0.14 & 0.86 & -0.14 & -0.14 \\ -0.14 & -0.14 & 0.86 & -0.14 \\ -0.14 & -0.14 & -0.14 & 0.86 \end{bmatrix}$$

Since the configuration space has dimension  $n_f = n - n_c = 5 - 1 = 4$ , the matrix

<sup>7</sup> Similarly to Section 6.7, the configuration matrix has been found through the “`svd`” command in Matlab. All the parameters reported here are rounded to the second decimal unit.

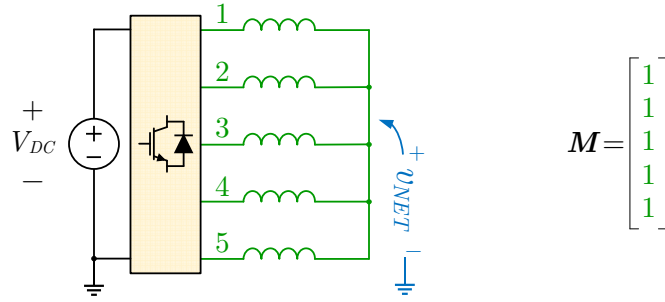


Fig. 7.9 – Schematic diagram and constraint matrix for the healthy configuration.

$\mathbf{L}'_f = \mathbf{U}_f^T \cdot \mathbf{L}' \cdot \mathbf{U}_f$  used in the MTPA algorithm is a  $4 \times 4$  symmetric matrix, whose coefficients are periodic functions of the rotor electrical position  $\theta_{el} = 2\theta$ . For each rotor position, the matrix has 4 unitary-norm linearly independent eigenvectors. In the initialization routine, these eigenvectors have been numerically evaluated for different rotor positions, in a way to find the ones corresponding to the maximum and minimum eigenvalues of  $\mathbf{L}'_f$ . The left subplot of Fig. 7.10 shows, in the whole range  $[-180^\circ; +180^\circ]$  of  $\theta_{el}$ , the eigenvalues of  $\mathbf{L}'_f$ , computed numerically. The maximum and minimum eigenvalues  $\nu_{\max}$  and  $\nu_{\min}$  are highlighted as thick solid lines. The corresponding eigenvector directions  $\hat{\mathbf{i}}_{f,\max}$  and  $\hat{\mathbf{i}}_{f,\min}$ , are shown in the right subplots of Fig. 7.10.

The optimal current vectors in the phase variable domain have been computed as  $\hat{\mathbf{i}}_{\max} = \mathbf{U}_f \cdot \hat{\mathbf{i}}_{f,\max}$  and  $\hat{\mathbf{i}}_{\min} = \mathbf{U}_f \cdot \hat{\mathbf{i}}_{f,\min}$ , coherently with (7.21), while the corresponding RMS currents, computed for constant positive and negative reference torques, have been computed as in (7.22). They are depicted in Fig. 7.11 in the whole range  $[-180^\circ, +180^\circ]$  and have been normalized by the square root of  $T_{em}^*$ .

Finally, the optimal phase currents set has been computed as  $\mathbf{i}^* = I_{RMS} \cdot \hat{\mathbf{i}}^*$ . The

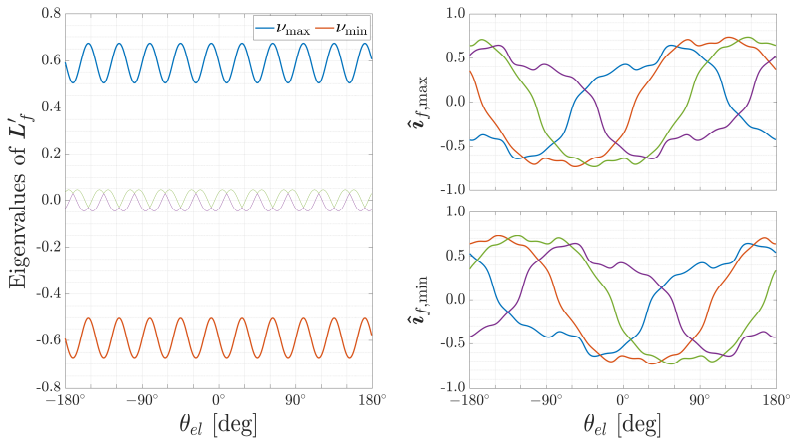


Fig. 7.10 – Eigenvalues of  $\mathbf{L}'_f$  (left) and eigenvectors  $\hat{\mathbf{i}}_{f,\max}$  and  $\hat{\mathbf{i}}_{f,\min}$  (right) in the whole range  $[-180^\circ, +180^\circ]$  of  $\theta_{el}$  for the machine healthy configuration.

corresponding waveforms and harmonic spectra are depicted in Fig. 7.12 for both positive and negative reference torques, once again normalized by  $\sqrt{T_{em}^*}$ .

From the analysis of these results, it is possible to clarify many properties of the MTPA solution explained in Section 7.2.3.

First, it can be seen in Fig. 7.10 that the eigenvalue  $\nu_{\max}$  is always positive, and that the eigenvalue  $\nu_{\min}$  is always negative. However, they are not constant with  $\theta_{el}$  but oscillate with a  $10\theta_{el}$  periodicity. As a consequence, the corresponding RMS currents  $I_{RMS}$ , depicted in Fig. 7.11, show the same  $10\theta_{el}$  periodicity, coherently with (7.22).

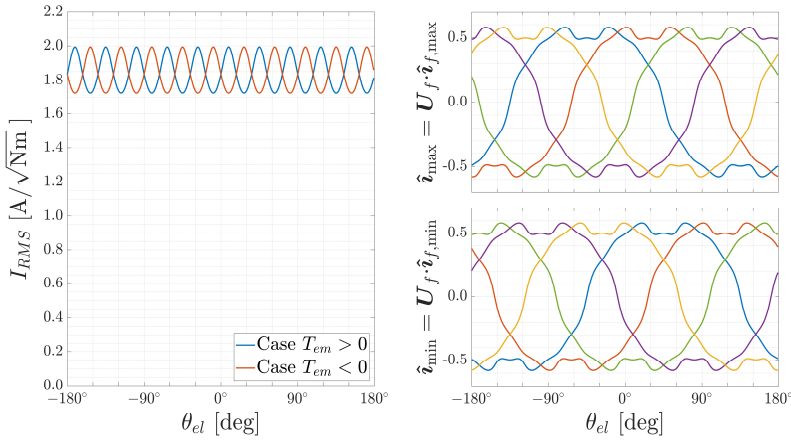


Fig. 7.11 – Overall machine RMS current (left) and optimal phase current vectors  $\hat{i}_{\max} = U_f \cdot \hat{i}_{f,\max}$  and  $\hat{i}_{\min} = U_f \cdot \hat{i}_{f,\min}$  (right) in the whole range  $[-180^\circ, +180^\circ]$  of  $\theta_{el}$  for the machine healthy configuration.

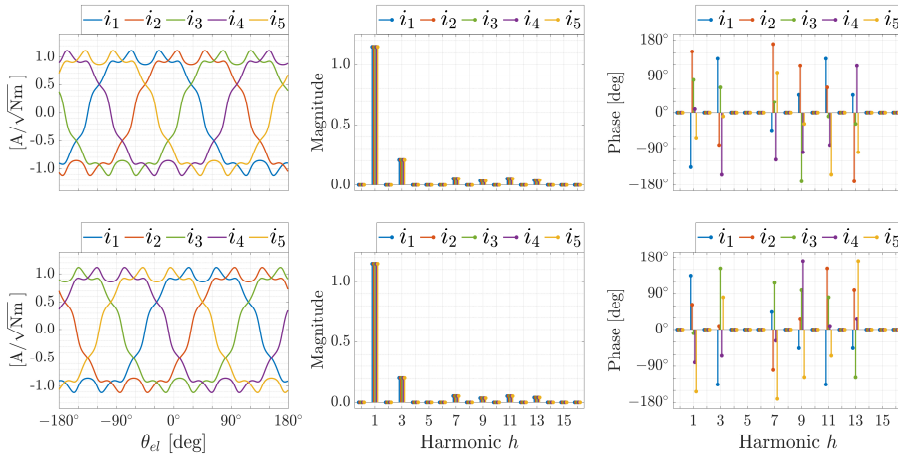


Fig. 7.12 – Optimal phase currents waveforms and harmonic spectra in the healthy machine configuration: (top) Positive reference torque  $T_{em}^* > 0$ ; (bottom) Negative reference torque  $T_{em}^* < 0$ .

These oscillations mean that, in different rotor positions, the RMS current required to generate the same electromagnetic torque may be different. As an example, to develop a torque of +1 Nm, when  $\theta_{el} = 0^\circ$ , the required RMS current is around 1.8 A, when  $\theta_{el} = +9^\circ$ , the required RMS current is around 2.0 A and when  $\theta_{el} = -9^\circ$ , the required RMS current is around 1.7 A.

Since  $|\nu_{\max}| \neq |\nu_{\min}|$ , in different rotor positions, opposite torque signs may require different RMS currents. For example, when  $\theta_{el} = 9^\circ$ , the development of  $T_{em}^* = +1$  Nm requires an overall equivalent RMS current of around 2.0 A, while the development of  $T_{em}^* = -1$  Nm requires an overall equivalent RMS current of around 1.7 A, indicating that this is a (locally) preferred spin direction. However, on average in a full rotor cycle, this local inequality is neutralized.

Finally, from Fig. 7.12 it can be seen that the reference currents are highly non-sinusoidal, and display many non-negligible odd-order harmonics. However, coherently with the five-phase machine symmetry, all the phase currents have the same waveform and are just mutually shifted from one another by  $72^\circ$ . Given the symmetry, the fifth harmonics (and their multiple integers) are homopolar components and, therefore, they are absent from the currents spectra. The optimal reference currents required to develop a negative torque have the same waveforms as the currents required to develop a positive torque, and are only mutually shifted by  $90^\circ$  from the first ones.

For the real-time implementation, the current references have been calculated via (7.21), where the versors  $\hat{\mathbf{i}}_{\max} = \mathbf{U}_f \cdot \hat{\mathbf{i}}_{f,\max}$  and  $\hat{\mathbf{i}}_{\min} = \mathbf{U}_f \cdot \hat{\mathbf{i}}_{f,\min}$  are reconstructed from the coefficients of the Fourier decompositions of the waveforms depicted in Fig. 7.11.

To validate the effectiveness of the proposed strategy, it has been experimentally compared with the sole use of sinusoidal currents and with a third-harmonic injection strategy based on the field-oriented analysis developed in [163]–[165]. The test has been executed by considering the steady-state behaviour of the machine at different speeds, while the loading torque has been realized by connecting the DC machine armature terminals to a  $20 \Omega$  resistor.

The experimental results obtained at 500 rpm are shown in Fig. 7.13; the results obtained at 750 rpm are shown in Fig. 7.14, and the results obtained at 1000 rpm are shown in Fig. 7.15. They show, for each of the considered torque control strategies, the machine phase currents  $i_1, \dots, i_5$ , the overall instantaneous RMS current  $I_{RMS}$  computed via (7.14) and the machine angular speed  $\omega$ . The solid lines represent the measured variables, while the black dashed lines represent the corresponding reference currents.

Additional measurements are depicted in Fig. 7.16, Fig. 7.17 and Fig. 7.18, which show (for the speeds of 500 rpm, 750 rpm and 1000 rpm, respectively) the oscilloscope captures of the currents  $i_1$  (dark blue traces),  $i_2$  (light blue traces), and  $i_3$  (magenta traces), and the electromagnetic torque  $T_m$  applied at the rotor shaft (green traces).

The difference between the three examined torque control strategies is evident in the waveforms of the phase currents, and it also affects the corresponding waveforms of  $I_{RMS}$ . Indeed, considering the proposed MTPA algorithm, it can be seen that the highly non-sinusoidal current waveforms (based on the references of Fig. 7.12) lead to the  $10\omega_{el}$  oscillation in  $I_{RMS}$ , coherently with the results of Fig. 7.11. On the contrary, this oscillation at  $10\omega_{el}$  is absent in case of both the sinusoidal currents strategy and the third harmonic injection strategy.

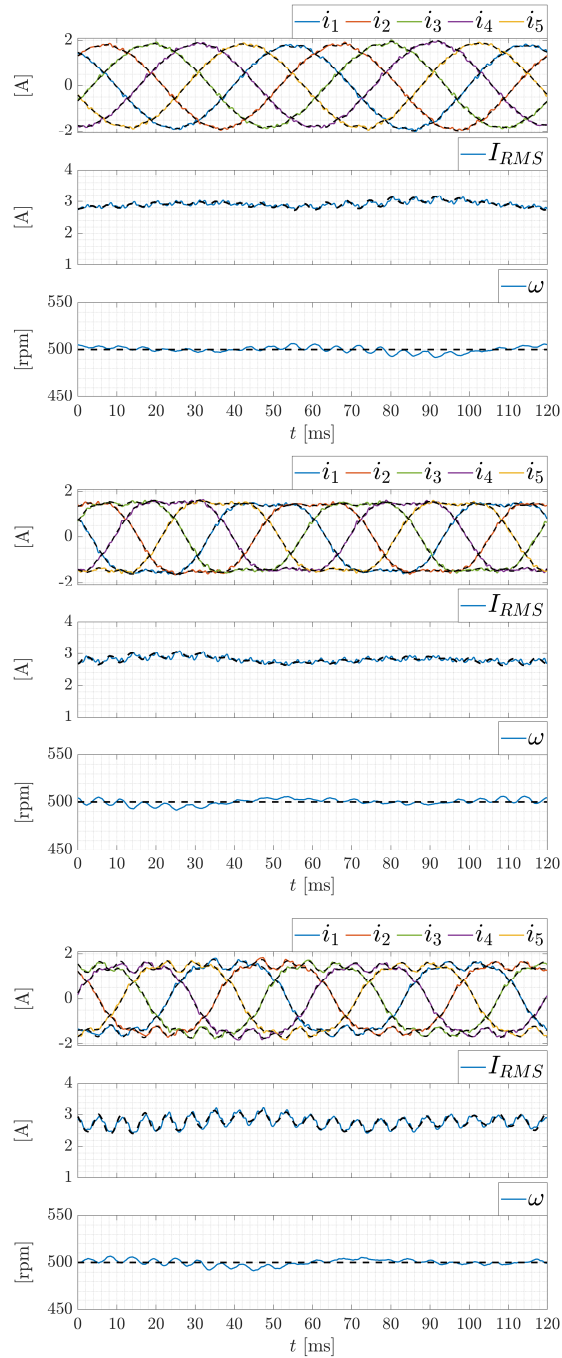


Fig. 7.13 – Steady-state results at 500 rpm: (top) Sinusoidal currents strategy; (middle) Third Harmonic Injection; (bottom) Proposed MTPA.

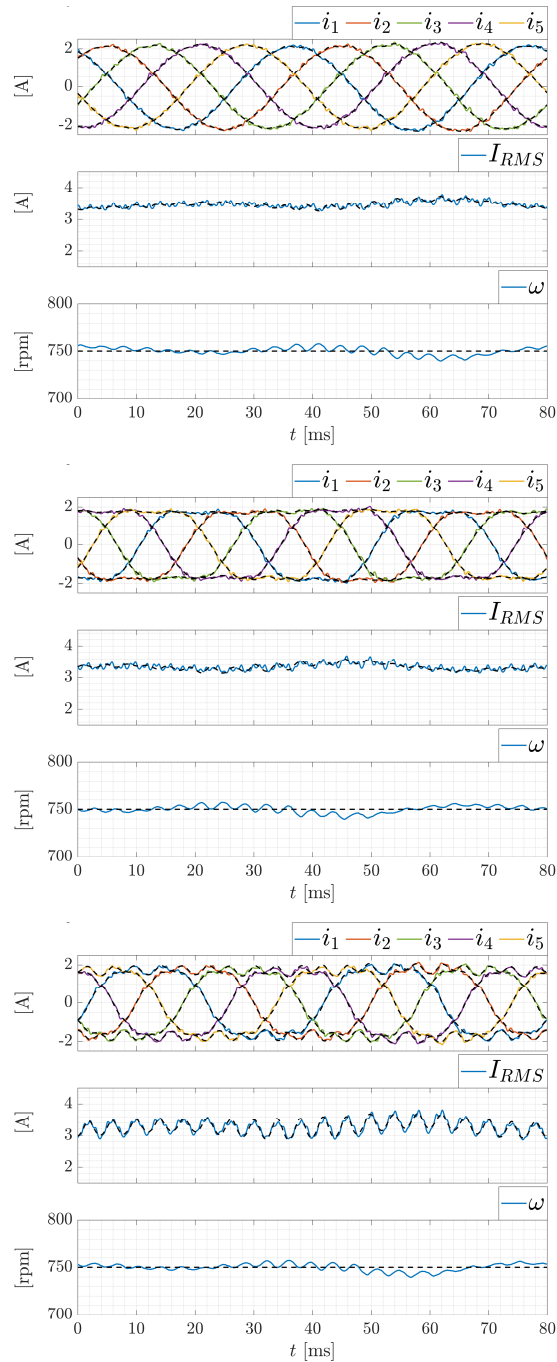


Fig. 7.14 – Steady-state results at 750 rpm: (top) Sinusoidal currents strategy; (middle) Third Harmonic Injection; (bottom) Proposed MTPA.

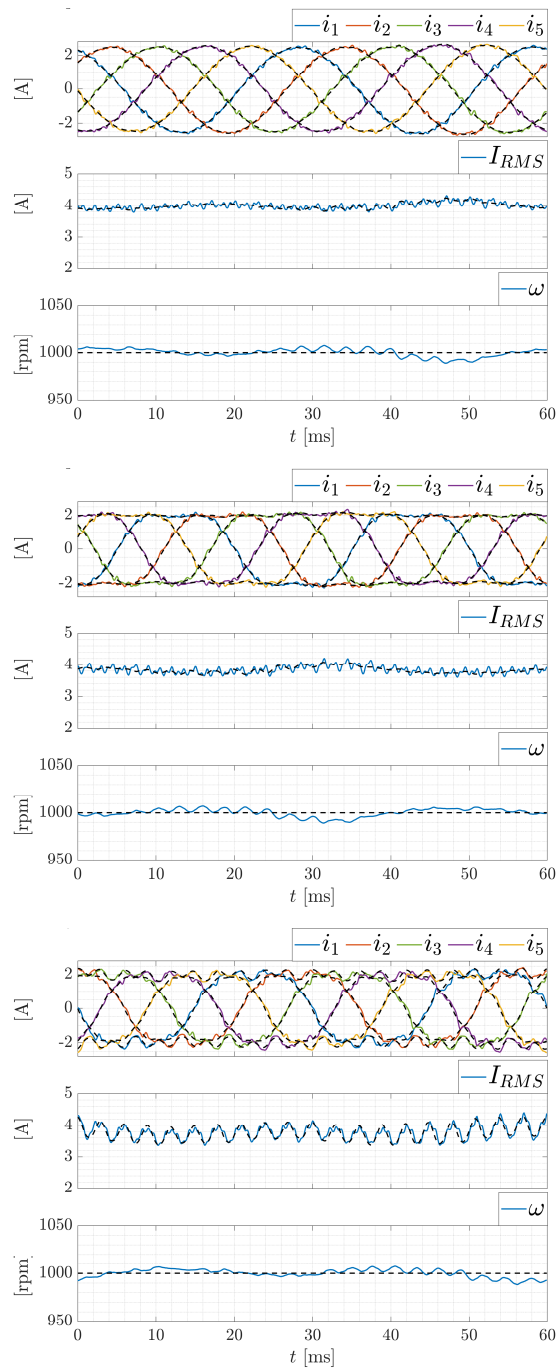


Fig. 7.15 – Steady-state results at 1000 rpm: (top) Sinusoidal currents strategy; (middle) Third Harmonic Injection; (bottom) Proposed MTPA.

No sensible difference between the three examined torque control strategies can instead be appreciated in the measured speeds. This indicates that the electromagnetic torque ripple (which is inevitably due to unmodelled phenomena, e.g., magnetic hysteresis of the iron) is not altered by the different strategies.

A comparison of the average RMS current per phase<sup>8</sup> obtained in a fundamental period for all the examined conditions is reported in Table 7.III. As can be seen, in all the examined conditions, the sinusoidal currents strategy is characterized by the highest values, the third harmonic injection strategy has intermediate results, and the proposed MTPA algorithm leads to the smallest currents. Then, the reduction of the RMS current

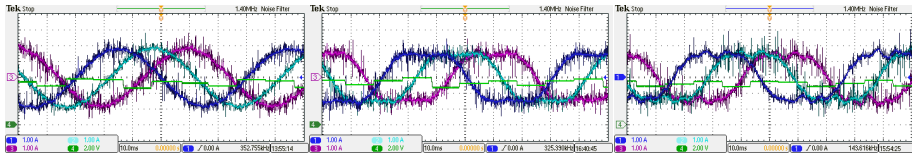


Fig. 7.16 – Oscilloscope captures at 500 rpm: (left) Sinusoidal currents strategy; (middle) Third Harmonic Injection; (right) Proposed MTPA.

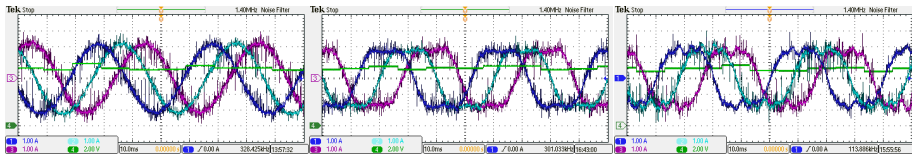


Fig. 7.17 – Oscilloscope captures at 750 rpm: (left) Sinusoidal currents strategy; (middle) Third Harmonic Injection; (right) Proposed MTPA.

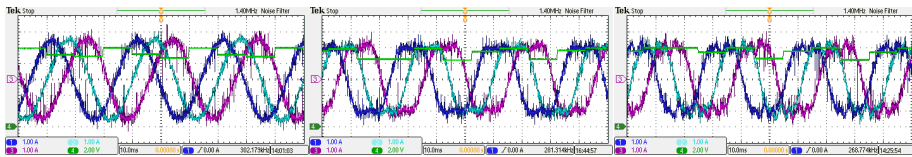


Fig. 7.18 – Oscilloscope captures at 1000 rpm: (left) Sinusoidal currents strategy; (middle) Third Harmonic Injection; (right) Proposed MTPA.

Table 7.III – COMPARISON OF THE AVERAGE RMS CURRENT PER PHASE.

Mechanical speed of the rotor	Sinusoidal Currents Strategy	Third Harmonic Injection	Proposed MTPA Algorithm
500 rpm	1.303 A	1.254 A	1.242 A
750 rpm	1.552 A	1.490 A	1.469 A
1000 rpm	1.787 A	1.714 A	1.693 A

<sup>8</sup> Note that these RMS values are referred to the behaviour of a single machine current, averaged in a fundamental period. They are different from the RMS current  $I_{RMS}$  defined in (7.14) and depicted in Fig. 7.11, which instead take into account the overall contribution of all the five machine currents in a specific rotor position (i.e at a specific time instant).

is also accompanied by a corresponding reduction of the overall machine losses. To be more specific, with respect to the sinusoidal currents strategy, the third harmonic injection can reduce the RMS currents by around 4%, which leads to a reduction of around 8% of the machine stator losses, while the proposed MTPA algorithm can lead to a reduction of around 5.5%, which leads to a losses reduction of around 10%.

### 7.6.2 Healthy configuration

This testing scenario is aimed at showing the effectiveness of the proposed control algorithm in a healthy machine configuration and at comparing it with a standard baseline controller architecture.

The test has been done in the same single-star configuration of Fig. 7.9, and the current references have been computed with the MTPA algorithm described in Section 7.2, whose waveforms have been depicted in Fig. 7.12. The proposed decoupled current control algorithm has been compared with a standard VSD-based controller.

The VSD-based controller has been realized by considering the Clarke's matrix:

$$C = \sqrt{\frac{2}{5}} \cdot \begin{bmatrix} \cos(0\alpha) & \cos(1\alpha) & \cos(2\alpha) & \cos(3\alpha) & \cos(4\alpha) \\ \sin(0\alpha) & \sin(1\alpha) & \sin(2\alpha) & \sin(3\alpha) & \sin(4\alpha) \\ \cos(0\alpha) & \cos(3\alpha) & \cos(6\alpha) & \cos(9\alpha) & \cos(12\alpha) \\ \sin(0\alpha) & \sin(3\alpha) & \sin(6\alpha) & \sin(9\alpha) & \sin(12\alpha) \\ 1/\sqrt{2} & 1/\sqrt{2} & 1/\sqrt{2} & 1/\sqrt{2} & 1/\sqrt{2} \end{bmatrix}$$

with  $\alpha = 2\pi/5$ . It can be verified that this matrix is orthogonal (i.e.,  $C^{-1} = C^T$ ). Both the reference and the measured currents are transformed in the VSD domain through the transformation (2.38), and the corresponding error components are processed by PI controllers working in the multiple synchronous domain. To be more specific, considering the harmonic mapping for a symmetrical five-phase system, the  $x1 - y1$  components have been processed with PI controllers in rotating frames synchronous with  $\theta_{el}$ ,  $-9\theta_{el}$ ,  $11\theta_{el}$  and  $-19\theta_{el}$  (i.e., with the progression  $10h \pm 1$ ), while the  $x3 - y3$  components have been processed with PI controllers in rotating frames synchronous with  $3\theta_{el}$ ,  $-7\theta_{el}$ ,  $13\theta_{el}$  and  $-17\theta_{el}$  (i.e., with the progression  $10h \pm 3$ ). The computed reference voltages have been summed and transformed back into the phase variable domain by (2.38).

The first set of tests has been done considering the dynamic response of the system to speed transients. The machine has been subject to a step change of the reference speed from  $-500$  rpm to  $+500$  rpm, while at the same time the DC machine armature terminals are again closed on a  $20 \Omega$  resistor (which, as also previously mentioned, generates a braking torque proportional to the speed with a proportionality gain of around  $0.04 \text{ Nm}/(\text{rad/s})$ ).

The results obtained with the proposed decoupled phase variable controller are depicted in Fig. 7.19, while the results obtained with the VSD-based controller are depicted in Fig. 7.20. The top subplots show the machine phase currents (solid lines) and the corresponding references (black dashed lines). The middle subplots show the developed electromagnetic torque  $T_{em}$  (solid line) and the controller reference torque  $T_{em}^*$  (black dashed line); the torque has been estimated by computing (7.4) with the measured currents. The bottom subplots show the machine angular speed  $\omega$  (solid line) and the corresponding reference speed  $\omega^*$  (black dashed line).

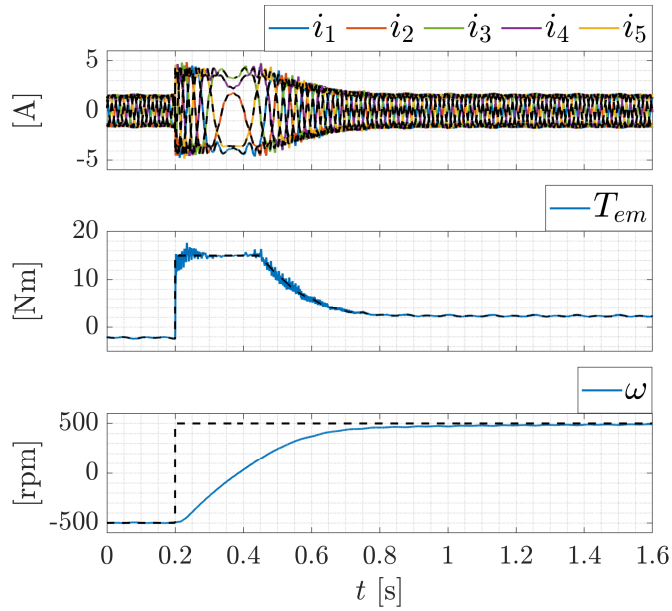


Fig. 7.19 – Experimental results obtained with the proposed decoupled phase variable controller (speed change from  $-500$  rpm to  $+500$  rpm).

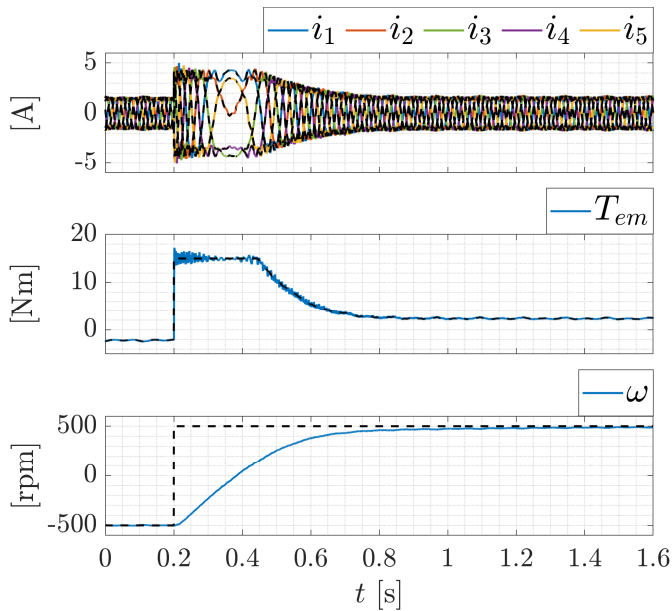


Fig. 7.20 – Experimental results obtained with the VSD-based controller (speed change from  $-500$  rpm to  $+500$  rpm).

As can be seen, both controller architectures produce very similar results.

After the speed reference change (at  $t = 0.2$  s) the torque reference jumps from  $-2$  Nm to the limit value of  $+15$  Nm and, consequently, the measured speed starts increasing. At around  $t = 0.45$  s the torque starts decreasing and finally stabilizes to around  $+2$  Nm when the speed inversion has been completed (at around  $t = 1$  s).

The only differences between the two approaches can be appreciated in the estimated torques during the initial transients, because of the different dynamic behaviour of the analysed current controllers. However, no sensible effect can instead be appreciated in the speed response.

Fig. 7.21 and Fig. 7.22 show the system responses in the same operating condition but for a reference speed change from  $-250$  rpm to  $+750$  rpm. Here, initially, the machine torque is around  $-1$  Nm, then at  $t = 0.2$  s it again jumps at the limit value of  $+15$  Nm and finally stabilizes at around  $+3$  Nm. Again, the two controllers show a similar dynamic behaviour.

An additional test has been done considering the dynamic response of the system to a load change. Here, the test has been carried out at the reference speed of  $750$  rpm by commanding (via RT Box platform) the closing of a contactor that connects an additional  $20 \Omega$  resistor to the DC machine armature terminals. In this way, the equivalent resistance applied at the DC machine armature terminals is  $10 \Omega$ , and the corresponding braking torque applied to the SynRM is changed from around  $3$  Nm to around  $6$  Nm.

The results obtained with the proposed decoupled phase variable controller are depicted in Fig. 7.23, while the results obtained with the VSD-based controller are depicted in Fig. 7.24.

Again, the two controller architectures show a similar behaviour. After the load change (at  $t = 0.2$  s), the machine speed drops to the minimum value of around  $710$  rpm, but is quickly driven back to the reference value of  $750$  rpm at around  $t = 1$  s, thanks to the action of the speed controller. The slightly smaller oscillation in the estimated torque with the proposed solution can be justified by considering that the adopted resonant actions, contrarily to the synchronous PI controller of the VSD-based solution, have an infinite gain for both positive and negative sequences actions, and can therefore better neutralize the machine non-idealities.

To better appreciate the dynamics of the machine currents, Fig. 7.25 shows a zoom of their evolution in the interval between  $0.2$  s and  $0.4$  s, when the reference torque is increased from around  $3$  Nm to around  $6$  Nm. It can be seen that all the currents follow the corresponding references, whose waveforms match the ones obtained with the previously analysed MTPA algorithm, and whose magnitude increase in time to counteract the speed drop.

These results clearly show that the proposed controller architecture has a satisfactory behaviour in an ordinary healthy machine configuration, and that it can match the same performances of a standard VSD-based controller.

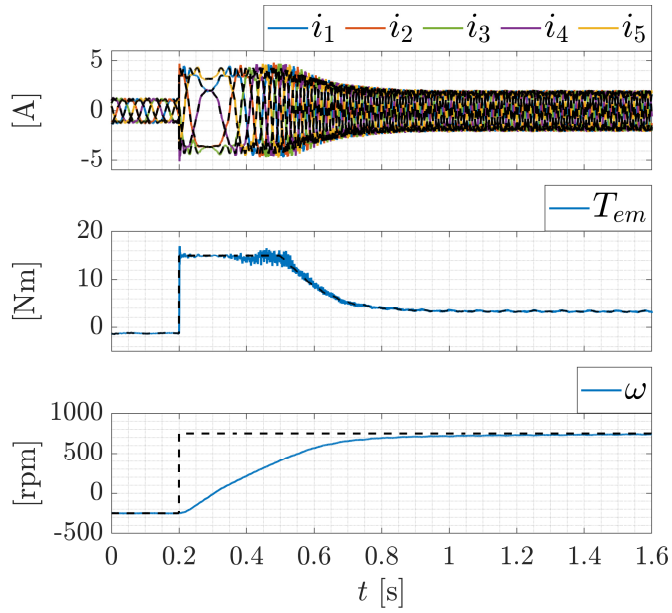


Fig. 7.21 – Experimental results obtained with the proposed decoupled phase variable controller (speed change from  $-500$  rpm to  $+500$  rpm).

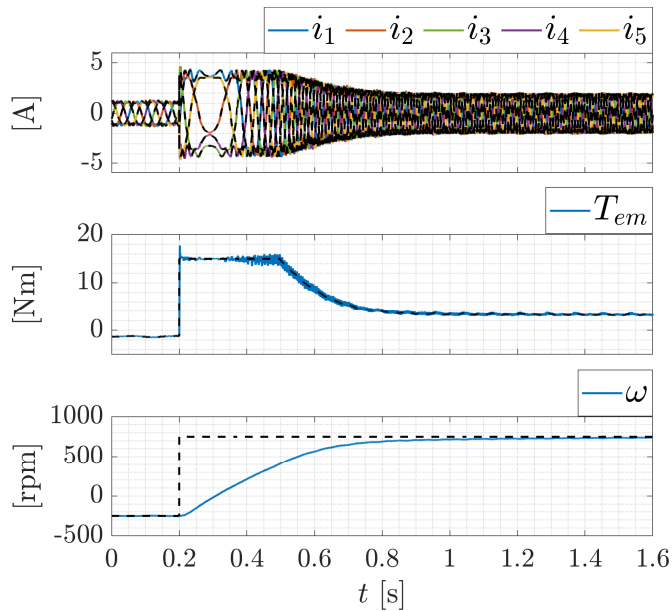


Fig. 7.22 – Experimental results obtained with the VSD-based controller (speed change from  $-250$  rpm to  $+750$  rpm).

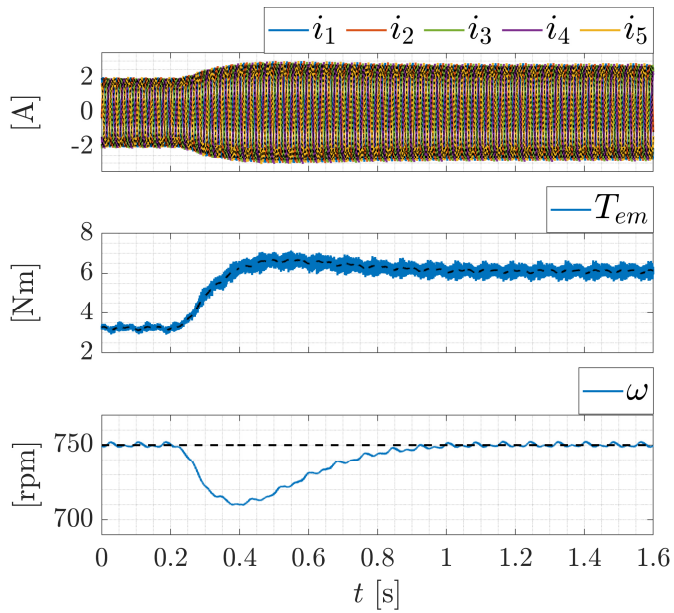


Fig. 7.23 – Experimental results obtained with the proposed decoupled phase variable controller (loading torque change).

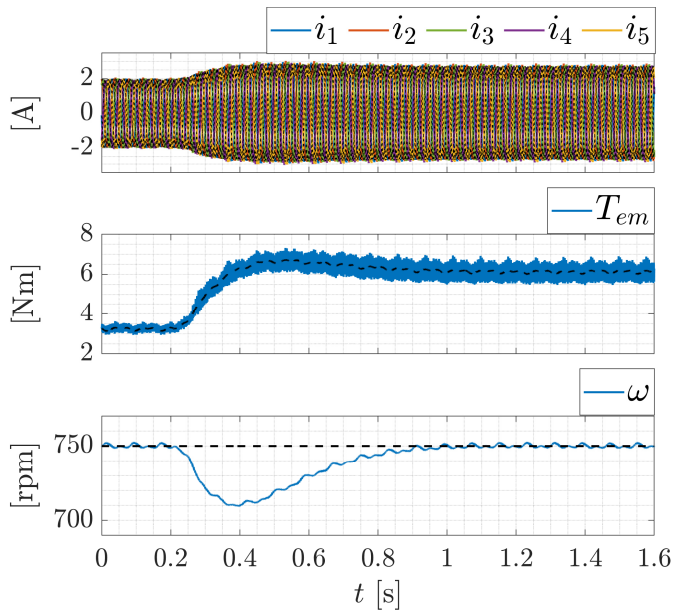


Fig. 7.24 – Experimental results obtained with the VSD-based controller (loading torque change).

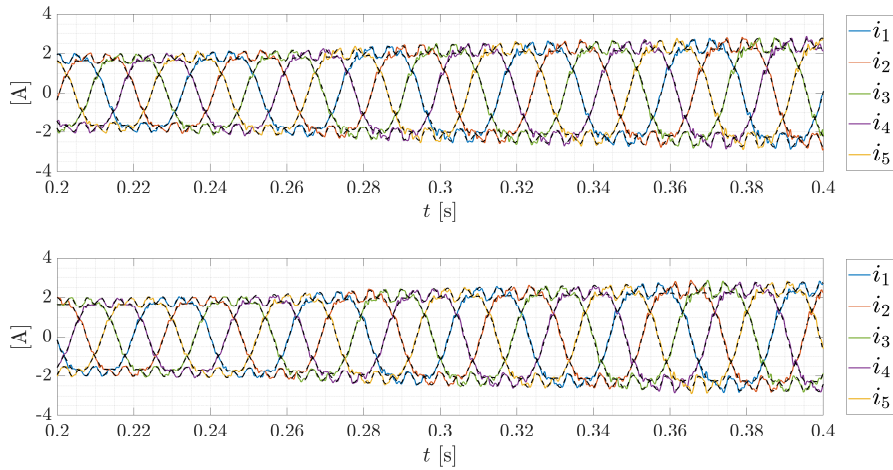


Fig. 7.25 – Currents evolution during the loading torque change: Top) Proposed decoupled phase variable control; Bottom) VSD-based control.

### 7.6.3 Post-fault configuration with one faulty phase

This testing scenario analyses the proposed controller in a post-fault configuration.

The machine configuration is changed by physically disconnecting phase 1. The winding configuration is depicted in Fig. 7.26, and the corresponding constraints and configuration matrices are:

$$M = \begin{bmatrix} 1 & 1 \\ 1 & 0 \\ 1 & 0 \\ 1 & 0 \\ 1 & 0 \end{bmatrix}, \quad U_f = \begin{bmatrix} 0 & 0 & 0 \\ -0.50 & -0.50 & -0.50 \\ 0.83 & -0.17 & -0.17 \\ -0.17 & 0.83 & -0.17 \\ -0.17 & -0.17 & 0.83 \end{bmatrix}$$

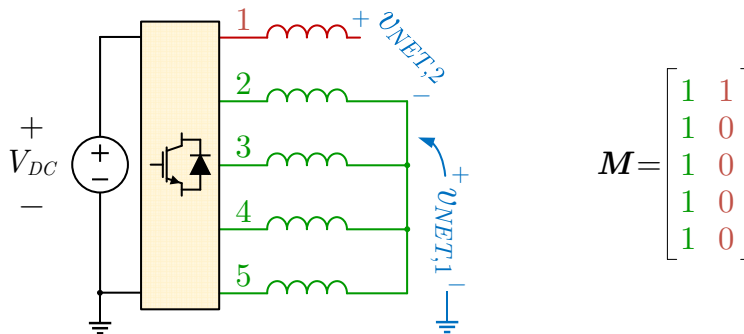


Fig. 7.26 – Schematic diagram and constraint matrix for the post-fault configuration with one faulty phase.

The MTPA algorithm proposed in Section 7.2 has again been implemented via (7.21). Similarly to the previous cases, an initialization routine has been executed to compute the versors  $\hat{\mathbf{i}}_{\max} = \mathbf{U}_f \cdot \hat{\mathbf{i}}_{f,\max}$  and  $\hat{\mathbf{i}}_{\min} = \mathbf{U}_f \cdot \hat{\mathbf{i}}_{f,\min}$  from the eigenvectors of the  $3 \times 3$  matrix  $\mathbf{L}'_f$ . The coefficients of their Fourier decomposition have been stored in the controller memory and reconstructed in real-time basing on the measured electrical rotor position  $\theta_{el} = 2\theta$ . They are graphically depicted in Fig. 7.27, together with the corresponding waveforms of  $I_{RMS}$ .

Again, it can be seen that  $I_{RMS}$  is strongly affected by the rotor position and that it locally differs between positive and negative torques.

The optimal phase currents waveforms obtained in this new configuration are depicted in Fig. 7.28. Now, coherently with the open-circuit constraint, the current  $i_1$  (and all its harmonics) are zero. The waveforms of the other currents, if compared to the waveforms depicted in Fig. 7.12 for the healthy machine configuration, have been severely altered by the fault.

For symmetry reasons, it can be noted that  $i_2$  and  $i_5$  have mirrored waveforms with respect to the electrical rotor position  $\theta_{el}$ . Similarly, also  $i_3$  and  $i_4$  have mirrored waveforms from one another, which are however sensibly different from  $i_2$  and  $i_5$ . If compared to the healthy configuration, the magnitude of all the harmonics is increased and also the harmonics with an order multiple of 5 are now present in the harmonic spectra<sup>9</sup>. Again, the waveforms obtained for negative reference torques are identical to the waveforms obtained for positive torques, and only shifted by  $90^\circ$ .

In this case, given the additional constraint  $i_1 = 0$ , the overall RMS current  $I_{RMS}$

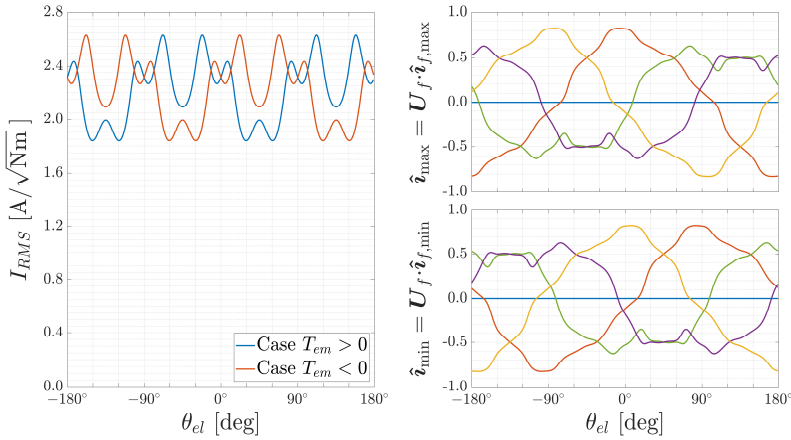


Fig. 7.27 – Overall machine RMS current (left) and optimal phase current versors  $\hat{\mathbf{i}}_{\max} = \mathbf{U}_f \cdot \hat{\mathbf{i}}_{f,\max}$  and  $\hat{\mathbf{i}}_{\min} = \mathbf{U}_f \cdot \hat{\mathbf{i}}_{f,\min}$  (right) in the whole range  $[-180^\circ, +180^\circ]$  of  $\theta_{el}$  for the post-fault configuration with one faulty phase.

<sup>9</sup> This could be expected because, given the lost of the machine symmetry after the fault, the harmonics with order multiple of 5 are not homopolar anymore.

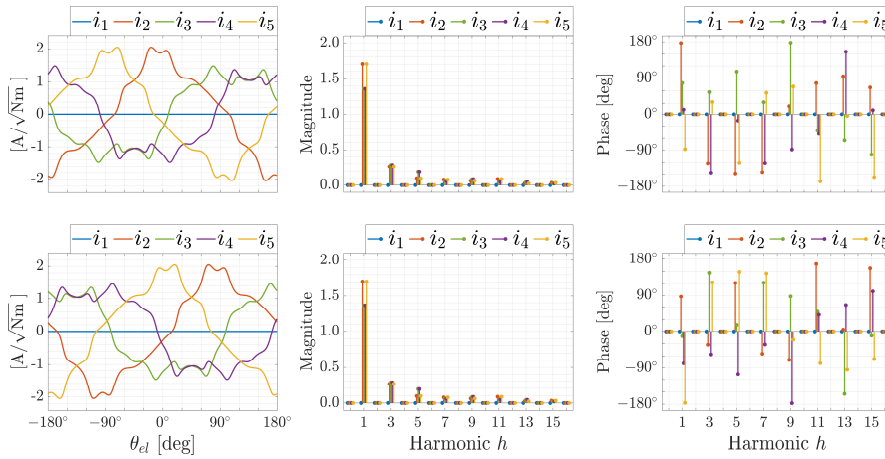


Fig. 7.28 – Optimal phase currents waveforms and harmonic spectra for the post-fault configuration with one faulty phase: (top) Positive reference torque  $T_{em}^* > 0$ ; (bottom) Negative reference torque  $T_{em}^* < 0$ .

provided by (7.14) is higher than in the previous case study, which also leads to higher machine losses. It has been estimated that, with respect to the healthy configuration, the average losses in a full rotor cycle are increased by around 46%. Moreover, similarly to the results obtained in Chapter 5 and in Chapter 6 for PMSMs, the symmetry loss following the fault makes the overall losses to be unequally shared by the remaining phases. In this case, phases 2 and 5 are each responsible for 30% of the losses, while phases 3 and 4 are each responsible for 20% of the losses.

The experimental validation has been done by considering the same testing scenarios analysed in Section 7.6.2. The dynamic responses following reference speed changes (with a DC loading resistor of 20  $\Omega$ ) are shown in Fig. 7.29 (from  $-500$  rpm to  $+500$  rpm) and in Fig. 7.30 (from  $-250$  rpm to  $+750$  rpm).

It can be noted that the mechanical behaviour of the machine following the reference speed change is similar to the healthy configuration analysed in Section 7.6.2. Only some small differences in the speed behaviour during the transients can be observed, and they are related to magnetic saturation phenomena. In other words, the higher machine currents in this faulty configuration (required to develop the same reference electromagnetic torque of the healthy case) affect the inductances with a corresponding deviation of the developed electromagnetic torque from the estimated one.

The dynamic responses following a loading torque change (obtained with a reference speed of 750 rpm by changing the value of the resistance applied at the DC machine terminals) are shown in Fig. 7.31. A zoomed version of the dynamics of the currents has been also reported in Fig. 7.32. The machine mechanical dynamics following the loading torque change is also very similar to the healthy configuration analysed in Section 7.6.2, and it can be seen that the proposed controller can effectively track the current references even in this post-fault configuration.

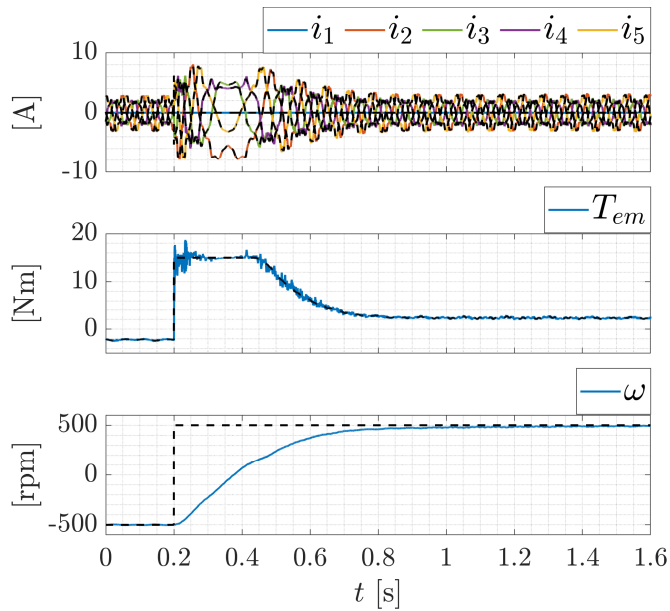


Fig. 7.29 – Experimental results obtained for the post-fault configuration with one faulty phase (speed change from  $-500$  rpm to  $+500$  rpm).

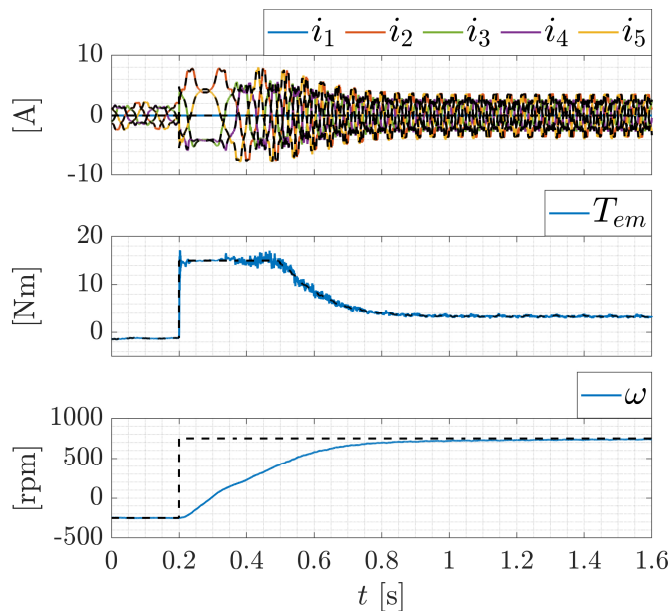


Fig. 7.30 – Experimental results obtained for the post-fault configuration with one faulty phase (speed change from  $-250$  rpm to  $+750$  rpm).

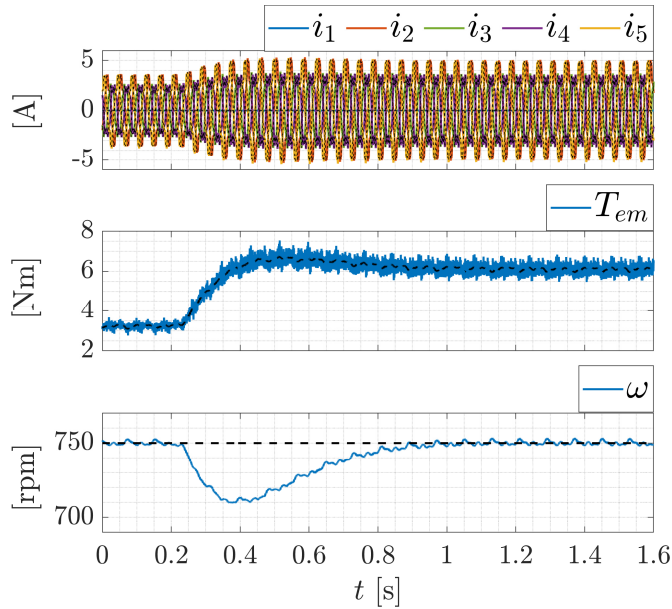


Fig. 7.31 – Experimental results obtained for the post-fault configuration with one faulty phase (loading torque change).

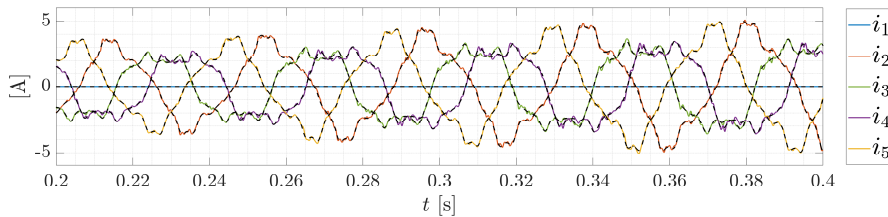


Fig. 7.32 – Currents evolution during the loading torque change for the post-fault configuration with one faulty phase.

#### 7.6.4 Post-fault configuration with two faulty phases

This testing scenario analyses the proposed controller performances in a heavy post-fault scenario.

In this test, the winding configuration is represented in Fig. 7.33. If compared to the previous case study, the configuration has been modified by physically disconnecting also the phase 3 of the machine, thus emulating a fault on two non-adjacent phases<sup>10</sup>.

The corresponding constraints and configuration matrices are:

<sup>10</sup> It has been numerically verified that, for the considered machine, the performances derating following the fault of two adjacent phases would be too limiting for experimental testing.

$$M = \begin{bmatrix} 1 & 1 & 0 \\ 1 & 0 & 0 \\ 1 & 0 & 1 \\ 1 & 0 & 0 \\ 1 & 0 & 0 \end{bmatrix}, \quad U_f = \begin{bmatrix} 0 & 0 \\ -0.58 & -0.58 \\ 0 & 0 \\ 0.79 & -0.21 \\ -0.21 & 0.79 \end{bmatrix}$$

Again, the MTPA implementation has been executed as in Section 7.6.2 and in Section 7.6.3. The overall machine RMS current  $I_{RMS}$  and the eigenvector directions  $\hat{i}_{\max}$  and  $\hat{i}_{\min}$  obtained by the MTPA algorithm in this new configuration are depicted in Fig. 7.34. The optimal current waveforms are depicted in Fig. 7.35.

In this case, both the currents  $i_1$  and  $i_3$  computed by the MTPA algorithm are zero, and all the torque development is achieved through the three remaining healthy phases. For symmetry reasons, the  $i_4$  and  $i_5$  have mirrored waveforms, which differ from  $i_2$ .

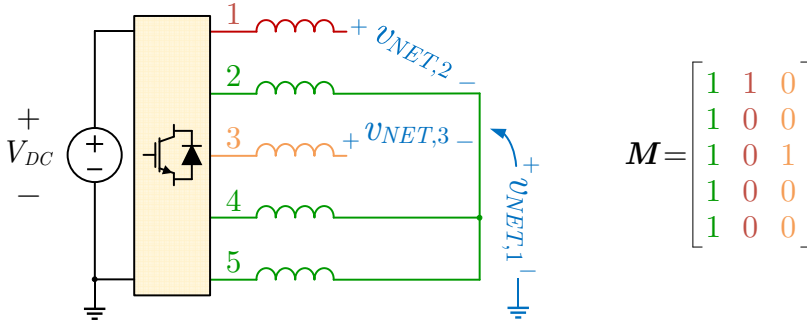


Fig. 7.33 – Schematic diagram and constraint matrix for the post-fault configuration with two faulty phases.

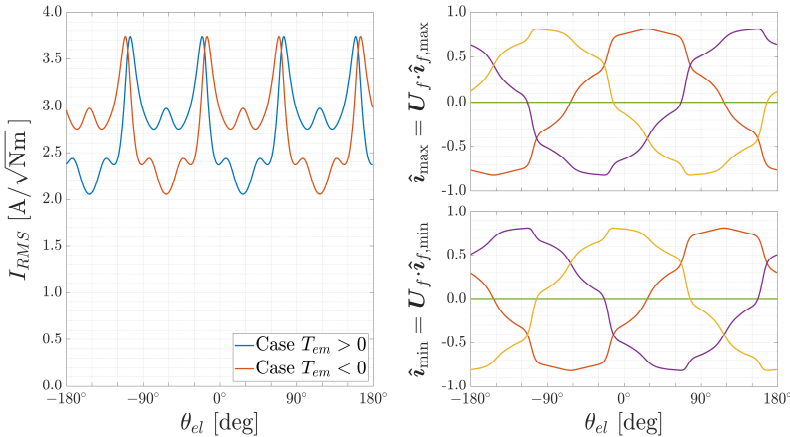


Fig. 7.34 – Overall machine RMS current (left) and optimal phase current vectors  $\hat{i}_{\max} = U_f \cdot \hat{i}_{f,\max}$  and  $\hat{i}_{\min} = U_f \cdot \hat{i}_{f,\min}$  (right) in the whole range  $[-180^\circ, +180^\circ]$  of  $\theta_{el}$  for the post-fault configuration with two faulty phases.

The overall RMS current is higher than in the previous cases, and it has been estimated that, if compared to the healthy configuration, the overall machine losses are increased by around 128%. In this case, the current  $i_2$  is responsible for around 28% of the overall losses, while the currents  $i_4$  and  $i_5$  are responsible for around 36% each.

Again, the machine has been experimentally tested with the same scenarios as in the previous cases. Fig. 7.36 and Fig. 7.37 show the results of the dynamical behaviour following a speed reference change from  $-500$  rpm to  $+500$  rpm and from  $-250$  rpm to  $+750$  rpm, respectively. Similarly to the results analysed in Section 7.6.2 and in Section 7.6.3, when the speed reference changes (at  $t = 0.2$  s), the reference torque increases to the limit value of  $15$  Nm but, contrarily to the previous results, the electromagnetic torque developed by the machine is unable to follow it. This is because the corresponding currents computed by the MTPA algorithm (which, in this post-fault configuration, would have been higher than the maximum feasible currents) have been limited in the range of  $\pm 8.5$  A. This software saturation generates the electromagnetic torque drops which can be seen in the middle subplots of Fig. 7.36 and Fig. 7.37. Consequently, the transient dynamics of the machine speed during the acceleration is different from the results of Section 7.6.2 and Section 7.6.3.

The machine response following a load step change has been here done with a reference speed of  $500$  rpm. The results are depicted in Fig. 7.38. The closing (via RT Box platform) of the DC machine contactor changes the applied torque from around  $2$  Nm to around  $4$  Nm, and the machine speed decreases to the minimum value of around  $470$  rpm. However, the speed controller, by properly increasing the reference torque  $T_{em}^*$  (and, consequently, the magnitude of the reference currents) is again capable of keeping back the speed to the reference value of  $500$  rpm at around  $t = 1$  s.

The zoomed view of the evolution of the currents is shown in Fig. 7.39. Again, it can be observed that the proposed current controller can properly make the currents of the healthy phases track the corresponding references.

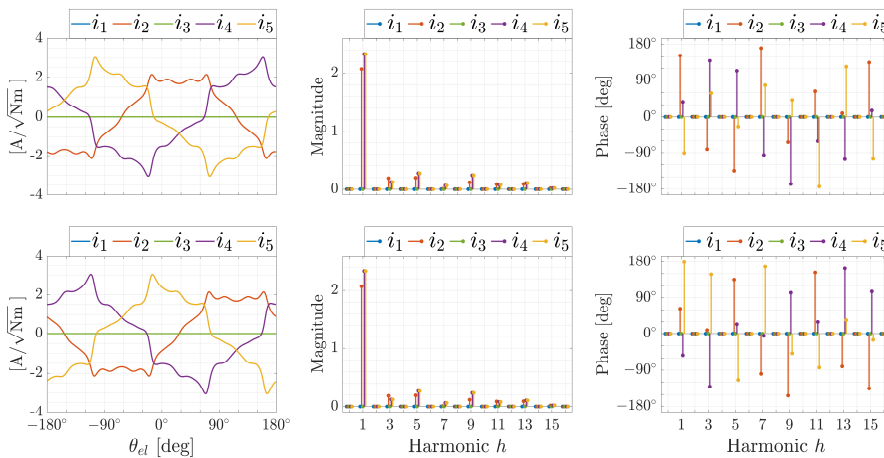


Fig. 7.35 – Optimal phase currents waveforms and harmonic spectra for the post-fault configuration with two faulty phases: (top) Positive reference torque  $T_{em}^* > 0$ ; (bottom) Negative reference torque  $T_{em}^* < 0$ .

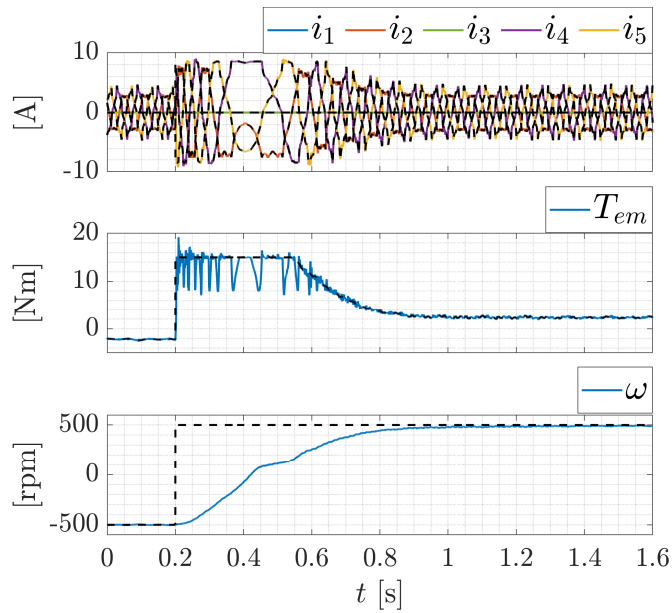


Fig. 7.36 – Experimental results obtained for the post-fault configuration with two faulty phases (speed change from  $-500$  rpm to  $+500$  rpm).

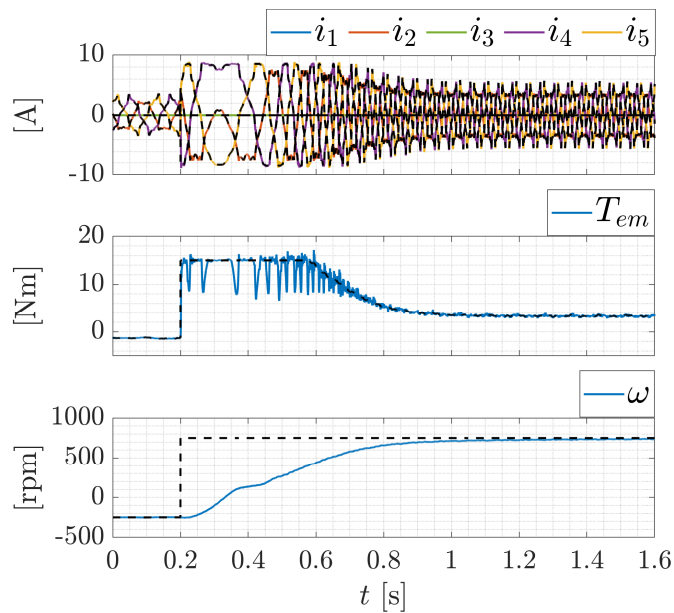


Fig. 7.37 – Experimental results obtained for the post-fault configuration with two faulty phases (speed change from  $-250$  rpm to  $+750$  rpm).

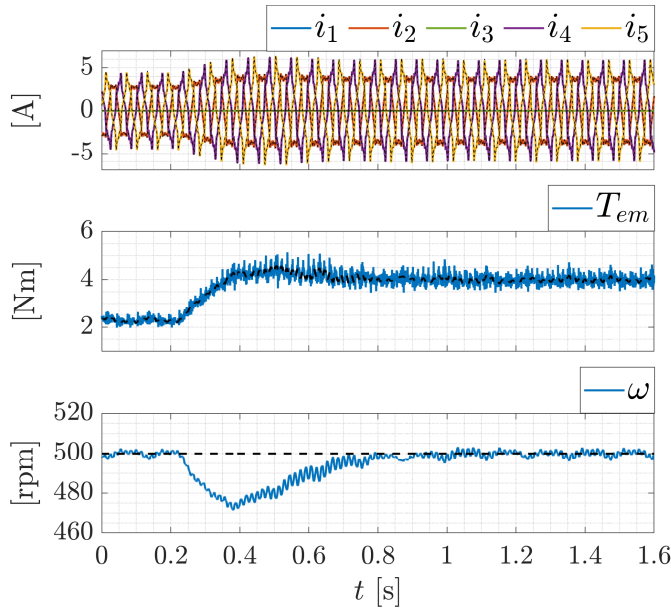


Fig. 7.38 – Experimental results obtained for the post-fault configuration with two faulty phases (loading torque change).

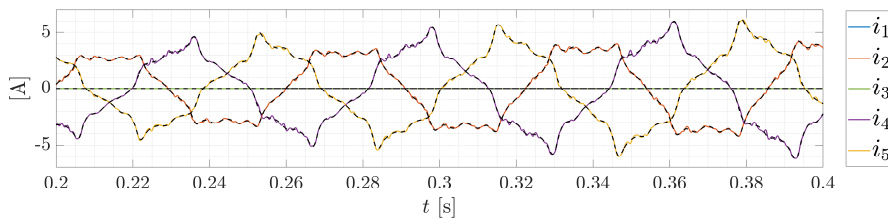


Fig. 7.39 – Currents evolution during the loading torque change for the post-fault configuration with two faulty phases.

## 7.7 Summary and remarks

This chapter has presented a *generalized control algorithm for a multiphase SynRM drive*. The approach is the direct extension of the decoupled phase variable control developed in Chapter 6 for PMSM drives. It is entirely derived in the phase variable domain and explicitly considers the hardware connection among the phase windings and with the supplying power converter.

First, the mathematical model of the drive has been derived. The machine model is the particularization of the general model developed in Chapter 2, while the drive architecture has been analysed through the multiport network approach of Chapter 4.

Then, an *MTPA algorithm* has been presented to compute the machine current references to develop a desired electromagnetic torque. Similarly to Chapter 6, the

approach has been formalized as a constrained optimization problem aimed at minimizing the overall machine RMS current while, at the same time, developing the desired reference torque and satisfying the algebraic constraints introduced by the drive hardware configuration. It has been solved analytically and it has been shown that the optimal solution depends on the *eigenvalues* and *eigenvectors* of the matrix  $\mathbf{L}'_f(\theta) = \mathbf{U}_f^T \cdot \mathbf{L}'(\theta) \cdot \mathbf{U}_f$ , with  $\mathbf{L}'(\theta) = \partial \mathbf{L} / \partial \theta$ .

The current controller has then been developed. The proposed controller is the same as the one proposed in Chapter 6, and is based on a *decoupling algorithm* (which considers both the machine magnetic interaction and the network electrical interactions) and on a *decoupled current controller* (implemented with a proportional action, an integral action, and multiple resonant actions). The only differences here are the  $\theta$ -dependence of the inductances matrix  $\mathbf{L}(\theta)$  and the different expression for the motional-induced back-EMFs set  $\mathbf{e}$ .

The whole control algorithm has been experimentally validated with a five-phase SynRM drive. Several testing scenarios have been analysed and discussed in detail. All the results are satisfactory and coherent with the theoretical analysis. Some comparisons have also been considered both with other torque control strategies and with standard current control algorithms.

# 8 Conclusions

Multiphase drives are nowadays one of the most relevant research topics in the electrical engineering scientific community. Thanks to the many benefits they offer over standard three-phase drives, it is possible to witness a progressive interest and spread of their implementation in many areas, ranging from industrial to traction applications, and especially in presence of high-power and/or high-reliability requirements. However, their control is generally more challenging than in standard three-phase configurations, because of the higher number of degrees of freedom and of the wider variety of different possible configurations.

The work presented in this Ph.D. thesis has dealt with the modelling and control of multiphase electric drives, with the aim of developing a generalized model-based approach that can be used in multiple configurations and scenarios. This chapter summarizes the main contents presented in this dissertation, highlights the major novelties and suggests some possible developments for future studies.

## 8.1 Summary of the thesis contents

The dissertation has been organized by first addressing the drive modelling, and then by focusing on the development of control algorithms.

The drive modelling has been intentionally developed in a generalized way, by introducing the required simplifying assumptions and by mathematically deriving the corresponding properties and results. It has been carried out by first separately modelling the electric machine and the power electronics converter, and then by formalizing their mutual interaction considering the drive topology.

The drive control has been introduced for multiphase PMSM drives. It has first been addressed with a standard field-oriented approach, specifically adapted to deal with asymmetrical PMSM configurations, and then by introducing an innovative control technique based on the decoupled control in the phase variable domain. This novel control technique has then been extended to multiphase SynRM drives.

In the following, a summary of the main content of each chapter is provided.

- Chapter 1 has provided an introduction to the main topics of this dissertation and has briefly addressed the state of the art presented in the technical literature. This review has addressed different aspects related to multiphase electric drives, like their application areas, the different machine and converter designs and architectures, the standard modelling and control approaches, and some post-fault operation criteria.
- Chapter 2 has developed the mathematical model of the electrical machine. The approach has been developed in the phase variable domain, and has been carried out with the standard tools of electromechanical conversion theory. The magnetic model of the machine has been obtained assuming a linear behaviour of the materials, and the analytical expressions of the fluxes and of the torque have been found through the energy conservation

principle, by referring to the electromagnetic coenergy of the system. From the expression of the induced fluxes, it has been possible to derive the induced back-EMFs, and then to recognize the transformer-induced and the motional-induced contributions. Different torque development mechanisms have also been presented and classified, both in relation to their mathematical dependence on the machine phase currents and in relation to the various possible interactions between the stator and the rotor. The resulting model (which is a system of differential and algebraic equations) can adequately describe the key functional aspects of multiple machine types and designs, and is therefore suited for control purposes. Finally, a brief mention of some of the typical transformations of the machine variable used in many standard multiphase analysis approaches has been provided.

- Chapter 3 has discussed the architectures and modulation strategies for power electronics converters employed in multiphase drives. The chapter has examined both two-level and multilevel VSI configurations, briefly explaining the benefits and limitations of the most common structures from the point of view of their control. Additionally, many different multiphase topologies have been presented, considering architectures with both single and multiple DC sources. The basic principles and properties of PWM algorithms have then been recalled, and a brief mention has also been given to carrier-based and space vector modulation techniques for two-level multiphase drives. Finally, the chapter has also presented some novel carrier-based modulation techniques for NPC and MPC multilevel converters, which have been developed while directly addressing the voltage equalization of the DC-bus capacitors. These techniques have been developed considering a multi-step approach, meaning that the leg output voltage can switch among multiple levels in the same modulation period. By exploiting this capability, the voltage equalization can always be guaranteed, but at the expense of a higher switching transitions rate. In this context, the proposed approaches have been conceived as a trade-off between the equalization effectiveness and the mitigation of this switching transitions increase.
- Chapter 4 has developed a novel methodology to analyse the electrical topology of a multiphase drive, which is based on the study of the connections between the multiphase machine and the power electronics converter through a multiport network approach. It has been shown how many hardware configurations, by introducing some constraints on the machine phase currents, modify the dynamical behaviour of the machine by acting as additional internal feedback terms for its mathematical model. Several architectures of practical interest have been exemplified with this approach, which has revealed to be a helpful tool for the analysis of a multiphase machine under various hardware topologies, coming either from different design choices or resulting from post-fault reconfigurations. Finally, the chapter has developed a different formulation of a multiphase

---

drive model subject to constraints on the phase currents, by introducing the concept of configuration space, which intrinsically considers the effect of such constraints and allows to mathematically formalize a reduced order model for the drive.

- Chapter 5 has focused on the development of a FOC algorithm for asymmetrical multiphase PMSMs. In this framework, a space-vector formalism has been introduced, and the VSD and rotational transformations of the machine variables have been based on the choice of a set of space-vector current components to be independently controlled. It has been shown that, for asymmetrical machine configurations, the transformation matrices chosen with a field-oriented approach may not be unitary, which considerably affect the machine modelling and control. Then, the chapter has presented and compared different torque control strategies for asymmetrical PMSMs, aimed at exploiting non-sinusoidal currents to develop the desired electromagnetic torque while, at the same time, optimizing some desired system performances. The current control algorithm has then been developed, and it has been shown how a standard scheme developed for symmetrical machines can be adapted to deal with asymmetrical configurations by introducing some additional compensation actions. The considered analysis has been tested, both numerically and experimentally, with an asymmetrical nine-phase PMSM with non-sinusoidal back-EMFs.
- Chapter 6 has presented an innovative control technique for a multiphase PMSM drive. This new approach is completely general with respect to the machine design and configuration, and has been directly rederived in the phase variable domain, without using any VSD and rotational transformation. An MTPA algorithm has been proposed to compute a set of current references to develop a desired electromagnetic torque while, at the same time, minimizing the machine RMS currents. The same strategy can also be easily extended to implement unequal torque-sharing strategies. The control of the machine phase currents has been based on a decoupling algorithm, with the aim to counteract the mutual coupling effects due both to the machine magnetic behaviour and to the electrical drive topology. A feedback regulator has then been designed to control the decoupled phase currents and, to guarantee the proper tracking of periodic references, the proposed solution has been based on the use of multiple resonant controllers. The conceived approach can easily generalize to different machine configurations and drive topologies, including post-fault operations, proving to be a viable alternative to standard control algorithms for multiphase drives. It has been successfully validated through an extensive set of experimental tests on an asymmetrical nine-phase PMSM.
- Chapter 7 has shown how the proposed phase variable control technique can be extended from PMSMs to SynRMs drives. In this case, both the

electromagnetic torque and the motional-induced back-EMFs are related to the variable reluctance effects, exhibited by a periodic dependence of the machine inductances on the rotor position. Then, the MTPA algorithm has been rederived. Again, it is aimed at the minimization of the machine RMS currents for a given reference torque but, given the different torque development mechanism, the corresponding solution and properties are different than in case of PMSMs. The current control is instead almost identical to the previously proposed scheme. It is again based on a decoupling algorithm and on a decoupled feedback controller acting on each single machine phases, and it only requires a different estimation for the motional-induced back-EMFs. The proposed approach has been successfully tested with a five-phase SynRM drive.

## 8.2 Original research contributions

This Ph.D. thesis has addressed the mathematical modelling and the control of multiphase electrical drive with an innovative approach.

Regarding the electrical drive modelling, the major novelty is represented by the *multiport network approach*, developed in Chapter 4 to analyse the mutual interactions between the machine and the converter according to different drive topologies. This approach, which is of general applicability, has made it possible to analytically formalize the effects of different drive configurations on the behaviour of the electrical machine, even in presence of one or more constraints on the machine phase currents introduced by the hardware architecture, which happens in many typical cases. In these circumstances, the introduction of the concept of configuration space can be helpful to identify the effects of such constraints on the machine model variables. Moreover, the proposed approach can also be easily adapted to drive reconfigurations, and therefore it can be exploited to deal with post-fault events.

Regarding the electric drive control, the major novelty is represented by the proposed *decoupled phase variable control*, developed in Chapter 6 for PMSMs and extended in Chapter 7 for SynRMs. This control approach, contrarily to most standard techniques, is directly derived in the phase variable domain, while explicitly considering the constraints imposed by the hardware topology. Thanks to its flexibility and generality, it can be easily adapted to different machine parameters and designs, to different drive topologies and to different control requirements. As proven through an extensive set of experimental tests, the proposed approach is a viable alternative to standard control algorithms for multiphase drives and it is especially suited to deal with asymmetrical and post-fault configurations.

This thesis has also presented many *enhanced torque control strategies*, aimed at developing the desired electromagnetic torque while, at the same time, optimizing the system energetic performances. Some of the proposed techniques have been derived with a standard field-oriented approach, by specifically identifying different space vector components to be exploited; other techniques have instead been derived by directly addressing the machine phase variables or the configuration space variables.

Finally, this dissertation has also briefly mentioned some novel *carrier-based*

---

*modulation techniques* for multilevel NPC and MPC converters, which have been derived to directly address the voltage equalization of the DC-bus capacitors and which have been developed as a side activity during the Ph.D. course.

## 8.3 Future developments

The work presented in this thesis reveals several possible future developments, concerning many different aspects. Further investigations can be especially addressed to the decoupled phase variable control, and include both the extension of the proposed approach to different multiphase drive architectures, and the study of alternative techniques for the torque development strategy and for the current control algorithm.

The extension of the decoupled phase variable control algorithm to *multiphase interior mounted PMSMs* can be handled by taking advantage of the results obtained for surface mounted PMSMs and SynRMs. In this case, the torque control strategy needs to be modified in a way to consider the contributions of both the permanent magnets and of the variable reluctance effects at the same time. The tracking of the optimal reference currents can instead be carried with the same controller architecture proposed in this thesis, and only requires a proper estimation of the motional-induced back-EMFs.

The extension of the decoupled phase variable control algorithm to *multiphase induction machines* is currently under development. In this case, the main challenge is that only the stator currents can be directly controlled by the supplying converter, while the rotor variables (i.e., the rotor fluxes and currents) can only be indirectly regulated through the effects of the inductive coupling effects. Consequently, the torque control strategy for the computation of the reference stator currents needs to be replaced with a simultaneous torque and flux control strategy, whose analytical derivation for a generalized configuration may be more difficult (especially in case of asymmetrical designs and post-fault scenarios).

For what concerns the torque control algorithm, all the analysed techniques have not considered the voltage saturation phenomenon, which restricts their application below a certain speed. Then, for high-speed operations, the current references computation algorithms should be modified by developing some *flux weakening strategies*. However, their mathematical formulation may not be straightforward in asymmetrical or post-fault configurations, which would make the development of a generalized approach more challenging.

Moreover, the optimization criterion to exploit the degrees of freedom offered by the multiphase configuration can also be modified to *maximize some different system performances*. For example, the problem can be formulated to minimize the highest peak stator current (instead of the overall RMS current) or to develop a Maximum-Torque-Per-Voltage (MTPV) algorithm.

Regarding the current controller, other *different decoupling algorithms* can be developed and compared, both in terms of performances and in terms of robustness to parameters uncertainty. For examples, alternative schemes can be realized by addressing the decoupling to the machine fluxes (instead of the machine currents) or by introducing additional terms to the machine or to the network compensation actions (e.g., by adding some damping terms to change the dynamical behaviour of the decoupled system).

Similarly, many alternatives can be analysed for the decoupled controller. As also formerly mentioned, they can either regard *different feedback control actions* (e.g., employing VPI controllers, repetitive controllers, etc...) or can involve the use of *different control architectures* (e.g., model-predictive approaches, dead-beat algorithms, sliding-mode controllers, etc...).

Finally, a more detailed machine model can be developed to also explicitly consider *non-linear effects* in the drive control algorithm (e.g., magnetic saturation phenomena).

# 9 Appendix

This Chapter contains additional material for the analysis of the presented dissertation. The first section covers some technical details mentioned in the previous chapters, while all the other sections group the mathematical proofs of several properties used in the thesis.

## 9.1 Additional considerations

### 9.1.1 Resonant controllers implementation

This section describes the algorithm which has been used to implement the resonant controllers in the experiments of Chapter 6.

The considered resonant controller structure is a dynamical system with a resonance for a given desired resonance frequency  $f_0$ . Its transfer functions in the Laplace domain and in the frequency domain are<sup>1</sup>:

$$\mathfrak{R}(s) = K_R \cdot \frac{s}{s^2 + \omega_0^2}, \quad \mathfrak{R}(j\omega) = K_R \cdot \frac{j\omega}{\omega_0^2 - \omega^2} \quad (9.1)$$

where  $K_R$  is a resonance gain and  $\omega_0 = 2\pi f_0$  is the angular frequency corresponding to  $f_0$ . Its Bode diagram is shown in Fig. 9.1.

For  $\omega \rightarrow \omega_0$  the magnitude of  $\mathfrak{R}(j\omega)$  tends to infinity. Thanks to this infinite gain, when used in a stable feedback control loop, the resonant controller allows a perfect tracking of sinusoidal reference signals with frequency  $f_0$  and a perfect rejection of sinusoidal disturbances with frequency  $f_0$ . For  $\omega \gg \omega_0$  and  $\omega \ll \omega_0$ , the magnitude of  $\mathfrak{R}(j\omega)$  tends to zero, and its effect on the feedback control loop becomes negligible.

Several different implementations can be used to obtain the equivalent behaviour of (9.1). However, not all the implementations are suited for variable frequency applications. Some possible implementations are given in [158], [161].

The implementation adopted for the control algorithm of Chapter 6 is based on the following expression:

$$y(t) = K_R \cdot \left[ \cos(\omega_0 t) \cdot \int \varepsilon(t) \cos(\omega_0 t) dt + \dots \right. \\ \left. \dots + \sin(\omega_0 t) \cdot \int \varepsilon(t) \sin(\omega_0 t) dt \right] \quad (9.2)$$

where  $\varepsilon(t)$  is the input error signal and  $y(t)$  is the control output signal.

The principle behind the implementation algorithm (9.2) is to identify the Fourier coefficients of the error signal  $\varepsilon(t)$  at the angular frequency  $\omega_0$  (which is done through the Fourier-like integrals) and to supply as a control signal a sinusoidal function at the angular frequency  $\omega_0$ , whose magnitude is modulated by these Fourier coefficients.

---

<sup>1</sup> Note that in this framework  $\omega$  is used to denote a generic angular frequency (i.e., contrarily to the previous chapters, it is unrelated to the electrical drive).

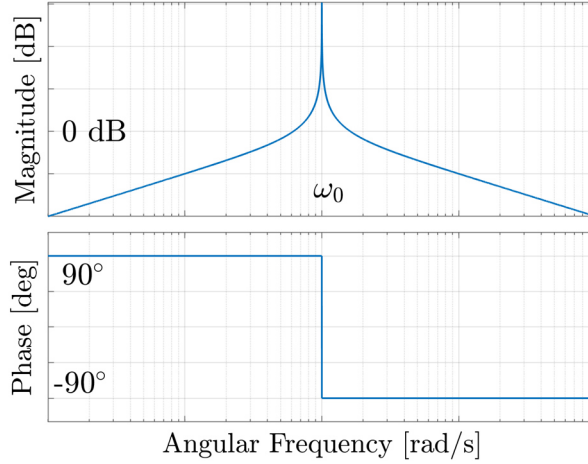


Fig. 9.1 – Bode diagram of a resonant controller (with  $K_R = 1$ ).

In other words, if the error signal  $\varepsilon(t)$  has a harmonic at frequency  $\omega_0$ , the results of the integrals grow linearly in time, and therefore  $y(t)$  is a sinusoidal function whose magnitude grows linearly in time, coherently with the behaviour of a resonant dynamical system. This linearly increasing output, by acting on the dynamical system under control, is stabilized only when the corresponding harmonic in the error function  $\varepsilon(t)$  is nullified. Under this point of view, a simple integrator can be interpreted as a particular case of (9.2) when  $\omega_0 = 0$ : in this case  $y(t)$  would be a DC signal (i.e., not sinusoidal) whose magnitude linearly increases with the DC component of the error signal  $\varepsilon(t)$ .

The validity of the algorithm can be mathematically justified by considering an error signal in the complex domain as  $\varepsilon(t) = E_M \cdot e^{j\omega t}$  and by computing the output signal of (9.2), which is:

$$\begin{aligned} y(t) &= K_R \cdot \left[ \cos(\omega_0 t) \cdot \int E_M \cdot e^{j\omega t} \cdot \cos(\omega_0 t) dt + \sin(\omega_0 t) \cdot \int E_M \cdot e^{j\omega t} \cdot \sin(\omega_0 t) dt \right] = \\ &= K_R \cdot \frac{E_M \cdot e^{j\omega t}}{\omega_0^2 - \omega^2} \cdot \left[ \cos(\omega_0 t) \cdot (\omega_0 \cdot \sin(\omega_0 t) + j\omega \cdot \cos(\omega_0 t)) + \dots \right. \\ &\quad \left. \dots + \sin(\omega_0 t) \cdot (j\omega \cdot \sin(\omega_0 t) + \omega_0 \cdot \cos(\omega_0 t)) \right] = E_M \cdot e^{j\omega t} \cdot K_R \cdot \frac{j\omega}{\omega_0^2 - \omega^2} \end{aligned}$$

This means that the frequency response of (9.2) is equal to the desired frequency response of (9.1).

Since, for the control algorithm proposed in Chapter 6, the resonance frequency is linked to the rotor angular speed, all the terms  $\omega_0 t$  can be simply replaced by a multiple integer of the rotor position  $\theta$ . In other words, to synchronize the resonance frequency  $\omega_0$  with the  $h$ -th multiple integer of the machine angular speed, the algorithm implementation (9.2) is simplified to:

$$y(t) = K_R \cdot \left[ \cos(h\theta) \cdot \int \varepsilon(t) \cos(h\theta) dt + \sin(h\theta) \cdot \int \varepsilon(t) \sin(h\theta) dt \right] \quad (9.3)$$

and the corresponding block diagram is depicted in Fig. 9.2. With this implementation,

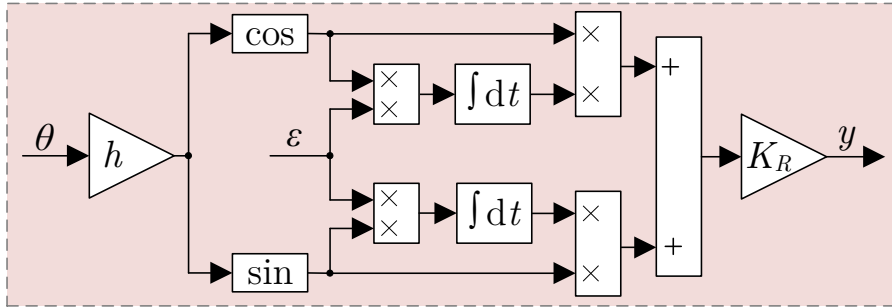


Fig. 9.2 – Resonant controller implementation.

similarly to an integral controller implemented in the synchronous domain, the frequency tuning is automatically done through the rotor position  $\theta$ .

Note that, in presence of multiple resonant actions, the computation of the terms  $\cos(h\theta)$  and  $\sin(h\theta)$  in (9.3) can be obtained from  $\cos(\theta)$  and  $\sin(\theta)$  by using the multiple-angle formulas of sine and cosine functions. This can be particularly convenient for real-time implementations, because it allows replacing the calculation of many trigonometric functions (which may be computationally demanding) with simple algebraic expressions (i.e., sums and products), thus allowing for a much faster and efficient execution.

For the experiments of Chapter 6, the integrals in (9.3) have been discretized with the trapezoidal method. It has also been found that no sensible difference was obtained by using other discretization methods (e.g., forward Euler and backward Euler). A compensation of the phase delay introduced by the discrete-time implementation and by the pulse-width-modulation (i.e.,  $1.5\omega T_s$ ) has revealed useful to improve the controller stability of the high-order resonant actions. This is coherent with the analogous results given in [161] for different resonant controller implementations.

### 9.1.2 Torquemeter measurement

This section clarifies some observations regarding the torque measurements obtained in Section 6.7.

The measurements have been obtained by a torque meter positioned between the shaft of the multiphase machine under analysis and the shaft of the DC machine used for mechanical loading.

The mechanical model of both machines can be analysed by referring to the expressions (5.42) and (5.44), which are here reported:

$$\begin{aligned}
 J \cdot \frac{d\omega}{dt} + F(\omega) \cdot \omega &= T_{em} - T_m \\
 J_m \cdot \frac{d\omega}{dt} + F_m(\omega) \cdot \omega &= T_m - T_{load}
 \end{aligned}
 \tag{9.4}$$

Part of the electromagnetic torque  $T_{em}$  developed by the multiphase machine through the electromechanical conversion is used to compensate the multiphase machine inertial torque  $J \cdot d\omega/dt$  and friction  $F(\omega) \cdot \omega$ , while the remaining part  $T_m$  acts as a motoring

torque contribution for the coupled DC machine. This torque  $T_m$  is itself used in part to compensate the DC machine inertial torque  $J_m \cdot d\omega/dt$  and friction  $F_m(\omega) \cdot \omega$ , and in part to compensate the loading torque  $T_{load}$  generated by electromechanical conversion by the DC machine (whose armature terminals are connected to an external resistor through a controllable contactor).

The measurement obtained with the torque meter is the torque  $T_m$  transferred between the two shafts. It is intrinsically different from both the electromagnetic torques  $T_{em}$  and  $T_{load}$  applied by the two electrical machines, because it does not take into account the inertial and friction contributions.

To better clarify this statement, it is possible to refer to the simulation of the mechanical system shown in Fig. 9.3. In this simulation, the mechanical system (purple blocks) has been represented by splitting the overall drive train into the PMSM and DC machine components. An idealized torque sensor has been inserted between them.

The PMSM torque is developed by introducing the same “Speed Controller” block which has been used in the experiments of Chapter 6 and by neglecting the electrical dynamics. In other words, for simplicity reasons, it is assumed that the output of the Speed Controller block is the same electromagnetic torque  $T_{em}$  developed by the machine.

The DC machine torque, which in the experiments of Chapter 6 has been realized by connecting the DC machine terminals to an external  $25 \Omega$  resistor, has been simulated through a controlled torque whose value is proportional to the DC machine speed and is such that, at the speed of 500 rpm, the developed torque is around 2.1 Nm. It represents the applied loading torque  $T_{load}$  of (9.4).

The inertia and friction contributions of both machines have been set coherently with the estimated data provided in Section 6.6.

The simulation has been set to emulate the dynamical testing scenarios of the experiments discussed in Section 6.7. Initially, the system is in steady-state conditions at  $-500$  rpm and the external resistor on the DC machine is not connected. Then, at 100 ms, the reference speed is changed to 500 rpm. Finally, at 600 ms, the braking torque of the DC machine is activated.

The simulation results are depicted in Fig. 9.4 (left). They are compared with the corresponding experimental results obtained in Section 6.7.1 for the single-star connection of the multiphase PMSM, represented in Fig. 9.4 (right). These experimental results have also been represented in Fig. 6.18 and Fig. 6.19. It is here recalled that the measured speed  $\omega$  has been obtained with a Omron E6B2-CWZ1X incremental encoder, with a resolution of 1000 pulses/revolution, while the measured torque  $T_m$  has been obtained with a Magtrol Torquemaster TM 210 has positioned between the PMSM and the DC machine rotor shafts. The electromagnetic torque  $T_{em}$  has instead been estimated by computing the analytical expression (6.4) of the torque with the set of measured PMSM currents.

As can be noted, the qualitative behaviour of the simulated mechanical system is very similar to the corresponding experimental results.



## 9.2 Chapter 2 Proofs

This section contains the proof of the properties stated in Chapter 2 - Electrical Machine Model.

### 9.2.1 Power balance equation for an electrical machine

Considering a motoring power flow convention, it is possible to write the following power balance equation:

$$p_{el} = p_m + p_\omega + p_R + p_F + p_{em} \quad (9.5)$$

where:

- $p_{el} = \sum_{k=1}^n i_k \cdot v_k$  represents the *input electrical power* absorbed from the network,
- $p_m = T_m \cdot \omega$  represents the *output mechanical power* delivered at the rotor shaft,
- $p_\omega = \frac{d}{dt} \left( \frac{1}{2} J \cdot \omega^2 \right)$  represents the *kinetic mechanical power* absorbed to accelerate the rotor mass (i.e., to increase the *kinetic energy*  $\frac{1}{2} J \cdot \omega^2$ ),
- $p_R = \sum_{k=1}^n R_k \cdot i_k^2$  represents the *Joule losses* in the machine windings,
- $p_F = F(\omega) \cdot \omega^2$  represents the *mechanical friction losses*, and
- $p_{em} = dW_{em}/dt$  represents the *electromagnetic power* absorbed by the machine (i.e., to change the *electromagnetic energy*  $W_{em}$ ).

It is here shown that the net electromagnetic power absorbed by the machine is given by the expression (2.5).

**Proof.** By considering the electrical equations (2.1), the input power absorbed from the electrical network can be explicitly found to be:

$$p_{el} = \sum_k i_k \cdot u_k = \mathbf{i}^T \cdot \mathbf{v} = \mathbf{i}^T \cdot \mathbf{R} \cdot \mathbf{i} + \mathbf{i}^T \cdot \frac{d\phi}{dt}$$

The term  $\mathbf{i}^T \cdot \mathbf{R} \cdot \mathbf{i} = \sum_{k=1}^n R_k \cdot i_k^2$  can be recognized to be the overall Joule losses  $p_R$ .

Similarly, by considering the mechanical equation (2.4), the output mechanical power  $p_m$  delivered at the rotor shaft can be explicitly computed:

$$p_m = T_m \cdot \omega = T_{em} \cdot \omega - F \cdot \omega^2 - J \cdot \omega \cdot \frac{d\omega}{dt}$$

The term  $F \cdot \omega^2$  can be recognized to be the machine friction losses  $p_F$ , while the term  $J \cdot \omega \cdot d\omega/dt = \frac{d}{dt} \left( \frac{1}{2} J \cdot \omega^2 \right)$  represents the mechanical power  $p_\omega$  to accelerate the rotor mass.

By substituting these explicit expressions in the power balance equation (9.5) and by properly grouping the various terms it results:

$$\begin{aligned}
 \frac{dW_{em}}{dt} &= p_{em} = p_{el} - p_m - p_\omega - p_R - p_F = \\
 &= \mathbf{i}^T \cdot \mathbf{R} \cdot \mathbf{i} + \mathbf{i}^T \cdot \frac{d\phi}{dt} - T_{em} \cdot \omega + F \cdot \omega^2 + J \cdot \omega \cdot \frac{d\omega}{dt} - p_\omega - p_R - p_F = \\
 &= \left( \mathbf{i}^T \cdot \frac{d\phi}{dt} - T_{em} \cdot \omega \right) - (p_R - \mathbf{i}^T \cdot \mathbf{R} \cdot \mathbf{i}) - (p_F - F \cdot \omega^2) - \left( p_\omega - J \cdot \omega \cdot \frac{d\omega}{dt} \right) = \\
 &= \mathbf{i}^T \cdot \frac{d\phi}{dt} - T_{em} \cdot \omega = \mathbf{i}^T \cdot \frac{d\phi}{dt} - T_{em} \cdot \frac{d\theta}{dt}
 \end{aligned}$$

□

### 9.2.2 Orthogonality of conservative and solenoidal fields

It is here proven that, given a conservative vector field  $\vec{A}$  and a solenoidal vector field  $\vec{B}$  in a closed domain  $\mathfrak{D}$  with the boundary condition  $\vec{B} \cdot \hat{n} = 0$  on  $\partial\mathfrak{D}$ , then it results:

$$\iiint_{\mathfrak{D}} \vec{A} \cdot \vec{B} \, dV = 0 \tag{9.6}$$

**Proof.** The property (9.6) follows from the vector manipulations:

$$\begin{aligned}
 \iiint_{\mathfrak{D}} \vec{A} \cdot \vec{B} \, dV &= \left( \begin{array}{l} \vec{A} \text{ is conservative:} \\ \vec{A} = \nabla f \end{array} \right) \\
 &= \iiint_{\mathfrak{D}} \nabla f \cdot \vec{B} \, dV = \left( \begin{array}{l} \text{Vector Identity:} \\ \nabla \cdot (f \vec{B}) = \nabla f \cdot \vec{B} + f(\nabla \cdot \vec{B}) \end{array} \right) \\
 &= \iiint_{\mathfrak{D}} [\nabla \cdot (f \vec{B}) - f(\nabla \cdot \vec{B})] \, dV = \left( \begin{array}{l} \vec{B} \text{ is solenoidal:} \\ \nabla \cdot \vec{B} = 0 \end{array} \right) \\
 &= \iiint_{\mathfrak{D}} \nabla \cdot (f \vec{B}) \, dV = \left( \begin{array}{l} \iiint_{\mathfrak{D}} \nabla \cdot \vec{v} \, dV = \oint_{\partial\mathfrak{D}} \vec{v} \cdot \hat{n} \, dS \end{array} \right) \\
 &= \oint_{\partial\mathfrak{D}} f \vec{B} \cdot \hat{n} \, dS = 0 \left( \begin{array}{l} \text{Boundary Condition:} \\ \vec{B} \cdot \hat{n} = 0 \text{ on } \partial\mathfrak{D} \end{array} \right)
 \end{aligned}$$

□

### 9.2.3 Uniqueness of the MQS solution

It is here proven that the MQS system:

$$\left\{ \begin{array}{l} \oint_{S_\tau} \vec{B} \cdot \hat{n} \, dS = 0 \\ \oint_{S_\gamma} \vec{H} \cdot \hat{t} \, dl = \iint_{S_\gamma} \vec{J}_f \cdot \hat{n} \, dS \\ \vec{B} = \mu \vec{H} + \vec{B}_{PM} \text{ (with } \mu > 0) \\ \vec{B} \cdot \hat{n} = 0 \text{ on } \partial\mathfrak{D} \end{array} \right. \tag{9.7}$$

which, in the linear approximation, describes the magnetic behaviour of an electrical machine with the simultaneous presence of current-carrying windings and permanent magnets [129], has a unique solution.

**Proof.** Suppose there exist two solutions  $(\vec{H}^{(1)}, \vec{B}^{(1)})$  and  $(\vec{H}^{(2)}, \vec{B}^{(2)})$ . Both solutions satisfy the system of equations (9.7). The difference fields defined as  $(\vec{H}^{(3)}, \vec{B}^{(3)}) =$

$(\vec{H}^{(1)} - \vec{H}^{(2)}, \vec{B}^{(1)} - \vec{B}^{(2)})$  satisfy the following homogeneous system of equations:

$$\begin{cases} \oint_{S_\tau} \vec{B}^{(3)} \cdot \hat{n} \, dS = 0 \\ \oint_\gamma \vec{H}^{(3)} \cdot \hat{t} \, dl = 0 \\ \vec{B}^{(3)} = \mu \vec{H}^{(3)} \quad (\text{with } \mu > 0) \\ \vec{B}^{(3)} \cdot \hat{n} = 0 \quad \text{on } \partial\mathfrak{D} \end{cases}$$

Meaning that the field  $\vec{H}^{(3)}$  is conservative and the field  $\vec{B}^{(3)}$  is solenoidal. Then, by computing the total energy stored in the system and applying the property (9.6) it results that:

$$W_{em} = \iiint_{\mathfrak{D}} \frac{1}{2} \frac{B^{(3)2}}{\mu} \, dV = \frac{1}{2} \iiint_{\mathfrak{D}} \frac{\vec{B}^{(3)} \cdot \vec{B}^{(3)}}{\mu} \, dV = \frac{1}{2} \iiint_{\mathfrak{D}} \vec{B}^{(3)} \cdot \vec{H}^{(3)} \, dV = 0$$

but since the first term is a squared quantity, the only way for this integral to be zero is to have  $\vec{B}^{(3)} = 0$ , which also implies  $\vec{H}^{(3)} = 0$ . This means that  $\vec{H}^{(1)} = \vec{H}^{(2)}$  and that  $\vec{B}^{(1)} = \vec{B}^{(2)}$ . Then, the solution to (9.7) is unique.  $\square$

## 9.2.4 Electromagnetic energy and coenergy properties

The coefficients of the electromagnetic energy and coenergy expressions (2.25) and (2.26) can be computed from the integrals (2.19) and (2.20) with the magnetic field  $\vec{H}$  and the magnetic flux density field  $\vec{B}$  given by (2.24), resulting in:

$$\begin{aligned} W_{em}^{(0)} &= \iiint_{\mathfrak{D}} \frac{1}{2} \mu H^{(0)2} \, dV & W'_{em}{}^{(0)} &= \iiint_{\mathfrak{D}} \frac{1}{2} \frac{B^{(0)2}}{\mu} \, dV \\ W_{em,k}^{(1)} &= \iiint_{\mathfrak{D}} \mu \vec{H}^{(0)} \cdot \vec{h}^{(k)} \, dV & W'_{em,k}{}^{(1)} &= \iiint_{\mathfrak{D}} \frac{1}{\mu} \vec{B}^{(0)} \cdot \vec{b}^{(k)} \, dV \\ W_{em,k_1,k_2}^{(2)} &= \iiint_{\mathfrak{D}} \frac{1}{2} \mu \vec{h}^{(k_1)} \cdot \vec{h}^{(k_2)} \, dV & W'_{em,k_1,k_2}{}^{(2)} &= \iiint_{\mathfrak{D}} \frac{\vec{b}^{(k_1)} \cdot \vec{b}^{(k_2)}}{2\mu} \, dV \end{aligned} \quad (9.8)$$

where it is worth recalling that the fields  $(\vec{H}^{(0)}, \vec{B}^{(0)})$  are the solutions to the MQS problem (9.7) in absence of currents, while the fields  $(\vec{h}^{(k)}, \vec{b}^{(k)})$  (with  $k = 1, \dots, n$ ) are the solution of the MQS problem (9.7) in presence of the sole  $k$ -th current and in absence of permanent magnetization. This means that:

$$\begin{cases} \oint_{S_\tau} \vec{B}^{(0)} \cdot \hat{n} \, dS = 0 \\ \oint_\gamma \vec{H}^{(0)} \cdot \hat{t} \, dl = 0 \\ \vec{B}^{(0)} = \mu \vec{H}^{(0)} + \vec{B}_{PM} \\ \vec{B}^{(0)} \cdot \hat{n} = 0 \quad \text{on } \partial\mathfrak{D} \end{cases} \quad \text{and} \quad \begin{cases} \oint_{S_\tau} \vec{b}^{(k)} \cdot \hat{n} \, dS = 0 \\ \oint_\gamma \vec{h}^{(k)} \cdot \hat{t} \, dl = \iint_{S_\gamma} \vec{j}_{f,k} \cdot \hat{n} \, dS \\ \vec{b}^{(k)} = \mu \vec{h}^{(k)} \\ \vec{b}^{(k)} \cdot \hat{n} = 0 \quad \text{on } \partial\mathfrak{D} \end{cases} \quad (9.9)$$

The properties (2.27) of the electromagnetic energy and coenergy coefficients (9.8) are here proven.

**Proof.** First, consider the symmetry properties  $W_{em,k_1,k_2}^{(2)} = W_{em,k_2,k_1}^{(2)}$  and  $W'_{em,k_1,k_2}{}^{(2)} = W'_{em,k_2,k_1}{}^{(2)}$ . They can be directly derived from the expressions (9.8) considering that the dot product is commutative (i.e.,  $\vec{h}^{(k_1)} \cdot \vec{h}^{(k_2)} = \vec{h}^{(k_2)} \cdot \vec{h}^{(k_1)}$  and  $\vec{b}^{(k_1)} \cdot \vec{b}^{(k_2)} = \vec{b}^{(k_2)} \cdot \vec{b}^{(k_1)}$ ).

Consider the property  $W_{em,k_1,k_2}^{(2)} = W'_{em,k_1,k_2}{}^{(2)}$ . The fields  $(\vec{h}^{(k_1)}, \vec{b}^{(k_1)})$  and  $(\vec{h}^{(k_2)}, \vec{b}^{(k_2)})$  are both solutions of the demagnetized MQS problem (9.7) with  $\vec{B}_{PM} = 0$ . This means that  $\vec{b}^{(k_1)} = \mu \vec{h}^{(k_1)}$  and  $\vec{b}^{(k_2)} = \mu \vec{h}^{(k_2)}$ . Then, by simple algebraic manipulations, it results:

$$\begin{aligned} W_{em,k_1,k_2}^{(2)} &= \iiint_{\mathcal{D}} \frac{1}{2} \mu \vec{h}^{(k_1)} \cdot \vec{h}^{(k_2)} dV = \iiint_{\mathcal{D}} \frac{1}{2\mu} (\mu \vec{h}^{(k_1)}) \cdot (\mu \vec{h}^{(k_2)}) dV = \\ &= \iiint_{\mathcal{D}} \frac{1}{2\mu} \vec{b}^{(k_1)} \cdot \vec{b}^{(k_2)} dV = W'_{em,k_1,k_2}{}^{(2)} \end{aligned}$$

which is the symmetry property of (2.27).

Consider now the property  $W_{em,k}^{(1)} = 0$ . The fields  $(\vec{H}^{(0)}, \vec{B}^{(0)})$  are the solution of the MQS problem (9.7) with all the currents being zero. This means that the magnetic field  $\vec{H}^{(0)}$  is conservative. The fields  $(\vec{h}^{(k)}, \vec{b}^{(k)})$  are the solution of the demagnetized MQS problem (9.7) with  $\vec{B}_{PM} = 0$ , meaning that  $\vec{b}^{(k)} = \mu \vec{h}^{(k)}$ .

Since  $\vec{H}^{(0)}$  is conservative and  $\vec{b}^{(k)}$  is solenoidal, by applying (9.6) it results:

$$W_{em,k}^{(1)} = \iiint_{\mathcal{D}} \mu \vec{H}^{(0)} \cdot \vec{h}^{(k)} dV = \iiint_{\mathcal{D}} \vec{H}^{(0)} \cdot (\mu \vec{h}^{(k)}) dV = \iiint_{\mathcal{D}} \vec{H}^{(0)} \cdot \vec{b}^{(k)} dV = 0$$

which is the aforementioned property of the energy coefficients.

Finally, consider the property  $W_{em}^{(0)} + W'_{em}{}^{(0)} = \iiint_{\mathcal{D}} (B_{PM}^2/2\mu) dV$ . The fields  $(\vec{H}^{(0)}, \vec{B}^{(0)})$  are the solution of the MQS problem (9.7) with all the currents being zero. This means that the magnetic field  $\vec{H}^{(0)}$  is conservative and  $\vec{B}^{(0)}$  is solenoidal.

By applying the property (9.6) the computation of the energy coefficient results in:

$$\begin{aligned} W_{em}^{(0)} &= \iiint_{\mathcal{D}} \frac{1}{2} \mu H^{(0)2} dV = \iiint_{\mathcal{D}} \frac{1}{2} (\mu \vec{H}^{(0)}) \cdot \vec{H}^{(0)} dV = \iiint_{\mathcal{D}} \frac{1}{2} (\vec{B}^{(0)} - \vec{B}_{PM}) \cdot \vec{H}^{(0)} dV = \\ &= \frac{1}{2} \iiint_{\mathcal{D}} \vec{B}^{(0)} \cdot \vec{H}^{(0)} dV - \iiint_{\mathcal{D}} \frac{1}{2} \vec{B}_{PM} \cdot \vec{H}^{(0)} dV = - \iiint_{\mathcal{D}} \frac{1}{2} \vec{B}_{PM} \cdot \vec{H}^{(0)} dV \end{aligned}$$

Similarly, the computation of the coenergy coefficient results in:

$$\begin{aligned} W'_{em}{}^{(0)} &= \iiint_{\mathcal{D}} \frac{1}{2\mu} B^{(0)2} dV = \iiint_{\mathcal{D}} \frac{1}{2} \left( \frac{\vec{B}^{(0)}}{\mu} \right) \cdot \vec{B}^{(0)} dV = \iiint_{\mathcal{D}} \frac{1}{2} \left( \vec{H}^{(0)} + \frac{\vec{B}_{PM}}{\mu} \right) \cdot \vec{B}^{(0)} dV = \\ &= \frac{1}{2} \iiint_{\mathcal{D}} \vec{H}^{(0)} \cdot \vec{B}^{(0)} dV + \iiint_{\mathcal{D}} \frac{1}{2\mu} \vec{B}_{PM} \cdot \vec{B}^{(0)} dV = \iiint_{\mathcal{D}} \frac{1}{2\mu} \vec{B}_{PM} \cdot \vec{B}^{(0)} dV \end{aligned}$$

By summing these two terms it results:

$$\begin{aligned} W_{em}^{(0)} + W'_{em}{}^{(0)} &= \iiint_{\mathcal{D}} \frac{1}{2\mu} \vec{B}_{PM} \cdot \vec{B}^{(0)} dV - \iiint_{\mathcal{D}} \frac{1}{2} \vec{B}_{PM} \cdot \vec{H}^{(0)} dV = \\ &= \iiint_{\mathcal{D}} \frac{1}{2} \vec{B}_{PM} \cdot \left( \frac{\vec{B}^{(0)}}{\mu} - \vec{H}^{(0)} \right) dV = \iiint_{\mathcal{D}} \frac{1}{2\mu} B_{PM}^2 dV \end{aligned}$$

which is the last property to be proven.  $\square$

## 9.2.5 Inductances matrix properties

It is here proven that the inductances matrix  $\mathbf{L}$  is symmetric and positive definite.

**Proof.** First, consider the symmetry property. From the definition (2.28) it immediately results that:

$$L_{k_1, k_2} = 2 \cdot W'_{em, k_1, k_2} = 2 \cdot \iiint_{\mathfrak{D}} \frac{\vec{b}^{(k_1)} \cdot \vec{b}^{(k_2)}}{2\mu} dV = 2 \cdot W'_{em, k_2, k_1} = L_{k_2, k_1}$$

Consider now the positive definiteness property. The inductances matrix coefficient can be computed by solving the MQS model of the machine in absence of permanent magnetization effects. The solution to this problem is given by (2.24) with  $\vec{H}^{(0)} = 0$  and  $\vec{B}^{(0)} = 0$ . Then, the electromagnetic energy stored in the demagnetized model is:

$$W_{em} = \iiint_{\mathfrak{D}} \frac{1}{2} \mu H^2 dV = \sum_{k_1=1}^n \sum_{k_2=1}^n W_{em, k_1, k_2}^{(2)} \cdot i_{k_1} \cdot i_{k_2} = \frac{1}{2} \cdot \mathbf{i}^T \cdot \mathbf{L} \cdot \mathbf{i}$$

Since  $\mu > 0$ , the integral is always non-negative and is zero only in absence of any magnetic field  $\vec{H}$  in the whole machine domain  $\mathfrak{D}$ . The presence of any current always leads to the generation of a magnetic field<sup>2</sup>. Then, for any  $n \times 1$  currents vector  $\mathbf{i} \neq \mathbf{0}$ , it results  $\mathbf{i}^T \cdot \mathbf{L} \cdot \mathbf{i} > 0$ , meaning that  $\mathbf{L}$  is positive definite. □

## 9.2.6 Torque expression from the electromagnetic energy

It is here proven that the electromagnetic torque expression computed as  $T_{em} = -\partial W_{em} / \partial \theta$  with respect to the energy expression (2.31) is equivalent to the expression (2.33) computed as  $T_{em} = \partial W'_{em} / \partial \theta$  to the coenergy expression (2.32).

**Proof.** The torque computation through the energy expression first requires to reformulate (2.31) in terms of the machine fluxes  $\phi$  instead of the machine currents  $\mathbf{i}$ . By inverting the relation (2.29) it results that:

$$\mathbf{i} = \mathbf{\Gamma}(\theta) \cdot [\phi - \psi_{PM}(\theta)]$$

where it is worth recalling that  $\mathbf{\Gamma}(\theta) = \mathbf{L}^{-1}(\theta)$  is the reluctances matrix, which is symmetric and positive definite. By substituting this expression in (2.31) it results that:

$$\begin{aligned} W_{em} &= W_{em}^{(0)}(\theta) + \frac{1}{2} \cdot \mathbf{i}^T \cdot \mathbf{L}(\theta) \cdot \mathbf{i} = \\ &= W_{em}^{(0)}(\theta) + \frac{1}{2} \cdot [\phi - \psi_{PM}(\theta)]^T \cdot \mathbf{\Gamma}(\theta) \cdot \mathbf{L}(\theta) \cdot \mathbf{\Gamma}(\theta) \cdot [\phi - \psi_{PM}(\theta)] = \\ &= W_{em}^{(0)}(\theta) + \frac{1}{2} \cdot [\phi - \psi_{PM}(\theta)]^T \cdot \mathbf{\Gamma}(\theta) \cdot [\phi - \psi_{PM}(\theta)] \end{aligned}$$

By applying the  $\theta$ -derivative (2.8) with fixed fluxes it results that:

<sup>2</sup> The only exception would be verified when the field generated by one current perfectly cancels out the field generated by another one in the whole machine domain. However, this behaviour (which would lead to a semi-positive definite matrix) would be an unrealistic model.

$$T_{em} = -\frac{\partial W_{em}}{\partial \theta} = -\frac{\partial W_{em}^{(0)}}{\partial \theta} + \left(\frac{\partial \psi_{PM}}{\partial \theta}\right)^T \cdot \mathbf{\Gamma}(\theta) \cdot [\phi - \psi_{PM}(\theta)] + \dots \\ \dots - \frac{1}{2} \cdot [\phi - \psi_{PM}(\theta)]^T \cdot \frac{\partial \mathbf{\Gamma}}{\partial \theta} \cdot [\phi - \psi_{PM}(\theta)]$$

Similarly to (2.33), the torque is given by three contributions:

- the term  $-\partial W_{em}^{(0)}/\partial \theta$ , which is independent of the fluxes,
- the term  $(\partial \psi_{PM}/\partial \theta)^T \cdot \mathbf{\Gamma}(\theta) \cdot [\phi - \psi_{PM}(\theta)]$ , which is linearly varying with the fluxes,
- the term  $-(1/2) \cdot [\phi - \psi_{PM}(\theta)]^T \cdot (\partial \mathbf{\Gamma}/\partial \theta) \cdot [\phi - \psi_{PM}(\theta)]$ , which is quadratically varying with the fluxes.

The first torque contribution, thanks to (2.27), can be rewritten as:

$$-\frac{\partial W_{em}^{(0)}}{\partial \theta} = -\frac{\partial}{\partial \theta} \left( \iiint_{\mathcal{Q}} \frac{1}{2} \frac{B_{PM}^2}{\mu} dV - W_{em}^{(0)}(\theta) \right) = \frac{\partial W_{em}'^{(0)}}{\partial \theta}$$

because the integral  $\iiint_{\mathcal{Q}} (B_{PM}^2/2\mu)dV$  does not depend on the rotor position  $\theta$ . It is equal to the current independent term  $T_0(\theta)$  in (2.33).

The second torque contribution can be rewritten as:

$$\left(\frac{\partial \psi_{PM}}{\partial \theta}\right)^T \cdot \mathbf{\Gamma}(\theta) \cdot [\phi - \psi_{PM}(\theta)] = \mathbf{f}_{PM}^T(\theta) \cdot \mathbf{i}$$

where  $\mathbf{f}_{PM}(\theta) = \partial \psi_{PM}/\partial \theta$ . It is equal to the term in (2.33) which is linearly varying with the machine currents.

The third torque contribution can be rewritten as:

$$-\frac{1}{2} \cdot [\phi - \psi_{PM}(\theta)]^T \cdot \frac{\partial \mathbf{\Gamma}}{\partial \theta} \cdot [\phi - \psi_{PM}(\theta)] = -\frac{1}{2} \cdot \mathbf{i}^T \cdot \mathbf{L}(\theta) \cdot \frac{\partial \mathbf{\Gamma}}{\partial \theta} \cdot \mathbf{L}(\theta) \cdot \mathbf{i}$$

The  $\theta$ -derivative of the inductances matrix  $\mathbf{L}(\theta)$  can be rewritten as:

$$\mathbf{L}'(\theta) = \frac{\partial \mathbf{L}}{\partial \theta} = \frac{\partial}{\partial \theta} \left[ \mathbf{L}(\theta) \cdot \mathbf{\Gamma}(\theta) \cdot \mathbf{L}(\theta) \right] = \\ = 2 \cdot \frac{\partial \mathbf{L}}{\partial \theta} \cdot \mathbf{\Gamma}(\theta) \cdot \mathbf{L}(\theta) + \mathbf{L}(\theta) \cdot \frac{\partial \mathbf{\Gamma}}{\partial \theta} \cdot \mathbf{L}(\theta) = \\ = 2 \cdot \mathbf{L}'(\theta) + \mathbf{L}(\theta) \cdot \frac{\partial \mathbf{\Gamma}}{\partial \theta} \cdot \mathbf{L}(\theta)$$

meaning that  $\mathbf{L}(\theta) \cdot (\partial \mathbf{\Gamma}/\partial \theta) \cdot \mathbf{L}(\theta) = -\mathbf{L}'(\theta)$ . By substituting in the previous expression, it results that:

$$-\frac{1}{2} \cdot [\phi - \psi_{PM}(\theta)]^T \cdot \frac{\partial \mathbf{\Gamma}}{\partial \theta} \cdot [\phi - \psi_{PM}(\theta)] = \frac{1}{2} \cdot \mathbf{i}^T \cdot \mathbf{L}'(\theta) \cdot \mathbf{i}$$

which is the term in (2.33) quadratically varying with the currents. □

### 9.2.7 Fixed reference frame transformation parameters

It is here proven that, by applying the transformation (2.36) to the phase variable model of the electrical machine (2.35), the transformed model is given by (2.37) and the

parameters are<sup>3</sup>:

$$\begin{aligned}
\tilde{\mathbf{f}}_{PM}(\theta) &= \mathbf{T} \cdot \mathbf{f}_{PM}(\theta) \\
\tilde{\mathbf{R}} &= \mathbf{T} \cdot \mathbf{R} \cdot \mathbf{T}^{-1} \\
\tilde{\mathbf{L}}(\theta) &= \mathbf{T} \cdot \mathbf{L}(\theta) \cdot \mathbf{T}^{-1} \\
\tilde{\mathbf{L}}'_E(\theta) &= \mathbf{T} \cdot \mathbf{L}'(\theta) \cdot \mathbf{T}^{-1} \\
\tilde{\mathbf{L}}'_T(\theta) &= \mathbf{T}^{-\text{T}} \cdot \mathbf{L}'(\theta) \cdot \mathbf{T}^{-1} \\
\tilde{\mathbf{Y}} &= \mathbf{T}^{-\text{T}} \cdot \mathbf{T}^{-1}
\end{aligned} \tag{9.10}$$

*Proof.* Consider the phase variable model (2.35). By applying the transformation  $\mathbf{x} = \mathbf{T}^{-1} \cdot \tilde{\mathbf{x}}$  to both the machine voltages and currents, the electrical equation is modified to:

$$\mathbf{L}(\theta) \cdot \frac{d}{dt}(\mathbf{T}^{-1} \cdot \tilde{\mathbf{i}}) + \mathbf{R} \cdot (\mathbf{T}^{-1} \cdot \tilde{\mathbf{i}}) + \mathbf{e} = (\mathbf{T}^{-1} \cdot \tilde{\mathbf{v}})$$

Since  $\mathbf{T}$  is constant, the matrix  $\mathbf{T}^{-1}$  can be taken out from the time derivative. By pre-multiplying both sides for  $\mathbf{T}$  it results that:

$$(\mathbf{T} \cdot \mathbf{L}(\theta) \cdot \mathbf{T}^{-1}) \cdot \frac{d\tilde{\mathbf{i}}}{dt} + (\mathbf{T} \cdot \mathbf{R} \cdot \mathbf{T}^{-1}) \cdot \tilde{\mathbf{i}} + (\mathbf{T} \cdot \mathbf{e}) = \tilde{\mathbf{v}}$$

which is the first equation of (2.37) with the parameters  $\tilde{\mathbf{L}}(\theta)$  and  $\tilde{\mathbf{R}}$  defined in (9.10). The transformed motional back-EMFs vector  $\tilde{\mathbf{e}}$  is:

$$\tilde{\mathbf{e}} = \mathbf{T} \cdot \mathbf{e} = \omega [\mathbf{T} \cdot \mathbf{f}_{PM}(\theta)] + \omega [\mathbf{T} \cdot \mathbf{L}'(\theta) \cdot \mathbf{T}^{-1}] \cdot \tilde{\mathbf{i}}$$

which is the second equation of (2.37), with  $\tilde{\mathbf{f}}_{PM}(\theta)$  and  $\tilde{\mathbf{L}}'_E(\theta)$  defined in (9.10).

With the same substitutions, the torque expression becomes:

$$\begin{aligned}
T_{em} &= T_0(\theta) + (\mathbf{T}^{-1} \cdot \tilde{\mathbf{f}}_{PM})^{\text{T}} \cdot (\mathbf{T}^{-1} \cdot \tilde{\mathbf{i}}) + \frac{1}{2} (\mathbf{T}^{-1} \cdot \tilde{\mathbf{i}})^{\text{T}} \cdot \mathbf{L}'(\theta) \cdot (\mathbf{T}^{-1} \cdot \tilde{\mathbf{i}}) = \\
&= T_0(\theta) + \tilde{\mathbf{f}}_{PM}^{\text{T}} \cdot [(\mathbf{T}^{-1})^{\text{T}} \cdot \mathbf{T}^{-1}] \cdot \tilde{\mathbf{i}} + \frac{1}{2} \tilde{\mathbf{i}}^{\text{T}} \cdot [(\mathbf{T}^{-1})^{\text{T}} \cdot \mathbf{L}'(\theta) \cdot \mathbf{T}^{-1}] \cdot \tilde{\mathbf{i}}
\end{aligned}$$

which is the third equation of (2.37) with the parameters  $\tilde{\mathbf{Y}}$  and  $\tilde{\mathbf{L}}'_T(\theta)$  defined in (9.10).  $\square$

## 9.2.8 Moving reference frame transformation parameters

It is here proven that, by applying the transformation (2.39) to the phase variable model of the electrical machine (2.35), the transformed model is given by (2.40) and the parameters are:

$$\begin{aligned}
\tilde{\mathbf{f}}_{PM}(\theta, \vartheta) &= \mathbf{T}(\vartheta) \cdot \mathbf{f}_{PM}(\theta) \\
\tilde{\mathbf{R}}(\vartheta) &= \mathbf{T}(\vartheta) \cdot \mathbf{R} \cdot \mathbf{T}^{-1}(\vartheta) \\
\tilde{\mathbf{L}}(\theta, \vartheta) &= \mathbf{T}(\vartheta) \cdot \mathbf{L}(\theta) \cdot \mathbf{T}^{-1}(\vartheta) \\
\tilde{\mathbf{L}}'_{E1}(\theta, \vartheta) &= \mathbf{T}(\vartheta) \cdot \mathbf{L}'(\theta) \cdot \mathbf{T}^{-1}(\vartheta) \\
\tilde{\mathbf{L}}'_{E2}(\theta, \vartheta) &= \mathbf{T}(\vartheta) \cdot \mathbf{L}(\theta) \cdot \frac{\partial}{\partial \vartheta} [\mathbf{T}^{-1}(\vartheta)] \\
\tilde{\mathbf{L}}'_T(\theta, \vartheta) &= \mathbf{T}^{-\text{T}}(\vartheta) \cdot \mathbf{L}'(\theta) \cdot \mathbf{T}^{-1}(\vartheta) \\
\tilde{\mathbf{Y}}(\vartheta) &= \mathbf{T}^{-\text{T}}(\vartheta) \cdot \mathbf{T}^{-1}(\vartheta)
\end{aligned} \tag{9.11}$$

<sup>3</sup> The notation  $\mathbf{T}^{-\text{T}}$  stands for  $\mathbf{T}^{-\text{T}} = (\mathbf{T}^{-1})^{\text{T}} = (\mathbf{T}^{\text{T}})^{-1}$ .

**Proof.** Consider the phase variable model (2.35). By applying the inverse transformation  $\mathbf{x} = \mathbf{T}^{-1}(\vartheta) \cdot \tilde{\mathbf{x}}$  to both the machine voltages and currents, the electrical equation is modified to:

$$\mathbf{L}(\theta) \cdot \frac{d}{dt} [\mathbf{T}^{-1}(\vartheta) \cdot \tilde{\mathbf{i}}] + \mathbf{R} \cdot [\mathbf{T}^{-1}(\vartheta) \cdot \tilde{\mathbf{i}}] + \mathbf{e} = [\mathbf{T}^{-1}(\vartheta) \cdot \tilde{\mathbf{v}}]$$

Since the matrix  $\mathbf{T}$  depends on the variable parameter  $\vartheta$ , the time derivative is decomposed as:

$$\frac{d}{dt} [\mathbf{T}^{-1}(\vartheta) \cdot \tilde{\mathbf{i}}] = \frac{d}{dt} [\mathbf{T}^{-1}(\vartheta)] \cdot \tilde{\mathbf{i}} + \mathbf{T}^{-1}(\vartheta) \cdot \frac{d\tilde{\mathbf{i}}}{dt} = \Omega \cdot \frac{\partial}{\partial \vartheta} [\mathbf{T}^{-1}(\vartheta)] \cdot \tilde{\mathbf{i}} + \mathbf{T}^{-1}(\vartheta) \cdot \frac{d\tilde{\mathbf{i}}}{dt}$$

with  $\Omega = d\vartheta/dt$ . By substituting this expression and by multiplying both sides for  $\mathbf{T}(\vartheta)$  it results that:

$$\begin{aligned} & [\mathbf{T}(\vartheta) \cdot \mathbf{L}(\theta) \cdot \mathbf{T}^{-1}(\vartheta)] \cdot \frac{d\tilde{\mathbf{i}}}{dt} + [\mathbf{T}(\vartheta) \cdot \mathbf{R} \cdot \mathbf{T}^{-1}(\vartheta)] \cdot \tilde{\mathbf{i}} + \dots \\ & \dots + \Omega \left\{ \mathbf{T}(\vartheta) \cdot \mathbf{L}(\theta) \cdot \frac{\partial}{\partial \vartheta} [\mathbf{T}^{-1}(\vartheta)] \right\} \cdot \tilde{\mathbf{i}} + \mathbf{T}(\vartheta) \cdot \mathbf{e} = \tilde{\mathbf{v}} \end{aligned}$$

If the term dependent by  $\Omega$  is grouped into  $\tilde{\mathbf{e}}$ , this is the first equation of (2.40) with the parameters  $\tilde{\mathbf{L}}(\theta, \vartheta)$  and  $\tilde{\mathbf{R}}(\vartheta)$  defined in (9.11). The transformed back-EMFs vector is therefore defined as:

$$\begin{aligned} \tilde{\mathbf{e}} &= \mathbf{T}(\vartheta) \cdot \mathbf{e} + \Omega \left\{ \mathbf{T}(\vartheta) \cdot \mathbf{L}(\theta) \cdot \frac{\partial}{\partial \vartheta} [\mathbf{T}^{-1}(\vartheta)] \right\} \cdot \tilde{\mathbf{i}} = \\ &= \omega [\mathbf{T}(\vartheta) \cdot \mathbf{f}_{PM}(\theta)] + \omega [\mathbf{T}(\vartheta) \cdot \mathbf{L}'(\theta) \cdot \mathbf{T}^{-1}(\vartheta)] \cdot \tilde{\mathbf{i}} + \Omega \left\{ \mathbf{T}(\vartheta) \cdot \mathbf{L}(\theta) \cdot \frac{\partial}{\partial \vartheta} [\mathbf{T}^{-1}(\vartheta)] \right\} \cdot \tilde{\mathbf{i}} \end{aligned}$$

which is the second equation of (2.40) with the parameters  $\tilde{\mathbf{f}}_{PM}(\theta, \vartheta)$ ,  $\tilde{\mathbf{L}}'_{E1}(\theta, \vartheta)$  and  $\tilde{\mathbf{L}}'_{E2}(\theta, \vartheta)$  defined in (9.11).

With the same substitutions, the torque expression becomes:

$$\begin{aligned} T_{em} &= T_0(\theta) + [\mathbf{T}^{-1}(\vartheta) \cdot \tilde{\mathbf{f}}_{PM}]^T \cdot [\mathbf{T}^{-1}(\vartheta) \cdot \tilde{\mathbf{i}}] + \frac{1}{2} [\mathbf{T}^{-1}(\vartheta) \cdot \tilde{\mathbf{i}}]^T \cdot \mathbf{L}'(\theta) \cdot [\mathbf{T}^{-1}(\vartheta) \cdot \tilde{\mathbf{i}}] = \\ &= T_0(\theta) + \tilde{\mathbf{f}}_{PM}^T \cdot \{[\mathbf{T}^{-1}(\vartheta)]^T \cdot \mathbf{T}^{-1}(\vartheta)\} \cdot \tilde{\mathbf{i}} + \frac{1}{2} \tilde{\mathbf{i}}^T \cdot \{[\mathbf{T}^{-1}(\vartheta)]^T \cdot \mathbf{L}'(\theta) \cdot \mathbf{T}^{-1}(\vartheta)\} \cdot \tilde{\mathbf{i}} \end{aligned}$$

which is the third equation of (2.40), with  $\tilde{\mathbf{Y}}(\vartheta)$  and  $\tilde{\mathbf{L}}'_T(\theta, \vartheta)$  defined in (9.11).

□

## 9.3 Chapter 3 Proofs

This section contains the proof of the properties stated in Chapter 3 - Converter Architectures and Modulation Techniques.

### 9.3.1 PWM for a two-level VSI leg

It is here proven that, for a generic  $k$ -th two-level inverter leg (with  $k = 1, \dots, m$ ) controlled with a PWM technique, if the bandwidth of the reference voltage  $u_k^*(t)$  is low enough with respect to the modulation frequency  $f_{PWM}$ , then the low-frequency content of the leg output voltage  $u_k(t)$  matches the harmonic content of the reference voltage  $u_k^*(t)$ . In other words, the output voltage can be expressed through (3.4) and the residual voltage  $\Delta u_k(t)$  has an harmonic content that is only located at high frequencies.

**Proof.** Consider a generic  $k$ -th two-level converter leg controlled with a PWM technique working in symmetrical regular sampling mode with a triangular carrier<sup>4</sup>. The leg output voltage generated by the PWM technique is a sequence of rectangular pulses. All the pulses have the same height, equal to the DC-bus voltage  $V_{DC}$ . Given (3.3), the width of the rectangular pulse in the  $h$ -th modulation period is:

$$T_{ON}[h] = T_{PWM} \cdot d_{ON}[h] = \frac{1}{f_{PWM}} \cdot \frac{u^*(t_h)}{V_{DC}}$$

The  $h$ -th modulation period lasts from the instant  $t_h$  to the instant  $t_{h+1} = t_h + T_{PWM}$ . Each pulse is centred around the midpoint of the modulation interval, located at  $(t_h + t_{h+1})/2 = t_h + T_{PWM}/2$ . By placing the time origin in a way that  $t_0 = 0$ , then  $t_h = hT_{PWM}$  and the output voltage can be expressed as:

$$\begin{aligned} u(t) &= \sum_{h=-\infty}^{+\infty} V_{DC} \cdot \text{rect}_{T_{ON}[h]} \left( t - \frac{t_h + t_{h+1}}{2} \right) = \\ &= \sum_{h=-\infty}^{+\infty} V_{DC} \cdot \text{rect}_{T_{ON}[h]} \left( t - hT_{PWM} - \frac{T_{PWM}}{2} \right) \end{aligned}$$

where  $\text{rect}_{\Delta T}(t)$  is the *rectangle function*, which describes a rectangular pulse centred at the time  $t = 0$ , with magnitude 1 and time width  $\Delta T$  (denoted as the subscript of the function  $\text{rect}(t)$ ).

The harmonic content of the reference voltage  $u^*(t)$  (i.e., of the smooth signal to be applied) is identified by its Fourier transform:

$$U^*(f) = \mathcal{F}[u^*(t)](f) = \int_{-\infty}^{+\infty} u^*(t) \cdot e^{-j2\pi f t} dt$$

Similarly, the harmonic content of the actual leg voltage  $u(t)$  (i.e., of the sequence of rectangular pulses) is also identified by its Fourier transform. By recalling that the Fourier transform of a rectangular pulse is the *normalized sine cardinal function*:

<sup>4</sup> A similar reasoning can also be applied for other PWM working modes. The leg subscript  $k$  will be omitted for notation compactness.

$$\mathcal{F}[\text{rect}_{\Delta T}(t)](f) = \Delta T \cdot \text{sinc}(f \Delta T) = \Delta T \cdot \frac{\sin(\pi f \Delta T)}{\pi f \Delta T}$$

and by recalling the time delay property of the Fourier transformation

$$\mathcal{F}[x(t - \tau)](f) = \mathcal{F}[x(t)](f) \cdot e^{-j2\pi f \tau}$$

the explicit computation of the harmonic spectra of  $u(t)$  results in:

$$\begin{aligned} \mathcal{U}(f) &= \mathcal{F}[u(t)](f) = \\ &= \mathcal{F}\left[\sum_{h=-\infty}^{+\infty} V_{DC} \cdot \text{rect}_{T_{ON}[h]}\left(t - h T_{PWM} - \frac{T_{PWM}}{2}\right)\right](f) = \\ &= \sum_{h=-\infty}^{+\infty} V_{DC} \cdot \mathcal{F}\left[\text{rect}_{T_{ON}[h]}\left(t - h T_{PWM} - \frac{T_{PWM}}{2}\right)\right](f) = \\ &= \sum_{h=-\infty}^{+\infty} V_{DC} \cdot \mathcal{F}[\text{rect}_{T_{ON}[h]}(t)](f) \cdot e^{-j(h T_{PWM} + \frac{T_{PWM}}{2})} = \\ &= \sum_{h=-\infty}^{+\infty} V_{DC} \cdot T_{ON}[h] \cdot \text{sinc}(f \cdot T_{ON}[h]) \cdot e^{-j h T_{PWM}} \cdot e^{-j \frac{T_{PWM}}{2}} = \\ &= \sum_{h=-\infty}^{+\infty} T_{PWM} \cdot u^*(h T_{PWM}) \cdot \text{sinc}\left(\frac{f}{f_{PWM}} \cdot \frac{u^*(h T_{PWM})}{V_{DC}}\right) \cdot e^{-j h T_{PWM}} \cdot e^{-j \frac{T_{PWM}}{2}} \end{aligned}$$

Each term of this infinite sum represents the Fourier transform contribution of the reference voltage  $u^*$ , sampled at the  $h$ -th instant  $h T_{PWM}$ , shifted by the time delay  $h T_{PWM}$  (related to the  $h$ -th modulation interval) and  $T_{PWM}/2$  (related to the center of the rectangular pulse) and weighted (for each frequency  $f$ ) by the non-linear function  $T_{PWM} \cdot \text{sinc}((f/f_{PWM}) \cdot (u^*(h T_{PWM})/V_{DC}))$ .

By directly comparing the harmonic spectra  $\mathcal{U}(f)$  and  $\mathcal{U}^*(f)$  it is not immediate to derive any conclusion. The comparison requires defining an additional auxiliary term. By considering an idealized sampling process, obtained in the distribution domain by multiplying the reference (i.e., smooth) signal  $u^*(t)$  with a periodic sequence of *Dirac pulses* of area  $T_{PWM}$  and of period  $T_{PWM}$ , it is possible to define idealized sampled signal:

$$u_{\delta}(t) = u^*(t) \cdot T_{PWM} \cdot \sum_{h=-\infty}^{+\infty} \delta(t - h T_{PWM}) = \sum_{h=-\infty}^{+\infty} T_{PWM} \cdot u^*(h T_{PWM}) \cdot \delta(t - h T_{PWM})$$

where  $\delta(t)$  is the unitary-area *Dirac pulse* located at  $t = 0$ .

As known, the Fourier transform of an idealized sampled signal is the periodic replica of the Fourier transform of the original (i.e., smooth) signal. Therefore, the Fourier transform of  $u_{\delta}(t)$  can be written as:

$$\begin{aligned} \mathcal{U}_{\delta}(f) &= \mathcal{F}[u_{\delta}(t)](f) = \mathcal{F}\left[u^*(t) \cdot T_{PWM} \cdot \sum_{h=-\infty}^{+\infty} \delta(t - h \cdot T_{PWM})\right](f) = \\ &= \sum_{h=-\infty}^{+\infty} \mathcal{F}[u^*(t)](f - h \cdot f_{PWM}) = \sum_{h=-\infty}^{+\infty} \mathcal{U}^*(f - h \cdot f_{PWM}) \end{aligned}$$

and, if the bandwidth of the reference voltage  $u^*(t)$  is low enough with respect to  $f_{PWM}$ , then there is no aliasing<sup>5</sup> and it results that:

$$\mathcal{U}_\delta(f) \cong \mathcal{U}^*(f) \quad \text{for } f < f_{PWM}$$

The same Fourier transform, however, can also be expressed differently. Indeed, by recalling that  $\mathcal{F}[\delta(t)](f) = 1$ , it is possible to directly apply the Fourier transform to the Dirac pulse sequence  $u_\delta(t)$ , which results in:

$$\begin{aligned} \mathcal{U}_\delta(f) &= \mathcal{F}[u_\delta(t)](f) = \\ &= \mathcal{F}\left[\sum_{h=-\infty}^{+\infty} T_{PWM} \cdot u^*(h T_{PWM}) \cdot \delta(t - h T_{PWM})\right](f) = \\ &= \sum_{h=-\infty}^{+\infty} T_{PWM} \cdot u^*(h T_{PWM}) \cdot \mathcal{F}[\delta(t - h T_{PWM})](f) = \\ &= \sum_{h=-\infty}^{+\infty} T_{PWM} \cdot u^*(h T_{PWM}) \cdot \mathcal{F}[\delta(t)](f) \cdot e^{-j h T_{PWM}} = \\ &= \sum_{h=-\infty}^{+\infty} T_{PWM} \cdot u^*(h T_{PWM}) \cdot e^{-j h T_{PWM}} \end{aligned}$$

Each term of this infinite sum represents the Fourier transform contribution of the reference voltage  $u^*$ , sampled at the  $h$ -th instant  $h T_{PWM}$ , shifted by the time delay  $h T_{PWM}$  (related to the  $h$ -th modulation interval) and weighted by  $T_{PWM}$ .

By comparing this last expression of  $\mathcal{U}_\delta(f)$  with the Fourier transform  $\mathcal{U}(f)$  of the pulse-width modulated signal  $u(t)$  (previously found), it can be recognized that many terms are similar to each other. Moreover, for low frequencies,  $f/f_{PWM} \ll 1$  and, since  $0 \leq u^* \leq V_{DC}$ , the normalized sine cardinal function which appears in the expression of  $\mathcal{U}(f)$  can be approximated as:

$$\text{sinc}\left(\frac{f}{f_{PWM}} \cdot \frac{u^*(h T_{PWM})}{V_{DC}}\right) \cong 1$$

Then, by comparing  $\mathcal{U}(f)$  and  $\mathcal{U}_\delta(f)$  it results that:

$$\begin{aligned} \mathcal{U}(f) &\cong \sum_{h=-\infty}^{+\infty} T_{PWM} \cdot u^*(h T_{PWM}) \cdot e^{-j h T_{PWM}} \cdot e^{-j \frac{T_{PWM}}{2}} = \\ &= \left[ \sum_{h=-\infty}^{+\infty} T_{PWM} \cdot u^*(h T_{PWM}) \cdot e^{-j h T_{PWM}} \right] \cdot e^{-j \frac{T_{PWM}}{2}} = \\ &= \mathcal{U}_\delta(f) \cdot e^{-j \frac{T_{PWM}}{2}} \quad \text{for } f \ll f_{PWM} \end{aligned}$$

As a result, thanks to the introduction of the signal  $u_\delta(t)$ , it has been shown that:

<sup>5</sup> For the *Nyquist-Shannon Theorem*, to avoid any aliasing phenomena, the frequency  $f_{max}$  identifying the bandwidth of the signal should be lower than the *Nyquist frequency*, which for the present analysis is equal to  $f_{PWM}/2$ .

$$\mathcal{U}(f) \cong \mathcal{U}_\delta(f) \cdot e^{-j\frac{T_{PWM}}{2}} \cong \mathcal{U}^*(f) \cdot e^{-j\frac{T_{PWM}}{2}} \quad \text{for } f \ll f_{PWM}$$

To summarize, it has been shown that, if the original (i.e., smooth) signal has a narrow bandwidth with respect to  $f_{PWM}$ , then:

- the low-frequency harmonic spectrum of the pulse-width-modulated signal (i.e., the sequence of rectangular pulses) is similar to the harmonic spectra of the idealized sampled signal (i.e., the sequence of Dirac pulses) and just delayed by  $T_{PWM}/2$ ,
- the low-frequency harmonic spectrum of the idealized sampled signal (i.e., the sequence of Dirac pulses) is similar to the harmonic spectra of the original signal (i.e., the smooth reference signal), and then
- the low-frequency harmonic spectrum of the pulse-width-modulated signal (i.e., the sequence of rectangular pulses) is similar to the harmonic spectra of the original signal (i.e., the smooth reference signal) and just delayed by  $T_{PWM}/2$ .

Therefore, by anti-transforming the previous result back into the time domain, it results that:

$$u(t) = \mathcal{F}^{-1}[\mathcal{U}(f)](t) \cong \mathcal{F}^{-1}\left[\mathcal{U}^*(f) \cdot e^{-j\frac{T_{PWM}}{2}}\right](t) = u^*\left(t - \frac{T_{PWM}}{2}\right)$$

which is the result given in (3.4).

By definition, the residual voltage  $\Delta u(t)$  is given by the difference between the pulse-width-modulated signal  $u(t)$  and the shifted reference signal  $u^*(t - T_{PWM}/2)$ , which is:

$$\Delta u(t) = \mathcal{F}^{-1}\left[\mathcal{U}(f) - \mathcal{U}^*(f) \cdot e^{-j\frac{T_{PWM}}{2}}\right](t)$$

and, since at low frequencies  $\mathcal{U}(f) \cong \mathcal{U}^*(f) \cdot e^{-j\frac{T_{PWM}}{2}}$ , the harmonic content of  $\Delta u(t)$  is only located at high frequencies, and can be therefore filtered by the supplied load.  $\square$

### 9.3.2 Common-mode voltage limits

It is here proven that, given a set  $\tilde{\mathbf{u}}^* = [\tilde{u}_1^*, \tilde{u}_2^*, \dots, \tilde{u}_m^*]^T$  of reference leg voltages, the feasible range for the common-mode voltage component  $u_{CM}^*$  which can be injected is given by (3.7).

Naturally, for the leg voltages to be feasible, it must result:

$$-\min\{\tilde{\mathbf{u}}^*\} \leq V_{DC} - \max\{\tilde{\mathbf{u}}^*\} \quad \Rightarrow \quad \max\{\tilde{\mathbf{u}}^*\} - \min\{\tilde{\mathbf{u}}^*\} \leq V_{DC}$$

meaning that the maximum phase-to-phase voltage must be lower than the total DC-bus voltage.

**Proof.** The reference leg voltages after the common-mode injection are:

$$u_k^* = \tilde{u}_k^* + u_{CM}^* \quad (\text{with } k = 1, \dots, m)$$

Since it must result  $0 \leq u_k^* \leq V_{DC}$  for all converter legs, this means that  $u_{CM}^*$  must be in a certain feasible range. This range can be found by referring to the extreme minimum and maximum leg voltages as:

---

$$\begin{cases} \min\{\tilde{\mathbf{u}}^*\} = \min\{\tilde{\mathbf{u}}^*\} + u_{CM}^* \geq 0 \\ \max\{\tilde{\mathbf{u}}^*\} = \max\{\tilde{\mathbf{u}}^*\} + u_{CM}^* \leq V_{DC} \end{cases} \Rightarrow \begin{cases} u_{CM}^* \geq -\min\{\tilde{\mathbf{u}}^*\} \\ u_{CM}^* \leq V_{DC} - \max\{\tilde{\mathbf{u}}^*\} \end{cases}$$

which is the range provided in (3.7).

□

## 9.4 Chapter 4 Proofs

This section contains the proof of the properties stated in Chapter 4 - Electrical Network Model.

### 9.4.1 Tellegen's theorem (virtual powers conservation)

This section recalls *Tellegen's theorem* for the *virtual powers conservation*, which is an important and well-known result for an electric circuit [166]–[168].

Consider the same electrical circuit in two different operating conditions, here referred through the superscripts ( $'$ ) and ( $''$ ), respectively. By using the passive sign notation for all the circuit elements, the first operating condition is characterized by the voltages and currents set  $(\mathbf{v}', \mathbf{i}')$ , while the second operating condition is characterized by the voltages and currents set  $(\mathbf{v}'', \mathbf{i}'')$ .

The circuit overall *Virtual Powers* are defined as:

$$\hat{P}''' = \mathbf{v}'^T \cdot \mathbf{i}'' = \sum_{k=1}^m v'_k \cdot i''_k \quad \text{and} \quad \hat{P}''' = \mathbf{v}''^T \cdot \mathbf{i}' = \sum_{k=1}^m v''_k \cdot i'_k \quad (9.12)$$

where  $m$  is the total number of elements in the circuit.

Tellegen's theorem states that the overall virtual powers are zero:

$$\hat{P}_{12} = \hat{P}_{21} = 0 \quad (9.13)$$

When only a single operating condition is considered,  $\mathbf{v}' = \mathbf{v}'' = \mathbf{v}$  and  $\mathbf{i}' = \mathbf{i}'' = \mathbf{i}$ . Then, the virtual powers are equal to the real power absorbed by the circuit and Tellegen's theorem corresponds to the conservation of energy principle of physical systems.

A classic proof of this theorem is here recalled.

**Proof.** Any electric circuit can be associated with an ordered graph. Generally speaking, the graph has  $n$  nodes and  $m$  branches. The branches directions can be associated with the flow of the currents. By using the passive sign convention for all the circuit elements, the orientations of the voltages are automatically determined.

The *Incidence Matrix*  $\mathbf{A}$  related to the graph is a  $n$  that:

$$A_{hk} = \begin{cases} +1 & \text{if the branch } h \text{ points out from the node } k \\ -1 & \text{if the branch } h \text{ points to the node } k \\ 0 & \text{if the branch } h \text{ is not connected to the node } k \end{cases}$$

The set of circuit currents  $\mathbf{i}$  satisfies *Kirchhoff's Current Law*, which can be expressed as:

$$\mathbf{A} \cdot \mathbf{i} = \mathbf{0}$$

The set of circuit voltages  $\mathbf{v}$  satisfies Kirchhoff's Voltage Law, and each voltage can be therefore expressed as the difference of the electric potentials in two corresponding nodes. They can be expressed as:

$$\mathbf{v} = \mathbf{A}^T \cdot \mathbf{u}$$

where  $\mathbf{u}$  is the set of electric potentials at the circuit nodes.

These properties are true regardless of the operating condition, meaning that:

$$\mathbf{A} \cdot \mathbf{i}' = \mathbf{0}, \quad \mathbf{A} \cdot \mathbf{i}'' = \mathbf{0}, \quad \mathbf{v}' = \mathbf{A}^T \cdot \mathbf{u}', \quad \mathbf{v}'' = \mathbf{A}^T \cdot \mathbf{u}''$$

The virtual powers can be therefore expressed as:

$$\begin{aligned} \hat{P}''' &= \mathbf{v}'^T \cdot \mathbf{i}'' = (\mathbf{A}^T \cdot \mathbf{u}') \cdot \mathbf{i}'' = \mathbf{u}'^T \cdot (\mathbf{A} \cdot \mathbf{i}'') = \mathbf{u}'^T \cdot \mathbf{0} = 0 \\ \hat{P}''' &= \mathbf{v}''^T \cdot \mathbf{i}' = (\mathbf{A}^T \cdot \mathbf{u}'') \cdot \mathbf{i}' = \mathbf{u}''^T \cdot (\mathbf{A} \cdot \mathbf{i}') = \mathbf{u}''^T \cdot \mathbf{0} = 0 \end{aligned}$$

which is the property stated by the theorem. □

### 9.4.2 Reciprocity properties for two-port networks

This section recalls the *reciprocity properties* for linear a-dynamical two-port electrical networks [166], [167].

A linear a-dynamical two-port network is an electric system that only contains passive linear elements (i.e., resistors) and can be accessed externally by two couples of terminals (i.e., two *ports*). The two ports, further on referred by the subscripts 1 and 2, can be supplied by voltage or current sources. For an independent voltage source, the current absorbed by the network is the *complementary variable*. Similarly, for an independent current source, the voltage at the port terminals is the complementary variable<sup>6</sup>.

If both ports are supplied by voltage sources, the two-port network is mathematically represented by the *Conductances Matrix*:

$$\begin{bmatrix} i_1 \\ i_2 \end{bmatrix} = \begin{bmatrix} G_{11} & G_{12} \\ G_{21} & G_{22} \end{bmatrix} \cdot \begin{bmatrix} v_1 \\ v_2 \end{bmatrix} \quad (9.14)$$

and the reciprocity property states that  $G_{12} = G_{21}$ .

If both ports are supplied by current sources, the two-port network is mathematically represented by the *Resistances Matrix*:

$$\begin{bmatrix} v_1 \\ v_2 \end{bmatrix} = \begin{bmatrix} R_{11} & R_{12} \\ R_{21} & R_{22} \end{bmatrix} \cdot \begin{bmatrix} i_1 \\ i_2 \end{bmatrix} \quad (9.15)$$

and the reciprocity property states that  $R_{12} = R_{21}$ .

If one port is supplied by a voltage source and the other port is supplied by a current source, the two-port network is mathematically represented by the *Hybrid Matrix*:

$$\begin{bmatrix} i_1 \\ v_2 \end{bmatrix} = \begin{bmatrix} H_{11} & H_{12} \\ H_{21} & H_{22} \end{bmatrix} \cdot \begin{bmatrix} v_1 \\ i_2 \end{bmatrix} \quad (9.16)$$

and the reciprocity property states that  $H_{12} = -H_{21}$ .<sup>7</sup>

<sup>6</sup> It is important to emphasize that the network ports are identified through the passive sign notation, which corresponds to the active sign notation for the sources connected to the ports.

<sup>7</sup> This is also called *Anti-reciprocity* property. The same property also applies if the port 1 is fed by a current source and the port 2 is fed by a voltage source.

**Proof.** Any linear a-dynamical network is characterized by a certain number  $n$  of internal elements, each of which can be modelled through a resistance  $R_k$  (with  $k = 1, \dots, n$ ). Their voltages and currents can be denoted as  $v_{R,k}$  and  $i_{R,k}$  and, given Ohm's law,  $v_{R,k} = R_k \cdot i_{R,k}$ .

First, refer to the conductances matrix formulation (9.14). Consider two operating conditions, denoted through the superscripts ( $'$ ) and ( $''$ ). The first operating condition is given by  $v'_1 = V_1 \neq 0$  and  $v'_2 = 0$ . From (9.14) it results that  $i'_1 = G_{11} \cdot V_1$  and  $i'_2 = G_{21} \cdot V_1$ . The second operating condition is given by  $v''_1 = 0$  and  $v''_2 = V_2 \neq 0$ . From (9.14) it results that  $i''_1 = G_{12} \cdot V_2$  and  $i''_2 = G_{22} \cdot V_2$ . By applying Tellegen's theorem (9.13) to the two operating conditions it results that:

$$0 = v'_1 \cdot i''_1 + v'_2 \cdot i''_2 - \sum_{k=1}^n v'_{R,k} \cdot i''_{R,k} = G_{12} \cdot V_1 \cdot V_2 - \sum_{k=1}^n R_k \cdot i'_{R,k} \cdot i''_{R,k}$$

$$0 = v''_1 \cdot i'_1 + v''_2 \cdot i'_2 - \sum_{k=1}^n v''_{R,k} \cdot i'_{R,k} = G_{21} \cdot V_2 \cdot V_1 - \sum_{k=1}^n R_k \cdot i''_{R,k} \cdot i'_{R,k}$$

By comparing the two expressions, it results:

$$G_{12} = \frac{1}{V_1 \cdot V_2} \cdot \sum_{k=1}^n R_k \cdot i'_{R,k} \cdot i''_{R,k} = G_{21}$$

which is the reciprocity property of the conductances matrix.

Refer now to the resistances matrix formulation (9.15). Again, consider two operating conditions, denoted through the superscripts ( $'$ ) and ( $''$ ). The first operating condition is given by  $i'_1 = I_1 \neq 0$  and  $i'_2 = 0$ . From (9.15) it results that  $v'_1 = R_{11} \cdot I_1$  and  $v'_2 = R_{21} \cdot I_1$ . The second operating condition is given by  $i''_1 = 0$  and  $i''_2 = I_2 \neq 0$ . From (9.15) it results that  $v''_1 = R_{12} \cdot I_2$  and  $v''_2 = R_{22} \cdot I_2$ . By applying Tellegen's theorem (9.13) to the two operating conditions it results that:

$$0 = v'_1 \cdot i''_1 + v'_2 \cdot i''_2 - \sum_{k=1}^n v'_{R,k} \cdot i''_{R,k} = R_{21} \cdot I_1 \cdot I_2 - \sum_{k=1}^n R_k \cdot i'_{R,k} \cdot i''_{R,k}$$

$$0 = v''_1 \cdot i'_1 + v''_2 \cdot i'_2 - \sum_{k=1}^n v''_{R,k} \cdot i'_{R,k} = R_{12} \cdot I_2 \cdot I_1 - \sum_{k=1}^n R_k \cdot i''_{R,k} \cdot i'_{R,k}$$

and, by comparing the two expressions, it results:

$$R_{12} = \frac{1}{I_1 \cdot I_2} \cdot \sum_{k=1}^n R_k \cdot i'_{R,k} \cdot i''_{R,k} = R_{21}$$

which is the reciprocity property of the resistances matrix.

Finally, refer to the hybrid matrix formulation (9.16). Again, consider two operating conditions, denoted through the superscripts ( $'$ ) and ( $''$ ). The first operating condition is given by  $v'_1 = V_1 \neq 0$  and  $i'_2 = 0$ . From (9.16) it results that  $i'_1 = H_{11} \cdot V_1$  and  $v'_2 = H_{21} \cdot V_1$ . The second operating condition is given by  $v''_1 = 0$  and  $i''_2 = I_2 \neq 0$ . From (9.16) it results that  $i''_1 = H_{12} \cdot I_2$  and  $v''_2 = H_{22} \cdot I_2$ . By applying Tellegen's theorem (9.13) to the two operating conditions it results that:

$$0 = v'_1 \cdot i''_1 + v'_2 \cdot i''_2 - \sum_{k=1}^n v'_{R,k} \cdot i''_{R,k} = (H_{12} + H_{21}) \cdot V_1 \cdot I_2 - \sum_{k=1}^n R_k \cdot i'_{R,k} \cdot i''_{R,k}$$

$$0 = v''_1 \cdot i'_1 + v''_2 \cdot i'_2 - \sum_{k=1}^n v''_{R,k} \cdot i'_{R,k} = - \sum_{k=1}^n R_k \cdot i''_{R,k} \cdot i'_{R,k}$$

and, by comparing the two expressions, it results

$$H_{12} + H_{21} = \frac{1}{V_1 \cdot I_2} \cdot \sum_{k=1}^n R_k \cdot i'_{R,k} \cdot i''_{R,k} = 0$$

meaning that  $H_{12} = -H_{21}$ , which is the reciprocity property of the hybrid matrix.  $\square$

### 9.4.3 Reciprocity properties for multiport networks

The reciprocity properties stated for linear a-dynamical two-port networks are here extended for linear a-dynamical multiport networks.

A linear a-dynamical multi-port network is an electric system that only contains passive linear elements (i.e., resistors) and can be accessed externally by  $m$  couples of terminals (i.e.,  $m$  ports). Each terminal can be supplied either by a voltage or by a current source.

The  $m$  ports can be divided into two subsets. The  $m_V$  ports supplied by independent voltage sources are denoted by the subscript  $V$ ; the supplying set is  $\mathbf{v}_V$  and the complementary set is  $\mathbf{i}_V$ . The  $m_I$  ports supplied by independent current sources are denoted by the subscript  $I$ ; the supplying set is  $\mathbf{i}_I$  and the complementary set is  $\mathbf{v}_I$ . Naturally, it must result  $m_V + m_I = m$ , but the size  $m_V$  or  $m_I$  of a single set can vary from 0 to  $m$ .

The general formulation of this multiport system is obtained by the *Hybrid Matrix*:

$$\begin{bmatrix} \mathbf{i}_V \\ \mathbf{v}_I \end{bmatrix} = \begin{bmatrix} \mathbf{H}_{VV} & \mathbf{H}_{VI} \\ \mathbf{H}_{IV} & \mathbf{H}_{II} \end{bmatrix} \cdot \begin{bmatrix} \mathbf{v}_V \\ \mathbf{i}_I \end{bmatrix} = \begin{bmatrix} \mathbf{G}_{VV} & \mathbf{H}_{VI} \\ \mathbf{H}_{IV} & \mathbf{R}_{II} \end{bmatrix} \cdot \begin{bmatrix} \mathbf{v}_V \\ \mathbf{i}_I \end{bmatrix} \quad (9.17)$$

where:

- $\mathbf{H}_{VV} = \mathbf{G}_{VV}$  is the  $m_V \times m_V$  *Partial Conductances Matrix*,
- $\mathbf{H}_{II} = \mathbf{R}_{II}$  is the  $m_I \times m_I$  *Partial Resistances Matrix*,
- $\mathbf{H}_{VI}$  is the  $m_V \times m_I$  *Currents to Voltages Partial Hybrid Matrix*,
- $\mathbf{H}_{IV}$  is the  $m_I \times m_V$  *Voltages to Currents Partial Hybrid Matrix*.

The *Reciprocity Properties* for the multiport representation (9.17) is:

$$\mathbf{G}_{VV} = \mathbf{G}_{VV}^T, \quad \mathbf{R}_{II} = \mathbf{R}_{II}^T, \quad \mathbf{H}_{VI} = -\mathbf{H}_{IV}^T \quad (9.18)$$

meaning that the relationship among the same kind of sources is symmetric, while the relationship among different kind of sources is related to an anti-transposition<sup>8</sup>.

The same property holds in case of multiple subsets. Also, when  $m_V = m$  and  $m_I = 0$  the reciprocity property (9.18) particularizes into the symmetry of the overall network

<sup>8</sup> This is not an anti-symmetry property, since the hybrid matrices  $\mathbf{H}_{IV}$  and  $\mathbf{H}_{VI}$  may not be square matrices.

conductances matrix, while when  $m_V = 0$  and  $m_I = m$  it particularizes into the symmetry of the overall network resistances matrix.

The properties (9.18) are here proved.

**Proof.** Consider two generic ports, here referred through the subscripts  $h \in \{1, \dots, m\}$  and  $k \in \{1, \dots, m\}$ . The mutual interaction between the two ports is obtained when all the other sources are zero. This means that all the other voltage-driven ports are short-circuited and all the other current-driven ports are left in open-circuit. Then, the overall multiport network is transformed into an equivalent two-port network, where the reciprocity properties defined in Section 9.4.2 hold. As a result:

- if both the ports are voltage-driven, then  $H_{hk} = H_{kh}$  (thus explaining why  $\mathbf{G}_{VV} = \mathbf{G}_{VV}^T$ ),
- if both the ports are current-driven, then also  $H_{hk} = H_{kh}$  (thus explaining why  $\mathbf{R}_{II} = \mathbf{R}_{II}^T$ ),
- if one port is voltage driven and the other is current-driven, then  $H_{hk} = -H_{kh}$  (thus explaining why  $\mathbf{H}_{IV} = -\mathbf{H}_{VI}^T$ ).

□

#### 9.4.4 Auxiliary network voltages expression

It is here proven that, given the electrical machine model (2.35), the auxiliary network voltages  $\mathbf{v}_{NET}$  in a constrained configuration obeying (4.8) can be expressed as (4.14) and the equivalent network parameters in (4.16) would be expressed as (4.17).

**Proof.** From (4.13), the machine voltages can be expressed as:

$$\mathbf{v}_{EM} = \mathbf{N} \cdot \mathbf{v}_{VSI} - \mathbf{R}_{NET} \cdot \mathbf{i}_{EM} - \mathbf{M} \cdot \mathbf{v}_{NET}$$

From (2.35), the machine voltages can also be expressed as:

$$\mathbf{v}_{EM} = \mathbf{L}_{EM} \cdot \frac{d\mathbf{i}_{EM}}{dt} + \mathbf{R}_{EM} \cdot \mathbf{i}_{EM} + \mathbf{e}_{EM}$$

By matching the two expressions and by isolating the currents time derivative  $\mathbf{L}_{EM} \cdot (d\mathbf{i}_{EM}/dt)$ , it results:

$$\mathbf{L}_{EM} \cdot \frac{d\mathbf{i}_{EM}}{dt} = \mathbf{N} \cdot \mathbf{v}_{VSI} - (\mathbf{R}_{EM} + \mathbf{R}_{NET}) \cdot \mathbf{i}_{EM} - \mathbf{e}_{EM} - \mathbf{M} \cdot \mathbf{v}_{NET}$$

Both expressions can be multiplied by  $\mathbf{\Gamma}_{EM} = \mathbf{L}_{EM}^{-1}$  resulting in:

$$\frac{d\mathbf{i}_{EM}}{dt} = \mathbf{\Gamma}_{EM} \cdot [\mathbf{N} \cdot \mathbf{v}_{VSI} - (\mathbf{R}_{EM} + \mathbf{R}_{NET}) \cdot \mathbf{i}_{EM} - \mathbf{e}_{EM}] - \mathbf{\Gamma}_{EM} \cdot \mathbf{M} \cdot \mathbf{v}_{NET}$$

By left-multiplying this last expression by  $\mathbf{M}^T$  and by recalling that, because of the currents constraint equation (4.8)  $\mathbf{M}^T \cdot \mathbf{i}_{EM} = \mathbf{0}$ , it results that:

$$\begin{aligned} \mathbf{0} &= \frac{d}{dt}(\mathbf{M}^T \cdot \mathbf{i}_{EM}) = \mathbf{M}^T \cdot \frac{d\mathbf{i}_{EM}}{dt} = \\ &= \mathbf{M}^T \cdot \mathbf{\Gamma}_{EM} \cdot [\mathbf{N} \cdot \mathbf{v}_{VSI} - (\mathbf{R}_{EM} + \mathbf{R}_{NET}) \cdot \mathbf{i}_{EM} - \mathbf{e}_{EM}] - (\mathbf{M}^T \cdot \mathbf{\Gamma}_{EM} \cdot \mathbf{M}) \cdot \mathbf{v}_{NET} \end{aligned}$$

By isolating  $\mathbf{v}_{NET}$  this expression can be written as:

$$(\mathbf{M}^T \cdot \boldsymbol{\Gamma}_{EM} \cdot \mathbf{M}) \cdot \mathbf{v}_{NET} = \mathbf{M}^T \cdot \boldsymbol{\Gamma}_{EM} \cdot [\mathbf{N} \cdot \mathbf{v}_{VSI} - (\mathbf{R}_{EM} + \mathbf{R}_{NET}) \cdot \mathbf{i}_{EM} - \mathbf{e}_{EM}]$$

The matrix  $(\mathbf{M}^T \cdot \boldsymbol{\Gamma}_{EM} \cdot \mathbf{M})$  which pre-multiplies  $\mathbf{v}_{NET}$  is symmetric because  $\boldsymbol{\Gamma}_{EM} = \boldsymbol{\Gamma}_{EM}^T$ . Also, it is positive definite, because  $\boldsymbol{\Gamma}_{EM}$  is positive definite and any quadratic form  $\mathbf{x}^T \cdot (\mathbf{M}^T \cdot \boldsymbol{\Gamma}_{EM} \cdot \mathbf{M}) \cdot \mathbf{x}$  with  $\mathbf{x} \neq 0$  can be rewritten as

$$\mathbf{x}^T \cdot (\mathbf{M}^T \cdot \boldsymbol{\Gamma}_{EM} \cdot \mathbf{M}) \cdot \mathbf{x} = (\mathbf{M} \cdot \mathbf{x})^T \cdot \boldsymbol{\Gamma}_{EM} \cdot (\mathbf{M} \cdot \mathbf{x}) > 0$$

where  $\mathbf{M} \cdot \mathbf{x} \neq \mathbf{0}$  because  $\mathbf{M}$  is, by definition, a full-ranked matrix. Therefore,  $(\mathbf{M}^T \cdot \boldsymbol{\Gamma}_{EM} \cdot \mathbf{M})$  is invertible, and therefore it is possible to explicitly compute  $\mathbf{v}_{NET}$  as:

$$\mathbf{v}_{NET} = (\mathbf{M}^T \cdot \boldsymbol{\Gamma}_{EM} \cdot \mathbf{M})^{-1} \cdot \mathbf{M}^T \cdot \boldsymbol{\Gamma}_{EM} \cdot [\mathbf{N} \cdot \mathbf{v}_{VSI} - (\mathbf{R}_{EM} + \mathbf{R}_{NET}) \cdot \mathbf{i}_{EM} - \mathbf{e}_{EM}]$$

which is the expression provided in (4.14).

With the definition of the network internal feedback matrix  $\mathbf{F}$  given in (4.15), the term  $\mathbf{M} \cdot \mathbf{v}_{NET}$  which appears in the expression of the machine voltages  $\mathbf{v}_{EM}$  is:

$$\mathbf{M} \cdot \mathbf{v}_{NET} = \mathbf{F} \cdot [\mathbf{N} \cdot \mathbf{v}_{VSI} - (\mathbf{R}_{EM} + \mathbf{R}_{NET}) \cdot \mathbf{i}_{EM} - \mathbf{e}_{EM}]$$

By substituting in (4.13) and by doing some algebraic manipulations it results that:

$$\begin{aligned} \mathbf{v}_{EM} &= \mathbf{N} \cdot \mathbf{v}_{VSI} - \mathbf{R}_{NET} \cdot \mathbf{i}_{EM} - \mathbf{M} \cdot \mathbf{v}_{NET} = \\ &= [(\mathbf{I} - \mathbf{F}) \cdot \mathbf{N}] \cdot \mathbf{v}_{VSI} - [(\mathbf{I} - \mathbf{F}) \cdot \mathbf{R}_{NET} - \mathbf{F} \cdot \mathbf{R}_{EM}] \cdot \mathbf{i}_{EM} + [\mathbf{F} \cdot \mathbf{e}_{EM}] = \\ &= \mathbf{N}_{ext} \cdot \mathbf{v}_{VSI} - \mathbf{R}_{NET,ext} \cdot \mathbf{i}_{EM} + \mathbf{e}_{EM,ext} \end{aligned}$$

which is the expression (4.16) with the parameters  $\mathbf{N}_{ext}$ ,  $\mathbf{R}_{NET,ext}$  and  $\mathbf{e}_{EM,ext}$  of (4.17).  $\square$

### 9.4.5 Full order electrical drive model parameters

It is here proven that in a constrained network, given the electrical machine voltages set  $\mathbf{v}_{EM}$  expressed by (2.35), the overall drive model can be written as per (4.19).

**Proof.** By substituting the expression (4.16) in (4.13) it results that:

$$\begin{aligned} \mathbf{L}_{EM} \cdot \frac{d\mathbf{i}_{EM}}{dt} + \mathbf{R}_{EM} \cdot \mathbf{i}_{EM} + \mathbf{e}_{EM} &= \mathbf{v}_{EM} = \\ &= \mathbf{N} \cdot \mathbf{v}_{VSI} - \mathbf{R}_{NET} \cdot \mathbf{i}_{EM} - \mathbf{M} \cdot \mathbf{v}_{NET} = \\ &= \mathbf{N}_{ext} \cdot \mathbf{v}_{VSI} - \mathbf{R}_{NET,ext} \cdot \mathbf{i}_{EM} + \mathbf{e}_{EM,ext} = \\ &= (\mathbf{I} - \mathbf{F}) \cdot \mathbf{N} \cdot \mathbf{v}_{VSI} - (\mathbf{I} - \mathbf{F}) \cdot \mathbf{R}_{NET} \cdot \mathbf{i}_{EM} + \mathbf{F} \cdot \mathbf{R}_{EM} \cdot \mathbf{i}_{EM} - \mathbf{F} \cdot \mathbf{e}_{EM} \end{aligned}$$

By grouping the homologous terms and by isolating the converter voltages set  $\mathbf{v}_{VSI}$  on the right side, this expression can be rewritten as:

$$\mathbf{L}_{EM} \cdot \frac{d\mathbf{i}_{EM}}{dt} + (\mathbf{I} - \mathbf{F}) \cdot [(\mathbf{R}_{EM} + \mathbf{R}_{NET}) \cdot \mathbf{i}_{EM} + \mathbf{e}_{EM}] = (\mathbf{I} - \mathbf{F}) \cdot \mathbf{N} \cdot \mathbf{v}_{VSI}$$

which is the full-order model expressed in (4.19).  $\square$

### 9.4.6 Range and null-space relationships

Given a  $r \times c$  matrix  $\mathbf{A}$ , it is here proven that:

$$\mathcal{R}^\perp(\mathbf{A}) = \mathcal{N}(\mathbf{A}^\top), \quad \text{and} \quad \mathcal{R}(\mathbf{A}) = \mathcal{N}^\perp(\mathbf{A}^\top) \quad (9.19)$$

where  $\mathcal{R}(\star)$  denotes the *range*,  $\mathcal{N}(\star)$  denotes the *null-space*, and  $\star^\perp$  denotes the orthogonal complement.

**Proof.** The proof focuses on the first property of (9.19).

First, it is here proven that  $\mathcal{R}^\perp(\mathbf{A}) \subseteq \mathcal{N}(\mathbf{A}^\top)$ .

Consider a generic vector  $\mathbf{y} \in \mathcal{R}^\perp(\mathbf{A})$ . By definition,  $\mathbf{y}$  is orthogonal to any  $\mathbf{x} \in \mathcal{R}(\mathbf{A})$ , meaning that the scalar product  $\mathbf{y}^\top \cdot \mathbf{x}$  is zero. Consider the vector defined as  $\mathbf{x} = \mathbf{A} \cdot \mathbf{A}^\top \cdot \mathbf{y}$ . Since it is obtained by pre-multiplying the vector  $(\mathbf{A}^\top \cdot \mathbf{y})$  by  $\mathbf{A}$ ,  $\mathbf{x}$  belongs to  $\mathcal{R}(\mathbf{A})$ , therefore:

$$0 = \mathbf{y}^\top \cdot \mathbf{x} = \mathbf{y}^\top \cdot (\mathbf{A} \cdot \mathbf{A}^\top \cdot \mathbf{y}) = (\mathbf{A}^\top \cdot \mathbf{y})^\top \cdot (\mathbf{A}^\top \cdot \mathbf{y}) = \|\mathbf{A}^\top \cdot \mathbf{y}\|^2$$

Therefore,  $\mathbf{A}^\top \cdot \mathbf{y} = \mathbf{0}$ , meaning that  $\mathbf{y} \in \mathcal{N}(\mathbf{A}^\top)$ . Since this is true for any  $\mathbf{y} \in \mathcal{R}^\perp(\mathbf{A})$ , it means that  $\mathcal{R}^\perp(\mathbf{A}) \subseteq \mathcal{N}(\mathbf{A}^\top)$ .

It is now proven that  $\mathcal{N}(\mathbf{A}^\top) \subseteq \mathcal{R}^\perp(\mathbf{A})$ .

By definition, if  $\mathbf{y} \in \mathcal{N}(\mathbf{A}^\top)$  it means that  $\mathbf{A}^\top \cdot \mathbf{y} = \mathbf{0}$ . Then, for any vector  $\mathbf{x}$ , it results:

$$0 = \mathbf{x}^\top \cdot \mathbf{0} = \mathbf{x}^\top \cdot (\mathbf{A}^\top \cdot \mathbf{y}) = (\mathbf{x}^\top \cdot \mathbf{A}^\top) \cdot \mathbf{y} = \mathbf{y}^\top \cdot (\mathbf{A} \cdot \mathbf{x})$$

Since the vector  $\mathbf{A} \cdot \mathbf{x}$  belongs to  $\mathcal{R}(\mathbf{A})$  and  $\mathbf{y}$  is orthogonal to any vector built as  $\mathbf{A} \cdot \mathbf{x}$ , it means that  $\mathbf{y} \in \mathcal{R}^\perp(\mathbf{A})$ . Given that this is true for any  $\mathbf{y} \in \mathcal{N}(\mathbf{A}^\top)$ , it means that  $\mathcal{N}(\mathbf{A}^\top) \subseteq \mathcal{R}^\perp(\mathbf{A})$ .

Having shown that  $\mathcal{R}^\perp(\mathbf{A}) \subseteq \mathcal{N}(\mathbf{A}^\top)$  and  $\mathcal{N}(\mathbf{A}^\top) \subseteq \mathcal{R}^\perp(\mathbf{A})$ , it must necessarily result  $\mathcal{R}^\perp(\mathbf{A}) = \mathcal{N}(\mathbf{A}^\top)$ , which is the first property of (9.19).

It is now possible to immediately prove the second part of (9.19). Since, for any vector space  $\mathcal{S}$ , it results  $\mathcal{S} = (\mathcal{S}^\perp)^\perp$ , from the first property of (9.19), it derives that:

$$\mathcal{R}(\mathbf{A}) = (\mathcal{R}^\perp(\mathbf{A}))^\perp = (\mathcal{N}(\mathbf{A}^\top))^\perp = \mathcal{N}^\perp(\mathbf{A}^\top)$$

which is the second property of (9.19). □

### 9.4.7 Left singular vectors properties

It is here proven that, given the  $n \times n_c$  constraint matrix  $\mathbf{M}$  and computing its singular value decomposition according to (4.21), then the properties (4.22), (4.23) and (4.24) are verified.

**Proof.** The matrix  $\mathbf{U}$  has been split as  $\mathbf{U} = [\mathbf{U}_c \quad \mathbf{U}_f]$ , where  $\mathbf{U}_c$  is the set of the first  $n_c$  left singular vectors of  $\mathbf{M}$  and  $\mathbf{U}_f$  is the set of the last  $n_f = n - n_c$  left singular vectors of  $\mathbf{M}$ .

Since, as a consequence of the singular value decomposition,  $\mathbf{U}$  is unitary, then  $\mathbf{U}^\top \cdot \mathbf{U} = \mathbf{I}$ . By writing the same expression in terms of  $\mathbf{U}_c$  and  $\mathbf{U}_f$  it results that:

$$\mathbf{U} \cdot \mathbf{U}^T = \begin{bmatrix} \mathbf{U}_c^T \\ \mathbf{U}_f^T \end{bmatrix} \cdot [\mathbf{U}_c \ \mathbf{U}_f] = \begin{bmatrix} (\mathbf{U}_c^T \cdot \mathbf{U}_c) & (\mathbf{U}_c^T \cdot \mathbf{U}_f) \\ (\mathbf{U}_f^T \cdot \mathbf{U}_c) & (\mathbf{U}_f^T \cdot \mathbf{U}_f) \end{bmatrix} = \begin{bmatrix} \mathbf{I} & \mathbf{0} \\ \mathbf{0} & \mathbf{I} \end{bmatrix}$$

and by equating term to term it results that:

$$\mathbf{U}_c^T \cdot \mathbf{U}_c = \mathbf{I}, \quad \mathbf{U}_f^T \cdot \mathbf{U}_f = \mathbf{I}, \quad \mathbf{U}_c^T \cdot \mathbf{U}_f = \mathbf{0}, \quad \mathbf{U}_f^T \cdot \mathbf{U}_c = \mathbf{0}$$

which are the properties of (4.22).

Since  $\mathbf{U}$  is unitary, it also results that  $\mathbf{U}^T \cdot \mathbf{U} = \mathbf{I}$ . Therefore, by expanding the product in terms of  $\mathbf{U}_c$  and  $\mathbf{U}_f$  it results that:

$$\mathbf{I} = \mathbf{U}^T \cdot \mathbf{U} = [\mathbf{U}_c \ \mathbf{U}_f] \cdot \begin{bmatrix} \mathbf{U}_c^T \\ \mathbf{U}_f^T \end{bmatrix} = \mathbf{U}_c \cdot \mathbf{U}_c^T + \mathbf{U}_f \cdot \mathbf{U}_f^T$$

which is the property (4.23).

As per (4.21), the constraint matrix is  $\mathbf{M} = \mathbf{U}_c \cdot \tilde{\Sigma} \cdot \mathbf{V}^T$ . By pre-multiplying  $\mathbf{M}$  by  $\mathbf{U}_f^T$  it results that:

$$\mathbf{U}_f^T \cdot \mathbf{M} = \mathbf{U}_f^T \cdot \mathbf{U}_c \cdot \tilde{\Sigma} \cdot \mathbf{V}^T = (\mathbf{U}_f^T \cdot \mathbf{U}_c) \cdot \tilde{\Sigma} \cdot \mathbf{V}^T = \mathbf{0} \cdot \tilde{\Sigma} \cdot \mathbf{V}^T = \mathbf{0}$$

which, once transposed, is the first property of (4.24).

By pre-multiplying  $\mathbf{M}$  by  $\mathbf{U}_c^T$  it results that:

$$\mathbf{U}_c^T \cdot \mathbf{M} = \mathbf{U}_c^T \cdot \mathbf{U}_c \cdot \tilde{\Sigma} \cdot \mathbf{V}^T = (\mathbf{U}_c^T \cdot \mathbf{U}_c) \cdot \tilde{\Sigma} \cdot \mathbf{V}^T = \mathbf{I} \cdot \tilde{\Sigma} \cdot \mathbf{V}^T = \tilde{\Sigma} \cdot \mathbf{V}^T$$

which, once transposed (since  $\tilde{\Sigma} = \tilde{\Sigma}^T$ ), is the second property of (4.24). □

### 9.4.8 Configuration spaces basis

It is here proven that, given the  $n \times n$  left singular vectors matrix  $\mathbf{U} = [\mathbf{U}_c \ \mathbf{U}_f]$  corresponding to the  $n \times n_c$  constraint matrix  $\mathbf{M}$ , then the  $n \times n_f$  matrix  $\mathbf{U}_f$  is a basis of the configuration space  $\mathcal{N}(\mathbf{M}^T)$  and the  $n \times n_c$  matrix  $\mathbf{U}_c$  is a basis of the complementary configuration space  $\mathcal{N}^\perp(\mathbf{M}^T) = \mathcal{R}(\mathbf{M})$ .

**Proof.** For any vector  $\mathbf{x} \in \mathbb{R}^n$ , since  $\mathbf{U}$  is a  $n \times n$  unitary matrix, it is possible to associate a unique vector  $\mathbf{y} \in \mathbb{R}^n$  such that:

$$\mathbf{x} = \mathbf{U} \cdot \mathbf{y} \iff \mathbf{y} = \mathbf{U}^{-1} \cdot \mathbf{x} = \mathbf{U}^T \cdot \mathbf{x}$$

The vector  $\mathbf{y}$  represents the same vector  $\mathbf{x}$  in the new reference frame defined by  $\mathbf{U}$ . It can be split into two sub-vectors  $\mathbf{y}_c$  and  $\mathbf{y}_f$ , with dimension  $n_c \times 1$  and  $n_f \times 1$ , respectively. Therefore, it results that:

$$\mathbf{x} = \mathbf{U} \cdot \mathbf{y} = [\mathbf{U}_c \ \mathbf{U}_f] \cdot \begin{bmatrix} \mathbf{y}_c \\ \mathbf{y}_f \end{bmatrix} = \mathbf{U}_c \cdot \mathbf{y}_c + \mathbf{U}_f \cdot \mathbf{y}_f$$

which is the same expression of (4.25).

Given (4.21), the constraint matrix can be expressed through its singular value decomposition as  $\mathbf{M} = \mathbf{U}_c \cdot \tilde{\Sigma} \cdot \mathbf{V}^T$ . If  $\mathbf{x} \in \mathcal{N}(\mathbf{M}^T)$  it means that  $\mathbf{M}^T \cdot \mathbf{x} = \mathbf{0}$ . Therefore,

by expanding this product and by recalling the properties (4.22) it results:

$$\begin{aligned}\mathbf{0} &= \mathbf{M}^T \cdot \mathbf{x} = (\mathbf{U}_c \cdot \tilde{\Sigma} \cdot \mathbf{V}^T)^T \cdot (\mathbf{U}_c \cdot \mathbf{y}_c + \mathbf{U}_f \cdot \mathbf{y}_f) = \\ &= (\mathbf{V} \cdot \tilde{\Sigma}) \cdot [(\mathbf{U}_c^T \cdot \mathbf{U}_c) \cdot \mathbf{y}_c + (\mathbf{U}_c^T \cdot \mathbf{U}_f) \cdot \mathbf{y}_f] = (\mathbf{V} \cdot \tilde{\Sigma}) \cdot \mathbf{y}_c\end{aligned}$$

Since both  $\mathbf{V}$  and  $\tilde{\Sigma}$  are  $n_c \times n_c$  invertible matrices, it results:

$$\mathbf{y}_c = (\mathbf{V} \cdot \tilde{\Sigma})^{-1} \cdot \mathbf{0} = \mathbf{0}$$

By denoting as  $\mathbf{u}_{f,k}$  the  $k$ -th column of  $\mathbf{U}_f$  (with  $k = 1, \dots, n_f$ ), the vector  $\mathbf{x}$  can be expressed as:

$$\mathbf{x} = \mathbf{U}_f \cdot \mathbf{y}_f = \sum_{k=1}^{n_f} \mathbf{u}_{f,k} \cdot y_{f,k}$$

meaning that  $\mathbf{x}$  is a linear combination of the vectors  $\mathbf{u}_{f,k}$ , each of which is weighted by  $y_{f,k}$ . Since this is true for any  $\mathbf{x} \in \mathcal{N}(\mathbf{M}^T)$ , it can be deduced that the set of  $\mathbf{u}_{f,k}$  is a basis of the configuration space  $\mathcal{N}(\mathbf{M}^T)$ .

If a vector  $\mathbf{y} \in \mathcal{R}(\mathbf{M})$ , by definition, it means that there exists a  $n_c \times 1$  vector  $\mathbf{z}$  such that  $\mathbf{y} = \mathbf{M} \cdot \mathbf{z}$ . By expanding  $\mathbf{M}$  it results that:

$$\mathbf{y} = \mathbf{M} \cdot \mathbf{z} = (\mathbf{U}_c \cdot \tilde{\Sigma} \cdot \mathbf{V}^T) \cdot \mathbf{z} = \mathbf{U}_c \cdot (\tilde{\Sigma} \cdot \mathbf{V}^T \cdot \mathbf{z})$$

and, by denoting as  $\mathbf{w}_c = \tilde{\Sigma} \cdot \mathbf{V}^T \cdot \mathbf{z}$  and as  $\mathbf{u}_{c,k}$  (with  $k = 1, \dots, n_c$ ) the columns of  $\mathbf{U}_c$ , the vector  $\mathbf{y}$  can be written as:

$$\mathbf{y} = \mathbf{U}_c \cdot \mathbf{w}_c = \sum_{k=1}^{n_c} \mathbf{u}_{c,k} \cdot w_{c,k}$$

meaning that  $\mathbf{y}$  is a linear combination of the vectors  $\mathbf{u}_{c,k}$ , each of which is weighted by  $w_{c,k}$ . Since this is true for any  $\mathbf{y} \in \mathcal{R}(\mathbf{M})$ , it can be deduced that the set of  $\mathbf{u}_{c,k}$  is a basis of the complementary configuration space  $\mathcal{R}(\mathbf{M}) = \mathcal{N}^\perp(\mathbf{M}^T)$ .  $\square$

### 9.4.9 Reduced order electrical drive model parameters

It is here proven that in a constrained network, the electrical drive model in the configuration space satisfies the equation (4.31), with the equivalent parameters defined in (4.32). It is also shown that the equivalent inductances matrix  $\mathbf{L}_{EM,f}$  is symmetric and positive definite, meaning that it can be inverted.

**Proof.** The machine electrical equations can be written as per (4.18):

$$\mathbf{L}_{EM} \cdot \frac{d\mathbf{i}_{EM}}{dt} + \mathbf{R}_{EM} \cdot \mathbf{i}_{EM} + \mathbf{e}_{EM} = \mathbf{N} \cdot \mathbf{v}_{VSI} - \mathbf{R}_{NET} \cdot \mathbf{i}_{EM} - \mathbf{M} \cdot \mathbf{v}_{NET}$$

By pre-multiplying both sides of the equation by  $\mathbf{U}_f^T$  and by considering that, given the constraints, the machine currents can be expressed as per (4.29) in the form  $\mathbf{i}_{EM} = \mathbf{U}_f \cdot \mathbf{i}_{EM,f}$ , it results that:

$$\begin{aligned} & \mathbf{U}_f^T \cdot \mathbf{L}_{EM} \cdot \frac{d}{dt}(\mathbf{U}_f \cdot \mathbf{i}_{EM,f}) + \mathbf{U}_f^T \cdot \mathbf{R}_{EM} \cdot (\mathbf{U}_f \cdot \mathbf{i}_{EM,f}) + \mathbf{U}_f^T \cdot \mathbf{e}_{EM} = \\ & = \mathbf{U}_f^T \cdot \mathbf{N} \cdot \mathbf{v}_{VSI} - \mathbf{U}_f^T \cdot \mathbf{R}_{NET} \cdot (\mathbf{U}_f \cdot \mathbf{i}_{EM,f}) - (\mathbf{U}_f^T \cdot \mathbf{M}) \cdot \mathbf{v}_{NET} \end{aligned}$$

As per (4.24),  $\mathbf{U}_f^T \cdot \mathbf{M} = \mathbf{0}$  and the auxiliary network voltages term is neutralized. By isolating the input term depending on  $\mathbf{v}_{VSI}$  on the right side of the equation and by considering that  $\mathbf{U}_f$  is constant (since it only depends on the network configuration), the dynamical equation can be rewritten as:

$$\begin{aligned} & (\mathbf{U}_f^T \cdot \mathbf{L}_{EM} \cdot \mathbf{U}_f) \frac{d\mathbf{i}_{EM,f}}{dt} + (\mathbf{U}_f^T \cdot \mathbf{R}_{EM} \cdot \mathbf{U}_f) \cdot \mathbf{i}_{EM,f} + (\mathbf{U}_f^T \cdot \mathbf{e}_{EM}) + \dots \\ & \dots + (\mathbf{U}_f^T \cdot \mathbf{R}_{NET} \cdot \mathbf{U}_f) \cdot \mathbf{i}_{EM,f} = (\mathbf{U}_f^T \cdot \mathbf{N}) \cdot \mathbf{v}_{VSI} \end{aligned}$$

which is equal to the equation (4.31) with the equivalent parameters defined in (4.32).

The equivalent inductances matrix of the model is defined in (4.32) as  $\mathbf{L}_{EM,f} = \mathbf{U}_f^T \cdot \mathbf{L}_{EM} \cdot \mathbf{U}_f$ . Since  $\mathbf{L}_{EM}$  is symmetric, then:

$$\mathbf{L}_{EM,f}^T = (\mathbf{U}_f^T \cdot \mathbf{L}_{EM} \cdot \mathbf{U}_f)^T = \mathbf{U}_f^T \cdot \mathbf{L}_{EM}^T \cdot \mathbf{U}_f = \mathbf{U}_f^T \cdot \mathbf{L}_{EM} \cdot \mathbf{U}_f = \mathbf{L}_{EM,f}$$

meaning that also  $\mathbf{L}_{EM,f}$  is symmetric. Since  $\mathbf{U}_f$  is a  $n \times n_f$  full-ranked matrix, given any  $n_f \times 1$  vector  $\mathbf{x} \neq \mathbf{0}$  it results that  $\mathbf{y} = \mathbf{U}_f \cdot \mathbf{x} \neq \mathbf{0}$ . Therefore, since  $\mathbf{L}_{EM}$  is positive definite, any quadratic form of  $\mathbf{L}_{EM,f}$  can be written as:

$$\begin{aligned} \mathbf{x}^T \cdot \mathbf{L}_{EM,f} \cdot \mathbf{x} &= \mathbf{x}^T \cdot (\mathbf{U}_f^T \cdot \mathbf{L}_{EM} \cdot \mathbf{U}_f) \cdot \mathbf{x} = \\ &= (\mathbf{U}_f \cdot \mathbf{x})^T \cdot \mathbf{L}_{EM} \cdot (\mathbf{U}_f \cdot \mathbf{x}) = \mathbf{y}^T \cdot \mathbf{L}_{EM} \cdot \mathbf{y} > 0 \end{aligned}$$

meaning that  $\mathbf{L}_{EM,f}$  is positive definite, too. Being  $\mathbf{L}_{EM,f}$  both symmetric and positive definite, it is invertible. □

## 9.5 Chapter 5 Proofs

This section contains the proof of the properties stated in Chapter 5 - Field Oriented Control of Asymmetrical PMSMs.

### 9.5.1 Torque expression in the space vector formalism

It is here proven that the analytical expression of the electromagnetic torque developed by a multiphase PMSM can be written as (5.11), which represents the superposition of all the (infinite) spatial harmonics contributions.

**Proof.** Considering the torque expression (5.8), the definitions of the currents space vectors (5.9) and their expression in the multiple synchronous domain (5.10), it results:

$$\begin{aligned}
 T_{em} &= P_p \cdot \sum_{k=1}^n \frac{\partial \psi_{PM,k}}{\partial \theta_{el}} \cdot i_k = \\
 &= -P_p \cdot \sum_{k=1}^n \left[ \sum_{h=1}^{+\infty} h \cdot \Psi_{Mh} \cdot \sin(h \cdot (\theta_{el} - \alpha_k) + \varphi_h) \right] \cdot i_k = \\
 &= P_p \cdot \sum_{h=1}^{+\infty} h \cdot \Psi_{Mh} \cdot \left[ - \sum_{k=1}^n \sin(h \cdot (\theta_{el} - \alpha_k) + \varphi_h) \cdot i_k \right] = \\
 &= P_p \cdot \sum_{h=1}^{+\infty} h \cdot \Psi_{Mh} \cdot \left[ - \sum_{k=1}^n i_k \cdot \text{Im} \{ e^{h \cdot (\theta_{el} - \alpha_k) + \varphi_h} \} \right] = \\
 &= P_p \cdot \sum_{h=1}^{+\infty} h \cdot \Psi_{Mh} \cdot \text{Im} \left\{ - \sum_{k=1}^n i_k \cdot e^{-jh\alpha_k} \cdot e^{j(h\theta_{el} + \varphi_h)} \right\} = \\
 &= P_p \cdot \sum_{h=1}^{+\infty} h \cdot \Psi_{Mh} \cdot \text{Im} \left\{ \left[ \sum_{k=1}^n i_k \cdot e^{jh\alpha_k} \right] \cdot e^{-j(h\theta_{el} + \varphi_h)} \right\} = \\
 &= P_p \cdot \sum_{h=1}^{+\infty} h \cdot \Psi_{Mh} \cdot \text{Im} \left\{ \sqrt{\frac{n}{2}} \cdot \hat{i}_h \cdot e^{-j(h\theta_{el} + \varphi_h)} \right\} = \\
 &= P_p \cdot \sum_{h=1}^{+\infty} h \cdot \Psi_{Mh} \cdot \sqrt{\frac{n}{2}} \cdot \text{Im} \{ \hat{i}_h^{(dq)} \} = \\
 &= \sum_{h=1}^{+\infty} \left( \sqrt{\frac{n}{2}} \cdot P_p \cdot h \cdot \Psi_{Mh} \right) \cdot i_{qh} = \\
 &= \sum_{h=1}^{+\infty} \kappa_h \cdot i_{qh}
 \end{aligned}$$

which is the expression (5.11). □

### 9.5.2 Clarke matrices orthogonality for symmetrical machines

It is here proven that, considering a symmetrical machine, the generalized Clarke transformation matrices  $\mathbf{C}$  built as per (5.18) or as per (5.19) are orthogonal.

**Proof.** For a symmetrical machine configuration, the magnetic axis of the  $k$ -th phase winding can be written as  $\alpha_k = (k - 1) \cdot (2\pi/n)$ .

Consider two rows  $\mathbf{c}_{c,k}$  and  $\mathbf{c}_{c,h}$  of  $\mathbf{C}$  built with the cosine functions of the magnetic axes angles:

$$\begin{aligned}\mathbf{c}_{c,k} &= \sqrt{\frac{2}{n}} \cdot \left[ \cos\left(0 \cdot k \cdot \frac{2\pi}{n}\right) \cos\left(1 \cdot k \cdot \frac{2\pi}{n}\right) \cdots \cos\left((n-1) \cdot k \cdot \frac{2\pi}{n}\right) \right] \\ \mathbf{c}_{c,h} &= \sqrt{\frac{2}{n}} \cdot \left[ \cos\left(0 \cdot h \cdot \frac{2\pi}{n}\right) \cos\left(1 \cdot h \cdot \frac{2\pi}{n}\right) \cdots \cos\left((n-1) \cdot h \cdot \frac{2\pi}{n}\right) \right]\end{aligned}$$

The scalar product between  $\mathbf{c}_{c,h}$  and  $\mathbf{c}_{c,p}$  can be computed as:

$$\begin{aligned}\mathbf{c}_{c,k}^T \cdot \mathbf{c}_{c,h} &= \frac{2}{n} \sum_{r=1}^n \cos\left(r \cdot k \cdot \frac{2\pi}{n}\right) \cdot \cos\left(r \cdot h \cdot \frac{2\pi}{n}\right) = \\ &= \frac{2}{n} \sum_{r=1}^n \frac{e^{jr \cdot k \cdot \frac{2\pi}{n}} + e^{-jr \cdot k \cdot \frac{2\pi}{n}}}{2} \cdot \frac{e^{jr \cdot h \cdot \frac{2\pi}{n}} + e^{-jr \cdot h \cdot \frac{2\pi}{n}}}{2} = \\ &= \frac{1}{2n} \left( \sum_{r=1}^n e^{jr \cdot k \cdot \frac{2\pi}{n}} \cdot e^{jr \cdot h \cdot \frac{2\pi}{n}} + \sum_{r=1}^n e^{-jr \cdot k \cdot \frac{2\pi}{n}} \cdot e^{-jr \cdot h \cdot \frac{2\pi}{n}} \right) + \dots \\ &\dots + \frac{1}{2n} \left( \sum_{r=1}^n e^{jr \cdot k \cdot \frac{2\pi}{n}} \cdot e^{-jr \cdot h \cdot \frac{2\pi}{n}} + \sum_{r=1}^n e^{-jr \cdot k \cdot \frac{2\pi}{n}} \cdot e^{jr \cdot h \cdot \frac{2\pi}{n}} \right) = \\ &= \frac{1}{n} \operatorname{Re} \left( \sum_{r=1}^n e^{jr \cdot (k+h) \cdot \frac{2\pi}{n}} \right) + \frac{1}{n} \operatorname{Re} \left( \sum_{r=1}^n e^{jr \cdot (k-h) \cdot \frac{2\pi}{n}} \right)\end{aligned}$$

Each of the complex sums which appear in this expression represents the sum of a symmetric star of unitary norm complex vectors shifted by a multiple integer of  $2\pi/n$ .

The only way for these sums to be different from zero is that either  $(k+h)/n$  or  $(k-h)/n$  are integer numbers. This is never verified for the matrices built as per (5.18) or as per (5.19), unless it results  $k=h$  (i.e., for the self-related scalar product), for which it results:

$$\mathbf{c}_{c,k}^T \cdot \mathbf{c}_{c,k} = \frac{1}{n} \operatorname{Re} \left( \sum_{r=1}^n e^{jr \cdot (k-k) \cdot \frac{2\pi}{n}} \right) = \frac{1}{n} \cdot \sum_{r=1}^n 1 = \frac{1}{n} \cdot n = 1$$

Similar results can also be obtained for the sine terms. By considering the row vectors  $\mathbf{c}_{s,k}$  and  $\mathbf{c}_{s,h}$  of  $\mathbf{C}$  built as:

$$\begin{aligned}\mathbf{c}_{s,k} &= \sqrt{\frac{2}{n}} \cdot \left[ \sin\left(0 \cdot k \cdot \frac{2\pi}{n}\right) \sin\left(1 \cdot k \cdot \frac{2\pi}{n}\right) \cdots \sin\left((n-1) \cdot k \cdot \frac{2\pi}{n}\right) \right]^T \\ \mathbf{c}_{s,h} &= \sqrt{\frac{2}{n}} \cdot \left[ \sin\left(0 \cdot h \cdot \frac{2\pi}{n}\right) \sin\left(1 \cdot h \cdot \frac{2\pi}{n}\right) \cdots \sin\left((n-1) \cdot h \cdot \frac{2\pi}{n}\right) \right]^T\end{aligned}$$

their scalar product is:

$$\begin{aligned}
\mathbf{c}_{s,k}^T \cdot \mathbf{c}_{s,h} &= \frac{2}{n} \sum_{r=1}^n \sin\left(r \cdot k \cdot \frac{2\pi}{n}\right) \cdot \sin\left(r \cdot h \cdot \frac{2\pi}{n}\right) = \\
&= \frac{2}{n} \sum_{r=1}^n \frac{e^{jr \cdot k \frac{2\pi}{n}} - e^{-jr \cdot k \frac{2\pi}{n}}}{2j} \cdot \frac{e^{jr \cdot h \frac{2\pi}{n}} - e^{-jr \cdot h \frac{2\pi}{n}}}{2j} = \\
&= -\frac{1}{2n} \left( \sum_{r=1}^n e^{jr \cdot k \frac{2\pi}{n}} \cdot e^{jr \cdot h \frac{2\pi}{n}} + \sum_{r=1}^n e^{-jr \cdot k \frac{2\pi}{n}} \cdot e^{-jr \cdot h \frac{2\pi}{n}} \right) + \dots \\
&\dots + \frac{1}{2n} \left( \sum_{r=1}^n e^{jr \cdot k \frac{2\pi}{n}} \cdot e^{-jr \cdot h \frac{2\pi}{n}} + \sum_{r=1}^n e^{-jr \cdot k \frac{2\pi}{n}} \cdot e^{jr \cdot h \frac{2\pi}{n}} \right) = \\
&= -\frac{1}{n} \operatorname{Re} \left( \sum_{r=1}^n e^{jr \cdot (k+h) \frac{2\pi}{n}} \right) + \frac{1}{n} \operatorname{Re} \left( \sum_{r=1}^n e^{jr \cdot (k-h) \frac{2\pi}{n}} \right)
\end{aligned}$$

for which the same properties hold.

Finally, by considering the mutual interaction among sine and cosine terms, the scalar product between  $\mathbf{c}_{c,k}$  and  $\mathbf{c}_{s,h}$  is:

$$\begin{aligned}
\mathbf{c}_{c,k}^T \cdot \mathbf{c}_{s,h} &= \frac{2}{n} \sum_{r=1}^n \cos\left(r \cdot k \cdot \frac{2\pi}{n}\right) \cdot \sin\left(r \cdot h \cdot \frac{2\pi}{n}\right) = \\
&= \frac{2}{n} \sum_{r=1}^n \frac{e^{jr \cdot k \frac{2\pi}{n}} + e^{-jr \cdot k \frac{2\pi}{n}}}{2} \cdot \frac{e^{jr \cdot h \frac{2\pi}{n}} - e^{-jr \cdot h \frac{2\pi}{n}}}{2j} = \\
&= \frac{1}{2jn} \left( \sum_{r=1}^n e^{jr \cdot k \frac{2\pi}{n}} \cdot e^{jr \cdot h \frac{2\pi}{n}} - \sum_{r=1}^n e^{-jr \cdot k \frac{2\pi}{n}} \cdot e^{-jr \cdot h \frac{2\pi}{n}} \right) + \dots \\
&\dots - \frac{1}{2jn} \left( \sum_{r=1}^n e^{jr \cdot k \frac{2\pi}{n}} \cdot e^{-jr \cdot h \frac{2\pi}{n}} - \sum_{r=1}^n e^{-jr \cdot k \frac{2\pi}{n}} \cdot e^{jr \cdot h \frac{2\pi}{n}} \right) = \\
&= \frac{1}{n} \operatorname{Im} \left( \sum_{r=1}^n e^{jr \cdot (k+h) \frac{2\pi}{n}} \right) - \frac{1}{n} \operatorname{Im} \left( \sum_{r=1}^n e^{jr \cdot (k-h) \frac{2\pi}{n}} \right)
\end{aligned}$$

and, given the imaginary part operator, this result is always zero regardless of the values of  $h$  and  $k$ .

Note that the row of  $\mathbf{C}$  related to the zero-sequence component can be simply obtained as:

$$\begin{aligned}
\mathbf{C}_0 &= \frac{1}{\sqrt{n}} \cdot [1 \ 1 \ 1 \ 1 \ \dots \ 1 \ 1] = \\
&= \frac{1}{\sqrt{n}} \cdot \left[ \cos\left(0 \cdot 0 \cdot \frac{2\pi}{n}\right) \ \cos\left(1 \cdot 0 \cdot \frac{2\pi}{n}\right) \ \dots \ \cos\left((n-1) \cdot 0 \cdot \frac{2\pi}{n}\right) \right] = \frac{1}{\sqrt{2}} \cdot \mathbf{c}_{c,0}
\end{aligned}$$

and, in this case, by repeating the same procedure, the scalar product with any of the other rows is still zero, while the self-related scalar product is again 1 because when  $k = h = 0$  both  $k + h$  and  $k - h$  are 0. In other words, in the expression of the scalar product both the complex sum with  $(k + h)/n$  and the complex sum with  $(k - h)/n$  give non-zero terms, which balance the gain  $1/\sqrt{2}$  which multiplies  $\mathbf{c}_{c,0}$ .

Similarly, the row of  $\mathbf{C}$  related to the second zero-sequence component (if present) can be obtained as:

$$\begin{aligned} \mathbf{C}_0^- &= \frac{1}{\sqrt{n}} \cdot [1 \quad -1 \quad 1 \quad -1 \quad \dots \quad 1 \quad -1] = \\ &= \frac{1}{\sqrt{n}} \cdot \left[ \cos\left(0 \cdot \frac{n}{2} \cdot \frac{2\pi}{n}\right) \cos\left(1 \cdot \frac{n}{2} \cdot \frac{2\pi}{n}\right) \dots \cos\left((n-1) \cdot \frac{n}{2} \cdot \frac{2\pi}{n}\right) \right] = \frac{1}{\sqrt{2}} \cdot \mathbf{c}_{c,(n/2)} \end{aligned}$$

Again, the scalar product with any of the other rows of  $\mathbf{C}$  is zero, while the self-related scalar product is again 1 because when  $k = h = n/2$ , then  $k - h = 0$  and  $k + h = n$ . This again means that, in the expression of the scalar product, both the complex sum with  $(k + h)/n$  and the complex sum with  $(k - h)/n$  give non-zero terms, which balance the gain  $1/\sqrt{2}$  which multiplies  $\mathbf{c}_{c,(n/2)}$ .

As a result, it has been shown that the rows of the matrix  $\mathbf{C}$  built either as per (5.18) or as per (5.19) are orthogonal with one another and with a unitary norm. Therefore,  $\mathbf{C}^T \cdot \mathbf{C} = \mathbf{C} \cdot \mathbf{C}^T = \mathbf{I}$ , meaning that  $\mathbf{C}$  is a unitary matrix, for which  $\mathbf{C}^T = \mathbf{C}^{-1}$ .  $\square$

### 9.5.3 Inductances matrix diagonalization for symmetrical machines

It is here proven that, for a symmetrical machine, the VSD transformations (5.18) and (5.19), once applied to the electrical equations (5.20), diagonalize the inductances matrix  $\mathbf{L}$ .

**Proof.** For a symmetrical machine,  $\mathbf{L}$  is a circulant matrix, meaning that it can be written in the following form:

$$\mathbf{L} = \begin{bmatrix} L_{c,0} & L_{c,n-1} & L_{c,n-2} & \dots & L_{c,2} & L_{c,1} \\ L_{c,1} & L_{c,0} & L_{c,n-1} & \dots & L_{c,3} & L_{c,2} \\ L_{c,2} & L_{c,1} & L_{c,0} & \dots & L_{c,4} & L_{c,3} \\ \vdots & \vdots & \vdots & \ddots & \vdots & \vdots \\ L_{c,n-2} & L_{c,n-3} & L_{c,n-4} & \dots & L_{c,0} & L_{c,n-1} \\ L_{c,n-1} & L_{c,n-2} & L_{c,n-3} & \dots & L_{c,1} & L_{c,0} \end{bmatrix}$$

where  $L_{c,0}, L_{c,1}, \dots, L_{c,n-1}$  are inductances coefficients. This property is coming from the symmetry itself, because it is always possible to renumber the phase windings in a cyclical order and obtaining the same electrical behaviour and, therefore, the same inductances matrix.

For energetic reasons it has also been proven that  $\mathbf{L}$  is symmetric. As a result, the inductances terms also satisfy the following properties:

$$L_{c,1} = L_{c,n-1}, \quad L_{c,2} = L_{c,n-2}, \quad \dots, \quad L_{c,h} = L_{c,n-h} \quad (\forall h)$$

and the previous expression can be also rewritten as:

$$\mathbf{L} = \begin{bmatrix} L_{c,0} & L_{c,1} & L_{c,2} & \cdots & L_{c,2} & L_{c,1} \\ L_{c,1} & L_{c,0} & L_{c,1} & \cdots & L_{c,3} & L_{c,2} \\ L_{c,2} & L_{c,1} & L_{c,0} & \cdots & L_{c,4} & L_{c,3} \\ \vdots & \vdots & \vdots & \ddots & \vdots & \vdots \\ L_{c,2} & L_{c,3} & L_{c,4} & \cdots & L_{c,0} & L_{c,1} \\ L_{c,1} & L_{c,2} & L_{c,3} & \cdots & L_{c,1} & L_{c,0} \end{bmatrix}$$

Consider now the column vector built as:

$$\mathbf{c}_{c,1} = \left[ \cos\left(0 \cdot \frac{2\pi}{n}\right) \cos\left(1 \cdot \frac{2\pi}{n}\right) \cdots \cos\left((n-1) \cdot \frac{2\pi}{n}\right) \right]^T$$

which is proportional to the 1<sup>st</sup> row of the Clarke matrix  $\mathbf{C}$  built as per (5.18)-(5.19) with the cosine terms of the magnetic axes angles (the normalization term  $\sqrt{2/n}$  does not affect all the following results).

By computing the product of the 1<sup>st</sup> row of  $\mathbf{L}$  with  $\mathbf{c}_{c,1}$  it results:

$$[L_{c,0} \ L_{c,1} \ \cdots \ L_{c,2} \ L_{c,1}] \cdot \mathbf{c}_{c,1} = \sum_{k=0}^{n-1} L_{c,k} \cdot \cos\left(k \cdot \frac{2\pi}{n}\right) = L_{m1}$$

This term can be conveniently rewritten in the complex domain as:

$$L_{m1} = \sum_{k=0}^{n-1} L_{c,k} \cdot \cos\left(k \cdot \frac{2\pi}{n}\right) = \operatorname{Re} \left\{ \sum_{k=0}^{n-1} L_{c,k} \cdot e^{jk \cdot \frac{2\pi}{n}} \right\}$$

Because of the symmetry  $L_{c,h} = L_{c,n-h}$ , the complex sum in the previous expression is a real number. This is because the imaginary part of each term  $L_{c,h} \cdot e^{jk \cdot \frac{2\pi}{n}}$  is balanced by the imaginary part of the term  $L_{c,n-h} \cdot e^{j(n-h) \cdot \frac{2\pi}{n}} = L_{c,h} \cdot e^{j(n-h) \cdot \frac{2\pi}{n}}$ . As a result:

$$L_{m1} = \operatorname{Re} \left\{ \sum_{k=0}^{n-1} L_{c,k} \cdot e^{jk \cdot \frac{2\pi}{n}} \right\} = \sum_{k=0}^{n-1} L_{c,k} \cdot e^{jk \cdot \frac{2\pi}{n}}$$

By computing the product of the 2<sup>nd</sup> row of  $\mathbf{L}$  with  $\mathbf{c}_{c,1}$  it results:

$$\begin{aligned} [L_{c,1} \ L_{c,0} \ \cdots \ L_{c,3} \ L_{c,2}] \cdot \mathbf{c}_{c,1} &= \sum_{k=0}^{n-1} L_{c,k} \cdot \cos\left((k+1) \cdot \frac{2\pi}{n}\right) = \\ &= \operatorname{Re} \left\{ \sum_{k=0}^{n-1} L_{c,k} \cdot e^{jk \cdot \frac{2\pi}{n}} \cdot e^{j \frac{2\pi}{n}} \right\} = \operatorname{Re} \left\{ L_{m1} \cdot e^{j \frac{2\pi}{n}} \right\} = L_{m1} \cdot \cos(1 \cdot \alpha) \end{aligned}$$

Similarly, by computing the product of the 3<sup>rd</sup> row of  $\mathbf{L}$ , it results:

$$\begin{aligned} [L_{c,2} \ L_{c,1} \ \cdots \ L_{c,4} \ L_{c,3}] \cdot \mathbf{c}_{c,1} &= \sum_{k=0}^{n-1} L_{c,k} \cdot \cos\left((k+2) \cdot \frac{2\pi}{n}\right) = \\ &= \operatorname{Re} \left\{ \sum_{k=0}^{n-1} L_{c,k} \cdot e^{jk \cdot \frac{2\pi}{n}} \cdot e^{j2 \cdot \frac{2\pi}{n}} \right\} = \operatorname{Re} \left\{ L_{m1} \cdot e^{j2 \cdot \frac{2\pi}{n}} \right\} = L_{m1} \cdot \cos(2 \cdot \alpha) \end{aligned}$$

and so on for all the other rows.

As a result, by grouping the result of all the rows, it results that:

$$\mathbf{L} \cdot \mathbf{c}_{c,1} = L_{m1} \cdot \left[ \cos\left(0 \cdot \frac{2\pi}{n}\right) \cos\left(1 \cdot \frac{2\pi}{n}\right) \cdots \cos\left((n-1) \cdot \frac{2\pi}{n}\right) \right]^T = L_{m1} \cdot \mathbf{c}_{c,1}$$

and, by definition, this means that  $\mathbf{c}_{c,1}$  is an eigenvector of  $\mathbf{L}$  with eigenvalue  $L_{m1}$ .

Consider now another column vector built as:

$$\mathbf{C}_{s,1} = \left[ \sin\left(0 \cdot \frac{2\pi}{n}\right) \sin\left(1 \cdot \frac{2\pi}{n}\right) \cdots \sin\left((n-1) \cdot \frac{2\pi}{n}\right) \right]^T$$

which is proportional to the 2<sup>nd</sup> row of the Clarke matrix  $\mathbf{C}$  built as per (5.18)-(5.19) with the sine terms of the magnetic axes angles.

The product of the 1<sup>st</sup> row of  $\mathbf{L}$  with  $\mathbf{c}_{s,1}$  results in:

$$\begin{aligned} [L_{c,0} \ L_{c,1} \ \cdots \ L_{c,2} \ L_{c,1}] \cdot \mathbf{c}_{s,1} &= \sum_{k=0}^{n-1} L_{c,k} \cdot \sin\left(k \cdot \frac{2\pi}{n}\right) = \\ &= \text{Im} \left\{ \sum_{k=0}^{n-1} L_{c,k} \cdot e^{jk \frac{2\pi}{n}} \right\} = \text{Im}\{L_{m1}\} = 0 \end{aligned}$$

The product of the 2<sup>nd</sup> row of  $\mathbf{L}$  with  $\mathbf{c}_{s,1}$  is:

$$\begin{aligned} [L_{c,1} \ L_{c,0} \ \cdots \ L_{c,3} \ L_{c,2}] \cdot \mathbf{c}_{s,1} &= \sum_{k=0}^{n-1} L_{c,k} \cdot \sin\left((k+1) \cdot \frac{2\pi}{n}\right) = \\ &= \text{Im} \left\{ \sum_{k=0}^{n-1} L_{c,k} \cdot e^{jk \frac{2\pi}{n}} \cdot e^{j \frac{2\pi}{n}} \right\} = \text{Im} \{L_{m1} \cdot e^{j \frac{2\pi}{n}}\} = L_{m1} \cdot \sin(1 \cdot \alpha) \end{aligned}$$

and so on for all the other rows.

As a result, by grouping the result of all the rows, it results that:

$$\mathbf{L} \cdot \mathbf{c}_{s,1} = L_{m1} \cdot \left[ \sin\left(0 \cdot \frac{2\pi}{n}\right) \sin\left(1 \cdot \frac{2\pi}{n}\right) \cdots \sin\left((n-1) \cdot \frac{2\pi}{n}\right) \right]^T = L_{m1} \cdot \mathbf{c}_{s,1}$$

and, by definition, this means that  $\mathbf{c}_{s,1}$  is an eigenvector of  $\mathbf{L}$  with the same eigenvalue  $L_{m1}$  of  $\mathbf{c}_{c,1}$ .

The same reasoning can be repeated for all the rows of the generalized Clarke transformation matrix  $\mathbf{C}$ . In other words, all the rows of the matrix  $\mathbf{C}$  are eigenvectors of  $\mathbf{L}$  and the rows corresponding to the same space vector components have the same eigenvalue.

Since the matrices built as per (5.18) and as per (5.19) are unitary, then  $\mathbf{C}^{-1} = \mathbf{C}^T$ , meaning that the columns of  $\mathbf{C}^{-1}$  are  $n$  linearly independent eigenvectors of  $\mathbf{L}$  and, therefore, that the matrix product  $\mathbf{L}_{\text{VSD}} = \mathbf{C} \cdot \mathbf{L} \cdot \mathbf{C}^{-1}$  (which appears in the transformed model (5.20)) is the diagonalization of the inductances matrix  $\mathbf{L}$ . □

### 9.5.4 PM-induced back-EMFs for symmetrical machines

It is here proven that, for a symmetrical machine, if the even-order harmonics of the

PM-induced back-EMFs are absent, and if the odd-order harmonics with index  $h \leq n$  are negligible, then, by using the VSD transformation (5.19), it results that  $e_{dh} = 0$  and  $e_{qh} = \sqrt{n/2} \cdot h \omega_{el} \cdot \Psi_{Mh}$ .

**Proof.** The expression of the PM-induced back-EMF of the machine  $k$ -th phase is given by (5.4) and can be rewritten as:

$$\begin{aligned}
 e_k &= -\omega_{el} \cdot \sum_{h=1}^{+\infty} h \cdot \Psi_{Mh} \cdot \sin(h \cdot (\theta_{el} - \alpha_k) + \varphi_h) = \\
 &= -\sum_{h=1,3,\dots}^n E_h \cdot \sin(h \theta_{el} - h \alpha_k + \varphi_h) = \\
 &= -\sum_{h=1,3,\dots}^n E_h \cdot \text{Im}\{e^{j(h\theta_{el} + \varphi_h)} \cdot e^{-jh\alpha_k}\} = \\
 &= \sum_{h=1,3,\dots}^n -\frac{1}{2j} \cdot [E_h \cdot e^{j(h\theta_{el} + \varphi_h)} \cdot e^{-jh\alpha_k} - E_h \cdot e^{-j(h\theta_{el} + \varphi_h)} \cdot e^{jh\alpha_k}] = \\
 &= -\frac{1}{2j} \cdot \sum_{h=1,3,\dots}^n E_h \cdot e^{j(h\theta_{el} + \varphi_h)} \cdot e^{-jh\alpha_k} + \frac{1}{2j} \cdot \sum_{h=1,3,\dots}^n E_h \cdot e^{-j(h\theta_{el} + \varphi_h)} \cdot e^{jh\alpha_k}
 \end{aligned}$$

with  $E_h = \omega_{el} \cdot h \cdot \Psi_{Mh}$ .

To find the  $r$ -th order space vector of the induced voltages it is sufficient to apply the same formula (5.9), resulting in:

$$\begin{aligned}
 \underline{e}_r &= e_{xr} + j \cdot e_{yr} = \sqrt{\frac{2}{n}} \cdot \sum_{k=1}^n e_k \cdot e^{jr\alpha_k} = \\
 &= \sqrt{\frac{2}{n}} \cdot \sum_{k=1}^n -\frac{1}{2j} \cdot \sum_{h=1,3,\dots}^n E_h \cdot e^{j(h\theta_{el} + \varphi_h)} \cdot e^{-jh\alpha_k} \cdot e^{jr\alpha_k} + \dots \\
 &\dots + \sqrt{\frac{2}{n}} \cdot \sum_{k=1}^n \frac{1}{2j} \cdot \sum_{h=1,3,\dots}^n E_h \cdot e^{-j(h\theta_{el} + \varphi_h)} \cdot e^{jh\alpha_k} \cdot e^{jr\alpha_k} = \\
 &= \sum_{h=1,3,\dots}^n \left( -\sqrt{\frac{2}{n}} \cdot \frac{1}{2j} \cdot E_h \cdot e^{j(h\theta_{el} + \varphi_h)} \right) \cdot \sum_{k=1}^n e^{j(r-h)\alpha_k} + \dots \\
 &\dots + \sum_{h=1,3,\dots}^n \left( \sqrt{\frac{2}{n}} \cdot \frac{1}{2j} \cdot E_h \cdot e^{-j(h\theta_{el} + \varphi_h)} \right) \cdot \sum_{k=1}^n e^{j(r+h)\alpha_k}
 \end{aligned}$$

Given the symmetry of the magnetic axes, all the terms  $\sum_{k=1}^n e^{j(r\pm h)\alpha_k}$  with  $r \neq h$  are zero, while for  $h = r$  the sum is equal to  $n$ . Then, the previous expression simplifies to

$$\underline{e}_r = -\sqrt{\frac{2}{n}} \cdot \frac{1}{2j} \cdot E_r \cdot e^{j(r\theta_{el} + \varphi_r)} \cdot n = \sqrt{\frac{n}{2}} \cdot j \cdot E_r \cdot e^{j(r\theta_{el} + \varphi_r)}$$

The corresponding space vector can be written in the synchronous domain by just applying the transformation (5.10), resulting in:

$$\underline{e}_r^{(dq)} = e_{dr} + j \cdot e_{qr} = \underline{e}_r \cdot e^{-j(r\theta_{el} + \varphi_r)} = \sqrt{\frac{n}{2}} \cdot j \cdot E_r$$



Consider the non-diagonal term  $\mathbf{G}_{h,k}(\theta_{el}) = \mathbf{D}_h(\theta_{el}) \cdot \mathbf{Q}_{h,k} \cdot \mathbf{D}_k^T(\theta_{el})$ . Since  $\mathbf{D}_h(\theta_{el})$  is composed of only trigonometric functions varying with  $h\theta_{el}$  and  $\mathbf{D}_k(\theta_{el})$  is composed of only trigonometric functions varying with  $k\theta_{el}$ , then  $\mathbf{G}_{h,k}(\theta_{el})$  only contains products of trigonometric terms with different periods (e.g.,  $\cos(h\theta_{el}) \cdot \cos(k\theta_{el})$  and the other analogous combinations).

As a result, by averaging  $\mathbf{G}_{h,k}(\theta_{el})$  along a full  $2\pi$  cycle of  $\theta_{el}$ , they are zero:

$$\frac{1}{2\pi} \int_0^{2\pi} \mathbf{G}_{h,k}(\theta_{el}) \, d\theta_{el} = \mathbf{0}$$

which is the first property of  $\mathbf{G}(\theta_{el})$  to be proven.

Consider now the diagonal term  $\mathbf{G}_{h,h}(\theta_{el}) = \mathbf{D}_h(\theta_{el}) \cdot \mathbf{Q}_{h,h} \cdot \mathbf{D}_h^T(\theta_{el})$ . Since  $\mathbf{Q}_{h,h}$  is symmetric, this term can be analytically computed as:

$$\begin{aligned} \mathbf{G}_{h,h}(\theta_{el}) &= \mathbf{D}_h(\theta_{el}) \cdot \mathbf{Q}_{h,h} \cdot \mathbf{D}_h^T(\theta_{el}) = \\ &= \begin{bmatrix} \cos(\theta_h) & \sin(\theta_h) \\ -\sin(\theta_h) & \cos(\theta_h) \end{bmatrix} \cdot \begin{bmatrix} Q_{h,h}^{(1)} & Q_{h,h}^{(2)} \\ Q_{h,h}^{(2)} & Q_{h,h}^{(1)} \end{bmatrix} \cdot \begin{bmatrix} \cos(\theta_h) & -\sin(\theta_h) \\ \sin(\theta_h) & \cos(\theta_h) \end{bmatrix} = \\ &= \begin{bmatrix} Q_{h,h}^{(1)} + Q_{h,h}^{(2)} \cdot \sin(2\theta_h) & Q_{h,h}^{(2)} \cdot \cos(2\theta_h) \\ Q_{h,h}^{(2)} \cdot \cos(2\theta_h) & Q_{h,h}^{(1)} - Q_{h,h}^{(2)} \cdot \sin(2\theta_h) \end{bmatrix} \end{aligned}$$

It can be seen that the diagonal terms are purely trigonometric functions of  $h\theta_{el}$ , while the diagonal terms also have a constant term, which is the same for both elements. As a result, by averaging  $\mathbf{G}_{h,h}(\theta_{el})$  along a  $2\pi$  cycle of  $\theta_{el}$ , this results in a scalar matrix:

$$\frac{1}{2\pi} \int_0^{2\pi} \mathbf{G}_{h,h}(\theta_{el}) \, d\theta_{el} = \begin{bmatrix} Q_{h,h}^{(1)} & 0 \\ 0 & Q_{h,h}^{(1)} \end{bmatrix} = \begin{bmatrix} H_h & 0 \\ 0 & H_h \end{bmatrix} = H_h \cdot \mathbf{I}$$

which is the second property of  $\mathbf{G}(\theta_{el})$  to be proven.

As a result, the average power losses weighting matrix is diagonal. The positivity of the terms  $H_h$  can be directly derived by its energetic properties, since it results that  $P_R = R \cdot \mathbf{i}_{dq}^T \cdot \mathbf{H} \cdot \mathbf{i}_{dq} \geq 0$ .

□

### 9.5.6 Power losses expression for symmetrical machines

It is here shown that, for a symmetrical machine, the instantaneous power losses and the average power losses are equal and are proportional to the squared Euclidean norm of the synchronous current set  $\mathbf{i}_{dq}$ .

**Proof.** For a symmetrical  $n$ -phase machine the generalized Clarke transformation matrix  $\mathbf{C}$  is unitary, meaning that  $\mathbf{C}^{-1} = \mathbf{C}^T$ . By computing the instantaneous power losses weighting matrix  $\mathbf{G}(\theta_{el})$  it results that:

$$\begin{aligned}
\mathbf{G}(\theta) &= \mathbf{D}(\theta_{el}) \cdot \mathbf{C}^{-\text{T}} \cdot \mathbf{C}^{-1} \cdot \mathbf{D}^{\text{T}}(\theta_{el}) = \\
&= \mathbf{D}(\theta_{el}) \cdot (\mathbf{C}^{\text{T}})^{-1} \cdot \mathbf{C}^{-1} \cdot \mathbf{D}^{\text{T}}(\theta_{el}) = \\
&= \mathbf{D}(\theta_{el}) \cdot (\mathbf{C}^{-1})^{-1} \cdot \mathbf{C}^{-1} \cdot \mathbf{D}^{\text{T}}(\theta_{el}) = \\
&= \mathbf{D}(\theta_{el}) \cdot \mathbf{C} \cdot \mathbf{C}^{-1} \cdot \mathbf{D}^{\text{T}}(\theta_{el}) = \\
&= \mathbf{D}(\theta_{el}) \cdot \mathbf{D}^{\text{T}}(\theta_{el}) = \\
&= \mathbf{D}(\theta_{el}) \cdot \mathbf{D}^{-1}(\theta_{el}) = \\
&= \mathbf{I}
\end{aligned}$$

The average power losses weighting matrix  $\mathbf{H}$  is:

$$\mathbf{H} = \frac{1}{2\pi} \int_0^{2\pi} \mathbf{G}(\theta_{el}) \, d\theta_{el} = \frac{1}{2\pi} \int_0^{2\pi} \mathbf{I} \, d\theta_{el} = \mathbf{I} \cdot \frac{1}{2\pi} \int_0^{2\pi} d\theta_{el} = \mathbf{I}$$

As a result, the expressions (5.37) and (5.38) simply become:

$$P_R = p_R = R \cdot (\mathbf{i}_{dq}^{\text{T}} \cdot \mathbf{i}_{dq}) = R \cdot \|\mathbf{i}_{dq}\|^2$$

which is the simplified expression (5.41). □

### 9.5.7 Optimal third harmonic injection strategy solution

It is here proven that the optimal third harmonic injection ratio to minimize the average stator losses (5.51) in a multiphase PMSM is given by (5.57).

**Proof.** The analytical expression of the average power losses in terms of the injection ratio  $k = i_{q3}/i_{q1}$  is given by (5.56):

$$P_R(k) = R \cdot I_{RMS}^2(k) = R \cdot T_{em}^{*2} \cdot \frac{H_1 + H_3 \cdot k^2}{(\kappa_1 + k \cdot \kappa_3)^2}$$

The optimal injection ratio is found by nullifying the derivative of the function  $P_R(k)$ , which is:

$$0 = \frac{\partial P_R}{\partial k} = R \cdot T_{em}^{*2} \cdot \frac{(2 \cdot H_3 \cdot k) \cdot (\kappa_1 + k \cdot \kappa_3)^2 - 2 \cdot \kappa_3 \cdot (\kappa_1 + k \cdot \kappa_3) \cdot (H_1 + H_3 \cdot k^2)}{(\kappa_1 + k \cdot \kappa_3)^4}$$

The terms  $R \cdot T_{em}^{*2}$  and  $(\kappa_1 + k \cdot \kappa_3)^4$  are always non-negative and can be disregarded. The term  $(\kappa_1 + k \cdot \kappa_3)$  is different from zero, otherwise given (5.54) it would always lead to  $T_{em} = 0$ .

Therefore, the previous expression can be simplified to:

$$\begin{aligned}
0 &= 2 \cdot H_3 \cdot k \cdot (\kappa_1 + k \cdot \kappa_3)^2 - 2 \cdot \kappa_3 \cdot (\kappa_1 + k \cdot \kappa_3) \cdot (H_1 + H_3 \cdot k^2) = \\
&= H_3 \cdot k \cdot (\kappa_1 + k \cdot \kappa_3) - \kappa_3 \cdot (H_1 + H_3 \cdot k^2) = \\
&= (H_3 \cdot \kappa_1) \cdot k + (H_3 \cdot \kappa_3) \cdot k^2 - (H_1 \cdot \kappa_3) - (H_3 \cdot \kappa_3) \cdot k^2 = \\
&= (H_3 \cdot \kappa_1) \cdot k - (H_1 \cdot \kappa_3)
\end{aligned}$$

meaning that:

$$k = \frac{H_1 \cdot \kappa_3}{H_3 \cdot \kappa_1} = \frac{\kappa_3/\kappa_1}{H_3/H_1}$$

which is the expression (5.57). □

### 9.5.8 Optimal multi-harmonic injection strategy solution

It is here proven that the multi-harmonic injection strategy to minimize the average stator losses (5.38) in a multiphase PMSM provides the optimal reference currents set given by (5.64).

**Proof.** As stated in Section 5.2.3, the optimal multi-harmonic injection strategy (5.61) can be solved by using the Lagrange multipliers method, where the Lagrangian function is given by (5.62):

$$\mathcal{L}(\mathbf{i}_{dq}, \mu) = \frac{1}{2} \mathbf{i}_{dq}^T \cdot \mathbf{H} \cdot \mathbf{i}_{dq} - \mu \cdot (\boldsymbol{\kappa}^T \cdot \mathbf{i}_{dq} - T_{em}^*)$$

By nullifying the gradient of  $\mathcal{L}(\mathbf{i}_{dq}, \mu)$ , the linear algebraic system (5.63) is found, which is here recalled:

$$\begin{aligned} \frac{\partial \mathcal{L}}{\partial \mathbf{i}_{dq}} &= \mathbf{H} \cdot \mathbf{i}_{dq} - \mu \cdot \boldsymbol{\kappa} = \mathbf{0} \\ \frac{\partial \mathcal{L}}{\partial \mu} &= \boldsymbol{\kappa}^T \cdot \mathbf{i}_{dq} - T_{em}^* = 0 \end{aligned}$$

From the first equation, since  $\mathbf{H}$  is a positive definite diagonal matrix, it results:

$$\mathbf{i}_{dq} = \mu \cdot \mathbf{H}^{-1} \cdot \boldsymbol{\kappa}$$

By pre-multiplying this expression by  $\boldsymbol{\kappa}^T$  and by using the second equation of the system (5.63), it results that:

$$T_{em}^* = \boldsymbol{\kappa}^T \cdot \mathbf{i}_{dq} = \mu \cdot (\boldsymbol{\kappa}^T \cdot \mathbf{H}^{-1} \cdot \boldsymbol{\kappa})$$

Since  $(\boldsymbol{\kappa}^T \cdot \mathbf{H}^{-1} \cdot \boldsymbol{\kappa})$  is a positive-definite quadratic form, the previous expression can be solved for the Lagrange multiplier:

$$\mu = \frac{T_{em}^*}{\boldsymbol{\kappa}^T \cdot \mathbf{H}^{-1} \cdot \boldsymbol{\kappa}}$$

Once substituted back in the current expression, this gives:

$$\mathbf{i}_{dq} = \mu \cdot \mathbf{H}^{-1} \cdot \boldsymbol{\kappa} = \frac{\mathbf{H}^{-1} \cdot \boldsymbol{\kappa}}{\boldsymbol{\kappa}^T \cdot \mathbf{H}^{-1} \cdot \boldsymbol{\kappa}} \cdot T_{em}^*$$

which is the result provided in (5.64).

The overall machine power losses with this optimal synchronous current set are:

$$\begin{aligned} P_R^{(MHI)} &= R \cdot \mathbf{i}_{dq}^T \cdot \mathbf{H} \cdot \mathbf{i}_{dq} = \\ &= R \cdot \left( \frac{\mathbf{H}^{-1} \cdot \boldsymbol{\kappa}}{\boldsymbol{\kappa}^T \cdot \mathbf{H}^{-1} \cdot \boldsymbol{\kappa}} \cdot T_{em}^* \right)^T \cdot \mathbf{H} \cdot \left( \frac{\mathbf{H}^{-1} \cdot \boldsymbol{\kappa}}{\boldsymbol{\kappa}^T \cdot \mathbf{H}^{-1} \cdot \boldsymbol{\kappa}} \cdot T_{em}^* \right) = \\ &= R \cdot \left( \frac{T_{em}^*}{\boldsymbol{\kappa}^T \cdot \mathbf{H}^{-1} \cdot \boldsymbol{\kappa}} \right)^2 \cdot (\boldsymbol{\kappa}^T \cdot \mathbf{H}^{-1} \cdot \mathbf{H} \cdot \mathbf{H}^{-1} \cdot \boldsymbol{\kappa}) = \\ &= R \cdot \frac{T_{em}^{*2}}{(\boldsymbol{\kappa}^T \cdot \mathbf{H}^{-1} \cdot \boldsymbol{\kappa})^2} \cdot (\boldsymbol{\kappa}^T \cdot \mathbf{H}^{-1} \cdot \boldsymbol{\kappa}) = \\ &= R \cdot T_{em}^{*2} \cdot \frac{1}{\boldsymbol{\kappa}^T \cdot \mathbf{H}^{-1} \cdot \boldsymbol{\kappa}} \end{aligned}$$

which is the result provided in (5.66). □

### 9.5.9 Maximum torque per ampere strategy solution

It is here proven that the MTPA strategy developed in Section 5.2.4 for a multiphase PMSM can be reformulated as:

$$\min_{\hat{\mathbf{i}}_{dq}} \left\{ \hat{\mathbf{i}}_{dq}^T \cdot \hat{\mathbf{G}}(\theta_{el}) \cdot \hat{\mathbf{i}}_{dq} \right\} \quad \text{subject to} \quad \hat{\boldsymbol{\kappa}}^T \cdot \hat{\mathbf{i}}_{dq} = T_{em}^* \quad (9.20)$$

where:

- $\hat{\mathbf{i}}_{dq}$  is the  $(n-1) \times 1$  set obtained by discarding the last element of  $\mathbf{i}_{dq}$  (which is the zero-sequence current component  $i_0$ ),
- $\hat{\boldsymbol{\kappa}}$  is the  $(n-1) \times 1$  set obtained by discarding the last element of  $\boldsymbol{\kappa}$  (which would be the torque gain related to  $i_0$ ), and
- $\hat{\mathbf{G}}(\theta_{el})$  is the  $(n-1) \times (n-1)$  matrix obtained by neglecting the last row and the last column of  $\mathbf{G}(\theta_{el})$  (which would be related to the interaction between  $i_0$  and all the other components of  $\mathbf{i}_{dq}$  in the computation of the instantaneous power losses).

It is then proven that the resulting optimal reference synchronous currents set  $\hat{\mathbf{i}}_{dq}^*$  is given by (5.70) with  $\mathbf{G}'_{eq}(\theta_{el})$  given by (5.71).

**Proof.** The optimization problem (5.69) considers two constraints, being the torque development requirement  $\boldsymbol{\kappa}^T \cdot \mathbf{i}_{dq} = T_{em}^*$  and the zero-sequence constraint  $i_0 = 0$ .

The problem (5.69) can be reformulated more compactly by only considering the  $(n-1)$  degrees of freedom of  $\mathbf{i}_{dq}$ , consisting in all the space vector components  $\{i_{dh}, i_{qh}\}$  and in the second zero-sequence component  $i_0^-$  (if present). Indeed, by imposing  $i_0 = 0$ , both the instantaneous losses and the electromagnetic torque can be expressed as functions of  $\hat{\mathbf{i}}_{dq}$ , being:

$$p_R = R \cdot \mathbf{i}_{dq}^T \cdot \mathbf{G}(\theta_{el}) \cdot \mathbf{i}_{dq} = R \cdot \hat{\mathbf{i}}_{dq}^T \cdot \hat{\mathbf{G}}(\theta_{el}) \cdot \hat{\mathbf{i}}_{dq}$$

$$T_{em} = \boldsymbol{\kappa}^T \cdot \mathbf{i}_{dq} = \hat{\boldsymbol{\kappa}}^T \cdot \hat{\mathbf{i}}_{dq}$$

In other words, the problem (5.69) in terms of the  $n$ -dimensional set  $\mathbf{i}_{dq}$  can be replaced by the problem (9.20) in terms of the  $(n-1)$ -dimensional set  $\hat{\mathbf{i}}_{dq}$ .

This reduced-order MTPA problem (9.20) has the same structure as the multi-harmonic injection problem (5.61). As a result, it can be solved with the same approach based on the Lagrange multiplier method. The optimal reduced-order set has the form of (5.64), which is:

$$\hat{\mathbf{i}}_{dq}^* = \frac{\hat{\mathbf{G}}^{-1}(\theta_{el}) \cdot \hat{\boldsymbol{\kappa}}}{\hat{\boldsymbol{\kappa}}^T \cdot \hat{\mathbf{G}}^{-1}(\theta_{el}) \cdot \hat{\boldsymbol{\kappa}}} \cdot T_{em}^*$$

The corresponding  $n \times 1$  optimal synchronous current set  $\mathbf{i}_{dq}^*$  can be obtained by simply concatenating  $\hat{\mathbf{i}}_{dq}^*$  and  $i_0^* = 0$ .

By introducing the weighting matrix  $\mathbf{G}'_{eq}(\theta_{el})$  as per (5.71), it results that:

$$\mathbf{G}'_{eq}(\theta_{el}) \cdot \boldsymbol{\kappa} = \begin{bmatrix} \hat{\mathbf{G}}^{-1}(\theta_{el}) & \mathbf{0} \\ \mathbf{0} & 0 \end{bmatrix} \cdot \begin{bmatrix} \hat{\boldsymbol{\kappa}} \\ 0 \end{bmatrix} = \begin{bmatrix} \hat{\mathbf{G}}^{-1}(\theta_{el}) \cdot \hat{\boldsymbol{\kappa}} \\ 0 \end{bmatrix}$$

and, therefore

$$\boldsymbol{\kappa}^T \cdot \mathbf{G}'_{eq}(\theta_{el}) \cdot \boldsymbol{\kappa} = [\hat{\boldsymbol{\kappa}}^T \quad 0] \cdot \begin{bmatrix} \hat{\mathbf{G}}^{-1}(\theta_{el}) & \mathbf{0} \\ \mathbf{0} & 0 \end{bmatrix} \cdot \begin{bmatrix} \hat{\boldsymbol{\kappa}} \\ 0 \end{bmatrix} = \hat{\boldsymbol{\kappa}}^T \cdot \hat{\mathbf{G}}^{-1}(\theta_{el}) \cdot \hat{\boldsymbol{\kappa}}$$

As a result, the expression (5.70) is:

$$\begin{aligned} \hat{\mathbf{i}}_{dq}^*(\theta_{el}) &= \frac{\mathbf{G}'_{eq}(\theta_{el}) \cdot \boldsymbol{\kappa}}{\boldsymbol{\kappa}^T \cdot \mathbf{G}'_{eq}(\theta_{el}) \cdot \boldsymbol{\kappa}} \cdot T_{em}^* = \frac{\begin{bmatrix} \hat{\mathbf{G}}^{-1}(\theta_{el}) \cdot \hat{\boldsymbol{\kappa}} \\ 0 \end{bmatrix}}{\hat{\boldsymbol{\kappa}}^T \cdot \hat{\mathbf{G}}^{-1}(\theta_{el}) \cdot \hat{\boldsymbol{\kappa}}} \cdot T_{em}^* = \\ &= \begin{bmatrix} \hat{\mathbf{G}}^{-1}(\theta_{el}) \cdot \hat{\boldsymbol{\kappa}} \\ \hat{\boldsymbol{\kappa}}^T \cdot \hat{\mathbf{G}}^{-1}(\theta_{el}) \cdot \hat{\boldsymbol{\kappa}} \\ 0 \end{bmatrix} \cdot T_{em}^* = \begin{bmatrix} \hat{\mathbf{i}}_{dq}^* \\ 0 \end{bmatrix} \end{aligned}$$

which is the aforementioned concatenation of  $\hat{\mathbf{i}}_{dq}^*$  and  $\hat{i}_0^* = 0$ .

By discarding, for notation simplicity, the explicit dependence on  $\theta_{el}$ , the overall instantaneous power losses obtained with the optimal current set  $\hat{\mathbf{i}}_{dq}^*$  are:

$$\begin{aligned} p_R^{(MTPA)} &= R \cdot \hat{\mathbf{i}}_{dq}^{*T} \cdot \mathbf{G} \cdot \hat{\mathbf{i}}_{dq}^* = R \cdot \hat{\mathbf{i}}_{dq}^{*T} \cdot \hat{\mathbf{G}} \cdot \hat{\mathbf{i}}_{dq}^* = \\ &= R \cdot \begin{pmatrix} \hat{\mathbf{G}}^{-1} \cdot \hat{\boldsymbol{\kappa}} \\ \hat{\boldsymbol{\kappa}}^T \cdot \hat{\mathbf{G}}^{-1} \cdot \hat{\boldsymbol{\kappa}} \end{pmatrix}^T \cdot T_{em}^* \cdot \hat{\mathbf{G}} \cdot \begin{pmatrix} \hat{\mathbf{G}}^{-1} \cdot \hat{\boldsymbol{\kappa}} \\ \hat{\boldsymbol{\kappa}}^T \cdot \hat{\mathbf{G}}^{-1} \cdot \hat{\boldsymbol{\kappa}} \end{pmatrix} \cdot T_{em}^* \\ &= R \cdot \left( \frac{T_{em}^*}{\hat{\boldsymbol{\kappa}}^T \cdot \hat{\mathbf{G}}^{-1} \cdot \hat{\boldsymbol{\kappa}}} \right)^2 \cdot (\hat{\boldsymbol{\kappa}}^T \cdot \hat{\mathbf{G}}^{-1} \cdot \hat{\mathbf{G}} \cdot \hat{\mathbf{G}}^{-1} \cdot \hat{\boldsymbol{\kappa}}) = \\ &= R \cdot \frac{T_{em}^{*2}}{(\hat{\boldsymbol{\kappa}}^T \cdot \hat{\mathbf{G}}^{-1} \cdot \hat{\boldsymbol{\kappa}})^2} \cdot (\hat{\boldsymbol{\kappa}}^T \cdot \hat{\mathbf{G}}^{-1} \cdot \hat{\boldsymbol{\kappa}}) = \\ &= R \cdot T_{em}^{*2} \cdot \frac{1}{\hat{\boldsymbol{\kappa}}^T \cdot \hat{\mathbf{G}}^{-1} \cdot \hat{\boldsymbol{\kappa}}} = \\ &= R \cdot T_{em}^{*2} \cdot \frac{1}{\boldsymbol{\kappa}^T \cdot \mathbf{G}'_{eq}(\theta_{el}) \cdot \boldsymbol{\kappa}} \end{aligned}$$

which is the result provided in (5.72). □

### 9.5.10 Neutral point voltage compensation

It is here proven that the general formulation of the steady-state compensation of the neutral point potential shift is:

$$v_{NET}^* = \frac{[0 \ 0 \ \dots \ (0) \ 1] \cdot (\mathbf{u}_{dq} - \omega_{el} \cdot \mathbf{L}_{dq2}(\theta_{el}) \cdot \dot{\mathbf{i}}_{dq} - R \cdot \mathbf{i}_{dq} + \mathbf{e}_{dq})}{[0 \ 0 \ \dots \ (0) \ 1] \cdot \mathbf{g}(\theta_{el})} \quad (9.21)$$

This term can be used in (5.78) to compensate for the steady-state mutual coupling interaction due to the electrical windings connection in asymmetrical machine configurations.

**Proof.** The electrical equations of the machine in the multiple synchronous domain is given by (5.30), which is here recalled:

$$\begin{aligned} \mathbf{L}_{dq1}(\theta_{el}) \cdot \frac{d\mathbf{i}_{dq}}{dt} + \omega_{el} \cdot \mathbf{L}_{dq2}(\theta_{el}) \cdot \mathbf{i}_{dq} + R \cdot \mathbf{i}_{dq} + \mathbf{e}_{dq} &= \\ &= \mathbf{v}_{dq} = \mathbf{u}_{dq} - \mathbf{g}(\theta_{el}) \cdot v_{NET} \end{aligned}$$

In case of a constant synchronous reference current set  $\mathbf{i}_{dq}^*$  the steady-state effects can be obtained by disregarding the transformer induced back-EMFs  $\mathbf{L}_{dq1}(\theta_{el}) \cdot d\mathbf{i}_{dq}/dt$ . The term including  $v_{NET}$  can be also isolated on one side, resulting in the equation:

$$\mathbf{g}(\theta_{el}) \cdot v_{NET} = \mathbf{u}_{dq} - \omega_{el} \cdot \mathbf{L}_{dq2}(\theta_{el}) \cdot \mathbf{i}_{dq} + R \cdot \mathbf{i}_{dq} + \mathbf{e}_{dq}$$

This vector equation is a set of  $n$  scalar equations. To only select the equation of the zero-sequence component (which, considering the chosen VSD transformation, is the last one) it is sufficient to pre-multiply it by the row vector  $[0 \ 0 \ \dots \ (0) \ 1]$ , resulting in:

$$\begin{aligned} [0 \ 0 \ \dots \ (0) \ 1] \cdot \mathbf{g}(\theta_{el}) \cdot v_{NET} &= \\ &= [0 \ 0 \ \dots \ (0) \ 1] \cdot (\mathbf{u}_{dq} - \omega_{el} \cdot \mathbf{L}_{dq2}(\theta_{el}) \cdot \mathbf{i}_{dq} + R \cdot \mathbf{i}_{dq} + \mathbf{e}_{dq}) \end{aligned}$$

The term  $[0 \ 0 \ \dots \ (0) \ 1] \cdot \mathbf{g}(\theta_{el})$  is a scalar variable and, assuming it to be different from zero, it allows to compute the neutral point potential shift as:

$$v_{NET}^* = \frac{[0 \ 0 \ \dots \ (0) \ 1] \cdot (\mathbf{u}_{dq} - \omega_{el} \cdot \mathbf{L}_{dq2}(\theta_{el}) \cdot \mathbf{i}_{dq} - R \cdot \mathbf{i}_{dq} + \mathbf{e}_{dq})}{[0 \ 0 \ \dots \ (0) \ 1] \cdot \mathbf{g}(\theta_{el})}$$

which is the expression provided in (9.21).

□

## 9.6 Chapter 6 Proofs

This section contains the proof of the properties stated in Chapter 6 - Decoupled Phase Variable Control of PMSMs.

### 9.6.1 MTPA problem resolution

It is here proven that the analytical solution of the MTPA problem (6.14) is given by the expression (6.17).

**Proof.** As already stated in Section 6.2.1, the MTPA problem (6.14) can be solved by using the Lagrange's multiplier method. The chosen Lagrangian function  $\mathfrak{L}(\mathbf{i}, \mu, \boldsymbol{\nu})$  is given by the expression (6.15), which is here recalled:

$$\mathfrak{L}(\mathbf{i}, \mu, \boldsymbol{\nu}) = \frac{1}{2} \mathbf{i}^T \cdot \mathbf{i} - \mu \cdot (\mathbf{f}_{PM}^T \cdot \mathbf{i} - T_{em}^*) - \boldsymbol{\nu}^T \cdot (\mathbf{M}^T \cdot \mathbf{i})$$

By nullifying its gradient, the linear algebraic system (6.16) is obtained. This system is here recalled:

$$\begin{aligned} \frac{\partial \mathfrak{L}}{\partial \mathbf{i}} &= \mathbf{i} - \mu \cdot \mathbf{f}_{PM} - \mathbf{M} \cdot \boldsymbol{\nu} = \mathbf{0} \\ \frac{\partial \mathfrak{L}}{\partial \mu} &= \mathbf{f}_{PM}^T \cdot \mathbf{i} - T_{em}^* = 0 \\ \frac{\partial \mathfrak{L}}{\partial \boldsymbol{\nu}} &= \mathbf{M}^T \cdot \mathbf{i} = \mathbf{0} \end{aligned}$$

From the first equation of (6.16), it results that:

$$\mathbf{i} = \mu \cdot \mathbf{f}_{PM} + \mathbf{M} \cdot \boldsymbol{\nu}$$

By pre-multiplying both terms for  $\mathbf{M}^T$  and by substituting the last equation of (6.16) it results that:

$$\mathbf{0} = \mathbf{M}^T \cdot \mathbf{i} = \mathbf{M}^T \cdot \mu \cdot \mathbf{f}_{PM} + \mathbf{M}^T \cdot \mathbf{M} \cdot \boldsymbol{\nu}$$

This equation can be rewritten as:

$$\mathbf{M}^T \cdot \mathbf{M} \cdot \boldsymbol{\nu} = -\mu \cdot \mathbf{M}^T \cdot \mathbf{f}_{PM}$$

and solved in terms of the Lagrange multipliers set  $\boldsymbol{\nu}$  (related to the current constraints), resulting in:

$$\boldsymbol{\nu} = -\mu \cdot (\mathbf{M}^T \cdot \mathbf{M})^{-1} \cdot \mathbf{M}^T \cdot \mathbf{f}_{PM}$$

By substituting back in the expression of the currents set  $\mathbf{i}$  it results:

$$\begin{aligned} \mathbf{i} &= \mu \cdot \mathbf{f}_{PM} + \mathbf{M} \cdot \boldsymbol{\nu} = \\ &= \mu \cdot \mathbf{f}_{PM} + \mathbf{M} \cdot [-\mu \cdot (\mathbf{M}^T \cdot \mathbf{M})^{-1} \cdot \mathbf{M}^T \cdot \mathbf{f}_{PM}] = \\ &= \mu \cdot [\mathbf{I} - \mathbf{M} \cdot (\mathbf{M}^T \cdot \mathbf{M})^{-1} \cdot \mathbf{M}^T] \cdot \mathbf{f}_{PM} = \\ &= \mu \cdot \mathbf{W} \cdot \mathbf{f}_{PM} \end{aligned}$$

where  $\mathbf{W} = \mathbf{I} - \mathbf{M} \cdot (\mathbf{M}^T \cdot \mathbf{M})^{-1} \cdot \mathbf{M}^T$  is the MTPA weighting matrix defined in (6.18).

By pre-multiplying both terms of this last equation by  $\mathbf{f}_{PM}^T$  and by substituting the

second equation of (6.16) it results that:

$$T_{em}^* = \mathbf{f}_{PM}^T \cdot \mathbf{i} = \mathbf{f}_{PM}^T \cdot (\mu \cdot \mathbf{W} \cdot \mathbf{f}_{PM}) = \mu \cdot (\mathbf{f}_{PM}^T \cdot \mathbf{W} \cdot \mathbf{f}_{PM})$$

which can be solved in terms of the Lagrange multiplier  $\mu$  (related to the electromagnetic torque development requirement), resulting in:

$$\mu = \frac{T_{em}^*}{\mathbf{f}_{PM}^T \cdot \mathbf{W} \cdot \mathbf{f}_{PM}}$$

Finally, by substituting this term in the currents set expression it results that the only stationary point of the Lagrangian function is:

$$\mathbf{i} = \mu \cdot \mathbf{W} \cdot \mathbf{f}_{PM} = \frac{\mathbf{W} \cdot \mathbf{f}_{PM}}{\mathbf{f}_{PM}^T \cdot \mathbf{W} \cdot \mathbf{f}_{PM}} \cdot T_{em}^*$$

which is the expression provided in (6.17). As also explained in Section 6.2.1, since the minimizing function  $\mathbf{i}^T \cdot \mathbf{i}$  is convex, the only stationary point of  $\mathcal{L}(\mathbf{i}, \mu, \nu)$  is the only solution to the problem (6.14). □

### 9.6.2 MTPA weighting matrix and configuration space

It is here proven that the weighting matrix  $\mathbf{W}$  of the MTPA algorithm developed in Section 6.2.1 satisfies the relation:

$$\mathbf{W} = \mathbf{I} - \mathbf{M} \cdot (\mathbf{M}^T \cdot \mathbf{M})^{-1} \cdot \mathbf{M}^T = \mathbf{U}_f \cdot \mathbf{U}_f^T \quad (9.22)$$

It is here recalled that the matrix  $\mathbf{U}_f \cdot \mathbf{U}_f^T$  projects a  $n \times 1$  vector in the configuration space defined by the constraints matrix  $\mathbf{M}$ .

**Proof.** The constraints matrix  $\mathbf{M}$  can be written through the singular value decomposition (4.21) as:

$$\mathbf{M} = \mathbf{U}_c \cdot \tilde{\Sigma} \cdot \mathbf{V}^T$$

It is worth recalling that  $\tilde{\Sigma}$  is a diagonal invertible matrix,  $\mathbf{V}$  is a unitary matrix (i.e.,  $\mathbf{V}^T \cdot \mathbf{V} = \mathbf{V} \cdot \mathbf{V}^T = \mathbf{I}$  and  $\mathbf{V}^T = \mathbf{V}^{-1}$ ) and  $\mathbf{U}_c$  has orthonormal columns (i.e.,  $\mathbf{U}_c^T \cdot \mathbf{U}_c = \mathbf{I}$ , but  $\mathbf{U}_c \cdot \mathbf{U}_c^T \neq \mathbf{I}$ ).

By computing the term  $\mathbf{M} \cdot (\mathbf{M}^T \cdot \mathbf{M})^{-1} \cdot \mathbf{M}^T$  in (6.18) it results that:

$$\begin{aligned} \mathbf{M} \cdot (\mathbf{M}^T \cdot \mathbf{M})^{-1} \cdot \mathbf{M}^T &= \\ &= (\mathbf{U}_c \cdot \tilde{\Sigma} \cdot \mathbf{V}^T) \cdot (\mathbf{V} \cdot \tilde{\Sigma} \cdot \mathbf{U}_c^T \cdot \mathbf{U}_c \cdot \tilde{\Sigma} \cdot \mathbf{V}^T)^{-1} \cdot (\mathbf{V} \cdot \tilde{\Sigma} \cdot \mathbf{U}_c^T) = \\ &= (\mathbf{U}_c \cdot \tilde{\Sigma} \cdot \mathbf{V}^T) \cdot (\mathbf{V} \cdot \tilde{\Sigma} \cdot \tilde{\Sigma} \cdot \mathbf{V}^T)^{-1} \cdot (\mathbf{V} \cdot \tilde{\Sigma} \cdot \mathbf{U}_c^T) = \\ &= (\mathbf{U}_c \cdot \tilde{\Sigma} \cdot \mathbf{V}^T) \cdot (\mathbf{V} \cdot \tilde{\Sigma}^{-1} \cdot \tilde{\Sigma}^{-1} \cdot \mathbf{V}^T) \cdot (\mathbf{V} \cdot \tilde{\Sigma} \cdot \mathbf{U}_c^T) = \\ &= \mathbf{U}_c \cdot \tilde{\Sigma} \cdot \mathbf{V}^T \cdot \mathbf{V} \cdot \tilde{\Sigma}^{-1} \cdot \tilde{\Sigma}^{-1} \cdot \mathbf{V}^T \cdot \mathbf{V} \cdot \tilde{\Sigma} \cdot \mathbf{U}_c^T = \\ &= \mathbf{U}_c \cdot \tilde{\Sigma} \cdot \tilde{\Sigma}^{-1} \cdot \tilde{\Sigma}^{-1} \cdot \tilde{\Sigma} \cdot \mathbf{U}_c^T = \\ &= \mathbf{U}_c \cdot \mathbf{U}_c^T \end{aligned}$$

And, by recalling the property (4.23), it results that:

$$\mathbf{W} = \mathbf{I} - \mathbf{M} \cdot (\mathbf{M}^T \cdot \mathbf{M})^{-1} \cdot \mathbf{M}^T = \mathbf{I} - \mathbf{U}_c \cdot \mathbf{U}_c^T = \mathbf{U}_f \cdot \mathbf{U}_f^T$$

□

### 9.6.3 MTPA strategy in the configuration space

The MTPA strategy developed in Section 6.2.1 in the phase variable domain can be also entirely formalized in the configuration space. It is here proven that the optimal set of  $n_f$  free current components is:

$$\mathbf{i}_f^* = \frac{\mathbf{f}_{PM,f}}{\mathbf{f}_{PM,f}^T \cdot \mathbf{f}_{PM,f}} \cdot T_{em}^* \quad (9.23)$$

where  $\mathbf{f}_{PM,f} = \mathbf{U}_f^T \cdot \mathbf{f}_{PM}$  is the  $n_f \times 1$  set of normalized PM-induced back-EMFs components in the configuration space. It is also proven that the corresponding set of phase current  $\mathbf{i}^* = \mathbf{U}_f \cdot \mathbf{i}_f^*$  is equivalent to the result provided in the solution (6.17).

**Proof.** Consider the MTPA problem (6.14). If the  $n$  machine currents are subject to  $n_c$  algebraic constraints expressed as  $\mathbf{M}^T \cdot \mathbf{i} = \mathbf{0}$ , they can be expressed as  $\mathbf{i} = \mathbf{U}_f \cdot \mathbf{i}_f$ , where  $\mathbf{U}_f$  is the configuration matrix related to  $\mathbf{M}$  and  $\mathbf{i}_f$  is a vector of  $n_f = n - n_c$  components.

Since the  $n \times n_f$  configuration matrix is such that  $\mathbf{U}_f^T \cdot \mathbf{U}_f = \mathbf{I}$ , the overall machine RMS current can be reformulated as:

$$I_{RMS} = \sqrt{\mathbf{i}^T \cdot \mathbf{i}} = \sqrt{\mathbf{i}_f^T \cdot \mathbf{U}_f^T \cdot \mathbf{U}_f \cdot \mathbf{i}_f} = \sqrt{\mathbf{i}_f^T \cdot \mathbf{i}_f}$$

Similarly, the electromagnetic torque can be reformulated as:

$$T_{em} = \mathbf{f}_{PM}^T \cdot \mathbf{i} = \mathbf{f}_{PM}^T \cdot \mathbf{U}_f \cdot \mathbf{i}_f = (\mathbf{U}_f^T \cdot \mathbf{f}_{PM}) \cdot \mathbf{i}_f = \mathbf{f}_{PM,f} \cdot \mathbf{i}_f$$

As a result, the MTPA optimization problem (6.14) can be reformulated for the free current components  $\mathbf{i}_f$  as:

$$\min_{\mathbf{i}_f} \{\mathbf{i}_f^T \cdot \mathbf{i}_f\} \quad \text{subject to} \quad \mathbf{f}_{PM,f}^T \cdot \mathbf{i}_f = T_{em}^*$$

where the constraints  $\mathbf{M}^T \cdot \mathbf{i} = \mathbf{0}$  are intrinsically included.

This minimization problem is equivalent to the MTPA algorithm for an unconstrained reduced-order machine, and its solution is given by:

$$\mathbf{i}_f^* = \frac{\mathbf{f}_{PM,f}}{\mathbf{f}_{PM,f}^T \cdot \mathbf{f}_{PM,f}} \cdot T_{em}^*$$

By recalling the property (6.7), it can be immediately verified that the corresponding optimal phase currents set is:

$$\mathbf{i}^* = \mathbf{U}_f \cdot \mathbf{i}_f^* = \frac{\mathbf{U}_f \cdot \mathbf{f}_{PM,f}}{\mathbf{f}_{PM,f}^T \cdot \mathbf{f}_{PM,f}} \cdot T_{em}^* = \frac{(\mathbf{U}_f \cdot \mathbf{U}_f^T) \cdot \mathbf{f}_{PM}}{\mathbf{f}_{PM}^T \cdot (\mathbf{U}_f \cdot \mathbf{U}_f^T) \cdot \mathbf{f}_{PM}} \cdot T_{em}^* = \frac{\mathbf{W} \cdot \mathbf{f}_{PM}}{\mathbf{f}_{PM}^T \cdot \mathbf{W} \cdot \mathbf{f}_{PM}} \cdot T_{em}^*$$

which is the same result found as per (6.17). □

### 9.6.4 A sufficient condition for the decoupling algorithm application

It is here proven that, if the  $n \times m$  network interconnection matrix  $\mathbf{N}$  is a full-ranked matrix with  $m \geq n$ , then the equation (6.27) is solvable and the decoupling algorithm (6.22) can be applied (regardless of the machine parameters and on the hardware

constraints on the phase currents).

**Proof.** To apply the decoupling algorithm (6.22), the equation (6.27) must be solvable. It is then sufficient to show that there exists at least one solution for the linear system (6.27) of  $n_f$  equations in  $m$  variables.

Since  $\mathbf{N}$  is a full-ranked  $n \times m$  matrix, there exists its Moore-Penrose pseudo-inverse matrix  $\mathbf{N}^\dagger$  such that  $\mathbf{N} \cdot \mathbf{N}^\dagger = \mathbf{I}$ . Then, by recalling that  $\mathbf{U}_f^T \cdot \mathbf{U}_f = \mathbf{I}$ , a possible solution of (6.27) can be chosen as:

$$\mathbf{u}^* = \mathbf{N}^\dagger \cdot \mathbf{U}_f \cdot \mathbf{v}_f^*$$

Indeed, by direct substitution, it results that:

$$\mathbf{N}_f \cdot \mathbf{u}^* = \mathbf{U}_f^T \cdot \mathbf{N} \cdot \mathbf{N}^\dagger \cdot \mathbf{U}_f \cdot \mathbf{v}_f^* = \mathbf{U}_f^T \cdot \mathbf{U}_f \cdot \mathbf{v}_f^* = \mathbf{v}_f^*$$

Since there exists at least one solution of (6.27), the system is solvable and the decoupling algorithm (6.22) can be applied.  $\square$

### 9.6.5 Injection voltage general formulation

Given the decoupling equation (6.22), it is here shown that the general solution can be written as (6.29) with the minimum norm reference converter voltages set  $\mathbf{u}_{opt}^*$  expressed by (6.30) and with the injection voltages set  $\mathbf{u}_0^*$  expressed as per (6.31).

**Proof.** Since  $\mathbf{N}_f$  is a  $n_f \times m$  full-ranked matrix with  $m \geq n_f$ , there exists its pseudo-inverse  $\mathbf{N}_f^\dagger$  such that  $\mathbf{N}_f \cdot \mathbf{N}_f^\dagger = \mathbf{I}$ . Then, consider the  $m \times 1$  vector  $\mathbf{u}^*$  built as:

$$\mathbf{u}^* = \mathbf{u}_{opt}^* + \mathbf{u}_0^* = \mathbf{N}_f^\dagger \cdot \mathbf{v}_f^* + (\mathbf{I} - \mathbf{N}_f^\dagger \cdot \mathbf{N}_f) \cdot \mathbf{u}_{off}^*$$

By simple substitution, it results that:

$$\begin{aligned} \mathbf{N}_f \cdot \mathbf{u}^* &= \mathbf{N}_f \cdot \mathbf{N}_f^\dagger \cdot \mathbf{v}_f^* + \mathbf{N}_f \cdot (\mathbf{I} - \mathbf{N}_f^\dagger \cdot \mathbf{N}_f) \cdot \mathbf{u}_{off}^* = \\ &= \mathbf{v}_f^* + (\mathbf{N}_f - \mathbf{N}_f \cdot \mathbf{N}_f^\dagger \cdot \mathbf{N}_f) \cdot \mathbf{u}_{off}^* = \\ &= \mathbf{v}_f^* + (\mathbf{N}_f - \mathbf{N}_f) \cdot \mathbf{u}_{off}^* = \mathbf{v}_f^* \end{aligned}$$

This means that, for any choice of the  $m \times 1$  vector  $\mathbf{u}_{off}^*$ , the chosen vector  $\mathbf{u}^*$  is a solution of the linear system (6.27). In other words, the pre-multiplying matrix  $(\mathbf{I} - \mathbf{N}_f^\dagger \cdot \mathbf{N}_f)$  projects  $\mathbf{u}_{off}^*$  in the null-space of  $\mathbf{N}_f$  and nullifies its contribution to the overall windings voltages set  $\mathbf{v}_f$ .  $\square$

### 9.6.6 Voltage injection properties

It is here proven that the voltage vector  $\mathbf{u}^* = \mathbf{u}_{opt}^* + \mathbf{u}_0^*$  with  $\mathbf{u}_{opt}^*$  computed via (6.30) and  $\mathbf{u}_0^*$  chosen as per (6.31), is the solution to the problem (6.27) which minimizes the Euclidean norm  $\|\mathbf{u} - \mathbf{u}_{off}^*\|$ .

**Proof.** Consider the constrained optimization problem:

$$\min_{\mathbf{u}} \{ \|\mathbf{u} - \mathbf{u}_{off}^*\| \} \quad \text{subject to} \quad \mathbf{N}_f \cdot \mathbf{u} = \mathbf{v}_f^*$$

For a given  $\mathbf{u}_{off}^*$ , this problem can be reformulated with the simple variable change:

$$\mathbf{w} = \mathbf{u} - \mathbf{u}_{off}^* \quad \Leftrightarrow \quad \mathbf{u} = \mathbf{w} + \mathbf{u}_{off}^*$$

Then, by simple substitution, it results:

$$\min_{\mathbf{w}} \{\|\mathbf{w}\|\} \quad \text{s. t.} \quad \mathbf{N}_f \cdot \mathbf{w} = (\mathbf{v}_f^* - \mathbf{N}_f \cdot \mathbf{u}_{off}^*)$$

This is a standard minimization problem with linear constraints. The minimum norm solution is given by:

$$\mathbf{w}^* = \mathbf{N}_f^\dagger \cdot (\mathbf{v}_f^* - \mathbf{N}_f \cdot \mathbf{u}_{off}^*)$$

and the corresponding optimal solution  $\mathbf{u}^*$  is:

$$\begin{aligned} \mathbf{u}^* = \mathbf{w}^* + \mathbf{u}_{off}^* &= \mathbf{N}_f^\dagger \cdot \mathbf{v}_f^* - \mathbf{N}_f^\dagger \cdot \mathbf{N}_f \cdot \mathbf{u}_{off}^* + \mathbf{u}_{off}^* = \\ &= \mathbf{N}_f^\dagger \cdot \mathbf{v}_f^* + (\mathbf{I} - \mathbf{N}_f^\dagger \cdot \mathbf{N}_f) \cdot \mathbf{u}_{off}^* = \\ &= \mathbf{u}_{opt}^* + \mathbf{u}_0^* \end{aligned}$$

which is the provided expression. □

### 9.6.7 Full order decoupling algorithm formulation

It is here proven that, given the minimum norm voltages set  $\mathbf{u}_{opt}^*$  computed as (6.30) with respect to the reduced-order machine model (6.8), the corresponding formulation for the full-order model (6.6) is given by (6.35).

**Proof.** By recalling that the machine variables in the configuration space are expressed by (6.32), by direct substitution, it results:

$$\begin{aligned} \mathbf{u}_{opt}^* &= \mathbf{N}_f^\dagger \cdot \mathbf{v}_f^* = \mathbf{N}_f^\dagger \cdot (\mathbf{L}_f \cdot \delta \mathbf{i}_f^* + \mathbf{R}_f \cdot \mathbf{i}_f + \mathbf{e}_f) = \\ &= (\mathbf{U}_f^\top \cdot \mathbf{N})^\dagger \cdot [\mathbf{U}_f^\top \cdot \mathbf{L} \cdot \mathbf{U}_f \cdot \delta \mathbf{i}_f^* + \mathbf{U}_f^\top \cdot \mathbf{R} \cdot \mathbf{U}_f \cdot \mathbf{i}_f + \mathbf{U}_f^\top \cdot \mathbf{e}] = \\ &= [(\mathbf{U}_f^\top \cdot \mathbf{N})^\dagger \cdot \mathbf{U}_f^\top] \cdot [\mathbf{L} \cdot \delta \mathbf{i}^* + \mathbf{R} \cdot \mathbf{i} + \mathbf{e}] \end{aligned}$$

which is the expression (6.35). □

### 9.6.8 Decoupled system transfer function

It is here proven that, by modelling the modulation process through a simple time delay of  $\tau_{del}$ , the transfer function for the decoupled current control algorithm can be approximated through (6.42).

**Proof.** Given the system linearity, it is possible to derive the whole reasoning in the Laplace domain. For notation simplicity, in what follows the Laplace transformation of each time-varying variable will be denoted with the same notation of the variable itself (i.e.,  $\mathcal{L}[x(t)](s) \rightarrow x(s)$ ). Moreover, the reasoning will be conducted for the reduced-order model (6.8) and the reduced-order algorithm (6.22), and then it is finally extended to

the full-order model.

Given the time delay due to the sampling and modulation process, the decoupling voltages set  $\mathbf{u}(s)$  is linked to the reference decoupling voltages set  $\mathbf{u}^*(s)$  through the simple relation:

$$\mathbf{u}(s) = \mathbf{u}^*(s) \cdot e^{-s\tau_{del}}$$

The reference voltages set is expressed by (6.29)-(6.31) and is:

$$\begin{aligned} \mathbf{u}^*(s) &= \mathbf{u}_{opt}^*(s) + \mathbf{u}_0^*(s) = \\ &= \mathbf{N}_f^\dagger \cdot [\mathbf{L}_f \cdot \delta \mathbf{i}_f^*(s) + \mathbf{R}_f \cdot \mathbf{i}_f(s) + \mathbf{e}_f(s)] + (\mathbf{I} - \mathbf{N}_f^\dagger \cdot \mathbf{N}_f) \cdot \mathbf{u}_{off}^*(s) \end{aligned}$$

The reduced-order machine model in the Laplace domain is:

$$s\mathbf{L}_f \cdot \mathbf{i}_f(s) + \mathbf{R}_f \cdot \mathbf{i}_f(s) + \mathbf{e}_f(s) = \mathbf{v}_f(s) = \mathbf{N}_f \cdot \mathbf{u}(s)$$

By considering the pseudo-inverse matrix  $\mathbf{N}_f^\dagger$  properties, the right-side term can be computed to be:

$$\mathbf{N}_f \cdot \mathbf{u}(s) = \mathbf{N}_f \cdot \mathbf{u}^*(s) \cdot e^{-s\tau_{del}} = [\mathbf{L}_f \cdot \delta \mathbf{i}_f^*(s) + \mathbf{R}_f \cdot \mathbf{i}_f(s) + \mathbf{e}_f(s)] \cdot e^{-s\tau_{del}}$$

By substituting back and by grouping the various terms it results:

$$\mathbf{L}_f \cdot [s \mathbf{i}_f(s) - \delta \mathbf{i}_f^*(s) \cdot e^{-s\tau_{del}}] + (1 - e^{-s\tau_{del}}) \cdot [\mathbf{R}_f \cdot \mathbf{i}_f(s) + \mathbf{e}_f(s)] = \mathbf{0}$$

For a wide range of variability of the complex variable  $s$ , the term  $(1 - e^{-s\tau_{del}})$  is close to zero. Therefore, the previous relationship can be approximated as:

$$\mathbf{L}_f \cdot [s \mathbf{i}_f(s) - \delta \mathbf{i}_f^*(s) \cdot e^{-s\tau_{del}}] \cong \mathbf{0}$$

and, since  $\mathbf{L}_f$  is symmetric and positive definite, it means that:

$$s \mathbf{i}_f(s) - \delta \mathbf{i}_f^*(s) \cdot e^{-s\tau_{del}} \cong \mathbf{0}$$

Finally, by isolating the currents and by pre-multiplying for  $\mathbf{U}_f$ , it results that:

$$\mathbf{i}(s) = \mathbf{U}_f \cdot \mathbf{i}_f(s) \cong \mathbf{U}_f \cdot \delta \mathbf{i}_f^*(s) \cdot \frac{1}{s} \cdot e^{-s\tau_{del}} = \delta \mathbf{i}^*(s) \cdot \frac{1}{s} \cdot e^{-s\tau_{del}}$$

which, once expressed in components, is the result provided in (6.42). □

## 9.7 Chapter 7 Proofs

This section contains the proof of the properties stated in Chapter 7 - Decoupled Phase Variable Control of SynRMs.

### 9.7.1 Required RMS current for the torque development

It is here proven that, considering the electromagnetic torque equation (7.9) and expressing the free currents set as  $\hat{\mathbf{i}}_f = I_{RMS} \cdot \hat{\mathbf{i}}_f$  (as done in (7.18)), once the direction versor  $\hat{\mathbf{i}}_f$  is chosen, the corresponding RMS current  $I_{RMS}$  is given by (7.19).

**Proof.** By substituting the current expression (7.18) in the torque development requirement (7.9), it results that:

$$T_{em}^* = \frac{1}{2} \cdot \hat{\mathbf{i}}_f^T \cdot \mathbf{L}'_f \cdot \hat{\mathbf{i}}_f = \frac{1}{2} \cdot \hat{\mathbf{i}}_f^T \cdot \mathbf{L}'_f \cdot \hat{\mathbf{i}}_f \cdot I_{RMS}^2$$

The term  $I_{RMS}^2$  can be isolated, resulting in:

$$I_{RMS}^2 = \frac{2 \cdot T_{em}^*}{\hat{\mathbf{i}}_f^T \cdot \mathbf{L}'_f \cdot \hat{\mathbf{i}}_f}$$

This equation is only feasible if the scalar term  $(\hat{\mathbf{i}}_f^T \cdot \mathbf{L}'_f \cdot \hat{\mathbf{i}}_f)$  at the denominator has the same sign of the reference torque  $T_{em}^*$ . In this case, since by definition  $I_{RMS} \geq 0$ , the solution is given by the (7.19):

$$I_{RMS} = \sqrt{\frac{2 \cdot T_{em}^*}{\hat{\mathbf{i}}_f^T \cdot \mathbf{L}'_f \cdot \hat{\mathbf{i}}_f}}$$

□

### 9.7.2 Optimal MTPA current unit vectors

It is here proven that, considering the quadratic form  $(\hat{\mathbf{i}}_f^T \cdot \mathbf{L}'_f \cdot \hat{\mathbf{i}}_f)$ , with  $\hat{\mathbf{i}}_f$  being a unitary-norm  $n_f \times 1$  vector, then:

- its maximum is equal to the maximum eigenvalue  $\nu_{\max}$  of the matrix  $\mathbf{L}'_f$ , and it is obtained when  $\hat{\mathbf{i}}_f$  is equal to the corresponding eigenvector  $\hat{\mathbf{i}}_{f,\max}$ , and
- its minimum is equal to the minimum eigenvalue  $\nu_{\min}$  of the matrix  $\mathbf{L}'_f$ , and it is obtained when  $\hat{\mathbf{i}}_f$  is equal to the corresponding eigenvector  $\hat{\mathbf{i}}_{f,\min}$ .

**Proof.** The two cases can be analysed as the constrained optimization problems:

$$\max/\min_{\hat{\mathbf{i}}_f} \{ \hat{\mathbf{i}}_f^T \cdot \mathbf{L}'_f \cdot \hat{\mathbf{i}}_f \} \quad \text{subject to} \quad \hat{\mathbf{i}}_f^T \cdot \hat{\mathbf{i}}_f = 1$$

In both cases, these problems can be solved with the Lagrange's multiplier method by referring to the Lagrangian function:

$$\mathfrak{L}(\hat{\mathbf{i}}_f, \mu) = \frac{1}{2} \cdot \hat{\mathbf{i}}_f^T \cdot \mathbf{L}'_f \cdot \hat{\mathbf{i}}_f - \mu \cdot (\hat{\mathbf{i}}_f^T \cdot \hat{\mathbf{i}}_f - 1)$$

By nullifying the gradient of  $\mathfrak{L}(\hat{\mathbf{i}}_f, \mu)$  it results that:

$$\begin{aligned}\frac{\partial \mathfrak{L}}{\partial \hat{\mathbf{i}}_f} &= \mathbf{L}'_f \cdot \hat{\mathbf{i}}_f - \mu \cdot \hat{\mathbf{i}}_f = \mathbf{0} \\ \frac{\partial \mathfrak{L}}{\partial \mu} &= \hat{\mathbf{i}}_f^T \cdot \hat{\mathbf{i}}_f - 1 = 0\end{aligned}$$

The second equation is simply the unitary-norm constraint of  $\hat{\mathbf{i}}_f$ . The first equation can be instead rewritten as:

$$\mathbf{L}'_f \cdot \hat{\mathbf{i}}_f = \mu \cdot \hat{\mathbf{i}}_f$$

This is an eigenvalue equation, and means that the product  $\mathbf{L}'_f \cdot \hat{\mathbf{i}}_f$  is parallel to the versor  $\hat{\mathbf{i}}_f$  itself through the coefficient  $\mu$ .

All the eigenvectors of  $\mathbf{L}'_f$  are stationary points for the Lagrangian function  $\mathfrak{L}(\hat{\mathbf{i}}_f, \mu)$ . Since  $\mathbf{L}'_f$  is a  $n_f \times n_f$  symmetric matrix, it has  $n_f$  linearly independent eigenvectors corresponding to real eigenvalues. By denoting as  $\hat{\mathbf{i}}_{f,k}$  the eigenvector related to the  $k$ -th eigenvalue  $\nu_k$  (with  $k = 1, \dots, n_f$ ), the corresponding quadratic form is equal to:

$$\hat{\mathbf{i}}_{f,k}^T \cdot \mathbf{L}'_f \cdot \hat{\mathbf{i}}_{f,k} = \hat{\mathbf{i}}_{f,k}^T \cdot (\nu_k \cdot \hat{\mathbf{i}}_{f,k}) = \nu_k \cdot (\hat{\mathbf{i}}_{f,k}^T \cdot \hat{\mathbf{i}}_{f,k}) = \nu_k \cdot 1 = \nu_k$$

Since the eigenvalue  $\nu_k$  is equal to the result of the quadratic form, then it has been proven that:

- the maximum value of  $\hat{\mathbf{i}}_f^T \cdot \mathbf{L}'_f \cdot \hat{\mathbf{i}}_f$  is obtained for the maximum eigenvalue  $\nu_{\max}$  of  $\mathbf{L}'_f$ , which corresponds to the eigenvector  $\hat{\mathbf{i}}_{f,\max}$ , and
- the minimum value of  $\hat{\mathbf{i}}_f^T \cdot \mathbf{L}'_f \cdot \hat{\mathbf{i}}_f$  is obtained for the minimum eigenvalue  $\nu_{\min}$  of  $\mathbf{L}'_f$ , which corresponds to the eigenvector  $\hat{\mathbf{i}}_{f,\min}$ .

□

### 9.7.3 RMS current with the optimal MTPA solution

It is here proven that, provided the MTPA currents (7.21), the RMS overall machine RMS current is given by (7.22).

**Proof.** For any given versor  $\hat{\mathbf{i}}_f$  in the configuration space, the corresponding RMS current is expressed by (7.19). In the MTPA conditions, the versor  $\hat{\mathbf{i}}_f$  is chosen between the eigenvectors of  $\mathbf{L}'_f$ . Then, by definition, it results that:

$$\mathbf{L}'_f \cdot \hat{\mathbf{i}}_{f,\max} = \nu_{\max} \cdot \hat{\mathbf{i}}_{f,\max} \quad \text{and} \quad \mathbf{L}'_f \cdot \hat{\mathbf{i}}_{f,\min} = \nu_{\min} \cdot \hat{\mathbf{i}}_{f,\min}$$

As a result, the corresponding quadratic forms ( $\hat{\mathbf{i}}_f^T \cdot \mathbf{L}'_f \cdot \hat{\mathbf{i}}_f$ ) are equal to:

$$\begin{aligned}\hat{\mathbf{i}}_{f,\max}^T \cdot \mathbf{L}'_f \cdot \hat{\mathbf{i}}_{f,\max} &= \hat{\mathbf{i}}_{f,\max}^T \cdot (\nu_{\max} \cdot \hat{\mathbf{i}}_{f,\max}) = \nu_{\max} \cdot (\hat{\mathbf{i}}_{f,\max}^T \cdot \hat{\mathbf{i}}_{f,\max}) = \nu_{\max} \\ \hat{\mathbf{i}}_{f,\min}^T \cdot \mathbf{L}'_f \cdot \hat{\mathbf{i}}_{f,\min} &= \hat{\mathbf{i}}_{f,\min}^T \cdot (\nu_{\min} \cdot \hat{\mathbf{i}}_{f,\min}) = \nu_{\min} \cdot (\hat{\mathbf{i}}_{f,\min}^T \cdot \hat{\mathbf{i}}_{f,\min}) = \nu_{\min}\end{aligned}$$

Then, by substituting in (7.19) it results that:

$$I_{RMS} = \begin{cases} \sqrt{2 \cdot T_{em}^* / \nu_{\max}} & \text{if } T_{em}^* \geq 0 \\ \sqrt{2 \cdot T_{em}^* / \nu_{\min}} & \text{if } T_{em}^* < 0 \end{cases}$$

which is the expression (7.22).

□

# References

- [1] E. Levi, 'Multiphase Electric Machines for Variable-Speed Applications', *IEEE Trans. Ind. Electron.*, vol. 55, no. 5, pp. 1893–1909, May 2008, doi: 10.1109/TIE.2008.918488.
- [2] E. Levi, R. Bojoi, F. Profumo, H. Toliyat, and S. Williamson, 'Multiphase induction motor drives - A technology status review', *Electr. Power Appl. IET*, vol. 1, pp. 489–516, Aug. 2007, doi: 10.1049/iet-epa:20060342.
- [3] F. Barrero and M. J. Duran, 'Recent Advances in the Design, Modeling, and Control of Multiphase Machines—Part I', *IEEE Trans. Ind. Electron.*, vol. 63, no. 1, pp. 449–458, Jan. 2016, doi: 10.1109/TIE.2015.2447733.
- [4] M. J. Duran and F. Barrero, 'Recent Advances in the Design, Modeling, and Control of Multiphase Machines—Part II', *IEEE Trans. Ind. Electron.*, vol. 63, no. 1, pp. 459–468, Jan. 2016, doi: 10.1109/TIE.2015.2448211.
- [5] G. K. Singh, 'Multi-phase induction machine drive research—a survey', *Electr. Power Syst. Res.*, vol. 61, no. 2, pp. 139–147, Mar. 2002, doi: 10.1016/S0378-7796(02)00007-X.
- [6] R. Bojoi, S. Rubino, A. Tenconi, and S. Vaschetto, 'Multiphase electrical machines and drives: A viable solution for energy generation and transportation electrification', in *2016 International Conference and Exposition on Electrical and Power Engineering (EPE)*, Oct. 2016, pp. 632–639. doi: 10.1109/ICEPE.2016.7781416.
- [7] Z. Liu, Y. Li, and Z. Zheng, 'A review of drive techniques for multiphase machines', *CES Trans. Electr. Mach. Syst.*, vol. 2, no. 2, pp. 243–251, Jun. 2018, doi: 10.30941/CESTEMS.2018.00030.
- [8] R. Bojoi, F. Farina, F. Profumo, and A. Tenconi, 'Dual-Three Phase Induction Machine Drives Control--A Survey', *Ieej Trans. Ind. Appl.*, vol. 126, pp. 420–429, Jul. 2006, doi: 10.1541/ieejias.126.420.
- [9] B. Gamble, G. Snitchler, and T. MacDonald, 'Full Power Test of a 36.5 MW HTS Propulsion Motor', *IEEE Trans. Appl. Supercond.*, vol. 21, no. 3, pp. 1083–1088, Jun. 2011, doi: 10.1109/TASC.2010.2093854.
- [10] L. Parsa and H. A. Toliyat, 'Five-phase permanent magnet motor drives for ship propulsion applications', in *IEEE Electric Ship Technologies Symposium, 2005.*, Jul. 2005, pp. 371–378. doi: 10.1109/ESTS.2005.1524702.
- [11] A. C. Smith, S. Williamson, and C. G. Hodge, 'High torque dense naval propulsion motors', in *IEEE International Electric Machines and Drives Conference, 2003. IEMDC'03.*, Jun. 2003, vol. 3, pp. 1421–1427 vol.3. doi: 10.1109/IEMDC.2003.1210638.
- [12] F. Terrien, S. Siala, and P. Noy, 'Multiphase induction motor sensorless control for electric ship propulsion', in *Second International Conference on Power Electronics, Machines and Drives (PEMD 2004).*, Mar. 2004, vol. 2, pp. 556–561 Vol.2. doi: 10.1049/cp:20040348.

- 
- [13] F. Scuiller, J. Charpentier, and E. Semail, 'Multi-star multi-phase winding for a high power naval propulsion machine with low ripple torques and high fault tolerant ability', in *2010 IEEE Vehicle Power and Propulsion Conference*, Sep. 2010, pp. 1–5. doi: 10.1109/VPPC.2010.5729185.
- [14] J. Dai, S. W. Nam, M. Pande, and G. Esmaeili, 'Medium-Voltage Current-Source Converter Drives for Marine Propulsion System Using a Dual-Winding Synchronous Machine', *IEEE Trans. Ind. Appl.*, vol. 50, no. 6, pp. 3971–3976, Nov. 2014, doi: 10.1109/TIA.2014.2316361.
- [15] Shuai Lu and K. Corzine, 'Multilevel multi-phase propulsion drives', in *IEEE Electric Ship Technologies Symposium, 2005.*, Jul. 2005, pp. 363–370. doi: 10.1109/ESTS.2005.1524701.
- [16] S. Castellan, R. Menis, M. Pigani, G. Sulligoi, and A. Tassarolo, 'Modeling and Simulation of Electric Propulsion Systems for All-Electric Cruise Liners', in *2007 IEEE Electric Ship Technologies Symposium*, May 2007, pp. 60–64. doi: 10.1109/ESTS.2007.372064.
- [17] C. Bassi, A. Tassarolo, R. Menis, and G. Sulligoi, 'Analysis of different system design solutions for a high-power ship propulsion synchronous motor drive with multiple PWM converters', in *Railway and Ship Propulsion Electrical Systems for Aircraft*, Oct. 2010, pp. 1–6. doi: 10.1109/ESARS.2010.5665224.
- [18] G. Sulligoi, A. Tassarolo, V. Benucci, A. M. Trapani, M. Baret, and F. Luise, 'Shipboard Power Generation: Design and Development of a Medium-Voltage dc Generation System', *IEEE Ind. Appl. Mag.*, vol. 19, no. 4, pp. 47–55, Jul. 2013, doi: 10.1109/MIAS.2012.2215643.
- [19] G. Sulligoi, A. Tassarolo, V. Benucci, M. Baret, A. Reborra, and A. Taffone, 'Modeling, simulation and experimental validation of a generation system for Medium-Voltage DC Integrated Power Systems', in *2009 IEEE Electric Ship Technologies Symposium*, Apr. 2009, pp. 129–134. doi: 10.1109/ESTS.2009.4906505.
- [20] B. Andresen and J. Birk, 'A high power density converter system for the Gamesa G10x 4,5 MW wind turbine', in *2007 European Conference on Power Electronics and Applications*, Sep. 2007, pp. 1–8. doi: 10.1109/EPE.2007.4417312.
- [21] S. Brisset, D. Vizireanu, and P. Brochet, 'Design and Optimization of a Nine-Phase Axial-Flux PM Synchronous Generator With Concentrated Winding for Direct-Drive Wind Turbine', *IEEE Trans. Ind. Appl.*, vol. 44, no. 3, pp. 707–715, May 2008, doi: 10.1109/TIA.2008.921379.
- [22] X. Zeng, Y. Yongbing, Z. Hongtao, L. Ying, F. Luguang, and Y. Xu, 'Modeling and control of a multi-phase permanent magnet synchronous generator and efficient hybrid 3L-converters for large direct-drive wind turbines', *Electr. Power Appl. IET*, vol. 6, pp. 322–331, Jul. 2012, doi: 10.1049/iet-epa.2011.0145.
- [23] J. P. McSharry, P. S. Hamer, D. Morrison, J. Nessa, and J. G. Rigsby, 'Design, fabrication, back-to-back test of 14200-hp two-pole cylindrical-rotor synchronous motor for ASD application', *IEEE Trans. Ind. Appl.*, vol. 34, no. 3, pp. 526–533, May 1998, doi: 10.1109/28.673723.
- [24] R. Salisbury, T. Griffith, P. Rasmussen, and A. Fibbi, 'Design, manufacture, and test campaign of the world's largest LNG refrigeration compressor strings', *LNG*

- 
- J.*, p. 11, 2007.
- [25] A. Tassarolo, 'Modeling and analysis of multiphase electric machines for high-power applications', Ph.D. Thesis, Università degli studi di Trieste, 2011.
- [26] A. Tassarolo, G. Zocco, and C. Tonello, 'Design and testing of a 45-MW 100-Hz quadruple-star synchronous motor for a Liquefied Natural Gas turbo-compressor drive', in *SPEEDAM 2010*, Jun. 2010, pp. 1754–1761. doi: 10.1109/SPEEDAM.2010.5545129.
- [27] J.- Simond, A. Sapin, T. Xuan, R. Wetter, and P. Burmeister, '12-pulse LCI synchronous drive for a 20 MW compressor modeling, simulation and measurements', in *Fourtieth IAS Annual Meeting. Conference Record of the 2005 Industry Applications Conference, 2005.*, Oct. 2005, vol. 4, pp. 2302-2308 Vol. 4. doi: 10.1109/IAS.2005.1518781.
- [28] L. D. Camillis, M. Matuonto, A. Monti, and A. Vignati, 'Optimizing current control performance in double winding asynchronous motors in large power inverter drives', *IEEE Trans. Power Electron.*, vol. 16, no. 5, pp. 676–685, Sep. 2001, doi: 10.1109/63.949500.
- [29] E. Jung, H. Yoo, S. Sul, H. Choi, and Y. Choi, 'A Nine-Phase Permanent-Magnet Motor Drive System for an Ultrahigh-Speed Elevator', *IEEE Trans. Ind. Appl.*, vol. 48, no. 3, pp. 987–995, May 2012, doi: 10.1109/TIA.2012.2190472.
- [30] R. Bojoi, A. Cavagnino, A. Tenconi, A. Tassarolo, and S. Vaschetto, 'Multiphase electrical machines and drives in the transportation electrification', in *2015 IEEE 1st International Forum on Research and Technologies for Society and Industry Leveraging a better tomorrow (RTSI)*, Sep. 2015, pp. 205–212. doi: 10.1109/RTSI.2015.7325099.
- [31] R. Bojoi, L. Boggero, S. Comino, M. Fioriti, A. Tenconi, and S. Vaschetto, 'Multiphase Drives for Hybrid-Electric Propulsion in Light Aircrafts: a Viable Solution', in *2018 International Symposium on Power Electronics, Electrical Drives, Automation and Motion (SPEEDAM)*, Jun. 2018, pp. 613–619. doi: 10.1109/SPEEDAM.2018.8445241.
- [32] X. Huang, A. Goodman, C. Gerada, Y. Fang, and Q. Lu, 'Design of a Five-Phase Brushless DC Motor for a Safety Critical Aerospace Application', *IEEE Trans. Ind. Electron.*, vol. 59, no. 9, pp. 3532–3541, Sep. 2012, doi: 10.1109/TIE.2011.2172170.
- [33] C. Gerada, K. Bradley, X. Huang, A. Goodman, C. Whitley, and G. Towers, 'A 5-Phase Fault-Tolerant Brushless Permanent Magnet Motor Drive for an Aircraft Thin Wing Surface Actuator', in *2007 IEEE International Electric Machines Drives Conference*, May 2007, vol. 2, pp. 1643–1648. doi: 10.1109/IEMDC.2007.383676.
- [34] M. Galea, Z. Xu, C. Tighe, T. Hamiti, C. Gerada, and S. Pickering, 'Development of an aircraft wheel actuator for green taxiing', in *2014 International Conference on Electrical Machines (ICEM)*, Sep. 2014, pp. 2492–2498. doi: 10.1109/ICELMACH.2014.6960537.
- [35] M. Rottach, C. Gerada, and P. W. Wheeler, 'Design optimisation of a fault-tolerant PM motor drive for an aerospace actuation application', in *7th IET International Conference on Power Electronics, Machines and Drives (PEMD 2014)*, Apr. 2014, pp. 1–6. doi: 10.1049/cp.2014.0484.

- 
- [36] B. C. Mecrow *et al.*, ‘Design and testing of a four-phase fault-tolerant permanent-magnet machine for an engine fuel pump’, *IEEE Trans. Energy Convers.*, vol. 19, no. 4, pp. 671–678, Dec. 2004, doi: 10.1109/TEC.2004.832074.
- [37] G. J. Atkinson, B. C. Mecrow, A. G. Jack, D. J. Atkinson, P. Sangha, and M. Benarous, ‘The design of fault tolerant machines for aerospace applications’, in *IEEE International Conference on Electric Machines and Drives, 2005.*, May 2005, pp. 1863–1869. doi: 10.1109/IEMDC.2005.195974.
- [38] J. W. Bennett *et al.*, ‘Choice of drive topologies for electrical actuation of aircraft flaps and slats’, in *Second International Conference on Power Electronics, Machines and Drives (PEMD 2004).*, Mar. 2004, vol. 1, pp. 332–337 Vol.1. doi: 10.1049/cp:20040308.
- [39] R. Bojoi, A. Cavagnino, A. Tenconi, and S. Vaschetto, ‘Control of Shaft-Line-Embedded Multiphase Starter/Generator for Aero-Engine’, *IEEE Trans. Ind. Electron.*, vol. 63, no. 1, pp. 641–652, Jan. 2016, doi: 10.1109/TIE.2015.2472637.
- [40] G. Rizzoli, G. Serra, P. Maggiore, and A. Tenconi, ‘Optimized design of a multiphase induction machine for an open rotor aero-engine shaft-line-embedded starter/generator’, in *IECON 2013 - 39th Annual Conference of the IEEE Industrial Electronics Society*, Nov. 2013, pp. 5203–5208. doi: 10.1109/IECON.2013.6699980.
- [41] R. Bojoi, A. Cavagnino, M. Cossale, and A. Tenconi, ‘Multiphase starter generator for 48V mini-hybrid powertrain: Design and testing’, in *2014 International Symposium on Power Electronics, Electrical Drives, Automation and Motion*, Jun. 2014, pp. 1319–1324. doi: 10.1109/SPEEDAM.2014.6872029.
- [42] J. M. Miller, V. Stefanovic, V. Ostovic, and J. Kelly, ‘Design considerations for an automotive integrated starter-generator with pole-phase modulation’, in *Conference Record of the 2001 IEEE Industry Applications Conference. 36th IAS Annual Meeting (Cat. No.01CH37248)*, Sep. 2001, vol. 4, pp. 2366–2373 vol.4. doi: 10.1109/IAS.2001.955953.
- [43] A. Bruyere, E. Semail, A. Bouscayrol, F. Locment, J. M. Dubus, and J. C. Mipo, ‘Modeling and control of a seven-phase claw-pole integrated starter alternator for micro-hybrid automotive applications’, in *2008 IEEE Vehicle Power and Propulsion Conference*, Sep. 2008, pp. 1–6. doi: 10.1109/VPPC.2008.4677668.
- [44] N. Schofield, X. Niu, and O. Beik, ‘Multiphase machines for electric vehicle traction’, in *2014 IEEE Transportation Electrification Conference and Expo (ITEC)*, Jun. 2014, pp. 1–6. doi: 10.1109/ITEC.2014.6861840.
- [45] M. G. Simoes and P. Vieira, ‘A high torque low-speed multi-phase brushless machine a perspective application for electric vehicles’, in *2000 26th Annual Conference of the IEEE Industrial Electronics Society. IECON 2000. 2000 IEEE International Conference on Industrial Electronics, Control and Instrumentation. 21st Century Technologies*, Oct. 2000, vol. 2, pp. 1395–1400 vol.2. doi: 10.1109/IECON.2000.972325.
- [46] Y. Burkhardt, A. Spagnolo, P. Lucas, M. Zavesky, and P. Brockerhoff, ‘Design and analysis of a highly integrated 9-phase drivetrain for EV applications’, in *2014 International Conference on Electrical Machines (ICEM)*, Sep. 2014, pp. 450–456. doi: 10.1109/ICELMACH.2014.6960219.

- 
- [47] R. Bojoi, A. Tenconi, F. Profumo, and F. Farina, 'Dual-Source Fed Multi-phase Induction Motor Drive for Fuel Cell Vehicles: Topology and Control', in *2005 IEEE 36th Power Electronics Specialists Conference*, Jun. 2005, pp. 2676–2683. doi: 10.1109/PESC.2005.1582011.
- [48] C. C. Chan, J. Z. Jiang, G. H. Chen, X. Y. Wang, and K. T. Chau, 'A novel polyphase multipole square-wave permanent magnet motor drive for electric vehicles', *IEEE Trans. Ind. Appl.*, vol. 30, no. 5, pp. 1258–1266, Sep. 1994, doi: 10.1109/28.315237.
- [49] S. Z. Jiang, K. T. Chau, and C. C. Chan, 'Spectral analysis of a new six-phase pole-changing induction motor drive for electric vehicles', *IEEE Trans. Ind. Electron.*, vol. 50, no. 1, pp. 123–131, Feb. 2003, doi: 10.1109/TIE.2002.807662.
- [50] O. Dordevic, 'PWM strategies for Multilevel Multiphase AC drives', Ph.D. Thesis, Liverpool John Moores University, 2013.
- [51] M. J. Durán, S. Kouro, B. Wu, E. Levi, F. Barrero, and S. Alepuz, 'Six-phase PMSG wind energy conversion system based on medium-voltage multilevel converter', in *Proceedings of the 2011 14th European Conference on Power Electronics and Applications*, Aug. 2011, pp. 1–10.
- [52] B. Mwinyiwiwa, O. Ojo, and Z. Wu, 'A five phase three-level neutral point clamped converter using DSP and FPGA based control scheme', in *2006 37th IEEE Power Electronics Specialists Conference*, Jun. 2006, pp. 1–7. doi: 10.1109/pesc.2006.1711937.
- [53] Z. Oudjebour, E. M. Berkouk, N. Sami, S. Belgasmi, S. Arezki, and I. Messaïf, *Indirect space vector control of a double star induction machine fed by two five - levels NPC VSI*. 2004. doi: 10.13140/2.1.2828.0962.
- [54] S. Rubino, 'High Performance Control Techniques for Multiphase eDrives', Ph.D. Thesis, Politecnico di Torino, 2019.
- [55] A. Tessarolo, 'On the modeling of poly-phase electric machines through Vector-Space Decomposition: Theoretical considerations', in *2009 International Conference on Power Engineering, Energy and Electrical Drives*, Mar. 2009, pp. 519–523. doi: 10.1109/POWERENG.2009.4915234.
- [56] I. Zoric, M. Jones, and E. Levi, 'Phase voltage harmonic imbalance in asymmetrical multiphase machines with single neutral point', in *IECON 2016 - 42nd Annual Conference of the IEEE Industrial Electronics Society*, Oct. 2016, pp. 4343–4348. doi: 10.1109/IECON.2016.7793473.
- [57] I. Zoric, M. Jones, and E. Levi, 'Vector space decomposition algorithm for asymmetrical multiphase machines', in *2017 International Symposium on Power Electronics (Ee)*, Oct. 2017, pp. 1–6. doi: 10.1109/PEE.2017.8171682.
- [58] I. Zoric, 'Multiple three-phase induction generators for wind energy conversion systems', Ph.D. Thesis, Liverpool John Moores University, 2018.
- [59] M. Jones, S. N. Vukosavic, D. Dujic, and E. Levi, 'A Synchronous Current Control Scheme for Multiphase Induction Motor Drives', *IEEE Trans. Energy Convers.*, vol. 24, no. 4, pp. 860–868, Dec. 2009, doi: 10.1109/TEC.2009.2025419.
- [60] H. S. Che, E. Levi, M. Jones, W. Hew, and N. A. Rahim, 'Current Control Methods for an Asymmetrical Six-Phase Induction Motor Drive', *IEEE Trans. Power Electron.*, vol. 29, no. 1, pp. 407–417, Jan. 2014, doi: 10.1109/TPEL.2013.2248170.

- 
- [61] A. G. Yepes, J. Malvar, A. Vidal, O. López, and J. Doval-Gandoy, ‘Current Harmonics Compensation Based on Multiresonant Control in Synchronous Frames for Symmetrical  $n$ -Phase Machines’, *IEEE Trans. Ind. Electron.*, vol. 62, no. 5, pp. 2708–2720, May 2015, doi: 10.1109/TIE.2014.2365155.
- [62] A. G. Yepes, J. Doval-Gandoy, F. Baneira, D. Pérez-Estévez, and O. López, ‘Current harmonic compensation for  $n$ -phase machines with asymmetrical winding arrangement’, in *2016 IEEE Energy Conversion Congress and Exposition (ECCE)*, Sep. 2016, pp. 1–8. doi: 10.1109/ECCE.2016.7854979.
- [63] A. G. Yepes, J. Doval-Gandoy, F. Baneira, D. Pérez-Estévez, and O. López, ‘Current Harmonic Compensation for  $n$ -Phase Machines With Asymmetrical Winding Arrangement and Different Neutral Configurations’, *IEEE Trans. Ind. Appl.*, vol. 53, no. 6, pp. 5426–5439, Nov. 2017, doi: 10.1109/TIA.2017.2722426.
- [64] F. Barrero, M. R. Arahal, R. Gregor, S. Toral, and M. J. Duran, ‘A Proof of Concept Study of Predictive Current Control for VSI-Driven Asymmetrical Dual Three-Phase AC Machines’, *IEEE Trans. Ind. Electron.*, vol. 56, no. 6, pp. 1937–1954, Jun. 2009, doi: 10.1109/TIE.2008.2011604.
- [65] F. Barrero, M. R. Arahal, R. Gregor, S. Toral, and M. J. Duran, ‘One-Step Modulation Predictive Current Control Method for the Asymmetrical Dual Three-Phase Induction Machine’, *IEEE Trans. Ind. Electron.*, vol. 56, no. 6, pp. 1974–1983, Jun. 2009, doi: 10.1109/TIE.2009.2016505.
- [66] F. Barrero *et al.*, ‘An Enhanced Predictive Current Control Method for Asymmetrical Six-Phase Motor Drives’, *IEEE Trans. Ind. Electron.*, vol. 58, no. 8, pp. 3242–3252, Aug. 2011, doi: 10.1109/TIE.2010.2089943.
- [67] K. Hatua and V. T. Ranganathan, ‘Direct torque control schemes for split-phase induction machine’, *IEEE Trans. Ind. Appl.*, vol. 41, no. 5, pp. 1243–1254, Sep. 2005, doi: 10.1109/TIA.2005.855043.
- [68] H. A. Toliyat and Huangsheng Xu, ‘A novel direct torque control (DTC) method for five-phase induction machines’, in *APEC 2000. Fifteenth Annual IEEE Applied Power Electronics Conference and Exposition (Cat. No.00CH37058)*, Feb. 2000, vol. 1, pp. 162–168 vol.1. doi: 10.1109/APEC.2000.826100.
- [69] X. Kestelyn, E. Semail, and D. Loroil, ‘Direct torque control of multi-phase permanent magnet synchronous motor drive: application to a five-phase’, in *IEEE International Conference on Electric Machines and Drives, 2005.*, May 2005, pp. 137–143. doi: 10.1109/IEMDC.2005.195714.
- [70] L. Zheng, J. E. Fletcher, B. W. Williams, and X. He, ‘A Novel Direct Torque Control Scheme for a Sensorless Five-Phase Induction Motor Drive’, *IEEE Trans. Ind. Electron.*, vol. 58, no. 2, pp. 503–513, Feb. 2011, doi: 10.1109/TIE.2010.2047830.
- [71] F. Farina, R. Bojoi, A. Tenconi, and F. Profumo, ‘Direct Torque Control with Full Order Stator Flux Observer for Dual-Three Phase Induction Motor Drives’, *Ieej Trans. Ind. Appl.*, vol. 126, pp. 412–419, Jan. 2006, doi: 10.1541/ieejias.126.412.
- [72] R. Bojoi, F. Farina, G. Griva, F. Profumo, and A. Tenconi, ‘Direct torque control for dual three-phase induction motor drives’, *IEEE Trans. Ind. Appl.*, vol. 41, no. 6, pp. 1627–1636, Nov. 2005, doi: 10.1109/TIA.2005.858281.
- [73] R. Karampuri, J. Prieto, F. Barrero, and S. Jain, ‘Extension of the DTC Technique

- 
- to Multiphase Induction Motor Drives Using Any Odd Number of Phases', in *2014 IEEE Vehicle Power and Propulsion Conference (VPPC)*, Oct. 2014, pp. 1–6. doi: 10.1109/VPPC.2014.7007070.
- [74] Gao Liliang, J. E. Fletcher, and Zheng Libo, 'Low speed control improvements for classic Direct Torque Control of a 2-level 5-phase inverter-fed induction machine', in *2010 IEEE International Symposium on Industrial Electronics*, Jul. 2010, pp. 2172–2177. doi: 10.1109/ISIE.2010.5637793.
- [75] A. Taheri, A. Rahmati, and S. Kaboli, 'Comparison of Efficiency for Different Switching Tables in Six-Phase Induction Motor DTC Drive', *J. Power Electron.*, vol. 12, pp. 128–135, Jan. 2012, doi: 10.6113/JPE.2012.12.1.128.
- [76] A. Taheri, A. Rahmati, and S. Kaboli, 'Efficiency Improvement in DTC of Six-Phase Induction Machine by Adaptive Gradient Descent of Flux', *IEEE Trans. Power Electron.*, vol. 27, no. 3, pp. 1552–1562, Mar. 2012, doi: 10.1109/TPEL.2011.2163420.
- [77] R. H. Nelson and P. C. Krause, 'Induction Machine Analysis for Arbitrary Displacement Between Multiple Winding Sets', *IEEE Trans. Power Appar. Syst.*, vol. PAS-93, no. 3, pp. 841–848, May 1974, doi: 10.1109/TPAS.1974.293983.
- [78] G. K. Singh, K. Nam, and S. K. Lim, 'A simple indirect field-oriented control scheme for multiphase induction machine', *IEEE Trans. Ind. Electron.*, vol. 52, no. 4, pp. 1177–1184, Aug. 2005, doi: 10.1109/TIE.2005.851593.
- [79] G. Scarcella, G. Scelba, M. Cacciato, A. Spampinato, and M. M. Harbaugh, 'Vector Control Strategy for Multidirectional Power Flow in Integrated Multidrives Starter-Alternator Applications', *IEEE Trans. Ind. Appl.*, vol. 52, no. 6, pp. 4816–4826, Nov. 2016, doi: 10.1109/TIA.2016.2591908.
- [80] S. Rubino, R. Bojoi, A. Cavagnino, and S. Vaschetto, 'Asymmetrical twelve-phase induction starter/generator for more electric engine in aircraft', in *2016 IEEE Energy Conversion Congress and Exposition (ECCE)*, Sep. 2016, pp. 1–8. doi: 10.1109/ECCE.2016.7854889.
- [81] Y. Hu, Z. Q. Zhu, and M. Odavic, 'Comparison of Two-Individual Current Control and Vector Space Decomposition Control for Dual Three-Phase PMSM', *IEEE Trans. Ind. Appl.*, vol. 53, no. 5, pp. 4483–4492, Sep. 2017, doi: 10.1109/TIA.2017.2703682.
- [82] J. Karttunen, S. Kallio, P. Peltoniemi, P. Silventoinen, and O. Pyrhönen, 'Decoupled Vector Control Scheme for Dual Three-Phase Permanent Magnet Synchronous Machines', *IEEE Trans. Ind. Electron.*, vol. 61, no. 5, pp. 2185–2196, May 2014, doi: 10.1109/TIE.2013.2270219.
- [83] S. Rubino, O. Dordevic, E. Armando, R. Bojoi, and E. Levi, 'A Novel Matrix Transformation for Decoupled Control of Modular Multiphase PMSM Drives', *IEEE Trans. Power Electron.*, pp. 1–1, 2020, doi: 10.1109/TPEL.2020.3043083.
- [84] S. Rubino, O. Dordevic, R. Bojoi, and E. Levi, 'Modular Vector Control of Multi-Three-Phase Permanent Magnet Synchronous Motors', *IEEE Trans. Ind. Electron.*, pp. 1–1, 2020, doi: 10.1109/TIE.2020.3026271.
- [85] E. Levi, D. Dujic, M. Jones, and G. Grandi, 'Analytical Determination of DC-Bus Utilization Limits in Multiphase VSI Supplied AC Drives', *IEEE Trans. Energy Convers.*, vol. 23, no. 2, pp. 433–443, Jun. 2008, doi: 10.1109/TEC.2008.921557.

- 
- [86] A. Iqbal and E. Levi, 'Space vector modulation schemes for a five-phase voltage source inverter', in *2005 European Conference on Power Electronics and Applications*, Sep. 2005, p. 12 pp.-P.12. doi: 10.1109/EPE.2005.219194.
- [87] A. Iqbal and E. Levi, 'Space Vector PWM Techniques for Sinusoidal Output Voltage Generation with a Five-Phase Voltage Source Inverter', *Electr. Power Compon. Syst. - ELECTR POWER COMPON SYST*, vol. 34, pp. 119–140, Feb. 2006, doi: 10.1080/15325000500244427.
- [88] J. W. Kelly, E. G. Strangas, and J. M. Miller, 'Multiphase space vector pulse width modulation', *IEEE Trans. Energy Convers.*, vol. 18, no. 2, pp. 259–264, Jun. 2003, doi: 10.1109/TEC.2003.811725.
- [89] G. Grandi, G. Serra, and A. Tani, 'Space vector modulation of a seven-phase voltage source inverter', in *International Symposium on Power Electronics, Electrical Drives, Automation and Motion, 2006. SPEEDAM 2006.*, May 2006, pp. 1149–1156. doi: 10.1109/SPEEDAM.2006.1649941.
- [90] D. Dujic, M. Jones, and E. Levi, 'Space Vector PWM for Nine-Phase VSI with Sinusoidal Output Voltage Generation: Analysis and Implementation', in *IECON 2007 - 33rd Annual Conference of the IEEE Industrial Electronics Society*, Nov. 2007, pp. 1524–1529. doi: 10.1109/IECON.2007.4459905.
- [91] D. Dujic, M. Jones, and E. Levi, 'Generalised space vector PWM for sinusoidal output voltage generation with multiphase voltage source inverters', *Int. J. Ind. Electron. Drives*, vol. 1, p. 1, Jan. 2009, doi: 10.1504/IJIED.2009.515638.
- [92] Ó. Lopez, J. Alvarez, J. Doval-Gandoy, and F. D. Freijedo, 'Multilevel Multiphase Space Vector PWM Algorithm', *IEEE Trans. Ind. Electron.*, vol. 55, no. 5, pp. 1933–1942, May 2008, doi: 10.1109/TIE.2008.918466.
- [93] D. Dujic, 'Development of pulse-width-modulation techniques for multi-phase and multi-leg voltage source inverters', Ph.D. Thesis, Liverpool John Moores University, 2008.
- [94] S. Busquets-Monge and A. Ruderman, 'Carrier-based PWM strategies for the comprehensive capacitor voltage balance of multilevel multileg diode-clamped converters', in *2010 IEEE International Symposium on Industrial Electronics*, Jul. 2010, pp. 688–693. doi: 10.1109/ISIE.2010.5637187.
- [95] L. Gao and J. E. Fletcher, 'A Space Vector Switching Strategy for Three-Level Five-Phase Inverter Drives', *IEEE Trans. Ind. Electron.*, vol. 57, no. 7, pp. 2332–2343, Jul. 2010, doi: 10.1109/TIE.2009.2033087.
- [96] Qingguo Song, Xiaofeng Zhang, Fei Yu, and Chengsheng Zhang, 'Research on PWM techniques of five-phase three-level inverter', in *International Symposium on Power Electronics, Electrical Drives, Automation and Motion, 2006. SPEEDAM 2006.*, May 2006, pp. 561–565. doi: 10.1109/SPEEDAM.2006.1649835.
- [97] J. Huang and K. A. Corzine, 'A New Walking Pattern SVM Technique for Five-Phase Motor Drives', in *2008 IEEE Industry Applications Society Annual Meeting*, Oct. 2008, pp. 1–8. doi: 10.1109/08IAS.2008.189.
- [98] C. M. Hutson, G. K. Venayagamoorthy, and K. A. Corzine, 'Optimal SVM switching for a multilevel multi-phase machine using modified discrete PSO', in *2008 IEEE Swarm Intelligence Symposium*, Sep. 2008, pp. 1–6. doi: 10.1109/SIS.2008.4668326.

- 
- [99] J. I. Leon *et al.*, ‘Conventional Space-Vector Modulation Techniques Versus the Single-Phase Modulator for Multilevel Converters’, *IEEE Trans. Ind. Electron.*, vol. 57, no. 7, pp. 2473–2482, Jul. 2010, doi: 10.1109/TIE.2009.2034674.
- [100] Ó. López *et al.*, ‘Carrier-Based PWM Equivalent to Multilevel Multiphase Space Vector PWM Techniques’, *IEEE Trans. Ind. Electron.*, vol. 67, no. 7, pp. 5220–5231, Jul. 2020, doi: 10.1109/TIE.2019.2934029.
- [101] O. Dordevic, M. Jones, and E. Levi, ‘A comparison of PWM techniques for three-level five-phase voltage source inverters’, in *Proceedings of the 2011 14th European Conference on Power Electronics and Applications*, Aug. 2011, pp. 1–10.
- [102] M. Jones, O. Dordevic, N. Bodo, and E. Levi, ‘PWM Algorithms for Multilevel Inverter Supplied Multiphase Variable-Speed Drives’, *Electron. ETF*, vol. 16, Jun. 2012, doi: 10.7251/ELS1216022J.
- [103] I. López *et al.*, ‘Modulation Strategy for Multiphase Neutral-Point-Clamped Converters’, *IEEE Trans. Power Electron.*, vol. 31, no. 2, pp. 928–941, Feb. 2016, doi: 10.1109/TPEL.2015.2416911.
- [104] I. López *et al.*, ‘Generalized PWM-Based Method for Multiphase Neutral-Point-Clamped Converters With Capacitor Voltage Balance Capability’, *IEEE Trans. Power Electron.*, vol. 32, no. 6, pp. 4878–4890, Jun. 2017, doi: 10.1109/TPEL.2016.2599872.
- [105] J. I. Leon *et al.*, ‘Multilevel Multiphase Feedforward Space-Vector Modulation Technique’, *IEEE Trans. Ind. Electron.*, vol. 57, no. 6, pp. 2066–2075, Jun. 2010, doi: 10.1109/TIE.2009.2034171.
- [106] L. Zarri *et al.*, ‘Detection and Localization of Stator Resistance Dissymmetry Based on Multiple Reference Frame Controllers in Multiphase Induction Motor Drives’, *IEEE Trans. Ind. Electron.*, vol. 60, no. 8, pp. 3506–3518, Aug. 2013, doi: 10.1109/TIE.2012.2235393.
- [107] J. M. Apsley and S. Williamson, ‘Analysis of multi-phase induction machines with winding faults’, in *IEEE International Conference on Electric Machines and Drives, 2005.*, May 2005, pp. 249–255. doi: 10.1109/IEMDC.2005.195731.
- [108] D. Foito, J. Maia, V. Fernão Pires, and J. F. Martins, ‘Fault diagnosis in six-phase induction motor using a current trajectory mass center’, *Measurement*, vol. 51, pp. 164–173, May 2014, doi: 10.1016/j.measurement.2014.02.004.
- [109] I. González-Prieto, M. J. Duran, N. Rios-García, F. Barrero, and C. Martín, ‘Open-Switch Fault Detection in Five-Phase Induction Motor Drives Using Model Predictive Control’, *IEEE Trans. Ind. Electron.*, vol. 65, no. 4, pp. 3045–3055, Apr. 2018, doi: 10.1109/TIE.2017.2748052.
- [110] M. Salehifar, R. S. Arashloo, J. M. Moreno-Equilaz, V. Sala, and L. Romeral, ‘Fault Detection and Fault Tolerant Operation of a Five Phase PM Motor Drive Using Adaptive Model Identification Approach’, *IEEE J. Emerg. Sel. Top. Power Electron.*, vol. 2, no. 2, pp. 212–223, Jun. 2014, doi: 10.1109/JESTPE.2013.2293518.
- [111] H. S. Che, M. J. Duran, E. Levi, M. Jones, W. Hew, and N. A. Rahim, ‘Postfault Operation of an Asymmetrical Six-Phase Induction Machine With Single and Two Isolated Neutral Points’, *IEEE Trans. Power Electron.*, vol. 29, no. 10, pp. 5406–5416, Oct. 2014, doi: 10.1109/TPEL.2013.2293195.

- 
- [112] S. Dwari and L. Parsa, ‘An Optimal Control Technique for Multiphase PM Machines Under Open-Circuit Faults’, *IEEE Trans. Ind. Electron.*, vol. 55, no. 5, pp. 1988–1995, May 2008, doi: 10.1109/TIE.2008.920643.
- [113] X. Kestelyn and E. Semail, ‘A Vectorial Approach for Generation of Optimal Current References for Multiphase Permanent-Magnet Synchronous Machines in Real Time’, *IEEE Trans. Ind. Electron.*, vol. 58, no. 11, pp. 5057–5065, Nov. 2011, doi: 10.1109/TIE.2011.2119454.
- [114] S. Dwari and L. Parsa, ‘Fault-Tolerant Control of Five-Phase Permanent-Magnet Motors With Trapezoidal Back EMF’, *IEEE Trans. Ind. Electron.*, vol. 58, no. 2, pp. 476–485, Feb. 2011, doi: 10.1109/TIE.2010.2045322.
- [115] S. Mantero, A. Monti, and C. Spreafico, ‘DC-bus voltage control for double star asynchronous fed drive under fault conditions’, in *2000 IEEE 31st Annual Power Electronics Specialists Conference. Conference Proceedings (Cat. No.00CH37018)*, Jun. 2000, vol. 1, pp. 533–538 vol.1. doi: 10.1109/PESC.2000.878920.
- [116] F. Baudart, B. Dehez, E. Matagne, D. Telteu-Nedelcu, P. Alexandre, and F. Labrique, ‘Torque Control Strategy of Polyphase Permanent-Magnet Synchronous Machines With Minimal Controller Reconfiguration Under Open-Circuit Fault of One Phase’, *IEEE Trans. Ind. Electron.*, vol. 59, no. 6, pp. 2632–2644, Jun. 2012, doi: 10.1109/TIE.2011.2170393.
- [117] M. T. Abolhassani, ‘A novel multiphase fault tolerant high torque density permanent magnet motor drive for traction application’, in *IEEE International Conference on Electric Machines and Drives, 2005.*, May 2005, pp. 728–734. doi: 10.1109/IEMDC.2005.195803.
- [118] A. Cervone, O. Dordevic, and G. Brando, ‘General Approach for Modelling and Control of Multiphase PMSM drives’, *IEEE Trans. Power Electron.*, vol. 36, no. 9, pp. 10490–10503, Sep. 2021, doi: 10.1109/TPEL.2021.3063791.
- [119] A. Cervone, M. Slunjski, E. Levi, and G. Brando, ‘Optimal Third-Harmonic Current Injection for Asymmetrical Multiphase Permanent Magnet Synchronous Machines’, *IEEE Trans. Ind. Electron.*, vol. 68, no. 4, pp. 2772–2783, Apr. 2021, doi: 10.1109/TIE.2020.2982099.
- [120] A. Cervone, G. Brando, and O. Dordevic, ‘Hybrid Modulation Technique With DC-Bus Voltage Control for Multiphase NPC Converters’, *IEEE Trans. Power Electron.*, vol. 35, no. 12, pp. 13528–13539, Dec. 2020, doi: 10.1109/TPEL.2020.2992226.
- [121] A. Cervone, G. Brando, O. Dordevic, A. D. Pizzo, and S. Meo, ‘An Adaptive Multistep Balancing Modulation Technique for Multipoint-Clamped Converters’, *IEEE Trans. Ind. Appl.*, vol. 56, no. 1, pp. 465–476, Jan. 2020, doi: 10.1109/TIA.2019.2949980.
- [122] A. Cervone, M. Slunjski, E. Levi, and G. Brando, ‘Optimal Multi-Harmonic Current Injection Strategy for an Asymmetrical Nine-Phase PMSM’, in *2020 International Symposium on Power Electronics, Electrical Drives, Automation and Motion (SPEEDAM)*, Jun. 2020, pp. 787–792. doi: 10.1109/SPEEDAM48782.2020.9161890.
- [123] A. Cervone, M. Slunjski, E. Levi, and G. Brando, ‘Optimal Third-Harmonic Current Injection for an Asymmetrical Nine-phase PMSM with Non-Sinusoidal

- 
- back-EMF', in *IECON 2019 - 45th Annual Conference of the IEEE Industrial Electronics Society*, Oct. 2019, vol. 1, pp. 6223–6228. doi: 10.1109/IECON.2019.8927562.
- [124] A. Cervone, G. Brando, and O. Dordevic, 'A Hybrid Modulation Technique for the DC-Bus Voltage Balancing in a Three-Phase NPC Converter', in *IECON 2019 - 45th Annual Conference of the IEEE Industrial Electronics Society*, Oct. 2019, vol. 1, pp. 3312–3318. doi: 10.1109/IECON.2019.8927047.
- [125] G. Brando and A. Cervone, 'Novel Balancing Approach for Multilevel Diode Clamped Converters in Medium Voltage Hybrid STATCOM Application', in *IECON 2018 - 44th Annual Conference of the IEEE Industrial Electronics Society*, Oct. 2018, pp. 4473–4479. doi: 10.1109/IECON.2018.8592794.
- [126] G. Brando, A. Cervone, A. D. Pizzo, and S. Meo, 'An Adaptive Balancing Modulation for Multilevel Diode Clamped Converters without Common Mode Voltage Injection', in *2018 International Symposium on Power Electronics, Electrical Drives, Automation and Motion (SPEEDAM)*, Jun. 2018, pp. 678–684. doi: 10.1109/SPEEDAM.2018.8445262.
- [127] A. Fitzgerald, C. Kingsley, and S. Umans, *Electric Machinery*, 6° edizione. Boston, Mass: McGraw-Hill Education, 2002.
- [128] S. N. Vukosavic, *Electrical Machines*. New York: Springer-Verlag, 2013. doi: 10.1007/978-1-4614-0400-2.
- [129] H. A. Haus, J. R. Melcher, M. Zahn, and M. L. Silva, *Electromagnetic Fields and Energy*. Massachusetts Institute of Technology: MIT OpenCourseWare, 2008. [Online]. Available: <https://ocw.mit.edu/resources/res-6-001-electromagnetic-fields-and-energy-spring-2008/>
- [130] S. A. Gonzalez, S. A. Verne, and M. I. Valla, *Multilevel Converters for Industrial Applications*, 1° edizione. Boca Raton: CRC Press, 2013.
- [131] J. Rodriguez, Jih-Sheng Lai, and Fang Zheng Peng, 'Multilevel inverters: a survey of topologies, controls, and applications', *IEEE Trans. Ind. Electron.*, vol. 49, no. 4, pp. 724–738, Aug. 2002, doi: 10.1109/TIE.2002.801052.
- [132] Fang Zheng Peng, 'A generalized multilevel inverter topology with self voltage balancing', *IEEE Trans. Ind. Appl.*, vol. 37, no. 2, pp. 611–618, Mar. 2001, doi: 10.1109/28.913728.
- [133] A. Nabae, I. Takahashi, and H. Akagi, 'A New Neutral-Point-Clamped PWM Inverter', *IEEE Trans. Ind. Appl.*, vol. IA-17, no. 5, pp. 518–523, Sep. 1981, doi: 10.1109/TIA.1981.4503992.
- [134] E. Levi, 'Advances in Converter Control and Innovative Exploitation of Additional Degrees of Freedom for Multiphase Machines', *IEEE Trans. Ind. Electron.*, vol. 63, no. 1, pp. 433–448, Jan. 2016, doi: 10.1109/TIE.2015.2434999.
- [135] N. Bodo, 'PWM strategies for open-end winding multiphase drives', Ph.D. Thesis, Liverpool John Moores University, 2013.
- [136] E. Levi, N. Bodo, O. Dordevic, and M. Jones, 'Recent advances in power electronic converter control for multiphase drive systems', in *2013 IEEE Workshop on Electrical Machines Design, Control and Diagnosis (WEMDCD)*, Mar. 2013, pp. 158–167. doi: 10.1109/WEMDCD.2013.6525176.
- [137] D. G. Holmes, 'The general relationship between regular-sampled pulse-width-

- modulation and space vector modulation for hard switched converters', in *Conference Record of the 1992 IEEE Industry Applications Society Annual Meeting*, Oct. 1992, pp. 1002–1009 vol.1. doi: 10.1109/IAS.1992.244437.
- [138] J. Rodriguez, S. Bernet, B. Wu, J. O. Pontt, and S. Kouro, 'Multilevel Voltage-Source-Converter Topologies for Industrial Medium-Voltage Drives', *IEEE Trans. Ind. Electron.*, vol. 54, no. 6, pp. 2930–2945, Dec. 2007, doi: 10.1109/TIE.2007.907044.
- [139] S. Kouro *et al.*, 'Recent Advances and Industrial Applications of Multilevel Converters', *IEEE Trans. Ind. Electron.*, vol. 57, no. 8, pp. 2553–2580, Aug. 2010, doi: 10.1109/TIE.2010.2049719.
- [140] B. P. McGrath and D. G. Holmes, 'Multicarrier PWM strategies for multilevel inverters', *IEEE Trans. Ind. Electron.*, vol. 49, no. 4, pp. 858–867, Aug. 2002, doi: 10.1109/TIE.2002.801073.
- [141] S. Kouro, P. Lezana, M. Angulo, and J. Rodriguez, 'Multicarrier PWM With DC-Link Ripple Feedforward Compensation for Multilevel Inverters', *IEEE Trans. Power Electron.*, vol. 23, no. 1, pp. 52–59, Jan. 2008, doi: 10.1109/TPEL.2007.911834.
- [142] N. Celanovic and D. Boroyevich, 'A comprehensive study of neutral-point voltage balancing problem in three-level neutral-point-clamped voltage source PWM inverters', *IEEE Trans. Power Electron.*, vol. 15, no. 2, pp. 242–249, Mar. 2000, doi: 10.1109/63.838096.
- [143] J. Pou, D. Boroyevich, and R. Pindado, 'Effects of imbalances and nonlinear loads on the voltage balance of a neutral-point-clamped inverter', *IEEE Trans. Power Electron.*, vol. 20, no. 1, pp. 123–131, Jan. 2005, doi: 10.1109/TPEL.2004.839823.
- [144] J. Pou, D. Boroyevich, and R. Pindado, 'Effects of imbalances and nonlinear loads on the voltage balance of a neutral-point-clamped inverter', in *IEEE 34th Annual Conference on Power Electronics Specialist, 2003. PESC '03.*, Jun. 2003, vol. 1, pp. 53–58 vol.1. doi: 10.1109/PESC.2003.1218273.
- [145] C. Newton and M. Sumner, 'Neutral point control for multi-level inverters: theory, design and operational limitations', in *IAS '97. Conference Record of the 1997 IEEE Industry Applications Conference Thirty-Second IAS Annual Meeting*, Oct. 1997, vol. 2, pp. 1336–1343 vol.2. doi: 10.1109/IAS.1997.629031.
- [146] C. Wang and Y. Li, 'Analysis and Calculation of Zero-Sequence Voltage Considering Neutral-Point Potential Balancing in Three-Level NPC Converters', *IEEE Trans. Ind. Electron.*, vol. 57, no. 7, pp. 2262–2271, Jul. 2010, doi: 10.1109/TIE.2009.2024093.
- [147] J. Lee, S. Yoo, and K. Lee, 'Novel Discontinuous PWM Method of a Three-Level Inverter for Neutral-Point Voltage Ripple Reduction', *IEEE Trans. Ind. Electron.*, vol. 63, no. 6, pp. 3344–3354, Jun. 2016, doi: 10.1109/TIE.2016.2530038.
- [148] J. Zaragoza, J. Pou, S. Ceballos, E. Robles, C. Jaen, and M. Corbalan, 'Voltage-Balance Compensator for a Carrier-Based Modulation in the Neutral-Point-Clamped Converter', *IEEE Trans. Ind. Electron.*, vol. 56, no. 2, pp. 305–314, Feb. 2009, doi: 10.1109/TIE.2008.2009195.
- [149] J. Pou *et al.*, 'Fast-Processing Modulation Strategy for the Neutral-Point-Clamped Converter With Total Elimination of Low-Frequency Voltage Oscillations in the

- 
- Neutral Point’, *IEEE Trans. Ind. Electron.*, vol. 54, no. 4, pp. 2288–2294, Aug. 2007, doi: 10.1109/TIE.2007.894788.
- [150] W. Jiang, X. Huang, J. Wang, J. Wang, and J. Li, ‘A Carrier-Based PWM Strategy Providing Neutral-Point Voltage Oscillation Elimination for Multi-Phase Neutral Point Clamped 3-Level Inverter’, *IEEE Access*, vol. 7, pp. 124066–124076, 2019, doi: 10.1109/ACCESS.2019.2938623.
- [151] S. Busquets-Monge, R. Griñó, J. Nicolas-Apruzzese, and J. Bordonau, ‘Decoupled DC-Link Capacitor Voltage Control of DC–AC Multilevel Multileg Converters’, *IEEE Trans. Ind. Electron.*, vol. 63, no. 3, pp. 1344–1349, Mar. 2016, doi: 10.1109/TIE.2015.2495295.
- [152] M. Slunjski, O. Dordevic, M. Jones, and E. Levi, ‘Symmetrical/Asymmetrical Winding Reconfiguration in Multiphase Machines’, *IEEE Access*, vol. 8, pp. 12835–12844, 2020, doi: 10.1109/ACCESS.2020.2965652.
- [153] A. Tassarolo, ‘On the modeling of poly-phase electric machines through Vector-Space Decomposition: Numeric application cases’, in *2009 International Conference on Power Engineering, Energy and Electrical Drives*, Mar. 2009, pp. 524–528. doi: 10.1109/POWERENG.2009.4915235.
- [154] G. Grandi, G. Serra, and A. Tani, ‘General Analysis of Multi-Phase Systems Based on Space Vector Approach’, in *2006 12th International Power Electronics and Motion Control Conference*, Aug. 2006, pp. 834–840. doi: 10.1109/EPEPEMC.2006.4778503.
- [155] M. Slunjski, M. Jones, and E. Levi, ‘Analysis of a Symmetrical Nine-phase Machine with Highly Non-Sinusoidal Back-Electromotive Force’, in *IECON 2018 - 44th Annual Conference of the IEEE Industrial Electronics Society*, Oct. 2018, pp. 6229–6234. doi: 10.1109/IECON.2018.8591091.
- [156] M. Slunjski, M. Jones, and E. Levi, ‘Control of a Symmetrical Nine-phase PMSM with Highly Non-Sinusoidal Back-Electromotive Force Using Third harmonic Current Injection’, in *IECON 2019 - 45th Annual Conference of the IEEE Industrial Electronics Society*, Oct. 2019, vol. 1, pp. 969–974. doi: 10.1109/IECON.2019.8927642.
- [157] M. Slunjski, O. Stiscia, M. Jones, and E. Levi, ‘General Torque Enhancement Approach for a Nine-Phase Surface PMSM with Built-in Fault Tolerance’, *IEEE Trans. Ind. Electron.*, pp. 1–1, 2020, doi: 10.1109/TIE.2020.3007053.
- [158] A. G. Yepes, F. D. Freijedo, Ó. Lopez, and J. Doval-Gandoy, ‘High-Performance Digital Resonant Controllers Implemented With Two Integrators’, *IEEE Trans. Power Electron.*, vol. 26, no. 2, pp. 563–576, Feb. 2011, doi: 10.1109/TPEL.2010.2066290.
- [159] C. Lascu, L. Asiminoaei, I. Boldea, and F. Blaabjerg, ‘High Performance Current Controller for Selective Harmonic Compensation in Active Power Filters’, *IEEE Trans. Power Electron.*, vol. 22, no. 5, pp. 1826–1835, Sep. 2007, doi: 10.1109/TPEL.2007.904060.
- [160] A. G. Yepes, ‘Digital Resonant Current Controllers for Voltage Source Converters’, Ph.D. Thesis, University of Vigo, 2011.
- [161] A. G. Yepes, F. D. Freijedo, J. Doval-Gandoy, Ó. López, J. Malvar, and P. Fernandez-Comesaña, ‘Effects of Discretization Methods on the Performance of

- 
- Resonant Controllers', *IEEE Trans. Power Electron.*, vol. 25, no. 7, pp. 1692–1712, Jul. 2010, doi: 10.1109/TPEL.2010.2041256.
- [162] P. Bolzern, R. Scattolini, and N. Schiavoni, *Fondamenti di controlli automatici*, 4° edizione. Milano: McGraw-Hill Education, 2015.
- [163] H. A. Toliyat, L. Xu, and T. A. Lipo, 'A five-phase reluctance motor with high specific torque', *IEEE Trans. Ind. Appl.*, vol. 28, no. 3, pp. 659–667, May 1992, doi: 10.1109/28.137454.
- [164] H. A. Toliyat, S. P. Waikar, and T. A. Lipo, 'Analysis and simulation of five-phase synchronous reluctance machines including third harmonic of airgap MMF', *IEEE Trans. Ind. Appl.*, vol. 34, no. 2, pp. 332–339, Mar. 1998, doi: 10.1109/28.663476.
- [165] Longya Xu, 'Rotor structure selections of nonsine five-phase synchronous reluctance machines for improved torque capability', *IEEE Trans. Ind. Appl.*, vol. 36, no. 4, pp. 1111–1117, Jul. 2000, doi: 10.1109/28.855967.
- [166] L. O. Chua, C. A. Desoer, and E. S. Kuh, *Linear and Non-Linear Circuits*. New York: McGraw-Hill College, 1987.
- [167] M. De Magistris and G. Miano, *Circuiti: Fondamenti di circuiti per l'Ingegneria*. Springer Science & Business Media, 2007.
- [168] L. O. Chua and P.-M. Lin, *Computer-Aided Analysis of Electronic Circuits: Algorithms and Computational Techniques*. Englewood Cliffs, N.J: Prentice Hall, 1975.

# Acknowledgments

The conclusion of this Ph.D. course represents the end of a long journey and, at the same time, the starting point for my future. These years have not been easy, but all the experiences I made, both professionally and personally, have contributed to my personal growth, and have sensibly changed me.

Naturally, this journey would not have been possible without all the people I have met during this period, to which I express my most sincere gratitude.

First, I would like to thank my advisor, *Prof. Gianluca Brando*. His help and support have always been fundamental during these years. He taught me to approach the research by investigating any problem under many perspectives, and not to hesitate to explore different point of views. I know that I can always count on him.

I also express my sincere gratitude to *Dr. Obrad Dordevic*. Just saying that he has been a true friend and that he has immensely helped me, would be a huge understatement. He is a person with great competence, teaching skills and patience, and none of this work would have been possible without him.

I would also like to thank all the other members of the Department of Electrical Engineering and Information Technology of the University of Naples Federico II, who have been like a second family to me.

I sincerely thank *Prof. Andrea Del Pizzo*, *Prof. Renato Rizzo*, *Prof. Santolo Meo* and *Prof. Ciro Attaianese* for their immense knowledge and helpful teachings, and *Prof. Adolfo Dannier*, *Prof. Diego Iannuzzi* and *Dr. Marino Coppola* for their great experience.

A special credit goes to *Dr. Luigi Pio Di Noia* and *Dr. Ivan Spina*. Their enthusiasm and motivation continuously inspire me to become a better researcher.

I would also like to thank the other Ph.D. student of the department, *Pasquale Franzese*, *Emanuele Fedele*, *Nicola Isernia* and *Antonio Di Pasquale*, who have shared this journey with me.

My deep gratitude also goes the other wonderful people I met during my stay at the Liverpool John Moores University, and especially to *Prof. Emil Levi*, who has been an inspirational model for me, and to *Dr. Marko Slunjski* and *Ornella Stiscia*, whose friendship greatly contributed to enjoy my period abroad.

Finally, a huge thank you is to be given to *my parents*, for their love and support during these years.